

Copyright
by
Michael Rasch
2012

**The Dissertation Committee for Michael Rasch Certifies that this is the approved
version of the following dissertation:**

**Assembly of Colloidal Nanocrystals into Phospholipid Structures and
Photothermal Materials**

Committee:

Brian A. Korgel, Supervisor

Thomas Truskett

Charles B. Mullins

Katherine Willets

Jennifer Maynard

**Assembly of Colloidal Nanocrystals into Phospholipid Structures and
Photothermal Materials**

by

Michael Rasch, B.Ch.E.; M.S.E.

Dissertation

Presented to the Faculty of the Graduate School of
The University of Texas at Austin
in Partial Fulfillment
of the Requirements
for the Degree of

Doctor of Philosophy

**The University of Texas at Austin
August, 2012**

Dedication

Dedicated to my wife and family.

Acknowledgements

I am grateful to a number of people for enabling me to reach this point in my career. First, my graduate advisor Dr. Brian Korgel, who provided me with a wealth of opportunities and support to pursue my research interests, develop research skills, and collaborate with other scientists and institutions. Second, I grateful to my committee members for their support, and the entire staff of the Department of Chemical Engineering and the Center for Nanotechnology and Molecular Science for keeping the departments organized and functioning. Next, I would like to thank Dr. Jordi Arbiol and his colleagues for hosting me at the University of Barcelona in Spain, which was a wonderful experience and I could not have progressed without his laboratory's assistance with cryo electron microscopy imaging. Furthermore, I am grateful to the Texas A&M Microscopy and Imaging Center for maintaining exceptional microscopy facilities, and I am particularly indebted to Dr. Zhiping Luo, whose patience and vast knowledge enabled me to become highly experienced and competent with cryo electron microscopy.

I am thankful to the many researchers who I was able to work with during my doctorate degree. The University of Texas scientists Dr. Dwight Romanovicz, Dr. Angela Bardo, Dr. JiPing Zhou, and Dr. Nate Miller were all helpful in enabling me to develop new research skills. Several past Korgel Lab members were helpful to me in establishing a productive research environment and enabling my progress including Doh C. Lee, Damon Smith, Dayne Fanfair, Danielle K. Smith, Hsing-Yu Tuan, Reken Patel, Bonil Koo, Andrew T. Heitsch, Aaron Chockla, Angela Holmberg, Jose L. Hueso, Yannika Marrs, and Kate Collier. Special gratitude is extended to Vahid Akhavan, Vince Holmberg, Matthew Panthani, and Brian Goodfellow for always being open to frequent discussions about current research and lab issues. I am grateful to the current Korgel lab

members who have been helpful, including Yixuan Yu, Christian Bosoy, Colin Hessel, Jackson Stolle, Taylor Harvey, Kate Shipman, Tim Bogart, Justin Harris, Chet Steinhagen, and Xiotang Yu, and Julian Villarreal. I am also grateful to Dr. Maynard's past and current students Jamie Sutherland, Tarik Khan, Jen Pai, and Ben Roy for teaching me about cell culture techniques. Finally, my wife and parents deserve much appreciation for their interest and support of my goals.

Assembly of Colloidal Nanocrystals into Phospholipid Structures and Photothermal Materials

Michael Rasch, Ph.D.

The University of Texas at Austin, 2012

Supervisor: Brian A. Korgel

There has been growing interest in developing colloidal metal and semiconductor nanocrystals as biomedical imaging contrast agents and therapeutics, since light excitation can cause the nanocrystals to fluoresce or heat up. Recent advances in synthetic chemistry produced fluorescent 2-4 nm diameter silicon and 1-2 nm diameter CuInSSe nanocrystals, as well as 16 nm diameter copper selenide (Cu_{2-x}Se) nanocrystals exhibiting strong absorbance of near infrared light suitable for biomedical applications. However, the syntheses yield nanocrystals that are stabilized by an adsorbed layer of hydrocarbons, making the nanocrystals hydrophobic and non-dispersible in aqueous solution. Encapsulating these nanocrystals in amphiphilic polymer micelles enables the nanocrystals to disperse in water. Subsequently, the Si nanocrystals were injected into tissue to demonstrate fluorescence imaging, the photothermal transduction efficiency of copper selenide nanocrystals was characterized in water, and the copper selenide nanocrystals were used to enhance the photothermal destruction of cancer cells *in vitro*. The polymer-encapsulated copper selenide nanocrystals were found to have higher photothermal transduction efficiency than 140 nm diameter Au nanoshells, which have been widely investigated for photothermal therapy.

Combining the optical properties of metal and semiconductor nanocrystals with the drug-carrying capability of lipid vesicles has received attention lately since it may create a nanomaterial capable of performing simultaneous drug delivery, optical contrast enhancement, and photo-induced therapy. Hydrophobic, dodecanethiol-coated Au nanocrystals were dispersed in water with phosphatidylcholine lipids and characterized using cryo transmission electron microscopy. 1.8 nm diameter Au nanocrystals completely load the bilayer of unsaturated lipid vesicles when the vesicles contain residual chloroform, and without chloroform the nanocrystals do not incorporate into the vesicle bilayer. 1.8 nm Au nanocrystals dispersed in water with saturated lipids to form lipid-coated nanocrystal agglomerates, which sometimes adhered to vesicles, and the shape of the agglomerates varied from linear nanocrystal chains, to flat sheets, to spherical clusters as the lipid fatty acid length was increased from 12 to 18 carbons. Including squalene formed lipid-stabilized emulsion droplets which were fully loaded with the Au nanocrystals. Results with 4.1 nm Au and 2-3 nm diameter Si nanocrystals were similar, but these nanocrystals could not completely load the bilayers of unsaturated lipids.

Table of Contents

Table of Contents	ix
List of Figures	xv
Chapter 1: Introduction	1
1.1: Nanocrystal Specifications for Biomedical Applications	1
1.2: Plasmonic Nanocrystals for Photothermal Therapy	7
1.3: Fluorescent Nanocrystals for Imaging and Detection.....	10
1.4: Nanoparticle Vehicles for Drug Delivery and Encapsulation	13
1.5: Dissertation Overview	18
1.6: References.....	19
PHOTOTHERMAL NANOPARTICLES AND AMPHIPHILIC POLYMER COATING	24
Chapter 2: Limitations on the Optical Tunability of Small Diameter Gold Nanoshells	24
2.1: Introduction.....	24
2.2: Experimental Details	27
2.2.1: Chemicals.....	27
2.2.2: Silica-coated Iron Oxide Nanocrystal Synthesis	27
2.2.3: Microemulsion-assisted Synthesis of Silica Colloid Particles ..	30
2.2.4: Commercial Silica Preparation	31
2.2.5: Determining Silica Nanoparticle Concentration.....	32
2.2.6: Silica Surface Modification with 3-(aminopropyl)trimethoxysilane	32
2.2.7: Au Nanocrystal Seed Formation.....	33
2.2.8: Au Nanoshell Formation.....	34
2.2.9: Ionic Strength Calculation of the Gold Hydroxide Solution	37
2.2.10: Materials Characterization.....	39
2.3: Results and Discussion	39
2.3.1: Au Nanoshell Formation and Morphology	39
2.3.2: Au Nanoshell Optical Properties	43

2.3.3: Mie Theory Calculations of Au Nanoshell Optical Properties	48
2.3.4: Diluting the Nanoshell Growth Solution	51
2.3.5: Model for Size-Dependent Nanoshell Aggregation	53
2.4: Conclusions	62
2.5: References	63
Chapter 3: Copper Selenide Nanocrystals for Photothermal Therapy	68
3.1: Introduction	68
3.2: Experimental Details	69
3.2.1: Chemicals	69
3.2.2: Cu _{2-x} Se Nanocrystal Synthesis	70
3.2.3: Gold Nanoshell Synthesis	71
3.2.4: Gold Nanorod Synthesis	72
3.2.5: Commercial Gold Nanorods and Nanoshells	72
3.2.6: Amphiphilic Polymer Synthesis	73
3.2.7: Cu _{2-x} Se Nanocrystal Polymer Coating	73
3.2.8: Material Characterization	74
3.2.9: Photothermal Heating and Transduction Efficiency	78
3.2.10: <i>In Vitro</i> Cytotoxicity Studies	78
3.2.11: <i>In Vitro</i> Photothermal Therapy with Cu _{2-x} Se Nanocrystals	79
3.3: Results and Discussion	80
3.3.1: Cu _{2-x} Se Nanocrystal Characterization	80
3.3.2: Cu _{2-x} Se Nanocrystal Stability and Amphiphilic Polymer Coating	90
3.3.3: Gold Nanoshell and Nanorod Characterization	94
3.3.4: Photothermal Heating and Transduction Efficiency	95
3.3.5: Cu _{2-x} Se Nanocrystal Biocompatibility	103
3.3.6: Photothermal Therapy with Cu _{2-x} Se Nanocrystals	104
3.4: Conclusions	106
3.5: References	107

Chapter 4: Encapsulating Semiconductor Nanocrystals in Polymer Micelles.....	111
4.1: Introduction.....	111
4.2: Experimental Details	113
4.2.1: Chemicals.....	113
4.2.2: Amphiphilic Polymer Synthesis and Characterization	114
4.2.3: Dodecanethiol-coated CuInS _x Se _{2-x} Nanocrystal Synthesis	116
4.2.4: Dodecane-coated Si Nanocrystal Synthesis.....	117
4.2.5: Nanocrystal Characterization.....	118
4.2.6: Amphiphilic Polymer Coating	121
4.3: Results and Discussion	123
4.3.1: Amphiphilic Polymer Characterization	123
4.3.2: Nanocrystal Characterization.....	128
4.3.3: Nanocrystal Polymer Coating	133
4.3.4: Stability of Polymer Coated Nanocrystals	138
4.4: Conclusions.....	142
4.5: References.....	142
LOADING VESICLES AND EMULSION DROPLETS WITH NANOCRYSTALS.....	147
Chapter 5: Chloroform Enhances Incorporation of Hydrophobic Au Nanocrystals into Unsaturated Phosphatidylcholine Vesicles.....	147
5.1: Introduction.....	147
5.2: Experimental Details	150
5.2.1: Chemicals.....	150
5.2.2: Au Nanocrystal Synthesis.....	150
5.2.3: Vesicle Formation with Egg Phosphatidylcholine (eggPC) ...	153
5.2.4: Vesicle Formation with Dioleoylphosphatidylcholine (DOPC)	155
5.2.5: Light Microscopy.....	159
5.2.6: Centrifugal Separation	160
5.2.7: CryoTEM Imaging.....	160
5.2.8: Dynamic Light Scattering (DLS).....	161
5.2.9: NMR Spectroscopy.....	163

5.2.10: Lipid and Nanocrystal Monolayer Compression	164
5.3: Results and Discussion	165
5.3.1: Au Nanocrystal Characterization.....	165
5.3.2: EggPC Lipid and 1.8 nm Au Nanocrystals.....	169
5.3.3: Chloroform Solvent Vapor Annealing Improves Nanocrystal Incorporation into DOPC Vesicles	178
5.3.4: Optimum DOPC Concentration	191
5.3.5: Solvent Vapor Annealing of Nanocrystal/Lipid Films Under Various Conditions	192
5.3.6: Pressure-Area Isotherms of DOPC/Nanocrystal Langmuir Blodgett Films	199
5.4: Conclusions.....	201
5.5: References.....	202
Chapter 6 Au Nanocrystal Assembly with Saturated Lipids and Oil Droplets...	208
6.1: Introduction.....	208
6.2: Experimental Details	210
6.2.1: Chemicals.....	210
6.2.2: Au Nanocrystal Synthesis.....	210
6.2.3: Saturated Lipid Vesicle Formation	210
6.2.4: Squalene Emulsions.....	213
6.2.5: Material Characterization	213
6.3: Results and Discussion	213
6.3.1: Aggregates of Saturated Phosphatidylcholine and 1.8 nm Au Nanocrystals.....	213
6.3.2: Lipid-Squalene Oil Droplets with Au Nanocrystals	216
6.3.3: Buoyancy of 1.8 nm Au nanocrystal-loaded squalene/lipid droplets	222
6.3.4: Saturated Lipids, Oil Droplets, and 4.1 nm Au Nanocrystals..	226
6.4: Conclusions.....	230
6.5: References.....	232

Chapter 7 Octylglucoside-Assisted Loading of Au Nanocrystals in Phosphatidylcholine Vesicles	235
7.1: Introduction.....	235
7.2: Experimental Details	237
7.2.1: Chemicals.....	237
7.2.2: Au Nanocrystal Synthesis.....	237
7.2.3: Vesicle Formation.....	238
7.2.4: Au-loaded Detergent Micelles	238
7.2.5: Incorporation of Au Nanocrystals into Vesicles by Detergent Dialysis	240
7.2.6: Characterization	242
7.3: Results and Discussion	242
7.3.1: EggPC Vesicle Characterization and Detergent Titration	242
7.3.2: Au-loaded Detergent Micelles	246
7.3.3: Au Nanocrystal Incorporation into Vesicles at 8.5 mM EggPC Concentration (2100 Lipid Molecules per Nanocrystal)	250
7.3.4: Au Nanocrystal Incorporation into Vesicles at 25-75 mM EggPC Concentration (1250-3250 Lipid Molecules per Nanocrystal)	255
7.3.5: Nanocrystal Clustering Mechanism in Lipid Bilayers (Raft Formation).....	266
7.4: Conclusions.....	268
7.5: References.....	270
Chapter 8: Assembling Fluorescent Semiconductor Nanocrystals with Phosphatidylcholine and Squalene Droplets for Cell Labeling	272
8.1: Introduction.....	272
8.2: Experimental Details	274
8.2.1: Chemicals.....	274
8.2.2: Nanocrystal Synthesis.....	275
8.2.3: Nile Red Synthesis.....	276
8.2.4: Formation of Lipid Dispersions and Squalene Emulsions.....	278
8.2.5: Material Characterization	278
8.2.6: HL60 Cell Culture	279
8.2.7: Cell Labeling and Imaging	279

8.3: Results and Discussion	280
8.3.1: Nile Red Dye Synthesis	280
8.3.2: CdSe Nanocrystal Synthesis	283
8.3.3: Vesicles and Emulsion Particles Loaded with Nile Red Dye	285
8.3.4: Vesicles and Emulsion Particles Loaded with CdSe	285
8.3.5: Vesicles and Emulsion Particles Loaded with CIS Nanocrystals	292
8.3.6: Vesicles and Emulsion Particles Loaded with Si.....	299
8.3.7: HL60 Cell Labeling with Fluorescent Lipid Aggregates and Emulsion Particles	311
8.4: Conclusions.....	317
8.5: References.....	319
Chapter 9: Conclusions and Future Work.....	323
9.1: Conclusions.....	323
9.1.1: Amphiphilic Polymer Coating.....	323
9.1.2: Au Nanoshells, Au Nanorods, and Cu _{2-x} Se Nanocrystals for Photothermal Therapy.....	324
9.1.3: Loading Hydrophobic Au Nanocrystals into Phospholipid Vesicles	325
9.1.4: Loading Hydrophobic Semiconductor Nanocrystals into Phospholipid Vesicles.....	327
9.2: Future Work.....	323
9.2.1: Polymer-coated Nanocrystals and Photothermal Therapy.....	330
9.2.2: Nanocrystal-loaded Vesicles.....	331
9.3: References.....	334
Appendix.....	336
Bibliography	348
Vita	384

List of Figures

Figure 1.1:	The relative size of nanocrystals in biology.	2
Figure 1.2:	Summary of nanocrystal surface stabilization.	7
Figure 1.3:	Illustration of plasmon generation in a spherical metal nanocrystal.....	8
Figure 1.4:	Illustration of Au nanorods and nanoshells.	9
Figure 1.5:	Simple energy band diagrams to illustrate the valence and conduction bands of metals and semiconductors.....	12
Figure 1.6:	Structure of surfactant aggregates versus the molecular shape.	15
Figure 2.1:	TEM image of iron oxide nanocrystals.....	29
Figure 2.2:	TEM image of Au nanocrystal seeds	34
Figure 2.3:	Photograph of aqueous dispersions of Au nanoshells grown on 118 nm diameter silica spheres.	36
Figure 2.4:	Photograph of aqueous dispersions of Au nanoshells grown on 38 nm diameter silica spheres.	36
Figure 2.5:	TEM images of silica particles with varying size coated with Au nanoshells.....	41
Figure 2.6:	Illustration of Au nanoshell deposition on a silica particle or silica-coated iron oxide particle.....	42
Figure 2.7:	Measured absorbance spectra of silica spheres coated with varying Au shell thickness.	47
Figure 2.8:	Absorbance spectra for 118 nm core diameter nanoshells, measured experimentally and calculated from Mie theory.	49
Figure 2.9:	Absorbance spectra for 38 nm core diameter nanoshells, measured experimentally and calculated from Mie theory	50

Figure 2.10: Mie theory calculations for absorbance spectra of 74 nm core diameter nanoshells with different core/shell ratios	50
Figure 2.11: Absorbance spectra of Au nanoshells grown on 118 nm diameter silica cores. The volume of the Au shell growth solution was diluted by a factor of 2 or 8.....	52
Figure 2.12: Dilution of small diameter nanoshells (28 nm silica core) during Au shell growth.....	53
Figure 2.13: Model geometry of silica particles covered by a sheath layer of Au nanocrystals that was used to determine the pair inter-particle potentials	54
Figure 2.14: Calculated pair inter-particle potential, van der Waals attraction, and electrostatic double-layer repulsion for silica core diameters noted in the legend. Calculations were performed for silica spheres coated with APTS at pH of 3.....	61
Figure 2.15: Calculated pair inter-particle potential, van der Waals attraction, and electrostatic double-layer repulsion for silica core diameters noted in the legend. Calculations were performed for silica spheres decorated with 3 nm Au nanocrystals (30% coverage) at pH of 7	62
Figure 3.1: Synthesis scheme and TEM images of Cu _{2-x} Se nanocrystals	81
Figure 3.2: X-ray diffraction patterns for Cu _{2-x} Se nanocrystals synthesized using different reaction times, solvent purity, and temperature	82
Figure 3.3: TGA of Cu _{2-x} Se nanocrystals and pure oleylamine	85
Figure 3.4: Room temperature UV-vis-NIR absorbance spectra for Cu _{2-x} Se nanocrystals in toluene at various solution concentrations to determine the Cu _{2-x} Se nanocrystal extinction coefficient.....	87

Figure 3.5: Plots of linear fits to sets of absorbance versus concentration data at three different wavelengths for Cu _{2-x} Se nanocrystal dispersions in toluene.....	87
Figure 3.6: Absorbance and molar extinction coefficient for Cu _{2-x} Se nanocrystals plotted against wavelength.....	89
Figure 3.7: Amphiphilic polymer encapsulation of Cu _{2-x} Se nanocrystals	92
Figure 3.8: Low resolution TEM at 25°C of amphiphilic polymer-coated Cu _{2-x} Se nanocrystals dried from water onto a TEM grid.....	93
Figure 3.9: Absorbance of Cu _{2-x} Se nanocrystal dispersions over time	94
Figure 3.10: TEM images of Au nanoshells and nanorods	95
Figure 3.11: (A) Absorbance spectra of polymer-coated Cu _{2-x} Se nanocrystals, Au nanoshells, and Au nanorods. (B) The photothermal response of the dispersions in (A) obtained by irradiating 300 µL aliquots of each solution for 5 minutes with a 800 nm diode laser	97
Figure 3.12: (A) Steady-state heating data for Au nanoshells, Au nanorods, and Cu _{2-x} Se nanocrystals. (B) Plot for the photothermal transduction efficiencies obtained for the Cu _{2-x} Se nanocrystals, Au nanorods, and Au nanoshells	98
Figure 3.13: Bright field optical microscopy images of human colorectal cancer cells incubated with 39 mg/L polymer coated Cu _{2-x} Se nanocrystals in PBS.	104
Figure 3.14: Comparison of photothermal destruction of human colorectal cancer cells without and with the addition of 2.8×10^{15} Cu _{2-x} Se nanocrystals per liter	106
Figure 4.1: Reaction scheme for the synthesis of the amphiphilic polymer	115

Figure 4.2: Illustration of Si nanocrystal formation	118
Figure 4.3: Schematic illustration of hydrophobic nanocrystals, dispersing in aqueous buffer solution with an amphiphilic polymer coating.....	122
Figure 4.4: ^1H NMR characterization of the amphiphilic polymer dissolved in CDCl_3	124
Figure 4.5: ATR-FTIR characterization of the amphiphilic polymer, compared to reference FTIR spectra of succinic acid, succinic anhydride, and N-Butyl propionamide.	125
Figure 4.6: MALDI mass spectrometry analysis of the amphiphilic polymer ..	128
Figure 4.7: SAXS characterization of Si nanocrystals dispersed in toluene	129
Figure 4.8: Spectra for Si nanocrystal absorbance, photoluminescence emission, and photoluminescence excitation	131
Figure 4.9: TEM characterization of CIS nanocrystals	132
Figure 4.10: Spectra for CIS nanocrystal absorbance, photoluminescence emission, and photoluminescence excitation	133
Figure 4.11: Florescence of polymer-coated Si.....	135
Figure 4.12: CryoTEM imaging of polymer micelles made with Si.....	136
Figure 4.13: Grey-scale CCD images of biological tissue injected with polymer-coated Si nanocrystals.....	137
Figure 4.14: Polymer-coated CIS absorbance, photoluminescence emission, and photoluminescence excitation	138
Figure 4.15: Effect of ionic strength on the photoluminescence intensity and absorbance of aphiphilic polymer-coated Si nanocrystals.....	139
Figure 4.16: Effect of varying pH on the photoluminescence intensity and absorbance of amphiphilic polymer-coated Si nanocrystals.....	140

Figure 4.17: Confocal fluorescence microscope image of polymer-coated CIS nanocrystals flocculated with 50 mM CaCl ₂	141
Figure 4.18: Amphiphilic polymer coated Si nanocrystals. (Top): Flocculation induced by HCl. (Bottom): Mixing Si nanocrystals with BSA does not result in Si flocculation.	142
Figure 5.1: Structure of the predominant lipid in eggPC, containing 1 saturated 16 carbon fatty acid and 1 mono-unsaturated 18 carbon fatty acid	154
Figure 5.2: Illustration of DOPC lipid and gold (Au) nanocrystals used for vesicle formation.....	156
Figure 5.3: Sketch of solvent vapor annealing apparatuses	158
Figure 5.4: TEM and SAXS characterization of Au nanocrystals used in these studies	167
Figure 5.5: Optical absorbance spectra of the Au nanocrystals used in these studies	168
Figure 5.6: TGA of Au nanocrystals, dodecanethiol, and hexadecanethiol	168
Figure 5.7: Photograph of aqueous dispersions of pure eggPC vesicles prepared by extrusion, and eggPC vesicles prepared by co-extrusion with Au nanocrystals (1500 lipid molecules per nanocrystal).....	170
Figure 5.8: CryoTEM images of eggPC vesicles prepared by extrusion in the (A) absence and (B-G) presence of Au nanocrystals	171
Figure 5.9: TEM images of Au nanocrystals and eggPC lipids dried onto a carbon- coated Ni grid at room temperature	173
Figure 5.10: Dispersion of eggPC and 1.8 nm diameter Au nanocrystals. Prior to hydration and vesicle formation, the eggPC and nanocrystal film was dried for over 12 hours to remove trace amounts of chloroform	176

Figure 5.11: Dispersions of eggPC and 1.8 nm diameter Au nanocrystals. Prior to hydration and vesicle formation, the eggPC and Au nanocrystal film was only dried for 15 minutes.....	177
Figure 5.12: Light microscopy images of dried DOPC lipid/Au nanocrystal films..	179
Figure 5.13: CryoTEM images of DOPC vesicles prepared in the presence of alkanethiol-coated 1.8 nm diameter Au nanocrystals	180
Figure 5.14: Separation of Au nanocrystal-loaded DOPC vesicles from nanocrystal-free vesicles.....	182
Figure 5.15: CryoTEM imaging of DOPC vesicles prepared with dodecanethiol-coated 4.1 nm diameter Au nanocrystals	184
Figure 5.16: Illustration of pathways to vesicle formation and nanocrystal incorporation that depend on solvent vapor annealing and nanocrystal size	185
Figure 5.17: Dynamic light scattering (DLS) of DOPC lipid/nanocrystal dispersions	187
Figure 5.18: ^{31}P and ^1H NMR characterization of DOPC dispersions prepared in D_2O with and without dodecanethiol-coated 1.8 nm Au nanoparticles..	190
Figure 5.19: Dispersions of DOPC and 1.8 nm Au nanocrystals prepared in DI water after chloroform annealing, with varying lipid concentration	192
Figure 5.20: Light microscopy analysis of varying drying conditions for films of DOPC and 1.8 nm diameter Au nanocrystals drop cast on glass from a liquid chloroform dispersion.....	193

Figure 5.21: Light microscopy analysis showing that chloroform vapor annealed DOPC-nanocrystal films do not revert to their initial, microphase-separated structure when placed under vacuum after annealing.....	195
Figure 5.22: CryoTEM images of Au nanocrystal-loaded DOPC vesicles prepared by annealing with dichloromethane vapor instead of chloroform	196
Figure 5.23: Light microscopy analysis of dry films of DOPC and dodecanethiol-coated Au nanocrystals exposed to various solvent vapors	198
Figure 5.24: Compression of LB films of DOPC lipid and dodecanethiol-coated 1.8 nm Au nanocrystals at a water/air interface.....	200
Figure 6.1: Light microscopy images of saturated lipid and Au nanocrystal films prepared on cover glass by drying from chloroform dispersion at different temperatures	211
Figure 6.2: CryoTEM images of aggregated 1.8 nm diameter Au nanocrystals formed with various phosphatidylcholine lipids with saturated hydrocarbon chains	214
Figure 6.3: Vesicles prepared with only dilauroyl-phosphatidylcholine.....	216
Figure 6.4: CryoTEM images of dimyristoyl-phosphatidylcholine dispersed in water with squalene in the absence of Au nanocrystals.....	217
Figure 6.5: CryoTEM images of squalene/DMPC lipid droplets with dodecanethiol-coated Au nanocrystals	218
Figure 6.6: CryoTEM images of squalene emulsion droplets loaded with dodecanethiol-coated Au nanocrystals and stabilized with either DLPC or DPPC	219
Figure 6.7: Illustration of lipid/Au nanocrystal assemblies observed by cryoTEM	221

Figure 6.8: Settling velocities calculated for the different types of lipid particles observed by cryoTEM.....	223
Figure 6.9: CryoTEM images of aggregated 4.1 nm diameter Au nanocrystals formed with various phosphatidylcholine lipids with saturated hydrocarbon chains	228
Figure 6.10: CryoTEM images of squalene emulsion droplets loaded with dodecanethiol-coated 4.1 nm diameter Au nanocrystals stabilized with DPPC.....	229
Figure 6.11: CryoTEM images of triolein emulsion droplets loaded with dodecanethiol-coated 4.1 nm diameter Au nanocrystals stabilized with DPPC.....	230
Figure 7.1: Illustration of how detergents influence the structure of lipid molecule aggregates	236
Figure 7.2: CryoTEM images of pure, aqueous eggPC vesicles extruded through 50 nm diameter pores.....	243
Figure 7.3: DLS of extruded eggPC vesicles dispersed in deionized water at different concentrations	244
Figure 7.4: DLS characterization of titrating vesicles with OCG detergent	246
Figure 7.5: DLS of pure OCG micelles (no Au nanocrystals)	247
Figure 7.6: DLS of OCG-Au nanocrystal micelles prepared at different concentrations	248
Figure 7.7: ^1H NMR characterization of OCG detergent.....	249
Figure 7.8: Photographs of dialysis tubings loaded with OCG-stabilized Au nanocrystals.....	251

Figure 7.9: CryoTEM images of eggPC vesicles after dialysis with OCG-Au micelles. The eggPC concentration was 8.5 mM, the Au nanocrystal concentration was 4 μ M, and the initial OCG concentration was 20 mM	253
Figure 7.10: More cryoTEM iages of eggPC vesicles after dialysis with OCG-Au micelles. The eggPC concentration was 8.5 mM, the Au nanocrystal concentration was 4 μ M, and the initial OCG concentration was 20 mM	254
Figure 7.11: CryoTEM images of eggPC vesicles after dialysis with OCG-Au micelles. The eggPC concentration was 25 mM, the Au nanocrystal concentration was 20 μ M, and the initial OCG concentration was 150 mM	256
Figure 7.12: CryoTEM images of eggPC vesicles after dialysis with OCG-Au micelles. The eggPC concentration was 25 mM, the Au nanocrystal concentration was 20 μ M, and the initial OCG concentration was 250 μ M	259
Figure 7.13: CryoTEM images of eggPC vesicles after dialysis with OCG-Au micelles. The eggPC concentration was 75 mM, the Au nanocrystal concentration was 20 μ M, and the initial OCG concentration was 150 μ M	261
Figure 7.14: CryoTEM images of eggPC vesicles after dialysis with OCG-Au micelles. The eggPC concentration was 75 mM, the Au nanocrystal concentration was 20 μ M, and the initial OCG concentration was 250 μ M	263

Figure 7.15: CryoTEM of Au nanocrystal chains found outside of vesicles after dialysis of 75 mM eggPC vesicles and OCG-Au micelles (250 mM OCG initially).....	264
Figure 7.16: Schematic illustration of the encapsulation of OCG-Au nanocrystal micelles inside the egPC vesicles formed during detergent depletion, which beings with rupture vesicles.	265
Figure 7.17: Schematic illustration considering three hypothetical states in which hydrophobic Au nanocrystals could exist, without considering the presence of detergent	267
Figure 8.1: Schematic illustration of the synthesis of Nile Red dye by heating Nile Blue dye in sulfuric acid	277
Figure 8.2: Photoluminescence spectra and molar absorption coefficient of the Nile Red dye dissolved in chloroform	281
Figure 8.3: FTIR spectra of Nile Red and Nile Blue dyes	282
Figure 8.4: Photoluminescence and absorbance spectra of CdSe nanocrystals	284
Figure 8.5: TEM image of CdSe nanocrystals coated with TOPO and TDPA ligands	284
Figure 8.6: Photograph of a dispersion of vesicles loaded with Nile Red dye..	285
Figure 8.7: CdSe nanocrystals dispersed at 3 mg/mL concentration in aqueous lipid vesicles and emulsion particles	286
Figure 8.8: CryoTEM images of CdSe nanocrystals dispersed with DMPC lipid in water.....	288
Figure 8.9: CryoTEM images of CdSe nanocrystals dispersed with DPPC lipid in water.....	289

Figure 8.10: CryoTEM images of CdSe nanocrystals dispersed in water with DOPC lipid after annealing with chloroform vapor	290
Figure 8.11: CryoTEM images of CdSe nanocrystals incorporated into squalene emulsion droplets, stabilized by DPPC lipid	291
Figure 8.12: Photograph of dodecanethiol-coated CIS nanocrystals dispersed in aqueous vesicles and squalene emulsions at 4 mg/mL concentration ..	293
Figure 8.13: CryoTEM images of CIS nanocrystals loaded in squalene droplets, stabilized by DLPC lipid.....	294
Figure 8.14: CryoTEM images of CIS nanocrystals loaded in squalene droplets, stabilized by DMPC lipid.....	295
Figure 8.15: CryoTEM images of CIS nanocrystals dispersed with DSPC lipid and squalene (25°C).....	296
Figure 8.16: CryoTEM images of CIS nanocrystals dispersed with DSPC lipid and squalene (58°C).....	297
Figure 8.17: CryoTEM images of CIS nanocrystals dispersed with DOPC lipids after annealing a dry CIS/DOPC film with chloroform vapor.	298
Figure 8.18: Photograph of aqueous dispersions of Si nanocrystals and lipid.....	299
Figure 8.19: CryoTEM images of dodecane-coated Si nanocrystals dispersed in water with DOPC lipid after chloroform annealing.	300
Figure 8.20: CryoTEM images of dodecane-coated Si nanocrystals dispersed in water with DLPC lipid	302
Figure 8.21: CryoTEM of dodecane-coated Si nanocrystals dispersed in DPPC vesicles in water.....	303

Figure 8.22: CryoTEM of dodecane-coated Si nanocrystals dispersed in water with DSPC lipid	304
Figure 8.23: CryoTEM of Si nanocrystals coated with a 100:1 mixture of dodecane and undecanoic acid and dispersed in DPPC vesicles	305
Figure 8.24: CryoTEM of dodecane-coated Si nanocrystals dispersed in water with a 4:1 mixture of DPPC and DPPG lipids.....	306
Figure 8.25: CryoTEM of dodecane-coated Si nanocrystals dispersed in water with a 4:1 mixture of DPPC and eDMPC lipids.....	307
Figure 8.26: CryoTEM of dodecane-coated Si nanocrystals dispersed in water with DMPC lipid and 1% squalene by volume.....	309
Figure 8.27: CryoTEM of dodecane-coated Si nanocrystals dispersed in water with DPPC lipid and 5% squalene by volume	310
Figure 8.28: Live HL-60 cells imaged with confocal fluorescence microscopy.....	313
Figure 8.29: Confocal fluorescence microscopy images of live HL-60 cells mixed with Nile Red-loaded squalene droplets coated by a mixture of cationic and zwitterionic lipids.....	314
Figure 8.30: Confocal fluorescence microscopy of Nile Red-loaded squalene emulsion droplets coated by a mixture of cationic and zwitterionic lipids	315
Figure 8.31: Confocal fluorescence microscopy images of live HL-60 cells mixed with squalene droplets loaded with Si nanocrystals and coated by a mixture of cationic and zwitterionic lipids	316
Figure A.1: Experimental DLS data plotted for each dispersion, along with the fitted light scattering model overlaid on the measured data.	341

Figure A.2: Comparison of the least squares fit parameters (χ^2) of two different DLS models – a single exponential (one particle size) and a double exponential (two particle sizes) – fit to the experimental DLS data shown in Figure A.1.	342
Figure A.3: DLS data of DOPC and hexadecanethiol-coated 1.8 nm NPs dispersed in water immediately after chloroform annealing.	343
Figure A.4: DLS data of the DOPC and DOPC-Au nanocrystal samples prepared for NMR characterization.	344
Figure A.5: CryoTEM images of DLPC vesicles prepared with 1.8 nm Au nanocrystals and chloroform vapor annealing. The nanocrystals are primarily observed in lipid-coated chains, just as in the absence of chloroform annealing. However, a few Au-loaded vesicles were found in the sample as well (bottom row).	346

Chapter 1: Introduction

1.1 Nanocrystal Specifications for Biomedical Applications

The design, fabrication, and characterization of inorganic nanomaterials has been researched extensively during the past few decades because nanomaterials have interesting optical and electronic properties compared to bulk solids of the same elemental composition.¹⁻⁵ These properties combined with their small size make nanomaterials useful for applications in biomedical imaging and therapy.^{3,6,7} As illustrated in Figure 1.1, nanomaterials have spatial dimensions between 1 and 100 nm in length,⁸ making them suitable for binding to individual biological macromolecules,^{7,9} which have similar dimensions.¹⁰ Nanometer-sized inorganic crystals stabilized as colloids (nanocrystals) have been shown to enter cells,^{6,11} and many researchers have exploited the optical properties of nanocrystals to label disease markers on cells and within biological tissues.¹²⁻¹⁴

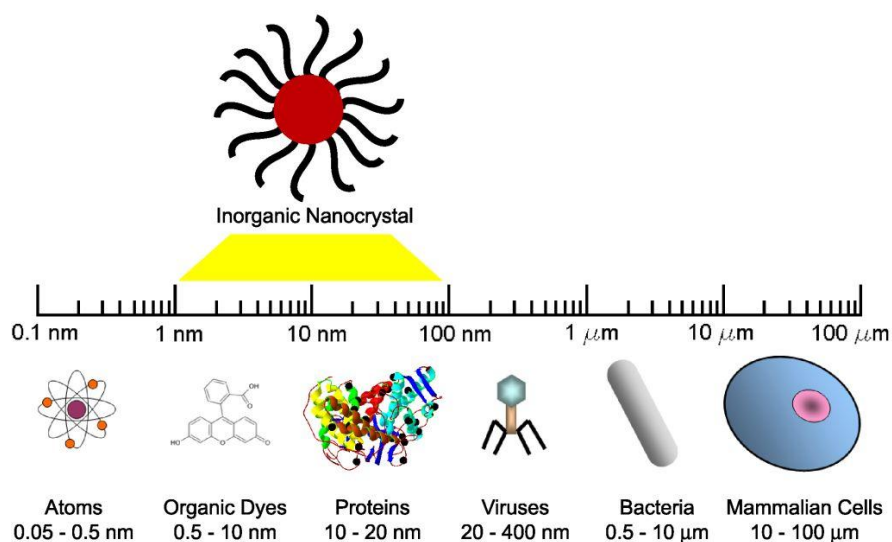


Figure 1.1. The relative size of nanocrystals in biology. The nanocrystal is drawn with a red core representing the inorganic atoms, and with black organic ligands coating the surface. Illustration adapted from the Life Technologies Corporation website and re-drawn.¹⁵

For biomedical imaging and labeling, nanocrystals must bind to a target and be detected by imaging equipment.⁸ To detect the nanocrystals during imaging, they must have some unique measurable property, such as enhanced absorbance or fluorescence relative to background signal.^{8,9} To use nanocrystals for therapy, the nanocrystals must include a detachable drug payload,¹⁶ or they must respond to a therapeutic stimulus, such as by heating in response to electromagnetic radiation.^{12,17} Some of the latest developments have focused on producing nanomaterials that can carry out multiple functions,^{4,18-20} such as simultaneously responding to multiple imaging techniques (e.g. MRI, light scattering, *and* fluorescence) while delivering therapy.^{16,21} Strategies for producing these complex multi-component nanomaterials require hybridizing distinct

material domains into a single nanometer-sized structure, and this has been accomplished by linking together separate nanocrystals with chemical bonds,²² encapsulating multiple types of nanocrystals in surfactant micelles,^{16,23,24} or growing nanometer-thick inorganic layers of different materials on top of a nanocrystal core (core/shell particles).^{4,18,22,25} Regardless of whether the nanomaterial is single- or multi-component, it must accumulate at the targeted site for effective imaging and site-specific therapy. Binding is controlled by designing the nanocrystal surface chemistry to ensure that the nanocrystal attaches to the biological target.^{11,17,26}

Controlling the nanocrystal surface chemistry is necessary for stabilizing nanocrystal colloids and directing their binding to specific sites.^{26,27} Nanocrystals are attracted to one another across a medium by van der Waals forces.²⁸ A repulsive force must exist between nanocrystals in a colloid to counterbalance the attractive force,²⁸ in order to prevent nanocrystal aggregation and precipitation as outlined in Figure 1.2. A repulsive force can be produced by either electrostatic or steric stabilization of the nanocrystal surface. Electrostatic stabilization requires that the nanocrystal surface be coated with an adsorbed electric double layer of ions, and nanocrystal aggregation is prevented by the osmotic pressure that builds up when the electric double layers of two nanocrystals start to overlap.²⁸ Water is an ideal medium for electrostatic stabilization, since it is a good solvent for the adsorbed ions. In low polarity organic solvents (e.g. octadecene), which are often used for nanocrystal synthesis at high temperatures (>100°C), electrostatic stabilization is complicated by the poor solubility of ions, and therefore steric stabilization using organic molecules is more effective. For steric

stabilization, small organic ligands such as fatty acids, alkyl amines, alkenes, or alkanethiols are bound to the nanocrystal by association of the ligand's functional group with the inorganic atoms on the nanocrystal surface. When two ligand-coated nanocrystals approach one another, a repulsive osmotic pressure builds up due to the unfavorable entropy of compressing the ligands and forces the nanocrystals apart.²⁸ Steric or electrostatic stabilization alone does not necessarily make the nanocrystals bind to a biological target such as a cell surface protein – usually the nanocrystal surface must be coated further with site-specific targeting molecules.^{6,13}

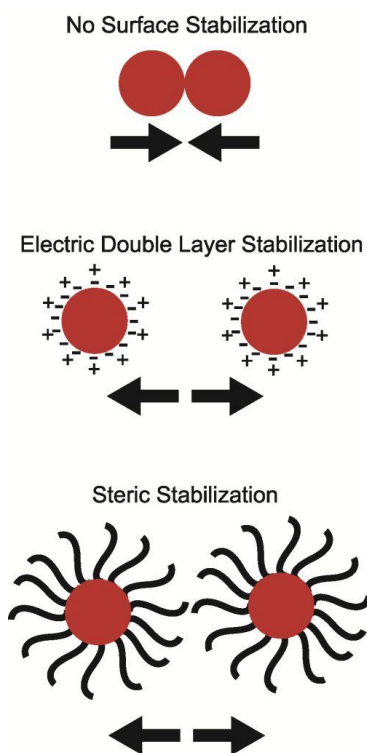


Figure 1.2. Summary of nanocrystal surface stabilization. The black arrows represent the direction of the net force per particle at an arbitrary distance greater than about 1 nm. Nanocrystals that have a bare surface of only inorganic atoms are attracted by van der Waals forces, and without any repulsive force the nanocrystals will collide and stick together, forming an aggregate. Nanocrystals stabilized by an electric double layer have an adsorbed layer of ions, while sterically stabilized nanocrystals are coated with organic ligands (black lines).

Nanocrystal surfaces stabilized by electrostatic or steric forces are conjugated to biological molecules (antibodies, peptides, nucleic acid aptamers, etc.)^{13,17,27,29} by three possible mechanisms – electrostatic adsorption, hydrophobic assembly, and covalent grafting. Electrostatic adsorption occurs when a nanocrystal and bio-macromolecule having opposite surface charges adhere to one another.³⁰ The electrostatic adsorption is

entropically favored, because when the two oppositely charged surfaces make contact, the numerous counterions on each surface (for example Na^+ adsorbed to an anionic surface) are released into solution and become fully solvated.^{31,32} Electrostatic adsorption has been used to link cell-targeting peptides to nanocrystals,³⁰ though this attachment is reversible and sensitive to pH and ionic strength.³² Hydrophobic assembly is used when the nanocrystal surface is coated with non-polar ligands,³³ such as linear alkanes. Surfactants such as phospholipids, detergents, and amphiphilic polymers can coat the hydrophobic nanocrystal surface to make the nanocrystal disperse in water, though the surfactants themselves usually do not have a molecular domain that binds to specific biological targets.³⁴⁻³⁶ Instead, the surfactant molecules may contain reactive functional groups (amine, carboxyl, etc.) that can be attached to targeting bio-molecules by covalent grafting.³⁷ Covalent grafting relies on cross-linking functional groups on bio-molecules to functional groups on the surface of nanocrystals.²⁷ For example, nanocrystals coated with carboxylic acids have been cross-linked to amine groups in the streptavidin protein after activation by a carbodiimide, producing a streptavidin-nanocrystal conjugate that can bind to biotin-labeled antibodies adhering to a cell surface.^{13,37} An important concern when attaching bio-molecules to nanocrystals is whether the bio-molecules lose their activity when bound to the surface.^{38,39} For example, antibody-nanocrystal conjugates must be capable of binding to the antibody's target in order to attain site-specific imaging and therapy.¹³

1.2 Plasmonic Nanocrystals for Photothermal Therapy

Inorganic nanocrystals are being considered for enhancing photothermal therapy.¹² Photothermal heating of nanocrystal dispersions occurs when the nanocrystals absorb light energy and convert the energy into heat, which dissipates to the surroundings.⁴⁰ When light strikes a nanocrystal, some photons are absorbed and some are scattered without absorption. In metal nanocrystals such as Au at room temperature, some of the energy levels in the conduction band are occupied by electrons, and the electromagnetic field from the absorbed light will cause the conduction band electrons to oscillate relative to the position of the atomic nuclei as illustrated in Figure 1.3.^{41,42} This collective oscillation of the conduction band electrons in a metal is called a plasmon, and the frequency of oscillation corresponds to a maximum in the nanocrystal's light absorbance spectrum at a particular wavelength where the light resonates with the plasmon.^{41,42} The oscillating electrons are scattered by the atomic nuclei in the nanocrystal, therefore the oscillations are damped and the energy lost due to damping is released as heat.^{41,43}

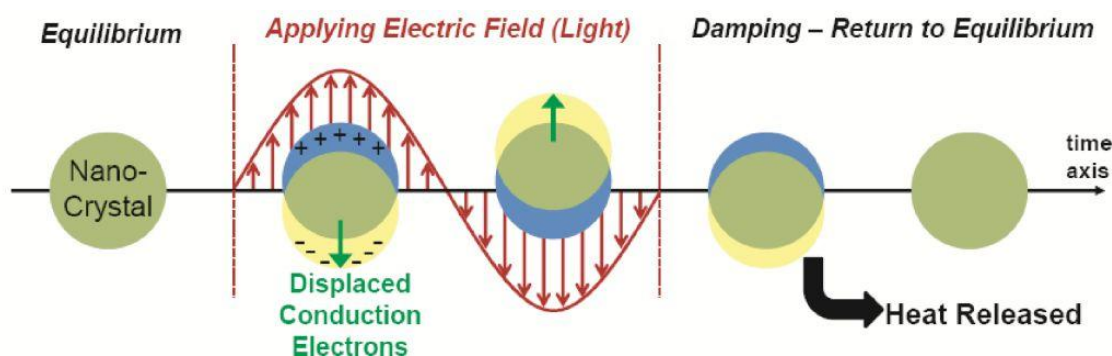


Figure 1.3. Illustration of plasmon generation in a spherical metal nanocrystal. The electrons occupying the conduction band energy levels are illustrated in yellow, while the atomic nuclei are blue. The plasmon is the collective oscillation of the conduction band electrons, and this is induced by light's oscillation electromagnetic field. The plasmon oscillation is damped within the metal nanocrystal, and the damping causes the absorbed light energy to be lost as heat to the surroundings. Illustration adapted from Kelly et al. and redrawn with modifications.⁴⁴

Both metal and doped semiconductor nanocrystals can exhibit a plasmon and have been investigated for photothermal therapy.^{21,45,46} Photothermal heating of Au metal nanocrystals has been widely studied,^{40,47} and some commonly used Au nanomaterials are illustrated in Figure 1.4. Au nanorods have a plasmon resonance wavelength that can be tuned from visible to near-infrared wavelengths, depending on the nanorod length,^{12,41} which is typically 60-80 nm. Au nanoshells consist of a nanometer-thick layer of Au deposited on the surface of a silicon dioxide sphere.⁴⁸ The nanoshells have a plasmon resonance wavelength that can be tuned throughout the visible to the near-infrared spectrum by controlling the thickness of the Au shell.⁴⁹⁻⁵¹ Most Au nanoshell syntheses reported in the literature produce nanoshell diameters of 120 nm or larger. In each of

these structures, the plasmon resonance is due to the collective oscillation of conduction band electrons in Au.

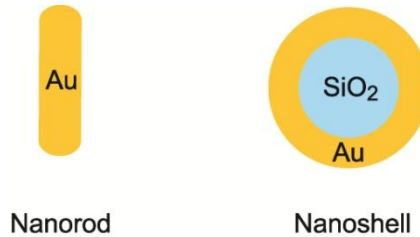


Figure 1.4. Illustration of Au nanorods and nanoshells. Au nanorods typically have an aspect ratio (length/width) of 2-5. Both Au nanoshells and nanorods are synthesized in aqueous solution from water-soluble HAuCl_4 . The nanoshells are stabilized by electric double layer forces after synthesis,⁵⁰ while nanorods are synthesized using the surfactant cetyltrimethylammonium bromide (not drawn) to provide steric stabilization.⁵²

In contrast to Au, a new type of nanomaterial that has emerged for photothermal therapy is the degenerately doped semiconductor. For example, 16 nm diameter nanocrystals made of Cu_{2-x}Se (where $x \sim 1.8$) contain a few Cu^{2+} nuclei substituted into a Cu_2Se crystal.⁴⁶ According to Talapin's work, a plasmon does not occur in Cu_2Se ;⁴⁶ it is a semiconductor, which has an energy barrier (band gap) separating valence band electrons from the conduction band where electrons have a higher mobility.⁵³ However, when the nanocrystal is doped with Cu^{2+} ions, these ions create vacancies in the valence band energy levels (holes) in the crystal structure that exhibit damped oscillations in an applied electromagnetic field just as do the conduction electrons in Au metal nanocrystals,⁴⁶ making photothermal heating possible.⁴⁵

The motivation for using these nanocrystals to improve photothermal therapy is to localize the nanocrystals to diseased tissue to achieve enhanced heating at the targeted

site under laser irradiation, while minimizing heating of adjacent healthy tissue that is not loaded with nanocrystals.⁴⁰ Therefore nanocrystals sensitize the targeted tissue to photothermal heating by providing improved absorption of laser light, which is important because often diseased and healthy tissues absorb the same amount of light in the absence of nanocrystals.⁵⁴ The heat released during photothermal heating with nanocrystals is intended to kill malignant cells by denaturing proteins essential to their survival.^{55,56} Heating above 40°C will cause cell damage, while heating above 45°C is necessary to kill cells *in vitro*.^{55,57} Solid tumors have been grown in nude mice, and it was shown that regular photothermal treatments over 10 days can cause the tumor to stop growing and fall off.⁵⁸ An important design criterion for *in vivo* applications of the photothermal nanoparticles is the overall nanoparticle size, since particle diameters between 5-100 nm are considered ideal for penetrating tissue while avoiding rapid renal clearance from circulation.^{50,59} This issue has prompted interest in developing smaller size Au nanoshells and the degenerately doped semiconductor nanocrystals for photothermal therapy.

1.3 Fluorescent Nanocrystals for Imaging and Detection

For biomedical imaging, semiconductor nanocrystals (quantum dots) have been widely investigated as fluorescent labels.^{6,14} Fluorescence from semiconductors occurs after light absorption excites valence electrons into the conduction band.⁵³ Unlike the electrons in metals that have no band gap separating valence electrons from the

conduction band, the electrons in semiconductors do have to overcome the band gap energy in order to enter the conduction band energy levels, as illustrated in Figure 1.5. When light strikes a semiconductor nanocrystal, if the photon energy exceeds the band gap energy then valence electrons will be promoted to the conduction band, thereby generating a (conduction band electron)-(valence band hole) pair called an exciton.⁵³ The exciton is analogous to the excited state in molecules. Within a few hundred picoseconds,⁶⁰ the electron-hole pair collide and recombine, releasing a photon of lower energy than the incident light as the electron returns to the valence band (ground state).⁵³ The band gap energy, and consequently the wavelength of emitted photons, depends on the elemental composition and the size of the nanocrystal, the latter being due to quantum confinement of the exciton to the physical dimensions of the crystal.^{13,61} Therefore, the color of fluorescent nanocrystals can be tuned by controlling the elemental composition and size through synthesis conditions.¹⁴

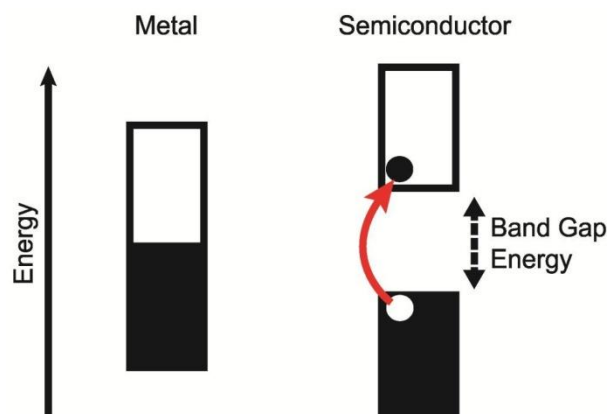


Figure 1.5. Simple energy band diagrams to illustrate the valence and conduction bands metals and semiconductors. Each band represents very closely spaced electron energy levels within the nanocrystal, essentially forming a continuum of possible states. The valence band is the black box, and it is filled with electrons. The conduction band is the open box, containing available energy levels for electrons. In metals, the amount of energy separating the conduction and valence bands is close to or equal to zero. In semiconductors, the valence and conduction bands are separated by the band gap energy. In semiconductors, valence band electrons can be excited with energy exceeding the band gap (like photoexcitation) and promoted to the conduction band. In contrast to bulk solids, nanocrystals contain a discrete number of atoms, and therefore discrete energy levels will be present at the band edges.⁶²

For fluorescence-based imaging applications, quantum dots can serve as alternatives to traditional small molecule organic dyes and fluorescent proteins. A thorough review of the tradeoffs between using quantum dots versus organic fluorophores was published recently.⁶³ Organic dye molecules are smaller than quantum dots and often more easily linked to biological targets. However, quantum dots exhibit more desirable optical properties than organic dyes such as improved brightness, better photostability, broad excitation spectra, and narrow, symmetric emission spectra.⁶³ The broad excitation

spectrum arises because quantum dots just need the light to have energy in excess of the band gap to generate an exciton, and it is beneficial because multiple colors of quantum dots often can be excited with light at a single wavelength, simplifying labeling experiments that use different colors to label distinct targets.⁶⁴

A key unresolved issue with quantum dots is their poorly characterized toxicity relative to the organic dyes. The most commonly studied quantum dot materials are the cadmium chalcogenides (S, Se, Te), and the high toxicity of cadmium metal raises global health concerns.⁶⁵ Literature sources on CdSe quantum dot toxicity often contradict one another though, likely because the toxicity can be influenced by numerous factors including quantum dot size, charge, concentration, surface coating, mechanical stability, and stability against oxidation that may differ from one batch of nanocrystals to the next.^{66,67} In spite of the fact that the reports are contradictory, many researchers have begun to investigate the application of cadmium-free semiconductor nanocrystals (Si, CuInSeS, ZnSe, etc.) for fluorescent labeling in biomedical imaging,⁶⁸ however progress so far has been marginal and warrants further study.

1.4 Nanoparticle Vehicles for Drug Delivery and Encapsulation

Drug molecules can be coupled to fluorescent or photothermal nanocrystals, providing drug-based therapy in addition to the functions of the nanocrystal.⁶⁹ This coupling can be accomplished by encapsulating the drug in a matrix such as a porous

solid,^{70,71} dendrimer,⁷² emulsion particle,^{16,73} micelle,^{74,75} or vesicle,^{76,77} and then fusing the encapsulant with the nanocrystal. Developing methods to fuse nanocrystals with such encapsulants is one focus of this dissertation, particularly using emulsion particles, micelles, and vesicles.

Micelles and vesicles form by the self-assembly of surfactant molecules in water, when the surfactant concentration exceeds the critical micelle concentration.²⁸ Common surfactants include detergents, amphiphilic polymers, and phospholipids, and these molecules are typically composed of a polar group covalently attached to one or more non-polar alkane chains. The surfactants self-assemble in water into aggregates in order to minimize the contact of the alkane chains with water while maximizing hydration of the polar groups.^{10,78} Consequently, the molecular shape of the amphiphiles dictates the whether they will form micelles, vesicles, or other structures.²⁸ The molecular shape is characterized by the packing factor, $P = V/(L \cdot A)$, where V is the volume of the surfactant molecule's hydrocarbon chains, L is the length of the hydrocarbon region, and A is the area that the polar head group occupies in the aggregate structure.²⁸ The relationship between packing factor and the structure of pure surfactant aggregates is summarized in Figure 1.6.



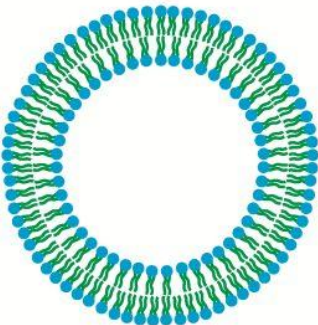
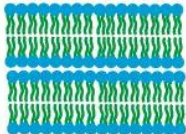
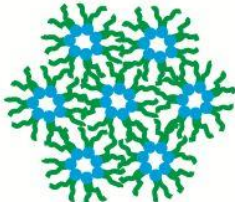
<u>Packing Factor, P</u>	<u>Aggregate Structure</u>	
0 - 1/3		Spherical Micelle
1/3 - 1/2		Cylindrical Micelle
1/2 - 1		Curved Bilayers, Vesicles
~1		Planar Bilayers
>1		Inverted Micelles

Figure 1.6. Structure of surfactant aggregates versus the molecular shape, quantified as the packing parameter $P = V/(L \cdot A)$. For example, surfactants with a large headgroup area A , short hydrocarbon chain length L and volume V , will pack into spherical micelles. Adapted from Israelachvili and redrawn, with modifications.²⁸

Among the different structures described in Figure 1.6, vesicles are interesting because they have both a hydrophobic and a hydrophilic compartment, corresponding to the lipid bilayer interior and the enclosed water cavity respectively. Therefore vesicles are attractive for drug delivery because they can encapsulate water soluble drugs and carry hydrophobic drugs, hydrophobic nanocrystals, or proteins in the bilayer as well. While several studies have featured the use of phospholipid vesicles to disperse nanocrystals,^{77,79-82} there have been no detailed studies that investigate how varying key parameters – such as nanocrystal size, bilayer thickness, bilayer fluidity, and the presence of additives – influence the incorporation of hydrophobic nanocrystals into vesicles. According to recent theoretical calculations, each of those parameters should contribute to the incorporation of hydrophobic nanocrystals into lipid bilayers.⁸³

Controlling the bilayer fluidity requires careful consideration of the lipid properties. The fluidity of the lipid bilayer depends on the length and unsaturation of the fatty acid chains, as well as temperature. The fatty acid chain length and unsaturation affect the temperature at which the chains transition from an ordered gel phase (L_β) to the disordered liquid crystalline phase (L_α).^{84,85} Lipid bilayers in the L_β phase are rigid, the viscosity is very high, and lipid diffusion is slow. Lipid bilayers in the L_α phase are flexible, with lower viscosity and faster lipid diffusion than the L_β phase.^{84,86} The lipid bilayer phase behavior is important to consider for processing vesicles – it is much easier to disperse lipids in water and form vesicles when the lipids are in the L_α phase.

Several methods are established for forming aqueous phospholipid vesicles. The first step involves dispersing dry lipids in water above the critical micelle concentration

(usually on the order of nanomolar for phospholipids). There is not a strong thermodynamic driving force for lipids to self-assemble into vesicles of a particular size, therefore mechanical shear forces (ultrasonication, extrusion) are used to fragment larger, micrometer-sized vesicles into smaller ones to obtain vesicles in the 50-200 nm diameter range.^{28,87} Alternatively, dry lipids can be dispersed in water using a micelle-forming detergent (octylglucoside, sodium cholate, Triton X-100, etc.). The lipids incorporate into the detergent micelles, and removal of the detergent by slow dialysis over 24-48 hours causes the lipid mole fraction in the micelles to increase over time until they aggregate into lipid vesicles.^{87,88} Careful control of the lipid:detergent molar ratio and dialysis rate can produce vesicles with low polydispersity in the 50-100 nm diameter range.⁸⁹ The dialysis technique is often used for incorporating detergent-solubilized membrane proteins into vesicles,^{90,91} however vesicle formation by mechanical agitation often can be completed much faster (a few minutes) and it avoids the possibility of residual detergent impurities being retained in the vesicles.

Stabilization of vesicle dispersions has similarities to stabilizing nanocrystal colloids, but there are some additional considerations. Vesicles with lipid bilayers in the L_α phase are not rigid like hard spheres; rather, they are somewhat elastic and can compress and deform before restoring to their average spherical shape. When two vesicles approach one another, the undulation of their lipid bilayers can induce hydrodynamic forces through the medium that repel the vesicles.²⁸ Even vesicles having a zwitterionic lipid bilayer and no steric stabilization can remain stably dispersed in solution due to these undulation forces between vesicles. Though if the lipids are cooled

to the L_{β} phase, zwitterionic vesicles without steric stabilization will tend to adhere to one another and eventually precipitate from solution.

Besides forming micelles and vesicles, phospholipid and detergent surfactants can stabilize emulsion particles in water for encapsulating hydrophobic drugs. Emulsion particles consist of a low polarity oil droplet coated by a monolayer of surfactant.⁷³ The oil typically has a very high oil/water partition coefficient and a very high interfacial tension with water (γ). Coalescence of oil droplets lowers the average Laplace pressure ($\Pi = 2\gamma/R$)⁹² by forming droplets with larger radii (R), so it is thermodynamically favorable for an emulsified oil phase to separate from water into a bulk liquid. Surfactants reduce the driving force for coalescence by lowering the interfacial tension of emulsion particles and providing steric or electrostatic barriers at the droplet surface, requiring a high activation barrier for droplet coalescence and thereby making the emulsion particles metastable.⁹² Metastable oil/water emulsions have been used to deliver hydrophobic drugs and vaccines to organisms in several studies,⁷³ and emulsion particles have hosted hydrophobic nanocrystals.¹⁶ However, detailed structural studies are lacking that investigate how hydrophobic nanocrystals associate with emulsion particles, and whether hydrophobic nanocrystals alter the emulsion particle structure.

1.5 Dissertation Overview

The synthesis of Au nanoshells of different sizes is presented in Chapter 2, showing that the synthesis chemistry places a limit on the minimum nanoshell size that can be

obtained. The synthesis and stabilization of Cu_{2-x}Se nanocrystals is presented in Chapter 3, along with photothermal heating studies comparing the heating efficiency of Au nanoshells, Au nanorods, and Cu_{2-x}Se nanocrystals.

Chapter 4 discusses the encapsulation of various semiconductor nanocrystals in an amphiphilic polymer coating. Chapters 5-7 are devoted to characterizing how Au nanocrystals incorporate into phospholipid vesicles and squalene emulsion droplets. Chapter 8 presents results on how semiconductor nanocrystals incorporate into vesicles and emulsions. Chapter 9 summarizes the main conclusions of this dissertation and makes some suggestions for future work.

1.6 References

- (1) Yin, Y.; Alivisatos, A. P. *Nature* 2005, *437*, 664-670.
- (2) Burda, C.; Chen, X.; Narayanan, R.; El-Sayed, M. A. *Chemical Reviews* 2005, *105*, 1025-1102.
- (3) Daniel, M.; Astruc, D. *Chemical Reviews* 2004, *104*, 293-346.
- (4) Chaudhuri, R. G.; Paria, S. *Chemical Reviews* 2012, *112*, 2373-2433.
- (5) Reiss, P.; Protiere, M.; Li, L. *Small* 2009, *5*, 154-168.
- (6) Smith, A. M.; Duan, H. W.; Mohs, A. M.; Nie, S. M. *Advanced Drug Delivery Reviews* 2008, *60*, 1226-1240.
- (7) Jain, P. K.; Huang, X. H.; El-Sayed, I. H.; El-Sayed, M. A. *Accounts of Chemical Research* 2008, *41*, 1578-1586.
- (8) Hurst, S. J. *Biomedical Nanotechnology Methods and Protocols*; Human Press: New York, 2011.
- (9) Gill, R.; Zayats, M.; Willner, I. *Angewandte Chemie-International Edition* 2008, *47*, 7602-7625.
- (10) Nelson, P. *Biological Physics: Energy, Information, Life*; W. H. Freeman and Company: New York, 2004.
- (11) Delehanty, J. B.; Mattoussi, H.; Medintz, I. L. *Analytical and Bioanalytical Chemistry* 2009, *393*, 1091-1105.
- (12) Huang, X.; El-Sayed, I. H.; Qian, W.; El-Sayed, M. A. *Journal of the American Chemical Society* 2006, *128*, 2115-2120.

- (13) Medintz, I. L.; Uyeda, H. T.; Goldman, E. R.; Mattoussi, H. *Nature Materials* 2005, 4, 435-446.
- (14) Michalet, X.; Pinaud, F. F.; Bentolila, L. A.; Tsay, J. M.; Doose, S.; Li, J. J.; Sundaresan, G.; Wu, A. M.; Gambhir, S. S.; Weiss, S. *Science* 2005, 307, 538-544.
- (15) Qdot Nanocrystals Technology Overview. Life Technologies Corporation. Accessed July 9, 2012.
<http://www.invitrogen.com/site/us/en/home/brands/Molecular-Probes/Key-Molecular-Probes-Products/Qdot/Technology-Overview.html#size>
- (16) Gianella, A.; Jarzyna, P. A.; Mani, V.; Ramachandran, S.; Calcagno, C.; Tang, J.; Kann, B.; Dijk, W. J. R.; Thijssen, V. L.; Griffioen, A. W.; Storm, G.; Fayad, Z. A.; Mulder, W. J. M. *ACS Nano* 2011, 5, 4422-4433.
- (17) El-Sayed, I. H.; Huang, X. H.; El-Sayed, M. A. *Cancer Letters* 2006, 239, 129-135.
- (18) Heitsch, A. T.; Smith, D. K.; Patel, R. N.; Ress, D.; Korgel, B. A. *Journal of Solid State Chemistry* 2008, 181, 1590-1599.
- (19) Yu, M. K.; Park, J.; Jon, S. *Theranostics* 2012, 2, 3-44.
- (20) Cheon, J.; Lee, J.-H. *Accounts of Chemical Research* 2008, 41, 1630-1640.
- (21) Park, J.-H.; von Maltzahn, G.; Ong, L. L.; Centrone, A.; Hatton, T. A.; Ruoslahti, E.; Bhatia, S. N.; Sailor, M. J. *Advanced Materials* 2010, 22, 880-885.
- (22) Lee, J. E.; Lee, N.; Kim, T.; Kim, J.; Hyeon, T. *Accounts of Chemical Research* 2011, 44, 893-902.
- (23) Park, J. H.; von Maltzahn, G.; Ruoslahti, E.; Bhatia, S. N.; Sailor, M. J. *Angewandte Chemie-International Edition* 2008, 47, 7284-7288.
- (24) Erogbogbo, F.; Ken-Tye, Y.; Hu, R.; Law, W.; Ding, H.; Chang, C.; Prasad, P. N.; Swihart, M. T. *ACS Nano* 2010, 4, 5131-5138.
- (25) Gao, J.; Gu, H.; Xu, B. *Accounts of Chemical Research* 2009, 42, 1097-1107.
- (26) Liu, R. H.; Kay, B. K.; Jiang, S. Y.; Chen, S. F. *Mrs Bulletin* 2009, 34, 432-440.
- (27) Erathodiyil, N.; Ying, J. Y. *Accounts of Chemical Research* 2011, 44, 925-935.
- (28) Israelachvili, J. N. *Intermolecular and Surface Forces*; 2nd ed.; Academic press Inc.: San Diego, 1992.
- (29) Chu, T. C.; Shieh, F.; Lavery, L. A.; Levy, M.; Richards-Kortum, R.; Korgel, B. A.; Ellington, A. D. *Biosensors & Bioelectronics* 2006, 21, 1859-1866.
- (30) Goldman, E. R.; Mattoussi, H.; Anderson, G. P.; Medintz, I. L.; Mauro, J. M. In *NanoBiotechnology Protocols*; Rosenthal, S. J., Wright, D. W., Eds.; Humana Press: Totowa, 2005, p 19.
- (31) Haugen, A.; May, S. *Journal of Chemical Physics* 2007, 127, -.
- (32) Sens, P.; Joanny, J.-F. *Physical Review Letters* 2000, 84, 4862-4865.
- (33) Rasch, M. R.; Rossinyol, E.; Hueso, J. L.; Goodfellow, B. W.; Arbiol, J.; Korgel, B. A. *Nano Letters* 2010, ASAP.

- (34) Hessel, C. M.; Rasch, M. R.; Hueso, J. L.; Goodfellow, B. W.; Akhavan, V.; Puvanakrishnan, P.; Tunnell, J. W.; Korgel, B. A. *Small* 2010, 6, 2026-2034.
- (35) Kairdolf, B. A.; Smith, A. M.; Nie, S. *Journal of the American Chemical Society* 2008, 130, 12866-+.
- (36) Erogbogbo, F.; Yong, K. T.; Roy, I.; Xu, G. X.; Prasad, P. N.; Swihart, M. T. *Acs Nano* 2008, 2, 873-878.
- (37) Wu, X. Y.; Liu, H. J.; Liu, J. Q.; Haley, K. N.; Treadway, J. A.; Larson, J. P.; Ge, N. F.; Peale, F.; Bruchez, M. P. *Nature Biotechnology* 2003, 21, 452-452.
- (38) Sapsford, K. E.; Spindel, S.; Jennings, T.; Tao, G.; Triulzi, R. C.; Algar, W. R.; Medintz, I. L. *Sensors* 2011, 11, 7879-7891.
- (39) Hermanson, G. T. *Bioconjugate Techniques*; Second ed.; Academic Press, Inc.: San Diego, 2008.
- (40) Huang, X. H.; Jain, P. K.; El-Sayed, I. H.; El-Sayed, M. A. *Lasers in Medical Science* 2008, 23, 217-228.
- (41) Link, S.; El-Sayed, M. A. *International Reviews in Physical Chemistry* 2000, 19, 409-453.
- (42) Garcia, M. A. *Journal of Physics D-Applied Physics* 2011, 44, 283001.
- (43) Alper, J.; Hamad-Schifferli, K. *Langmuir* 2010, 26, 3786-3789.
- (44) Kelly, K. L.; Coronado, E.; Zhao, L. L.; Schatz, G. C. *Journal of Physical Chemistry B* 2003, 107, 668-677.
- (45) Hessel, C. M.; Pattani, V. P.; Rasch, M. R.; Panthani, M. G.; Koo, B.; Tunnell, J. W.; Korgel, B. A. *Nano Letters* 2011, 11, 2560-2566.
- (46) Kriegel, I.; Jiang, C.; Rodriguez-Fernandez, J.; Schaller, R. D.; Talapin, D. V.; da Como, E.; Feldmann, J. *Journal of the American Chemical Society* 2012, 134, 1583-1590.
- (47) Hirsch, L. R.; Stafford, R. J.; Bankson, J. A.; Sershen, S. R.; Rivera, B.; Price, R. E.; Hazle, J. D.; Halas, N. J.; West, J. L. *Proceedings of the National Academy of Sciences of the United States of America* 2003, 100, 13549-13554.
- (48) Brinson, B. E.; Lassiter, J. B.; Levin, C. S.; Bardhan, R.; Mirin, N.; Halas, N. J. *Langmuir* 2008, 24, 14166-14171.
- (49) Westcott, S. L.; Oldenburg, S. J.; Lee, T. R.; Halas, N. J. *Langmuir* 1998, 14, 5396-5401.
- (50) Rasch, M. R.; Sokolov, K. V.; Korgel, B. A. *Langmuir* 2009, 25, 11777-11785.
- (51) Lal, S.; Clare, S. E.; Halas, N. J. *Accounts of Chemical Research* 2008, 41, 1842-1851.
- (52) Smith, D. K.; Miller, N. R.; Korgel, B. A. *Langmuir* 2009, 25, 9518-9524.
- (53) Pierret, R. F. *Semiconductor Fundamentals*; Addison-Wesley Publishing Co.: New York, 1988; Vol. 1.
- (54) Freeman, C.; Halperin, E. C.; Brady, L. W.; Wazer, D. E. *Perez and Brady's Principles and Practice of Radiation Oncology*; Wolters Kluwer Health/Lippincott Williams & Wilkins: Philadelphia, 2008.

- (55) Jori, G.; Spikes, J. D. *Journal of Photochemistry and Photobiology B: Biology* 1990, 6, 93-101.
- (56) Hantash, B. M.; Mahmood, M. B. *Dermatologic Surgery* 2007, 33, 525-534.
- (57) Landry, J.; Samson, S.; Chretien, P. *Cancer Research* 1990, 46, 324-327.
- (58) Nadejda, R.; JinZhong, Z. *Science in China Series B-Chemistry* 2009, 52, 1559-1575.
- (59) Choi, H. S.; Liu, W.; Misra, P.; Tanaka, E.; Zimmer, J. P.; Ipe, B. I.; Bawendi, M. G.; Frangioni, J. V. *Nature Biotechnology* 2007, 25, 1165-1170.
- (60) Donega, C. D.; Bode, M.; Meijerink, A. *Physical Review B* 2006, 74, 085320.
- (61) Smith, A. M.; Nie, S. *Accounts of Chemical Research* 2010, 43, 190-200.
- (62) Alivisatos, A. P. *Science* 1996, 271, 933-937.
- (63) Resch-Genger, U.; Grabolle, M.; Cavaliere-Jaricot, S.; Nitschke, R.; Nann, T. *Nature Methods* 2008, 5, 763-775.
- (64) Rauf, S.; Glidle, A.; Cooper, J. M. *Advanced Materials* 2009, 21, 4020-+.
- (65) Satarug, S.; Baker, J. R.; Urbenjapol, S.; Haswell-Elkins, M.; Reilly, P. E. B.; Williams, D. J.; Moore, M. R. *Toxicology Letters* 2003, 137, 65-83.
- (66) Hardman, R. *Environmental Health Perspectives* 2006, 114, 165-172.
- (67) Derfus, A. M.; Chan, W. C. W.; Bhatia, S. N. *Nano Letters* 2004, 4, 11-18.
- (68) O'Farrell, N.; Houlton, A.; Horrocks, B. R. *International Journal of Nanomedicine* 2006, 1, 451-472.
- (69) Jarzyna, P. A.; Skajaa, T.; Gianella, A.; Cormode, D. P.; Samber, D. D.; Dickson, S. D.; Chen, W.; Griffioen, A. W.; Fayad, Z. A.; Mulder, W. J. M. *Biomaterials* 2009, 30, 6947-6954.
- (70) Anglin, E. J.; Cheng, L. Y.; Freeman, W. R.; Sailor, M. J. *Advanced Drug Delivery Reviews* 2008, 60, 1266-1277.
- (71) Zhao, Y.; Trewyn, B. G.; Slowing, I. I.; Lin, V. S. Y. *Journal of the American Chemical Society* 2009, 131, 8398-8400.
- (72) Patri, A. K.; Kulowska-Latallo, J. F.; Baker, J. R. J. *Advanced Drug Delivery Reviews* 2005, 57, 2203-2214.
- (73) Fox, C. B. *Molecules* 2009, 14, 3286-3312.
- (74) Yokoyama, M. *Expert Opinion in Drug Delivery* 2010, 7, 145-158.
- (75) Rangel-Yagui, C. O.; Pessoa, A. J.; Tavares, L. C. *Journal of Pharmacy and Pharmaceutical Sciences* 2005, 8, 147-163.
- (76) Torchilin, V. P.; Sawant, R. R. *Soft Matter* 2010, 6, 4026-4044.
- (77) Amstad, E.; Kohlbrecher, J.; Muller, E.; Schweizer, T.; Textor, M.; Reimhult, E. *Nano Letters* 2011, 11, 1664-1670.
- (78) Chandler, D. *Nature* 2005, 437, 640-647.
- (79) Chen, Y.; Bose, A.; Bothun, G. D. *ACS Nano* 2010, 4, 3215-3221.
- (80) Mueller, W.; Koynov, K.; Fischer, K.; Hartmann, S.; Pierrat, S.; Basche, T.; Maskos, M. *Macromolecules* 2009, 42, 357-361.

- (81) Gopalakrishnan, G.; Danelon, C.; Izewska, P.; Prummer, M.; Bolinger, P. Y.; Geissbuhler, I.; Demurtas, D.; Dubochet, J.; Vogel, H. *Angewandte Chemie-International Edition* 2006, 45, 5478-5483.
- (82) Al-Jamal, W. T.; Kostarelos, K. *Nanomedicine* 2007, 2, 85-98.
- (83) Wi, H. S.; Lee, K.; Pak, H. K. *Journal of Physics-Condensed Matter* 2008, 20, 494211.
- (84) Marsh, D. *CRC Handbook of Lipid Bilayers*; CRC Press, Inc.: Boca Raton, FL, 1990.
- (85) Marsh, D. *Chemistry and Physics of Lipids* 1991, 57, 109-120.
- (86) Marsh, D. *Biophysical Journal* 2007, 93, 3884-3899.
- (87) Lasic, D. D. *Biochemical Journal* 1988, 256, 1-11.
- (88) Ollivon, M.; Eidelman, O.; Blumenthal, R.; Walter, A. *Biochemistry* 1988, 27, 1695-1703.
- (89) Korgel, B. A.; van Zanten, J. H.; Monbouquette, H. G. *Biophys J* 1998, 74, 3264-3272.
- (90) Paternostre, M. T.; Roux, M.; Rigaud, J. L. *Biochemistry* 1988, 27, 2668-2677.
- (91) Mimms, L. T.; Zampighi, G.; Nozaki, Y.; Tanford, C.; Reynolds, J. A. *Biochemistry* 1981, 20, 833-840.
- (92) McClements, D. J. *Food Emulsions: Principles, Practice, and Techniques*; CRC Press LLC: Boca Raton, 1999.

Chapter 2: Limitations on the Optical Tunability of Small Diameter Gold Nanoshells[§]

2.1 Introduction

Gold (Au) nanoshells are plasmonic materials that strongly absorb and scatter visible and near-IR light with size-tunable color.¹⁻⁶ Au nanoshells are typically made by coating a nanoparticle of a low dielectric constant material like silica with Au; the core/shell size ratio determines the nanoshell plasmon resonance frequency.^{2,3,7} Metal nanoshells can be conjugated with biological molecules using relatively straightforward chemistry,⁸⁻¹² and since nanoshells can be made with plasmon resonances at wavelengths that are particularly transparent for tissue (the near infrared, between 700 nm and 1000 nm),^{13,14} they have been explored for use as optical scattering contrast agents for tumor cell imaging.^{8,15} Additionally, medical therapeutics might also be combined with imaging, as Au nanoshells could serve as vehicles for drug delivery or for minimally-invasive photothermal therapy since light excitation leads to local heating that can be used for targeted cell death.^{14,16-19}

When Au nanoshells with plasmon resonance at near infrared wavelengths (700-1000 nm) are synthesized, they typically have a diameter between 120 nm to 1 μ m in diameter.^{1-4,6} For *in vivo* medical applications, Au nanoshells in this size range have limited access to the site of interest from the blood stream,^{6,14,20,21} as there are problems with systemic delivery associated with quick clearance from the blood by liver and

[§] Portions of this chapter appear in the following publication: Rasch, M.R.; Sokolov, K.; Korgel, B.A. *Langmuir* (2009), 25, 11777-11785. M.R. Rasch performed the experiments. All authors contributed to writing the text. B.A. Korgel and K. Sokolov provided funding through research grants.

spleen²²⁻²⁶ and limited diffusion of such big particles in tissue.²⁷⁻²⁹ Considering also the various molecular coatings, such as polyethylene glycol (PEG) to suppress immune response and other moieties needed for directed binding to biological targets, such as antibodies, aptamers or peptide fragments,^{16,30-33} (which can add another 40 nm or so to the bare particle diameter)^{34,35} nanoshells with smaller diameters, of 10 to 60 nm prior to bioconjugation, are better suited for *in vivo* medical applications.

There are only a few reports of nanoshells with diameters of 10 to 60 nm.³⁶⁻³⁹ Xia, et al.³⁹ recently reported Au nanoshells on 32 nm diameter silica-coated Au particles. The optical absorption peak was relatively broad with a maximum wavelength of 681 nm. Their transmission electron microscopy (TEM) showed that the nanoshells were not spherical, and the limited optical tunability was attributed in part to rough surfaces and agglomeration. Alternatives to the use of silica core particles for making smaller diameter Au nanoshells have also been reported; for instance, Au nanoshells ranging from 45 to 60 nm in diameter were made by depositing Au on 9 nm diameter iron oxide nanoparticles.^{37,38} The plasmon wavelength range for these nanoshells was again relatively limited, from 535 and 540 nm—comparable to the plasmon resonance wavelengths of solid Au nanoparticles—because of their small core/shell thickness ratios. Hollow Au nanoshells have also recently been made by galvanic displacement of silver or cobalt nanospheres.^{5,36} The nanoshells grown from cobalt spheres ranged from 58 nm to 60 nm in diameter with plasmon peak wavelengths ranging from 530 to 630 nm and the nanoshells produced from silver spheres were 10-20 nm in diameter with a plasmon resonances that could be tuned between 550 and 800 nm. These are promising results,

but the structural stability of such *unsupported* nanoshells remains to be tested and may present a problem for *in vivo* medical applications. Furthermore, a silica core can incorporate smaller nanocrystals of different materials, like magnets or luminescent semiconductors within the nanoshell that can provide added functionality, for multimodal medical imaging contrast with both optical and magnetic signatures for example.^{20,40}

Considering the stability, biocompatibility, and potential for development into a multi-functional material by manipulating the core material composition of the silica-supported Au nanoshells, we aimed to understand the limitations of this system for obtaining small diameter (20 to 60 nm diameter) Au nanoshells with size-tunable optical resonances from visible to NIR frequencies. In this chapter, it is demonstrated that Au nanoshells can be grown on silica spheres as small as 30 nm in diameter and on 40 nm diameter silica spheres encapsulating 5 nm diameter magnetic iron oxide nanocrystals. However, as the nanoshell diameter decreased, the plasmon peak was found to be tunable out to increasingly shorter wavelengths. As the silica core diameter becomes smaller, the geometric ratio of the Au shell thickness to the diameter becomes increasingly limited by the ~2 nm diameter Au nanocrystals used to seed shell growth—the shell simply cannot be made small enough to shift the plasmon to NIR wavelengths. The smaller diameter nanoshells are also found to be highly susceptible to aggregation—to a much greater extent than the larger diameter nanoshells. With model calculations of the size-dependent inter-particle potential, it is revealed that larger nanoshells are more stable than smaller nanoshells during synthesis because of more effective charge double-layer

repulsion. These factors lead to fundamental challenges in the synthesis of smaller diameter Au nanoshells with NIR plasmon resonances.

2.2 Experimental Details

2.2.1 Chemicals

Octyl ether (99%) and oleic acid ($\geq 99\%$) were purchased from Fluka. Iron pentacarbonyl ($\text{Fe}(\text{CO})_5$, 99.999%), tetraethylorthosilicate (TEOS, 98%), IgePal CO-520 ($M_n \sim 441$), tetrakis(hydroxymethyl)phosphonium chloride (THPC, 80% solution in water), sodium hydroxide pellets (97+%), tetrachloroauric acid ($\text{HAuCl}_4 \cdot 3\text{H}_2\text{O}$, 99.9+%), tris(2',2'-bipyridyl)dichlororuthenium(II) hexahydrate (Rubpy, 99.95%), n-hexanol (anhydrous, $\geq 99\%$), Triton X-100 (97+%), 4-(2-hydroxyethyl)-1-piperazineethanesulfonic acid (HEPES), and 3-aminopropyltrimethoxysilane (APTS, 97%) were purchased from Sigma Aldrich. Cyclohexane (99.9%), potassium carbonate (anhydrous, 99.8%), and formaldehyde solution (37% w/w in water) were obtained from Fisher Scientific. Ammonium hydroxide (NH_4OH , 28% in water) was purchased from EM Science. Colloidal silica particles (product name OrganosilicasolTM IPA-ST-ZL, 30% w/w SiO_2 in isopropanol, 70-100 nm particle diameter) were obtained from Nissan Chemical Company. All chemicals were used as received. Doubly-distilled, deionized (18 M Ω resistance), 0.2-micron filtered water (DI- H_2O) was used for all preparations.

2.2.2 Silica-coated Iron Oxide Nanocrystal Synthesis

Iron oxide nanocrystal synthesis and subsequent silica coating was performed using published procedures.^{41,42}

Hydrophobic 5 nm diameter iron oxide nanocrystals were first prepared on a Schlenk line under nitrogen atmosphere. 10 mL octyl ether and 0.9588 mL oleic acid were added to a 3-neck flask fitted with a cooling water condenser and two rubber septa. A thermocouple was fed through one septum and allowed to contact the solution, and the condenser was connected to a stopcock with Teflon valve. The system was purged of oxygen by connecting the stopcock to the Schlenk line, closing the stopcock valve and pulling vacuum, switching to nitrogen flow and opening the stopcock valve for a few minutes, and repeating these steps for three additional cycles. Subsequently, the solution was heated to 100°C under magnetic stirring using a heating mantle, which was powered by a variable autotransformer linked to the thermocouple by an electronic temperature controller. As soon as the solution temperature stabilized at 100°C for five minutes, 0.2 mL of iron pentacarbonyl was then injected into the flask and the mixture was heated to 297°C.⁴³ During heating, the reaction mixture proceeds through a series of color changes from orange to clear yellow, and finally black at the final temperature setting. The heating rate is important: the autotransformer was set to 70% power output and the solution reached its temperature set point after 30-40 minutes. The mixture was refluxed at 297°C for one hour, then the heating mantle was removed and the mixture was allowed to cool under nitrogen by equilibrating the flask with room temperature air. When the solution temperature reached 70°C, the reaction mixture was exposed to oxygen by disconnecting the open stopcock from the Schlenk line. Once the reaction mixture cooled to room temperature, it was poured into a centrifuge tube and centrifuged with ethanol antisolvent (4 mL per 1 mL of reaction product) at 8000 rpm for 5 minutes at 20°C. The

black precipitate was suspended in 10 mL hexane and re-precipitated with ethanol as just described at least four times, then finally dispersed in cyclohexane and stored in a parafilm-sealed glass vial. The iron oxide nanocrystals had a mean diameter of 5.0 ± 0.8 nm, determined by TEM. Figure 2.1 shows a typical TEM image of the iron oxide nanocrystals.

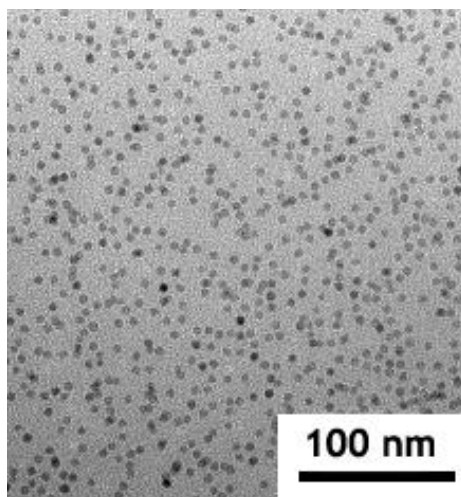


Figure 2.1. TEM image of iron oxide nanocrystals. Average diameter = 5.0 ± 0.8 nm.

To coat the iron oxide nanocrystals with silica, 16.2 mL of cyclohexane was first added to a 20 mL screwcap glass vial. With magnetic stirring, 0.800 mL Igepal, 37.7 μ L iron oxide nanocrystals (15.5 mg/mL in cyclohexane), 0.130 mL of ammonium hydroxide (28% in water), and 0.100 mL of TEOS were added to the vial in precisely that order. The microemulsions were covered and stirred for 2 days. The nanoparticles were extracted with about 5 mL of methanol. The nanoparticles were purified by adding 20 mL of hexane per 5 mL of extracted methanol dispersion. The solutions were centrifuged at 2500 rpm for 6 hours. The precipitate was collected and re-dispersed in 5 mL ethanol.

Hexane was added as an antisolvent to re-precipitate the nanoparticles. This dispersion was centrifuged again to isolate the precipitated nanoparticles. This purification procedure was repeated three times to remove unreacted TEOS and excess Igepal. The final nanoparticle product was re-dispersed in 5 mL of ethanol. High centrifugation speeds, complete drying (rotary evaporation), and an extensive number of centrifugation cycles were all seen to make the silica particles very difficult to redisperse in any solvent, so these actions should be avoided with all of the silica nanoparticle preparations.

2.2.3 Microemulsion-Assisted Synthesis of Silica Colloid Particles

30 nm diameter silica particles were synthesized in microemulsion media using the published procedures.⁴⁴ Two mL of Igepal, 0.325 mL of NH_4OH (28% w/w) and 0.250 mL of TEOS (0.250 mL) were added sequentially to 41 mL of cyclohexane. After stirring this cyclohexane solution for two days, the silica particles were extracted from the organic phase with ~5 mL methanol. The particles were isolated and purified as described for the silica-coated iron oxide.

Larger diameter (70 nm) silica particles were also made by a microemulsion method, but required a different surfactant combination.⁴⁵ The published procedures had incorporated a fluorescent dye, Rubpy, and therefore this procedure was followed exactly as described, including the addition of Rubpy, since the silica chemistry is sensitive to any chemical changes. First, 7.5 mL cyclohexane, 1.8 mL n-hexanol, 1.77 mL Triton X-100, 0.48 mL Rubpy (20 mM, aq), and 0.20 mL of TEOS were placed under magnetic stirring for 20 minutes in a conical flask. Next, 0.060 mL of ammonium hydroxide was added and the reaction was stirred for 24 hours. Subsequently, an equal volume (11.65

mL) of acetone was added to the completed reaction with vortexing to break the microemulsion. The dye-doped silica nanoparticles were collected by centrifuging at 3000 rpm for 30 minutes, the supernatant was discarded, and the particles were then suspended in 5 mL of ethanol. 20 mL of hexane was added, the particles were centrifuged again at the same parameters, and the supernatant was discarded. The particles were suspended in 5 mL ethanol, and the centrifugation cycle was repeated two more times.

2.2.4 Commercial Silica Preparation

The commercial silica colloid IPA-ST-ZL is supplied as an isopropanol dispersion. Prior to gold shell growth, these silica particles need to be purified by size selective precipitation and suspended in ethanol for surface modification. 20 mL of hexane was added to 5 mL of ST-ZL isopropanol-based colloid and centrifuged for 1 hour at 2500 rpm. The supernatant was discarded and the white precipitate was re-dispersed in 5 mL of ethanol with mild sonication. The concentrated sample was further purified through size selective precipitation to collect the largest silica spheres. Hexane was added dropwise to the nanoparticles until observing a slight change in turbidity (typically after adding ~0.5 mL), the particles were centrifuged for 1 hour at 2500 rpm and the precipitate was collected by pouring off the supernatant. The precipitated nanoparticles were dispersed in 5 mL ethanol, and the observed average particle diameter was 118 ± 5 nm from TEM measurement.

2.2.5 Determining Silica Nanoparticle Concentration

The number concentration of silica nanoparticles was important to keep track of during synthesis, particularly for keeping the total silica surface area constant during Au nanoparticle attachment and Au shell deposition for the various particle sizes. Mass concentration of silica colloid (prior to APTS surface passivation) was determined by drying 1.0 mL of nanoparticle dispersion using a rotary evaporator and measuring the weight of the dried sample. Nanoparticle number concentration was found by dividing the mass concentration by the bulk density of silica (2.2 g/cm^3) and the average volume per silica particle determined from TEM measurement. A similar procedure was carried out for the silica-coated iron oxide sample, including the iron oxide core size and bulk density (5.24 g/cm^3) in the calculation. Note that the un-passivated (hydroxyl terminated) silica particles dried to a film do not re-disperse well in ethanol or water, and were never introduced back into the particle dispersion from which they were taken.

2.2.6 Silica Surface Modification with 3-(aminopropyl)trimethoxysilane

Prior to Au shell deposition, the silica particles were functionalized with amines (APTS) using a modification of the procedures described by Lee for attaching octyltrimethoxysilane (OTMOS) to silica spheres.⁴² This method was more reproducible than previously reported methods of refluxing silica spheres in APTS,³⁹ and thus more effective for reproducibly achieving high surface coverage of Au nanocrystals on the amine-terminated silica particles in the next step. 0.10 mL of 30% NH_4OH (aq) was added to 10 mL of a 1 mg/mL dispersion of purified silica particles under magnetic stirring.⁴⁶ 0.5 mL of 10% v/v of APTS in ethanol was added dropwise to the dispersion.

The dispersion was stirred for 24 hours. The nanoparticles were then precipitated by adding 40 mL of hexane and centrifuging at 3000 rpm for one hour. After discarding the supernatant, the particles were suspended in 5 mL ethanol with sonication. This precipitation was repeated 2 times, after which the particles were re-dispersed with sonication in 10 mL DI-H₂O (1 mg/mL APTS-silica). The pH of this suspension is typically ~10, which is above the pK_a of the amine. Therefore, to protonate the amine for better dispersibility, the pH was reduced to ~3 by adding a few drops of concentrated HCl and sonicating the suspension.

2.2.7 Au Nanocrystal Seed Formation

A few days in advance of shell growth, Au seeds were prepared as previously described.⁴⁷ 45 mL of DI-H₂O was poured into a conical flask and stirred. 0.5 mL of 1M NaOH was added, followed by 1 mL of a THPC solution (12 µL of 80% THPC per mL of DI-H₂O). The mixture was stirred for 5 minutes before adding 2 mL of a fresh 1% w/w HAuCl₄ (aq) solution. After 15 minutes, the solution turned dark brown, indicating the formation of small (2-3 nm) gold seed particles. This colloidal Au dispersion was stored at 4°C for a week until use, as suggested in the literature.^{14,16,48} A TEM image of the Au nanocrystal seeds is in Figure 2.2.

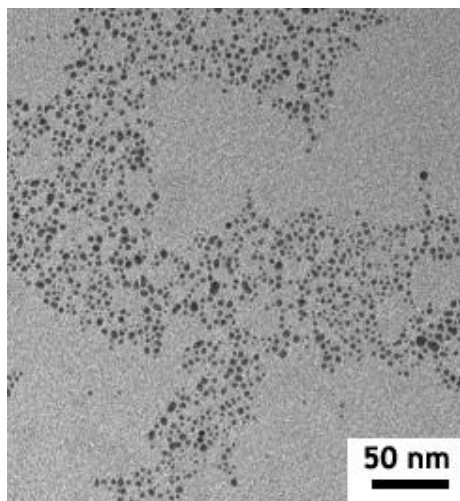


Figure 2.2. TEM image of Au nanocrystal seeds. The average diameter is 2.9 ± 0.3 nm from measuring 110 nanocrystals.

2.2.8 Au Nanoshell Formation

Au nanoshells were prepared following the methods developed by Xia.³⁹ Shell growth is carried out on silica nanoparticles that are surface-modified with exposed amines. A gold nanoparticle seed layer is first adsorbed onto the silica particle surface, followed then by the addition of a gold salt shell growth solution. Note that shell growth is extremely sensitive to the details of the procedures and need to be carefully followed.

The gold hydroxide solution for shell deposition was prepared one day prior to shell deposition. 25 mg of potassium carbonate was dissolved in 100 mL DI-H₂O, followed by the addition of 1.5 mL of a 1.0 % w/w HAuCl₄ solution. After stirring for ~30 minutes, the solution appears colorless, indicating that hydrolysis of AuCl₄⁻ has occurred.⁴⁷ This gold hydroxide solution was then stored for 24 hours in the dark and used immediately. Storing the gold hydroxide solution for more than 2-3 days leads to a

faint pink color and a solution that is no longer suitable for gold shell deposition, as evidenced by formation of a nanoshell reaction product having low optical tunability, and this is confirmed by other sources.⁴⁸

Prior to shell growth, Au seed particles were adsorbed to silica particles.³⁹ The APTS-treated silica particles were mildly sonicated for 20 minutes to ensure uniform particle dispersion and then 2.5 mL of the APTS-silica dispersion ($\sim 100 \text{ cm}^2$ silica surface area per mL solution) was added to a 15 mL centrifuge tube, followed immediately by the addition of 5.0 mL of THPC Au colloid.⁴⁹ The pH was re-adjusted (if necessary) to 3.0 with a few drops of concentrated HCl, and the dispersion was gently shaken for 2 minutes before storing in the dark overnight at 4°C. The resulting nanoparticle product was isolated by centrifugation at 2500 rpm for 3 hours. The supernatant was discarded and the precipitate was re-dispersed with sonication in 2.5 mL DI-H₂O. This centrifugation and re-dispersing cycle was repeated two more times to remove any unattached gold remaining, as indicated by a colorless supernatant above the precipitate.

For Au nanoshell growth, 4 mL of the as-prepared gold hydroxide reactant solution was added to a 20 mL glass vial and placed under magnetic stirring.³⁹ After sonicating for 20 minutes, Au-decorated silica was then added to this reactant solution with amounts that depended on the desired Au shell thickness, from 0.01 mL to 1.5 mL. The pH was adjusted from ~ 6.0 to 8.0 by adding 1-2 μL of NH₄OH (aq, 30% w/w), as recommended by ref 6 to inhibit homogeneous Au particle nucleation. 10 μL of formaldehyde was then immediately added. The dispersion changes from colorless to

blue over the course of about 10 minutes. The nanoshell product was isolated by centrifugation at 2500 rpm for 1 hour. After discarding the supernatant, the precipitate of Au nanoshells was redispersed in 4 mL of DI-H₂O with sonication. As shown in Figures 2.3 and 2.4, the nanoshell dispersions varied in color from blue to red, with the red color corresponding to the thickest Au shells. The nanoshells would sediment at a rate that depended on the particle size: the largest diameter nanoshells had much better dispersibility than the smallest diameter nanoshells. The poorer dispersibility of the smaller diameter nanoshells is the result of their extensive aggregation.

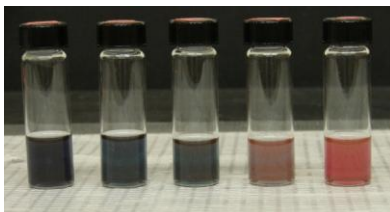


Figure 2.3. Photograph of aqueous dispersions of Au nanoshells grown on 118 nm diameter silica spheres. The amount of gold per silica surface area used during the shell deposition increases from left to right: 26, 35, 56, 110, 430 nmol Au per cm² silica, respectively.

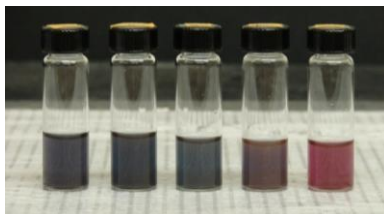


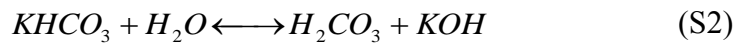
Figure 2.4. Photograph of aqueous dispersions of Au nanoshells grown on 38 nm diameter silica spheres. The amount of gold per silica surface area used during the shell deposition increases from left to right: 4.3, 26, 35, 56, 110 nmol Au per cm² silica, respectively.

2.2.9 Ionic Strength Calculation of the Gold Hydroxide Solution

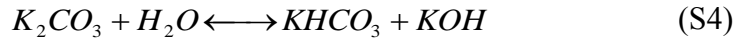
An estimate of the ionic strength of the Au nanoshell growth solution was needed to calculate the electric double layer potential in chapter 2.3. The expression for the ionic strength (I) for a solution with N charged species is

$$I = \frac{1}{2} \cdot \sum_{i=1}^N C_i \cdot z_i^2 \quad (S1)$$

where C_i is the concentration of species i and z_i is its charge.⁵⁰ The gold hydroxide solution was prepared by stirring 25 mg of potassium carbonate in 100 mL DI water for 10 minutes, then adding 1.5 mL of a 1.0 % w/w HAuCl_4 solution. When potassium carbonate is first added, $[\text{K}^+]$ is 3.6 mM and $[\text{CO}_3^{2-}]$ is 1.8 mM, and the ionic strength is 5.4 mM. The carbonate anion equilibrates with water to give hydrogen carbonate and carbonic acid. The equilibrium expressions, Equations S2 and S4, were used to model the system, with $K_{b1} = 5 \times 10^{-8}$ mM and $K_{b2} = 0.213$ mM:⁵⁰



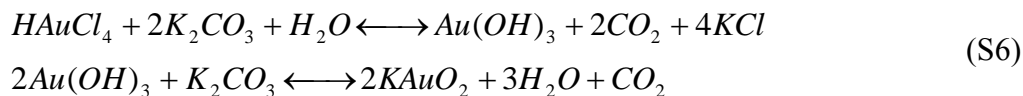
$$K_{b1} = \frac{[\text{H}_2\text{CO}_3] \cdot [\text{OH}^-]}{[\text{HCO}_3^-]} \cdot \frac{\gamma_{\text{H}_2\text{CO}_3} \gamma_{\text{OH}^-}}{\gamma_{\text{HCO}_3^-}} \quad (S3)$$



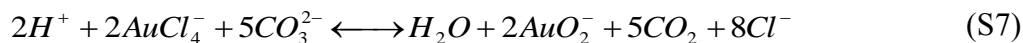
$$K_{b2} = \frac{[\text{HCO}_3^-] \cdot [\text{OH}^-]}{[\text{CO}_3^{2-}]} \cdot \frac{\gamma_{\text{HCO}_3^-} \gamma_{\text{OH}^-}}{\gamma_{\text{CO}_3^{2-}}} \quad (S5)$$

The ionic strength of the potassium carbonate solution was determined by iteratively solving Equations S1, S3, and S5. With an initial guess of 5.4 mM for the ionic strength, the tabulated activity coefficients are $\gamma_{HCO_3^-} = 0.928$, $\gamma_{CO_3^{2-}} = 0.742$, and $\gamma_{OH^-} = 0.926$.⁵⁰ These values of γ were used to calculate the concentration of each species based on the initial mass of potassium carbonate, and then solving for the ionic strength. This process was repeated until the value for the ionic strength converged. The calculated ionic strength before adding the 1% w/w HAuCl₄ is 4.9 mM.

After adding hydrogen tetrachloroaurate to the potassium carbonate solution, Au atoms associate with hydroxyls. The chemical reactions that take place in this gold salt solution are:⁵¹



The net chemical reaction is equation S7.



As reaction S7 shifts to the right with time, the ionic strength decreases. Consider if reaction S7 proceeds from left to right in stoichiometric amounts. The -2 charged carbonate species are oxidized to leave only ions with valences of ± 1 , causing the ionic strength to drop by about 58%. While we do not have the equilibrium constants for the expressions in S6, evaluating the ionic strength based on the initial preparation conditions yields an estimate of the maximum ionic strength attained in the gold salt solution. The addition of gold chloride initially raises the ionic strength to about 5.3 mM, and then

decreases over time. A 50-60% reduction in ionic strength will not have a significant effect on the trends in particle stability versus size discussed in Chapter 2.3; order of magnitude *increases* in ionic strength would be needed to change the trend in the stability of the nanoshells to aggregation.

2.2.10 Materials Characterization

The nanoparticles were characterized using transmission electron microscopy (TEM) and UV-visible-NIR optical absorbance spectroscopy. TEM samples were prepared by drop-casting 5 μL of a nanocrystal dispersion on 200 mesh carbon-coated copper TEM grids (Electron Microscopy Sciences) held at their edge with anti-capillary tweezers. To create a thin nanocrystal film on the grid, the droplet was drawn off slowly by touching a clean piece of filter paper to the edge of the grid. Low-resolution TEM images were taken using a Philips 208 TEM, equipped with an AMT Advantage HR model CCD camera, at 80 kV accelerating voltage. High resolution TEM images were acquired with a JEOL 2010F TEM at 200 kV using a Gatan multipole scanning CCD camera. Absorbance spectra were acquired with a Cary 500 spectrophotometer using quartz cuvettes with 10 mm optical path lengths.

2.3 Results and Discussion

2.3.1 Au Nanoshell Formation and Morphology

Figure 2.5 shows TEM images of Au nanoshells on silica particles with decreasing diameter, from 118 nm to 28 nm. The roughness of the Au nanoshells

increased as the silica particle diameter was decreased and there was much more aggregation of the smaller diameter nanoshells. A variety of different synthetic parameters were modified to try to eliminate the aggregation and nanoshell roughness,⁵² but it could not be avoided. Aggregation in particular was found to be a major problem associated with the smaller diameter particles as discussed in more detail below.

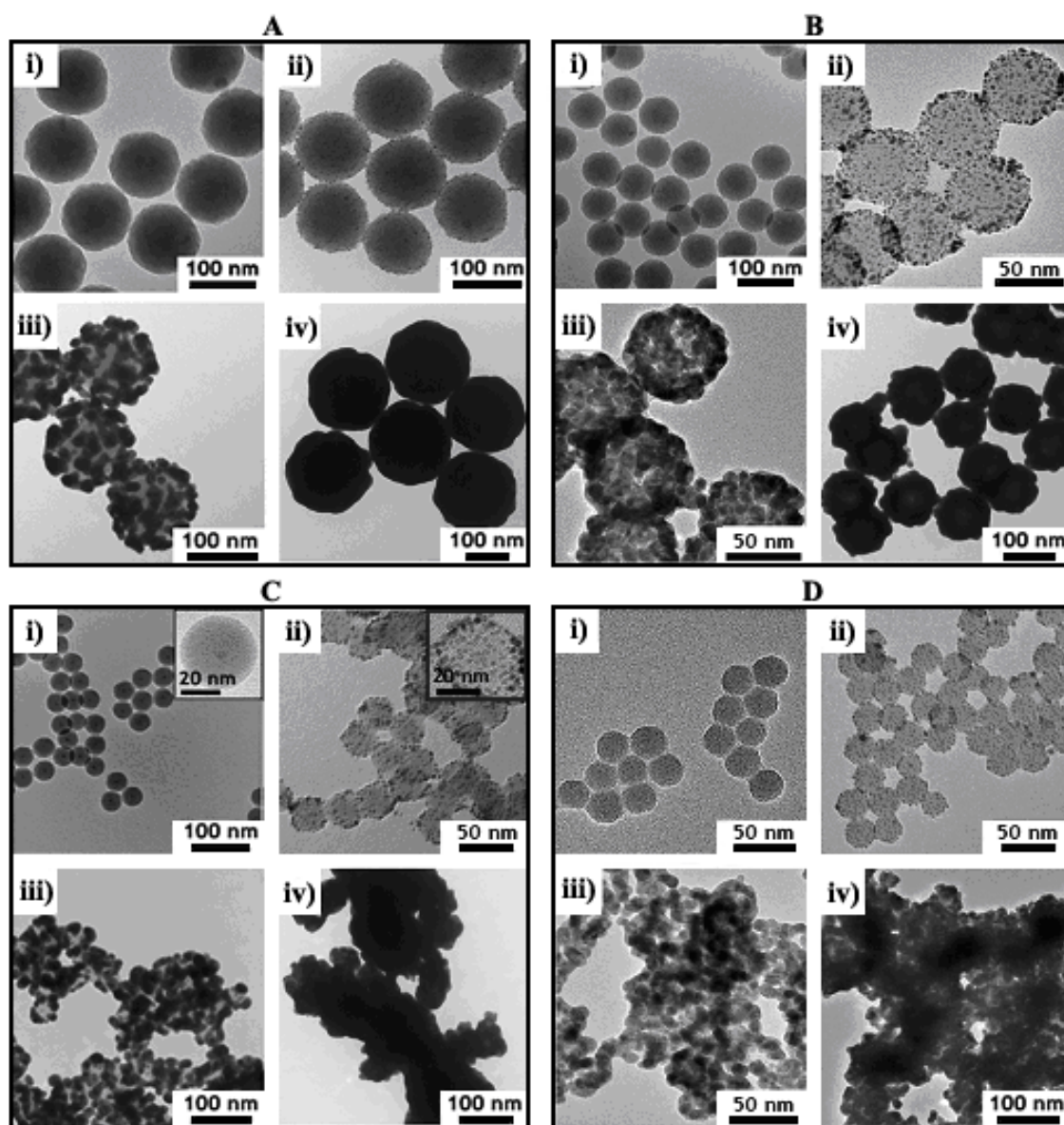


Figure 2.5. TEM images of silica particles with varying size—(A): 118 ± 5 nm; (B) 74 ± 3 nm; (C) 38 ± 1 nm with 5.0 ± 0.8 nm diameter iron oxide core; (D) 28 ± 1 nm—coated with Au nanoshells. Each frame shows the nanoshells at different stages of the deposition process: (i) bare silica; (ii) Au nanocrystal-decorated silica; (iii) partial Au shell growth; (iv) complete Au shell formation.

Figure 2.6 illustrates the nanoshell growth process. Silica spheres are first decorated with Au nanocrystals that are used to seed the deposition of the Au shell. TEM images of silica spheres coated with their Au seed layers prior to nanoshell deposition are shown in Figure 1. The seed layer coverage is relatively sparse, with only 20-30% coverage (based on TEM images), which is consistent with previous reports.^{1,53} The surface coverage of the Au seed particles is most likely limited by their charge double-layer repulsion.^{54,55} The Au seed particle surface coverage does not vary significantly with silica particle diameter.

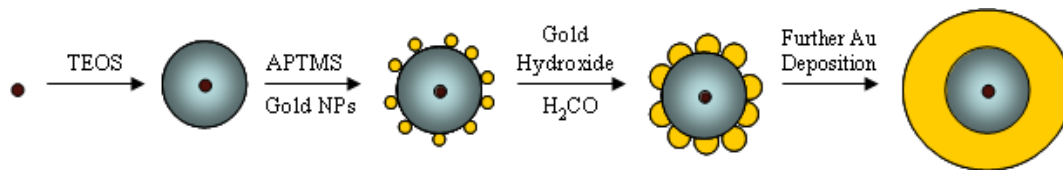


Figure 2.6. Illustration of Au nanoshell (yellow) deposition on a silica particle (gray) or silica-coated iron oxide (brown) particle. Gold hydroxide is reduced in solution with formaldehyde, which deposits Au onto the nanoparticle (NP) seeds on the silica particle surface. Nanoshell growth is complete when sufficient gold hydroxide has been added so that the seeds coalesce into a continuous shell (final step).

In the initial stages of shell growth, Au deposits isotropically on each spherical seed particle that eventually becomes large enough to fuse with their neighbors into a semi-continuous film on the silica surface (Figure 2.5, proceeding from panels (ii) to (iii)). Additional Au deposition fills the voids in the Au film to form a continuous Au shell (Figure 2.5, panels (iv)). In practice, the amount of Au deposited on the silica

particles is manipulated by changing the ratio of Au-primed silica cores (Figure 2.5(ii)) to the amount of the gold reactant solution added for nanoshell growth. There did not appear to be any core silica particle size dependence on the actual Au deposition itself, although the smaller diameter Au nanoshells were found to be rougher than the larger diameter shells. The variation in thickness of the Au seed layer is likely responsible for the observed roughness of the nanoshells. Since the variation in shell thickness from the seed layer is the same for all shells, it is more pronounced when the seed has a smaller diameter, giving an apparently rougher surface. The Au shell roughness appears to be directly related to the monodispersity of the Au seed colloid and Au clustering on the silica surface.

2.3.2 Au Nanoshell Optical Properties

The Au nanoshell plasmon absorbance peak shifts to shorter wavelengths as the size ratio of the core radius/shell thickness decreases.^{2,3,7} Figure 2.7 shows the UV-Vis-NIR optical absorbance spectra of aqueous dispersions of Au nanoshells grown on silica particles of varying diameter. The maximum red-shift of the plasmon absorbance peak decreased as the nanoshell diameter decreased. Since the Au nanoshells are limited to a minimum thickness by the seed particle diameter, the largest attainable core/shell ratio decreases as the silica particle diameter decreases; thus, resulting in shorter wavelength surface plasmon resonances as the silica particle diameter decreased. This is one reason that the plasmon resonance cannot be tuned as far to the red for nanoshells with decreasing diameter. The seed particle diameter fixes the lower limit to the Au shell thickness. If 2 nm diameter Au seeds could somehow be tightly packed on the silica

particle surface to form a complete Au shell, then the Au nanoshells on 28 nm diameter silica spheres would have a core radius/shell thickness ratio of 7, which would correspond to a plasmon peak wavelength at ~ 790 nm according to Mie theory calculations (Chapter 2.3.3).⁵⁶ It is not, however, possible to pack these seed particles into a complete layer on the surface as a shell, and the final Au shell thickness is larger than the initial seed particle diameter. The thinnest Au shells that were obtained on the 118 nm diameter silica particles were 11 nm (TEM measurement), corresponding to a core/shell ratio of 5.4. Based on Mie theory calculations, a core/shell ratio of about 4.5 is needed to achieve a plasmon resonance at 700 nm, which corresponds to Au shell thicknesses of 3.1 and 4.2 nm for the 28 and 38 nm diameter silica spheres, respectively. Uniform Au shells thinner than 10 nm were not experimentally obtainable on any silica core size.

As discussed previously, the different Au shell thicknesses were deposited by varying the number of Au-decorated silica seed particles added to the nanoshell solution. In each spectrum of Figure 2.7, the mole percent of Au added per seed particle is indicated, relative to the amount of Au used to make the nanoshells with the most red-shifted plasmon resonance wavelength (100%). The plasmon resonance wavelength decreases as more Au is deposited on uniform nanoshells, as a result of reducing their core/shell size ratio. This characteristic shifting of the plasmon resonance is observed for all Au nanoshells, regardless of the silica particle diameter. Patchy, incomplete Au nanoshells have plasmon resonance frequencies in-between those of silica spheres with an adsorbed layer of separated 2 nm Au nanoparticles and those of uniform Au

nanoshells. The smaller diameter nanoshells also exhibit a flattening of the absorbance peak at longer wavelengths compared to the larger nanoshells and Mie theory predictions, which is characteristic of aggregation.^{6,57}

Table 2.1 summarizes the lowest energy plasmon peak wavelengths obtained for the different-sized nanoshells. The largest (118 nm core diameter) nanoshells exhibited the most red-shifted plasmon peak at 733 nm. For each nanoshell size, the experimentally measured plasmon peak wavelengths listed in Table 2.1 were used to estimate the core/shell ratios from Mie theory, as described in Chapter 2.3.3. These estimated core/shell ratios correspond to a thinner layer of Au deposition per silica particle than observed by TEM. In the case of the 74 nm diameter nanoshells, Mie theory does not predict a single plasmon resonance peak at 697 nm for any core/shell ratio, suggesting that the Au shells may still be incomplete for this sample. The absorbance peaks for the 28, 38, and 118 nm diameter Au nanoshells can all be matched to a core/shell ratio using Mie theory, but the theory predicts much sharper peaks and long wavelength shoulders that are not observed experimentally. These features are probably lost to peak broadening due to aggregation and surface roughness, which are discussed further below.

TEM analysis of the Au shell thickness is difficult for the heavily aggregated 28-38 nm core diameter nanoshells, and only a few nanoshells can be distinguished on a typical TEM image for size measurement. However, the TEM estimates and Mie theory predictions for the core/shell ratios do not agree well for the nanoshells with core diameters smaller than 100 nm. As seen in Figure 2.5, the 28-74 nm diameter nanoshells had very rough surfaces and exhibited some aggregation, which likely made the plasmon

absorbance peak more red-shifted than expected. Rough edges around the nanoshell surface provide sites for localized electric field enhancements, similar to the more extreme case of Au nanostars,⁵⁸ creating plasmon oscillation modes at longer wavelengths than expected for Au nanoshells with smooth surfaces. Nanoshell aggregates also possess longer wavelength plasmon resonances due to additional oscillation modes associated with their complex geometry.^{2,57} Both roughness and aggregation promote broadened, red-shifted absorbance peaks for the 28-74 nm diameter nanoshells, causing Mie theory to over-estimate the core/shell ratio when the shells are assumed to be smooth and monodisperse.

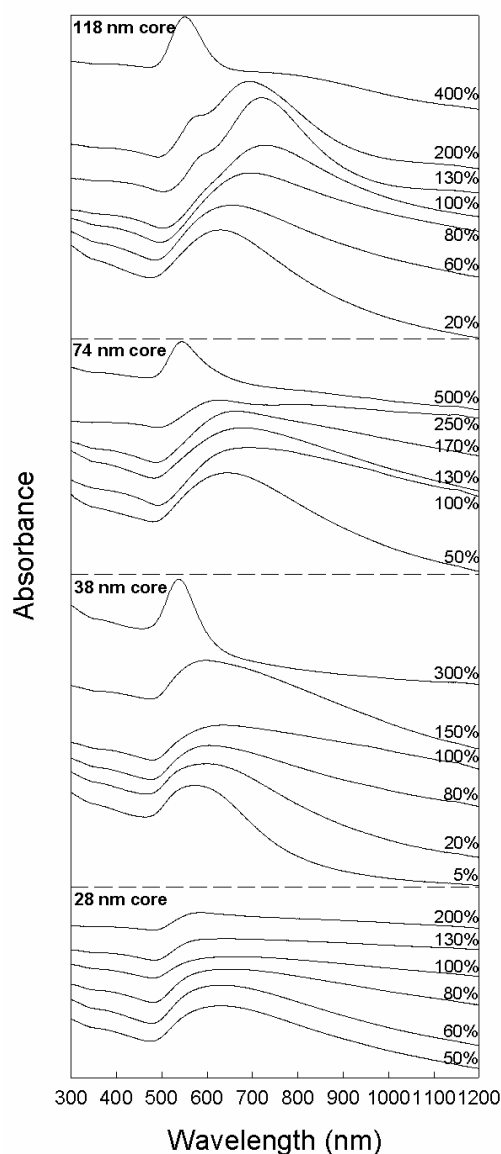


Figure 2.7. Measured absorbance spectra of silica spheres coated with varying Au shell thickness. Nanoshells with the most red-shifted plasmon peak are labeled as “100% complete” as incomplete nanoshells exhibit plasmon peaks at lower wavelength than the complete shells and the plasmon peak shifts back to the blue as the nanoshell thickness is further increased. The 100% complete samples for 118, 74, 38, and 28 nm core sizes correspond to 110, 30, 35, and 14 nmol of Au per cm² of silica used during shell deposition, respectively. The absorbance axis scale is linear.

Table 2.1. The lowest energy plasmon peak position (λ_{max}) observed for each nanoshell as a function of silica particle size.

Silica Diameter (nm)	Silica Particle Concentration during Growth* ($\times 10^{10}$ NP/mL)	Total Silica Surface Area during Growth* (cm^2/mL)	Nanoshell Extinction Peak, λ_{max} (nm)	Core/shell Ratio Calculated from λ_{max} †	Core/shell Ratio Estimate from TEM†
28	100	25	653	3.1	1.1 \pm 0.4
38	30	14	644	1.9	1.0 \pm 0.3
74	9	15	697	N/A‡	3.6 \pm 0.7
118	2	9	733	6.6	5.4 \pm 1.8

* Refers to the Au-decorated silica spheres added to the Au shell growth solution.

† Ratio is silica core radius divided by Au shell thickness. Mie theory calculations were performed to match λ_{max} to a core/shell ratio for smooth, non-aggregated nanoshells (Chapter 2.3.3).

‡ The plasmon absorbance peak for this sample was not within the range of λ_{max} predicted by Mie theory for this size. See Figure 6 in Chapter 2.3.3.

2.3.3 Mie Theory Calculations of Au Nanoshell Optical Properties

An online Mie Theory Calculator was used to predict the absorbance spectra for the different silica core sizes with varying Au shell thicknesses.^{7,59} For each silica core size, the Au shell thickness was adjusted in the program until the maximum in the predicted absorbance spectrum matched the maximum in the experimentally measured spectrum. The program requires inputs of absorbance wavelength, material complex refractive indices, and nanoshell dimensions to calculate the absorption of the core/shell

particle. Producing a full, detailed absorbance spectrum by this approach can be tedious, since the program allows input of only one wavelength at a time. Instead, the maximum absorbance was obtained for each nanoshell size by computing the absorbance at 50 nm intervals, starting at 400 nm wavelength and ending at 800 nm, and then narrowing the wavelength interval where the absorbance is highest. Examples of full predicted spectra overlaid with the experimentally measured spectra are shown in Figures 2.8, 2.9, and 2.10.

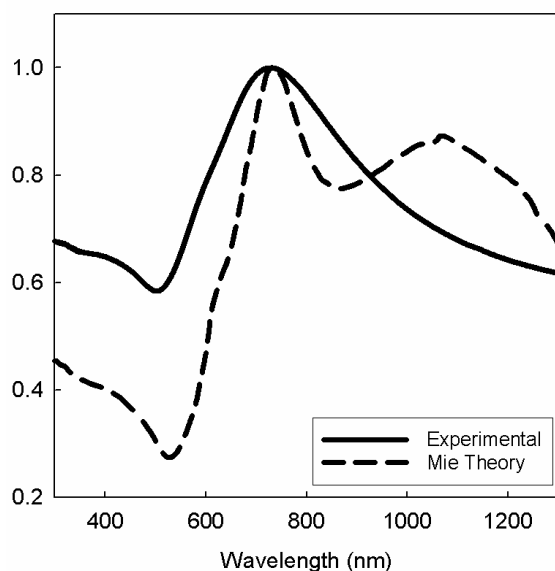


Figure 2.8. Absorbance spectra for 118 nm core diameter nanoshells, determined experimentally (solid line) and from Mie theory (dashed line). The core/shell ratio taken from the Mie theory calculation was obtained by matching the plasmon resonance wavelength with the experimental value.

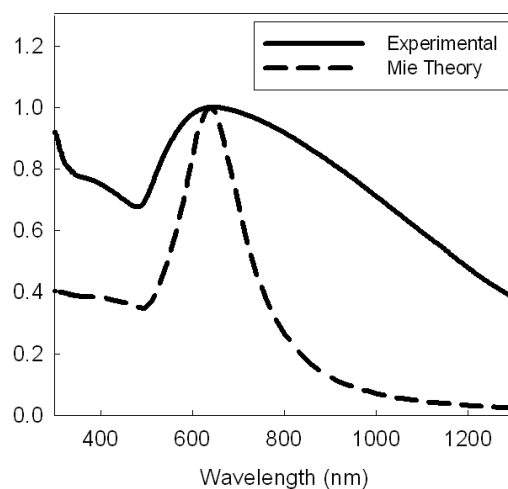


Figure 2.9. Absorbance spectra for 38 nm core diameter nanoshells, determined experimentally (solid line) and from Mie theory (dashed line). The core/shell ratio taken from the Mie theory calculation was obtained by matching the plasmon resonance wavelength with the experimental value.

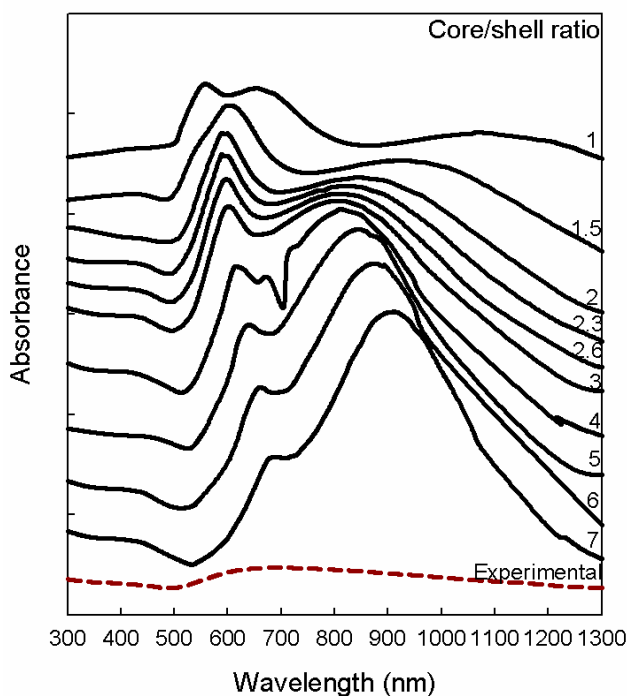


Figure 2.10. Mie theory predictions for absorbance spectra of 74 nm core diameter nanoshells with different core/shell ratios, compared to the spectrum obtained experimentally (dashed curve) with the most red-shifted plasmon resonance peak.

The experimentally measured spectra were typically broader and flatter than the spectra predicted by Mie theory. The 118 nm diameter nanoshells are predicted to have a second plasmon resonance peak around 1100 nm, but only the higher energy peak at 730 nm was observed. The calculated absorbance spectra for the 74 nm diameter nanoshells could not be tuned via the core/shell ratio to exactly match the plasmon resonance wavelength of the experimentally measured spectrum, as seen in Figure 2.10. The 74 nm diameter nanoshells may have incomplete Au shells, which would blue-shift the plasmon absorbance peak relative to Au nanoshells with a complete Au layer of the same thickness. The Mie theory calculations do not account for nanoshell surface roughness, incomplete Au shells, or nanoshell aggregation, which are all apparent in these samples based on TEM imaging.

2.3.4 Diluting the Nanoshell Growth Solution

We tried diluting the nanoshell growth solution to reduce the aggregation that occurred during Au shell deposition. First, we tested the effect of dilution on Au shell deposition with the largest silica spheres (118 nm diameter). During dilution the following parameters were held constant – the pH (~8.0, adjusted with dilute NH_4OH and monitored by pH paper), the concentration of reducing agent, and the ratio of Au ion concentration to silica particles. The shell growth medium was diluted using one of three different solutions prior to adding the formaldehyde reducing agent: 1) DI water (adjusted to pH = 8.0 with 1M aqueous NaOH), 2) aqueous potassium carbonate (1.8

mM, the same concentration for preparing the gold hydroxide solution), and 3) an aqueous HEPES buffer (50 mM, pH = 8.0). For the 118 nm nanoshells, dilution of the shell deposition reaction produced marginal changes in the plasmon resonance wavelength, as shown in Figure 2.11. This is not surprising, because TEM imaging (Figure 2.5) showed that the 118 nm nanoshells are not aggregating during growth. Unfortunately, diluting the small silica spheres (30 nm diameter) with DI water (pH = 8) yielded a nanoshell product with a very weak, blue-shifted plasmon absorbance peak relative to the case with no dilution (Figure 2.12). Therefore dilution does not reduce aggregation of the small Au nanoshells.

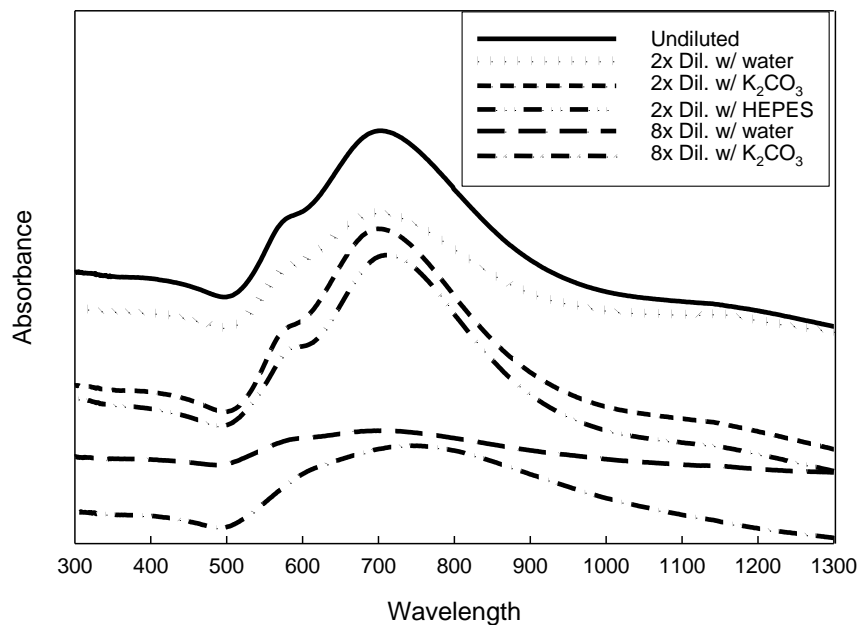


Figure 2.11. Absorbance spectra of Au nanoshells grown on 118 nm diameter silica cores. The volume of the Au shell growth solution was diluted by factors of 2 or 8. The 8x diluted HEPES did not work.

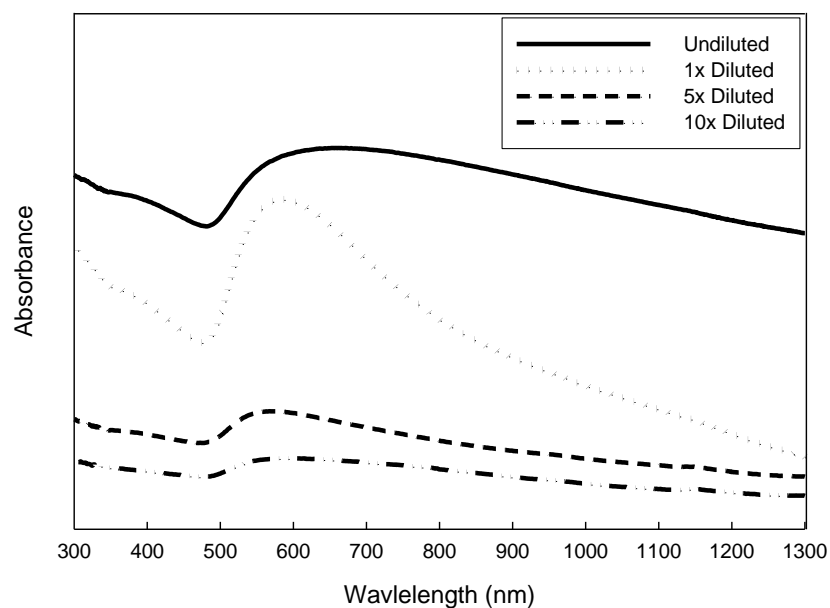


Figure 2.12. Dilution of the small diameter nanoshells (28 nm silica core) during Au shell growth using deionized water adjusted to pH = 8 using 1M NaOH (aq).

2.3.5 Model for Size-Dependent Nanoshell Aggregation

After many experimental trials to deposit Au nanoshells on silica particles less than 60 nm in diameter, it became clear that these smaller diameter Au-coated silica particles were much more prone to aggregation than the larger diameter nanoshells. Calculation of the interparticle potential energy as a function of nanoshell diameter reveals why this is the case. Due to their higher surface curvature, the smaller diameter nanoshells have a more diffuse charge double-layer and as a result are not as well stabilized from aggregation as the larger diameter particles, despite their weaker van der Waals attraction compared to the larger diameter nanoshells.

The pair interparticle potential V_{net} , can be approximated as the sum of an (attractive) van der Waals V_A , potential and a (repulsive) double-layer potential V_E .⁶⁰

$$V_{net} = V_A + V_E \quad (2.1)$$

The next few sections of this chapter describe the derivation of mathematical expressions for each term in equation 2.1, and subsequently the calculation of V_{net} for Au nanoshells and silica spheres decorated with Au nanocrystals as drawn in Figure 2.13. Table 2.2 summarizes the parameters used in the derived equations throughout this chapter.

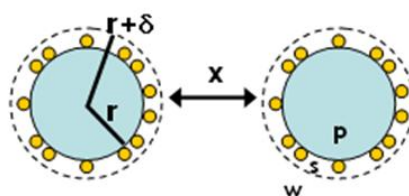


Figure 2.13. Model geometry of silica particles (material, p ; radius, r) covered by a sheath layer of Au nanocrystals (material, s ; thickness, δ) that was used to determine the pair inter-particle potentials. Material s is a composite layer made of Au nanocrystals covering 30% of the silica surface and separated by solvent. The nanoparticle surfaces are separated by a distance x across the water medium (material, w). The overall nanoparticle radius is $r + \delta$.

Table 2.2. Parameters used to model nanoshell aggregation.

Parameter	Description	Value	Reference
kT	Thermal energy	4.04×10^{-21} J	61
e	Fundamental charge	1.60×10^{-19} C	61
ϵ_0	Vacuum permittivity	8.85×10^{-12} C ² /N-m ²	61
ϵ_{rel}	Solvent relative dielectric constant	80.1	61
L	Avogadro's number	6.02×10^{23} mol ⁻¹	61
I	Solvent ionic strength	~5 mM	See Chapter 2.2.8
ϕ	Au nanocrystal surface coverage	30%	6,39
ρ_g	Au bulk density	19.3 g/cm ³	61
ρ_w	Water bulk density	0.997 g/cm ³	61
M_g	Au molar mass	196.97 g/mol	61
M_w	Water molar mass	18.02 g/mol	61
η_w	Water viscosity	0.89 cP	61
δ	Thickness of Au nanocrystal layer	3 nm	TEM measurement
A_g	Au Hamaker constant <i>in vacuo</i>	48×10^{-20} J	See Chapter 2.3.4 text
A_w	Water Hamaker constant <i>in vacuo</i>	3.7×10^{-20} J	62
A_p	Silica Hamaker constant <i>in vacuo</i>	14.7×10^{-20} J	62

Magnetic Dipole Potential. For the silica-coated iron oxide nanoparticles, the coupling between the magnetic dipoles of the iron oxide cores gives a negligible contribution to equation 2.1 due to the absence of an applied magnetic field and the large thickness of the silica layer. The interaction potential V_m between two magnetic nanoparticles (labeled 1 and 2) is¹³

$$\frac{V_m}{kT} = \frac{\gamma}{4\pi} \cdot (2 \cdot \cos \theta_1 \cdot \cos \theta_2 - \sin \theta_1 \cdot \sin \theta_2 \cdot \cos \alpha) \quad (2.2)$$

$$\gamma = \frac{\mu_0 \cdot m_s^2 \cdot \left(\frac{\pi}{6} \cdot D_m\right)^2}{kT \cdot (x + 2 \cdot t)^3} \quad (2.3)$$

θ_i is the angle between the i th nanoparticle's magnetic dipole moment and a distance vector connecting the nanoparticle centers, and α is the azimuthal angle between the magnetic dipole moments. μ_0 is the magnetic constant ($4\pi \times 10^{-7}$ N/A²), x is the distance between the surfaces of the silica-coated iron oxide nanoparticles, t is the thickness of the silica layer (~ 16.5 nm), D_m is the diameter of the magnetic nanocrystal core (5.0 nm), and m_s is the specific magnetization of the iron oxide core (3.1×10^5 A/m)¹³. At room temperature, γ has its maximum value of 0.0035 at zero separation between the silica-coated iron oxide particles ($x = 0$ nm). Since the parenthetical term in equation 2.2 can have a magnitude of at most 2 ($\theta_1 = \theta_2 = 0$), the maximum magnetic attraction between silica-coated iron oxide nanoparticles is only a very small fraction of kT , $5.6 \times 10^{-4} kT$. The magnetic dipole forces are even smaller for typical inter-particle separations in solution, and furthermore, are weaker for larger diameter silica particles, and were therefore neglected from the calculations.

Derivation of the Electric Double-layer Potential. V_E between two particles of equal radius r , separated by a distance x as illustrated in Figure 2.13, is^{60,63}

$$V_E = \begin{cases} \left(2\pi \cdot \varepsilon_{rel} \cdot \varepsilon_0 \cdot \zeta^2\right) \cdot r \cdot \ln[1 + \exp(-\kappa \cdot x)] & \text{for } \kappa \cdot r > 5 \\ \frac{4\pi \cdot \varepsilon_{rel} \cdot \varepsilon_0}{x + 2 \cdot r} \cdot \left(\frac{k \cdot T \cdot r \cdot Y}{e}\right)^2 \cdot \exp(-\kappa \cdot x) & \text{for } \kappa \cdot r < 5 \end{cases} \quad (2.4)$$

where κ is the inverse Debye length and Y is a function,

$$\kappa = \left[\frac{1000 \cdot e^2 \cdot L \cdot 2I}{\varepsilon_{rel} \cdot \varepsilon_0 \cdot k \cdot T} \right]^{1/2}, \quad (2.5)$$

$$Y = \frac{8 \tanh\left(\frac{e \cdot \zeta}{4 \cdot k \cdot T}\right)}{1 + \left[1 - \frac{(2 \cdot \kappa \cdot r + 1)}{(\kappa \cdot r - 1)} \tanh^2\left(\frac{e \cdot \zeta}{4 \cdot k \cdot T}\right)\right]} \quad (2.6)$$

Table 2.2 provides a description of the parameters. In Chapter 2.2.8, the solvent ionic strength I was estimated to be ≤ 5 mM during Au nanoshell growth, and also ~ 5 mM during Au nanocrystal attachment to the APTS-silica.

Derivation of the Van der Waals Potential. V_A is determined for silica particles coated with Au seed particles, like those illustrated in Figure 2.13. The Hamaker attractive potential V_A of a core/shell particle is⁶⁴

$$V_A = -\frac{1}{12} \left[H_s \cdot (A_s^{1/2} - A_w^{1/2})^2 + H_p \cdot (A_p^{1/2} - A_s^{1/2})^2 + (H_{p1s2} + H_{p2s1}) \cdot (A_p^{1/2} - A_s^{1/2}) \cdot (A_s^{1/2} - A_w^{1/2}) \right] \quad (2.7)$$

The *in vacuo* Hamaker constants for water (A_w), silica (A_p), and gold (A_g) are listed in Table 2.2. The value for the gold *in vacuo* Hamaker constant ($A_g = A_{11}$) is obtained by solving equation 2.8, using the *in vacuo* Hamaker constant of water ($A_w = A_{33} = 3.7 \times 10^{-20} \text{ J}$)⁶⁴ and the gold Hamaker constant reported in aqueous medium ($A_{\text{gold-water-gold}} = 25 \times 10^{-20} = A_{131}$):^{60,65,66}

$$A_{131} = A_{11} + A_{33} - 2\sqrt{A_{11}A_{33}} \quad (2.8)$$

The Hamaker constant A_s , of the gold/water sheath layer drawn in Figure 2.13 is:⁶⁴

$$A_s = \left(\frac{N_g}{N_g^0} \cdot A_g^{1/2} + \frac{N_w}{N_w^0} \cdot A_w^{1/2} \right)^2 \quad (2.9)$$

N_w^0 and N_g^0 are the number densities of pure water (H_2O molecules per cm^3) and solid Au (Au atoms per cm^3) respectively, and N_w and N_g are the number densities of water and Au in the sheath layer. The number n of Au nanocrystals on each silica particle is based on the area of the Au nanocrystals projected onto the silica particle surface, which is given in simplified form by equation 2.10.

$$n = \frac{2 \cdot \phi}{\left[1 - \cos \left(\sin^{-1} \left(\frac{\delta}{2r} \right) \right) \right]} \quad (2.10)$$

It follows that the Au and water concentrations in the sheath layer are represented by equations 2.11 and 2.12. Note that bare silica spheres can be represented by setting n equal to zero.

$$N_g = \frac{\rho_g \cdot L}{M_g} \cdot \frac{n \cdot \delta^3}{8 \cdot [(r + \delta)^3 - r^3]} \quad (2.11)$$

$$N_w = \frac{\rho_w \cdot L}{M_w} \cdot \left[1 - \frac{M_g}{\rho_g \cdot L} \cdot N_g \right] \quad (2.12)$$

The Hamaker functions in equation 2.11 for the sheath-sheath (H_s), particle-particle (H_p), and particle-sheath (H_{ps}) interactions are determined from equations 2.13-2.15.

$$H_i = \frac{y}{y^2 + yz + y} + \frac{z}{y^2 + yz + y + z} + 2 \ln \left[\frac{y^2 + yz + y}{y^2 + yz + y + z} \right] \quad (2.13)$$

$$y = \frac{\Delta}{2R_1}, \quad z = \frac{R_2}{R_1} \quad (2.14)$$

$$\begin{aligned} i = s, \quad \Delta = x, \quad R_1 = r + \delta, \quad R_2 = r + \delta \\ i = p, \quad \Delta = x + 2\delta, \quad R_1 = r, \quad R_2 = r \\ i = p_1 s_2, \quad \Delta = x + \delta, \quad R_1 = r, \quad R_2 = r + \delta \\ i = p_2 s_1, \quad \Delta = x + \delta, \quad R_1 = r + \delta, \quad R_2 = r \end{aligned} \quad (2.15)$$

In the above equation, i denotes the type of material – s refers to the sheath layer and p refers to the silica nanoparticle. The parameters x , r , and δ correspond to the particle geometry and were illustrated in Figure 2.13.

Calculation of the Net Inter-particle Potential. Calculations of V_{net} as a function of silica core diameter are plotted in Figures 2.5 and 2.6. Figure 2.14 represents bare silica particles (no adsorbed Au), while Figure 2.15 represents the Au-coated silica particles illustrated in Figure 2.13. For all of the nanoparticle diameters shown in Figure 2.14, there is a repulsive peak in $V_{net}(x)$, but it is weaker for silica nanoparticles with decreased diameter. The repulsive peak for the 30 nm diameter silica particles reaches a maximum at about $10\ kT$ (260 meV) versus about $25\ kT$ for the 120 nm diameter silica particles. Since this barrier represents an activation energy for particle aggregation,⁶⁷ the 30 nm diameter particles are more likely to aggregate with each inter-particle collision in solution than the 120 nm diameter silica particles. The Au-decorated silica spheres also exhibit this dramatic difference in stability with differing particle diameter.

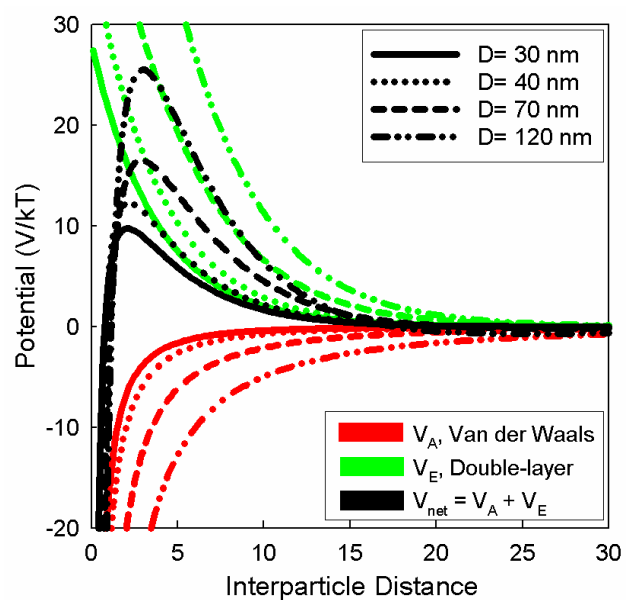


Figure 2.14. Pair inter-particle potential (black curves), van der Waals attraction (red curves) and electrostatic double-layer repulsion (green) calculated using Eqns 2.1-2.15 for silica core diameters noted in the legend. Calculations were performed for silica spheres coated with APTS at pH of 3: $\zeta=42$ mV.^{68,69}

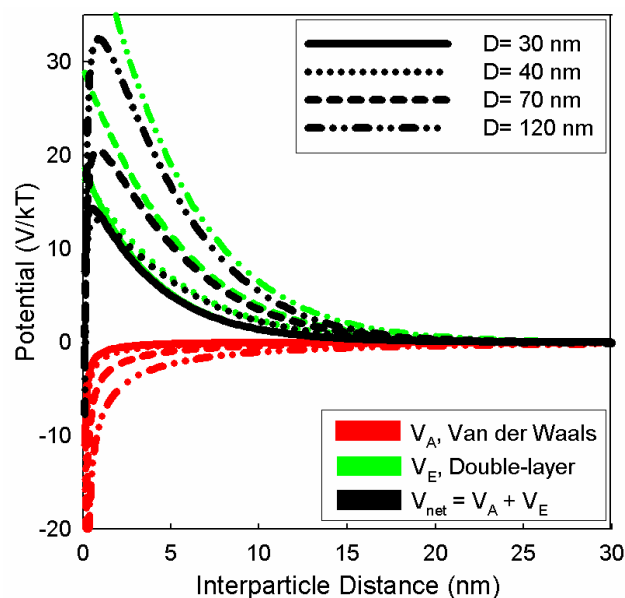


Figure 2.15. Pair interparticle potential (black curves), van der Waals attraction (red lines), and electrostatic double-layer repulsion (green) calculated using Eqns 2.1-2.15 for silica core diameters shown in the legend. The calculations are for silica spheres decorated with 3 nm Au nanocrystals (30% coverage) at pH of 7: $\zeta = -32.5$ mV.^{68,69}

2.4 Conclusions

As their diameter decreases from 120 nm to 30 nm, Au nanoshells are more prone to aggregation during the Au shell deposition step. Rather extensive aggregation is observed by TEM and is apparent from their absorbance spectra. Model calculations of the inter-particle potential revealed that the significant aggregation of smaller diameter Au nanoshells is related to the more diffuse charge double layer of the smaller particles. The collisions between 30 nm diameter nanoshells are inhibited by a smaller energy

barrier, making them more likely to aggregate than the 120 nm diameter nanoshells with each collision in solution.

The smaller diameter nanoshells also exhibit less optical tunability of their plasmon absorbance peak to the red than larger diameter nanoshells. The core/shell size ratio dictates the plasmon peak energy and the size of the gold seeds provides a lower limit to nanoshell thickness. In practice, the shells are thicker than this as a result of the shell deposition process, with a minimum thickness of ~10 nm. This limits the plasmon resonance frequency well into the visible wavelength range for the smallest diameter 30 nm silica spheres.

To obtain small diameter Au nanoshells with strong absorption near the NIR wavelengths, smaller Au nanoparticle seeds are needed in order to obtain higher core/shell size ratios. This is a challenge, but perhaps more significantly, a high nanoshell aggregation rate would still be a problem. Perhaps one approach that might enable stable small diameter Au nanoshells (20-60 nm in diameter) to be synthesized would be the use of a surfactant- or microemulsion-based reaction media that provides steric stabilization of the growing shells, as opposed to charge stabilization. This chemistry has yet to be developed, but should be possible unless steric stabilization creates a physical barrier to the deposition of Au.

2.5 References

(1) Oldenburg, S. J.; Averitt, R. D.; Westcott, S. L.; Halas, N. J. *Chemical Physics Letters* **1998**, 288, 243-247.

- (2) Oldenburg, S. J.; Jackson, J. B.; Westcott, S. L.; Halas, N. J. *Applied Physics Letters* **1999**, *75*, 2897-2899.
- (3) Prodan, E.; Radloff, C.; Halas, N. J.; Nordlander, P. *Science* **2003**, *302*, 419-422.
- (4) Nehl, C. L.; Grady, N. K.; Goodrich, G. P.; Tam, F.; Halas, N. J.; Hafner, J. H. *Nano Letters* **2004**, *4*, 2355-2359.
- (5) Liang, H.; Wan, L.; Bai, C.; Jiang, L. *Journal of Physical Chemistry B* **2005**, *109*, 7795-7800.
- (6) Yong, K. T.; Sahoo, S. K.; Swihart, M. T.; Prasad, P. N. *Colloids and Surfaces a-Physicochemical and Engineering Aspects* **2006**, *290*, 89-105.
- (7) Jain, P. K.; Lee, K. S.; El-Sayed, I. H.; El-Sayed, M. A. *Journal of physical Chemistry B* **2006**, *110*, 7238-7248.
- (8) Loo, C.; Lin, A.; Hirsch, L. R.; Lee, M.; Barton, J. K.; Halas, N. J.; West, J. L.; Drezek, R. A. *Cancer Research and Treatment* **2004**, *3*, 33-40.
- (9) Wang, Y.; Qian, W.; Tan, Y.; Ding, S. *Biosensors & Bioelectronics* **2008**, *23*, 1166-1170.
- (10) Slocik, J. M.; Tam, F.; Halas, N. J.; Naik, R. R. *Nano Letters* **2007**, *7*, 1054-1058.
- (11) Levin, C. S.; Bishnoi, S. W.; Grady, N. K.; Halas, N. J. *Analytical Chemistry* **2006**, *78*, 3277-3281.
- (12) Levin, C. S.; Kundu, J.; Janesko, B. G.; Scuseria, G. E.; Raphael, R. M.; Halas, N. J. *Journal of Physical Chemistry B* **2008**, *112*, 14168-14175.
- (13) Cubeddu, R.; Pifferi, A.; Taroni, P.; Torricelli, A.; Valentini, G. *Applied Physics Letters* **1999**, *74*, 874-876.
- (14) Hirsch, L. R.; Stafford, R. J.; Bankson, J. A.; Sershen, S. R.; Rivera, B.; Price, R. E.; Hazle, J. D.; Halas, N. J.; West, J. L. *Proceedings of the National Academy of Sciences of the United States of America* **2003**, *100*, 13549-13554.
- (15) Loo, C.; Lowery, A.; Halas, N. J.; West, J. L.; Drezek, R. A. *Nano Letters* **2005**, *5*, 709-711.
- (16) O'Neal, D. P.; Hirsch, L. R.; Halas, N. J.; Payne, J. D.; West, J. L. *Cancer Letters* **2004**, *209*, 171-176.
- (17) Halas, N. J. *Mrs Bulletin* **2005**, *30*, 362-367.
- (18) Liao, H.; Nehl, C. L.; Hafner, J. H. *Nanomedicine* **2006**, *1*, 201-208.
- (19) Fortina, P.; Kricka, L. J.; Graves, D. J.; Park, J.; Hyslop, T.; Tam, F.; Halas, N. J.; Surrey, S.; Waldman, S. A. *Trends in Biotechnology* **2007**, *25*, 145-152.
- (20) Ji, X. J.; Shao, R. P.; Elliott, A. M.; Stafford, R. J.; Esparza-Coss, E.; Bankson, J. A.; Liang, G.; Luo, Z. P.; Park, K.; Markert, J. T.; Li, C. *Journal of Physical Chemistry C* **2007**, *111*, 6245-6251.
- (21) Wang, Y.; Qian, W.; Tan, Y.; Ding, S.; Zhang, H. *Talanta* **2007**, *72*, 1134-1140.
- (22) Arruebo, M.; Fernandes-Pacheko, R.; Ibarra, M. R.; Santamaria, J. *Nano Today* **2007**, *2*, 22-32.

- (23) Schipper, M. L.; Iyer, G.; Koh, A. L.; Cheng, Z.; Ebenstein, Y.; Aharoni, A.; Keren, S.; Bentolila, L. A.; Li, J. Q.; Rao, J. H.; Chen, X. Y.; Banin, U.; Wu, A. M.; Sinclair, R.; Weiss, S.; Gambhir, S. S. *Small* **2009**, *5*, 126-134.
- (24) Choi, H. S.; Liu, W.; Misra, P.; Tanaka, E.; Zimmer, J. P.; Ipe, B. I.; Bawendi, M. G.; Frangioni, J. V. *Nature Biotechnology* **2007**, *25*, 1165-1170.
- (25) Sadauskas, E.; Wallin, H.; Stoltenberg, M.; Vogel, U.; Doering, P.; Larsen, A.; Danscher, G. *Particle and Fiber Toxicology* **2007**, *4*, 10.
- (26) Balogh, L.; Nigavekar, S. S.; Nair, B. M.; Lesniak, W.; Zhang, C.; Sung, L. Y.; Kariapper, M. S. T.; El-Jawahri, A.; Llanes, M.; Bolton, B.; Mamou, F.; Tan, W.; Huston, A.; Minc, L.; Khan, M. K. *Nanomedicine* **2007**, *3*.
- (27) Buzea, C.; Pacheco, I. I.; Robbie, K. *Biointerphases* **2007**, *2*, Mr17-Mr71.
- (28) Chan, V. S. W. *Regulatory Toxicology and Pharmacology* **2006**, *46*, 218-224.
- (29) Banerjee, R. *Nanomedicine* **2006**, *1*, 481-485.
- (30) Katz, E.; Willner, I. *Angewandte Chemie-International Edition* **2004**, *43*, 6042-6108.
- (31) Chu, T. C.; Shieh, F.; Lavery, L. A.; Levy, M.; Richards-Kortum, R.; Korgel, B. A.; Ellington, A. D. *Biosensors & Bioelectronics* **2006**, *21*, 1859-1866.
- (32) Winter, J. O.; Liu, T. Y.; Korgel, B. A.; Schmidt, C. E. *Advanced Materials* **2001**, *13*, 1673-1677.
- (33) Winter, J.; Schmidt, C.; Korgel, B. *Quantum Dots, Nanoparticles and Nanowires* **2004**, 789, 119-122 429.
- (34) McCarthy, J. R.; Kelly, K. A.; Sun, E. Y.; Weissleder, R. *Nanomedicine* **2007**, *2*, 153-167.
- (35) Duguet, E.; Vasseur, S.; Mornet, S.; Devoisselle, J. *Nanomedicine* **2006**, *1*, 157-168.
- (36) Liu, Z.; Song, H.; Yu, L.; Yang, L. *Applied Physics Letters* **2005**, *86*, 113109.
- (37) Lyon, J. L.; Fleming, D. A.; Stone, M. B.; Sciffer, P.; Williams, M. E. *Nano Letters* **2004**, *4*, 719-723.
- (38) Larson, T. A.; Bankson, J. A.; Aaron, J.; Sokolov, K. *Nanotechnology* **2007**, *18*, 325101.
- (39) Xia, X.; Liu, Y.; Backman, V.; Ameer, G. A. *Nanotechnology* **2006**, *17*, 5435-5440.
- (40) Heitsch, A. T.; Smith, D. K.; Patel, R. N.; Ress, D.; Korgel, B. A. *Journal of Solid State Chemistry* **2008**, *181*, 1590-1599.
- (41) Hyeon, T.; Lee, S. S.; Park, J.; Chung, Y.; Bin Na, H. *Journal of the American Chemical Society* **2001**, *123*, 12798-12801.
- (42) Lee, D. C.; Mikulec, F. V.; Pelaez, J. M.; Koo, B.; Korgel, B. A. *Journal of Physical Chemistry B* **2006**, *110*, 11160-11166.
- (43) Warning: Iron pentacarbonyl is a highly flammable, very toxic chemical that must be handled with caution.

- (44) Arriagada, F. J.; Osseo-Asare, K. *Journal of Colloid and Interface Science* **1999**, *211*, 210-220.
- (45) Lian, W.; Litherland, S. A.; Badrane, H.; Tan, W.; Wu, D.; Baker, H. V.; Gulig, P. A.; Lim, D. V.; Jin, S. *Analytical Biochemistry* **2004**, *334*, 135-144.
- (46) The APTS coating was performed with 1 mg/mL silica for all sizes of silica particles, despite the variation in total silica surface area. The referenced procedure for the OTMOS coating provided about 2.8 micromoles of OTMOS per mm² of silica. For the 30 nm silica spheres (10 mL, 1 mg/mL), the given reactant ratios provide 3.2 micromoles APTS per mm² of silica. At the same mass concentration (1 mg/mL), the larger silica spheres then have extra APTS per mm² relative to the 30 nm silica spheres. This did not appear to give the larger spheres any advantage over the smaller-sized silica for attachment of Au nanoparticles.
- (47) Duff, D. G.; Baiker, A.; Edwards, P. P. *Langmuir* **1993**, *9*, 2301-2309.
- (48) Brinson, B. E.; Lassiter, J. B.; Levin, C. S.; Bardhan, R.; Mirin, N.; Halas, N. J. *Langmuir* **2008**, *24*, 14166-14171.
- (49) The Au nanoparticle seeds were exposed to the same APTS-silica surface area during their attachment, regardless of the silica particle size. This was to ensure consistent Au attachment during this step. Calculation of nanoparticle concentration and surface area are described in the Supporting Information. A large excess of Au nanoparticles are used for attachment, and silica surface area concentrations in the range of 100-500 cm²/mL provided about the same Au surface coverage. Concentrations of silica surface area lower than this range did not improve the Au surface coverage.
- (50) Harris, D. C. *Quantitative Chemical Analysis*; W. H. Freeman: New York, 2003.
- (51) Christina, V.; Green, C. S. *Journal of Laboratory and Clinical Medicine* **1928**, *13*, 678.
- (52) Note
- (53) Grabar, K. C.; Smith, P. C.; Musick, M. D.; Davis, J. A.; Walter, D. G.; Jackson, M. A.; Guthrie, A. P.; Natan, M. J. *Journal of the American Chemical Society* **1996**, *118*, 1148-1153.
- (54) Sudhir, B.; Kumar, S. *Resonance* **2002**, *7*, 67-81.
- (55) Westcott, S. L.; Oldenburg, S. J.; Lee, T. R.; Halas, N. J. *Langmuir* **1998**, *14*, 5396-5401.
- (56) Note
- (57) Lassiter, J. B.; Aizpurua, J.; Hernandez, L. I.; Brandl, D. W.; Romero, I.; Lal, S.; Hafner, J. H.; Nordlander, P.; Halas, N. J. *Nano Letters* **2008**, *8*, 1212-1218.
- (58) Kumar, P. S.; Pastoriza-Santos, I.; Rodriguez-Gonzalez, B.; Garcia de Abajo, F. J.; Liz-Marzan, L. M. *Nanotechnology* **2008**, *19*, 015606.
- (59) Charamisinau, I.; Happawana, G.; Evans, G.; Rosen, A.; Hsi, R. A.; Bour, D. *Applied Optics* **2005**, *44*, 5055-5068.
- (60) Kim, T.; Lee, K.; Gong, M.; Joo, S. *Langmuir* **2005**, *21*, 9524-9528.
- (61) *CRC Handbook of Chemistry and Physics*; 91st ed.; CRC Press: Boca Raton, FL, 2011.

- (62) Vincent, B. *Journal of Colloid and Interface Science* **1973**, 42, 270-285.
- (63) Lee, K.; Sathyagal, A. N.; McCormick, A. V. *Colloids and Surfaces a-Physicochemical and Engineering Aspects* **1998**, 144, 115-125.
- (64) Suhara, T.; Shimano, F.; Sato, Y.; Fukui, H.; Yamaguchi, M. *Colloids and Surfaces a-Physicochemical and Engineering Aspects* **1996**, 119, 105-114.
- (65) Biggs, S.; Mulvaney, P. *Journal of Chemical Physics* **1994**, 100, 8501-8505.
- (66) Wall, J. F.; Grieser, F.; Zukoski, C. F. *Journal of the Chemical Society-Faraday Transactions* **1997**, 93, 4017-4020.
- (67) Valioulis, I. A.; List, E. J. *Advances in Colloid and Interface Science* **1984**, 20, 1-20.
- (68) Wu, Z.; Xiang, H.; Kim, T.; Chun, M.; Lee, K. *Journal of Colloid and Interface Science* **2006**, 304, 119-124.
- (69) Park, S.; Park, M.; Han, P.; Lee, S. *Bulletin of the Korean Chemical Society* **2006**, 27, 1341-1345.

Chapter 3: Copper Selenide Nanocrystals for Photothermal Therapy[§]

3.1 Introduction

Over the last decade, numerous researchers have been investigating the development of inorganic nanocrystal-based therapeutics to fight cancer.¹ Nanocrystals can enhance the heating and destruction of cancer cells under irradiation with near-infrared (NIR) light, and this is potentially useful for targeting cell death to tumors without damaging adjacent healthy tissue.²⁻⁴ Importantly, nanocrystals that are useful for photothermal therapy must have strong light absorption, particularly at wavelengths in the NIR between 650-950 nm where the absorbance of tissue is at a minimum.⁵

Several types of gold (Au) nanocrystals have large optical extinction coefficients at NIR wavelengths, such as Au nanoshells,⁶ nanorods,⁷ and nanocages.^{8,9} These Au nanocrystals have been widely studied for application in optical diagnostic imaging and therapy, since they can be excited with light at their plasmon resonance frequency to produce both considerable light scattering and heat. The Au nanocrystals are further interesting because their plasmon resonance frequency can be tuned by controlling the nanocrystal size and shape through synthesis parameters.^{10,11} However, Au nanoshells and nanorods are rather large – nanoshells are over 100 nm in diameter,^{10,12,13} and nanorods typically have a 10 nm diameter and 50 nm length.¹⁴ Ideally nanocrystals should have a diameter between 10 – 50 nm to increase bloodstream circulation time,¹⁵⁻¹⁷

[§] Portions of this chapter appear in the following publication: Hessel, C.M.; Pattani, V.P.; Rasch, M.; Panthani, M.G.; Koo, B.; Tunnell, J.W.; Korgel, B.A. *Nano Letters* (2011), 11, 2560-2566. The experiments were performed by C.M. Hessel, V.P. Pattani, M. Rasch, M.G. Panthani, and B. Koo. The publication's text was written by C.M. Hessel, V.P. Pattani, M. Rasch, J.W. Tunnell, and B.A. Korgel. Funding was provided by research grants to J.W. Tunnell and B.A. Korgel.

since larger nanoparticles are removed by the reticuloendothelial system (primarily the liver and spleen) and smaller particles by the renal system.¹⁸⁻²⁰ In addition, Au nanorods are coated by the cetyltrimethylammonium bromide (CTAB) surfactant, which is cytotoxic and difficult to remove completely from nanorod dispersions without compromising the nanorod stability.¹³

Besides Au, other nanomaterials such as germanium nanocrystals,²¹ porous silicon,²² graphene flakes,²³ carbon nanotubes,^{4,24} copper(II) sulfide nanocrystals,²⁵ and carbon-coated iron cobalt nanocrystals²⁶ can generate heat and kill cancer cells during irradiation with NIR light. However there is still a need to develop biocompatible nanocrystals in the 10 – 50 nm diameter size range for photothermal therapy, and copper-based semiconductors have been recognized as biocompatible alternatives to Cd-based nanocrystals as contrast agents for *in vivo* cancer imaging.^{25,27-30} Recently the potential of copper(II) sulfide for photothermal therapy was investigated, but the photothermal transduction efficiency of this nanomaterial was limited.²⁵ In this chapter, it is demonstrated that Cu_{2-x}Se nanocrystals have comparable photothermal transduction efficiency to Au nanorods and nanoshells. When excited by a NIR laser at 800 nm, the Cu_{2-x}Se nanocrystals demonstrate significant heating that kills human colorectal cancer cells.

3.2 Experimental Details

3.2.1 Chemicals

Methanol (Sigma, 99%), ethanol (Sigma, 99%), Poly(isobutylene-alt-maleic anhydride) (Mw~6000 Da, 39 monomer units per molecule, Sigma), anhydrous

tetrahydrofuran (Sigma, $\geq 99.9\%$), anhydrous chloroform (Sigma, $\geq 99\%$), sodium hydroxide pellets (Sigma, $\geq 98\%$), boric acid (Sigma, 99%), copper chloride (anhydrous, beads, $\geq 99.99\%$), selenourea (ACROS, 99.9+%), oleylamine (Sigma, 70%), 3-aminopropyltrimethoxysilane (Sigma, 97%), ammonium hydroxide (Sigma, 28%, ACS reagent grade), ethanol (Sigma, reagent grade), hydrochloric acid (Sigma, 37%, reagent grade), gold (III) chloride trihydrate (Aldrich, $\geq 99.9\%$), potassium carbonate (Sigma, $\geq 99.0\%$, ACS reagent grade), formaldehyde (Sigma, 37 wt. %, ACS reagent grade), cetyltrimethylammonium bromide (Sigma, $\geq 99\%$), sodium borohydride (Sigma, 98%), silver nitrate (Sigma, $\geq 99.0\%$, ACS reagent grade), ascorbic acid (Sigma, $\geq 99.0\%$) and phosphate-buffered saline powder (Sigma) were purchased and used as received. All aqueous solutions were prepared using deionized (DI) water having an 18 M Ω resistance.

3.2.2 Cu_{2-x}Se Nanocrystal Synthesis

All precursor mixtures were prepared in a nitrogen filled glovebox (< 1 ppm O₂) and transferred to a Schlenk line. In a typical synthesis the copper and selenium reactant mixtures were prepared in parallel and combined by hot injection to induce nucleation and growth. The copper reactant was prepared by combining 0.198 g (1 mmol) of CuCl and 10 mL of oleylamine in a 125 mL three neck round bottom flask. The mixture was heated to 130 °C for 10 minutes under nitrogen and vigorous stirring. CuCl dissolved at ~ 90 °C to form a yellow/blue solution. The solution was cooled to 100 °C prior to selenium injection. The selenium reactant was prepared by combining 0.123 g (1.0 mmol) of selenourea and 1 mL of oleylamine in a 25 mL 3 neck round bottom flask. The mixture was heated to 200 °C for 10 min under nitrogen and vigorous stirring. At ~ 170 °C the

selenourea dissolved and the solution became dark brown/red. The solution was cooled to 160 °C, drawn into a syringe, and rapidly injected into the flask containing CuCl and oleylamine. The solution became black upon injection and was heated to 240 °C for 30 min. The flask was removed from the heating mantle and allowed to cool to room temperature. The nanocrystals were precipitated by the addition of 20 mL ethanol, followed by centrifugation at 8000 rpm for 1 min. The blue supernatant was discarded and the green/black nanocrystals were dispersed in anhydrous chloroform. Prior to characterization and polymer coating the dispersions were centrifuged at 8000 rpm for 5 min to remove aggregated, poorly-capped nanocrystals. A typical reaction yields about 100 mg of nanocrystals. Several batches of nanocrystals were prepared for this investigation; some batches were prepared by the author of this dissertation, and some were prepared by Colin Hessel.

3.2.3 Gold Nanoshell Synthesis

Gold nanoshells were grown around amine-passivated silica core particles as described in Chapter 2. Briefly, 100 nm diameter colloidal silica spheres (Nissan Chemical Co.) were reacted with 3-aminopropyltrimethoxysilane and NH₄OH in ethanol for 12 hr. The silica spheres were precipitated by centrifugation and dispersed in deionized water titrated to pH 4 with 1 mM HCl. The amine-passivated silica spheres were mixed with an aqueous solution of 2 nm Au nanoparticles to promote Au surface adsorption. The Au-decorated silica spheres were purified from the excess Au nanoparticles by centrifugation and dispersed in deionized water. Au nanoshells were grown by mixing the Au decorated silica spheres with Au plating solution (0.4 mM

HAuCl₄ in 1.8 mM K₂CO₃), followed by the addition of 30% formaldehyde solution that served as the reducing agent. The Au nanoshells were collected by centrifugation at 3000g for 5 minutes and dispersed in deionized water. The Au nanoshell thickness was tuned to approximately 10 nm by varying the amount of Au-decorated silica spheres added to the Au plating solution.

3.2.4 Gold Nanorod Synthesis

Gold nanorods passivated with cetyltrimethylammonium bromide (CTAB) were synthesized as previously described.¹¹ In brief, a 10.6 mL aqueous Au nanocrystal seed solution was prepared by mixing HAuCl₄ (0.24 mM) with NaBH₄ (0.57 mM) in the presence of CTAB (94 mM). The 10.3 mL rod growth solution was prepared by combining CTAB (98 mM), HAuCl₄ (0.49 mM), AgNO₃ (0.094 mM), and ascorbic acid (0.54 mM) in deionized water. Nanorod growth was initiated by injecting a 12 μ L aliquot of the seed solution into the growth solution, gently mixing for 2-3 seconds, and then storing at 27°C for at least 12 hours. The nanorods were collected by centrifuging to a pellet at 8000g for 10 minutes, and then dispersed in deionized water. The nanorod dimensions were tuned to 49 \times 13 nm (aspect ratio: 3.8) by varying the amounts of AgNO₃ or seed solution added to the growth solution.

3.2.5 Commercial Gold Nanorods and Nanoshells

Concentrated Au nanorod and nanoshell solutions were obtained from Nanospectra Biosciences, Inc. (Houston, TX). The fabrication process for both nanoparticles has been discussed in detail previously.^{6,31} The Au nanorods are 23 \times 7 nm

(aspect ratio: 3.3). The nanoshells are 145 nm in diameter, with an 8 nm thick Au shell. The Au nanorods and nanoshells are conjugated with Polyethylene Glycol.

3.2.6 Amphiphilic Polymer Synthesis

The amphiphilic polymer synthesis was adapted from a published protocol.³² In a capped, single neck round bottom flask, 100 mL of anhydrous THF, 15 mmol (3.45 mL) of oleylamine, and 3.084 g of poly(isobutylene-alt-maleic anhydride) (20 mmol of monomer units) were added sequentially to form a turbid white solution. The flask was sonicated for 1 min to suspend the insoluble polymer, and was heated at 60 °C for 3 hr under vigorous stirring. The suspension became clear after 15 minutes of stirring. After 3 hours, the solution was cooled to room temperature and reduced in volume to 20 mL with a rotary evaporator. The clear solution was stirred again at 60 °C for 12 hours under vigorous stirring to ensure complete coupling between the polymer and oleylamine. The solution was cooled to room temperature and the remaining solvent was removed with a rotary evaporator, yielding the pale yellow, solid amphiphilic polymer. The solid polymer was transferred to a nitrogen filled glove box (< 0.1 ppm O₂) and dissolved in 25 mL of anhydrous CHCl₃ to give a monomer unit concentration of 0.8 M. The amphiphilic polymer solution was stored in a glass vial within the glovebox until use.

3.2.7 Cu_{2-x}Se Nanocrystal Polymer Coating

The Cu_{2-x}Se nanocrystal polymer coating was adapted from a protocol previously applied to other hydrophobic nanocrystal materials.³² In a 50 mL round bottom flask, 53 µL of the amphiphilic polymer stock solution (0.8 M monomer units in CHCl₃), 0.40 mL

of the oleylamine passivated nanocrystals (4.0 mg/mL in anhydrous CHCl_3), and 2.55 mL of anhydrous CHCl_3 were combined and vortexed with magnetic stirring for 15 minutes at room temperature. The solvent was removed by rotary evaporation to yield a green Cu_{2-x}Se -polymer film on the inner wall of the flask. 2.0 mL of aqueous sodium borate buffer (SBB, 50 mM borate, pH 12) was added to the flask and stirred for 15 minutes at room temperature to disperse the Cu_{2-x}Se -polymer. Once suspended, 13.0 mL of DI water was added to the flask to dilute the nanocrystals. The aqueous Cu_{2-x}Se nanocrystal solution was passed through a 0.2 μm -pore syringe filter (Corning, PES membrane), followed by a 0.1 μm -pore syringe filter (Whatman, inorganic membrane). The filtered nanocrystal solution was placed in an ultracentrifugation filter (Amicon Ultra, regenerated cellulose membrane, 50 kDa molecular weight cutoff) and centrifuged at 4000g for 4 minutes at room temperature. The colorless filtrate was discarded, and the concentrated nanocrystal retentate solution was diluted to 15.0 mL with aqueous, sterile-filtered phosphate buffered saline (PBS, 150 mM, pH 7.4). The ultracentrifugal filtration process was repeated two more times using PBS to dilute the nanocrystal retentate solution. The nanocrystal solution was dialyzed against PBS at 150 mM and pH 7.4 for 24 hr. The final aqueous nanocrystal solution was stored in a glass vial under ambient conditions until use.

3.2.8 Material Characterization

Electron Microscopy. The Cu_{2-x}Se nanocrystals were examined by low and high resolution transmission electron microscopy (TEM and HRTEM). TEM images were acquired with either a Phillips EM208 TEM operated at 80 kV accelerating voltage or a

JEOL 2010F TEM operated at 200 kV. The latter was operated by Matthew Panthani.

The nanocrystals were imaged on 200 mesh continuous carbon-coated copper TEM grids (Electron Microscopy Sciences, catalog # CF200-Cu-50), drop-cast from 5 μ L of dilute chloroform dispersions of the Cu_{2-x}Se nanocrystals. In the case of the aqueous polymer-coated nanocrystals, a negative staining procedure was used to visualize the polymer coating. A 5 μ L drop of aqueous sample was placed on a carbon-coated copper TEM grid and incubated under ambient conditions for 1 minute. A torn piece of filter paper was used to wick off the liquid from the edge of the TEM grid, and the grid was incubated another minute. Then, 5 μ L of a 1.0% w/w aqueous solution of ammonium molybdate (Electron Microscopy Sciences) was added to the grid. After 5 seconds, the liquid was carefully wicked off of the grid using a fresh piece of filter paper, and the grid was allowed to dry in air for over an hour.

Powder X-ray Diffraction. XRD experiments were performed by Colin Hessel. The data was obtained for 5 mg of Cu_{2-x}Se nanocrystals on quartz substrates using a Bruker-Nonius D8 Advance diffractometer. Scans of $2\theta^\circ$ were performed from $10 - 90^\circ$ in $0.02 (2\theta^\circ)$ increments at a scan rate of $12.0^\circ/\text{minute}$ for 6 hours.

Thermogravimetric Analysis (TGA). TGA was performed by drying 3 mg of Cu_{2-x}Se from a chloroform dispersion in a 70 μ L alumina crucible at room temperature, loading the crucible into a Mettler Toledo TGA-1, and heating the crucible from room

temperature to 800°C under 1 mL/minute N₂(g) purge while measure sample mass and temperature versus time.

Inductive-coupled plasma mass spectrometry (ICP-MS). ICP-MS was performed on the polymer-coated Cu_{2-x}Se nanocrystals by adjusting the absorbance at 800 nm to 1.0 and then digesting the inorganic material. Digestion was performed in containers cleaned with trace metal purity nitric acid and deionized water. The trace metal purity nitric acid (69% v/v) was used in all steps. The nanocrystals were concentrated on a centrifuge filter (100 kDa molecular weight cutoff) and dispersed in 10 mL deionized water two times, in order to remove salts from the dispersion. A 0.5 mL sample of aqueous polymer-coated Cu_{2-x}Se nanocrystals was added to a clean 50 mL round bottom flask, and the water was removed by rotary evaporation at 20 mbar pressure and 40°C temperature. Next 3.0 mL of nitric acid (69%) was added to the dry nanocrystal film, the flask was sealed with a glass stopper and wrapped with parafilm, and then it was stored for 2 days to digest the nanocrystals. Subsequently, 86 mL of deionized water was added to a clean plastic bottle, followed by 2.5 mL of the digested nanocrystal solution. The sample was submitted to the ICP-MS analysis facility in the University of Texas Geology Department for characterization. In addition, Cu and Se standards were prepared at 200 ppb concentration by dissolving high purity Cu⁰ and Se⁰ solids in nitric acid and diluting with nitric acid (2% v/v in deionized water) in a clean plastic bottle. For the Cu standard, ICP-MS analysis detected that [Cu] = 216 ppb and [Se] = 0.1 ppb. For the Se standard, ICP-

MS analysis detected [Cu] = 0.2 ppb and [Se] = 204 ppb, verifying correct calibration of the instrument.

Absorbance Spectroscopy, Light Scattering, and Zeta Potential. Absorbance spectra were acquired either with a Cary 500 UV/vis spectrophotometer or a Beckman Coulter DU720 using a quartz cuvette with a 10 mm optical path length. Zeta potential was measured by laser Doppler anemometry using a Zetasizer Nano ZS instrument (Malvern). Polymer-coated Cu_{2-x}Se nanocrystals dispersed in deionized water ($\sim 10^{16}$ nanocrystals/mL) were loaded into a disposable folded capillary cell (Malvern, 1.5 mL volume) equipped with two electrodes. The cell was placed in the Zetasizer, which applied an alternating electric field across the cell. Particle mobility in the electric field was measured with the Zetasizer by recording the phase shift of an incident laser beam. Particle mobility was then converted to zeta potential by the Zetasizer software using Smoluchowski theory.³³ The average hydrodynamic diameter of the polymer coated Si nanocrystals in PBS was measured by dynamic light scattering using the Zetasizer instrument. The particles were placed in the disposable capillary cell at about 10^{16} nanocrystals/mL concentration for light scattering measurements. The Zetasizer detected the intensity of backscattered photons at a 173° angle from an incident 4 mW He-Ne (633 nm) laser over a time interval of 10 seconds, using a sample time (τ) of 0.5 microseconds. The hydrodynamic diameter was then extracted from the light scattering data using the method of cumulants.³⁴

3.2.9 Photothermal Heating and Transduction Efficiency

Photothermal heating experiments were performed with Varun Pattani in Professor James Tunnell's research lab in the University of Texas Biomedical Engineering department. The heating characteristics of all photothermal materials were measured with an infrared camera (FLIR Systems SC4000, Boston, MA), using an 800 nm diode-laser (Opto Power Corp., Tucson, AZ) focused to 6 mm with a biconvex lens as the excitation source. All materials were dispersed in deionized water to an optical density (OD) equal to 1.0 at 800 nm and prior to measurement. Solutions were sonicated for 1 min and 300 μ L aliquots were transferred to a 96-well plate. Deionized water was used as the control. The laser power was calibrated to a fluence rate of 2 W/cm² with a power meter (Newport Corp., Irvine, CA). Measurements were collected by irradiating each well for 5 min and simultaneously collecting the solution temperature using the infrared camera and ThermoVision software (FLIR Sys., Boston, MA). All comparisons and analyses were performed in MATLAB (The Mathworks Inc., Natick, MA).

3.2.10 *In Vitro* Cytotoxicity Studies

Cytotoxicity studies were performed by Varun Pattani in Professor James Tunnell's research lab in the University of Texas Biomedical Engineering department. Human colorectal carcinoma HCT-116 cells (ATCC, Manassas, VA) were grown in 12-well plates in McCoy's 5A Modified Medium (ATCC) supplemented with fetal bovine serum (10% /volume) (Invitrogen, Carlsbad, CA) and penicillin streptomycin (1% /volume) (Invitrogen). Cells incubated for approximately two days until 80% confluence was reached. After the desired confluence was reached, the medium was removed and the

cells rinsed with phosphate buffered saline (PBS) (Thermo Fisher Scientific, Waltham, MA), and charged a combination of new media (0.375 mL) along with a volume of Cu_{2-x}Se dispersion (0.125 mL, 157 mg/L) to give a solution concentration of 39 mg/L (2.8×10^{15} NCs/L, equivalent concentration to 0.25 OD by absorbance spectroscopy). Cells were incubated for 0.5 hr, 1 hr, 3 hr, and 6 hr at 37°C. Control cells received fresh nanoparticle-free supplemented media and were incubated for 6 hours. After the incubation the media was replaced to remove all unbound Cu_{2-x}Se nanocrystals. The cells were exposed to a membrane permeability stain, Trypan blue (Invitrogen), to assess cell death. Dead cells absorb the dye, exhibiting a blue color, whereas viable cells look clear and normal under a brightfield microscope. The cells were incubated for 3 min with Trypan Blue, rinsed with PBS, and quickly imaged. Brightfield images were collected with a brightfield microscope (Carl Zeiss AG Invertoskop D, Germany) equipped with a Powershot G12 camera (Canon Inc, Tokyo, Japan).

3.2.11 *In Vitro* Photothermal Therapy with Cu_{2-x}Se Nanocrystals

Photothermal therapy studies were performed by Varun Pattani in Professor James Tunnell's research lab in the University of Texas Biomedical Engineering department. For the photothermal therapy experiments, cells were cultured by the above method by adding Cu_{2-x}Se nanocrystals to the supplemented medium at the equivalent concentration of 0.25 OD. The cells containing Cu_{2-x}Se nanocrystals were incubated 30 min at 37°C. Control cells received fresh nanoparticle-free supplemented medium and were incubated as well for 30 minutes. After incubation the nanoparticle medium was replaced to remove all unbound nanoparticles, and added fresh supplemented medium to

the cells. The cells were placed under the infrared camera and irradiated with the NIR diode laser (ThorLabs L808P1WJ, Newton, NJ) for 5 minutes at 30 W/cm^2 and a 1 mm circular spot. The irradiation was performed on both the cells that received the nanoparticle medium as well as the control cells. Cells were incubated for one hr at 37°C to allow any cell death processes to occur. The cells were exposed to the Trypan Blue by the same method as above to observe cell death. All imaging was performed with a brightfield microscope equipped with a Canon Powershot G12.

3.3 Results and Discussion

3.3.1 Cu_{2-x}Se Nanocrystal Characterization

Structural Characterization. The Cu_{2-x}Se nanocrystals were synthesized by arrested precipitation in a hot organic solvent. On the basis of a modification of methods developed for CuInS_2 and $\text{Cu}(\text{In}_x\text{Ga}_{1-x})\text{Se}_2$ nanocrystals,^{35,36} two hot reaction reactant solutions of copper(I) chloride and selenourea in oleylamine are combined to form a dark green colloidal dispersion of oleylamine-capped Cu_{2-x}Se nanocrystals, as diagrammed in Figure 3.1. TEM images show that the nanocrystals are predominantly spherical in shape with crystalline cores having an average diameter of $16 \pm 1 \text{ nm}$. The crystal structure, composition (Cu/Se ratio), and the particle shape were found to vary with subtle differences in reactant purity, supplier, injection temperature, and oxygen content, similar to what Manna and co-workers also recently observed in their Cu_{2-x}Se nanocrystal synthesis.³⁷ The Cu/Se ratios in the nanocrystals measured using ICP-MS were found to vary, with Cu/Se ratios as low as $\text{Cu}_{1.67}\text{Se}$ in some cases. A collection of XRD patterns

from Cu_{2-x}Se nanocrystals synthesized under modified reaction conditions is listed in Figure 3.2 and Table 2.1. There does not appear to be an obvious correlation between nanocrystal size, shape, XRD pattern, and λ_{max} . Despite these variations, all of the Cu_{2-x}Se nanocrystals were found to exhibit qualitatively similar absorbance spectra with an intense NIR absorbance peak and produced similar photoinduced heating.

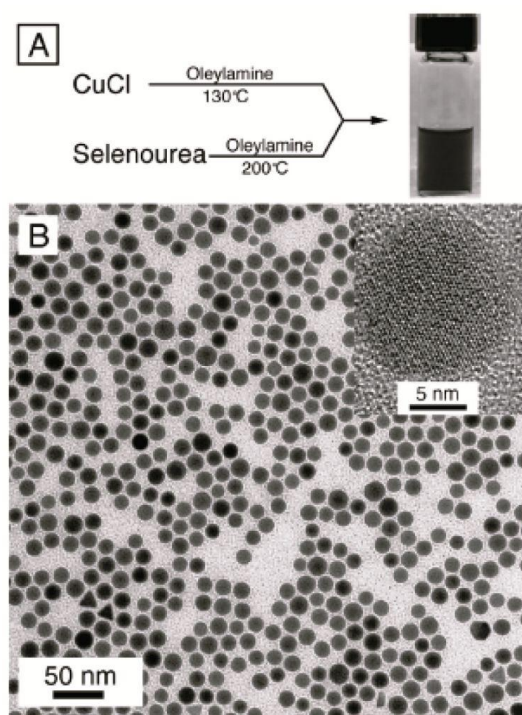


Figure 3.1. (A) Synthesis scheme for the Cu_{2-x}Se nanocrystals, and a vial of the oleylamine-coated nanocrystals dispersed in chloroform. (B) TEM images of Cu_{2-x}Se nanocrystals. The average nanocrystals diameter is 16 ± 1 nm. Images produced by Colin Hessel and Matthew Panthani.

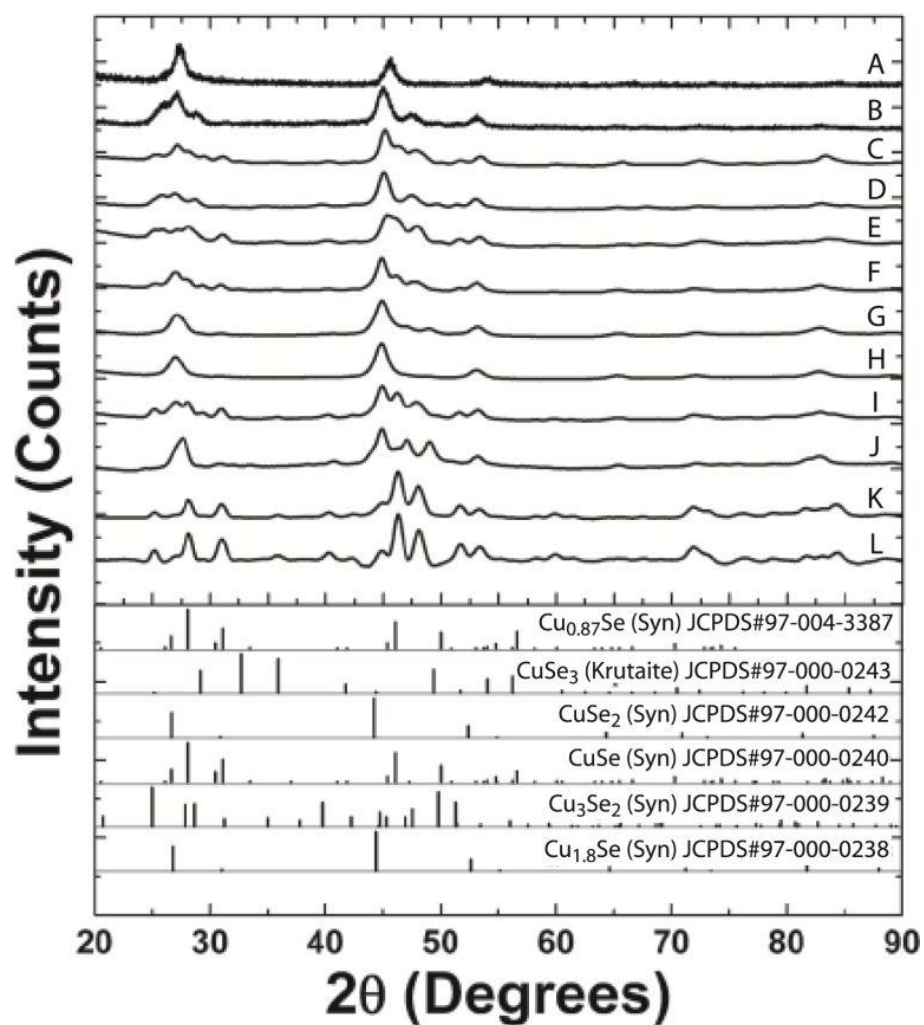


Figure 3.2. X-ray diffraction patterns for Cu_{2-x}Se nanocrystals synthesized using different reaction times, solvent purity, and temperature. The synthesis conditions corresponding to each curve (A-L) are listed in Table 3.1. XRD peak positions for various phases of Cu_{2-x}Se are included for reference. Data collected and graphed by Colin Hessel.

Table 3.1. Reaction conditions, solvent purity, nanocrystal diameter and morphology, and absorbance peak maxima wavelength (λ_{max}) for the copper selenide reactions corresponding to the data in Figure 3.2.

Reaction	Reaction Time (min.)	Reaction Temperature (°C)	Oleylamine Purity	Morphology	Diameter (nm)	λ_{max} (nm)
A	30	220	99.97	sphere	12	1000
B	30	220	99.97	sphere	12	1000
C	60	240	99.97	sphere	12	1100
D	30	240	99.97	sphere	12	1050
E	30	240	99.7	irregular*	na*	1100
F	15	240	98	irregular*	na*	1150
G	30	240	98	sphere	14	1200
H	30	240	98	disc	10	1250
I	90	240	98	disc, sphere	12	1250
J	60	240	98	disc, sphere	13	1100
K	30	240	98	irregular*	na*	1250
L	60	240	99.9	sphere	11	1050

* These batches of nanocrystals were of poor quality – very heterogeneous in size and shape.

Thermogravimetric Analysis (TGA)

The Cu_{2-x}Se nanocrystals were heated to 800°C in a TGA experiment to vaporize the oleylamine and determine the mass fraction of oleylamine relative to Cu_{2-x}Se in the

nanocrystals. The TGA heating curves are plotted in Figure 3.3. In spite of purging the TGA furnace with nitrogen, the nanocrystals still seem to oxidize while heated from room temperature to about 100°C, based on the increase in mass. Oxidation of Cu₂Se in air has been demonstrated.³⁸ It is probable that this oxygen contamination comes from the nitrogen tank feeding the instrument – high purity nitrogen gas still contains trace amounts of oxygen because it is prepared by distilling from air.³⁹ In spite of some initial oxidation, the mass change from 150°C to 600°C is due to vaporization of oleylamine bound to the copper selenide as well as excess oleylamine (not bound). The vaporization of excess oleylamine is distinguished from bound oleylamine by comparing to the TGA curve of pure oleylamine heated at the same rate. The excess oleylamine should be completely vaporized by 250°C, and the bound oleylamine vaporizes over the temperature range marked by the arrows in Figure 3.3. The change in sample mass percentage due to excess plus bound oleylamine is 10%, and this was taken to be the total oleylamine mass fraction in the sample. Above 600°C, the mass decreases significantly, and we attribute this to vaporization of selenium from the nanocrystals, given that pure selenium's vapor pressure increases from 100 Pa to 10 kPa over the 600 – 800°C temperature range. The mass loss over 600-800°C is about 25%, while for Cu₂Se the mass fraction of Se is expected to be 38%, so only a portion of the Se vaporizes from the Cu_{2-x}Se nanocrystals over this temperature range (not surprising, since the Se will have to diffuse out of the solid nanocrystals to vaporize).

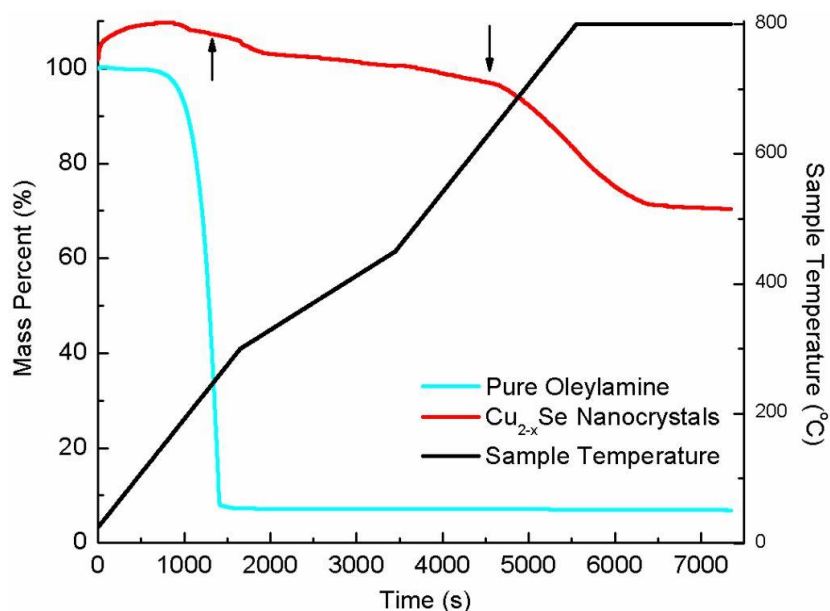


Figure 3.3. TGA of Cu_{2-x}Se nanocrystals and pure oleylamine. The arrows indicate the temperature range over which oleylamine bound to the nanocrystals vaporizes. At temperatures lower than marked by the left arrow, the copper selenide oxidizes and excess oleylamine vaporizes. At temperatures greater than the right arrow, selenium starts to vaporize.

Absorption Coefficient.

The molar extinction coefficient of the Cu_{2-x}Se nanocrystals (ϵ_m) was determined by measuring the absorbance spectra for various solutions with different nanocrystal concentrations, as shown in Figure 3.4. The extinction coefficient in terms of nanocrystal mass (ϵ) was obtained by fitting absorbance versus concentration data to the Beer Lambert Law.

$$A(\lambda) = \epsilon(\lambda) \cdot L \cdot C \quad (3.1)$$

Where A is the absorbance at wavelength λ , L is the cuvette pathlength (1 cm), and C is the nanocrystal concentration (g/L). For Cu_{2-x}Se nanocrystals in toluene, the concentration of nanocrystals was determined by taking a 1 mL aliquot of the dispersion, drying it completely on a rotary evaporator in a vial of known mass, and then measuring the mass of nanocrystals in the vial on a balance. The extinction coefficient (ϵ in L/g-cm units) was determined by evaluating the slope of Absorbance versus Concentration data at each wavelength in the spectrum, as shown in Figure 3.5. This experimentally calculated extinction coefficient contains mass contributions from both the Cu_{2-x}Se nanocrystals and the oleylamine ligands (bound plus excess oleylamine). The mass fraction of Cu_{2-x}Se in the nanocrystals was determined by TGA to be about 90%, the diameter of Cu_{2-x}Se is 16 nm from TEM, and the bulk solid density of Cu_{2-x}Se is 5.8 g/cm³,⁴⁰ therefore the molar mass of the nanocrystals (M_{NC} , in units of grams per mole of nanocrystals) and the molar extinction coefficient were calculated using the following expressions:

$$M_{NC} = \left(\frac{\frac{\pi}{6} (16 \text{ nm})^3}{\text{Nanocrystal}} \right) \cdot \left(\frac{10^{-21} \text{ cm}^3}{\text{nm}^3} \right) \cdot \left(\frac{5.8 \text{ g Cu}_{2-x}\text{Se}}{\text{cm}^3} \right) \left(\frac{1 \text{ g Nanocrystals}}{0.9 \text{ g Cu}_{2-x}\text{Se}} \right) \left(\frac{6.02 \times 10^{23} \text{ Nanocrystals}}{\text{mole}} \right) = 8.0 \times 10^6 \text{ g / mole}$$

(3.2)

$$\epsilon_m \left(\text{L mol}^{-1} \text{ cm}^{-1} \right) = \epsilon \left(\text{L g}^{-1} \text{ cm}^{-1} \right) \cdot M_{NC}$$

(3.3)

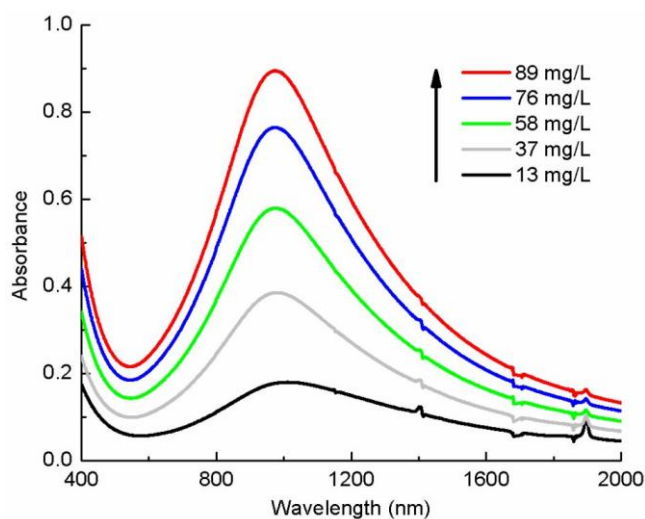


Figure 3.4. Room temperature UV-vis-NIR absorbance spectra for Cu_{2-x}Se nanocrystals in toluene at various solution concentrations to determine the Cu_{2-x}Se nanocrystal extinction coefficient.

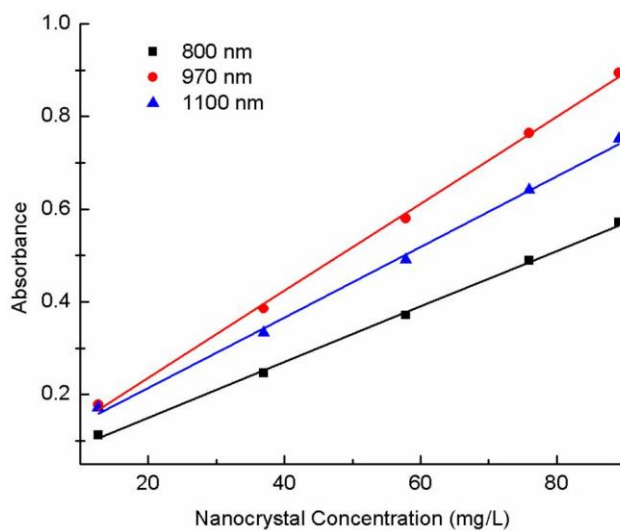


Figure 3.5 Plots of linear fits to sets of absorbance versus concentration data at three different wavelengths for Cu_{2-x}Se nanocrystal dispersions in toluene. The wavelengths are 800 nm (black, squares), 970 nm (red, circles), and 1100 nm (blue, triangles).

The molar extinction coefficient versus wavelength measured for Cu_{2-x}Se nanocrystals in toluene is plotted in Figure 3.6. There is a broad absorbance peak centered at 970 nm with monotonically rising absorbance at wavelengths below 500 nm. Similar absorbance features were observed by Manna and co-workers³⁷ and Garcia and co-workers⁴¹ and were assigned to direct and indirect interband transitions for Cu_{2-x}Se . Bulk Cu_{2-x}Se has direct and indirect band gap energies of 2.1 to 2.3 eV (540 to 590 nm) and 1.2 to 1.4 eV (1030 to 880 nm), respectively. We also assign the low wavelength (less than 600 nm) absorbance to interband optical transitions. However, we assign the NIR absorbance peak to a surface plasmon resonance. Cu_{2-x}Se is a p-type semiconductor with a relatively high carrier (holes) concentration and exhibits strong free carrier absorption,⁴² which in the case of the Cu_{2-x}Se nanocrystals results in a surface plasmon resonance. Nanocrystals of analogous non-stoichiometric copper sulfides (Cu_{2-x}S) in which Cu deficiencies also lead to high densities of holes have also exhibited NIR absorbance peaks.⁴³⁻⁴⁵ The NIR absorption band from Cu_{2-x}S was also originally assigned to an indirect interband transition;⁴³⁻⁴⁵ however, Burda and co-workers have clarified using Drude theory that the NIR absorption is actually a surface plasmon resonance.⁴⁵ Very recently, Luther and co-workers revealed that Cu_{2-x}S nanocrystals with vacancy concentrations of $\sim 10^{21}$ holes/cm³ exhibit surface plasmon resonance bands, thus confirming that sub-stoichiometric copper(I) chalcogenides have absorption characteristics similar to those of metals.⁴⁶ The high molar extinction coefficients measured for the Cu_{2-x}Se nanocrystals (Table 3.2) are also consistent with plasmon

absorption⁴⁶ and are orders of magnitude higher than expected for an indirect optical transition and considerably higher than strongly absorbing organic dyes or direct band gap semiconductor quantum dots (Table 3.2).

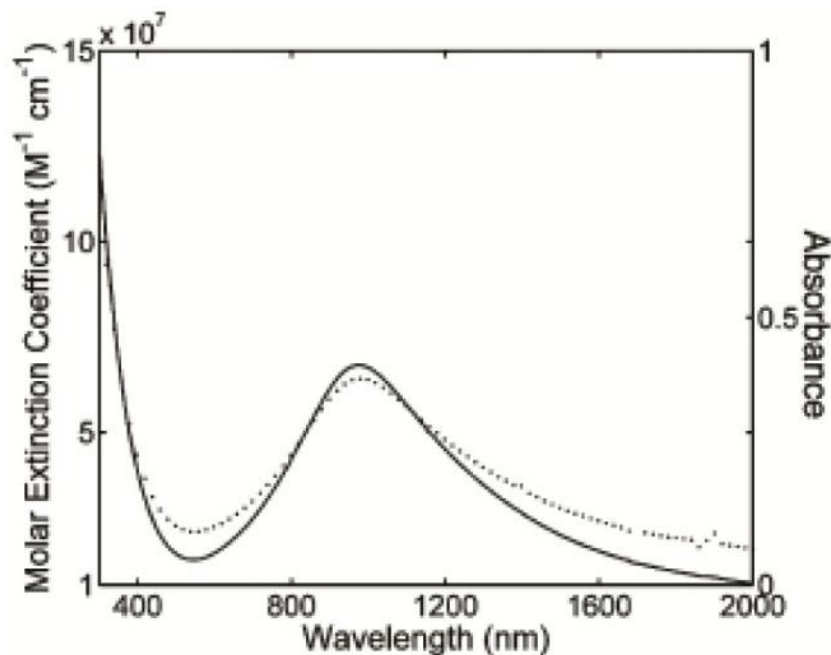


Figure 3.6. Absorbance (dotted line) and molar extinction coefficient (solid line) for $Cu_{2-x}Se$ nanocrystals plotted against wavelength. The molar extinction coefficient was calculated for $Cu_{2-x}Se$ nanocrystals in chloroform as described in the text. The molar extinction coefficient reaches a maximum of $7.7 \times 10^7 M^{-1}cm^{-1}$ at 970 nm. The absorbance spectrum is of $Cu_{2-x}Se$ nanocrystals coated with amphiphilic polymer and dispersed in water. Plot was generated by Colin Hessel.

Table 3.2. Molar Extinction Coefficients (per mole of Molecules of Nanocrystals) of Common Photoabsorbers, Including Molecular Dyes, Direct Bandgap Semiconductors, and Photothermal Materials

Photoabsorber	Dimension (nm)	Molar Extinction Coefficient ($M^{-1}cm^{-1}$)	Wavelength (nm)
Rhodamine 6G ⁴⁷	Molecular	1.2×10^5	530
Malachite Green ⁴⁷	Molecular	1.5×10^5	617
CdX (X = S, Se, Te) ⁴⁸	R = 2	$2 - 5 \times 10^5$	Exciton maximum
Carbon nanotubes ⁴	R = 0.6, L = 150	7.9×10^6	808
Copper selenide	R = 8	7.7×10^7	970
Gold nanospheres ⁴⁹	R = 20	7.7×10^9	530
Gold nanorods ⁵⁰	R = 5, L = 27	1.9×10^9	650
Gold nanoshells ⁵¹	R ₁ = 55, R ₂ = 65	2×10^{11}	800

3.3.2 Cu_{2-x}Se Nanocrystal Stability and Amphiphilic Polymer Coating

The hydrophobic oleylamine-coated Cu_{2-x}Se nanocrystals were coated with amphiphilic polymer composed of a poly(maleic anhydride) backbone with hydrophilic carboxylic acid groups and hydrophobic oleylamine side chains using techniques described previously.⁵² For a polymer-coated Cu_{2-x}Se dispersion with an absorbance of 1.0 at 800 nm, the concentrations of Cu and Se were determined by ICP-MS analysis to be 530 μ M (34 μ g/mL) and 320 μ M (25 μ g/mL) respectively, so the nanocrystal

stoichiometry is $\text{Cu}_{1.67}\text{Se}$. A sketch of the polymer coating process is shown in Figure 3.7. The polymer forms micelles in water, which encapsulate the nanocrystals as shown in the TEM image of Figure 3.8. Either individual nanocrystals or small clusters (2-5 per cluster) of nanocrystals are encapsulated in micelles – that is, no massive aggregates of nanocrystals with 100 or more nanocrystals are present (these would be removed by the filtration process during encapsulation procedure). The amphiphilic polymer coating enables dispersion of the nanocrystals in aqueous media under physiological conditions i.e., phosphate buffered saline (PBS) at pH 7.4 and 150 mM ionic strength.⁵² The polymer coating does not affect the wavelength of the NIR absorbance peak compared to the toluene dispersions of nanocrystals, as shown in Figure 3.6. In PBS, the polymer-coated nanocrystals have a hydrodynamic diameter of 39 nm and a zeta potential of -40 mV according to dynamic light scattering and electrophoretic mobility measurements, respectively. Therefore, the Cu_{2-x}Se nanocrystals are well stabilized in water by the anionic polymer coating. Unfortunately, many empty polymer micelles, with size comparable to the polymer-coated nanocrystals, are retained with the nanocrystals after filtration.

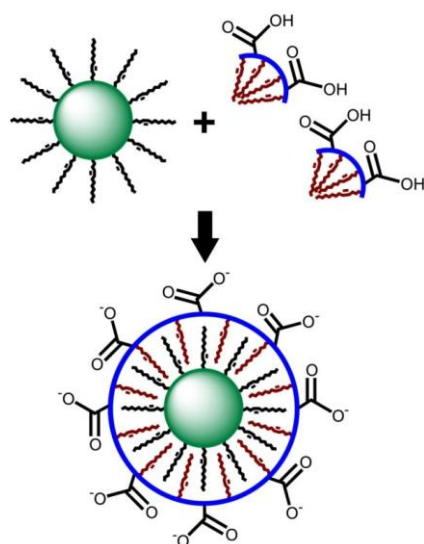


Figure 3.7. Amphoteric polymer encapsulation of Cu_{2-x}Se nanocrystals. Combining oleylamine-coated Cu_{2-x}Se nanocrystals (green sphere) and the amphiphilic poly(maleic anhydride)-based polymer leads to encapsulation of the Cu_{2-x}Se nanocrystals within a hydrophilic, carboxylic acid coated exterior that enables the nanocrystals to disperse in aqueous media.

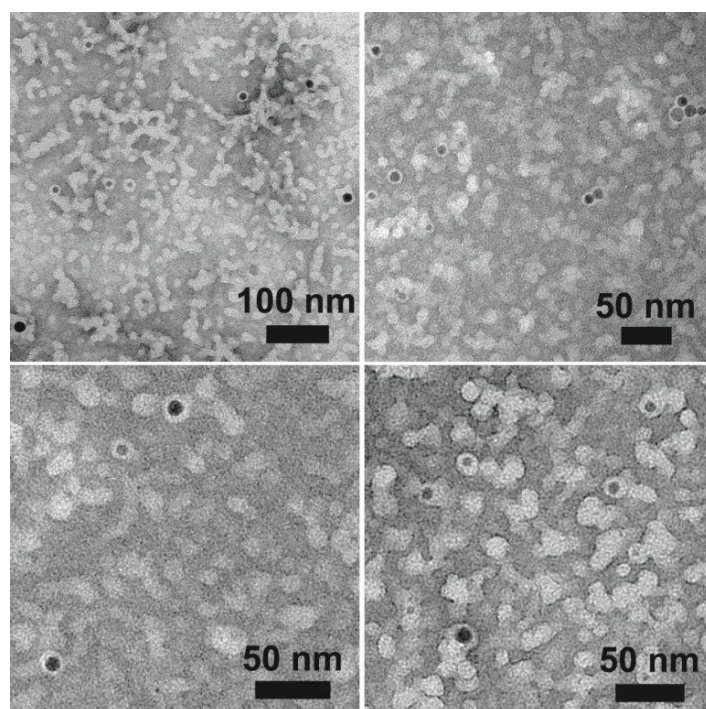


Figure 3.8. Low Resolution TEM at 25°C of amphiphilic polymer-coated Cu_{2-x}Se nanocrystals dried from water onto a TEM grid. The background was stained with ammonium molybdate to provide negative contrast to the amphiphilic polymer, showing that there are empty micelles present alongside the polymer-coated nanocrystals. The average thickness of the polymer coating is 3.0 ± 0.5 nm.

The stability of the Cu_{2-x}Se nanocrystals within the polymer micelles was demonstrated by measuring absorbance versus time. The absorbance of the polymer-coated Cu_{2-x}Se nanocrystal dispersion is plotted versus time in Figure 3.9, showing that the nanocrystals remain well-dispersed in water without destruction or dissolution of the Cu_{2-x}Se core. In comparison, the absorbance versus time also is plotted in Figure 3.9 for Cu_{2-x}Se dispersed in chloroform by sonication immediately prior to the start of the measurements. For the chloroform dispersion of just oleylamine-coated Cu_{2-x}Se

nanocrystals, the absorbance decreases rapidly over 24 hours as the nanocrystals settle out of solution.

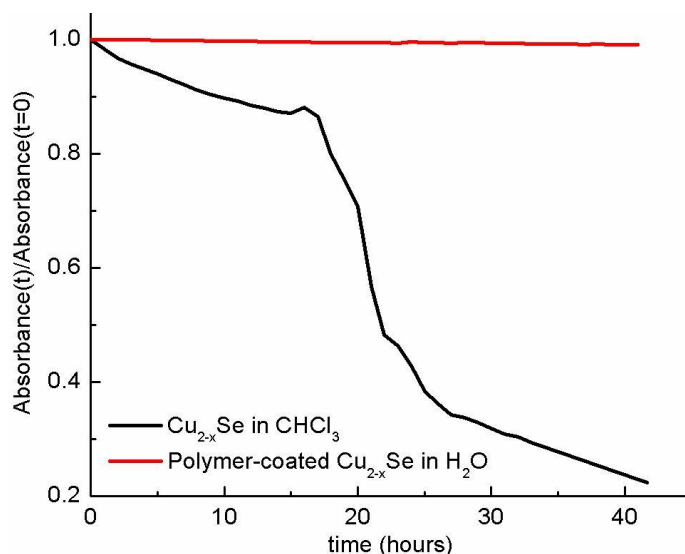


Figure 3.9. Absorbance of Cu_{2-x}Se nanocrystal dispersions over time. The absorbance is normalized to the initial absorbance at 0 hours, which was adjusted to be between 0.8 – 1.0 before starting the experiment. The nanocrystal dispersions were left undisturbed in the absorbance spectrophotometer for the duration of the measurement. The Cu_{2-x}Se nanocrystals dispersed in chloroform are coated with oleylamine only and there is no amphiphilic polymer present.

3.3.3 Gold Nanoshell and Nanorod Characterization

Electron Microscopy. TEM characterization of Au nanoshells and nanorods is provided in Figure 3.10. The synthesized Au nanorods had an average length of 49 nm and diameter of 13 nm, while the synthesized nanoshells had a 135 nm diameter (Au plus SiO_2) and an approximate shell thickness of 10 nm. The commercial Au nanorods had an

average length of 23 nm and diameter of 7 nm, while the commercial nanoshells had a 145 nm diameter (Au plus SiO₂) and a shell thickness of 7.5 nm.

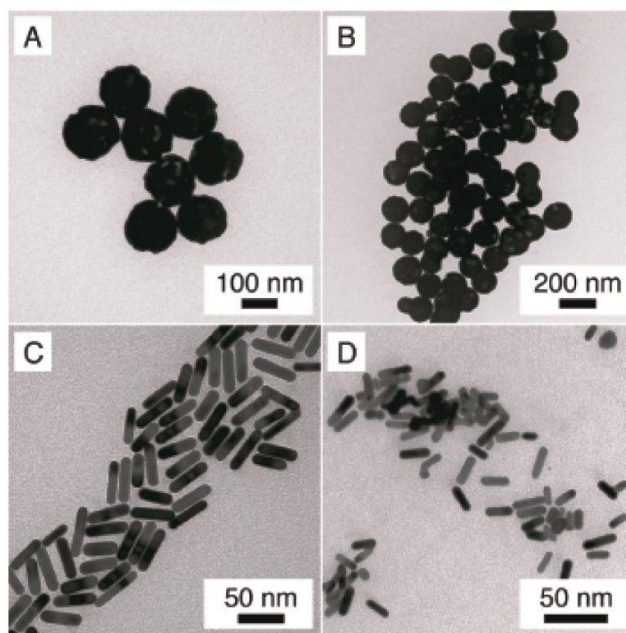


Figure 3.10. TEM images of Au nanoshells and nanorods. Synthesized Au nanoshells (A) are 135 nm in diameter with a shell thickness of about 10 nm, while commercially obtained Au nanoshells (B) are 145 nm in diameter with a 7.5 nm Au shell thickness. Synthesized Au nanorods (C) have a 49 nm length and 13 nm diameter, while the commercial nanorods (D) have a 23 nm length and 7 nm diameter.

3.3.4 Photothermal Heating and Transduction Efficiency

A significant amount of heat was evolved when the NIR plasmon resonance of the nanocrystals was optically excited. Photothermal heating of polymer-coated Cu_{2-x}Se nanocrystals was measured by irradiating an aqueous dispersion with 800 nm light near

the plasmon band at low fluence (2 W/cm^2) for 5 minutes. The optical density of the nanocrystal dispersion was adjusted to 1.0 at the excitation wavelength. Figure 3.11 shows the measured temperature of the dispersion as a function of irradiation time. Five minutes of light exposure raised the temperature by 22°C , which compares quite favorably with the photothermal heating of the Au nanoshells and Au nanorods that were synthesized and obtained commercially.^{10,11} As shown in Figure 3.11, under similar illumination conditions with the optical densities of the Au nanorods and nanoshells also adjusted to 1.0 at the excitation wavelength of 800 nm to normalize the photothermal responses of all of the materials, the Au nanoshells increased the temperature by 13°C (synthesized) and 15°C (commercial), and Au nanorods by 20°C (synthesized) and 22°C (commercial) after 5 minutes.

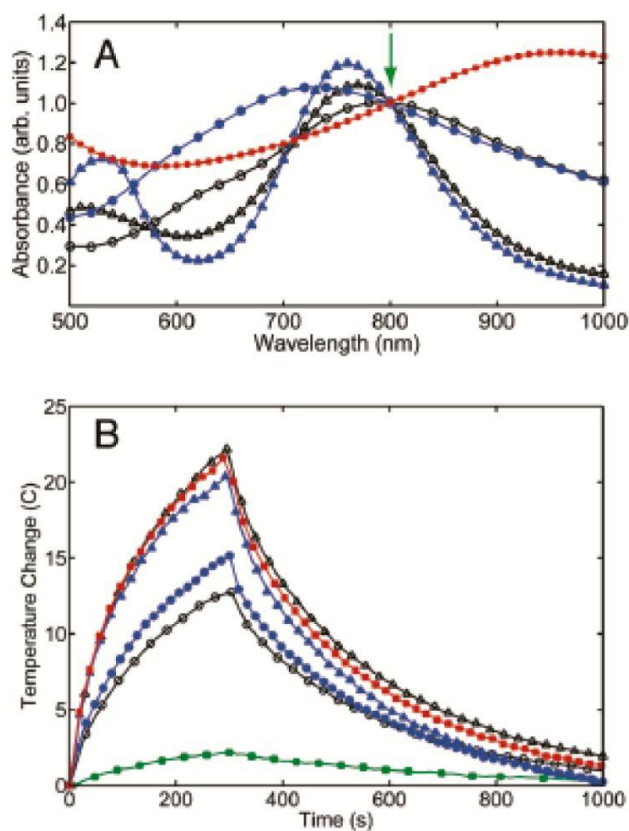


Figure 3.11. (A) Absorbance spectra of polymer-coated Cu_{2-x}Se nanocrystals (red, solid squares), commercial Au nanoshells (blue, solid circles) and Au nanorods (blue, solid triangles), and synthesized Au nanoshells (black, hollow circle) and Au nanorods (black, hollow triangle) dispersed in deionized water. The nanocrystal concentration in the dispersions was adjusted to an absorbance equal to 1.0 at 800 nm (green arrow). (B) The photothermal response of the dispersions in (A) obtained by irradiating 300 μ L aliquots of each solution for 5 minutes with an 800 nm diode laser (6 mm spot size, fluence of 2 W/cm²). The temperature was monitored with an infrared imaging camera. The laser heating of water (green, solid squares) contributes about 2.5°C to the overall change in temperature during the 5 minute of irradiation. The data were collected by Varun Pattani and the plots were sketched by Colin Hessel.

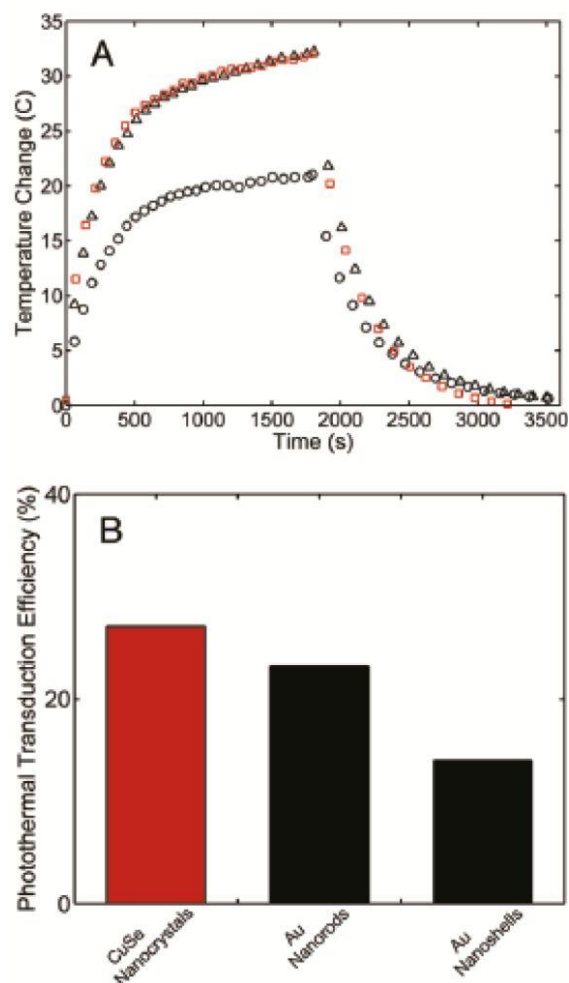


Figure 3.12. (A) Steady state heating data for commercial Au nanoshells (black circles), commercial Au nanorods (black triangles), and Cu_{2-x}Se nanocrystals (red squares). Dispersions of nanocrystals (300 μ L) were irradiated with 800 nm light (2 W/cm², 6 mm spot size) for 1800 seconds and then the laser was switched off. The heat transfer coefficient (hA) was determined by fitting the equation 3.8 to the Temperature versus Time data after 1800 seconds. The photothermal transduction efficiency was then determined by substituting the steady-state temperature during laser irradiation into equation 3.10. (B) Plot of the photothermal transduction efficiencies obtained for the Cu_{2-x}Se nanocrystals, commercial Au nanorods, and commercial Au nanoshells. The data were collected by Varun Pattani and the plots were sketched by Colin Hessel.

The photothermal transduction efficiencies of the Cu_{2-x}Se nanocrystals and the commercial Au-based nanoparticles were also measured and found to be quite similar. Similar to Roper and co-workers,⁵³ nanoparticle dispersions were illuminated until reaching a steady-state temperature. The light source was then removed and the temperature decrease was monitored to determine the rate of heat transfer from the system. Figure 3.12 shows the typical thermal profiles of the different nanoparticles. From an energy balance on the system, the photothermal transduction efficiency was calculated. The total energy balance is equation 3.4,

$$\sum_i m_i C_{p,i} \frac{dT}{dt} = Q_{in,np} + Q_{in,surround} - Q_{out} \quad (3.4)$$

The sum in the left hand side of equation 3.4 is over all components of the dispersion, though the density of water (997 mg/mL at room temperature) is on the order of 10⁴ times higher than the concentration of Cu and Se atoms (chapter 3.3.2) and about 10² times higher than the salt concentration (150 mM). So, all components besides water were considered negligible in equation 3.4. The variables m and C_p in Equation 3.4 are then the mass and heat capacity of water, and T is the water temperature. $Q_{in,np}$ is the photothermal energy input from the nanocrystals, and is described by equation 3.5, where I is the laser power (in mW), A_λ is the absorbance at the laser excitation wavelength of 800 nm, and η is the photothermal transduction efficiency – the fraction of absorbed light energy that is converted into heat. The middle term in parenthesis on the right hand side of equation 3.5 represents the fraction of light at 800 nm that is absorbed by the solution.

$$Q_{in,np} = I(1 - 10^{-A_\lambda})\eta \quad (3.5)$$

The term Q_{out} represents the heat lost to the surroundings, and is listed in Equation 3.6 where h is the heat transfer coefficient, A is the surface area of the solution's container, and $T_{surround}$ is the ambient surrounding temperature.

$$Q_{out} = hA(T - T_{surround}) \quad (3.6)$$

The lumped quantity hA was determined by measuring the rate of temperature drop after removing the light source. In the absence of laser excitation, equation 3.4 becomes the following:

$$mC_p \frac{dT}{dt} = -Q_{out} = -hA(T - T_{surround}) \quad (3.7)$$

Integrating equation 3.7,

$$T - T_{surround} = \exp\left(-\frac{hA}{mC_p}t\right) \quad (3.8)$$

Equation 3.8 was fit to the data in Figure 3.12A, beginning from when the laser is switched off at 30 minutes (1800 seconds). The heat transfer coefficients (hA) are tabulated in Table 3.3 for each type of nanoparticle dispersion. The values are very similar for the three different nanoparticle dispersions, reflecting the fact that the sample cell geometry is the same in each case.

Table 3.3. Heat Transfer Coefficients for Cu_{2-x}Se, Au Nanorods, and Au Nanoshells determined from the cooling curves shown in Figure 3.12. Fitting was performed by Varun Pattani.

Material	Heat transfer coefficient (mW/°C)
Cu _{2-x} Se	3.668
Au nanorods	3.389
Au nanoshells	4.306

During heating, when the sample reaches its maximum steady-state temperature (T_{max}), the rate of photothermal heating is then equal to the rate of heat transfer out of the system.

$$Q_{in,np} + Q_{in,surround} = I(1 - 10^{-A_\lambda})\eta + Q_{in,surround} = hA(T_{max} - T_{surround}) \quad (3.9)$$

The term $Q_{in,surround}$ is the energy absorbed by water in the absence of nanoparticles, and this is determined from a control experiment – heating pure water to T_{max} with the laser, determining hA from the cooling rate, and then setting $\eta = 0$ in equation 3.9 to calculate $Q_{in,surround}$ (determined to be 25.1 mW). Finally, the photothermal transduction efficiency for the dispersions with nanocrystals can be computed from equation 3.10 after measuring the corresponding T_{max} . Figure 3.12B reports the photothermal transduction efficiencies measured for the Cu_{2-x}Se nanocrystals (22%), and commercial Au nanoshells (13%) and nanorods (21%).

$$\eta = \frac{hA(T_{\max} - T_{\text{surround}}) - Q_{\text{in,surround}}}{I(1 - 10^{-A_\lambda})} \quad (3.10)$$

The photothermal transduction efficiency of the Cu_{2-x}Se nanocrystals of 22% is nearly equivalent to Au nanorods (21%) and noticeably higher than Au nanoshells (13%). Halas and co-workers have reported similar differences in the photothermal transduction efficiencies between Au nanoshells and nanorods, and have shown the amount of heat generated experimentally is almost 3-fold less than what is theoretically predicted.⁵⁴ The lower η for Au nanoshells compared to the nanorods and Cu_{2-x}Se nanocrystals is due to the larger contribution of light scattering to the optical cross-section that does not contribute to heating. Since the nanoparticle dispersions had the same optical density at the excitation wavelength, the same amount of light was attenuated in each measurement (Figure 3.11A). However, the Au nanoshells are significantly larger (73 nm radius) than the Au nanorods (6.0 nm effective radius)⁵⁵ and the Cu_{2-x}Se nanocrystals ($r = 8$ nm). The size-dependence of the extinction coefficient and the relative amounts of light scattering and absorption have been extensively studied for Au nanostructures and is well understood.⁵⁶⁻⁵⁸ El-Sayed and co-workers for example have illustrated how particle size affects the plasmonic properties of gold nanoparticles by normalizing the extinction coefficient to the particle volume and considering the relative contributions from light scattering.⁴⁹ They observed that Au nanorods have a normalized extinction coefficient (μ_{ext}) of 1021 μm^{-1} , which is the sum of normalized absorption ($\mu_{\text{abs}} = 986 \mu\text{m}^{-1}$) and scattering ($\mu_{\text{sca}} = 34 \mu\text{m}^{-1}$) coefficients, and that Au nanoshells have a normalized extinction coefficient of 58 μm^{-1} , which is the sum of normalized absorption and

scattering coefficients of 36 and 23 μm^{-1} , respectively. Therefore, the higher photothermal efficiency of nanorods compared to nanoshells is consistent with their higher absorption compared to scattering (96% vs 60%, respectively).⁴⁹ Like the Au nanorods, the Cu_{2-x}Se nanocrystals are small enough that the majority of optical extinction is due to light absorption related to the plasmon resonance.

3.3.5 Cu_{2-x}Se Nanocrystal Biocompatibility

A Trypan blue staining protocol was used to test the effect of polymer-coated Cu_{2-x}Se nanocrystals on the viability of HCT-116 (human colorectal carcinoma) cells. Cells were cultured until they were 80% confluent, and then both fresh media and Cu_{2-x}Se dispersed in PBS were injected. The PBS dispersion of Cu_{2-x}Se had an absorbance of 1.0 at 800 nm, and it was diluted to one fourth this concentration when mixed with the cells (about 39 mg/L Cu_{2-x}Se in the cell culture). Cells were incubated with the nanocrystals for 0.5, 1, 3, and 6 hours at 37°C. In a control experiment, cells were given fresh nanoparticle-free media and incubated for 6 hours as well. After the incubation period, the media was replaced to remove unbound nanoparticles. Subsequently, Trypan blue dye was added to assess cell viability. The dye is absorbed by dead cells, causing them to appear blue, while the dye does not penetrate viable cells, and it possible to distinguish live and dead cells under a bright-field microscope. Figure 3.13 shows bright-field images of HCT-116 cells after incubation with polymer-coated Cu_{2-x}Se nanocrystals. The cell viability assay indicates that incubation of HCT-116 cells with the nanocrystals

show no signs of cytotoxicity up to 6 hours, and only a slight increase in cell death at 6 hours compared to the control.

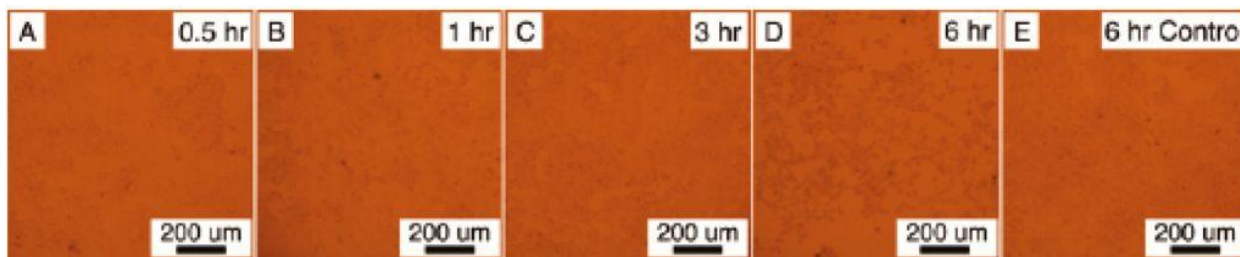


Figure 3.13. Bright field optical microscopy images of human colorectal cancer cells (HCT-116) incubated with 39 mg/L polymer coated Cu_{2-x}Se nanocrystals in PBS for 0.5 (A), 1 (B), 3 (C), and 6 hours (D). A control sample (E) was incubated for 6 hours and did not receive Cu_{2-x}Se nanocrystals. Cells were incubated for the predetermined time and stained with Trypan blue to visualize cell death. There is not a significant number of stained cells in samples treated with the nanocrystals relative to the control, suggesting that the nanocrystals are not acutely toxic. Light microscopy images were acquired by Varun Pattani.

3.3.6 Photothermal Therapy with Cu_{2-x}Se Nanocrystals

The polymer-coated Cu_{2-x}Se nanocrystals, dispersed in PBS, were added to HCT-116 cells and illuminated with 800 nm light to determine if they would promote photothermal cell death. In photothermal therapy, NIR light is used to excite the nanocrystals and create local temperature increases to destroy diseased cells. Cells grown in a 12-well plate were combined with media (0.375 mL) and Cu_{2-x}Se nanocrystals in PBS (0.125 mL) at a solution concentration of 39 mg/L (2.8×10^{15} NC/L) and were incubated for 0.5 hours at 37°C. Cells were irradiated for five minutes with and without

Cu_{2-x}Se nanocrystals at 30 W/cm². Bright-field images were collected, at the same coordinates on the substrate as the laser spot, of cells stained with Trypan Blue after irradiation. The imaging showed that all cells within the area of the laser spot exhibited cell death. Exposure of the cells to the NIR laser in the absence of nanocrystals did not result in cell death at the area of the laser spot, as shown in Figure 3.14. The power threshold for nontargeted photothermal cell destruction using an 800 nm laser was 30 W/cm² for 5 minutes. These conditions are slightly more moderate than what is reported for nontargeted *in vitro* photothermal destruction of cells with Au nanoshells (35 W/cm² for 7 minutes) or targeted *in vitro* photothermal therapy with hollow Au nanoshells (40 W/cm², 5 minutes).⁵⁹

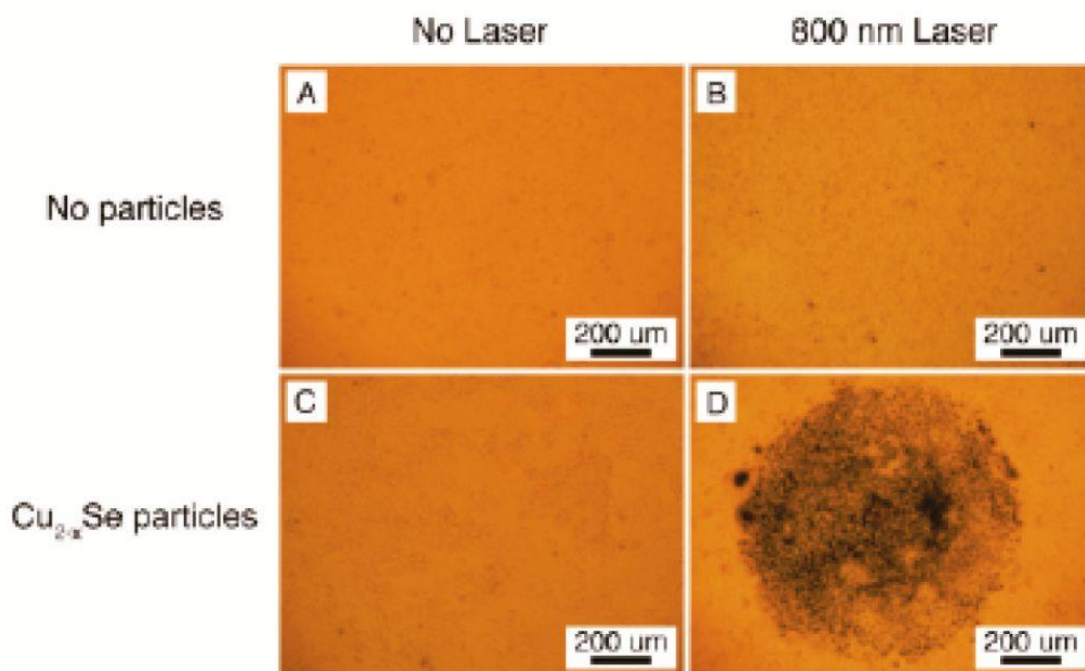


Figure 3.14. Comparison of photothermal destruction of human colorectal cancer cells (HCT-116) without (top row, A and B) and with (bottom row, C and D) the addition of 2.8×10^{15} Cu_{2-x}Se nanocrystals/L. Cells irradiated at 30 W/cm^2 with an 800 nm diode laser for 5 minutes (circular spot size of 1 mm) were stained with Trypan blue dye to visualize cell death and imaged with an inverted microscope in bright field mode. Significant cell death is observed with 30 W/cm^2 irradiation in the sample containing nanocrystals. The light microscopy images were acquired by Varun Pattani.

3.4 Conclusions

Amphiphilic polymer-coated Cu_{2-x}Se nanocrystals exhibit an intense NIR absorbance peak and significant photothermal heating, comparable to Au nanorods and Au nanoshells. NIR photoexcitation of the Cu_{2-x}Se nanocrystals in the presence of human colorectal cancer cells led to significant cell death, verifying that the nanocrystals have the potential for photothermal therapy. The potential for Cu_{2-x} as an *in vivo*

therapeutic is highlighted by its small hydrodynamic diameter that will lead to prolonged blood circulation times when additional non-immunogenic or cell targeting molecules are grafted to the carboxyl groups on the amphiphilic polymer coating, in order to achieve targeted photothermal therapy. However, much work needs to be done with these nanocrystals to evaluate their chronic toxicity and to develop bio-molecule conjugation strategies.

3.5 References

- (1) Jain, P. K.; El-Sayed, I. H.; El-Sayed, M. A. *Nano Today* **2007**, 2, 18-29.
- (2) Huang, X.; El-Sayed, I. H.; Qian, W.; El-Sayed, M. A. *Journal of the American Chemical Society* **2006**, 128, 2115-2120.
- (3) Gobin, A. M.; Lee, M. H.; Halas, N. J.; James, W. D.; Drezek, R. A.; West, J. L. *Nano Letters* **2007**, 7, 1929-1934.
- (4) Kam, N. W. S.; O'Connell, M.; Wisdom, J. A.; Dai, H. J. *Proceedings of the National Academy of Sciences of the United States of America* **2005**, 102, 11600-11605.
- (5) Weissleder, R. *Nature Biotechnology* **2001**, 19, 316-317.
- (6) Oldenburg, S. J.; Averitt, R. D.; Westcott, S. L.; Halas, N. J. *Chemical Physics Letters* **1998**, 288, 243-247.
- (7) Huang, X. H.; Neretina, S.; El-Sayed, M. A. *Advanced Materials* **2009**, 21, 4880-4910.
- (8) Chen, J. Y.; Wang, D. L.; Xi, J. F.; Au, L.; Siekkinen, A.; Warsen, A.; Li, Z. Y.; Zhang, H.; Xia, Y. N.; Li, X. D. *Nano Letters* **2007**, 7, 1318-1322.
- (9) Chen, J. Y.; Glaus, C.; Laforest, R.; Zhang, Q.; Yang, M. X.; Gidding, M.; Welch, M. J.; Xia, Y. N. *Small* **2010**, 6, 811-817.
- (10) Rasch, M. R.; Sokolov, K. V.; Korgel, B. A. *Langmuir* **2009**, 25, 11777-11785.
- (11) Smith, D. K.; Miller, N. R.; Korgel, B. A. *Langmuir* **2009**, 25, 9518-9524.
- (12) Loo, C.; Lin, A.; Hirsch, L. R.; Lee, M.; Barton, J. K.; Halas, N. J.; West, J. L.; Drezek, R. A. *Cancer Research and Treatment* **2004**, 3, 33-40.
- (13) Alkilany, A. M.; Nagaria, P. K.; Hexel, C. R.; Shaw, T. J.; Murphy, C. J.; Wyatt, M. D. *Small* **2009**, 5, 701-708.
- (14) Nikoobakht, B.; El-Sayed, M. A. *Chemistry of Materials* **2003**, 15, 1957-1962.

- (15) Soo Choi, H.; Liu, W.; Mista, P.; Tanaka, E.; Zimmer, J. P.; Itty, I. B.; Bawendi, M. G.; Frangioni, J. V. *Nature Biotechnology* **2007**, *25*, 1165-1170.
- (16) Jiang, W.; Kim, B. Y. S.; Rutka, J. T.; Chan, W. C. W. *Nature Nanotechnology* **2008**, *3*, 145-150.
- (17) Gao, H. J.; Shi, W. D.; Freund, L. B. *Proceedings of the National Academy of Sciences of the United States of America* **2005**, *102*, 9469-9474.
- (18) Osaki, F.; Kanamori, T.; Sando, S.; Sera, T.; Aoyama, Y. *Journal of the American Chemical Society* **2004**, *126*, 6520-6521.
- (19) Sadauskas, E.; Wallin, H.; Stoltenberg, M.; Vogel, U.; Doering, P.; Larsen, A.; Danscher, G. *Particle and Fiber Toxicology* **2007**, *4*, 10.
- (20) De Jong, W. H.; Hagens, W. I.; Krystek, P.; Burger, M. C.; Sips, A.; Geertsma, R. E. *Biomaterials* **2008**, *29*, 1912-1919.
- (21) Lambert, T. N.; Andrews, N. L.; Gerung, H.; Boyle, T. J.; Oliver, J. M.; Wilson, B. S.; Han, S. M. *Small* **2007**, *3*, 691-699.
- (22) Lee, C.; Kim, H.; Hong, C.; Kim, M.; Hong, S.; Lee, D. H.; Lee, W. I. *Journal of Materials Chemistry* **2008**, *18*, 4790-4795.
- (23) Yang, K.; Zhang, S. A.; Zhang, G. X.; Sun, X. M.; Lee, S. T.; Liu, Z. A. *Nano Letters* **2010**, *10*, 3318-3323.
- (24) Moon, H. K.; Lee, S. H.; Choi, H. C. *ACS Nano* **2009**, *3*, 3707-3713.
- (25) Li, Y. B.; Lu, W.; Huang, Q. A.; Huang, M. A.; Li, C.; Chen, W. *Nanomedicine* **2010**, *5*.
- (26) Sherlock, S. P.; Tabakman, S. M.; Xie, L.; Dai, H. *ACS Nano* **2011**, *5*, 1505-1512.
- (27) Derfus, A. M.; Chan, W. C. W.; Bhatia, S. N. *Nano Letters* **2004**, *4*, 11-18.
- (28) Li, L.; Daou, T. J.; Texier, I.; Tran, T. K. C.; Nguyen, Q. L.; Reiss, P. *Chemistry of Materials* **2009**, *21*, 2422-2429.
- (29) Pons, T.; Pic, E.; Lequex, N.; Cassette, E.; Bezdetnaya, L.; Guillemin, G.; Marchal, F.; Dubertret, B. *ACS Nano* **2010**, *4*, 2531-2538.
- (30) Cassette, E.; Pons, T.; Bouet, C.; Helle, M.; Bezdetnaya, L.; Marchal, F.; Dubertret, B. *Chemistry of Materials* **2010**, *22*, 6117-6124.
- (31) Jana, N. R.; Gearheart, L.; Murphy, C. J. *Journal of Physical Chemistry B* **2001**, *105*, 4065-4067.
- (32) Lin, C. A. J.; Sperling, R. A.; Li, J. K.; Yang, T. Y.; Li, P. Y.; Zanella, M.; Chang, W. H.; Parak, W. G. J. *Small* **2008**, *4*, 334-341.
- (33) Smoluchowski, M. V. *Bulletin International de l'Academie des sciences de Cracovie* **1903**, 184.
- (34) Frisken, B. J. *Applied Optics* **2001**, *40*, 4087-4091.
- (35) Panthani, M. G.; Akhavan, V.; Goodfellow, B. W.; Schmidtke, J. P.; Dunn, L.; Dodabalapur, A.; Barbara, P. F.; Korgel, B. A. *Journal of the American Chemical Society* **2008**, *130*, 16770-16777.
- (36) Koo, B.; Patel, R. N.; Korgel, B. A. *Journal of the American Chemical Society* **2009**, *131*, 3134-3135.

- (37) Deka, S.; Genovese, A.; Zhang, Y.; Miszta, K.; Bertoni, G.; Krahne, R.; Giannini, C.; Manna, L. *Journal of the American Chemical Society* **2010**, *132*, 8912-8914.
- (38) Kriegel, I.; Jiang, C.; Rodriguez-Fernandez, J.; Schaller, R. D.; Talapin, D. V.; da Como, E.; Feldmann, J. *Journal of the American Chemical Society* **2012**, *134*, 1583-1590.
- (39) Our lab observes oxidation with many different kinds of nanocrystals in the TGA in spite of purging with nitrogen gas. This issue is not limited to the copper selenide nanocrystals.
- (40) *CRC Handbook of Chemistry and Physics*; 91st ed.; CRC Press: Boca Raton, FL, 2011.
- (41) Garcia, M. A. *Journal of Physics D-Applied Physics* **2011**, *44*, 283001.
- (42) Jagminas, A.; Juskenas, R.; Gailiute, I.; Statkute, G.; Tomasiunas, R. *Journal of Crystal Growth* **2006**, *294*, 343-348.
- (43) Kuzuya, T.; Itoh, K.; Sumiyama, K. *Journal of Colloid and Interface Science* **2008**, *319*, 565-571.
- (44) Klimov, V.; Bolivar, P. H.; Kurz, H.; Karavanskii, V.; Krasovskii, V.; Korkishko, Y. *Applied Physics Letters* **1995**, *67*, 653-655.
- (45) Zhao, Y.; Pan, H.; Lou, Y.; Qiu, X.; Zhu, J.; Burda, C. J. *Journal of the American Chemical Society* **2009**, *131*, 4253-4261.
- (46) Luther, J. M.; Jain, P. K.; Ewers, T.; Alivisatos, A. P. *Nature Materials* **2011**, *10*, 361-366.
- (47) Du, H.; Fuh, R. C. A.; Li, J. Z.; Corkan, L. A.; Lindsey, J. S. *Photochemistry and Photobiology* **1998**, *68*, 141-142.
- (48) Yu, W. W.; Qu, L. H.; Guo, W. Z.; Peng, X. G. *Chemistry of Materials* **2003**, *15*, 2854-2860.
- (49) Jain, P. K.; Lee, K. S.; El-Sayed, I. H.; El-Sayed, M. A. *Journal of physical Chemistry B* **2006**, *110*, 7238-7248.
- (50) Nikoobakht, B.; Wang, J. P.; El-Sayed, M. A. *Chemical Physics Letters* **2002**, *366*, 17-23.
- (51) Hirsch, L. R.; Stafford, R. J.; Bankson, J. A.; Sershen, S. R.; Rivera, B.; Price, R. E.; Hazle, J. D.; Halas, N. J.; West, J. L. *Proceedings of the National Academy of Sciences of the United States of America* **2003**, *100*, 13549-13554.
- (52) Hessel, C. M.; Rasch, M. R.; Hueso, J. L.; Goodfellow, B. W.; Akhavan, V.; Puvanakrishnan, P.; Tunnell, J. W.; Korgel, B. A. *Small* **2010**, *6*, 2026-2034.
- (53) Roper, D. K.; Ahn, W.; Hoepfner, M. J. *Journal of Physical Chemistry C* **2007**, *111*, 3636-3641.
- (54) Cole, J. R.; Mirin, N. A.; Knight, M. W.; Goodrich, G. P.; Halas, N. J. *Journal of Physical Chemistry C* **2009**, *113*, 12090-12094.
- (55) Effective radius = $(\text{Volume} \cdot 3 / (4 \cdot \pi))^{1/3}$
- (56) Link, S.; El-Sayed, M. A. *Journal of Physical Chemistry B* **1999**, *103*, 8410-8426.

- (57) Link, S.; El-Sayed, M. A. *International Reviews in Physical Chemistry* **2000**, *19*, 409-453.
- (58) Bohren, C. F.; Huffman, D. R. *Absorption and Scattering of Light by Small Particles*; John Wiley: New York, 1983.
- (59) Melancon, M. P.; Lu, W.; Yang, Z.; Zhang, R.; Cheng, Z.; Elliot, A. M.; Stafford, J.; Olson, T.; Zhang, J. Z.; Li, C. *Molecular Cancer Therapeutics* **2008**, *7*, 1730-1739.

Chapter 4: Encapsulating Semiconductor Nanocrystals in Polymer Micelles

4.1 Introduction

Inorganic nanocrystals have been extensively studied for labeling applications in biology and medicine.¹⁻⁷ Noble metal, metal oxide, and semiconductor nanocrystals 1-100 nm in diameter have exceptional size-, shape-, and composition-dependent optical or magnetic properties compared to molecular probes,⁸⁻¹⁵ making these nanocrystals useful contrast-enhancing labels for fluorescence-based imaging and cell sorting,¹⁶⁻²² magnetic resonance imaging (MRI),²³⁻²⁵ or photothermal and photoacoustic imaging.²⁶⁻²⁹ Advances in organometallic synthesis have led to careful control over nanocrystals dimensions and composition,^{30,31} making it possible to synthesize an entire library of colloidal nanocrystals that have distinct properties. However, syntheses that provide the most careful control over the nanocrystal size, size distribution, and crystal structure take place in non-polar solvents and produce hydrophobic nanocrystals – coated with a monolayer of C₁₂-C₁₈ alkane stabilizing molecules – that are not immediately compatible with aqueous biological systems.^{3,11,32} Thus a fundamental challenge of utilizing colloidal nanocrystals for biomedical applications is to develop post-synthesis surface coatings that not only make the nanocrystals dispersible in aqueous biological media, but also offer reactive functional groups for interfacing the nanocrystals with biological targets.^{3,10}

[§] Portions of this chapter appear in the following publication: Hessel, C.M.; Rasch, M.R.; Hueso, J.L.; Goodfellow, B.W.; Akhavan, V.A.; Puvanakrishnan, P.; Tunnell, J.W.; Korgel, B.A. *Small* (2010), 6, 2026-2034. The experiments were performed by C.M. Hessel, M.R. Rasch, J.L. Hueso, B.W. Goodfellow, V.A. Akhavan, and P. Puvanakrishnan. The text was written by C.M. Hessel, M.R. Rasch, and B.A. Korgel. Funding was provided by research grants to J.W. Tunnell and B.A. Korgel.

In some recent reports using luminescent nanocrystals as biomedical imaging contrast agents, hydrophobic nanocrystals were coated with bulky surface ligands to facilitate biocompatibility and make them dispersible in water, but at the expense of significantly increasing the nanocrystal size. For example, Sailor and coworkers used fragments of porous Si coated in dextran polymer to image tumors in mouse,³³ and Swihart and coworkers incorporated aggregates of hydrophobic Si nanocrystals into phospholipid micelles conjugated with polyethylene glycol (PEG) to image pancreatic cancer cells *in vitro*.³⁴ In these cases, the contrast agents are relatively large, with diameters of more than 100 nm, making them susceptible to rapid clearance from circulation in the body by the reticuloendothelial system (RES).³⁵ The desired particle size for designing nanocrystals to penetrate into tissue and target cells is about 25-50 nm, since particles within this range are most efficient at entering cells by receptor-mediated endocytosis,³⁶⁻³⁹ particles larger than 100 nm are rapidly cleared from the body by the RES,³⁵ and particles smaller than 5.5 nm are rapidly filtered from blood by the kidneys.³⁶ Encapsulating hydrophobic, alkyl-passivated nanocrystals within amphiphilic polymer micelles achieves biocompatibility and water-dispersibility without compromising a small hydrodynamic diameter.⁴⁰

Biocompatible polymers that previously have been used to coat hydrophobic nanocrystals (such as Si) have been synthesized in complicated ultraviolet light reactors,⁴¹ or with polymer cross-linking agents like ethyl-3-dimethylaminopropyl carbodiimide (EDC) that are removed by a slow post-synthesis dialysis procedure.^{40,42,43} Recent advances in polymer chemistry have eliminated the need for coupling agents,

complicated polymerizations, and clean-up processes.⁴⁴ For instance, Lin *et al* demonstrated a facile amphiphilic polymer synthesis using a poly(maleic anhydride) polymer backbone with a high specific reactivity for hydrophobic alkylamine side chains.⁴⁵ A two-step synthesis yields a low molecular weight amphiphilic polymer that spontaneously assembles into micelles in water and encapsulates hydrophobic nanocrystals, enabling the nanocrystals to disperse in water as well. The polymer backbone contains exposed carboxyl groups that provide a platform for further functionalization with cell-targeting biomolecules.^{45,46}

This chapter describes the synthesis of an amphiphilic polymer derived from a poly(maleic anhydride) backbone, characterization of the polymer, and application to the coating of hydrophobic nanocrystals. The coating strategy is extended to hydrophobic Si and CuInS_xSe_{2-x} (CIS) nanocrystals, which are promising new types of fluorescent nanocrystals for potential biomedical imaging applications that are free of toxic elements like the cadmium contained in commercially available quantum dot formulations. The fluorescence of Si and CIS nanocrystals is preserved during polymer encapsulation, which enables the nanocrystals to disperse in water. However, the stability of polymer-encapsulated nanocrystals is sensitive to pH and ionic strength.

4.2 Experimental Details

4.2.1 Chemicals

Amphiphilic Polymer. Dodecylamine (Sigma, 98%), anhydrous tetrahydrofuran (Sigma, ≥ 99.9%), anhydrous chloroform (Sigma, ≥ 99%), sodium hydroxide pellets (Sigma, ≥ 98%), boric acid (Sigma, 99%), poly(isobutylene-alt-maleic anhydride) (Mw~6 kDa, 39

monomer units per molecule, Sigma), and phosphate-buffered saline powder (Sigma) were used as received. Bovine serum albumin was from Jackson Laboratories. All aqueous solutions were prepared using deionized (DI) water having an 18 M Ω resistance.

CuInS_xSe_{2-x} Nanocrystals. 1-dodecanethiol (99%, Sigma), copper(II) acetylacetonate (Cu(acac)₂, 99.99%, Sigma), indium(III) acetylacetonate (In(acac)₃, 99.99%, Sigma), selenium powder (99.99%, Sigma), 1-octadecene (90%), tributylphosphine (TBP, 98%, Sigma), potassium ethyl xanthogenate (96%, Sigma), zinc(II) oleate (90%, Sigma), toluene (99%, Fisher Scientific), and ethanol (99%, Fisher Scientific) were used as received. A stock solution of 1M tributylphosphine selenide (TBP:Se) was prepared by dissolving 10 mmol of Se powder (790 mg) in 10 mL TBP inside a N₂-filled glovebox.

Si Nanocrystals. Fox17 (Dow Corning Corporation, 17% hydrogen silsesquioxane (HSQ) by weight in methylisobutylketone), methanol (Sigma, 99%), anhydrous ethanol (Sigma, > 99%), hydrofluoric acid (Sigma, 48%), 1-dodecene (Acros Organics, 93%), acetonitrile (Acros Organics, 99%), and Rhodamine 101 (Sigma, 99%) were used as received.

4.2.2 Amphiphilic Polymer Synthesis and Characterization

The amphiphilic polymer synthesis was adapted from a published protocol.⁴⁵ In a capped, single neck round bottom flask, anhydrous THF (100 mL), dodecylamine (15 mmol, 3.45 mL), and poly(isobutylene-*alt*-maleic anhydride) (20 mmol of monomer units, 3.084 g) were added sequentially to form a turbid white solution. The flask was sonicated for 1 minute to suspend the insoluble polymer, and it was heated at 60°C for 3 hours under vigorous stirring. The suspension became clear after 15 minutes of stirring,

indicating that the polymer became soluble in THF after covalently coupling to the hydrophobic dodecylamine molecules. We found that the mole ratio of dodecylamine to anhydride monomers (0.75 to 1) was important to achieve complete solubility of the polymer – at ratios of less than 0.6 moles dodecylamine per mole of anhydride, the polymer was not hydrophobic enough to completely dissolve in THF.⁴⁷ After 3 hours of stirring, the solution was cooled to room temperature and reduced in volume to 20 mL with a rotary evaporator. The clear solution was stirred again at 60°C for 12 hours under vigorous stirring to ensure complete coupling between the polymer and dodecylamine. The solution was cooled to room temperature and the remaining solvent was removed with a rotary evaporator, yielding the pale yellow, solid amphiphilic polymer. The solid polymer was transferred to a nitrogen filled glove box (< 1.0 ppm O₂) and dissolved in anhydrous CHCl₃ (25 mL) to give a monomer unit concentration of 0.8 M. The amphiphilic polymer solution was stored in a glass vial within the glovebox until use.

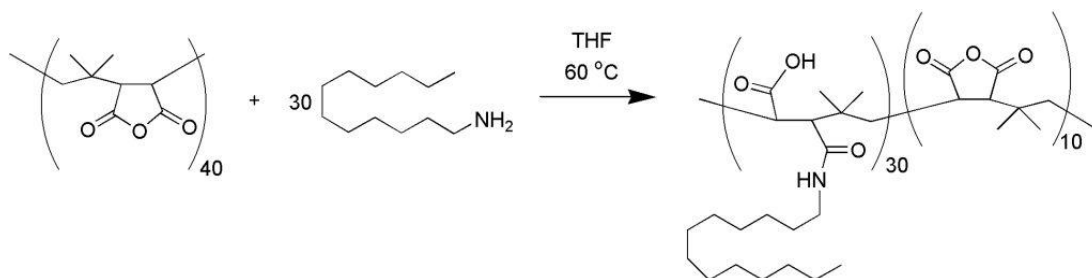


Figure 4.1. Reaction scheme for the synthesis of the amphiphilic polymer. Primary amines attack the anhydride rings of the polymer backbone. Each amine molecule forms one amide bond and one carboxylic acid due to ring opening.

For ¹H NMR, 0.5 mL of the 0.8 M amphiphilic polymer solution was placed in glass vial, and the chloroform was removed by rotary evaporation. The vial was stored in

a vacuum oven at 25°C for over 1 hour to remove residual chloroform in the polymer film. The dry polymer was dissolved in 1 mL of deuterated chloroform (CDCl_3), loaded into an NMR sample tube, and submitted to the University of Texas NMR facility in the Chemistry Department. For mass spectrometry, 1 mL of the 0.8 M polymer dissolved in chloroform was submitted to the University of Texas Mass Spectrometry facility in the Chemistry Department. The sample was analyzed using Matrix Assisted Laser Desorption Ion (MALDI) mass spectrometry. FTIR was performed in attenuated total internal reflectance (ATR) mode using a zinc sulfide crystal. First a background scan was collected by adding a few drops of chloroform to the crystal, letting the FTIR sample compartment purge for 10 minutes with the ATR crystal inside, and then collecting a scan. For the polymer sample, 0.1 mL of the 0.8 M sample of polymer was dried on a zinc sulfide crystal. The ATR crystal with dry polymer was left to purge with nitrogen in the (closed) FTIR sample compartment for 10 minutes, and then a scan was collected.

4.2.3 Dodecanethiol-coated CIS Nanocrystal Synthesis

The nanocrystals were synthesized by Matthew Panthani. 1.3 g $\text{Cu}(\text{acac})_2$, 2.5 g $\text{In}(\text{acac})_2$, 20 mL octadecene, and 10 mL dodecanethiol were placed in a 100 mL 3-neck round bottom flask. A Teflon magnetic stir bar was added, the flask was connected to a condenser, and it was sealed with rubber septa. A thermocouple was inserted through one of the septa. The flask was connected to a Schlenk line and equipped with a heating mantle. The flask was placed under vacuum (<500 mbar) and heated to 110°C for 1 hour while stirring. The flask was then heated to 180°C under $\text{N}_2(\text{g})$ atmosphere, at which point 10 mL of the 1M TBP:Se solution was injected. The temperature was increased to

220°C and allowed to react for 15 minutes. A ZnS shell precursor solution was prepared by combining zinc bis(ethyl xanthogenate) (100 mg), zinc (II) oleate (900 mg), ODE (10 mL), trioctylphosphine (3 mL) and oleylamine (1 mL). The CISS nanocrystals are coated with ZnS by cooling the reaction solution to 190°C and injecting this solution into the reaction flask. The mixture is stirred overnight to allow the shell to form. Subsequently, the heating mantle is removed and the flask is allowed to cool to room temperature. The nanocrystals are purified by mixing 5 mL of crude reaction solution with 20 mL of an ethanol/toluene solution (2:1 v/v) and centrifuging at 8000 rpm for 5 minutes. The precipitated nanocrystals are dispersed in about 1 mL of toluene, mixed with 10 mL ethanol, and precipitated a second time by centrifuging at 8000 rpm for 5 minutes. The nanocrystal precipitate is dispersed in toluene and stored in a glass vial. A typical reaction yield is 200 mg of nanocrystals.

4.2.4 Dodecane-coated Si Nanocrystal Synthesis

The Si nanocrystals were synthesized by Colin Hessel and Yixuan Yu using an established procedure.⁴⁸ First, 0.3 g of HSQ is decomposed by heating to 1100°C (18°C/min.) in a reducing atmosphere (7% H₂/93% N₂) and maintaining this temperature for 1 hour, yielding Si nanocrystals approximately 3 nm in diameter embedded in silica. HSQ is a silicon-rich oxide that disproportionates into SiO₂ and Si when heated, and at sufficient temperature, Si nanocrystals nucleate and crystallize within the SiO₂ matrix.^{49,50} The Si nanocrystals are liberated from the silica matrix by first grinding and shaking the matrix until it is broken up into 200 nm grains, and then the grains are etched with 10 mL of a hydrofluoric acid solution (1:1:1; 48% HF:H₂O:Acetonitrile) for 1.5

hours while stirring at 250 rpm. HF etches both Si and SiO₂, but SiO₂ etching is much faster due to the polarity difference between Si-Si and Si-O bonds.⁵¹ The Si nanocrystals were isolated from the etch solution by centrifugation at 8000 rpm for 2 minutes. The precipitate was rinsed twice with acetonitrile, dispersed in 12 mL of 1-dodecene, and degassed in a 3 neck round bottom flask by 4 freeze-pump-thaw cycles on a Schlenk line. The Si nanocrystals and dodecene were mixed at 190°C under nitrogen atmosphere for 3 hours to promote hydrosilylation. Subsequently, the dodecene-coated Si nanocrystals were washed three times by precipitation with a 2:1 ethanol:methanol mixture (15 mL) and finally dispersed in anhydrous chloroform. Figure 4.2 provides an illustration outlining the Si nanocrystal synthesis process.

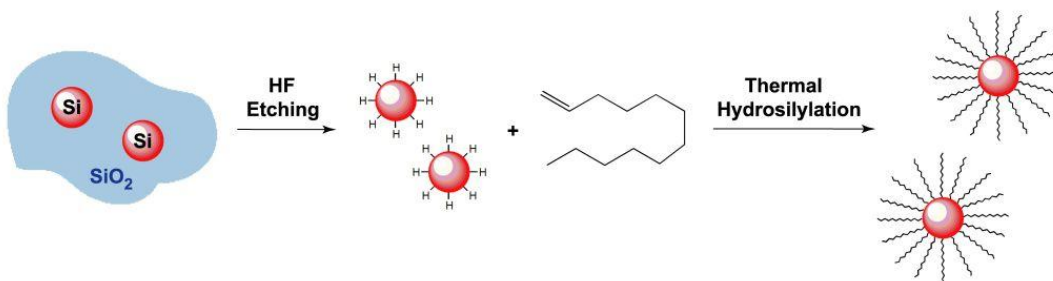


Figure 4.2. Illustration of Si nanocrystal formation. Si nanocrystals are liberated from a SiO₂ matrix by HF etching. The hydride-terminated Si nanocrystals are refluxed in 1-dodecene to attach a hydrophobic, covalently bonded alkyl monolayer via thermal hydrosilylation.

4.2.5 Nanocrystal Characterization

Room temperature TEM, absorbance spectroscopy, TGA, light scattering, and zeta potential measurements were performed as described in Chapter 3.

Cryo Transmission Electron Microscopy (CryoTEM). CryoTEM was performed at the Universidad Autonoma de Barcelona with Dr. Jordi Arbiol. A 2 μ L aliquot of an undiluted, aqueous nanoparticle solution was drop cast onto a holey carbon TEM grid, held with a pair of forceps. The forceps were loaded onto a Leica electron microscopy cryo preparation chamber (Leica EM CPC), which contained a liquid ethane bath cooled to between -178 and -180 °C using automated liquid nitrogen flow. The aqueous solution was quickly wicked off the grid with a piece of filter paper and plunged into the liquid ethane in one swift motion. The liquid ethane vitrified the aqueous solution trapped in the holes on the TEM grid. Keeping the grid submerged in a liquid nitrogen bath, the frozen grid was loaded into a TEM grid holder cooled with a liquid nitrogen reservoir, which keeps the water on the grid at a low enough temperature (around -196 °C) to remain amorphous once inside the TEM column. The cooled grid holder was then inserted into a JEOL 2010 TEM microscope for imaging. Places on the grid where the amorphous water was not too thick (> 1 micron) could be readily imaged, and the grids were scanned at low magnification to find these regions of low sample thickness. Rapid freezing was critical to avoid formation of ice crystals, and wicking off the aqueous sample before freezing was important to make sure that the sample was not too thick for the electron beam to pass through once converted to a glass.

Small Angle X-ray Scattering (SAXS). SAXS was performed by Brian Goodfellow. The nanocrystals were dispersed in toluene (5-10 mg/mL) in order to determine the mean particle diameter. The dispersions were enclosed in a stainless steel cell with Kapton windows. Measurements were performed using a Molecular Metrology system with a

rotating copper anode X-ray generator (Bruker Nonius, $\lambda = 1.54 \text{ \AA}$) operating at 3.0 kW. The scattered photons were collected on a 2D multiwire gas-filled detector (Molecular Metrology, Inc.) and the scattering angle was calibrated using a silver behenate standard. Experimental data were corrected for background scattering by measuring the scattering from pure toluene. Radial integrations of scattering intensity were performed using Datasqueeze software, in order to produce an $I(q)$ data set, where q is the scattering wave vector related to the X-ray wavelength λ and scattering angle θ as follows:⁵²⁻⁵⁵

$$q = \frac{4\pi}{\lambda} \sin\left(\frac{\theta}{2}\right) \quad (4.1)$$

Considering that the nanocrystals are a dilute dispersion of scatterers, the radially-integrated scattering intensity is modeled as a function of q and the nanocrystal radius (R) by equation 4.2.

$$I(q) \propto \int_0^{\infty} N(R) P(qR) R^6 dR \quad (4.2)$$

In equation 4.2, $P(qR)$ is the form factor. For solid homogeneous spheres,⁵²⁻⁵⁵

$$P(qR) = \left[3 \frac{\sin(qR) - qR \cos(qR)}{(qR)^3} \right]^2 \quad (4.3)$$

The term $N(R)$ is the number fraction of nanocrystals of radius R in the sample, which is typically assumed to have a Gaussian distribution with a mean radius \bar{R} and standard deviation σ :

$$N(R) = \frac{1}{\sigma\sqrt{2}} \exp\left[-\frac{(R - \bar{R})^2}{2\sigma^2}\right] \quad (4.4)$$

Equations 4.1 – 4.4 were fit to the experimental data to determine \bar{R} and σ .

Fluorescence Spectroscopy. Photoluminescence spectra were acquired on a Varian Cary Eclipse Fluorescence spectrophotometer using a quartz cuvette with a 10 mm optical path length. Nanocrystal quantum yields (QY_{NC}) were measured relative to the Rhodamine 101 dye ($QY_{dye} = 100\%$), using equation 4.5. The nanocrystals were dispersed in chloroform while the dye was separately dissolved in ethanol. First the absorbance of the dye (A_{dye}) was measured and adjusted to be between 0.01 – 0.10 at the excitation wavelength, and then the photoluminescence spectrum (intensity I versus photon energy E) was acquired with an excitation wavelength of 500 nm. The process was repeated using Si and CIS nanocrystals; for Si the excitation wavelength was 350 nm, while for CIS the excitation wavelength was 500 nm. In equation 4.5, the terms n_{CHCl_3} and n_{EtOH} are the refractive indexes of chloroform and ethanol respectively.⁵⁶

$$QY_{NC} = \frac{A_{dye} \int \frac{I_{NC}}{E} dE}{A_{NC} \int \frac{I_{dye}}{E} dE} \cdot \left(\frac{n_{CHCl_3}}{n_{EtOH}} \right)^2 \cdot QY_{dye} \quad (4.5)$$

4.2.6 Coating nanocrystals with polymer

Hydrophobic nanocrystals were coated with polymer following a recently developed protocol,⁴⁵ an illustration of the assembly is included in Figure 4.3. In a 50 mL round bottom flask, 53 μ L of the amphiphilic polymer stock solution (0.8M monomer units in chloroform) was diluted with 2 mL anhydrous chloroform, and then 3 mg of nanocrystals was added. The mixture was stirred at room temperature for 15 minutes. The solvent was removed by rotary evaporation to yield a nanocrystal-polymer film on

the inner flask wall. 2 mL of aqueous sodium borate buffer (SBB, 50 mM borate, pH 12) was injected into the flask, and it was stirred for about an hour at room temperature to disperse the nanocrystals and polymer. Once dispersed, DI water (13 mL) was added to the flask to dilute the nanocrystals. The nanocrystal dispersion was passed through a 0.2 μm -pore syringe filter (Whatman, inorganic membrane). The filtered nanocrystal solution was placed in an ultracentrifugation filter (Amicon Ultra, regenerated cellulose membrane, 50 kDa molecular weight cutoff) and centrifuged at 4000g for 4 minutes at room temperature. The colorless filtrate was discarded, and the concentrated nanocrystal solution retained on the filter was diluted to 15 mL with aqueous, sterile-filtered phosphate buffered saline (PBS, 150 mM, pH 7.4). The ultracentrifugal filtration process was repeated two more times using PBS to dilute the concentrated nanocrystals. The final aqueous nanocrystal dispersion was stored in a glass vial under ambient conditions until use.

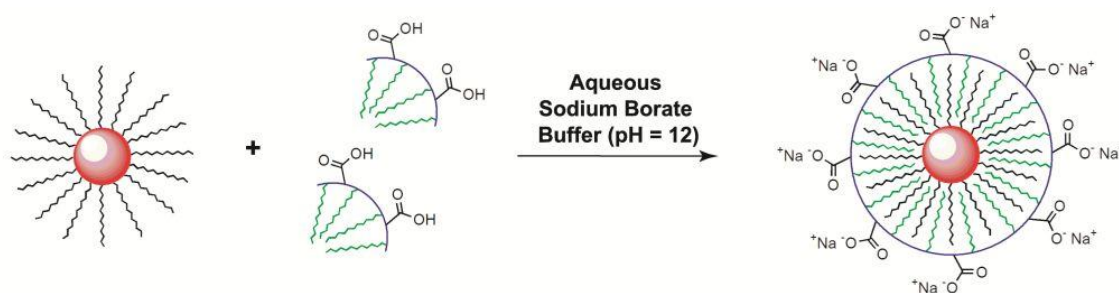


Figure 4.3. Schematic illustration of hydrophobic nanocrystals dispersing in aqueous buffer solution with an amphiphilic polymer coating.

4.3 Results and Discussion

4.3.1 Amphiphilic Polymer Characterization

Chemical analyses were performed on the amphiphilic polymer to confirm that the dodecylamine couples to the anhydrides in the polymer backbone, as diagrammed in Figure 4.1. Figure 4.4 shows a ^1H NMR spectrum of the amphiphilic polymer dissolved in CDCl_3 . In the ^1H NMR spectrum, broad magnetic resonance peaks corresponding to carboxylic acid COOH protons ($\delta_{\text{H}} = 14\text{--}17$ ppm) and amide N-H protons ($\delta_{\text{H}} = 6\text{--}9$ ppm) are identified, and the integrals of these peaks (minus the chloroform signal) are about equal in magnitude indicating that the polymer contains approximately the same number of carboxyl and amide groups as expected. The broad proton resonance peak at $\delta_{\text{H}} = 2\text{--}4$ ppm corresponds to protons attached to the anhydride rings and in the methyl group adjacent to nitrogen. The broad proton resonance peak at $\delta_{\text{H}} = 0\text{--}2$ ppm accounts for the remaining protons in the dodecyl and isobutyl groups in the polymer. The breadth of the proton NMR peaks is due to the polydispersity in the polymer structure.

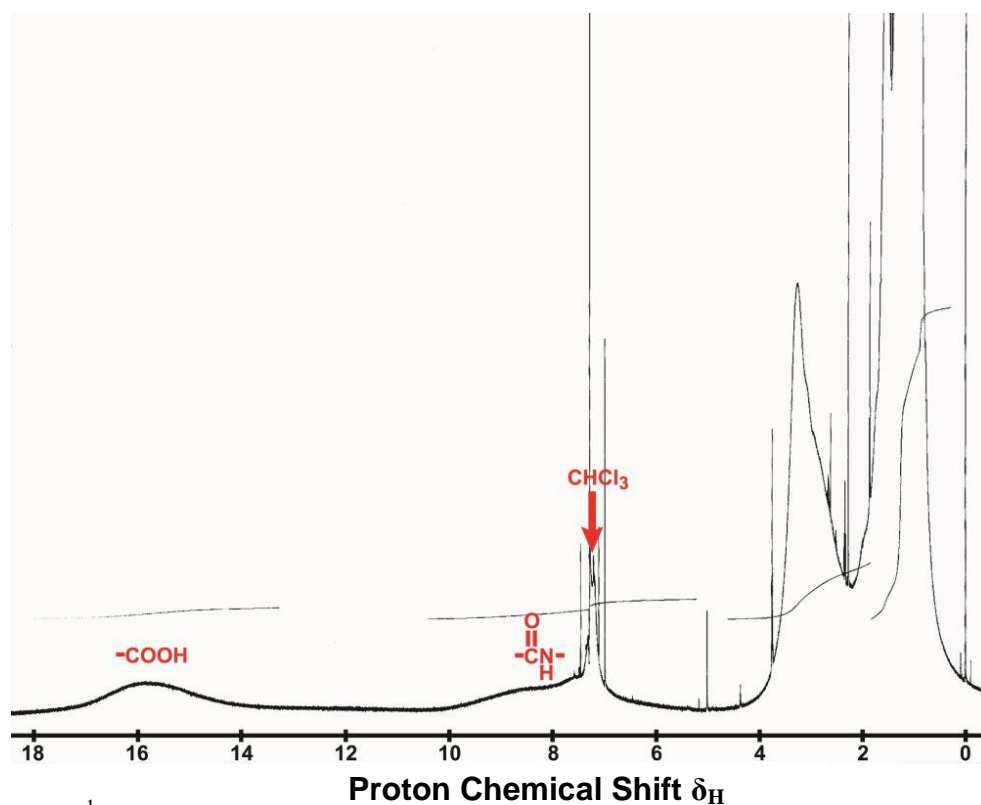


Figure 4.4. ^1H NMR characterization of the amphoteric polymer dissolved in CDCl_3 . The sample contains tetramethylsilane, having a signature peak at 0 ppm. The sample inevitably contains some contaminant CHCl_3 , which produces a sharp resonance peak at about 7-7.5 ppm as expected.

Figure 4.5 shows the ATR-FTIR spectrum of a dry film of amphiphilic polymer, which is compared to three reference FTIR spectra of simple chemical molecules having functional groups analogous to the anticipated structure of the amphiphilic polymer. The IR absorbance peaks in the polymer spectrum can be matched to peaks in the reference spectra. Importantly, the amide is identified by the N-H stretch ($3100 - 3500\text{ cm}^{-1}$) and the N-H bend ($1500 - 1650\text{ cm}^{-1}$).⁵⁸ The carboxylic acid is identified by the O-H stretch ($2200 - 2700\text{ cm}^{-1}$) and the C=O stretch ($1700 - 1780\text{ cm}^{-1}$).⁵⁸ Anhydrides are identified by the characteristic C=O stretch at $1800 - 1900\text{ cm}^{-1}$ and the C-O bends at $900 - 1100\text{ cm}^{-1}$. Interestingly, the carbonyl stretch of the amide group is not precisely positioned at 1650 cm^{-1} for the polymer, as expected from the reference spectrum of N-butyl propionamide. The amide carbonyl is conjugated to the backbone of the polymer, and it is recognized that conjugation will lower the carbonyl stretching frequency by about 50 cm^{-1} ,⁵⁸ so the amide's carbonyl stretch must be at 1600 cm^{-1} such that the absorbance peak appears merged with the peak for the N-H bend.

Mass spectrometry was used to further analyze the polymer structure and the results are displayed in Figure 4.6. The weight average molecular weight (Mw) of the poly(maleic anhydride) before reaction with amine is 6000 Da according to the supplier. After reacting 75% of the anhydride groups with dodecylamine, the polymer's average molecular weight should increase to 11560 Da. MALDI is an acceptable mass spectrometry mode for analyzing molecules larger than 10000 Da, and the polymer was run in negative ionization mode since the polymer's carboxyl groups are readily de-

protonated. However, ions with mass/charge (m/z) ratios larger than 3350 were not observed when the polymer was analyzed by MALDI. This is surprising, given that the poly(maleic anhydride) backbone alone should be at least 6000 Da. Looking carefully at the spacing between the peaks of ions in the mass spectrum, it is obvious that the mass difference between ions equals the mass of either un-reacted monomer units or monomer units conjugated to dodecylamine, as diagrammed in Figure 4.6. Therefore, the polymer's molecular ion may not be detected in MALDI because the polymer is heavily fragmented. In addition, the polymer may contain multiple charges since it has about 30 carboxyl groups available for de-protonation in negative-mode mass spectrometry. An 11000 – 12000 Da polymer that has 5 negative charges will have a peak at $m/z = 2200 - 2400$, which is comparable to the mass range of ions detected during MALDI. So mass spectrometry has provided further confirmation that the polymer contains a mixture of anhydride monomers and monomers conjugated to dodecylamine, however more progress is needed to accurately measure the polymer's molecular weight.

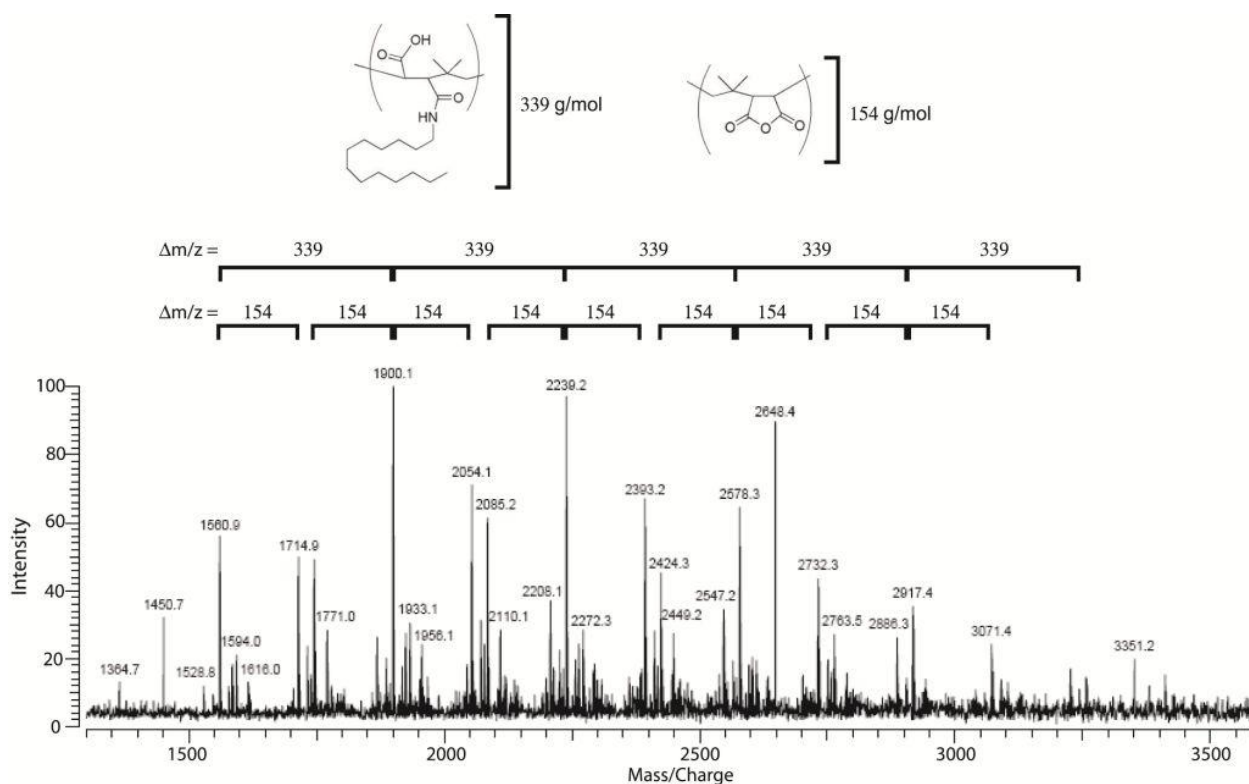


Figure 4.6. MALDI mass spectrometry analysis of the amphiphilic polymer. There is extreme fragmentation of the polymer, but by comparing the difference in m/z between peaks, it is obvious that the fragments are composed of the anhydride (154 g/mole) and carboxyl-amide functional groups (339 g/mole). Larger m/z fragments (> 3500) were not generated by this technique, so it was not possible to evaluate the m/z of the molecular ion.

4.3.2 Nanocrystal Characterization

Si Nanocrystals. The diameter of hydrophobic Si nanocrystals after hydrosilylation was determined by SAXS. Imaging Si nanocrystals in this size range by TEM is very difficult because there is a very low electron density difference between silicon and carbon, the typical TEM grid support. Not only is it difficult to resolve the nanocrystals themselves,

it is even more difficult to determine an accurate diameter from the edge of the nanocrystal, as needed to obtain a statistically meaningful measure of the nanocrystal size distribution in the sample. Grazing incidence small angle X-ray scattering (GISAXS) and transmission SAXS have been used to determine the size distribution of Si nanocrystals embedded in porous Si,⁵⁹ SiO₂,⁶⁰ and amorphous silicon matrices,⁶¹ however, SAXS has not been used before to determine the size distribution of sterically-stabilized silicon nanocrystals in a solvent dispersion. Figure 4.7 shows SAXS data for dodecene-coated Si nanocrystals dispersed in toluene. Fitting the scattering intensity $I(q)$ to equations 4.1 – 4.4 gave a mean nanocrystal diameter of 2.1 ± 0.6 nm.

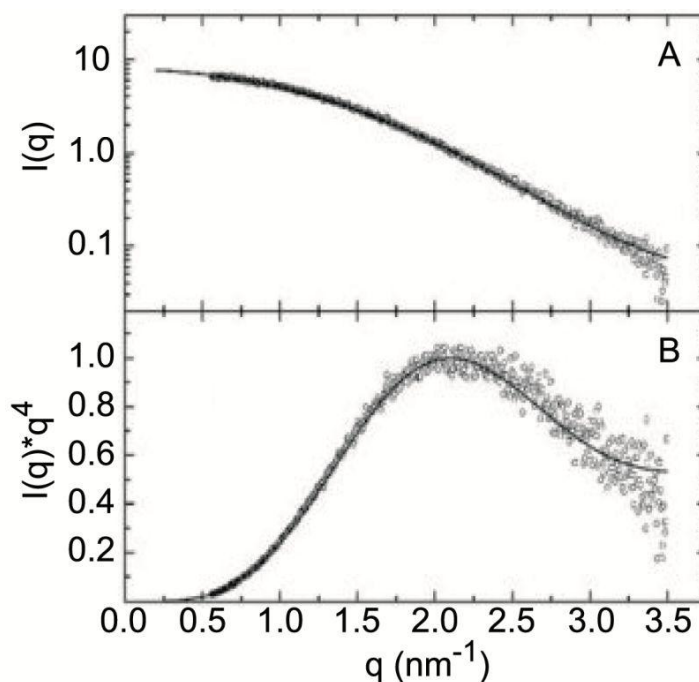


Figure 4.7. SAXS characterization of Si nanocrystals dispersed in toluene. (A) Radial integration of scattering intensity, plotted on a log scale. (B) Porod plot of scattering data. The scattering intensity is normalized to the maximum in the Porod plot. Fitted nanocrystal diameter is 2.1 ± 0.6 nm. Data collected by Brian Goodfellow.

The optical properties of the Si nanocrystals were measured before and after dodecene passivation. Figure 4.8 shows the UV-visible absorbance, photoluminescence emission (PL), and photoluminescence excitation (PLE) spectra of the nanocrystals dispersed in chloroform. Before and after dodecene passivation, the Si nanocrystals exhibit a very large Stokes shift of almost 300 nm between the PLE and PL spectra, and this is characteristic of most Si nanocrystal samples examined in the literature. Dodecene passivation caused both the PL and the PLE maximum to shift toward the red by about +60 nm, producing nanocrystals that fluoresce orange (648 nm PL maximum). Similar post-hydrosilylation red-shifts in PL spectra have also been observed by other groups, and it has been attributed to a small amount of surface oxidation during the passivation process. After dodecene passivation, the nanocrystals had a quantum yield of 8% relative to Rhodamine 101.

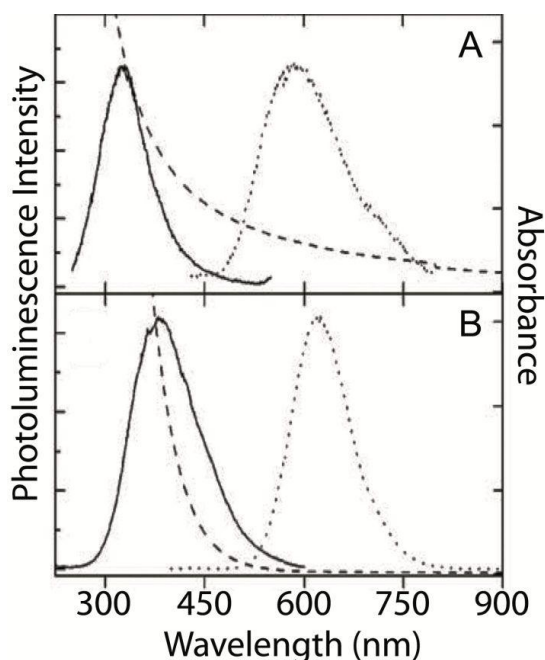


Figure 4.8. Spectra for Si nanocrystal absorbance (dashed line), photoluminescence emission (PL, dotted line), and photoluminescence excitation (PLE, solid line). (A) Si nanocrystals immediately after HF etching; the PL/PLE maxima are 590/320 nm. (B) Si nanocrystals after hydrosilylation with 1-dodecene; the PL/PLE maxima are 648/380 nm. Nanocrystals are dispersed in chloroform. Data collected by Colin Hessel.

CIS Nanocrystals. The CIS nanocrystals were imaged using TEM and the results are displayed in Figure 4.9, however the nanocrystals are difficult to image due to their very small size. The nanocrystals are more difficult to image than Au because CIS is not as dense (5.8 g/cm^3 , versus 19.7 g/cm^3 for Au)⁵⁶, and therefore CIS does not scatter as many electrons per unit volume as Au, giving CIS lower contrast than Au in TEM. Like Si nanocrystals, the mean diameter of CIS nanocrystals was determined by performing SAXS on a dilute dispersion of CIS nanocrystals in toluene, and the diameter was found to be $1.9 \pm 0.6 \text{ nm}$. The photoluminescence spectrum of the CIS nanocrystals is shown

in Figure 4.10. The CIS nanocrystals have a PL maximum at 720 nm, which is much further in to the red than the Si nanocrystals. The CIS nanocrystals also have a very broad PLE spectrum and can be excited between 350 – 600 nm, compared to the Si nanocrystals that have optimal excitation limited to 350 – 450 nm wavelengths. The quantum yield of the CIS nanocrystals (with the ZnS surface layer) is about 40% when excited at 500 nm.

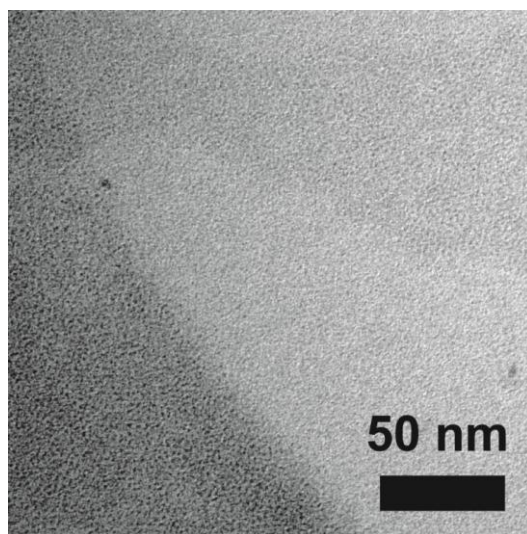


Figure 4.9. TEM characterization of CIS nanocrystals. Nanocrystals form a monolayer in the top right of the image, and nanocrystals are stacked on top of one another in the bottom left of the image. The CIS nanocrystals are very small and the size is difficult to image accurately by TEM.

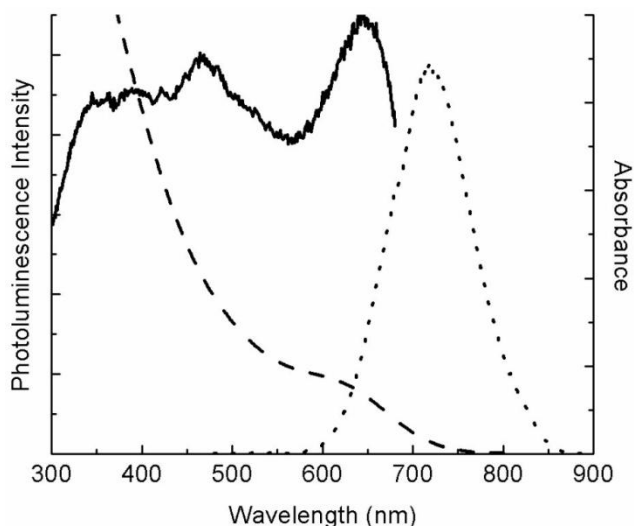


Figure 4.10. Spectra for CIS nanocrystal absorbance (dashed line), photoluminescence emission (PL, dotted line), and photoluminescence excitation (PLE, solid line). Nanocrystals are dispersed in chloroform.

4.3.3 Nanocrystal Polymer Coating

Si Nanocrystals. As shown in Figure 4.11, the PL emission wavelength of the polymer-coated Si nanocrystals dispersed in PBS was unchanged from that of the hydrophobic nanocrystals dispersed in chloroform. The quantum yield of the nanocrystals decreased only slightly to 3% when transferred to water. The dodecene-passivated nanocrystals do not disperse in water without the polymer coating – the nanocrystals form aggregates that are readily trapped within a 200 nm pore size filter (see photograph in Figure 4.11B). Polymer-coated Si nanocrystals form optically clear dispersions in PBS that easily pass through a 200 nm pore size filter and maintain their strong PL intensity. The hydrodynamic diameter was measured to be 17 nm by dynamic light scattering, and the zeta potential was -31 mV. Increasing the amount of Si nanocrystals per polymer (above

3 mg nanocrystals per 43 μ moles of monomer units) did not allow more nanocrystals to disperse in PBS – the additional nanocrystals simply formed large aggregates that were removed during the filtration process.

An aqueous dispersion of polymer-coated Si nanocrystals was vitrified and imaged using cryoTEM. The cryoTEM images are shown in Figure 4.12. The polymer micelles appear to be short threads or worm-like structures similar to recent reports on detergent micelles.^{62,63} The length of the micelles is around 10-20 nm, while the thickness is about 5 nm, and these results are consistent with the hydrodynamic diameter measured by light scattering. Unfortunately the location of the Si nanocrystals in the dispersion could not be identified, since the nanocrystals have low contrast relative to the hydrocarbon regions of the micelles where the nanocrystals are expected to reside.

Polymer-coated Si nanocrystals were injected into a model host and then imaged with a custom-built fluorescence imaging system to determine their potential as contrast agents for *in vivo* biological imaging.⁶⁴ Figure 4.13 shows a section of chicken tissue injected with Si nanocrystals imaged with a custom built wide field fluorescence imaging system. The fluorescence from the nanocrystals is readily observable in the tissue illuminated with a 337 nm laser and imaged with a 600 nm long pass filter to remove reflected light from the excitation source (Figure 4.13B).

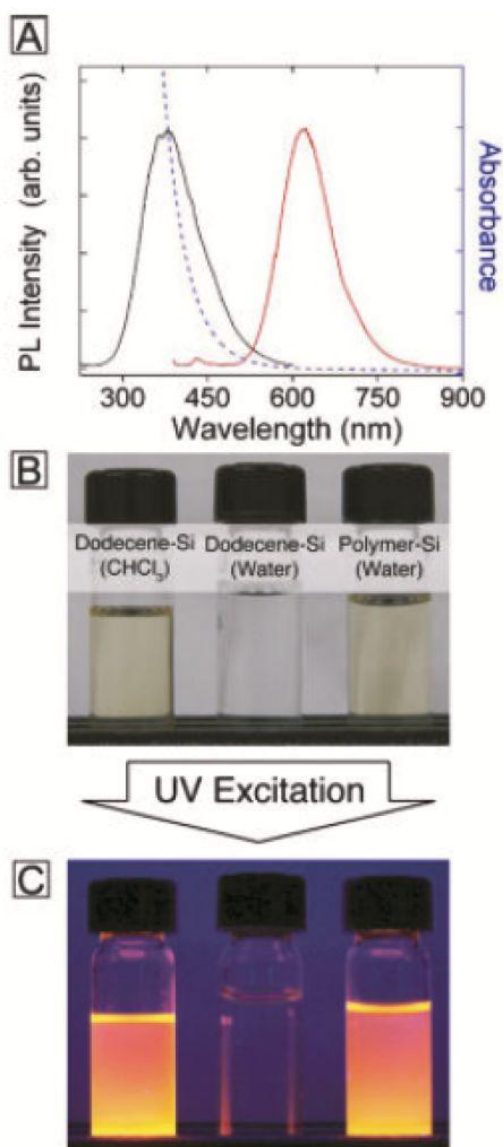


Figure 4.11. Fluorescence of polymer-coated Si. (A) Room temperature PL (red), PLE (black), and absorbance (blue) of polymer-coated Si nanocrystals dispersed in aqueous phosphate buffered saline (PBS) solution at pH 7. (B) Photographs of vials containing (from left to right) alkyl-passivated Si nanocrystals in chloroform, alkyl-passivated Si nanocrystals sonicated in PBS, and polymer-coated Si nanocrystals in PBS. The aqueous samples were passed through a 200 nm pore size filter. (C) Photographs of the vials shown in (B) illuminated by UV (350 nm) light.

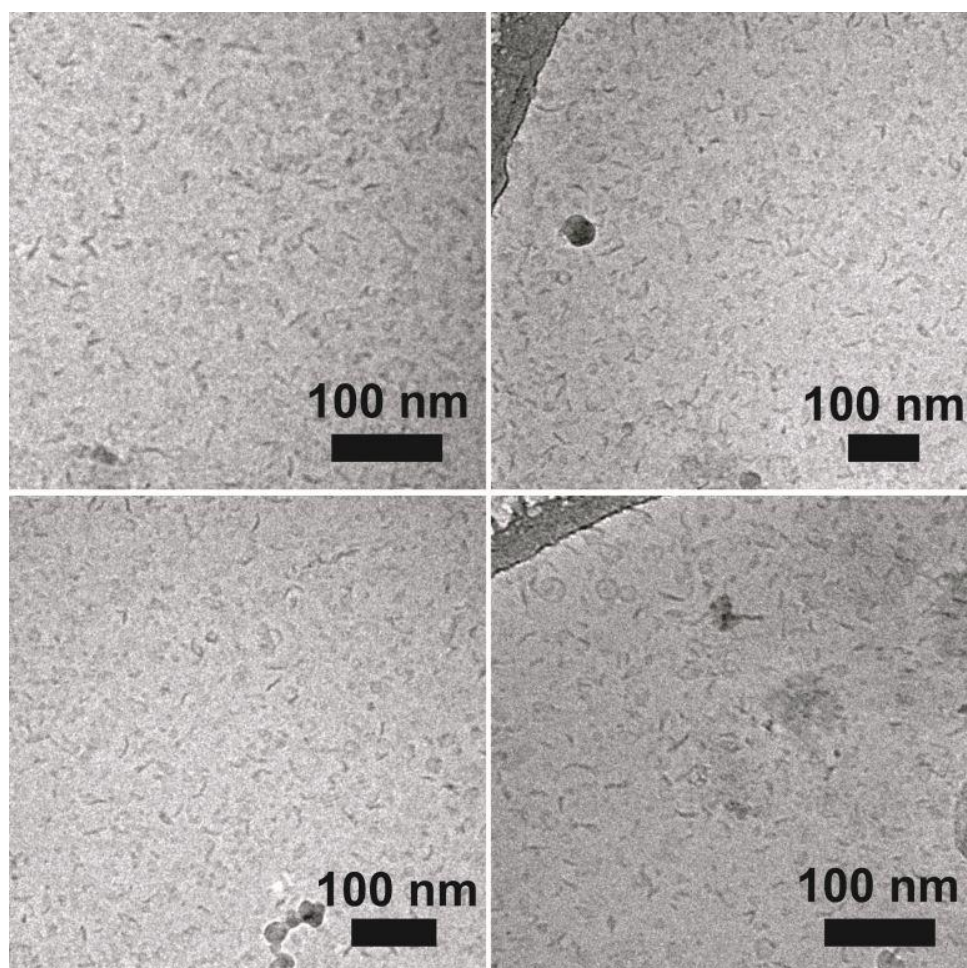


Figure 4.12. CryoTEM imaging of polymer micelles made with Si, dispersed in PBS. The polymer micelles appear to be thread- or disk-shaped structures.

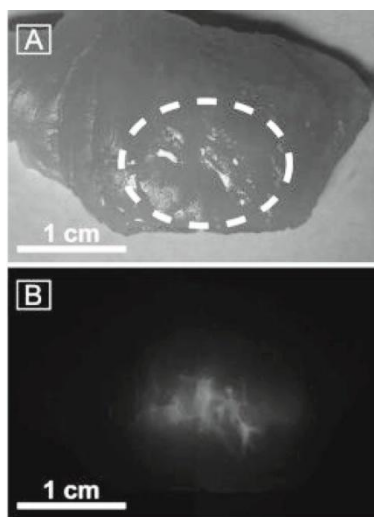


Figure 4.13. Grey-scale CCD images of biological tissue injected with polymer coated Si nanocrystals in PBS. The tissue is under (A) room light, and (B) UV illumination with a 337 nm pulsed nitrogen laser. Grey-scale fluorescence images were collected with a custom-built wide field fluorescence imaging system equipped with a 600 nm long pass filter to remove the excitation contribution from the image. The location of the injected Si nanocrystals is outlined in (A) for clarity. 150 μL of a PBS dispersion of polymer coated Si nanocrystals (10^{16} nanocrystals/mL) was injected 3 mm below the tissue surface. Image captured by Priya Puvanakrishnan.

CIS Nanocrystals. As shown in Figure 4.14, the PL emission wavelength of the polymer-coated CIS nanocrystals dispersed in PBS was unchanged from that of the hydrophobic nanocrystals dispersed in chloroform. The quantum yield of the nanocrystals decreased to 20% when transferred to water. Polymer-coated CIS nanocrystals form optically clear dispersions in PBS that easily pass through a 200 nm pore size filter and maintain their strong PL intensity.

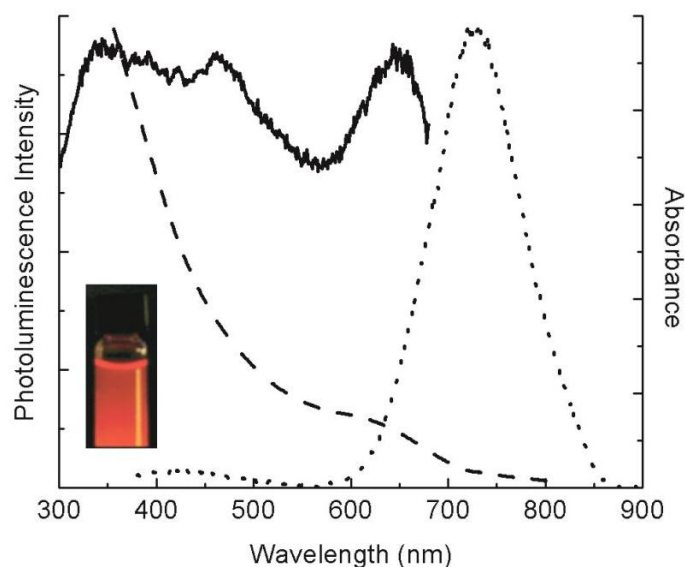


Figure 4.14. Polymer-coated CIS absorbance (dashed line), photoluminescence emission (PL, dotted line), and photoluminescence excitation (PLE, solid line). The nanocrystals are dispersed in PBS (aq).

4.3.4 Stability of Polymer Coated Nanocrystals

The PL and dispersion stability of polymer-coated Si nanocrystals were tested at various ionic strength and pH. For testing ionic strength, the nanocrystal dispersions (20 μL) were loaded into separate wells of a 96-well plate and diluted with 80 μL of NaCl(aq) solutions ranging from 250 mM – 5 M ionic strength. For testing pH, 20 μL of nanocrystal dispersion was loaded into separate wells and then diluted with 80 μL of sodium borate buffer (250 mM) ranging in pH from 7.0 – 12. The results of the ionic strength test are displayed in Figure 4.15, showing that the nanocrystals maintain their PL emission intensity up to 4 M, while the dispersion becomes more turbid above 2 M

indicating that polymer flocculates into larger aggregates. The results of the pH test are listed in Figure 4.16, showing that increasing pH does not cause flocculation of the nanocrystals but above pH 10 the emission starts to decline. Therefore, recommended handling conditions for the amphiphilic polymer coated nanocrystals are pH 7 – 10 and ionic strength of less than 2 M.

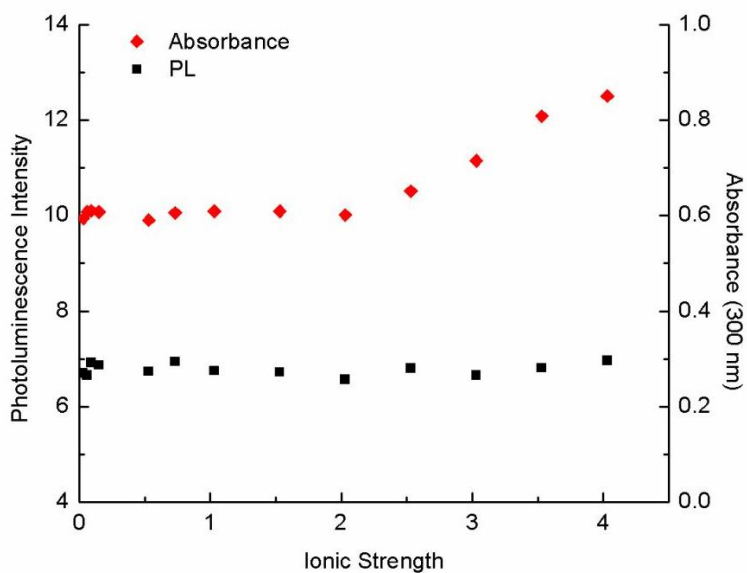


Figure 4.15. Effect of ionic strength on the photoluminescence intensity (380 nm excitation) and absorbance (turbidity, 300 nm) of amphiphilic polymer-coated Si nanocrystals.

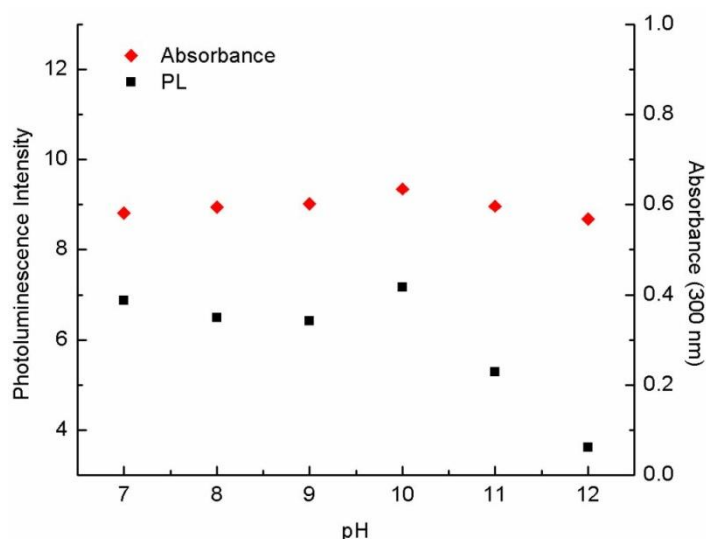


Figure 4.16. Effect of varying pH on the photoluminescence intensity (380 nm excitation) and absorbance (turbidity, 300 nm) of amphiphilic polymer-coated Si nanocrystals.

The results of the ionic strength test (Figure 4.15) suggest that the nanocrystals will flocculate when the electric double layer repulsions between polymer molecules is reduced by screening the charge on the carboxyl groups.⁶⁵ Flocculation can also be induced by cross-linking the carboxyl groups with divalent cations or hydrogen bonding at low pH. Figure 4.17 shows a confocal microscope image of a dispersion of polymer-coated CIS nanocrystals that were mixed with calcium chloride (50 mM Ca^{2+} , 3 mg/mL CIS). The dispersion contains fluorescent flocculates of nanocrystals that are around 10 μm in diameter. Divalent (and trivalent) cations are known to induce flocculation of colloid particles having a negative zeta potential – divalent cations adsorb to the colloid particles and reduce the thickness and density of the adsorbed layer of ions, weakening the inter-particle repulsive potential.^{66,67} The polymer coated nanocrystals are also

flocculated by lowering the pH below 7, which results in protonation and neutralization of the polymer's carboxyl groups. The top arrow of Figure 4.18 shows the flocculation of polymer coated Si nanocrystals when the pH is lowered from 7 to 3 by adding HCl. However, when a protein like bovine serum albumin (BSA, isoelectric point = 4.7) is included in the dispersion, the nanocrystals do not flocculate in spite of lowering the pH to 3. It was shown that BSA can adsorb to Au nanocrystals having a negative zeta potential,⁶⁸ therefore we suspect that the BSA adsorbs to the polymer-coated Si nanocrystals as well at neutral pH. When the pH is lowered to 3, apparently the adsorbed BSA keeps the polymer-coated nanocrystals from flocculating. Therefore, protein adsorption seems to provide a means of improving the stabilization of the polymer coated nanocrystals in aqueous solution.

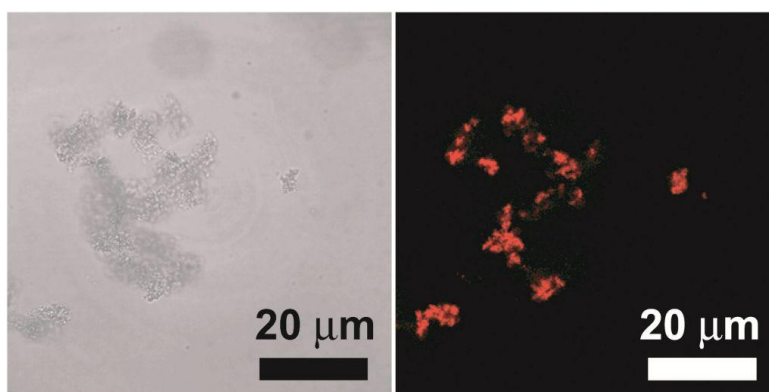


Figure 4.17. Confocal fluorescence microscope image of polymer-coated CIS nanocrystals flocculated with 50 mM CaCl_2 . The nanocrystals are excited with a 400 nm wavelength laser. Left panel: Transmitted light image. Right panel: Red light channel (650 – 800 nm).

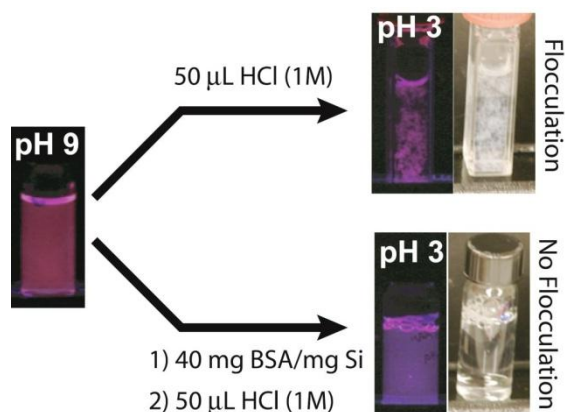


Figure 4.18. Amphiphilic polymer coated Si nanocrystals. Top: Flocculation induced by mixing 0.2 mg Si, 50 μmol HCl in 2 mL DI water. Bottom: Mixing 0.2 mg Si, 8 mg BSA, and 50 μmol HCl in 2 mL DI water does not result in Si flocculation.

4.4 Conclusions

The amphiphilic polymer coating enables hydrophobic Si and CIS nanocrystals to disperse in water, and the nanocrystals remain fluorescent. The nanocrystals are stable in water over a wide range of pH and ionic strength. The polymer-coated nanocrystals flocculate when exposed to calcium, or when the pH is lowered below neutral. BSA protein inhibits the flocculation of the nanocrystals, and therefore protein adsorption on the polymer-coated nanocrystals is worth further investigation for enhancing the nanocrystal stability.

4.5 References

- (1) Katz, E.; Willner, I. *Angewandte Chemie-International Edition* **2004**, *43*, 6042-6108.
- (2) Petros, R. A.; DeSimone, J. M. *Nature Reviews Drug Discovery* **2010**, *9*, 615-627.

- (3) Selvan, S. T.; Tan, T. T. Y.; Yi, D. K.; Jana, N. R. *Langmuir* **2010**, *26*, 11631-11641.
- (4) Gill, R.; Zayats, M.; Willner, I. *Angewandte Chemie-International Edition* **2008**, *47*, 7602-7625.
- (5) Yong, K. T.; Roy, I.; Swihart, M. T.; Prasad, P. N. *Journal of Materials Chemistry* **2009**, *19*, 4655-4672.
- (6) Jain, P. K.; Huang, X. H.; El-Sayed, I. H.; El-Sayed, M. A. *Accounts of Chemical Research* **2008**, *41*, 1578-1586.
- (7) Daniel, M.; Astruc, D. *Chemical Reviews* **2004**, *104*, 293-346.
- (8) Pankhurst, Q. A.; Thanh, N. K. T.; Jones, S. K.; Dobson, J. *Journal of Physics D-Applied Physics* **2009**, *42*, 220301.
- (9) Huang, X. H.; Neretina, S.; El-Sayed, M. A. *Advanced Materials* **2009**, *21*, 4880-4910.
- (10) Medintz, I. L.; Uyeda, H. T.; Goldman, E. R.; Mattoussi, H. *Nature Materials* **2005**, *4*, 435-446.
- (11) Michalet, X.; Pinaud, F. F.; Bentolila, L. A.; Tsay, J. M.; Doose, S.; Li, J. J.; Sundaresan, G.; Wu, A. M.; Gambhir, S. S.; Weiss, S. *Science* **2005**, *307*, 538-544.
- (12) Heitsch, A. T.; Smith, D. K.; Patel, R. N.; Ress, D.; Korgel, B. A. *Journal of Solid State Chemistry* **2008**, *181*, 1590-1599.
- (13) Bonnemain, B. *Journal of Drug Targeting* **1998**, *6*, 167-174.
- (14) Jain, P. K.; El-Sayed, I. H.; El-Sayed, M. A. *Nano Today* **2007**, *2*, 18-29.
- (15) Resch-Genger, U.; Grabolle, M.; Cavaliere-Jaricot, S.; Nitschke, R.; Nann, T. *Nature Methods* **2008**, *5*, 763-775.
- (16) Smith, A. M.; Duan, H. W.; Mohs, A. M.; Nie, S. M. *Advanced Drug Delivery Reviews* **2008**, *60*, 1226-1240.
- (17) Chattopadhyay, P. K.; Price, D. A.; Harper, T. F.; Betts, M. R.; Yu, J.; Gostick, E.; Perfetto, S. P.; Goepfert, P.; Koup, R. A.; De Rosa, S. C.; Bruchez, M. P.; Roederer, M. *Nature Medicine* **2006**, *12*, 972-977.
- (18) Medintz, I. L.; Mattoussi, H.; Clapp, A. R. *International Journal of Nanomedicine* **2008**, *3*, 151-167.
- (19) Wang, C.; Gao, X.; Su, X. G. *Analytical and Bioanalytical Chemistry* **2010**, *397*, 1397-1415.
- (20) Ho, Y. P.; Leong, K. W. *Nanoscale* **2010**, *2*, 60-68.
- (21) Frasco, M. F.; Chaniotakis, N. *Analytical and Bioanalytical Chemistry* **2010**, *396*, 229-240.
- (22) Edgar, R.; McKinstry, M.; Hwang, J.; Oppenheim, A. B.; Fekete, R. A.; Giulian, G.; Merrill, C.; Nagashima, K.; Adhya, S. *Proceedings of the National Academy of Sciences of the United States of America* **2006**, *103*, 4841-4845.
- (23) Lin, W. B.; Hyeon, T.; Lanza, G. M.; Zhang, M. Q.; Meade, T. J. *Mrs Bulletin* **2009**, *34*, 441-448.
- (24) Laurent, S.; Boutry, S.; Mahieu, I.; Vander Elst, L.; Muller, R. N. *Current Medicinal Chemistry* **2009**, *16*, 4712-4727.
- (25) Islam, T.; Josephson, L. *Cancer Biomarkers* **2009**, *5*, 99-107.

- (26) Tam, J. M.; Tam, J. O.; Murthy, A.; Ingram, D. R.; Ma, L. L.; Travis, K.; Johnston, K. P.; Sokolov, K. V. *ACS Nano* **2010**, *4*, 2178-2184.
- (27) Shah, J.; Park, S.; Aglyamov, S.; Larson, T.; Ma, L.; Sokolov, K.; Johnston, K.; Milner, T.; Emelianov, S. Y. *Journal of Biomedical Optics* **2008**, *13*, 034024.
- (28) Chamberland, D. L.; Agarwal, A.; Kotov, N.; Fowlkes, J. B.; Carson, P. L.; Wang, X. *Nanotechnology* **2008**, *19*, 095101.
- (29) Zharov, V. P.; Galanzha, E. I.; Shashkov, E. V.; Kim, J. W.; Khlebtsov, N. G.; Tuchin, V. V. *Journal of Biomedical Optics* **2007**, *12*, 051503.
- (30) Murray, C. B.; Kagan, C. R.; Bawendi, M. G. *Annual Review of Materials Science* **2000**, *30*, 545-610.
- (31) Xia, Y.; Xiong, Y.; Lim, B.; Skrabalak, S. E. *Angewandte Chemie-International Edition* **2009**, *48*, 60-103.
- (32) Muir, B. W.; Moffat, B. A.; Harbour, P.; Coia, G.; Zhen, G. L.; Waddington, L.; Scoble, J.; Krah, D.; Thang, S. H.; Chong, Y. K.; Mulvaney, P.; Hartley, P. *Journal of Physical Chemistry C* **2009**, *113*, 16615-16624.
- (33) Park, J. H.; Gu, L.; von Maltzahn, G.; Ruoslahti, E.; Bhatia, S. N.; Sailor, M. J. *Nature Materials* **2009**, *8*, 331-336.
- (34) Erogbogbo, F.; Yong, K. T.; Roy, I.; Xu, G. X.; Prasad, P. N.; Swihart, M. T. *Acs Nano* **2008**, *2*, 873-878.
- (35) Osaki, F.; Kanamori, T.; Sando, S.; Sera, T.; Aoyama, Y. *Journal of the American Chemical Society* **2004**, *126*, 6520-6521.
- (36) Soo Choi, H.; Liu, W.; Mista, P.; Tanaka, E.; Zimmer, J. P.; Itty, I. B.; Bawendi, M. G.; Frangioni, J. V. *Nature Biotechnology* **2007**, *25*, 1165-1170.
- (37) Sadauskas, E.; Wallin, H.; Stoltenberg, M.; Vogel, U.; Doering, P.; Larsen, A.; Danscher, G. *Particle and Fiber Toxicology* **2007**, *4*, 10.
- (38) Jiang, W.; Kim, B. Y. S.; Rutka, J. T.; Chan, W. C. W. *Nature Nanotechnology* **2008**, *3*, 145-150.
- (39) Gao, H. J.; Shi, W. D.; Freund, L. B. *Proceedings of the National Academy of Sciences of the United States of America* **2005**, *102*, 9469-9474.
- (40) Wu, X. Y.; Liu, H. J.; Liu, J. Q.; Haley, K. N.; Treadway, J. A.; Larson, J. P.; Ge, N. F.; Peale, F.; Bruchez, M. P. *Nature Biotechnology* **2003**, *21*, 452-452.
- (41) Li, Z. F.; Ruckenstein, E. *Nano Letters* **2004**, *4*, 1463-1467.
- (42) Zhang, X.; Neiner, D.; Wang, S.; Louie, A. Y.; Kauzlarich, S. M. *Nanotechnology* **2007**, *18*, 095601.
- (43) Gao, X.; Cui, Y.; Levenson, R. M.; Chung, L. W. K.; Nie, S. *Nature Biotechnology* **2004**, *22*, 969-976.
- (44) Sperling, R. A.; Pellegrino, T.; Li, J. K.; Chang, W. H.; Parak, W. J. *Advanced Functional Materials* **2006**, *16*, 943-948.
- (45) Lin, C. A. J.; Sperling, R. A.; Li, J. K.; Yang, T. Y.; Li, P. Y.; Zanella, M.; Chang, W. H.; Parak, W. G. J. *Small* **2008**, *4*, 334-341.
- (46) Hermanson, G. T. *Bioconjugate Techniques*; Second ed.; Academic Press, Inc.: San Diego, 2008.

- (47) Using more than 0.75 mole dodecylamine per mole anhydride did not seem to offer any benefit in this work. Increasing the amount of dodecylamine just increases the molecular weight of the polymer, which is not beneficial.
- (48) Hessel, C. M.; Rasch, M. R.; Hueso, J. L.; Goodfellow, B. W.; Akhavan, V.; Puvanakrishnan, P.; Tunnell, J. W.; Korgel, B. A. *Small* **2010**, *6*, 2026-2034.
- (49) Hessel, C. M.; Henderson, E. J.; Veinot, J. G. C. *Chemistry of Materials* **2006**, *18*, 6139-6146.
- (50) Hessel, C. M.; Henderson, E. J.; Veinot, J. G. C. *Journal of Physical Chemistry C* **2007**, *111*, 6956-6961.
- (51) Williams, K. R.; Gupta, K.; Wasilik, M. J. *Journal of Micromechanical Systems* **2003**, *12*, 761-778.
- (52) Korgel, B. A.; Fitzmaurice, D. *Physical Review B* **1999**, *59*, 14191-14201.
- (53) Korgel, B. A.; Fullam, S.; Connolly, S.; Fitzmaurice, D. *Journal of Physical Chemistry B* **1998**, *102*, 8379-8388.
- (54) Glatter, O.; Kratky, O.; Eds. *Small-Angle X-Ray Scattering*; Academic Press: New York, 1982.
- (55) Guinier, A.; Fournet, G. *Small-Angle Scattering of X-Rays*; Wiley: New York, 1955.
- (56) *CRC Handbook of Chemistry and Physics*; 91st ed.; CRC Press: Boca Raton, FL, 2011.
- (57) SDBSWeb : <http://riodb01.ibase.aist.go.jp/sdbs/> (National Institute of Advanced Industrial Science and Technology, July 2012)
- (58) Coates, J. In *Encyclopedia of Analytical Chemistry*; Meyers, R. A., Ed.; John Wiley & Sons Ltd: Chichester, 2000, p 10815-10837.
- (59) Matsumoto, T.; Suzuki, J. I.; Ohnuma, M.; Kanemitsu, Y.; Masumoto, Y. *Physical Review B* **2001**, *63*, 1953221-1953225.
- (60) Bernstorff, S.; Dubček, P.; Kovačević, I.; Radić, N.; Pivac, B. *Thin Solid Films* **2007**, *515*, 5637-5640.
- (61) Gracin, D.; Bernstorff, S.; Dubcek, P.; Gajovic, A.; Juraic, K. *Journal of Applied Crystallography* **2007**, *40*, s373-s376.
- (62) Pochan, D. J.; Cui, H.; Hodgdon, T. K.; Kaler, E. W.; Abezgauz, L.; Danino, D.; Lubovsky, M.; Talmon, Y. *Soft Matter* **2007**, *3*, 945-955.
- (63) Pochan, D. J.; Zhong, S. *Polymer Reviews* **2010**, *50*, 287-320.
- (64) Puvanakrishnan, P.; Park, J.; Diagaradjane, P.; Schwartz, J. A.; Coleman, C. L.; Gill-Sharp, K. L.; Sang, K. L.; Payne, J. D.; Krishnan, S.; Tunnell, J. W. *Journal of Biomedical Optics* **2009**, *14*, 024044.
- (65) Israelachvili, J. N. *Intermolecular and Surface Forces*; 2nd ed.; Academic press Inc.: San Diego, 1992.
- (66) Migo, V. P.; Del Rosario, E. J.; Matsumura, M. *Journal of Fermentation and Bioengineering* **1997**, *83*, 287-291.
- (67) Dickinson, E.; McClements, D. J. *Advances in Food Colloids*; Blackie Academic & Professional: Glasgow, 1996.

(68) Brewer, S. H.; Glomm, W. R.; Johnson, M. C.; Knag, M. K.; Franzen, S.
Langmuir **2005**, *21*, 9303-9307.

Chapter 5: Chloroform Enhances Incorporation of Hydrophobic Au Nanocrystals into Unsaturated Phosphatidylcholine Vesicles[§]

5.1 Introduction

Hybrids of vesicles, or liposomes, and inorganic nanocrystals have interesting implications for medical imaging, drug delivery, and nanotoxicology.¹ They should exhibit the well-established properties of vesicles, like the ability to encapsulate drugs for targeted delivery in the body,² while imparting new functionality, such as imaging contrast for real-time tracking *in vivo*,³⁻⁵ or a therapeutic response to external electromagnetic stimulation by heating or cooling.⁶⁻¹⁰ Studies of vesicle-nanocrystal hybrids could also provide fundamental insight about how nanomaterials distribute in live cells and organisms, with vesicles serving as models of naturally-occurring biological membranes.^{11,12}

Vesicle-nanocrystal hybrids can be created using several strategies.¹ For example, nanocrystals can be precipitated in-place within vesicles,¹³⁻²⁸ or they can be synthesized and then associated with vesicles, either by electrostatic adsorption²⁹⁻³⁵ or encapsulation^{36,37} of hydrophilic nanocrystals, or by insertion of hydrophobic nanocrystals into the non-polar interior of the lipid bilayer.^{3,5,38-41} Precipitation within the vesicles limits the nanocrystal chemistry to a relatively narrow range of materials because

[§] Portions of this chapter appear in the following two publications: (1) Rasch, M.R.; Rossinyol, E.; Hueso, J.L.; Goodfellow, B.W.; Arbiol, J.; Korgel, B.A. *Nanoletters* 2010, 10, 3733-3739; and (2) Rasch, M.R.; Yu, Y.; Bosoy, C.A.; Korgel, B.A. *Langmuir* 2012, submitted. In the respective publications, the experiments were performed by M.R. Rasch, E. Rossinyol, J.L. Hueso, B.W. Goodfellow, J. Arbiol, Y. Yu, and C.A. Bosoy. Both publications were written by M.R. Rasch and B.A. Korgel. Funding was provided by research grants to J. Arbiol and B.A. Korgel.

the synthesis must be carried out near room temperature in aqueous media.^{13-23,26,28} The reliance on hydrophilic nanocrystals is also limiting, as a much wider range of nanocrystal materials with the highest quality properties are obtained with hydrophobic capping ligands from synthetic reactions carried out in organic high boiling point solvents.⁴² Therefore, the ability to load hydrophobic nanocrystals into the lipid bilayer of vesicles provides a quite general route to vesicle-nanocrystal hybrids, making available a wide range of nanocrystal chemistry, including the prospect of loading different combinations of nanocrystals within each vesicle.

There are many examples in the literature of hydrophobic nanocrystals, including Au,^{37,39,43,44} Ag,^{45,46} CdSe,^{3,38,40,41,47} Si,⁴⁸ and Fe₂O₃,^{5,49,50} being dispersed in water with vesicle-forming surfactants. The structures of the resulting lipid-nanocrystal assemblies, however, are typically not well characterized, leaving fundamental questions about how hydrophobic nanocrystals really associate with liposomes and affect their stability. It is known that nanocrystals can disrupt vesicle formation under certain conditions; for example, hydrophobic nanocrystals larger than about 6 nm in diameter tend to induce lipid adsorption around the nanocrystals into micelle-like structures instead of vesicles.^{51,52} Lipid adsorption around smaller nanocrystals on the other hand, leads to too much curvature of the lipid membrane,^{51,53,54} and vesicles form instead of micelles, reportedly with hydrophobic nanocrystals embedded within the lipid bilayer.^{5,55,56} Molecular dynamics simulations have predicted that very small (~1 nm diameter) hydrophobic fullerenes can disperse in a lipid bilayer without significant distortion of the lipid bilayer,⁵⁷ but spherical nanocrystals of slightly larger size (i.e., 2~4 nm diameter)

should distort the packing of the hydrophobic chains. This is different than alkanes or membrane-spanning proteins that can simply insert in a bilayer parallel to the lipid molecules;⁵⁸⁻⁶¹ nanocrystals should force a molecular “unzipping”^{44,48,51} of the lipid bilayer that could also disrupt the integrity of the vesicles. Therefore, we sought to study phosphatidylcholine (PC) vesicles with dodecanethiol-coated Au nanocrystals as a model system, with the help of cryogenic transmission electron microscopy (cryoTEM) imaging, to understand in detail how hydrophobic nanocrystals interact with liposomes.

This chapter demonstrates the interaction of hydrophobic Au nanocrystals with vesicles prepared from two types of unsaturated lipids – PC derived from hen eggs (eggPC), and pure dioleoylphosphatidylcholine (DOPC). The results indicate that incorporating Au nanocrystals into these unsaturated lipid vesicles depends on the nanocrystal size and the presence of residual chloroform. Dodecanethiol-coated Au nanocrystals were synthesized with diameters of 1.8 nm and 4.0 nm using established methods.^{62,63} Au nanocrystals with a 1.8 nm diameter and hexadecanethiol coating were also synthesized. To form vesicles, the Au nanocrystals were mixed with PC lipids in chloroform solvent, dried to a film, dispersed in deionized water by ultrasonication, and then extruded through 100 nm diameter pores. The effect of residual chloroform was studied by controlled exposure of the dry lipid-nanocrystal film to organic solvent vapor (solvent vapor annealing). CryoTEM was used as the primary tool for structural characterization because it provides clear visualization of the vesicle-nanocrystal hybrids, with sufficient resolution to view individual nanocrystals and their location within the vesicles in their native environment.^{20,60,64-68}

5.2 Experimental Details

5.2.1 Chemicals

Hydrogen tetrachloroaurate trihydrate ($\text{HAuCl}_4 \cdot 3\text{H}_2\text{O}$, 99.999%), tetraoctylammonium bromide (TOAB, 98%), sodium borohydride (NaBH_4 , 98%), diethyl ether, 1-dodecanethiol (98%), 1-hexadecanethiol (95%), anhydrous chloroform (99%) and anhydrous dichloromethane were obtained from Sigma-Aldrich. Toluene, cyclohexane, hexanes, dichloromethane, acetone, ethanol (EtOH, 200 proof), isopropanol, and methanol were from Fisher Scientific. Egg-derived L- α -phosphatidylcholine (99% PC, 760.09 g/mole average molecular weight), and 1,2-dioleoyl-*sn*-glycero-3-phosphatidylcholine (DOPC, >99%) was obtained from Avanti Polar Lipids. Deionized (DI) water was obtained from a Barnstead Nanopure Filtration System operating at a 17 M Ω resistance. Deuterium oxide was from Cambridge Isotope Laboratory.

5.2.2 Au nanocrystal synthesis

1.8 nm diameter Au nanocrystals capped with dodecanethiol were synthesized following literature procedures.⁶⁹ In a 125 mL flask, 6.0 g of TOAB was dissolved in 73 mL of toluene by magnetic stirring (600 rpm). An aqueous gold solution (0.300 g $\text{HAuCl}_4 \cdot 3\text{H}_2\text{O}$ in 18 mL DI water) was added to the toluene phase and stirring was continued for 1 hour, resulting in complete phase transfer of the gold ions to the toluene phase. The toluene phase was extracted, placed in a clean flask, and stirred at 600 rpm. Next, 2.3 mmol of 1-dodecanethiol was injected into the stirring flask, and the toluene phase turned from red to colorless. After stirring for 15 minutes, an aqueous sodium

borohydride solution (0.346 g NaBH_4 in 18 mL DI water) was quickly poured into the toluene phase. Stirring was continued for 12 hours, and then the toluene phase was extracted and distributed into glass centrifuge tubes. Ethanol was added to each tube as an antisolvent (20 mL EtOH : 5 mL toluene). The tubes were centrifuged at 9000 rpm for 6 minutes, and the colorless supernatant was discarded. The gold nanocrystal precipitates were dispersed in 2 mL total of toluene, combined into one centrifuge tube, and centrifuged at 10000 rpm for 3 minutes. The supernatant of well-dispersed nanocrystals was transferred to a clean glass centrifuge tube. Size selective precipitation was performed by adding 500 μL of ethanol, centrifuging at 9000 rpm for 6 minutes, and transferring the supernatant to a new tube. The size selection was repeated 3 times, and each precipitate was dispersed in 2 mL of toluene.

Au nanocrystals with 4.1 nm diameter coated with dodecanethiol were prepared by modification of recent protocols.⁷⁰ In a 125 mL flask, 5.4 g of TOAB was dissolved in 49 mL of toluene by magnetic stirring (600 rpm). An aqueous gold solution (0.760 g $\text{HAuCl}_4 \cdot 3\text{H}_2\text{O}$ in 72 mL DI water) was added to the toluene phase and stirring was continued for 1 hour, resulting in complete phase transfer of the gold ions to the toluene phase. The toluene phase was extracted, placed in a clean flask, and stirred at 600 rpm. Next, an aqueous sodium borohydride solution (1.0 g sodium borohydride in 60 mL DI water) was quickly poured into the toluene phase. Stirring was continued for 10 minutes, the two phase liquid mixture was decanted off of the bulk gold precipitate, and then the toluene phase was extracted from the mixture, washed with three 20 mL aliquots of DI water, and collected in a clean flask. Then 2.0 mmoles of dodecanethiol was injected into

the toluene phase while stirring at 600 rpm. After 3 hours, the toluene phase was distributed into glass centrifuge tubes, centrifuged at 10000 rpm for 3 minutes, and the supernatant of well dispersed particles was collected. This dispersion was combined with ethanol (20 mL EtOH per 5 mL toluene), centrifuged at 8500 rpm for 6 minutes, and the colorless supernatant was discarded. The total gold precipitate was dispersed in 2 mL of toluene and then centrifuged at 10000 rpm for 3 minutes. The supernatant was collected and transferred to a clean glass centrifuge tube. Size selective precipitation was performed as described above, and the gold precipitates were dispersed and stored in toluene.

Au nanocrystals capped with 1-hexadecanethiol were prepared as described above for 1.8 nm nanocrystals with 2.3 mmol of the appropriate thiol. A 50:50 v/v mixture of acetone and isopropanol was used as the antisolvent to purify the nanocrystals because hexadecanethiol does not dissolve in ethanol. The particles were washed twice before carrying out a final precipitation with methanol.

Gold Nanocrystal Characterization. Gold nanocrystals were dried from toluene solvent onto 200 mesh carbon-coated copper grids (Electron Microscopy Sciences) and imaged by a FEI Tecnai Biotwin transmission electron microscope (TEM) operating at 80 kV. Small angle x-ray scattering (SAXS) was used to determine the mean crystalline core diameter of gold nanocrystals dispersed in toluene as described in Chapter 4.⁶⁹

Thermogravimetric analysis (TGA) was used to determine the weight fractions of Au and organic ligand. 1 mg of nanocrystals was placed in a 70 μ L alumina crucible (Mettler Toledo) and the solvent was evaporated. TGA measurements were conducted using a

Mettler Toledo TGA-1 with heating from 25–800°C at 10°C/minute under 5 mL/minute nitrogen gas flow.

5.2.3 Vesicle Formation with Egg Phosphatidylcholine (eggPC)

Au nanocrystals were dispersed in anhydrous chloroform at 6.0 mg/mL (120 μ M nanocrystals per volume for 1.8 nm diameter, DDT-passivated Au). 10 mg (13 μ mol) of eggPC lipid (Figure 5.1) was added to a 50 mL round bottom flask, and enough Au solution was added to achieve the desired lipid:nanocrystal mole ratio, which was varied from 5000:1 to 100:1. For example, a lipid:nanocrystal ratio of 100:1 required addition of 1.0 mL of the 6.0 mg/mL Au nanocrystals dispersed in chloroform. The eggPC and Au solution in the 50 mL flask was diluted to 1.0 mL total volume using anhydrous chloroform. The flask was then connected to a rotary evaporator and partially submerged in a 20 °C water bath to maintain constant temperature. The chloroform was evaporated by rotating the flask at ~1 revolution per second at about 200 mbar pressure until a dry film formed on the flask walls. Afterward, the flask was removed from the rotary evaporator, and the film was blown with a stream of Ar gas to purge the flask of chloroform vapor, because chloroform would sometimes condense in the flask even after several minutes under vacuum using an old rotary evaporator.

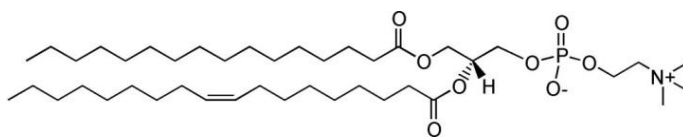


Figure 5.1. Structure of the predominant lipid in eggPC, containing 1 saturated 16 carbon fatty acid (palmitoyl, *sn1* position) and 1 mono-unsaturated 18 carbon fatty acid (oleoyl, *sn2* position). EggPC is composed of 99% glycerol-3-phosphatidylcholine lipids that have different fatty acid chains linked to the *sn1* and *sn2* positions of the glycerol group. Other less abundant fatty acids found in eggPC lipids at the *sn1* or *sn2* position include 18 carbon saturated chains (stearoyl), 18 carbon di-unsaturated chains (linoleoyl), and 20 carbon polyunsaturated alkane chains (arachidinoyl).⁷¹ The lamellar gel to liquid crystal phase transition temperature for eggPC is about -15°C, so eggPC will be in the liquid crystal phase at 25°C.⁷²

The lipid-nanocrystal film was hydrated by adding 1.0 mL of DI to the flask, then gently vortexing by hand for 1-2 minutes. The flask was immersed in a bath sonicator and sonicated for 2 minutes to disperse the lipid-nanocrystal film. The turbid lipid-nanocrystal dispersion was transferred to a 20 mL glass scintillation vial and sonicated further for 10 minutes in the bath sonicator. During this time, the turbid Au-lipid solution became translucent, indicating the break-up of large Au-lipid aggregates into nanometer-sized particles smaller than the wavelengths of visible light. For samples with very high Au concentration (lipid:nanocrystal ratio < 1500:1), the change in turbidity could only be seen at the water's meniscus, because the Au makes the color of the solution too dark to notice the turbidity. After sonication, the aqueous lipid-Au solutions were placed in a 1.5 mL plastic centrifuge tube, and centrifuged with a force of 600g for 5 minutes. The supernatant was collected and spun again at the 900g for 5 minutes. Au precipitated

during centrifugation when the lipid:nanocrystal ratio was less than 1500:1. The final supernatant was collected and used for extrusion.

The final lipid-nanocrystal supernatant was drawn into a 1.0 mL glass syringe, which was loaded onto an Avanti MiniExtruder (Avanti Polar Lipids, see manufacturer website for details). The syringe was depressed to pass the Au-lipid aggregates through a polycarbonate filter (100 nm diameter pore size) 21 times. The extruded Au-lipid solution was then extruded through a polycarbonate filter with 50 nm diameter pore size 21 more times. For lipid:nanocrystal mole ratios lower than 1500:1, Au fouled the filter and required that a higher pressure be exerted than when extruding samples with higher ratios of lipid:nanocrystal. The final aqueous Au-lipid dispersion was stored in a clean 1.5 mL plastic centrifuge tube until cryoTEM imaging.

5.2.4 Vesicle Formation with Dioleoylphosphatidylcholine (DOPC)

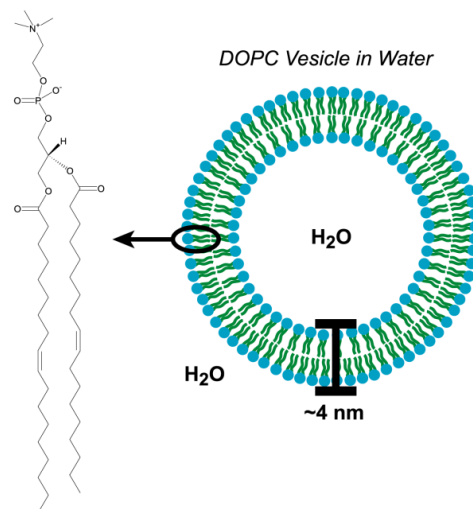
Vesicles were formed by dispersing a dry lipid-nanocrystal film in water. Films were prepared from a 1.0 mL chloroform dispersion containing 30 μmol of DOPC and 3 mg of gold nanocrystals (200 nanocrystals per lipid), illustrated in Figure 5.2. The 1 mL dispersion was placed in a 50 mL glass round bottom flask (Chemglass) and connected to a rotary evaporator (Buchi, new equipment purchased in 2011). Chloroform was evaporated with the rotary evaporator bath temperature at 25°C, 40 rpm rotation, and a pressure of 200 mbar. After 15 minutes, the flask was removed from the rotary evaporator, placed in a vacuum chamber for 12 hours (< 50 mbar pressure), and then subjected to solvent vapor annealing as described below.

Dioleoylphosphatidylcholine (DOPC) Lipid

Mol. Weight = 786.1 Da

$T_m = -20^\circ\text{C}$

CMC $\ll 1$ nM



Gold Nanocrystals:

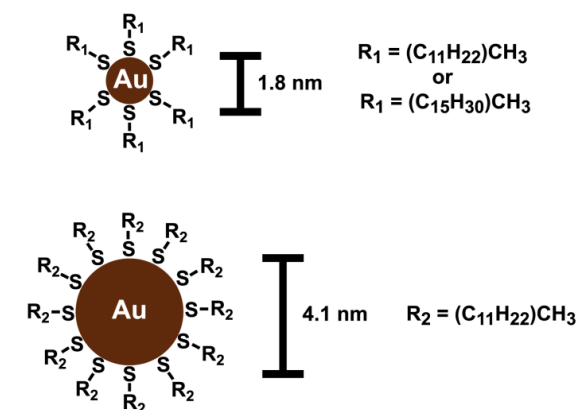


Figure 5.2. Illustration of DOPC lipid and gold (Au) nanocrystals used for vesicle formation. DOPC is a glycerol-3-phosphatidylcholine lipid with two mono-unsaturated fatty acid chains located at the *sn*1 and *sn*2 positions, and the hydrophilic phosphatidylcholine head group at the *sn*3 position. The DOPC molecular weight, critical micelle concentration (CMC), and lamellar gel to liquid crystal phase transition temperature (T_m) are derived from Marsh.⁷¹ The lipid bilayer thickness is based on measurements by Nagle et al.⁷³ The gold nanocrystal diameters are drawn to scale.

Lipid/nanocrystal films were annealed with chloroform vapor using the experimental setup illustrated in Figure 5.3A. The flask containing a dried lipid-nanocrystal film was placed on top of a glass bottle filled with liquid chloroform with the flask neck inserted into the bottle opening. The flask-bottle contact was wrapped with parafilm to help maintain constant chloroform vapor pressure. Solvent vapor annealing was performed for 60 minutes, and during the first 50 minutes of solvent vapor exposure, the films changed in appearance from opaque to translucent. Immediately after 60 minutes of solvent vapor annealing, the flask was separated from the glass bottle, 1.0 mL of DI water was added to the lipid/nanocrystal film, the flask opening was covered with parafilm and the film was sonicated for 10 min (Misonix bath sonicator, 600 mL water bath, 25-30°C temperature, 30 W power delivered to the sample).⁷⁴

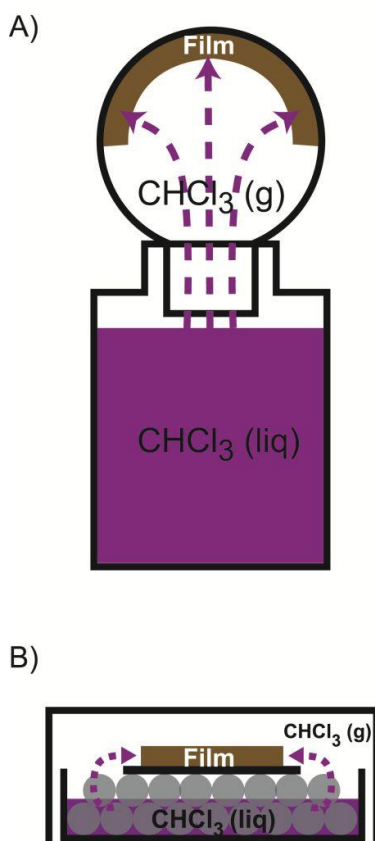


Figure 5.3. Sketch of solvent vapor annealing apparatuses, using chloroform as an example of an organic solvent. A) A glass bottle of liquid CHCl_3 is used for lipid/nanocrystal films prepared in 50 mL glass round-bottom flasks. The liquid level is typically 2-3 mm below the opening of the round-bottom flask, and the contact between the glass bottle and flask is sealed by wrapping with parafilm. B) A glass Petri dish containing 10 mL of liquid chloroform is used for annealing films prepared on glass cover slides. The cover slide (black) is placed face up on two layers of 5 mm diameter glass beads (grey), and the level of liquid chloroform is below the cover slide. The Petri dish is covered with a glass crystallization dish trap chloroform vapor inside.

After 10 min of ultrasonication, the aqueous lipid/nanocrystal dispersions were loaded into 2 mL plastic centrifuge tubes for purification from poorly dispersed

nanocrystals and extrusion. The dispersions were centrifuged at 2000g for 10 minutes, the supernatant was removed with a glass pipette and placed into a clean 2 mL centrifuge tube, and then it was centrifuged at 2000g a second time. The final supernatant was transferred to a clean 2 mL centrifuge tube using a glass pipette. Vesicles formation was completed by extruding the lipid/nanocrystal dispersions through a polycarbonate membrane with 100 nm diameter pores using a hand-powered MiniExtruder (Avanti).

5.2.5 Light Microscopy.

DOPC/nanocrystal films were imaged using a Leica DM2500 light microscope at 40x magnification in bright field mode. Images were captured using a Leica DFC 320 color camera. The lipid/nanocrystal films were prepared for light microscopy by dispersing lipids and nanocrystals in liquid chloroform and drop-casting 500 μ L onto a 24x50 mm (12 cm²) cover glass. The liquid chloroform was allowed to evaporate in a ventilated fume hood at room temperature (23°C) for 15 minutes. Once dry, the films were transferred to a room temperature vacuum oven and stored under vacuum for 12 hours.

Nanocrystal/lipid films were annealed with solvent vapor as illustrated in Figure 5.3B, using a glass petri dish filled with two complete layers of glass beads and liquid organic solvent in the dish. The liquid level was below the top layer of the beads. The cover glass coated with a dry lipid-nanocrystal film was placed face up on the top layer of glass beads. The Petri dish was covered by a glass crystallization dish, forming a closed container to trap the solvent vapor. The films were kept in the closed container until the

film appearance changed from opaque to translucent, typically 5 minutes. Once annealing was complete, the films were removed from the closed container for light microscopy imaging.

5.2.6 Centrifugal Separation. An extruded lipid/nanocrystal dispersion was placed in a plastic centrifuge tube and spun at 10000g for 60 minutes. The gold-loaded vesicles concentrate at the bottom of the centrifuge tube. The supernatant was transferred to a clean centrifuge tube using a glass pipette and centrifuged at 10000g for 60 minutes. The remaining Au-loaded vesicles concentrated at the bottom of the centrifuge tube. A blue-opalescent supernatant, containing mostly empty vesicles, was transferred by pipette to a clean centrifuge tube. The concentrated Au-loaded vesicles from both centrifugation steps were combined and diluted to 0.5 mL with DI water for cryoTEM imaging.

5.2.7 CryoTEM Imaging. CryoTEM imaging for the preliminary experiment with eggPC vesicles (see Chapter 5.3.2) was performed at the Universidad Autonoma de Barcelona as described in Chapter 4. Subsequent cryoTEM imaging with eggPC and DOPC vesicles was performed at the Texas A&M University, described as follows. An FEI Tecnai F20 transmission electron microscope was used, operating at 200 kV with a liquid nitrogen cooled stage. Specimens were prepared on C-flat holey carbon film TEM grids (Protochips, via Electron Microscopy Sciences) having a 1.2 μm holes separated by and a 1.3 μm . TEM grids were exposed to glow discharge plasma for 30 sec to improve wetting of the hydrophobic grids. The TEM samples were vitrified using an automated

Vitrobot (FEI). A 2.8 μL drop of lipid-nanocrystal dispersions was placed on a C-flat grid suspended in the Vitrobot chamber maintained at 22°C and 95-100% relative humidity. The Vitrobot blots the grid with filter paper (1 blot, 3.5 second blot time) and then plunges the grid into liquid ethane. The vitrified grid was transferred to a cryo grid storage box (Electron Microscopy Sciences) submerged in liquid nitrogen, where it was kept until imaging. The vitrified grid was transferred in liquid nitrogen to a Gatan CT3500 single tilt cryo TEM specimen holder on a cryo workstation (Gatan), followed by insertion into the microscope. Vesicles are imaged in the holey regions of the carbon film.

5.2.8 Dynamic Light Scattering (DLS). Clean, disposable, polystyrene, low-volume microcuvettes (Malvern) were used for DLS. The microcuvettes were cleaned by rinsing 5 times with 500 μL of DI water passed through a 100 nm pore size polyvinylidene fluoride syringe filter (Millipore). After rinsing, residual water was removed from the cuvettes by tapping the cuvette upside down on the benchtop. Cuvettes were filled with 50 μL of aqueous lipid/nanocrystal dispersion for DLS characterization.

DLS data were collected using a Zetasizer Nano ZS instrument (Malvern) operating at 25°C with a laser wavelength λ of 630 nm and a scattering angle θ of 173°. The instrument measures the correlation in light scattering intensity over time and reports the data as the intensity autocorrelation function given by equation 5.1.^{75,76} For each dispersion, $g_2(t)$ was measured in triplicate.

$$g_2(t) = \frac{\langle I(t)I(0) \rangle}{\langle I(0) \rangle^2} \quad (5.1)$$

The intensity autocorrelation function (g_2) is related to the electric field autocorrelation function (g_1) by the Siegert relationship, equation 5.2.⁷⁵ In equation 5.2, the β term is a constant.

$$g_2(t) = 1 + \beta \cdot |g_1(t)|^2 \quad (5.2)$$

Each scattering particle contributes a single exponential decay to the correlation in light scattering intensity, thus the general form of g_1 is the following:

$$g_1(t) = \sum_{i=1}^m A_i e^{-\Gamma_i t} \quad (5.3)$$

In Eqn (5.3), each particle size (i) has a constant pre-exponential term A_i and a scattering intensity decay rate Γ_i . Equation 5.4 shows how the decay rate is related to the scattering vector q and the particle diffusion coefficient D_i . Also, equation 5.4 employs the Stokes-Einstein relationship to relate the decay rate directly to the particle hydrodynamic diameter d_i .⁷⁵ The refractive index n , of water is 1.333, the dynamic viscosity η of water at 25°C is 0.89 cP, k is Boltzmann's constant ($1.38 \cdot 10^{-23}$ J/K), and T equals 298 K.

$$\Gamma_i = q^2 \cdot D_i = \left(\frac{4n}{\lambda} \sin\left(\frac{\theta}{2}\right) \right)^2 \cdot \left(\frac{kT}{3\eta \cdot d_i} \right) \quad (5.4)$$

The particle size is obtained by fitting equations 5.2-5.4 to the experimental data $g_2(t)$ given by equation 5.1. Unfortunately this problem has many solutions when $m > 3$ in equation 5.3, or if the particles are considered to have a multimodal, polydisperse size distribution. In this experiment though, we actually found that the DLS data were very

well represented by simply assuming that there are only two particle sizes, so that $m = 2$ in equation 5.3.^{77,78} In this case, the two pre-exponentials represent the relative amplitude of scattering from each particle size, so $A_I + A_{II} = 1$.^{79,80}

For each dispersion, equations 5.2-5.4 were fit to the three replicate measurements of $g_2(t)$ using non-linear least squares regression, assuming only non-negative solutions were valid. The regression minimized χ^2 in equation 5.5, the sum of the squared differences between the experimental correlation function $g_2(t)|_{\text{exp}}$ (equation 5.1) and the correlation function calculated by the model $g_2(t)|_{\text{model}}$ (equation 5.3).

$$\chi^2 = \sum \left(g_2(t)|_{\text{exp}} - g_2(t)|_{\text{model}} \right)^2 \quad (5.5)$$

For each dispersion, DLS was performed by taking three replicate measurements of the light scattering intensity correlation function (g_2), which is related to the intensity of scattered light $I(\tau)$ according to Eqn (5.1). DLS data were fit to a light scattering modeling derived from Eqns (5.2-5.3) by assuming that the scattering population consists of two different particle sizes ($i = I, II$) with pre-exponential constants A_i , and size-dependent constants Γ_i , that correspond to the relaxation rate of the light scattering intensity given in Eqn (5.4):⁷⁷⁻⁷⁹

$$g_2(\tau) - 1 = \beta \cdot [A_I \exp(-\Gamma_I \cdot \tau) + A_{II} \cdot \exp(-\Gamma_{II} \cdot \tau)]^2 \quad (5.6)$$

5.2.9 NMR Spectroscopy

Pure lipid and lipid/nanocrystal dispersions were prepared as described above, but using D₂O was used as the solvent instead of deionized water. The lipid dispersions were

pipetted into NMR liquid sample tubes (Wilmad) and submitted to the University of Texas-Chemistry Department's NMR facility for analysis. All spectra were collected at 27°C on a Varian Inova-500 spectrometer. The ^1H NMR spectra with ^{13}C decoupling were collected at 600 MHz using no spinning, 12.9 kHz spectral width, 4 kHz filter bandwidth, 3.57 s acquisition time, 0.020 relaxation delay, 64 transients with 32 transients collected before saving, 61 transmitter power, 1.4 kHz transmitter offset, and 11.6 μs pulse width.

5.2.10 Lipid and Nanocrystal Monolayer Compression

Monolayer compression experiments were carried out on a KSV Minitrough (maximum area=243 cm^2) with Teflon barriers, a platinum Wilhelmy plate, and a DI water sub-phase maintained at 25°C by a recirculating water bath. DOPC lipid and nanocrystals were dispersed in chloroform and spread on the trough by touching a single droplet of the dispersion to the surface of the water every 10 seconds. After spreading, the monolayer was allowed to equilibrate for at least 10 minutes. The barriers were compressed to an area of 63 cm^2 at a rate of 3.75 cm^2/min while recording surface pressure and area. LB monolayers with 10 mole% nanocrystals or less were prepared using nanocrystals dispersed in chloroform at 5 μM (0.28 mg/mL) and lipid dissolved separately in chloroform at 1 mM (0.79 mg DOPC/mL). The nanocrystals were spread first, followed by 30 nmol of lipid. For 25-100 mole% of nanocrystals, the 5 μM nanocrystal dispersion was too dilute to form a monolayer during compression on the Minitrough, so a 25 μM nanocrystal dispersion was prepared. For the monolayer with 50

mole% nanocrystals, it was difficult to spread the lipid after the gold nanocrystals without the surface pressure increasing over 1 mN/m before compression, which is detrimental to forming a monolayer according to the manufacturer. Because of this, the 50 mole% monolayer data was not included when comparing the experimental data of average area (nm^2 per number of moles of DOPC plus nanocrystals added to the trough) versus mole% to the calculated area for ideal mixing (A_{ideal}).

5.3 Results and Discussion

5.3.1 Au Nanocrystal Characterization

Three different Au nanocrystal samples were studied: (1) 1.8 nm diameter particles capped with dodecanethiol, (2) 1.8 nm diameter particles capped with hexadecanethiol and (3) 4.1 nm diameter nanocrystals capped with dodecanethiol. The average diameters of the nanocrystals were determined using both TEM and SAXS (Figure 5.4). Table 5.1 lists the average sizes determined from SAXS. Figure 5.5 shows the optical absorbance spectra of the gold nanocrystals, which further verify the nanocrystal sizes measured by TEM and SAXS. The 1.8 nm gold nanocrystal samples are too small to have a plasmon resonance, and the 4.1 nm nanocrystals have the characteristic Au nanocrystal plasmon peak at 520 nm.⁸¹ TGA (Figure 5.6) of the nanocrystals was used to ensure that each sample was free of unbound ligand and that the nanocrystals had similar ligand coverage. Table 5.1 lists the mass fraction of ligand expected for nanocrystals with a complete uniform thiol monolayer compared to the measured mass fraction, based on the Au nanocrystal size and assuming that each Au-

adsorbed thiol molecule occupies 0.16 nm^2 on the nanocrystal surface.^{82,83,84} The measured ligand content is within experimental error of the expected ligand content from calculation.

Table 5.1. Size and mass fraction of Au and organic in the nanocrystal samples measured by SAXS and TGA.

Measured SAXS Diameter, D (nm)	Thiol	Calculated Thiol Mass Percent (%)	Mass Fraction of Ligand Measured by TGA (%)‡
1.8 ± 0.2	$\text{C}_{12}\text{H}_{25}\text{SH}$	26 ± 9	27
1.8 ± 0.2	$\text{C}_{16}\text{H}_{33}\text{SH}$	31 ± 11	33
4.1 ± 0.8	$\text{C}_{12}\text{H}_{25}\text{SH}$	14 ± 9	21

‡ Quantities extracted from the data in Figure 5.6. The TGA balance has microgram precision, and the error in this measurement is negligible compared to the error in the calculated thiol mass percent. The thiol footprint on a Au surface was assumed to be $0.16 \pm 0.02 \text{ nm}^2/\text{thiol}$.^{83,84}

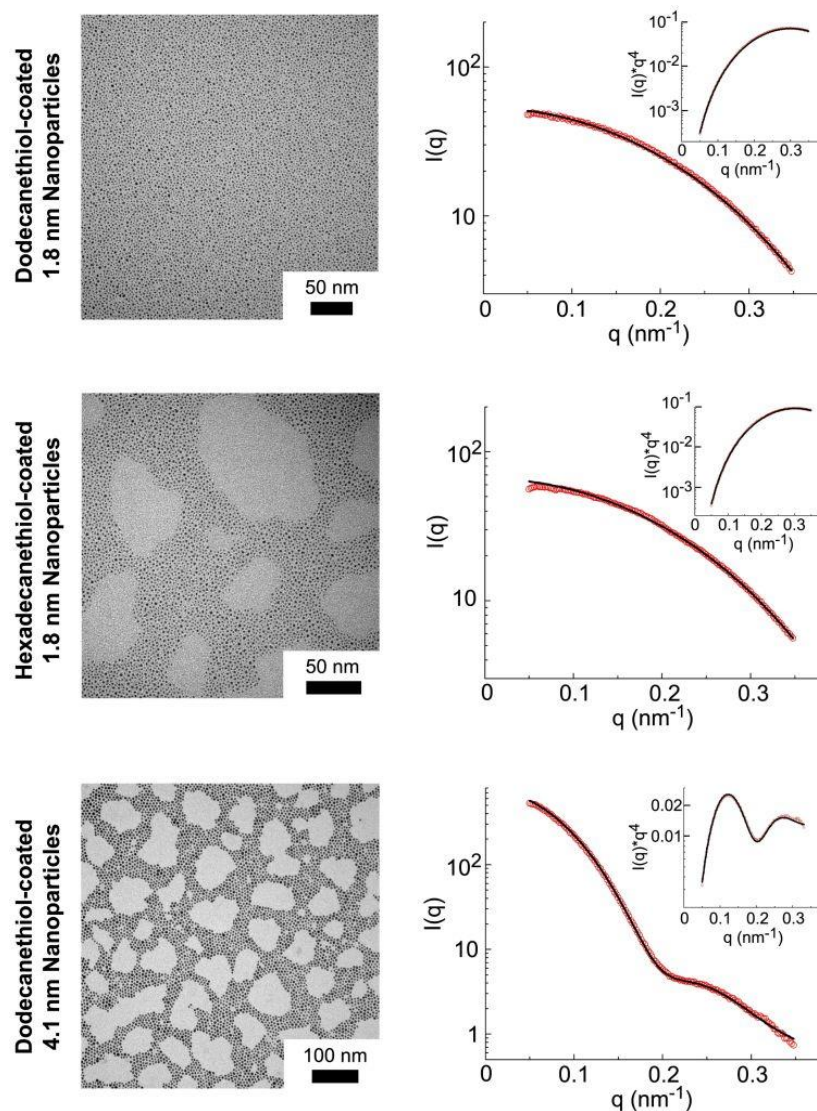


Figure 5.4. TEM and SAXS characterization of the Au nanocrystals used in these studies. The SAXS data were fit according to Equations 4.1 – 4.4 (Chapter 4) to obtain the mean nanocrystal diameters (D) and standard deviations (σ) listed in Table 1.

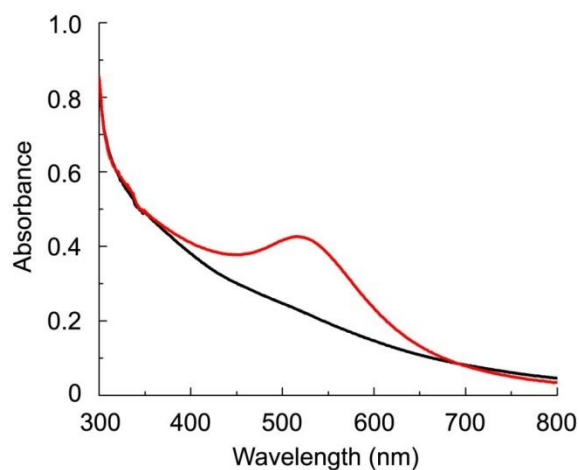


Figure 5.5. Optical absorbance spectra of the Au nanocrystals used in these studies. The black line is 1.8 nm gold nanocrystals and the red line is 4.1 nm gold nanocrystals. The spectra for the 1.8 nm gold nanocrystals coated with dodecanethiol and hexadecanethiol are identical.

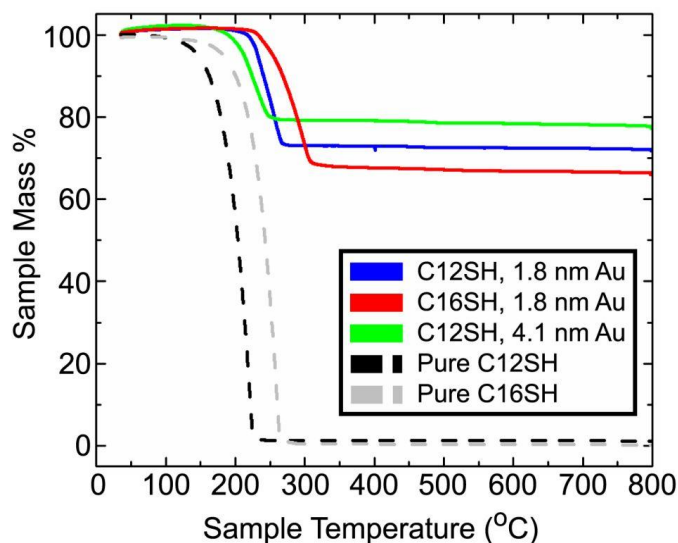


Figure 5.6. TGA of the alkanethiol-capped gold nanocrystals: dodecanethiol-coated 1.8 nm gold nanocrystals (blue), hexadecanethiol-coated 1.8 nm gold nanocrystals (red), and dodecanethiol-coated 4.1 nm gold nanocrystals (green). TGA of pure dodecanethiol (black) and hexadecanethiol (grey) Au are also plotted.

5.3.2 EggPC Lipid and 1.8 nm Au Nanocrystals

Preliminary Experiments without Rigorous Chloroform Removal. The preliminary experiments with eggPC and Au nanocrystals were performed while visiting a lab at the Universidad Autonoma de Barcelona. Figure 5.7 shows images of dispersions of eggPC vesicles prepared with and without nanocrystals. In Figure 5.7, samples A and B were prepared by extruding either pure lipid (A) or lipid with nanocrystals (B) through a membrane with 50 nm diameter pores after sonicating a lipid-nanocrystal film in deionized water. Both samples exhibit the characteristic opalescence of a vesicle dispersion, but Sample B has a brown color from the Au nanocrystals. The fact that the hydrophobic nanocrystals remain dispersed in the aqueous media implies that the lipid is associated with the nanocrystals. When the vesicles were prepared with lipid:nanocrystal ratios lower than 1500:1, some Au nanocrystals sedimented from the vesicle dispersion within a couple of days, though most of the nanocrystals remained dispersed by the lipid for weeks. Vesicle-nanocrystal hybrids made with higher lipid:nanocrystal ratios were stable, without any sedimentation, for weeks.

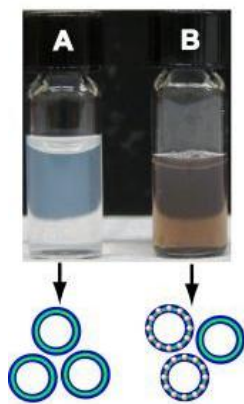


Figure 5.7. Photograph of aqueous dispersions of (A) pure eggPC vesicles prepared by extrusion, and (B) eggPC vesicles prepared by co-extrusion with Au nanocrystals (1500 lipid molecules per nanocrystal).

CryoTEM of nanocrystal-vesicle hybrids made by lipid:nanocrystal coextrusion (i.e., the vial in Figure 5.7B) showed that the vesicles were predominantly unilamellar, intact, and *densely loaded* with nanocrystals in the lipid bilayer. For comparison, Figure 5.8A shows cryo-TEM images of eggPC vesicles made without nanocrystals. The average diameter of the vesicles was similar for those prepared with and without nanocrystals— 60 ± 10 nm—which is slightly larger than the 50 nm pores in the polycarbonate filter used for extrusion. The nanocrystals did not appear to influence the vesicle diameter.

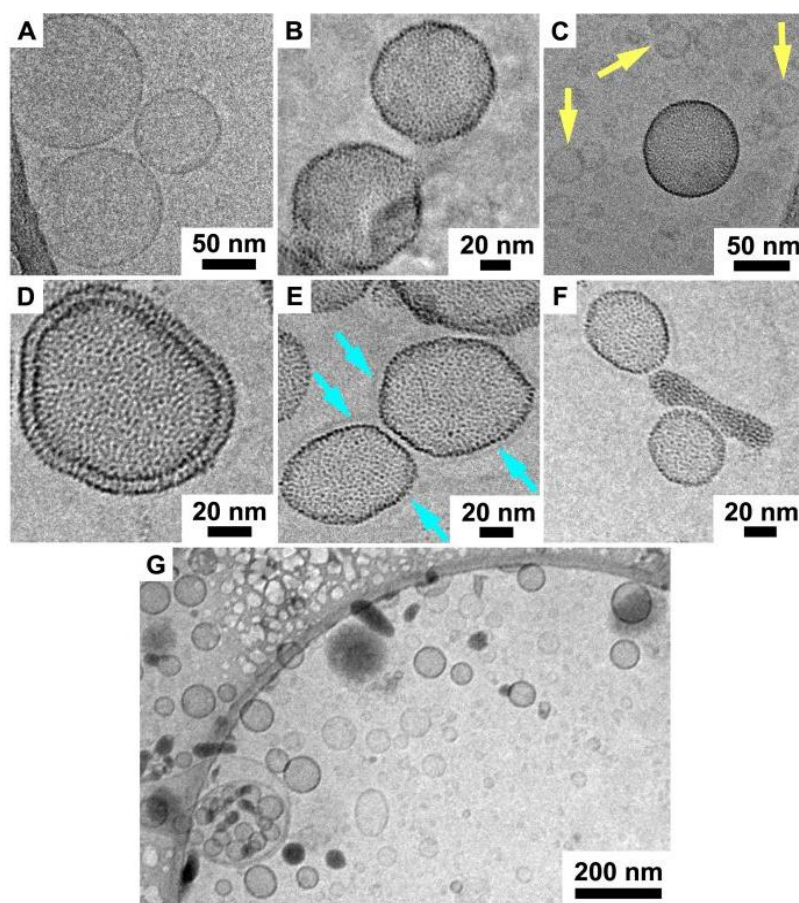


Figure 5.8. Cryo-TEM images of eggPC vesicles prepared by extrusion in the (A) absence and (B-G) presence of Au nanocrystals. Chloroform removal was not thorough vesicle preparation. Imaging was performed one day after preparing the vesicles. The samples imaged in (B) and (C) were made with a lipid:nanocrystal ratio of 1500, and the samples imaged in (D)-(G) were prepared with a lipid:nanocrystal ratio of 100. The arrows in (C) highlight vesicles that are free of nanocrystals surrounding one nanocrystal-loaded vesicle. The vesicle in (D) is bi-lamellar with both lipid bilayers loaded with nanocrystals. In (E), two nanocrystal-loaded vesicles are encapsulated within a lipid bilayer, labeled by blue arrows. In (F), two Au-loaded vesicles are accompanied by a nanocrystal agglomerate. The field of vesicles in (G) shows a mixture of nanocrystal agglomerates, nanocrystal-loaded vesicles, and nanocrystal-free vesicles. Imaging was performed at the Universidad Autonoma de Barcelona with Dr. Jordi Arbiol.

The vesicles prepared by co-extrusion with nanocrystals were either loaded with nanocrystals or were free of nanocrystals. Figures 5.8C and 5.8F show examples of this. Vesicles having only a few nanocrystals were not observed. A higher fraction of vesicles could be loaded with Au nanocrystals when the lipid:nanocrystal ratio was decreased, but empty vesicles were still observed, even when vesicles were extruded with only 100 lipid molecules per Au nanocrystal. It is possible that the apparent clustering of nanocrystals is due to incomplete mixing of the starting lipid-nanocrystal film as shown in Figure 5.9; however, the lipid-nanocrystal dispersion was well-sonicated prior to extrusion. When high concentrations of nanocrystals were added—with lower than 1500 lipid molecules per nanocrystal—worm-shaped agglomerates of Au nanocrystals were observed (average length 100 ± 50 nm, average width 30 ± 10 nm), as shown in Figure 5.8F. In Figure 5.8G, the nanocrystal-vesicle hybrid population made with a lipid:nanocrystal ratio of 100—the lowest molar ratio used—contains a mixture of nanocrystal agglomerates, vesicles fully-loaded with Au nanocrystals, and vesicles without any Au nanocrystals in the bilayer.

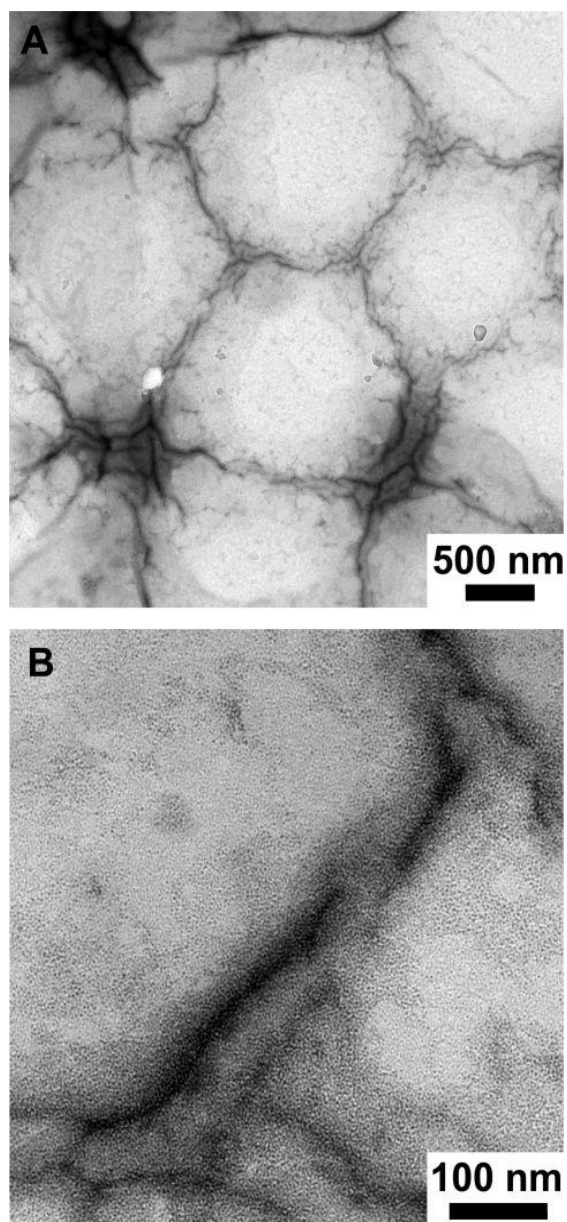


Figure 5.9. TEM images of Au nanocrystals and eggPC lipids dried onto a carbon-coated Ni grid at room temperature. 5 μ L of a chloroform solution containing Au nanocrystals (3 mg/mL) and eggPC lipid (5 mg/mL) was evaporated onto the grid. There is clustering of the Au nanocrystals in the lipid film during drying, forming patches in the film that are nanocrystal-rich and nanocrystal-deficient.

Other vesicle structures were observed in some instances as well, like the bilamellar vesicles shown in Figure 5.8D and the two separate nanocrystal-loaded vesicles in Figure 5.8E that are enveloped in a single lipid bilayer. In the bilamellar vesicle in Figure 5.8D, the separation between the concentric rings of nanocrystals is about 3.9 nm, which is near the expected thickness of a PC bilayer.⁷¹ The nanocrystals do not bridge the concentric bilayers of the bilamellar vesicle, which contrasts recent observations of much larger 8-14 nm diameter hydrophobic iron oxide nanocrystals spanning membranes when embedded in multilamellar vesicles.⁴⁷ The enveloped nanocrystal shells in Figure 5.8D nearly touch, but are separated by about 3.9 nm, which again corresponds to the thickness of a lipid bilayer, or equivalently, two lipid monolayers comprising the outer layer of each vesicle bilayer. Clearly, the hydrophobic nanocrystals are associating with the hydrophobic tails of the lipid and embedding within the bilayer.

Follow-up Experiments with Careful Control of Chloroform Removal. At first, the results shown in Figure 5.8 were difficult to reproduce when returning to the University of Texas at Austin. The experiments with (13 mM) eggPC and 1.8 nm diameter Au nanocrystals (200 lipids per nanocrystal) were repeated in Austin, but during formation of the eggPC and Au nanocrystal film, the films were stored under vacuum overnight to ensure complete removal of residual chloroform. The films were dispersed in deionized water by sonication and extruded through 50 nm pores, and the samples were imaged within 1 day of preparation at the Texas A&M Microscopy and Imaging Center. However, as shown in the top row of Figure 5.10, no Au-loaded vesicles were formed. Instead, the Au

nanocrystals assembled into solid lipid-coated agglomerates, as illustrated in Figure 5.10. Repeating the experiment again, but without placing the lipid-nanocrystal films under overnight vacuum to remove residual chloroform, produced the sample imaged in Figure 5.11. The sample that was not extensively dried of chloroform, shown in Figure 5.11, does form many Au nanocrystal-loaded vesicles, suggesting that chloroform plays some role in the vesicle loading process. The mechanism may involve a change in the lipid bilayer fluidity, improved mixing of the separate lipid components of eggPC, or improved mixing of Au nanocrystals and eggPC in the presence of chloroform. It is noteworthy that the eggPC and Au nanocrystals seem to phase separate when dried, as shown in the TEM image of Figure 5.9 where a Au nanocrystal and eggPC mixture was allowed to dry from chloroform onto a carbon-coated Ni TEM grid. This observation of phase separation prompted further investigations into controlling the mixing of lipids and nanocrystals during vesicle formation.

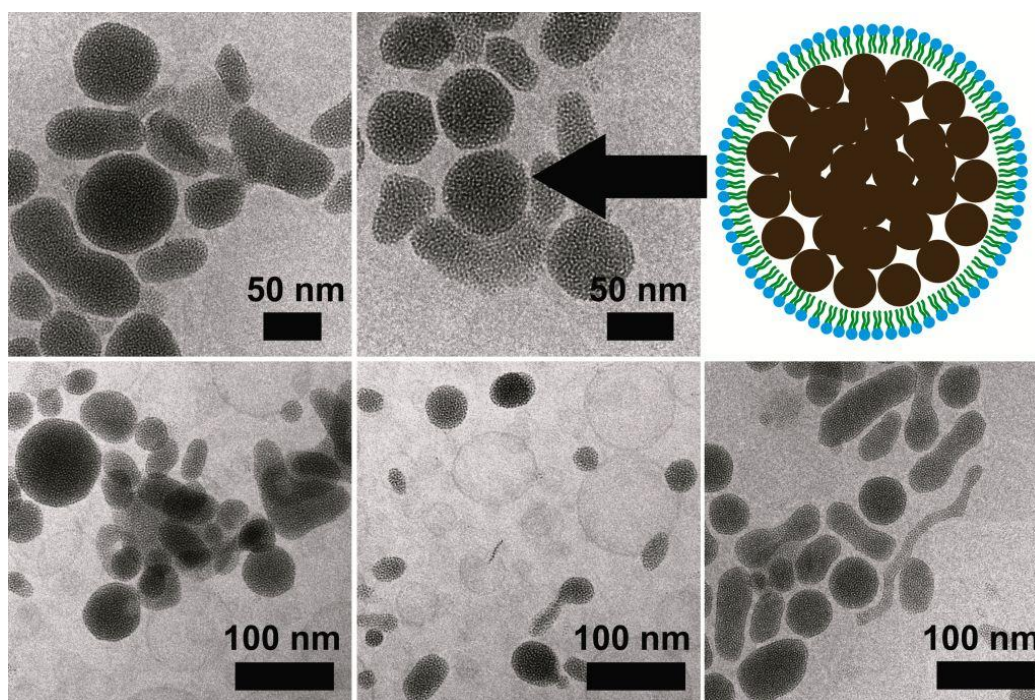


Figure 5.10. Dispersion of eggPC and 1.8 nm diameter Au nanocrystals. Prior to hydration and vesicle formation, the eggPC and nanocrystal film was dried for over 12 hours to remove trace amounts of chloroform. The illustration in the upper right panel is a Au nanocrystal agglomerate (Au = brown spheres) coated with lipid.

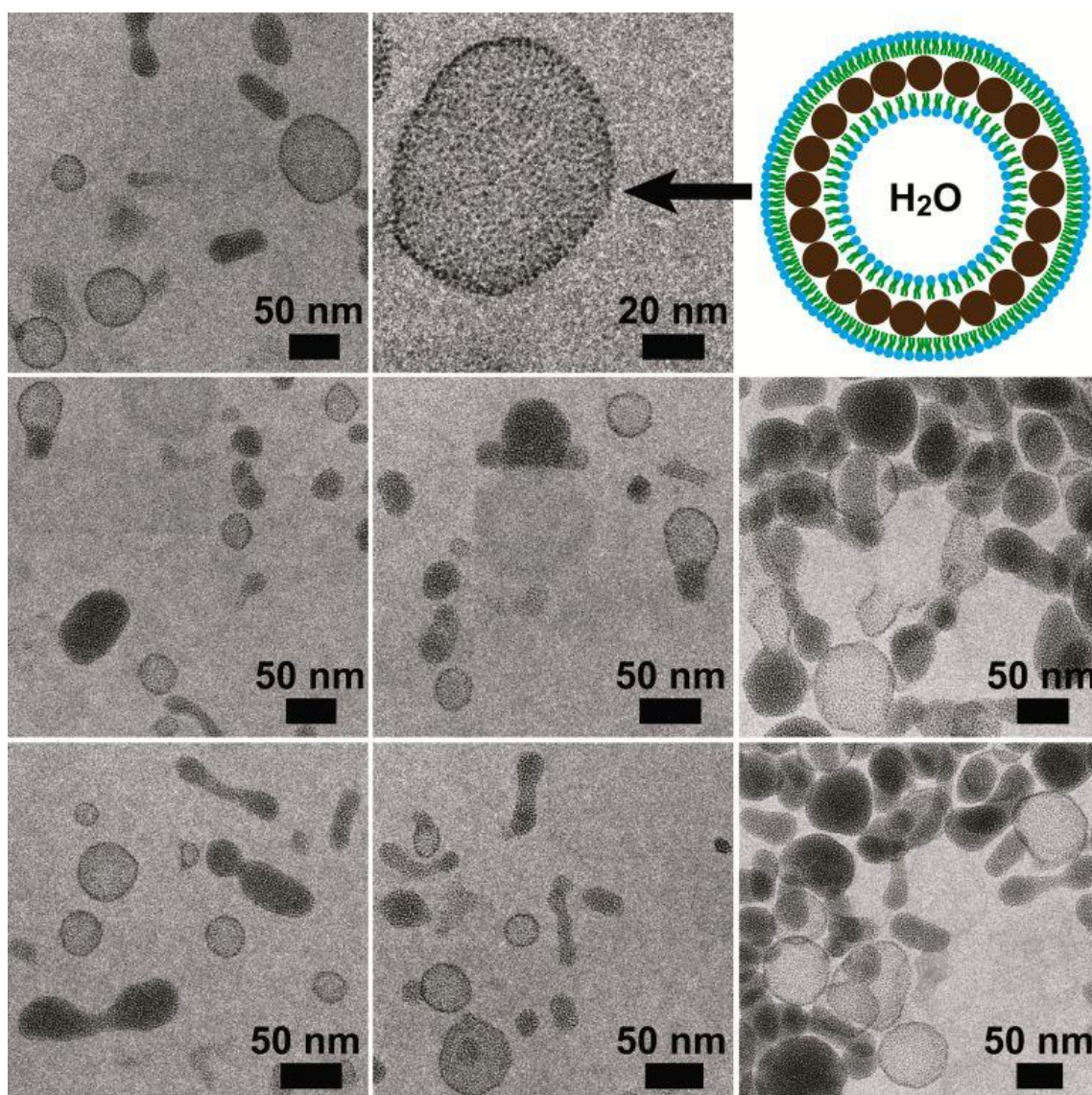


Figure 5.11. Dispersion of eggPC and 1.8 nm diameter Au nanocrystals. Prior to hydration and vesicle formation, the eggPC and Au nanocrystal film was only dried for 15 minutes. When the vacuum is removed at 15 minutes, chloroform tends to re-condense in the flask, and therefore the film contains residual chloroform vapor. The illustration in the upper right panel is lipid vesicle having a bilayer fully loaded with Au nanocrystals.

5.3.3 Chloroform solvent vapor annealing improves nanocrystal incorporation into DOPC vesicles.

Since the results shown in Chapter 5.3.2 suggest that chloroform influences incorporation of Au nanocrystals into unsaturated lipid bilayers, a procedure was developed to deliberately expose lipid-Au nanocrystal films to organic solvent vapor. The lipid was changed to DOPC to focus specifically on a single-component lipid that has one double bond in each fatty acid. Au nanocrystals of different diameters were investigated as well.

To form vesicles, the Au nanocrystals first were dispersed in chloroform with DOPC lipid and then dried for 12 hours under vacuum. During this drying process, the nanocrystals and lipid phase separate. Chloroform vapor annealing reverses the phase separation and re-disperses the nanocrystals in the DOPC lipid film, as shown in Figure 5.12. Vesicles formed from the phase-separated nanocrystal/DOPC films were predominantly free of nanocrystals, with a few Au agglomerates coated with lipid (illustrated in Figure 5.10). In contrast, the chloroform-annealed DOPC/nanocrystal films formed vesicles with significant incorporation of the 1.8 nm diameter dodecanethiol-capped nanocrystals, as shown in the middle row of cryo-TEM images in Figure 5.13.

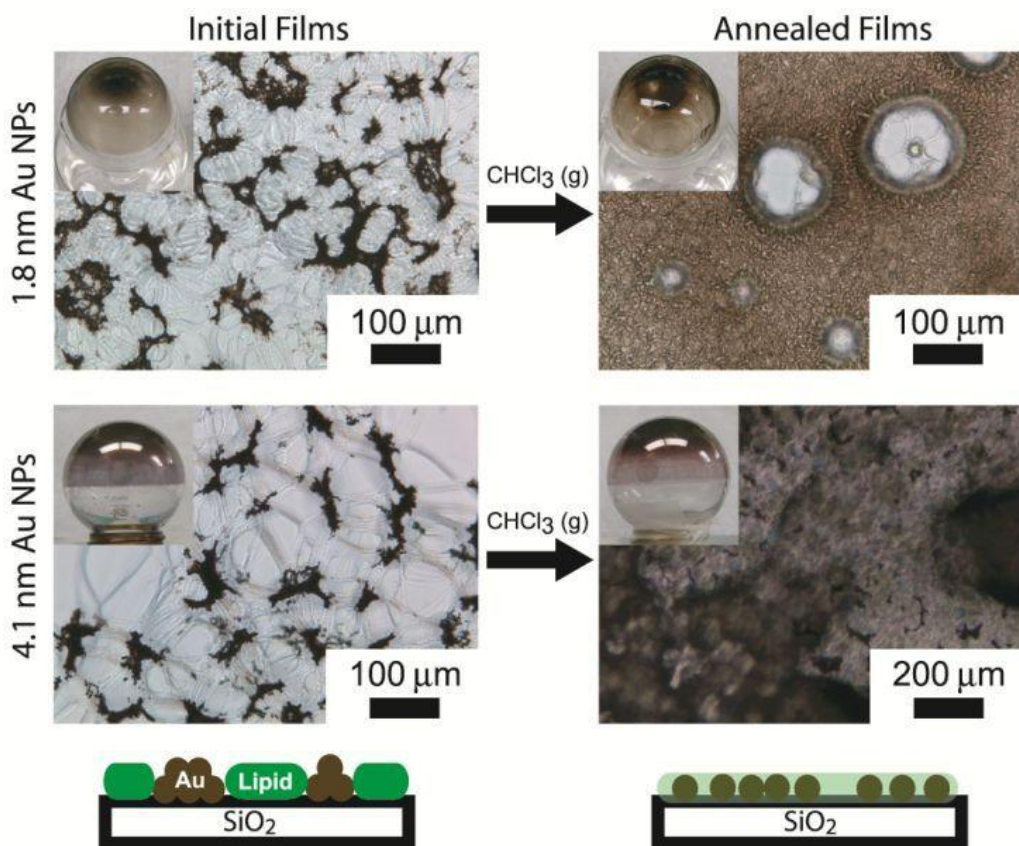


Figure 5.12. Light microscopy images of dried DOPC lipid/Au nanocrystal films after (a) complete drying followed by (b) exposure to chloroform vapor (i.e., solvent vapor “annealed” films).

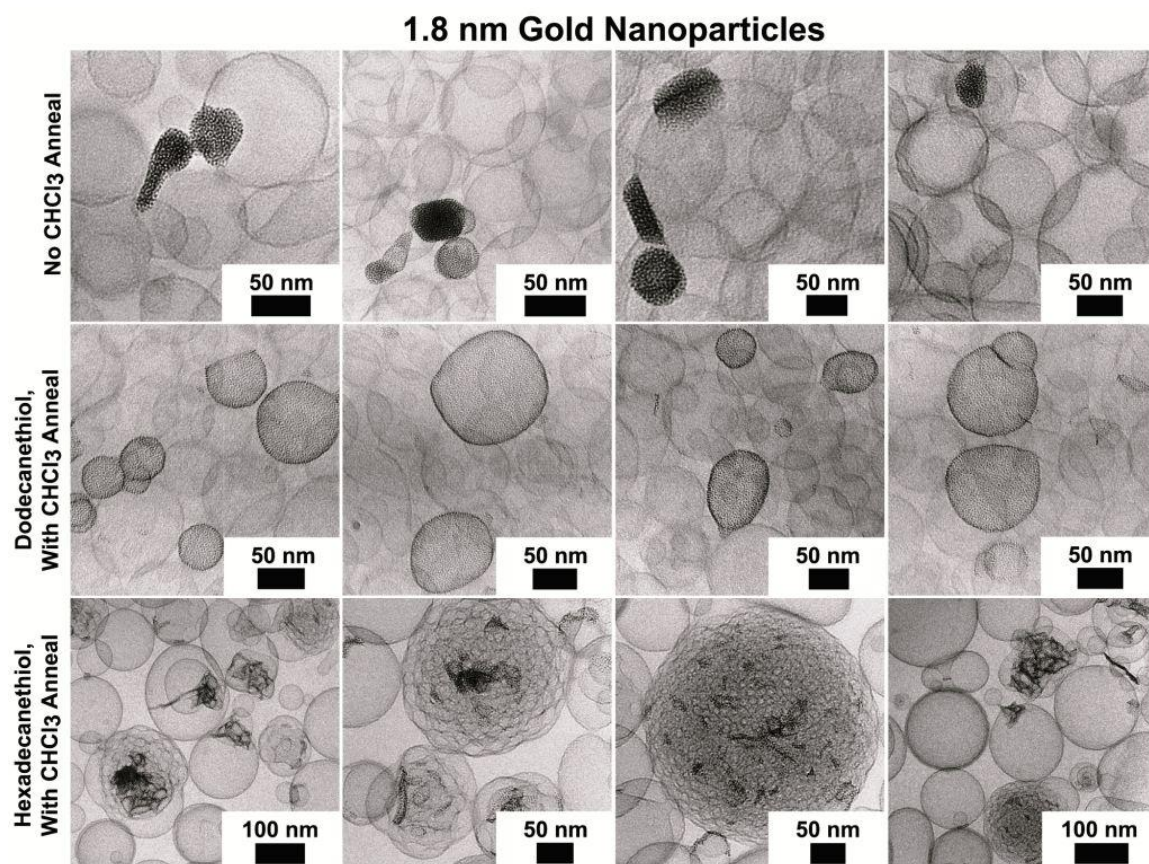


Figure 5.13. CryoTEM images of DOPC vesicles prepared in the presence of alkanethiol-coated 1.8 nm diameter Au nanocrystals. Only when lipid/nanocrystal films were annealed with chloroform vapor did the dodecanethiol-coated nanocrystals load the vesicle bilayers (middle row). Hexadecanethiol-coated nanocrystals caused intra-lamellar attachments to form between DOPC bilayers when annealed with chloroform (bottom row).

Centrifugal purification of nanocrystal-loaded DOPC vesicles. Nanocrystal-loaded and nanocrystal-free vesicles could be separated by centrifugation. As illustrated in Figure 5.14, vesicles loaded with nanocrystals are about 10-100 times heavier than the vesicles without nanocrystals (an 80 nm diameter Au-loaded vesicle will contain about 2000 nanocrystals using a nanocrystal area of 10 nm² from Langmuir Blodgett monolayer compression, see Chapter 5.3.6). Figure 5.14 shows cryo-TEM images of vesicles enriched with lipid bilayer-embedded nanocrystals obtained by centrifugal separation.

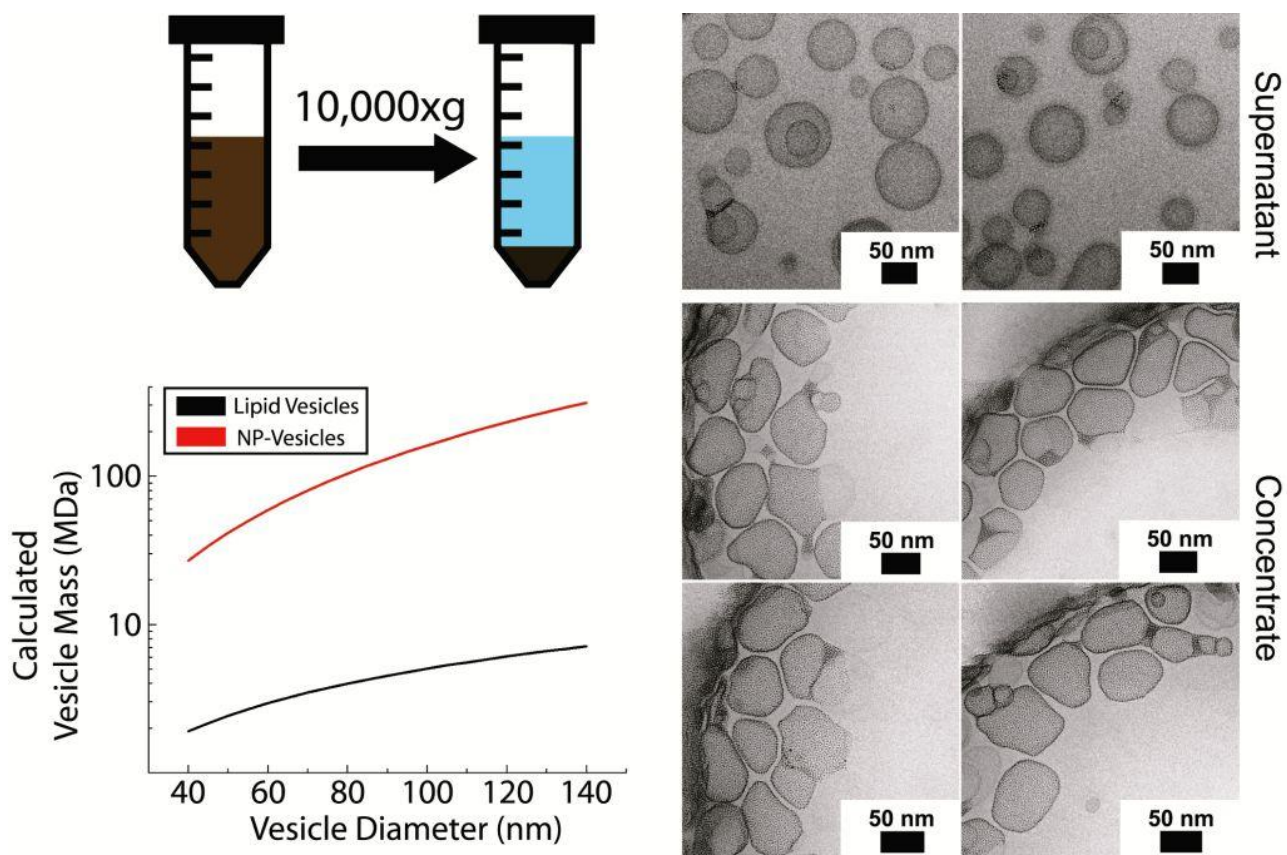


Figure 5.14. Separation of Au nanocrystal-loaded DOPC vesicles from nanocrystal-free vesicles. Black curve: pure DOPC vesicles, red curve: DOPC vesicles loaded with 1.8 nm diameter dodecanethiol-coated Au nanocrystals. High speed centrifugation (10,000g for 60 minutes) precipitates the heavier nanocrystal-loaded vesicles from the nanocrystal-free vesicles. The vesicle mass was determined by assuming that lipids occupy an area of 0.7 nm^2 with a 4 nm thick lipid bilayer,⁷³ with nanocrystals residing at the center of the lipid bilayer and occupying an area of 10 nm^2 , based on LB nanocrystal monolayers (See Chapter 5.3.6).⁸⁵ The nanocrystal molecular weight was taken to be 50 kDa/nanocrystal based on the TGA measurement of the ligand content (Table 5.1).

Influence of ligand chain length and nanocrystal size on vesicle incorporation. Au nanocrystals with 1.8 nm diameter cores and longer capping ligands of hexadecanethiol (C₁₆) did not incorporate into the DOPC vesicles after chloroform annealing. They tended to cluster at the intersection of multiple vesicle bilayers and induce the formation of lipid particles with many internal, intra-lamellar attachments as shown in the bottom row of Figure 5.13. Clustering of 6-10 nm diameter hydrophobic iron oxide nanocrystals between vesicle bilayers has been observed as well.^{10,49} Lipid particles with many internal, intra-lamellar attachments have also been formed by hydrophobic phytosterols and polyprenoids in glycerolipid particles.⁸⁶ The formation of intra-lamellar attachments suggests that the hexadecanethiol-coated nanocrystals destabilize the DOPC lipid bilayers when mixed with chloroform. Some lipid particles were 200 nm in diameter or larger, probably due to the aggregation of vesicles induced by the hexadecanethiol-coated gold nanocrystals, similar to a mechanism suggested for monoolein lipid.⁸⁶ According to Efrat et al., unilamellar monoolein vesicles loaded with phytosterol may fuse into larger vesicles with a few interlamellar attachments, followed by further fusion of bilayers within the vesicle to form a complex lipid particle with many interlamellar attachments.⁸⁶ Hexadecanethiol-capped Au nanocrystals are probably too large to insert in the lipid bilayer of the DOPC vesicles.^{87,88,51}

Even larger 4.1 nm Au nanocrystals capped with dodecanethiol also do not incorporate into the DOPC lipid bilayer. As the cryoTEM images in Figure 5.15 show, the nanocrystals tend to agglomerate and fuse to vesicle membranes or lead to fused lipid bilayers and intra-lamellar attachments within and between vesicles when annealed with

chloroform. Figure 5.16 summarizes the role of chloroform vapor annealing and the influence of nanocrystal size on the interaction between DOPC vesicles and the nanocrystals.

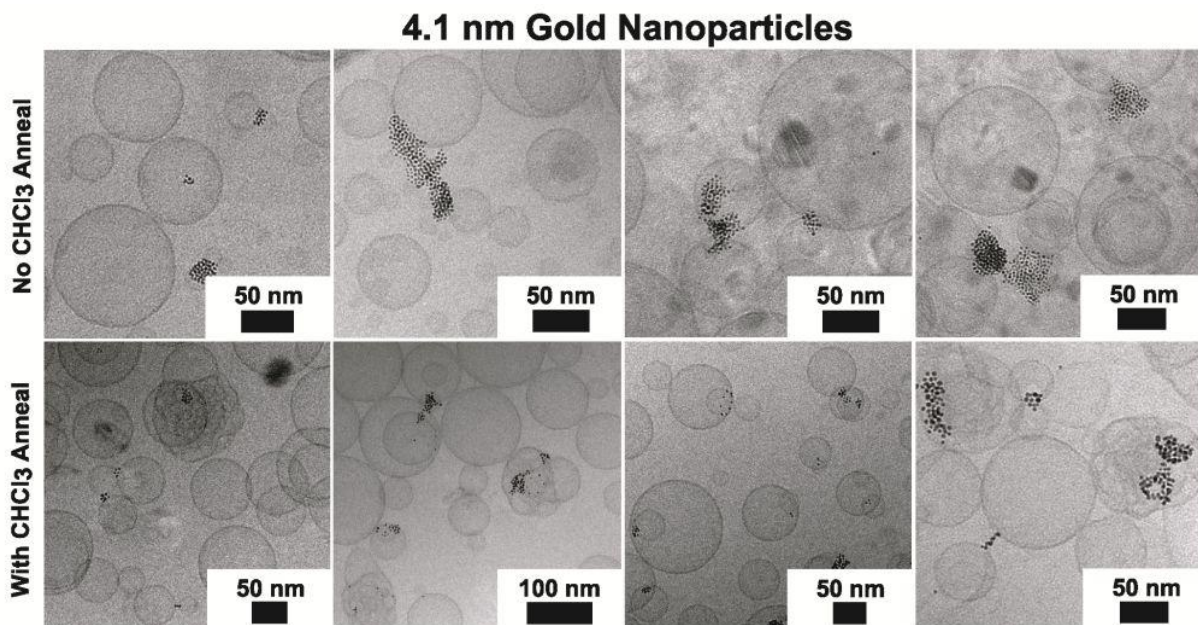


Figure 5.15. CryoTEM imaging of DOPC vesicles prepared with dodecanethiol-coated 4.1 nm diameter Au nanocrystals. The nanocrystals do not form loaded vesicles, though chloroform annealing encourages formation of intra-lamellar attachments between DOPC bilayers.

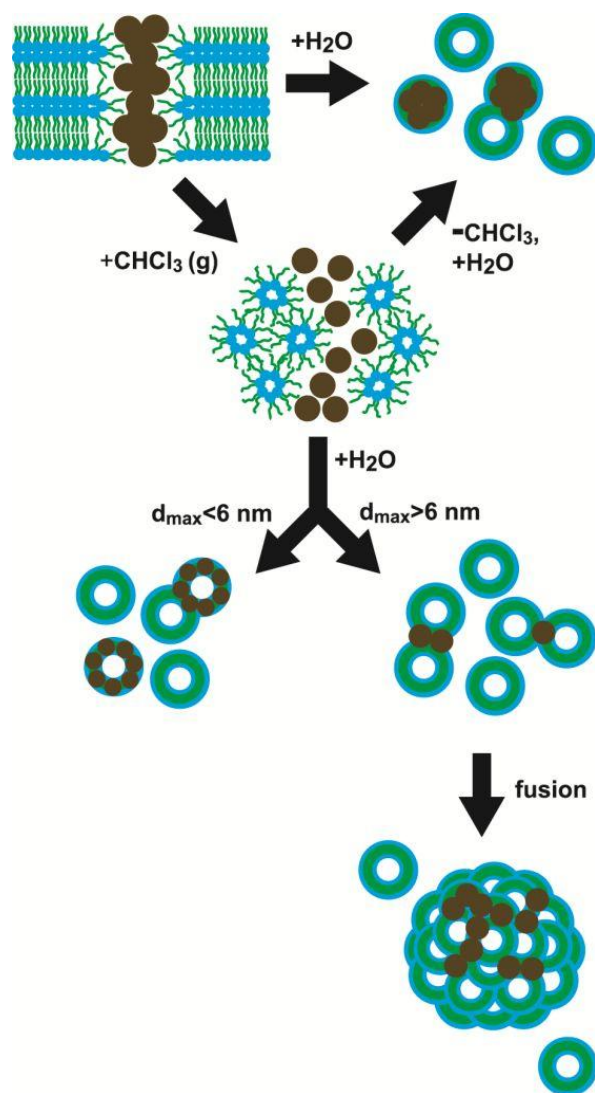


Figure 5.16. Illustration of pathways to vesicle formation and nanocrystal incorporation that depend on solvent vapor annealing and nanocrystal size. The nanocrystal diameter d_{max} , includes the fully extended length of the alkanethiol ligands. DOPC lipid adopts the inverted hexagonal phase in the anhydrous state after exposure to chloroform, similar to the lipid's behavior presence of dodecane at low water content.⁸⁹ As predicted by Wi,⁵¹ Au nanocrystals less than 6 nm incorporate into DOPC vesicle bilayers (with chloroform annealing), whereas nanocrystals larger than 6 nm de-stabilize DOPC bilayers to form lipid particles with many inter-lamellar attachments.

Rehydration and dispersion of lipid/nanocrystal films with chloroform vapor annealing. Chloroform vapor annealing of lipid/nanocrystal films led to much better aqueous dispersibility of both the smaller and larger Au nanocrystals. As shown in Figure 5.12, the 4.1 nm diameter nanocrystals also re-disperse in the lipid film upon chloroform annealing, as the film changes color from violet to red—a sign of de-aggregation of Au nanocrystals in the lipid film (Figure 5.12).⁹⁰⁻⁹² Even though the larger 4.1 nm diameter Au nanocrystals do not incorporate into the lipid membranes, the chloroform annealing process led to significantly better dispersibility of the nanocrystals with lipid in water. This was visually observed by the dark color of the dispersions (Figure 5.17) and DLS measurements of lipid/nanocrystal aggregate size. When the lipid/nanocrystal films were not annealed with chloroform vapor, there was very poor dispersibility and the lipid and nanocrystals formed very large aggregates (Figure 5.17). Chloroform vapor annealing produced DOPC/nanocrystal dispersions that passed easily through the extruder pores, consistent with their much better dispersibility.

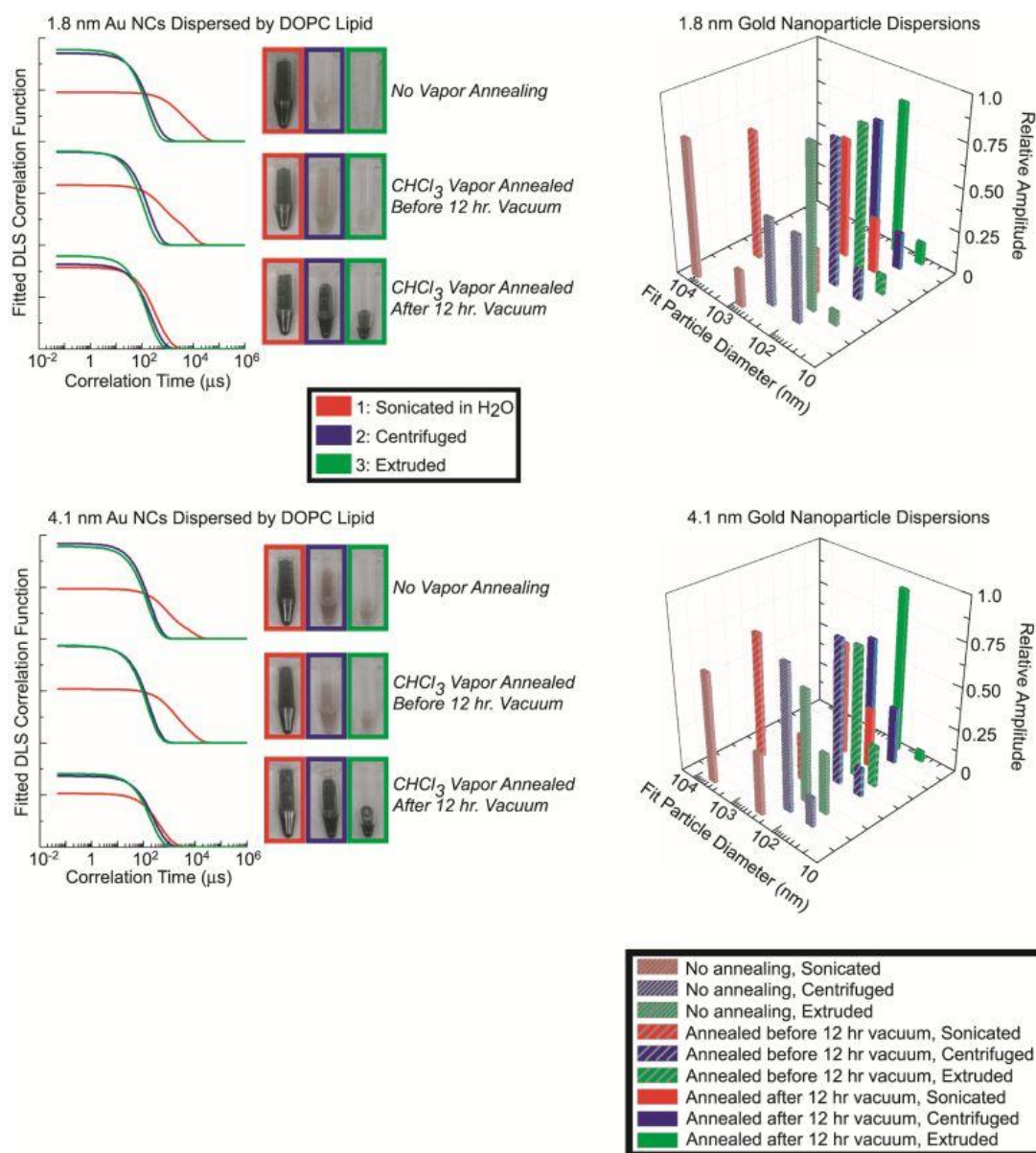


Figure 5.17. Dynamic light scattering (DLS) of DOPC lipid/nanocrystal dispersions. Immediately after the lipid/nanocrystal films were dried by rotary evaporation, they were either annealed with chloroform vapor and then vacuum dried for 12 hours, or vacuum dried for 12 hours followed by chloroform vapor annealing. One set of lipid/nanocrystal films were not exposed to chloroform vapor. The lipid/nanocrystal films were then rehydrated and sonicated (red), centrifuged after sonication (blue), or extruded after centrifugation (green). The plotted correlation functions are the best fit of Equation 5.6 to triplicate measurements of the scattering correlation function. Numerical values obtained from the data fits are tabulated in the Appendix.

Lipid/nanocrystal films exposed to chloroform vapor also took significantly longer to lift off the glass surface during sonication than films without chloroform annealing. The exposure to organic solvent leads to inverted hexagonal (H_{II}) and cubic (Q) phases of the DOPC lipid.^{89,93,94} Inverted H_{II} and Q phases do not disperse in water without the addition of stabilizing surfactant due to the exposed hydrophobic interfaces.⁹⁵ Bringing the phospholipids to full hydration requires a transition from the chloroform-swollen non-lamellar phase to the vesicle-forming L_{α} phase,^{89,96} which is a relatively slow process requiring the lipids to rearrange.^{97,98}

Role of solvent vapor annealing in nanocrystal loading of DOPC vesicles. Chloroform improves mixing of the nanocrystals and DOPC in the dried films and is also retained in the vesicles. Chloroform influences several properties of lipid membranes, which may further improve nanocrystal loading. Absorbed chloroform lowers the viscosity of lipid bilayers (increasing lipid lateral diffusivity),^{97,98} which should make the bilayers less resistant to the physical deformation of incorporating a hydrophobic nanocrystal. Chloroform has a slight preference to reside at the membrane-water interface,^{98,99} which should lower the pressure at the center of the bilayer and may encourage nanocrystal incorporation.^{100,101} Simulations of DOPC bilayers showed that chloroform encourages lipid to align more perpendicular to the membrane-water interface and increase the bilayer thickness.⁹⁸ In Figure 5.18, 1H NMR spectra of DOPC vesicles prepared in D_2O with and without nanocrystals confirm that chloroform is present in the DOPC/Au nanocrystal dispersions. The DOPC dispersions prepared with 1.8 nm Au nanocrystals

and chloroform annealing contained about 1 chloroform molecule per DOPC after the sonication step and then extrusion lowered the CHCl_3 :DOPC molar ratio to about 0.2. In ^{31}P NMR spectra, the ^{31}P resonance peak of the DOPC dispersions with chloroform vapor annealing was much broader when Au nanocrystals were present, even though the size of the vesicles was about the same with and without Au nanocrystals according to DLS (Appendix A). This suggests that the diffusion rate of the lipid phosphate groups is slower when nanocrystals are present – either that the lipids must be more ordered to support nanocrystals in the bilayer or the nanocrystals slow the lateral diffusivity of lipids in the bilayer.^{102,103}

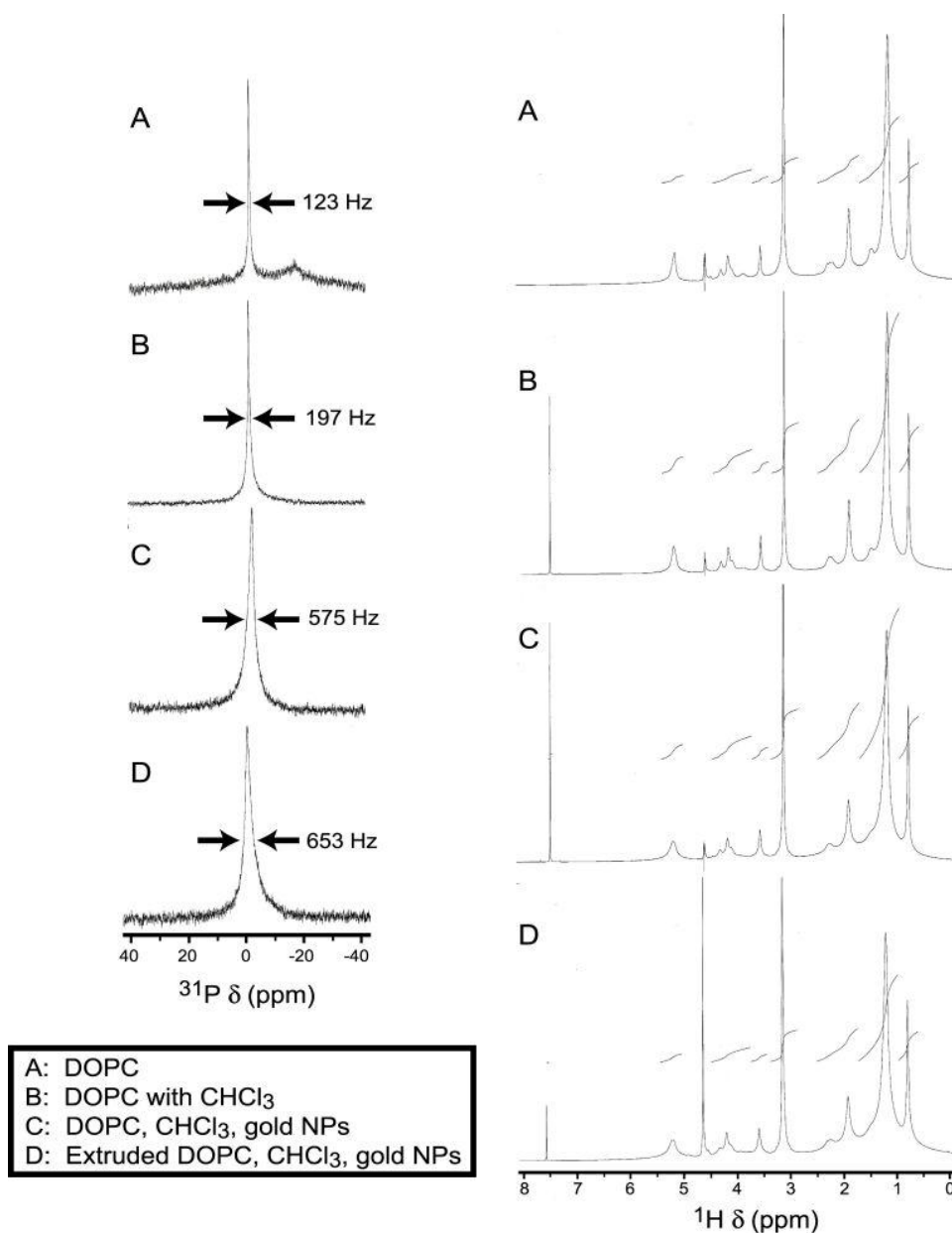


Figure 5.18. ^{31}P (left) and ^1H NMR (right) characterization of DOPC dispersions prepared in D_2O with and without dodecanethiol-coated 1.8 nm Au nanoparticles (NPs). Sample A was not prepared with absorbed chloroform, while samples B-D were prepared with absorbed chloroform vapor. The full width at half maximum is indicated for the peak in each ^{31}P spectrum. In the ^1H NMR spectrum, the resonance peak of chloroform is identified at $\delta = 7.6$ ppm.

5.3.4 Optimum DOPC Concentration.

The optimum concentration of DOPC lipid was determined for dispersing 3 mg of the 1.8 nm diameter dodecanethiol-coated Au nanocrystals. Dry films were prepared containing 3 mg of Au nanocrystals and 1 mmol, 10 mmol, 30 mmol, or 60 mmol of DOPC lipid. The films were annealed with chloroform vapor for 60 minutes, and then dispersed in 1 mL DI water by sonication. Immediately after dispersing by sonication, the dispersed DOPC-Au particles were all adjusted to 1 mM DOPC concentration by dilution with DI water, since the particle diffusion coefficient is concentration-dependent.¹⁰⁴ Fitting the DLS data reveals that the particle size decreases with increasing DOPC concentration: 125 nm (1 mM), 91 nm (10 mM), 59 nm (30 mM), 56 nm (60 mM). When the dispersions are centrifuged, most of the Au nanocrystals precipitate from the 1 mM DOPC sample, while most of the Au nanocrystals remain dispersed in the 30 mM and 60 mM samples as shown in Figure 5.19. Therefore, 30 mM DOPC provides better dispersibility of the Au nanocrystals than 1 or 10 mM DOPC. The 60 mM DOPC sample does not provide any significant improvement in dispersibility over the 30 mM DOPC sample, and so the additional lipid used in the 60 mM sample is unnecessary.

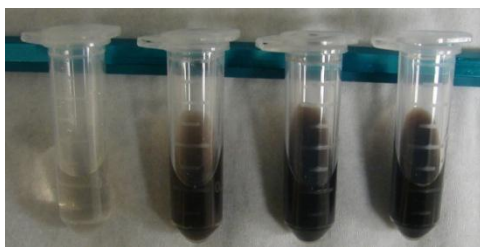


Figure 5.19. Dispersions of DOPC and 1.8 nm Au nanocrystals prepared in DI water after chloroform vapor annealing, with varying lipid concentration. The dispersions were dispersed by sonicating and centrifuged. The samples all were made with 3 mg of Au nanocrystals, and the lipid concentration was (from left to right) 1 mM, 10 mM, 30 mM, and 60 mM DOPC.

5.3.5 Solvent vapor annealing of nanocrystal/lipid films under various conditions.

A variety of conditions of solvent evaporation temperature and solvent annealing were studied. De-mixing of the nanocrystal and lipid occurred regardless of the solvent evaporation temperature (Figure 5.20). Others have also shown that zwitterionic phospholipids and nanocrystals tend to de-mix – for instance, hydrophilic silica nanocrystals have been observed to separate from phospholipids when dried from ethanol,^{105,106} and in Langmuir Blodgett (LB) monolayer films, hydrophobic gold nanocrystals phase separated from saturated phospholipids.¹⁰⁷

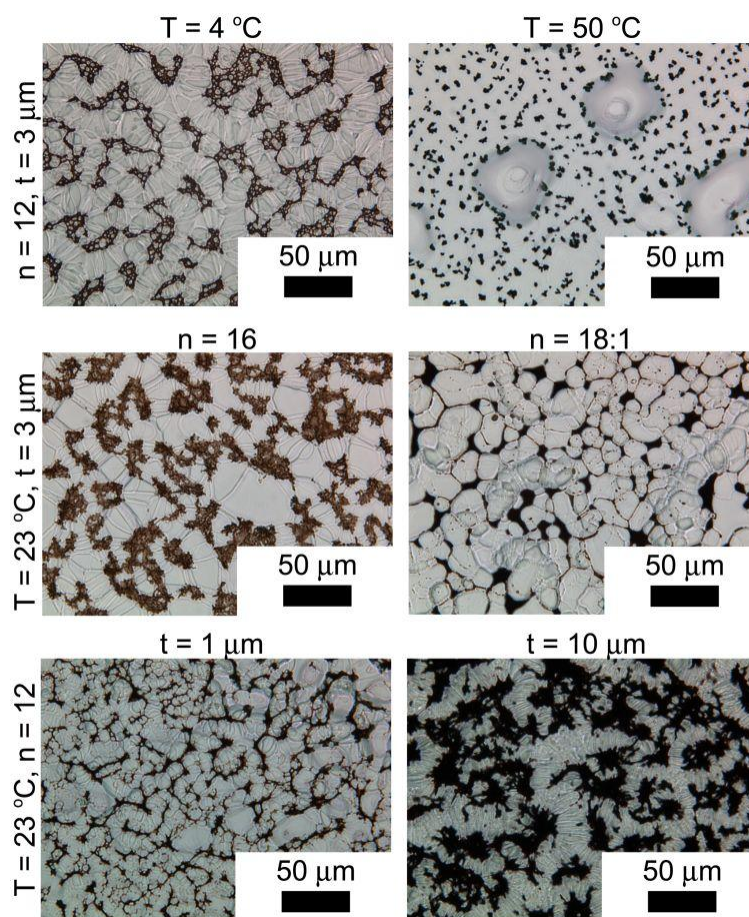


Figure 5.20. Light microscopy analysis of varying drying conditions for films of DOPC and 1.8 nm diameter Au nanocrystals drop cast on glass from a liquid chloroform dispersion. The drying variables included temperature (T), number of carbon atoms per thiol ligand ($n = 12$ for dodecanethiol, $n = 16$ for hexadecanethiol, $n = 18:1$ for 9-octadecene-1-thiol),¹⁰⁸ and average film thickness (t). The average film thicknesses ranged from 1 – 10 μm . The drying temperature was varied by drop-casting the dispersions in either a cold room (4°C) or an oven (50°C) at atmospheric pressure, after equilibrating the coverglass and dispersion at the drop-cast temperature for 10 minutes. Since the lipid molar volume (1.0 mg/mm^3)¹⁰⁹ and the substrate area were known, the film thickness was varied according to the concentration of lipid in the 500 μL chloroform dispersion – 1 mg lipid (1 μm thickness), 3 mg lipid (3 μm thickness), 10 mg lipid (10 μm thickness). In each case, 0.3 mg of nanocrystals was included per 1 mg of lipid. For comparison, lipid-nanocrystal films prepared in the glass round bottom flasks for making vesicles typically have 0.5 mg of lipid per cm^2 and 0.1 mg of nanocrystals per 1 mg of lipid.

The nanocrystals and lipid in solvent vapor “annealed” films remained well-mixed even after drying again under vacuum for 12 hours (Figure 5.21). From visual observation, the viscosity of the films during annealing remains very high, compared to when the lipids and nanocrystals are completely dispersed in 1 mL of liquid chloroform. The viscosity of a dispersion increases with the volume fraction of solid particles,^{110,111} and since the diffusion coefficient of solid particles in a fluid decreases with both increasing viscosity *and* increasing volume fraction,¹¹² the nanocrystals probably diffuse too slowly in the annealed film to re-arrange into the microscale phase separated arrangement seen in the top image of Figure 5.21. Other organic solvents, such as dichloromethane and toluene, were found to remix the lipid and nanocrystals,¹¹³ and others did not, including carbon tetrachloride, tetrachloroethylene, cyclohexane, hexanes, diethyl ether, ethanol, and acetone. Chloroform, dichloromethane, and toluene are low polarity molecules that have a non-zero dipole moment,¹¹⁴ and are good solvents for both lipid and nanocrystals.¹¹⁵ In fact, dichloromethane can be substituted for chloroform during the solvent vapor annealing to produce Au-loaded DOPC vesicles, as shown in Figure 5.22.

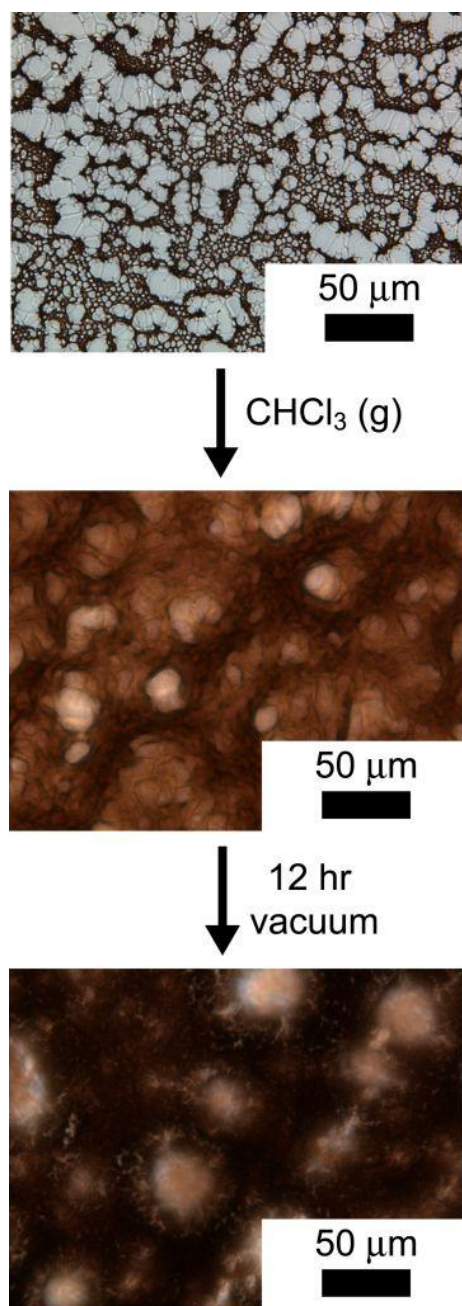


Figure 5.21. Light microscopy analysis showing that chloroform vapor annealed DOPC-nanocrystal films do not revert to their initial, microphase-separated structure when placed under vacuum after annealing. At 40x magnification, the annealed films appear homogeneous before and after vacuum.

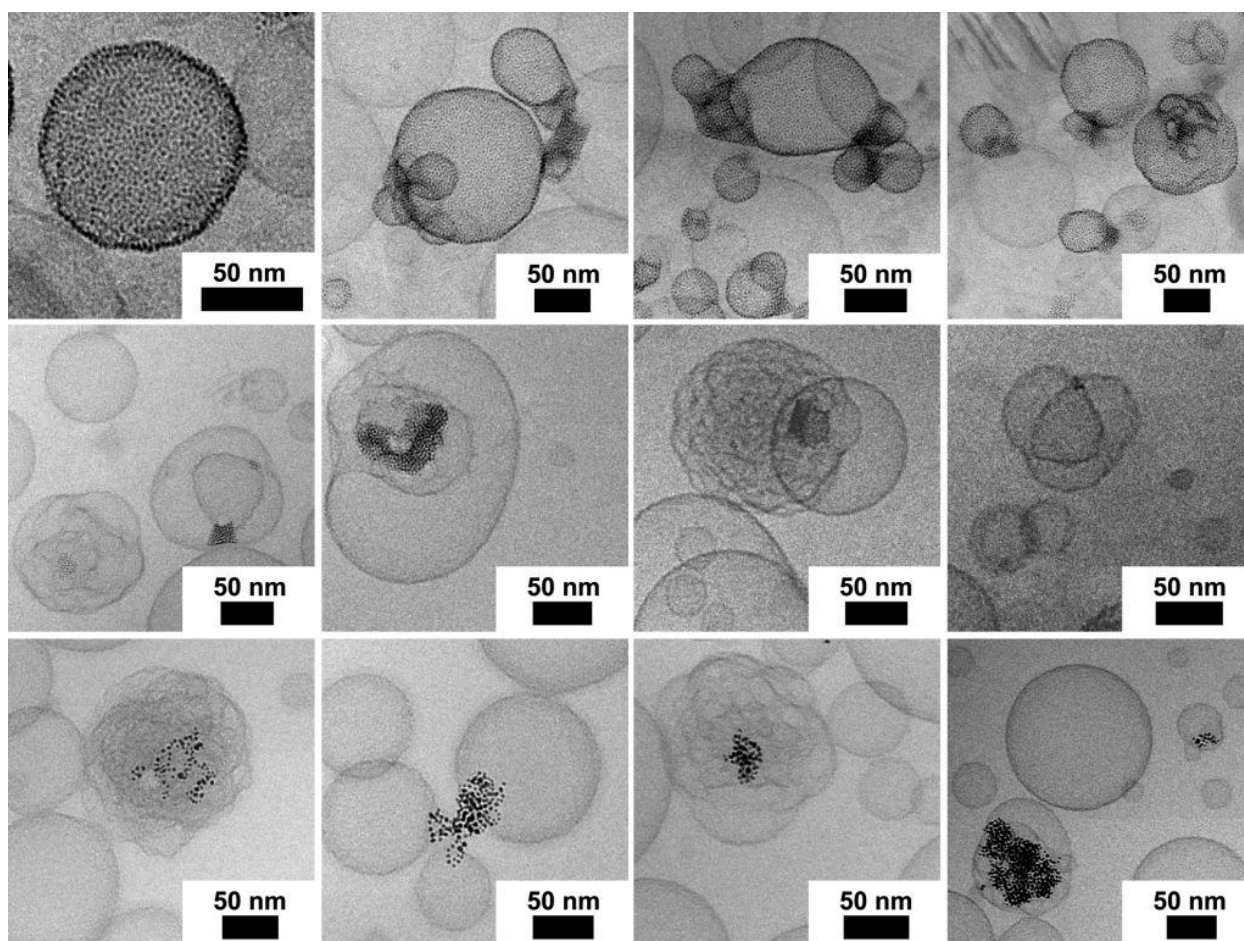


Figure 5.22. CryoTEM images of Au nanocrystal-loaded DOPC vesicles prepared by annealing with dichloromethane vapor instead of chloroform. Top row: dodecanethiol-coated 1.8 nm nanocrystals, middle row: hexadecanethiol-coated 1.8 nm nanocrystals, bottom row: dodecanethiol-coated 4.1 nm nanocrystals.

Chloroform and dichloromethane vapor annealing turned the films from opaque to glassy and transparent within 5 minutes, and they caused the films to bead up on the glass surface within 10 minutes. The appearance of the chloroform-annealed films did not change much in light microscopy after the annealed films were exposed to 12 hour vacuum, as shown in Figure 5.21. Toluene annealing was performed for 60 minutes

without causing the film to de-wet, and this is probably because toluene has a much lower vapor pressure and a lower dipole moment than chloroform and dichloromethane. Toluene also was not effective at improving the dispersibility of Au nanocrystals in DOPC vesicles. Other organic solvent vapors tested were allowed to anneal the films for 45-60 minutes, and they did not cause the films to become glassy or de-wet. Figure 5.23 shows that solvent vapor annealing with the other organic solvents only caused marginal changes in film morphology and did not cause substantial mixing of the separate lipid and nanocrystal microdomains. Diethyl ether, which also has a non-zero dipole moment, has a much lower refractive index than chloroform, dichloromethane and toluene, making it a relatively poor solvent for the nanocrystals.

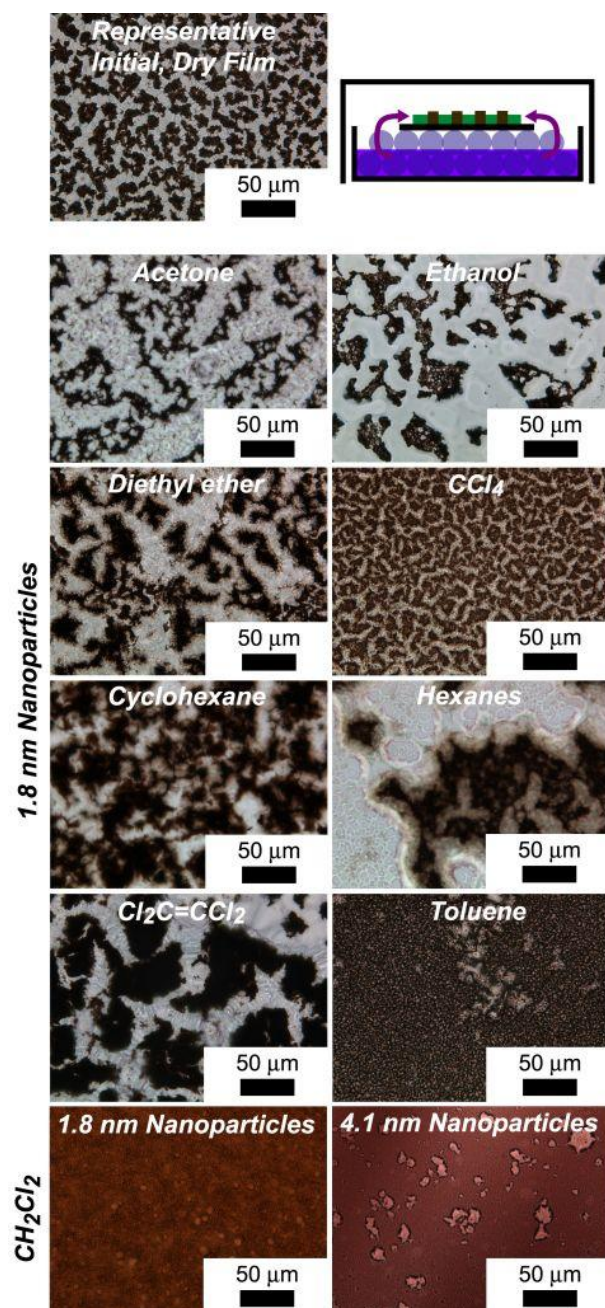


Figure 5.23. Light microscopy analysis of dry films of DOPC and dodecanethiol-coated Au nanocrystals exposed to various solvent vapors. The sketch at the top right illustrates the solvent vapor annealing apparatus, with purple arrows indicating the diffusion of solvent vapor to the film from the underlying liquid phase. Only toluene and dichloromethane vapor exposure led to significant mixing of lipid and nanocrystals.

5.3.6. Pressure-area isotherms of DOPC/nanocrystal Langmuir Blodgett Films.

LB films of DOPC and the 1.8 nm diameter dodecanethiol-capped Au nanocrystals were studied. The lipid/nanocrystal films were spread from chloroform dispersions on the water sub-phase. There was also phase separation between the lipid and the nanocrystals. The pressure-area isotherms of the LB films are shown in Figure 5.24. An ideal mixture of nanocrystals and lipid should have an area A_{ideal} , which is proportional to the mole fractions of lipid (x_{lipid}) and nanocrystals (x_{NPs}):^{116,117}

$$A_{ideal}(\pi) = x_{lipid}A_{lipid}(\pi) + x_{NPs}A_{NPs}(\pi) \quad (5.7)$$

A_{lipid} and A_{NPs} are the areas occupied per lipid molecule and per nanocrystals in a pure single component monolayer at surface pressure π . Deviations from A_{ideal} indicate attractive or repulsive interactions between the nanocrystals and lipid in the film. A plot of LB film area measured at 20 mN/m surface pressure with changing nanocrystal mole fraction in Figure 5.24B is consistent with equation 5.7, which means that either the nanocrystal and lipid are completely miscible or are completely immiscible.¹¹⁷ Furthermore, the buckling pressure did not vary with the amount of nanocrystals in the film and was always around 45 mN/m, which corresponds to the phase transition pressure for LB films of pure DOPC. The transition for a pure nanocrystal film is typically at about 15 mN/m.¹¹⁸ These data are also consistent with recent LB monolayer compression studies of saturated phospholipids and alkanethiol-capped Au nanocrystals in which phase separation was observed using microscopy.¹⁰⁷

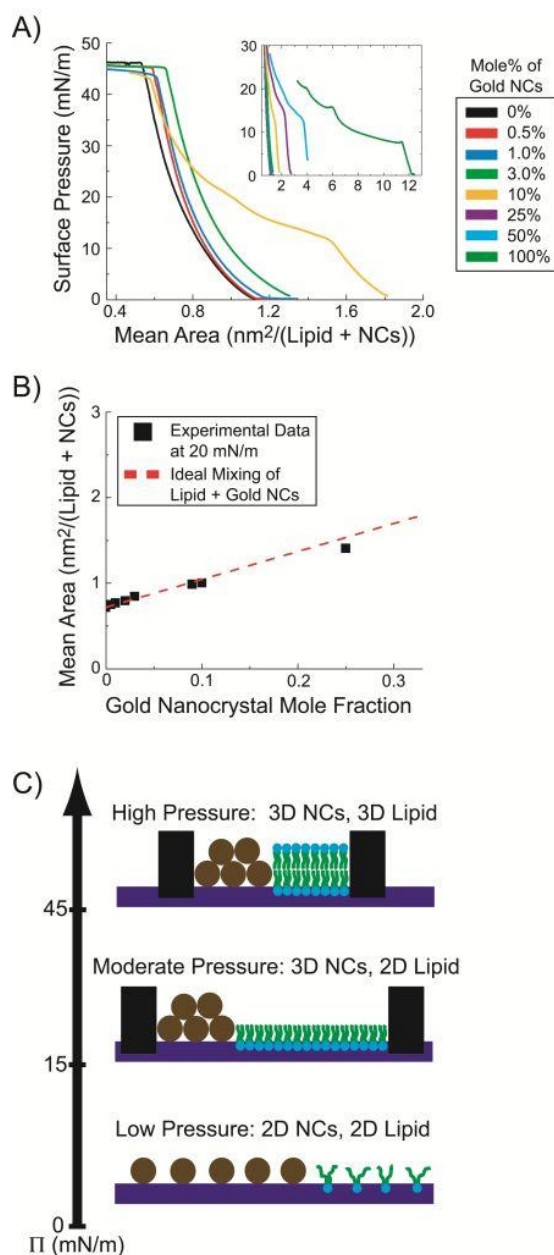


Figure 5.24. Compression of LB films of DOPC lipid and dodecanethiol-coated 1.8 nm Au nanocrystals at a water/air interface. (A) Surface pressure-area isotherms of monolayers with varying DOPC/nanocrystal ratio. (B) Mean area per DOPC lipid/nanocrystals at 20 mN/m pressure, plotted versus Au nanocrystal mole fraction. The data (solid squares) are taken from the plots in (A) and the dashed line plots the area calculated assuming ideal mixing (equation 5.7). (C) Illustration of the nanocrystal/lipid configurations at various pressure.

5.4 Conclusions

Dried films of hydrophobic, alkanethiol-coated gold nanocrystals and DOPC undergo micro-phase separation. Exposure to chloroform vapor, however, leads to mixing of the nanocrystals and lipid. Without chloroform vapor annealing, the lipid-nanocrystal films dispersed poorly in water and formed micrometer-size lipid-coated nanocrystal agglomerates. Lipid-nanocrystal films saturated with chloroform vapor on the other hand disperse well in water. Dodecanethiol-coated 1.8 nm diameter Au nanocrystals did not disrupt vesicle formation and the nanocrystals were observed to completely load the DOPC vesicle membranes vesicles. The larger hexadecanethiol-coated 1.8 nm diameter and dodecanethiol-coated 4.1 nm diameter Au nanocrystals, however, disrupted vesicle formation and tended to disperse as small clusters that fused multiple lipid bilayers.

These data show that there is a maximum nanocrystal size that can be incorporated into lipid bilayers,^{5,40} consistent with recent theoretical work.⁵¹ A recent study also showed that 2 nm diameter hydrophobic gold nanocrystals only inserted into a hydrated lamellar phase of sodium dodecyl sulfate and pentanol when swollen with dodecane solvent.¹¹⁹ The thickness of the swollen lamellae also depends on the amount of absorbed dodecane, and hydrophobic nanocrystals that were larger than the bilayer thickness did not incorporate into the membranes.

In terms of applications, chloroform is toxic and carcinogenic,¹²⁰⁻¹²² making these nanocrystal-loaded vesicles unsuitable for medical applications. Alternative preparative

conditions must be developed for forming nanocrystal-loaded vesicles with relevance to medical applications.

5.5 References

- (1) Al-Jamal, W. T.; Kostarelos, K. *Nanomedicine* **2007**, *2*, 85-98.
- (2) Torchilin, V. P. *Nature Reviews Drug Discovery* **2005**, *4*, 145-160.
- (3) Al-Jamal, W. T.; Al-Jamal, K. T.; Tian, B.; Lacerda, L.; Bomans, P. H.; Frederik, P. M.; Kostarelos, K. *ACS Nano* **2008**, *2*, 408-418.
- (4) McCarthy, J. R.; Kelly, K. A.; Sun, E. Y.; Weissleder, R. *Nanomedicine* **2007**, *2*, 153-167.
- (5) Amstad, E.; Kohlbrecher, J.; Muller, E.; Schweizer, T.; Textor, M.; Reimhult, E. *Nano Letters* **2011**, *11*, 1664-1670.
- (6) Duguet, E.; Vasseur, S.; Mornet, S.; Devoisselle, J. *Nanomedicine* **2006**, *1*, 157-168.
- (7) Park, J.; Estrada, A.; Sharp, K.; Sang, K.; Schwartz, J. A.; Smith, D. K.; Coleman, C.; Payne, J. D.; Korgel, B. A.; Dunn, A. K.; Tunnell, J. W. *Optics Express* **2008**, *16*, 1590-1599.
- (8) Huang, X. H.; Jain, P. K.; El-Sayed, I. H.; El-Sayed, M. A. *Lasers in Medical Science* **2008**, *23*, 217-228.
- (9) Pankhurst, Q. A.; Thanh, N. K. T.; Jones, S. K.; Dobson, J. *Journal of Physics D-Applied Physics* **2009**, *42*, 220301.
- (10) Chen, Y.; Bose, A.; Bothun, G. D. *ACS Nano* **2010**, *4*, 3215-3221.
- (11) Olbrich, K.; Rawicz, W.; Needham, D.; Evans, E. *Biophysical Journal* **2000**, *79*, 321-327.
- (12) Evans, E.; Heinrich, V.; Ludwig, F.; Rawicz, W. *Biophysical Journal* **2003**, *85*, 2342-2350.
- (13) Liu, H.; Graff, G. L.; Hyde, M.; Sarikaya, M.; Aksay, I. A. *Materials Synthesis Based on Biological Processes* **1991**, *218*, 115-121.
- (14) Yaacob, I. I.; Bhandarkar, S.; Bose, A. *Journal of Materials Research* **1993**, *8*, 573-577.
- (15) Tricot, Y. M.; Fendler, J. H. *Journal of Physical Chemistry* **1986**, *90*, 3369-3374.
- (16) Heywood, B. R.; Fendler, J. H.; Mann, S. *Journal of Colloid and Interface Science* **1990**, *138*, 295-298.
- (17) Hutchinson, J. L.; Mann, S.; Skarnulis, A. J.; Williams, R. J. P. *Journal of the Chemical Society, Chemical Communications* **1980**, 634-635.
- (18) Mann, S. *Nature* **1993**, *365*, 499-505.
- (19) Mann, S.; Hannington, J. P. *Journal of Colloid and Interface Science* **1988**, *122*, 326-335.

- (20) Kennedy, M. T.; Korgel, B. A.; Monbouquette, H. G.; Zasadzinski, J. A. *Chemistry of Materials* **1998**, *10*, 2116-2119.
- (21) Korgel, B. A.; Monbouquette, H. G. *Langmuir* **2000**, *16*, 3588-3594.
- (22) Watzke, H.; Fendler, J. H. *Journal of Physical Chemistry* **1987**, *91*, 854-861.
- (23) Korgel, B. A.; Monbouquette, H. G. *Journal of Physical Chemistry* **1996**, *100*, 346-351.
- (24) Song, Y. J.; Garcia, R. M.; Dorin, R. M.; Wang, H. R.; Qiu, Y.; Shelnutt, J. A. *Angewandte Chemie-International Edition* **2006**, *45*, 8126-8130.
- (25) Bota, A.; Varga, Z.; Goerigk, G. *Journal of Applied Crystallography* **2007**, *40*, S259-S263.
- (26) Mann, S.; Hannington, J. P.; Williams, R. J. P. *Nature* **1986**, *324*, 565-567.
- (27) Yang, P.; Lipowsky, R.; Dimova, R. *Small* **2009**, *5*, 2033-2037.
- (28) Chang, A. C.; Pfeiffer, W. F.; Guillaume, B.; Baral, S.; Fendler, J. H. *Journal of Physical Chemistry* **1990**, *94*, 4284-4289.
- (29) Al-Jamal, W. T.; Al-Jamal, K. T.; Bomans, P. H.; Frederik, P. M.; Kostarelos, K. *Small* **2008**, *4*, 1406-1415.
- (30) Wang, M. F.; Zhang, M.; Siegers, C.; Scholes, G. D.; Winnik, M. A. *Langmuir* **2009**, *25*, 13703-13711.
- (31) Pornpattananankul, D.; Olson, S.; Aryal, S.; Sartor, M.; Huang, C. M.; Vecchio, K.; Zhang, L. *Acs Nano* **2010**, *4*, 1935-1942.
- (32) Zhang, L. F.; Granick, S. *Nano Letters* **2006**, *6*, 694-698.
- (33) Volodkin, D. V.; Skirtach, A. G.; Mohwald, H. *Angewandte Chemie-International Edition* **2009**, *48*, 1807-1809.
- (34) Mornet, S.; Lambert, O.; Duguet, E.; Brisson, A. *Nano Letters* **2005**, *5*, 281-285.
- (35) Dietrich, C.; Angelova, M.; Pouligny, B. *Journal De Physique II* **1997**, *7*, 1651-1682.
- (36) Beaune, G.; Menager, C.; Cabuil, V. *Journal of Physical Chemistry B* **2008**, *112*, 7424-7429.
- (37) Paasonen, L.; Laaksonen, T.; Johans, C.; Yliperttula, M.; Kontturi, K.; Urth, A. *Journal of Controlled Release* **2007**, *122*, 86-93.
- (38) Feng, L. Y.; Kong, X. G.; Chao, K. F.; Sun, Y. J.; Zeng, Q. H.; Zhang, Y. L. *Materials Chemistry and Physics* **2005**, *93*, 310-313.
- (39) Binder, W. H.; Sachsenhofer, R.; Farnik, D.; Blaas, D. *Physical Chemistry Chemical Physics* **2007**, *9*, 6435-6441.
- (40) Gopalakrishnan, G.; Danelon, C.; Izewska, P.; Prummer, M.; Bolinger, P. Y.; Geissbuhler, I.; Demurtas, D.; Dubochet, J.; Vogel, H. *Angewandte Chemie-International Edition* **2006**, *45*, 5478-5483.
- (41) Mueller, W.; Koynov, K.; Fischer, K.; Hartmann, S.; Pierrat, S.; Basche, T.; Maskos, M. *Macromolecules* **2009**, *42*, 357-361.
- (42) Yin, Y.; Alivisatos, A. P. *Nature* **2005**, *437*, 664-670.

- (43) Park, S. H.; Oh, S. G.; Mun, J. Y.; Han, S. S. *Colloids and Surfaces B-Biointerfaces* **2006**, *48*, 112-118.
- (44) Von White, I. G.; Chen, Y.; Roder-Hanna, J.; Bothun, G. D.; Kitchens, C. L. *ACS Nano* **2012**, ASAP online.
- (45) Park, S. H.; Oh, S. G.; Suh, K. D.; Han, S. H.; Chung, D. J.; Mun, J. Y.; Han, S. S.; Kim, J. W. *Colloids and Surfaces B-Biointerfaces* **2009**, *70*, 108-113.
- (46) Bothun, G. D. *Journal of Nanobiotechnology* **2008**, *6*.
- (47) Bothun, G. D.; Rabideau, A. E.; Stoner, M. A. *Journal of Physical Chemistry B* **2009**, *113*, 7725-7728.
- (48) Jang, H.; Pell, L. E.; Korgel, B. A.; English, D. S. *Journal of Photochemistry and Photobiology a-Chemistry* **2003**, *158*, 111-117.
- (49) Krack, M.; Hohenberg, H.; Kornowski, A.; Lindner, P.; Weller, H.; Forster, S. *Journal of the American Chemical Society* **2008**, *130*, 7315-7320.
- (50) Zhang, X. W.; Yang, Y. F.; Tian, J.; Zhao, H. Y. *Chemical Communications* **2009**, 3807-3809.
- (51) Wi, H. S.; Lee, K.; Pak, H. K. *Journal of Physics-Condensed Matter* **2008**, *20*, 494211.
- (52) Levin, C. S.; Kundu, J.; Janesko, B. G.; Scuseria, G. E.; Raphael, R. M.; Halas, N. J. *Journal of Physical Chemistry B* **2008**, *112*, 14168-14175.
- (53) Deserno, M.; Gelbart, W. M. *Journal of Physical Chemistry B* **2002**, *106*, 5543-5552.
- (54) Roiter, Y.; Ornatska, M.; Rammohan, A. R.; Balakrishnan, J.; Heine, D. R.; Minko, S. *Nano Letters* **2008**, *8*, 941-944.
- (55) Ginzburg, V. V.; Balijepailli, S. *Nano Letters* **2007**, *7*, 3716-3722.
- (56) Alexeev, A.; Uspal, W. E.; Balazs, A. C. *Acs Nano* **2008**, *2*, 1117-1122.
- (57) Roiter, Y.; Ornatska, M.; Rammohan, A. R.; Balakrishnan, J.; Heine, D. R.; Minko, S. *Langmuir* **2009**, *25*, 6287-6299.
- (58) Aagaard, T. H.; Kristensen, M. N.; Westh, P. *Biophysical Chemistry* **2006**, *119*, 61-68.
- (59) McIntosh, T. J.; Simon, S. A.; MacDonald, R. C. *Biochim Biophys Acta* **1980**, *597*, 445-463.
- (60) Saxena, K.; Shipley, G. G. *Biochemistry* **1997**, *36*, 15940-15948.
- (61) Nelson, P. *Biological Physics: Energy, Information, Life*; W. H. Freeman and Company: New York, 2004.
- (62) Brust, M.; Walker, M.; Bethell, D.; Schiffrin, D. J.; Whyman, R. *Journal of the Chemical Society, Chemical Communications* **1994**, 801-802.
- (63) Sigman, M. B.; Saunders, A. E.; Korgel, B. A. *Langmuir* **2004**, *20*, 978-983.
- (64) Pochan, D. J.; Cui, H.; Hodgdon, T. K.; Kaler, E. W.; Abezgauz, L.; Danino, D.; Lubovsky, M.; Talmon, Y. *Soft Matter* **2007**, *3*, 945-955.
- (65) Jung, H. T.; Coldren, B.; Zasadzinski, J. A.; Iampietro, D. J.; Kaler, E. W. *Proceedings of the National Academy of Sciences of the United States of America* **2001**, *98*, 1353-1357.

- (66) Johnsson, M.; Edwards, K. *Biophysical Journal* **2003**, 85, 3839-3847.
- (67) Vinson, P. K.; Talmon, Y.; Walter, A. *Biophysical Journal* **1989**, 56, 669-681.
- (68) Pochan, D. J.; Zhong, S. *Polymer Reviews* **2010**, 50, 287-320.
- (69) Rasch, M. R.; Rossinyol, E.; Hueso, J. L.; Goodfellow, B. W.; Arbiol, J.; Korgel, B. A. *Nano Letters* **2010**, ASAP.
- (70) Smith, D. K.; Goodfellow, B. W.; Smilgies, D. M.; Korgel, B. A. *Journal of the American Chemical Society* **2009**, 131, 3281-3290.
- (71) Marsh, D. *CRC Handbook of Lipid Bilayers*; CRC Press, Inc.: Boca Raton, FL, 1990.
- (72) Abdulreda, M. H.; Moy, V. T. *Biophysical Journal* **2007**, 92, 4369-4378.
- (73) Nagle, J. F.; Pan, J.; Tristram-Nagle, S.; Kucerka, N. *Biophysical Journal* **2008**, 94, 117-124.
- (74) Taurozzi, J. S.; Hackley, V. A.; Wiesner, M. R. *Nanotoxicology* **2011**, 5, 711-729.
- (75) *Scattering in Polymeric and Colloidal Systems*; Brown, W.; Mortensen, K., Eds.; Gordon and Breach: Singapore, 2000.
- (76) *Characterization of Nanoparticles Intended for Drug Delivery*; McNeil, S. E., Ed.; Humana Press: Totawa, N.J., 2011.
- (77) Appell, J.; Porte, G.; Buhler, E. *Journal of Physical Chemistry B* **2005**, 109, 13186-13194.
- (78) Shukla, A.; Neubert, R. H. H. *Colloid and Polymer Science* **2006**, 284, 568-573.
- (79) Yan, Y. D.; Clarke, J. H. R. *Journal of Chemical Physics* **1990**, 93, 4501-4509.
- (80) Zulauf, M.; Eicke, H. F. *Journal of Physical Chemistry* **1979**, 83, 480-486.
- (81) Daniel, M.; Astruc, D. *Chemical Reviews* **2004**, 104, 293-346.
- (82) First, calculate the Au surface area per nanocrystal using the measured diameter, and divide by the thiol footprint to get thiol molecules per nanocrystal. Second, estimate the Au mass per nanocrystal by calculating Au volume from measured Au diameter, then multiply by the density of Au. Third, determine the thiol mass per nanocrystal from thiol molecular weight. Finally, use the Au mass and thiol mass per nanocrystal to calculate the thiol weight percent.
- (83) Korgel, B. A.; Fullam, S.; Connolly, S.; Fitzmaurice, D. *Journal of Physical Chemistry B* **1998**, 102, 8379-8388.
- (84) Saunders, A. E.; Korgel, B. A. *Journal of Physical Chemistry B* **2004**, 108, 16732-16738.
- (85) The amount of lipid in the nanoparticle-loaded vesicles was estimated to be the same as in a pure lipid vesicle of the same diameter, since the bilayer thickness of the nanoparticle-loaded vesicles is not known yet.
- (86) Efrat, R.; Kesselman, E.; Aserin, A.; Garti, N.; Danino, D. *Langmuir* **2009**, 25, 1316-1326.

- (87) Israelachvili, J. N. *Intermolecular and Surface Forces*; 2nd ed.; Academic press Inc.: San Diego, 1992.
- (88) Considering the thiols at full extension of their hydrocarbon chains.
- (89) Sjolund, M.; Lindblom, G.; Rilfors, L.; Arvidson, G. *Biophysical Journal* **1987**, *52*, 145-153.
- (90) Mirkin, C. A.; Hurst, S. J.; Hill, H. D.; Macfarlane, R. J.; Wu, J. S.; Dravid, V. P. *Small* **2009**, *5*, 2156-2161.
- (91) Jiang, M.; Liu, Z. *Journal of Materials Chemistry* **2007**, *17*, 4249-4254.
- (92) Mandal, T. K.; Si, S. *Langmuir* **2007**, *23*, 190-195.
- (93) Seddon, J. M. *Biochimica Et Biophysica Acta* **1990**, *1031*, 1-69.
- (94) Lohner, K. *Chemistry and Physics of Lipids* **1991**, *57*, 341-362.
- (95) Gustafsson, J.; Ljusberg-Wahren, H.; Almgren, M.; Larsson, K. *Langmuir* **1997**, *13*, 6964-6971.
- (96) Luzzati, V.; Tardieu, A. *Annual Review of Physical Chemistry* **1974**, *25*, 79-94.
- (97) Regen, S. L.; Turkyilmaz, S.; Chen, W. H.; Mitomo, H. *Journal of the American Chemical Society* **2009**, *131*, 5068-+.
- (98) Reigada, R. *Journal of Physical Chemistry B* **2011**, *115*, 2527-2535.
- (99) Phonphok, N.; Chidichimo, G.; Westerman, P. W. *Chemistry and Physics of Lipids* **1996**, *83*, 25-37.
- (100) Cantor, R. S. *Biochemistry* **1997**, *36*, 2339-2344.
- (101) Alakoskela, J. M.; Vitovic, P.; Kinnunen, P. K. J. *Chemmedchem* **2009**, *4*, 1224-1251.
- (102) Burnell, E. E.; Cullis, P. R.; Kruijff, B. D. *Biochim Biophys Acta* **1980**, *603*, 63-69.
- (103) Tilcock, C. P. S.; Cullis, P. R.; Gruner, S. M. *Chemistry and Physics of Lipids* **1986**, *40*, 47-56.
- (104) Pons, T.; Uyeda, H. T.; Medintz, I. L.; Mattoussi, H. *Journal of Physical Chemistry B* **2006**, *110*, 20308-20316.
- (105) Brinker, C. J.; Dunphy, D. R.; Alam, T. M.; Tate, M. P.; Hillhouse, H. W.; Smarsly, B.; Collord, A. D.; Carnes, E.; Baca, H. K.; Kohn, R.; Sprung, M.; Wang, J. *Langmuir* **2009**, *25*, 9500-9509.
- (106) Brinker, C. J.; Dunphy, D. R.; Garcia, F. L.; Jiang, Z.; Strzalka, J.; Wang, J. *Chemical Communications* **2011**, *47*, 1806-1808.
- (107) Jelinek, R.; Mogilevsky, A.; Volinsky, R.; Dayagi, Y.; Markovich, N. *Langmuir* **2010**, *26*, 7893-7898.
- (108) Au nanocrystals coated with 9-octadecene-1-thiol do not load DOPC vesicle bilayers.
- (109) Greenwood, A. I.; Tristram-Nagle, S.; Nagle, J. F. *Chemistry and Physics of Lipids* **2006**, *143*, 1-10.
- (110) Thomas, D. G. *Journal of Colloid and Interface Science* **1965**, *20*, 267.
- (111) Kitano, T.; Kataoka, T.; Shirota, T. *Rheologica Acta* **1981**, *20*, 207.

- (112) Deen, W. M. *Analysis of Transport Phenomena*; Oxford University Press Inc.: New York, 1998.
- (113) Chloroform and dichloromethane are rapidly absorbed into the films and mix the lipids and nanoparticles within 5-10 minutes. Toluene, due to its lower vapor pressure at room temperature, is absorbed more slowly and requires 60 minutes to mix the lipid and nanoparticles.
- (114) *CRC Handbook of Chemistry and Physics*; 91st ed.; CRC Press: Boca Raton, FL, 2011.
- (115) De Luca, G.; Pisula, W.; Credgington, D.; Treossi, E.; Fenwick, O.; Lazzerini, G. M.; Dabirian, R.; Orgiu, E.; Liscio, A.; Palermo, V.; Mullen, K.; Cacialli, F.; Samori, P. *Advanced Functional Materials* **2011**, *21*, 1279-1295.
- (116) Stillwell, W.; Shaikh, S. R.; Dumaual, A. C.; Janski, L. J. *Biochimica Et Biophysica Acta-Biomembranes* **2001**, *1512*, 317-328.
- (117) Hall, R. A.; Thistlethwaite, P. J.; Grieser, F. *Langmuir* **1993**, *9*, 2128-2132.
- (118) Kundu, S. K., S. *Langmuir* **2011**, *27*, 3930-3936.
- (119) Pansu, B.; Lecchi, A.; Constantin, D.; Clerc-Imperator, M.; Veber, M.; Dozov, I. *Journal of Physical Chemistry C* **2011**, ASAP, DOI: 10.1021/jp2046189.
- (120) Abbassi, R.; Chamkhia, N.; Sakly, M. *Toxicology and Industrial Health* **2010**, *26*, 487-496.
- (121) Beddowes, E. J.; Faux, S. P.; Chipman, J. K. *Toxicology* **2003**, *2003*, 101-115.
- (122) Aggazzotti, G.; Fantuzzi, G.; Tartoni, L.; Predieri, G. *Archives of Environmental Health: An International Journal* **1990**, *45*, 175-179.

Chapter 6: Au Nanocrystal Assembly with Saturated Lipids and Oil Droplets[§]

6.1 Introduction

Phosphatidylcholine lipids with saturated fatty acid chains are naturally-occurring,^{1-3,4} bio-degradable amphiphiles that aggregate into lipid bilayers when dispersed in water⁵⁻⁷ and form vesicles.^{8,9} The vesicles can serve as drug carriers by encapsulating hydrophilic molecules in an aqueous compartment or hosting hydrophobic molecules in the lipid bilayer.¹⁰⁻¹³ The lipid bilayer can also host hydrophobic metal,^{14,15} oxide,¹⁶ or semiconductor nanocrystals,^{17,18} which can give the vesicles new functionalities for biomedical imaging and therapy.^{19,20} Recently, it was reported that only hydrophobic nanocrystals smaller than about 5 nm diameter can incorporate into lipid bilayers,^{17,21} while larger nanocrystals aggregate and do not associate with the bilayers.¹⁶ However, the role of the lipid chemistry has not yet been considered, i.e., changes in lipid chain length and saturation. The fatty acid chain length of saturated phosphatidylcholine influences the thickness,⁷ elastic bending modulus,²² and melting temperature of bilayers,¹ so it seems likely that it would influence the incorporation of nanocrystals into the lipid bilayer.

This chapter shows that hydrophobic 1.8 nm Au nanocrystals do not fully load the lipid bilayer of vesicles of phosphatidylcholine lipids with saturated hydrocarbon chains, including dilauroyl-phosphatidylcholine (DLPC, C₁₂), dimyristoyl-phosphatidylcholine

[§] Portions of this chapter appear in the following publication: Rasch, M.R.; Bosoy, C.B.; Yu, Y.; Korgel, B.A. *Langmuir* 2012, submitted. The experiments were performed by M.R. Rasch, C.B. Bosoy, and Y. Yu. The publication's text was written by M.R. Rasch and B.A. Korgel. Funding was provided by research grants to B.A. Korgel.

(DMPC, C₁₄), dipalmitoyl-phosphatidylcholine (DPPC, C₁₆), and distearoyl-phosphatidylcholine (DSPC, C₁₈). The gold nanocrystals formed various lipid-stabilized agglomerates, sometimes fusing with lipid vesicle bilayers. The nanocrystal assembly structure depended on the hydrocarbon chain length of the lipid fatty acids. Lipid with the shortest fatty acid length studied, dilauroyl-phosphatidylcholine, created extended chains of gold nanocrystals. Lipid with slightly longer fatty acid chains created planar sheets of nanocrystals. Further increases of the fatty acid chain length led to spherical agglomerates.

We also tested whether the addition of the liquid hydrocarbon, squalene, influences the assembly of saturated lipids and dodecanethiol-coated Au nanocrystals. A recent study reported that 2 nm diameter hydrophobic Au nanocrystals can only incorporate into surfactant bilayers swollen with n-dodecane.²³ Squalene is a natural precursor to steroids and is frequently used to prepare oil-in-water emulsions for delivering hydrophobic drugs and vaccines.^{24,25} When squalene and phosphatidylcholine are dispersed in water, they form a mixture of lipid-coated squalene droplets and lipid vesicles,²⁴ and squalene does not interpenetrate the fatty acids of lipid monolayers or alter the lipid melting temperature.^{26,27} We find that squalene, saturated phosphatidylcholine lipid and Au nanocrystals form lipid-stabilized squalene droplets loaded with Au nanocrystals, similar to the therapeutic vegetable oil emulsions prepared with iron nanocrystals and phospholipid stabilizers that others have studied.²⁸⁻³⁰ Unique to our work however, the dodecanethiol-coated Au nanocrystals are located at the squalene-

water interface, and at low squalene concentration the nanocrystals pack tightly at the interface.

6.2 Experimental Details

6.2.1 Chemicals

Hydrogen tetrachloroaurate trihydrate ($\text{HAuCl}_4 \cdot 3\text{H}_2\text{O}$, 99.999%), tetraoctylammonium bromide (TOAB, 98%), sodium borohydride (NaBH_4 , 98%), squalene (99%), triolein (99%), and 1-dodecanethiol (98%) were obtained from Sigma-Aldrich. Chloroform, toluene, and ethanol (EtOH, 200 proof) were from Fisher Scientific. 1,2-dilauroyl-*sn*-glycero-3-phosphatidylcholine (DLPC, >99%), 1,2-dimyristoyl-*sn*-glycero-3-phosphatidylcholine (DMPC, >99%), 1,2-dipalmitoyl-*sn*-glycero-3-phosphatidylcholine (DPPC, >99%), and 1,2-distearoyl-*sn*-glycero-3-phosphatidylcholine (DSPC, >99%) were obtained from Avanti Polar Lipids. Deionized (DI) water was obtained from a Barnstead Nanopure Filtration System operating at a 17 M Ω resistance.

6.2.2 Au Nanocrystal Synthesis

The dodecanethiol-coated 1.8 nm and 4.1 nm diameter Au nanocrystals were synthesized as described in Chapter 5.2.

6.2.3 Saturated Lipid Vesicle Formation

Lipid films were dried from 1.0 mL chloroform dispersions of 30 μmol phosphatidylcholine (DLPC, DMPC, DPPC, or DSPC) and 3 mg of gold nanocrystals, corresponding to about 500 lipid molecules per nanocrystal. The 1 mL dispersion was placed in a 50 mL glass round bottom flask (Chemglass) and connected to a rotary

evaporator (Buchi). Chloroform was evaporated at different temperatures depending on the lipid: DLPC and DMPC at 5°C, DPPC at 50°C, DSPC at 60°C. Compared to drying at room temperature, these temperatures reduced the amount of phase separation between lipid and nanocrystals observed by light microscopy, producing more uniform films as shown in Figure 6.1. Once dry, the pressure in the flask was reduced to 50 mbar for 15 minutes. The flask was removed from the rotary evaporator and placed in a vacuum oven for 12 hours at room temperature to completely remove the chloroform.

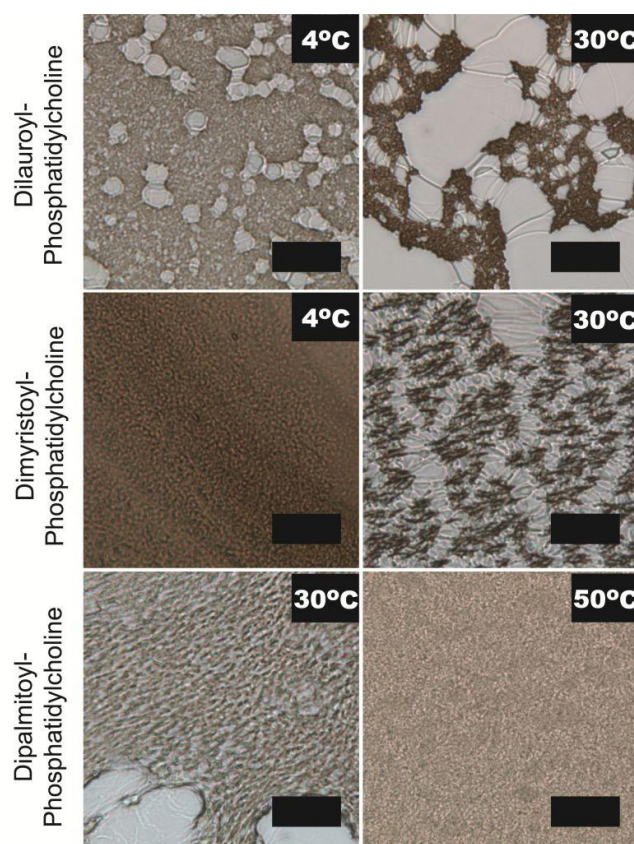


Figure 6.1. Light microscopy images of lipid and Au nanocrystal films prepared on cover glass by drying from a chloroform dispersion at different temperature. Scale bar: 25 μm .

Lipid films were hydrated with 1.0 mL of 0.1 μm pore-filtered DI water at the liquid crystal lamellar phase (L_α) temperature of each lipid:¹ DLPC at 25°C; DMPC at 30°C; DPPC at 50°C; and DSPC at 60°C.³¹ The flasks with the dry lipid-nanocrystal films were briefly warmed in a circulating water bath to the desired temperature, followed by addition of water at the same temperature. The film was completely wetted by gently rotating the flask while held in the water bath. Then, the flask was sealed with parafilm, transferred to an ultrasonicator bath (Misonix, 600 mL water bath) adjusted to the hydration temperature for each lipid, and sonicated until the lipid-nanocrystal film completely lifted off of the glass surface (3 minutes). Subsequently, the dispersion was transferred by glass pipette to a clean 20 mL scintillation vial warmed to the lipid hydration temperature.³² The scintillation vials have thinner walls and a flat bottom, which are better for transmitting ultrasonic waves than the round bottom flasks for reducing particle size.³³ The vial was sealed with parafilm and sonicated for an additional 12 minutes. The power delivered by the ultrasonicator was about 30 W,³⁴ calculated from the measured temperature rise of the bath versus time near 25°C according to Taurozzi et al.^{35,36}

After sonication, samples were transferred to 2 mL plastic centrifuge tubes, warmed to the hydration temperature in a water bath, and centrifuged at 1000g for 10 minutes to precipitate poorly dispersed nanocrystals. The supernatant was transferred to new tubes and maintained at the hydration temperature in a water bath. Samples were then extruded 10 times through two stacked polycarbonate membranes (100 nm diameter pores) using a stainless steel Lipex extruder (Northern Lipids), operating at 500 psi and

equilibrated to the lipid hydration temperature using a water jacket connected to a circulating water bath. After extrusion, the samples were allowed to cool to room temperature overnight prior to imaging the next day.

6.2.4 Squalene Emulsions

The vesicle formation process was repeated using 30 μmol of DLPC, DMPC, or DPPC, in addition to 3 mg of Au nanocrystals. Squalene was added to the chloroform dispersions of lipid and nanocrystals prior to rotary evaporation in varying amounts from 5, 10, 15, to 45 μL (0.5%, 1.0%, 1.5%, and 4.5% v/v respectively).

6.2.5 Material Characterization

The Au nanocrystals were characterized as described in Chapter 5. The vesicles were imaged using cryoTEM at Texas A&M Microscopy and Imaging Center, as described in Chapter 5.

6.3 Results and Discussion

6.3.1 Aggregates of Saturated Phosphatidylcholine and 1.8 nm Au Nanocrystals

Figure 6.2 shows cryoTEM images of saturated phosphatidylcholine lipids with various fatty acid chain length (C_{12} - C_{18}) combined with dodecanethiol-coated 1.8 nm diameter Au nanocrystals. The lipid forms vesicles, but the saturated phosphatidylcholine lipid vesicles are not fully loaded with Au nanocrystals in their lipid bilayer.¹⁴ The nanocrystals form various aggregated structures coated with lipid.

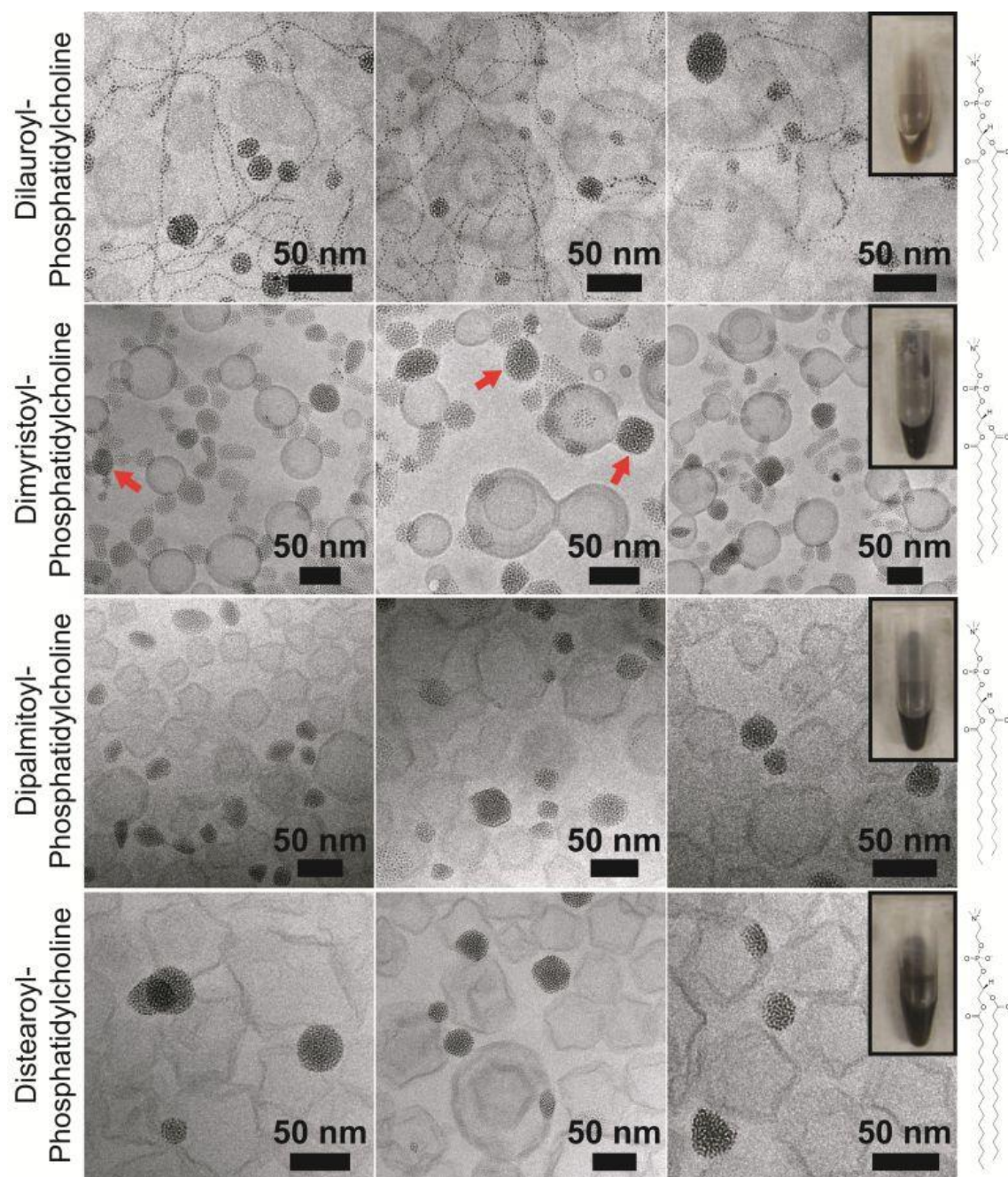


Figure 6.2. CryoTEM images of aggregated 1.8 nm diameter Au nanocrystals formed with various phosphatidylcholine lipids with saturated hydrocarbon chains. All aqueous dispersions were vitrified at 25°C. DLPC and DMPC are in the liquid crystal phase, while DPPC and DSPC are in the gel phase. Red arrows identify nanocrystal aggregates coated with a thin lipid layer. Photographs of the dispersions are shown in the insets.

Disetearoyl- and Dipalmitoyl Phosphatidylcholine Aggregates. The morphology of the lipid-coated gold nanocrystal agglomerates varied with fatty acid length. For DSPC (C_{18}) and DPPC (C_{16}), the nanocrystals form lipid-coated agglomerates ranging from 10 to 50 nm in diameter. Both DPPC and DSPC lipid are in the lamellar gel phase ($L_{\beta'}$) (at 25°C, the temperature of cryoTEM sample vitrification)¹ and the vesicles exhibit planar, faceted membranes as has been observed previously.³⁷ The lipid-coated nanocrystal aggregates also had faceted surfaces. About half of the nanocrystal agglomerates in each lipid sample were found to be fused to vesicle bilayers. This type of structure—of clustered nanocrystals associated with lipid bilayers—has been proposed as a way to minimize distortions in lipid packing.^{14,19}

Dimyristoyl- and Dilauroyl-Phosphatidylcholine Aggregates. The structures of the gold agglomerates with DMPC (C_{14}) and DLPC (C_{12}) differed significantly from those with DPPC and DSPC. DMPC and DLPC are both in the lamellar liquid crystal phase (L_{α}) at 25°C,¹ making their bilayers much more fluid than those of DPPC and DSPC.^{1,22} Accordingly, DLPC and DMPC vesicles are round and spherical, not faceted.^{38,39} The DMPC-coated nanocrystal agglomerates were either solid spherical agglomerates (highlighted with red arrows in Figure 6.2) or flat monolayer sheets. When these structures fuse with the DMPC vesicles, the nanocrystals appear to be budding off the pure lipid bilayer, as if being forced out of the vesicle membrane. Nanocrystals with DLPC formed chains. These chains often terminated in pure lipid bilayers or larger spherical nanocrystal agglomerates. Furthermore, the chains seemed to form an

interconnected network. The DLPC-stabilized Au nanocrystal chains resemble the thread-like micelles that form when eggPC vesicles are mixed with cetyltrimethylammonium chloride surfactant,⁴⁰ yet pure DLPC lipid chains were not observed (Figure 6.3). Perhaps the interfacial curvature of thread-like micelles of pure lipid is too significant and the core of Au nanocrystals reduces this to stabilize the structure.²²

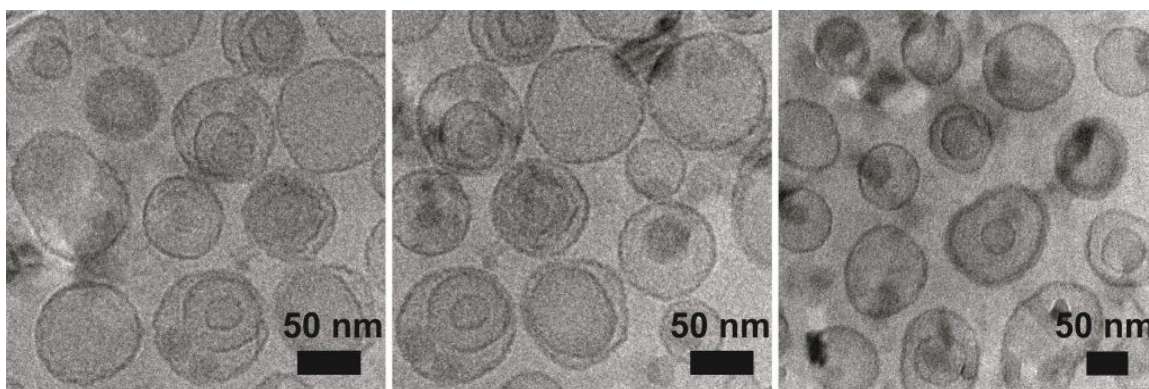


Figure 6.3. Vesicles prepared with only dilauroyl-phosphatidylcholine. There are no signs of thread-like micelles.

6.3.2 Lipid-Squalene Oil Droplets with Au nanocrystals.

Squalene was added to the dispersions to reduce the rigidity of the lipid bilayers. Addition of squalene however led to the formation of lipid-coated squalene (oil) droplets, as shown in Figures 6.4 and 6.5. The Au nanocrystals were observed to accumulate on the droplet surface. Figure 6.6 shows DLPC and DPPC lipid and squalene droplets as well. At high Au nanocrystal concentrations, the Au nanocrystals form a tightly packed monolayer at the droplet surface. Squalene disrupts the Au nanocrystal chains formed

with DLPC, although there were rare instances of Au nanocrystal chains still, as in the top right panel of Figure 6.6. The DPPC-squalene droplets loaded with Au nanocrystals were spherical and not faceted either above or below the $L_{\beta'}$ to L_{α} phase transition temperature of pure DPPC. This is another indication that the observed droplets are not vesicles, as squalene does not alter the phase transition temperature of DPPC,²⁶ and the nanocrystal-loaded droplet morphology remains spherical.

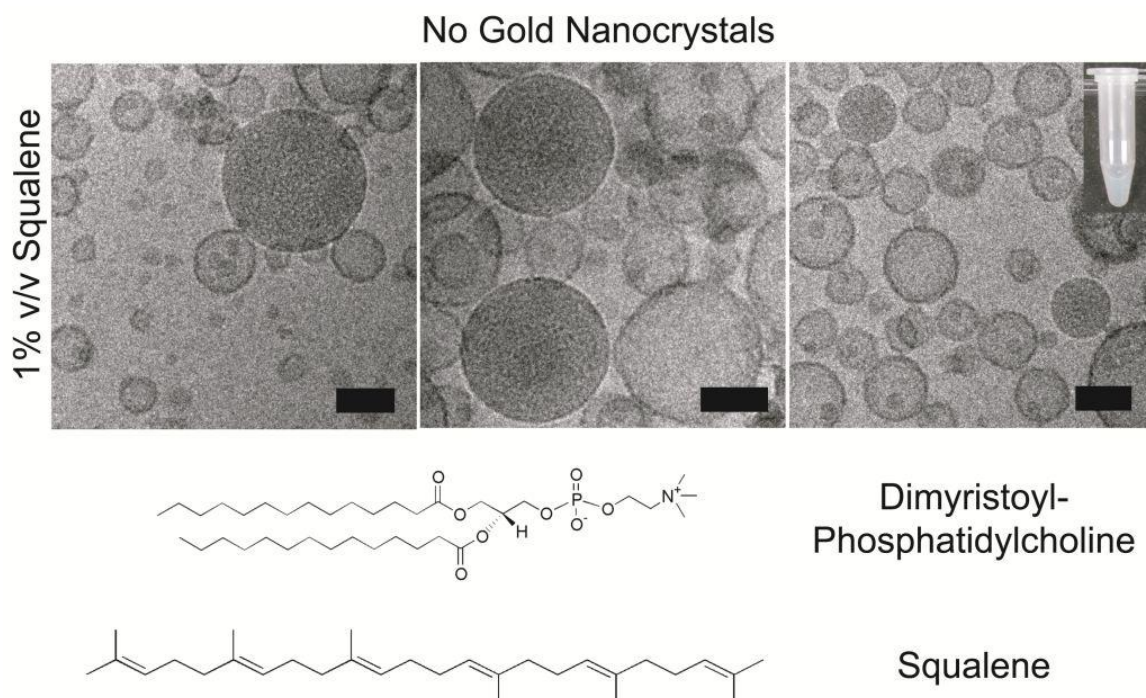


Figure 6.4. CryoTEM images of dimyristoyl-phosphatidylcholine dispersed in water with squalene in the absence of Au nanocrystals. Squalene droplets have high contrast throughout the center since they are filled with liquid hydrocarbon, while vesicles have the highest contrast around the circumference since the hydrocarbon. 50 nm scale bars.

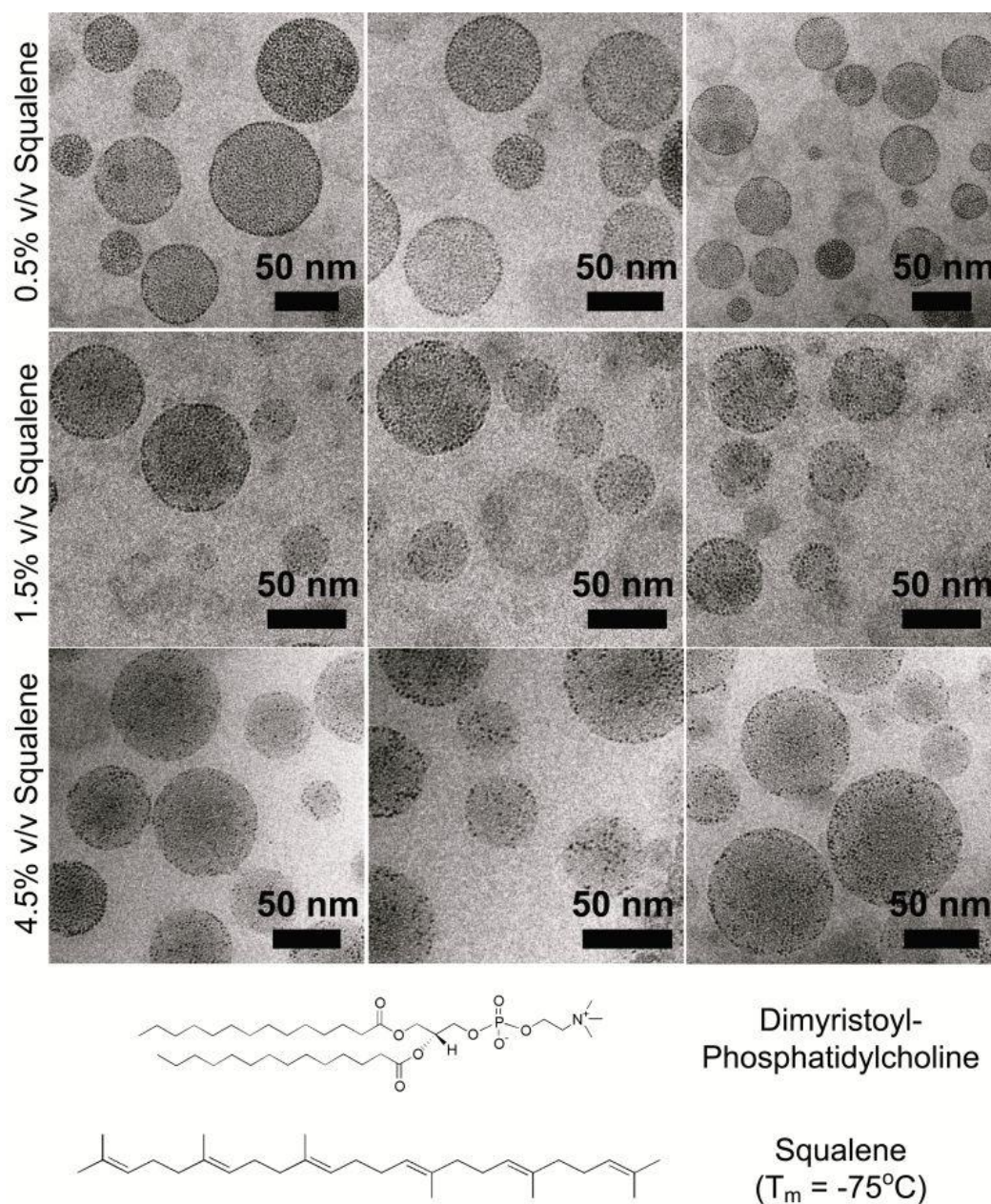


Figure 6.5. CryoTEM images of squalene/DMPC lipid droplets with dodecanethiol-coated Au nanocrystals. Each row of images corresponds to a different squalene concentration.

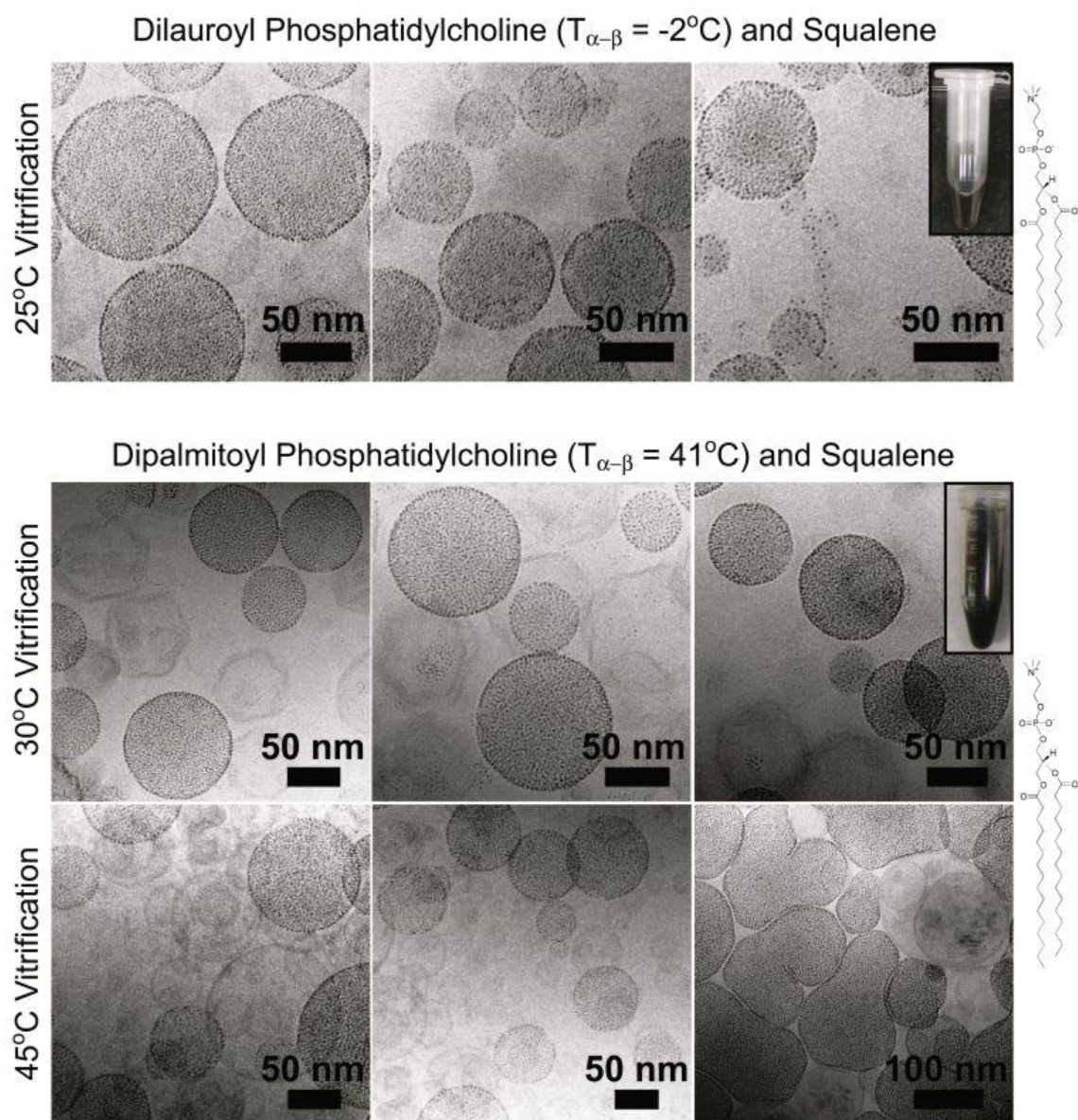
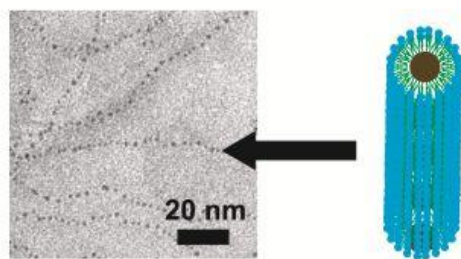


Figure 6.6. CryoTEM images of squalene emulsion droplets loaded with dodecanethiol-coated Au nanocrystals and stabilized with either DLPC or DPPC. The bottom right panel shows Au-loaded squalene droplets deforming when packed together in one region of the TEM grid. The squalene concentrations are all 1% v/v. The insets show photographs of the dispersions.

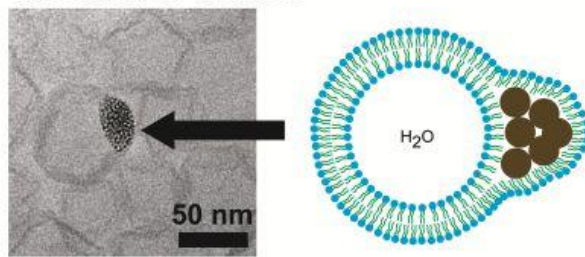
The partitioning of the hydrophobic nanocrystals to the squalene-water interface indicates that lipid is coating the droplets.^{41,42,43} Dodecanethiol-coated gold nanocrystals disperse in pure squalene, but squalene-nanocrystal mixtures did not emulsify in water without lipid. The positioning of the hydrophobic Au nanocrystals at the squalene-lipid interface increases the separation between the water and squalene phases, and also reduces the contact between lipid molecules and squalene, which do not mix according to recent studies.^{26,27} This is comparable to Pickering emulsions, which are stabilized by a combination of solid particles and surfactant, where the role of the surfactant is to change the interfacial tension so the particles reside at the oil/water interface to stabilize the emulsion.^{44,45}

Figure 6.7 summarizes the various saturated PC lipid-nanocrystal-squalene assemblies observed by cryoTEM. In each case, the lipid forms a coating around the assemblies and stabilizes their structure. The lipid chain length plays a determining role, varying the structure from chain-like aggregates to two-dimensional sheets of nanocrystals to three-dimensional solid aggregates of nanocrystals.

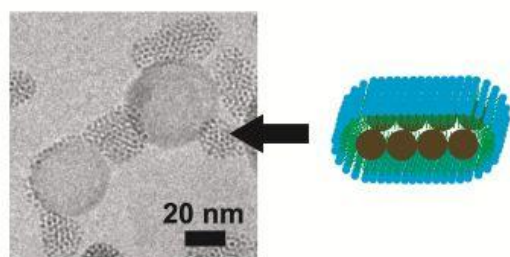
I) Lipid-Coated Au Chains



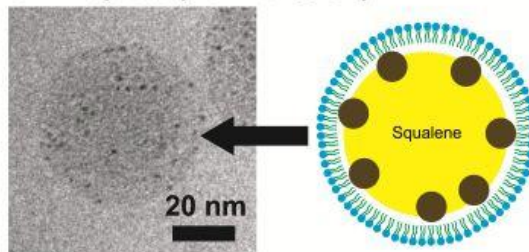
IV) Lipid-Coated Au Agglomerates Adsorbed to Vesicles



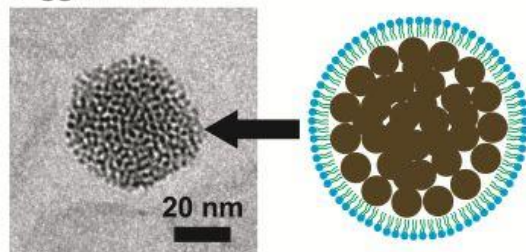
II) Lipid-Coated Au Sheets



V) Lipid-Coated, Au-loaded Oil Droplets (Low v/v% Oil)



III) Solid, Lipid-coated Au Agglomerates



VI) Lipid-coated, Au-loaded Oil Droplets (High v/v% Oil)

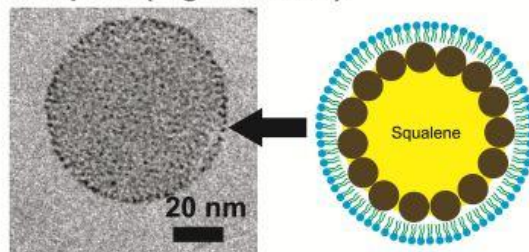


Figure 6.7. Lipid/Au nanocrystal assemblies observed by cryoTEM. The PC lipids are drawn with blue polar headgroups and green fatty acid chains. The gold nanocrystals are brown circles. Squalene is shown in yellow.

6.3.3 Buoyancy of 1.8 nm Au nanocrystal-loaded squalene/lipid droplets.

Lipid-coated squalene droplets were observed to cream (negative settling velocity), particularly when Au nanocrystals were not added. For example, significant creaming was observed within 24 hours if insufficient sonication power was delivered or Au nanocrystals were not incorporated into the emulsions. The Au nanocrystals alter the buoyancy of the squalene droplets. Figure 6.8 shows the settling velocity v , calculated for the various types of particles observed by cryoTEM. Assuming the particles do not interact,⁴⁶

$$v = \frac{F_{drag}}{3\pi\eta D} = \frac{(m_{squalene} + m_{lipid} + m_{Au} - m_{water})g}{3\pi\eta D} \quad (6.1)$$

D is the diameter of the lipid-coated particle, g is 9.8 m/s^2 , and η is the viscosity of water at 25°C ($0.89 \text{ mPa}\cdot\text{s}$). m_{water} is the mass of water displaced by the particle, m_{lipid} is the mass of lipid coating the particle, $m_{squalene}$ is the mass of squalene in the droplet, and m_{Au} is the mass of the Au nanocrystals per droplet. As shown in Figure 6.8, settling rate is size dependent. The lipid-coated Au agglomerates settle the fastest and the Au nanocrystals act as a weighting agent in the squalene droplets, preventing creaming until the droplet diameter exceeds 130 nm.

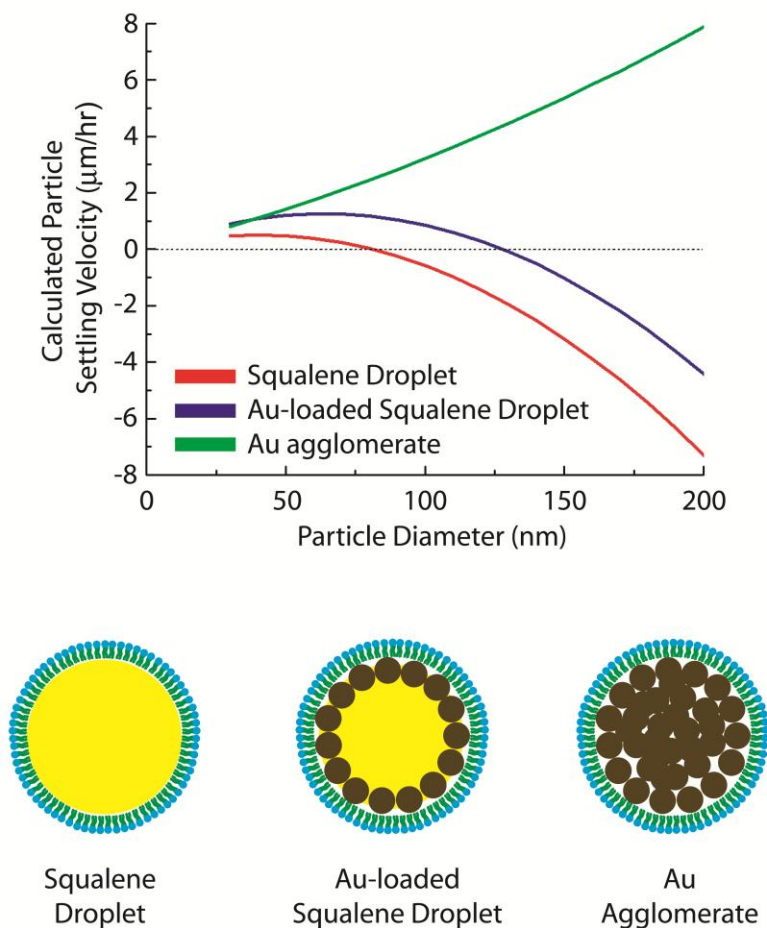


Figure 6.8. Settling velocities calculated for the different types of particles observed by cryoTEM. Positive velocity refers to motion in the direction of gravity and negative velocity refers to flotation or particle creaming. In the illustrations, lipids have a blue headgroup and green fatty acid chains, Au nanocrystals are brown circles, and squalene is yellow.

Derivation of expressions for the masses in equation 6.1, for each type of particle illustrated in Figure 6.8, proceeds as follows. The mass of water displaced by the particle is the product of the particle volume and the water density ($\rho_{\text{water}} = 0.997 \text{ g/mL}$):⁴⁷

$$m_{\text{water}} = \frac{\pi}{6} D^3 \rho_{\text{water}} \quad (6.2)$$

The mass of lipid coating the particles, m_{lipid} , is the product of the particle surface area (πD^2) and the lipid molecular weight ($M_{\text{lipid}} = 677.95$ Da for DMPC), divided by the lipid head group area ($\sigma_{\text{lipid}} = 3.6 \times 10^{23}$ nm² per mole of DMPC lipid).^{1,7} We take the lipid head group area measured in a lipid bilayer as an estimate for the head group area on the different types of particles.

$$m_{\text{lipid}} = \pi D^2 M_{\text{lipid}} \cdot \sigma_{\text{lipid}} \quad (6.3)$$

The mass of squalene (m_{squalene}) and Au nanocrystals (m_{Au}) are specific to the type of particle. For the squalene droplets drawn in Figure 6.8, the masses of squalene and Au are expressed as equation 6.4, where ρ_{squalene} is the squalene density (0.858 g/cm³)⁴⁷:

$$m_{\text{squalene}} = \frac{\pi}{6} D^3 \rho_{\text{squalene}} \quad , \quad m_{\text{Au}} = 0 \quad (6.4)$$

For the Au-loaded squalene droplet, first we estimate the number of Au nanocrystals per droplet N_{Au} as the total droplet surface area (πD^2) divided by the projected area per Au nanocrystal ($A_{\text{Au}} = (\pi/4) \cdot d_{\text{Au}}^2$). Next, we estimate the volume fraction of the droplet occupied by Au nanocrystals (Φ_{Au}), which is used to calculate the mass of squalene per droplet m_{squalene} by subtracting the volume of Au from the total droplet volume. Finally the total nanocrystal mass is determined as the product of the number of nanocrystals per droplet, the volume of Au atoms per nanocrystal, and the bulk density of Au divided by the weight percent of Au atoms per nanocrystal ($w_{\text{Au}} = 73\%$ by thermogravimetric analysis of a dry powder of the nanocrystals, see Chapter 5).

$$N_{Au} = \left(\frac{\pi D^2}{\frac{\pi}{4} d^2} \right) = \left(\frac{2D}{d} \right)^2 \quad (6.5)$$

$$\Phi_{Au} = \frac{N_{Au} \left(\frac{\pi}{6} d_{Au}^3 \right)}{\frac{\pi}{6} D^3} = \frac{4d_{Au}}{D} \quad (6.6)$$

$$m_{squalene} = \frac{\pi}{6} D^3 (1 - \Phi_{Au}) \rho_{squalene} \quad (6.7)$$

$$m_{Au} = N_{Au} \left(\frac{\pi}{6} \frac{d_{Au}^3 \cdot \rho_{Au}}{w_{Au}} \right) = \frac{2\pi D^2 \rho_{Au} d_{Au}}{3w_{Au}} \quad (6.8)$$

In the case of the lipid-coated Au agglomerates, the mass of squalene equals zero. To estimate the mass of the Au agglomerate versus agglomerate diameter (m_{Au}), first we assumed that the nanocrystals are randomly packed in the agglomerate so that the volume packing density of nanocrystals is $\varphi = 0.6$,^{48,49} defined as the total volume of nanocrystals in the agglomerate divided by the total agglomerate volume. The volume occupied by a single nanocrystal in the agglomerate is calculated by assuming each nanocrystal occupies the volume of a sphere with a diameter equal to the Au core diameter (d_{Au}) plus the d-spacing of the Au nanocrystals measured from grazing incidence small angle x-ray scattering of the dry DPPC-Au film ($d_{space} = 2.7$ nm). The d-spacing is less than the length of two fully-extended dodecanethiol ligands, which is about 3.3 nm,⁵⁰ so we assume that the void space in the Au agglomerate ($1-\varphi$) is occupied by the remaining

amount of dodecanethiol ligand not accounted for by the d-spacing. Therefore, the mass of nanocrystals in the agglomerate is just the number of Au nanocrystals per agglomerate multiplied by the mass per Au nanocrystal. It follows that the density of the agglomerate $\rho_{agglomerate}$ is the total nanocrystal mass divided by the total agglomerate volume (the total number of nanocrystals in the numerator and denominator cancel).

$$\rho_{agglomerate} = \frac{\varphi}{\frac{\pi}{6}(d_{Au} + d_{space})^3} \left(\frac{\pi}{6} \frac{d_{Au}^3 \cdot \rho_{Au}}{w_{Au}} \right) \quad (6.9)$$

$$m_{Au} = \frac{\pi}{6} D^3 \rho_{agglomerate} \quad (6.10)$$

6.3.4 Saturated Lipids, Oil Droplets, and 4.1 nm Au Nanocrystals

The experiments performed with the 1.8 nm diameter Au nanocrystals were repeated with 4.1 nm diameter Au nanocrystals. Figure 6.9 shows cryoTEM images of saturated phosphatidylcholine lipids with various fatty acid chain length (C₁₂-C₁₈) combined with dodecanethiol-coated 4.1 nm diameter Au nanocrystals. The lipid forms vesicles, and the nanocrystals form various aggregated structures coated with lipid. The results with DMPC, DPPC, and DSPC are similar to the observations with 1.8 nm Au nanocrystals – some of the lipid-coated 4.1 nm Au nanocrystal agglomerates are stuck to vesicle membranes, and some are completely dispersed in solution without attaching to vesicles. With DMPC, there are many irregularly shaped lipid-coated agglomerates with 4.1 nm diameter Au, whereas with 1.8 nm diameter Au the agglomerates are more

rounded and spherical. The 4.1 nm Au nanocrystals do not disperse well with the DLPC lipid or form Au chains, and most of the nanocrystals precipitate from solution during the centrifugation step of vesicle processing. The exact reason why the 4.1 nm nanocrystals do not form chains with the DLPC lipid is not clear, there are several factors that could participate: (1) The 4.1 nm diameter Au nanocrystals are much larger than the DLPC bilayer thickness (3.3 nm)⁷ compared to the 1.8 nm diameter nanocrystals, and may be excluded due to their size alone; (2) Since the van der Waals attractive force between particles increases proportionally to particle size,⁵⁰ and since both the 4.1 nm and 1.8 nm nanocrystals have the same ligand coating (dodecanethiol), then the 4.1 nm nanocrystals will have stronger inter-particle attractive forces and therefore a stronger tendency to aggregate than the 1.8 nm nanocrystals; (3) Since the inter-particle attractive force is greater for 4.1 nm than 1.8 nm Au nanocrystals, aggregates of the 4.1 nm nanocrystals will have a higher Young's modulus and therefore will be less deformable into thin chains compared to the 1.8 nm nanocrystals.⁵¹ These considerations, combined with the fact that DLPC has a higher critical micelle concentration and exchange rate between monomers and aggregates in bulk solvent (less time spent coating the surface of Au aggregates), may be responsible for the substantial aggregation and precipitation of 4.1 nm nanocrystals in dispersions of DLPC.

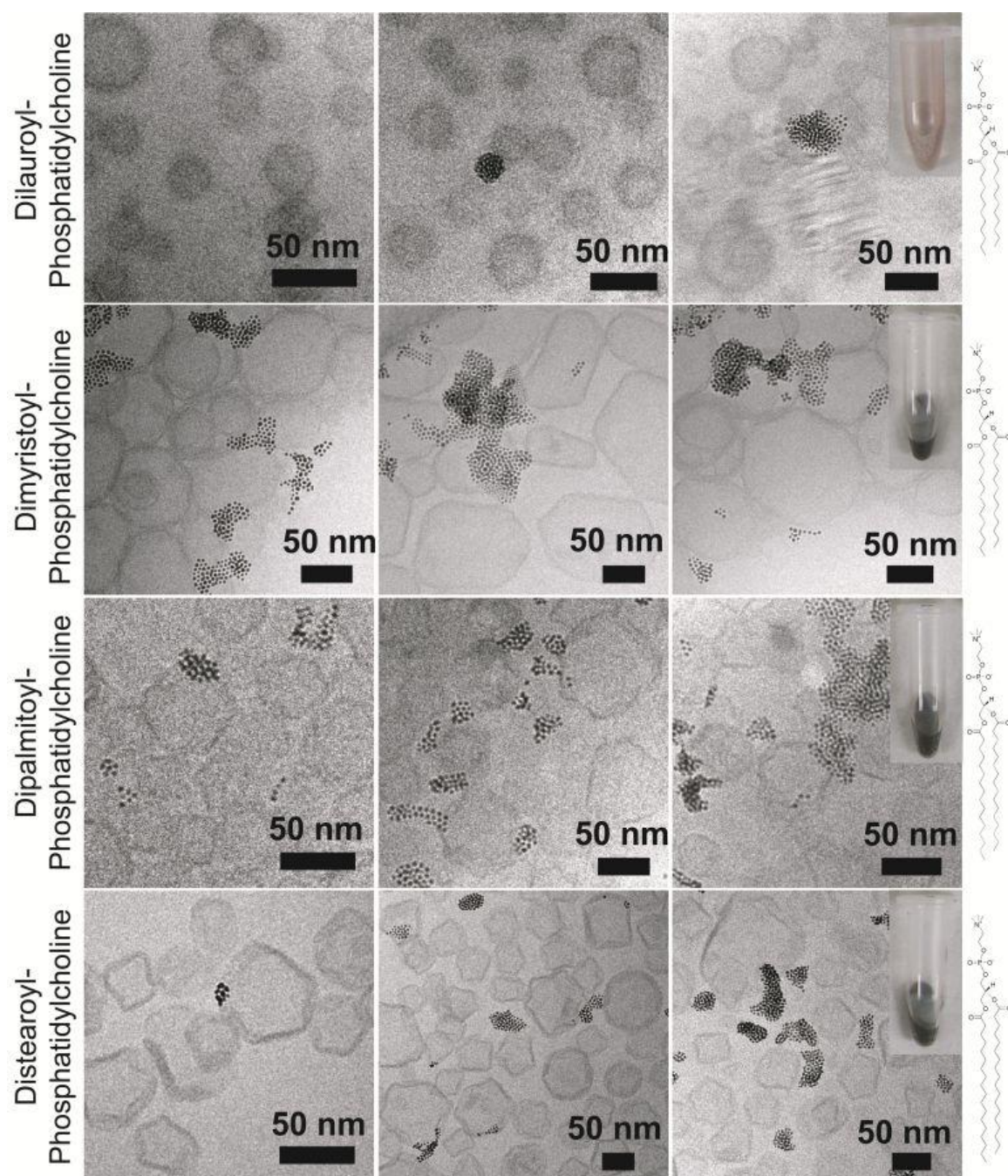


Figure 6.9. CryoTEM images of aggregated 4.1 nm diameter Au nanocrystals formed with various phosphatidylcholine lipids with saturated hydrocarbon chains. All aqueous dispersions were vitrified at 25°C. DLPC and DMPC are in the liquid crystal phase, while DPPC and DSPC are in the gel phase.

Similar to the results with 1.8 nm nanocrystals, the 4.1 nm diameter Au nanocrystals can also incorporate into lipid-coated squalene droplets, as shown in Figure 6.10. The emulsions were prepared with 5% v/v squalene in water and 3 mg of 4.1 nm diameter Au nanocrystals. Finally, squalene was replaced with triolein, and emulsions were formed at 5% v/v triolein, showing that Au nanocrystals can load the triolein droplets as well in Figure 6.11.

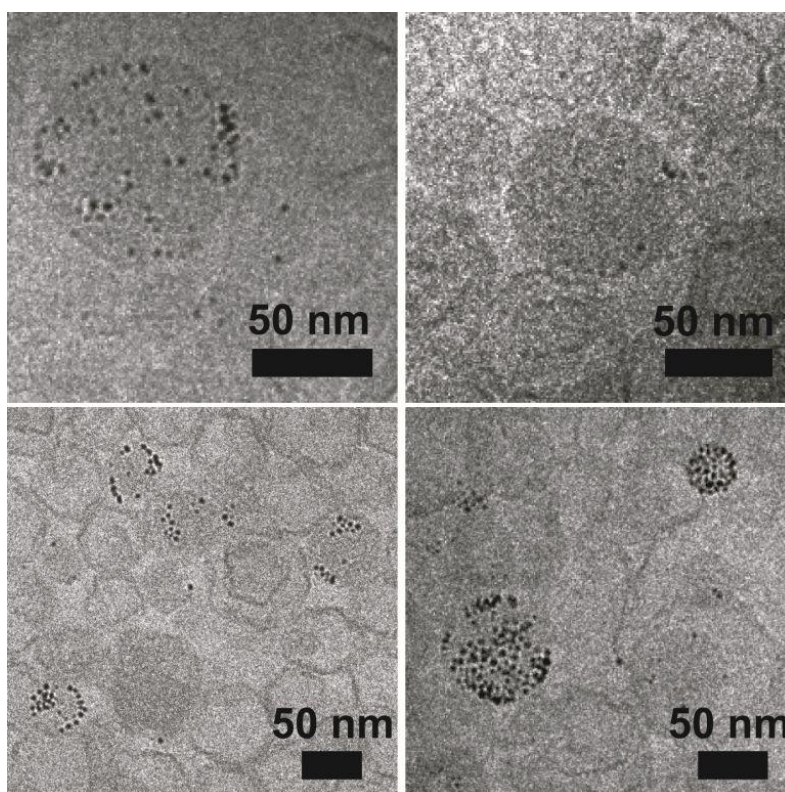


Figure 6.10. CryoTEM images of squalene emulsion droplets loaded with dodecanethiol-coated 4.1 nm diameter Au nanocrystals and stabilized with DPPC. The squalene concentrations are all 5% v/v.

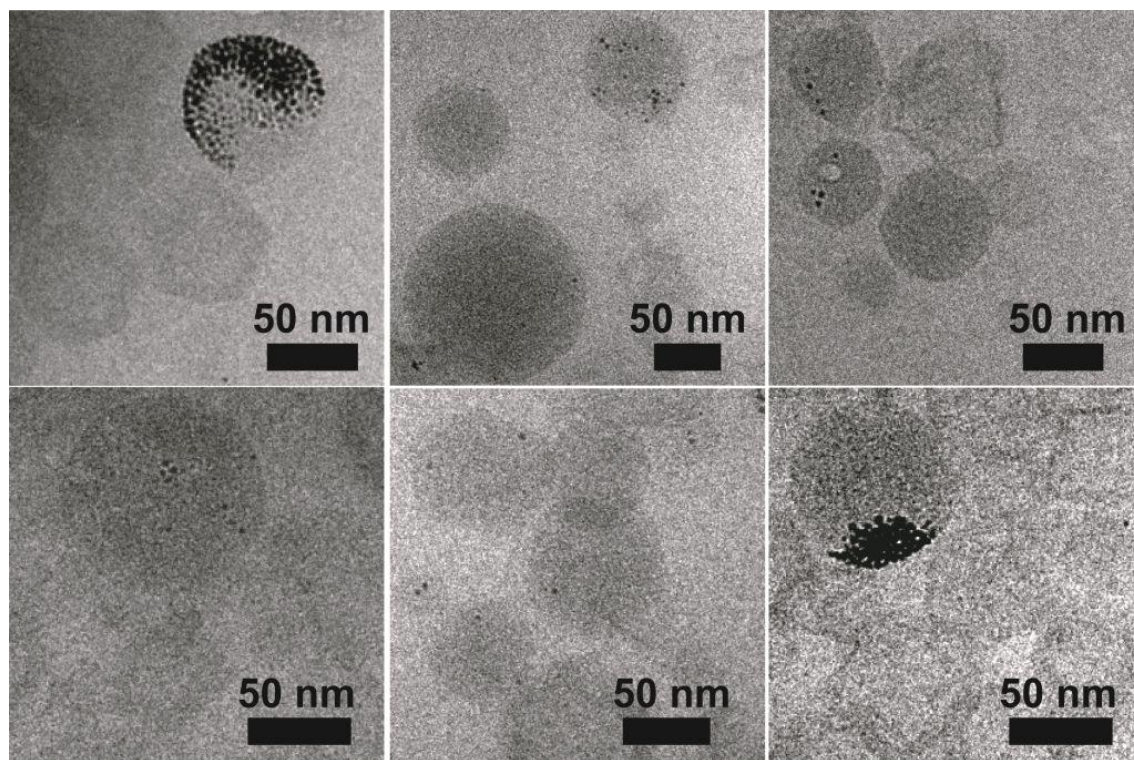


Figure 6.11. CryoTEM images of triolein emulsion droplets loaded with dodecanethiol-coated 4.1 nm diameter Au nanocrystals and stabilized with DPPC. The triolein concentrations are all 5% v/v.

6.4 Conclusions

Saturated phosphatidylcholine lipids DLPC, DMPC, DPPC, and DSPC assemble into vesicles, but do not incorporate dodecanethiol-capped (1.8 nm or 4.1 nm diameter) Au nanocrystals into their lipid bilayers. Instead, lipid/nanocrystal agglomerates form with different morphologies depending on the fatty acid chain length. DLPC (C_{12}) led to the formation of extended chains of 1.8 nm diameter nanocrystals, while 4.1 nm diameter nanocrystals did not form a stable dispersion with DLPC. DMPC (C_{14}) stabilized three-

dimensional aggregates or thin monolayer sheets of 1.8 nm and 4.1 nm nanocrystals. DPPC (C₁₆) and DSPC (C₁₈) only stabilized three-dimensional agglomerates of nanocrystals. In many case, the lipid-coated nanocrystal agglomerates partially fused with vesicles.

The lipids that formed membranes with more mechanical flexibility produced agglomerates with higher curvature surfaces. The 1.8 nm Au agglomerates made with DLPC resemble thread-like micelles typically prepared from detergents.⁴⁰ There must be a synergy between the lipid and 1.8 nm diameter nanocrystals leading to these structures since thread-like micelles do not form with pure DLPC, and these structures fail to form with larger nanocrystals. DMPC lipid forms slightly more rigid membranes than DLPC and stabilized planar sheets of Au nanocrystals. Others have incorporated CdSe nanocrystals into the bilayer of DMPC vesicles.^{17,21} The Au nanocrystals form only spherical agglomerates with both DPPC and DSPC, which do not have high curvature edges like the DMPC and DLPC structures, which is consistent with higher bending elasticity of DPPC and DSPC lipid assemblies at 25°C.

Squalene (or triolein) does not encourage nanocrystals to mix with the lipid bilayers and incorporate into vesicles. Instead, the squalene forms lipid-coated oil droplets, and the 1.8 nm Au nanocrystals incorporate into the droplets and assemble at the oil-water interface. Nanocrystal loaded emulsion particles have been established,²⁹ and so has the interfacial assembly of Au nanocrystals having mixed polar and non-polar surface functionalities to form Pickering emulsions.⁴³ However the assembly of entirely

hydrophobic Au nanocrystals at a lipid-coated oil-water interface seems to be a new concept. We predict that the Au nanocrystals alter the density and therefore the settling velocity of the oil droplets by a small amount, which may be exploited in future efforts to perform ultracentrifugal fractionation. Furthermore the Au nanocrystals assembled at the squalene-water interface may be useful as a barrier to controlled release of molecules dissolved in the squalene phase,^{20,27} though this remains to be demonstrated. Further work should be done with the 4.1 nm Au nanocrystals at varying oil:nanocrystal ratios to determine if they assemble at the interface as densely as do the 1.8 nm diameter Au nanocrystals.

6.5 References

- (1) Marsh, D. *CRC Handbook of Lipid Bilayers*; CRC Press, Inc.: Boca Raton, FL, 1990.
- (2) Cole, L. K.; Vance, J. E.; Vance, D. E. *Biochim Biophys Acta* **2012**, 1821, 754-761.
- (3) Dashiti, M.; Kulik, W.; Hoek, F.; Veerman, E. C.; Peppelenbosch, M. P.; Rezaee, F. *Scientific Reports* **2011**, 1, 1-11.
- (4) We refer only to fatty acids with an even number of carbon atoms throughout this text.
- (5) Hermansson, M.; Hokynar, K.; Somerharju, P. *Progress in Lipid Research* **2011**, 50, 240-257.
- (6) Bianco, I. D.; Fidelio, G. D.; Yu, R. K.; Maggio, B. *Biochemistry* **1991**, 30, 1709-1714.
- (7) Kucerka, N.; Nieh, M.-P.; Katsaras, J. *Biochimica Et Biophysica Acta* **2011**, 1808, 2761-2771.
- (8) Lasic, D. D. *Biochemical Journal* **1988**, 256, 1-11.
- (9) Torchilin, V. P.; Weissig, V. *Liposomes: A Practical Approach*; 2nd ed.; Oxford: New York, 2003.
- (10) Torchilin, V. P.; Sawant, R. R. *Soft Matter* **2010**, 6, 4026-4044.

- (11) Tsuchida, E.; Sou, K.; Nakagawa, A.; Sakai, H.; Komatsu, T.; Kobayashi, K. *Bioconjugate Chemistry* **2009**, *20*, 1419-1440.
- (12) Kudlicki, W.; Katzen, F.; Peterson, T. C. *Trends in Biotechnology* **2009**, *27*, 455-460.
- (13) Jesorka, A.; Orwar, O. *Annual Review of Analytical Chemistry* **2008**, *1*, 801-832.
- (14) Rasch, M. R.; Rossinyol, E.; Hueso, J. L.; Goodfellow, B. W.; Arbiol, J.; Korgel, B. A. *Nano Letters* **2010**, *10*, 3733-3739.
- (15) Park, S. H.; Oh, S. G.; Suh, K. D.; Han, S. H.; Chung, D. J.; Mun, J. Y.; Han, S. S.; Kim, J. W. *Colloids and Surfaces B-Biointerfaces* **2009**, *70*, 108-113.
- (16) Amstad, E.; Kohlbrecher, J.; Muller, E.; Schweizer, T.; Textor, M.; Reimhult, E. *Nano Letters* **2011**, *11*, 1664-1670.
- (17) Gopalakrishnan, G.; Danelon, C.; Izewska, P.; Prummer, M.; Bolinger, P. Y.; Geissbuhler, I.; Demurtas, D.; Dubochet, J.; Vogel, H. *Angewandte Chemie-International Edition* **2006**, *45*, 5478-5483.
- (18) Al-Jamal, W. T.; Al-Jamal, K. T.; Tian, B.; Lacerda, L.; Bomans, P. H.; Frederik, P. M.; Kostarelos, K. *ACS Nano* **2008**, *2*, 408-418.
- (19) Von White, I., G.; Chen, Y.; Roder-Hanna, J.; Bothun, G. D.; Kitchens, C. L. *ACS Nano* **2012**, *ASAP online*.
- (20) Chen, Y.; Bose, A.; Bothun, G. D. *ACS Nano* **2010**, *4*, 3215-3221.
- (21) Wi, H. S.; Lee, K.; Pak, H. K. *Journal of Physics-Condensed Matter* **2008**, *20*, 494211.
- (22) Marsh, D. *Biophysical Journal* **2007**, *93*, 3884-3899.
- (23) Pansu, B.; Lecchi, A.; Constantin, D.; Clerc-Imperator, M.; Veber, M.; Dozov, I. *Journal of Physical Chemistry C* **2011**, *ASAP*, DOI: 10.1021/jp2046189.
- (24) Fox, C. B. *Molecules* **2009**, *14*, 3286-3312.
- (25) Spanova, M.; Daum, G. *European Journal of Lipid Science and Technology* **2011**, *113*, 1299-1320.
- (26) Simon, S. A.; Lis, L. J.; MacDonald, R. C.; Kauffman, J. W. *Biophysical Journal* **1977**, *19*, 83-90.
- (27) Hauss, T.; Dante, S.; Dencher, N. A.; Haines, T. H. *Biochimica Et Biophysica Acta* **2002**, *1556*, 149-154.
- (28) Gianella, A.; Jarzyna, P. A.; Mani, V.; Ramachandran, S.; Calcagno, C.; Tang, J.; Kann, B.; Dijk, W. J. R.; Thijssen, V. L.; Griffioen, A. W.; Storm, G.; Fayad, Z. A.; Mulder, W. J. M. *ACS Nano* **2011**, *5*, 4422-4433.
- (29) Tilborg, G. A. F.; Cormode, D. P.; Jarzyna, P. A.; van der Toorn, A.; van der Pol, S. M. A.; van Bloois, L.; Fayad, Z. A.; Storm, G.; Mulder, W. J. M.; de Vries, H. E.; Dijkhuizen, R. M. *Bioconjugate Chemistry* **2012**, *23*, 941-950.
- (30) Woodward, R. T.; Olariu, C. I.; Hasan, E. A.; Yiu, H. H. P.; Rosseinsky, M. J.; Weaver, J. V. M. *Soft Matter* **2011**, *7*, 4335.
- (31) The lipids all disperse poorly in water at lower temperatures corresponding to the lamellar gel phase (L β ').

- (32) The scintillation vials, as well as the round bottom flasks, are thoroughly cleaned beforehand. They are sonicated in an aqueous solution of laboratory detergent, then rinsed 5 times with tap water and DI water, rinsed with EtOH, sonicated with chloroform, and then finally dried in an oven overnight.
- (33) Santos, H. M.; Lodeiro, C.; Capelo-Martinez, J.-L.; Capelo-Martinez, J.-L., Ed.; Wiley-VCH Verlag GmbH & Co.: Weinheim, 2009.
- (34) Sonication amplitude is reported on the instrument to be 42kHz.
- (35) Taurozzi, J. S.; Hackley, V. A.; Wiesner, M. R. *Nanotoxicology* **2011**, *5*, 711-729.
- (36) Heat loss to the surroundings will be minimal near room temperature, so the measured temperature rise will correlate better with the sonicator power.
- (37) Dubois, M.; Deme, B.; Gulik-Krzywicid, T.; Dedleu, J.-C.; Vautrin, C.; Desert, S.; Perez, E.; Zemb, T. *Nature* **2001**, *411*, 672-675.
- (38) Blaurock, A. E.; Gamble, R. C. *Journal of Membrane Biology* **1979**, *50*, 187-204.
- (39) Quemeneur, F.; Quilliet, C.; Faivre, M.; Viallat, A.; Pepin-Donat, B. *Physical Review Letters* **2012**, *108*, 108303.
- (40) Almgren, M.; Edwards, K.; Karlsson, G. *Colloids and Surfaces a-Physicochemical and Engineering Aspects* **2000**, *174*, 3-21.
- (41) Binks, B. P. *Current Opinion In Colloid & Interface Science* **2002**, *7*, 21-41.
- (42) Wang, J.; Yang, F.; Tan, J.; Liu, G.; Xu, J.; Sun, D. *Langmuir* **2010**, *26*, 5397-5404.
- (43) Glogowski, E.; He, J.; Russell, T. P.; Emrick, T. *Chemical Communications* **2005**, 4050-4052.
- (44) Tambe, D. E.; Sharma, M. M. *Journal of Colloid and Interface Science* **1993**, *157*, 244-253.
- (45) Pichot, R.; Spyropoulos, F.; Norton, I. T. *Journal of Colloid and Interface Science* **2010**, *352*, 128-135.
- (46) Mason, T. G.; Wilking, J. N.; Meleson, K.; Chang, C. B.; Graves, S. M. *Journal of Physics: Condensed Matter* **2006**, *18*, R635-R666.
- (47) *CRC Handbook of Chemistry and Physics*; 91st ed.; CRC Press: Boca Raton, FL, 2011.
- (48) Song, C.; Wang, P.; Makse, H. A. *Nature* **2008**, *453*, 629-632.
- (49) Silbert, L. E. *Soft Matter* **2010**, *6*, 2918-2924.
- (50) Israelachvili, J. N. *Intermolecular and Surface Forces*; 2nd ed.; Academic press Inc.: San Diego, 1992.
- (51) Marangoni, A. G.; Narine, S. S. In *Crystallization and Solidification Properties of Lipids*; Widlak, N., Hartel, R., Narine, S., Eds.; AOCS Press: Champaign, 2001, p 153-159.

Chapter 7: Octylglucoside-Assisted Loading of Au Nanocrystals in Phosphatidylcholine Vesicles[§]

7.1 Introduction

Vesicles have been used to host hydrophobic trans-membrane proteins,¹ and the hydrophobic proteins are incorporated into vesicles by transfer from a cell membrane to the vesicle bilayer by detergent micelles.²⁻⁶ Detergents spontaneously form micelles ($P < 0.3$, Chapter 1) when dissolved in pure water above the critical micelle concentration,⁷ they partition into lipid bilayers and lower the average molecular packing factor in the bilayer,^{8,9} causing the bilayer to break up and form mixed detergent-lipid micelles when the detergent:lipid ratio exceeds a critical amount.⁸ This process is diagrammed in Figure 7.1; when this is applied to cell membranes, the membrane-embedded proteins are incorporated (solubilized) in the mixed detergent-lipid micelles.^{2,5} The reverse process, extracting detergent from mixed detergent-lipid micelles, forms lipid bilayers and has been used to make vesicles.¹⁰⁻¹³ Detergent removal is often accomplished by dialysis,^{8,11} where the detergent-lipid mixed micelle dispersion is separated from a pure water reservoir by a semi-permeable membrane, which contains pores that only allow passage of detergent monomers and water (not whole mixed micelles). Over time, the detergent diffuses out of the mixed micelle dispersion and into the reservoir, causing the lipids and any solubilized hydrophobic proteins to aggregate into vesicles (Stages III-II-I-0

[§] Portions of this chapter appear in the following publication: Rasch, M.R.; Rossinyol, E.; Hueso, J.L.; Goodfellow, B.W.; Arbiol, J.; Korgel, B.A. *Nanoletters* 2010, *10*, 3733-3739. The experiments were performed by M.R. Rasch, E. Rossinyol, J.L. Hueso, B.W. Goodfellow, and J. Arbiol. The text was written by M.R. Rasch and B.A. Korgel. Funding was provided by research grants to J. Arbiol and B.A. Korgel.

consecutively in Figure 7.1).

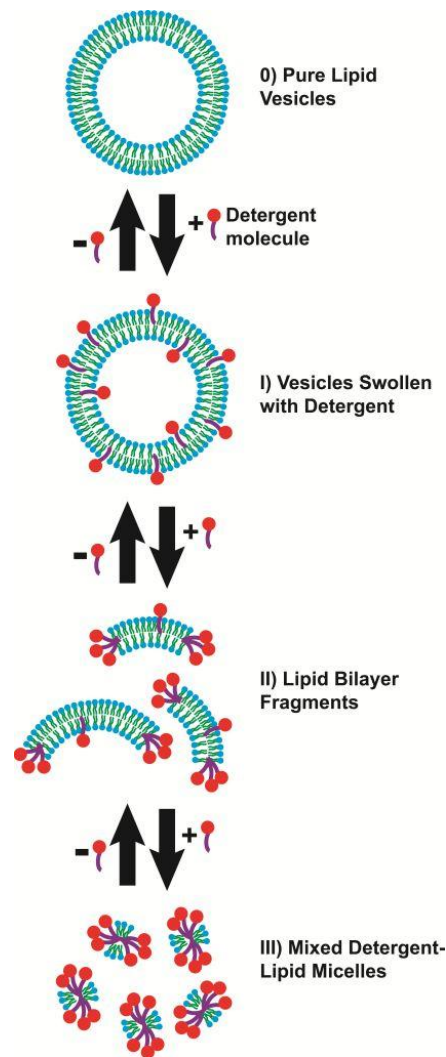


Figure 7.1. Illustration of how detergents influence the structure of lipid molecule aggregates. The plus and minus signs indicate addition or removal of detergent in the direction of the arrow, respectively. In stage II, the lipid bilayer fragments can take the form of cylindrical micelles,¹⁴ disc micelles,¹⁵ or planar lipid sheets¹⁶ depending on several factors including the type of detergent, the total lipid concentration, and the rate of change in detergent concentration, though clarifying these structure-processing relationships is the subject of many ongoing research efforts.¹⁵ Lipid molecules are drawn with a blue hydrophilic head group and green hydrocarbon tails. Detergent molecules are drawn with a red hydrophilic head group and purple hydrocarbon tail.

When hydrophobic nanocrystals are solubilized in detergent micelles, they can be incorporated into vesicles by detergent dialysis just as with hydrophobic proteins. This chapter presents results on the formation of aqueous phase octyl-glucopyranoside (OCG) detergent micelles containing 1.8 nm diameter, dodecanethiol-coated Au nanocrystals. When the detergent is removed by dialysis, the nanocrystals precipitate from solution unless lipids are present. The lipids stabilize the Au nanocrystals during detergent dialysis, and cryoTEM imaging reveals that the Au nanocrystals incorporate into lipid vesicles. The number of Au nanocrystals per vesicle depends on a combination of factors including the detergent:lipid ratio and the total lipid concentration. Interestingly, the nanocrystals cluster together in the lipid bilayers, forming nanocrystal rafts in the vesicles.

7.2 Experimental Details

7.2.1 Chemicals

Hen egg-derived phosphatidylcholine (eggPC, 99%) was from Avanti Polar Lipids. N-Octyl- β -D-glucopyranoside (OCG, 99%) was from Affymetrix. Regenerated cellulose dialysis tubing (6-8 kDa molecular weight cut-off) was from Spectrum Labs. All other materials are listed in Chapters 5.2.1 and 6.2.1.

7.2.2 Au nanocrystal Synthesis

The Au nanocrystal synthesis is detailed in Chapter 5.2.

7.2.3 Vesicle Formation

Vesicles made purely of eggPC lipid were formed by extrusion. Samples were prepared in DI water with either 13 mM (10 mg/mL) or 150 mM eggPC (114 mg/mL) concentration. First, a lipid film was formed by weighing dry eggPC powder and placing it in a clean 50 mL glass round bottom flask, adding 1.0 mL of chloroform, and evaporating the chloroform using rotary evaporation at room temperature, 1 revolution per second rotation speed, and 760 mm Hg vacuum pressure for 1 hour. Then 1.0 mL of DI water was added, and the lipid was dispersed by magnetic stirring for about 30 minutes. The aqueous lipid dispersion was then extruded 10 times through a filter with 100 nm diameter pores, and 21 more times through a filter with 50 nm diameter pores to form eggPC vesicles about 50 nm in diameter. The vesicle concentration (vesicles per liter) is determined by multiplying the lipid concentration by the number of lipid molecules per vesicle, which equals the vesicle bilayer surface area ($2\pi D^2$, D = vesicle diameter) divided by the area per lipid head group (0.63 nm^2 per lipid)¹⁷. For 50 nm diameter vesicles, there are about 25000 lipid molecules per vesicle.

7.2.4 Au-loaded Detergent Micelles

The detergent micelles were prepared at three different concentrations for this study: A) 0.75 mg/mL Au nanocrystals, 66 mM OCG; B) 2 mg/mL Au nanocrystals, 300 mM OCG; C) 2 mg/mL Au nanocrystals, 500 mM OCG.

A) 66 mM OCG, 0.75 mg/mL Au nanocrystals. 76 mg (0.26 mmol) of OCG was added to a 20 mL glass vial and dissolved in 1.0 mL of anhydrous chloroform. 0.22 mL of Au nanocrystals at 3.0 mg/mL was added to the vial, and the contents were stirred for about 5

minutes. Then 3.0 mL of DI water was added to the vial, forming a white turbid microemulsion while continuing to stir for another 5 minutes. Next the un-capped vial was immersed in a water bath at 60 °C to heat the contents of the stirring vial and evaporate the chloroform. After 10-15 minutes, the solution became completely translucent, and a convective air stream was blown over the stirring vial in the water bath for 3 minutes to help remove traces of chloroform. The final volume of the OCG-Au solution was adjusted to 3.0 mL with DI water in a 10 mL graduated cylinder, to account for evaporation of water while heating. The final Au nanocrystal concentration is 15 μ M.

B) 300 mM OCG, 2 mg/mL Au nanocrystals. 702 mg (2.45 mmol) of OCG was added to a 20 mL glass vial and dissolved in 4 mL of anhydrous chloroform. 16 mg of Au nanocrystals was added to the vial, and the contents were stirred for about 5 minutes.

Then 8.0 mL of DI water was added to the vial, forming a white turbid microemulsion while continuing to stir for another 5 minutes. Next the un-capped vial was immersed in a water bath at 60 °C to heat the contents of the stirring vial and evaporate the chloroform. After 10-15 minutes, the solution became completely translucent. Next, the sample was placed in a 50 mL round bottom flask, loaded on a rotary evaporator, and placed under vacuum at 80 mbar pressure for 30 minutes to remove trace amounts of chloroform. The final volume of the OCG-Au solution was adjusted to 3.0 mL with DI water in a 10 mL graduated cylinder, to account for evaporation of water while heating. The final Au nanocrystal concentration is 40 μ M.

C) 500 mM OCG, 2 mg/mL Au nanocrystals. Repeat the procedure for *B*, using 1.17 g of OCG. The final Au nanocrystal concentration is 40 μ M.

7.2.5 Incorporation of Au Nanocrystals into Vesicles by Detergent Dialysis

In the first experiment, vesicles are mixed with OCG-Au micelles with the OCG concentration being less than the amount needed to disassemble the vesicles (Stage I in Figure 7.1), and using low concentrations of nanocrystals (4 μM) and vesicles (0.34 μM assuming 50 nm diameter). In the second experiment, vesicles are mixed with OCG-Au micelles at much higher concentrations of nanocrystals (20 μM) and vesicles (1 μM and 3 μM , assuming 50 nm diameter vesicles). Considering the simple case of collisions between two particles, the collision rate is proportional to the product the particle concentrations;¹⁸ therefore, manipulating the concentration of Au nanocrystals and vesicles should influence the self-assembly.

Mixing Vesicles with OCG-Au Micelles: Low Concentration and no Vesicle Rupture.

EggPC vesicles were combined with OCG-Au micelles to allow a detergent:lipid mole ratio of 2.3 and a lipid:nanocrystal mole ratio of 2100. With a detergent:lipid ratio of 2.3 at an eggPC lipid concentration of 8.5 mM, the OCG should not rupture and disassemble the vesicles.^{10, 11} In one glass vial, 2.08 mL of the 50 nm diameter eggPC lipid vesicles (13 mM eggPC) was diluted with 0.15 mL DI water and placed under magnetic stirring. Then 0.97 mL of the OCG-Au micelle solution (66 mM OCG, 5.6 μM Au nanocrystals) was injected drop-wise into the vial of vesicles, bringing the concentration of each species in the vesicle solution to 8.5 mM PC, 20 mM OCG and 4 μM Au nanocrystals. The eggPC-OCG-Au solution was stirred for 5 minutes, and then loaded into a hydrated 5 cm segment of regenerated cellulose dialysis tubing, which was sealed at both ends with locking closures. The sealed dialysis bag was immersed in 1 L of DI water under

magnetic stirring. The 1 L of water was replaced every four hours, and the dialysis was carried out for 24 hours total. Afterward, the Au-vesicle solution was transferred to a 1.5 mL plastic centrifuge tube for storage. This entire dialysis procedure was repeated using 2.08 mL of DI water in place of the eggPC lipid vesicle solution to show that the Au nanocrystals aggregate during dialysis in the absence of eggPC vesicles.

Mixing Vesicles with OCG-Au Micelles: High Vesicle and Nanocrystal Concentration.

The 150 mM eggPC vesicle dispersion was added to 4 separate vials, as prescribed below. Two of the vials were diluted with deionized water to lower the eggPC concentration to 50 mM. The volume of vesicles in each vial is 800 μ L at this point, and magnetic stirring is initiated. Next, 800 μ L of OCG-Au micelle samples B (300 mM OCG) and C (500 mM OCG) are injected drop-wise into the vials as prescribed below. After about 30 seconds, the samples are transferred to dialysis tubing by a glass pipette and then dialyzed for over 24 hours against 1L of deionized water. The 1L of deionized water was replaced every 4 hours. Subsequently, the samples were transferred from the dialysis tubing to a 2 mL plastic centrifuge tube for immediate cryoTEM imaging.

Vial 1: 800 μ L (150 mM) egg PC, 800 μ L of OCG-Au micelle sample B (300 mM OCG, 40 μ M nanocrystals). After combining, [eggPC] = 75 mM, [OCG] = 150 mM, [nanocrystals] = 20 μ M.

Vial 2: 800 μ L (150 mM) egg PC, 800 μ L of OCG-Au micelle sample C (500 mM OCG, 40 μ M nanocrystals). After combining, [eggPC] = 75 mM, [OCG] = 250 mM, [nanocrystals] = 20 μ M.

Vial 3: 267 μL (150 mM) egg PC, 533 μL DI water, 800 μL of OCG-Au micelle sample

B. After combining, [eggPC] = 25 mM, [OCG] = 150 mM, [nanocrystals] = 20 μM .

Vial 4: 267 μL (150 mM) egg PC, 533 μL DI water, 800 μL of OCG-Au micelle sample

C. After combining, [eggPC] = 25 mM, [OCG] = 250 mM, [nanocrystals] = 20 μM .

7.2.6 Characterization

CryoTEM imaging, dynamic light scattering, and ^1H NMR measurements were performed as described in Chapter 5.2. The Rayleigh approximation was used to determine the most abundant hydrodynamic diameter from the fits to the light scattering data, which is valid for particles up to at least 150 nm.¹⁹ Dynamic light scattering data were not corrected for changes in viscosity or diffusion coefficient with particle concentration.

7.3 Results and Discussion

7.3.1 EggPC Vesicle Characterization and Detergent Titration

EggPC vesicles were prepared by extrusion the lipids through 50 nm diameter pores while dispersed in DI water. Figure 7.2 shows a typical cryoTEM image of the extruded eggPC vesicles dispersed in water. The average diameter of the spherical vesicles (not those undergoing deformations due to crowding on the TEM grid) is 62 ± 16 nm, which agrees well with DLS characterization of vesicle size. The DLS results are shown in Figure 7.3, indicating that the vesicle hydrodynamic diameter is between 60 –

70 nm over the lipid concentration range of 25 – 150 mM. The vesicle hydrodynamic diameter varies slightly with vesicle concentration because this value is obtained from measuring the vesicle diffusion coefficient, which has approximately a linear dependence on concentration.²⁰

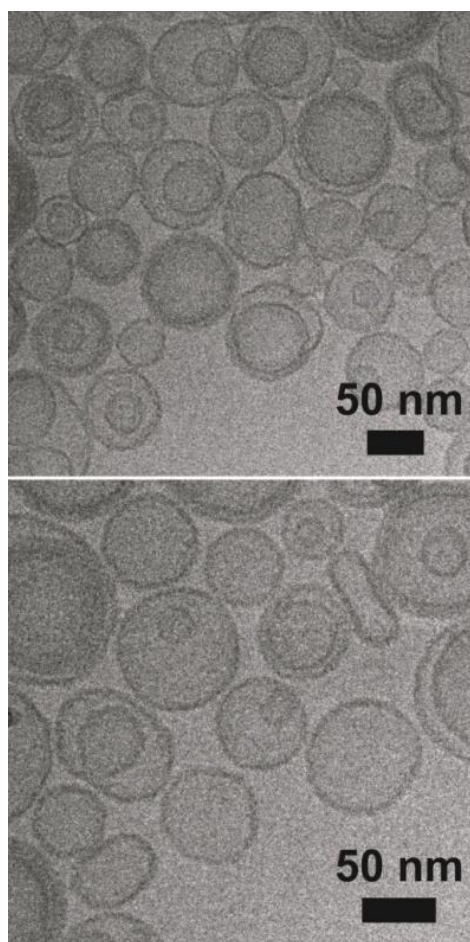


Figure 7.2. CryoTEM images of pure, aqueous eggPC vesicles extruded through 50 nm diameter pores.

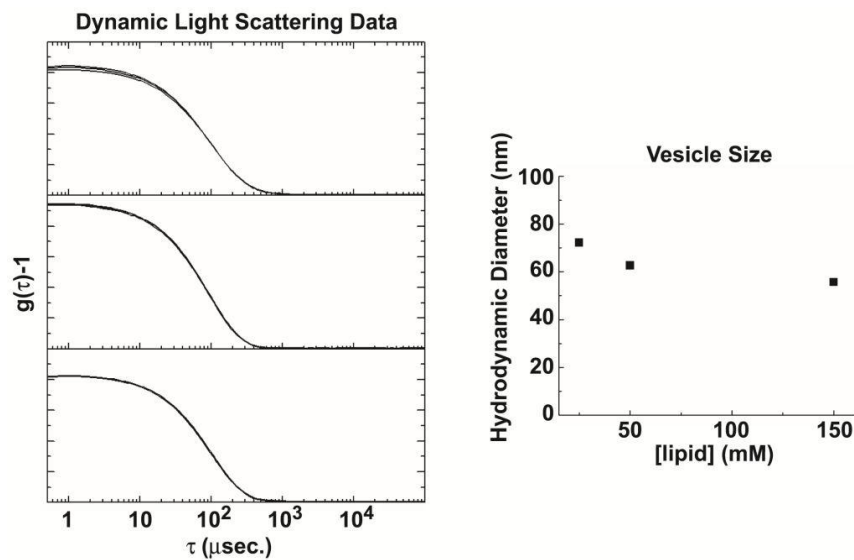


Figure 7.3. Dynamic light scattering of extruded eggPC vesicles dispersed in deionized water at different concentrations. A 150 mM eggPC sample was prepared and then diluted consecutively for these measurements. The left series of stacked plots displays the scattering intensity correlation coefficient versus correlation time, which are fitted to the vesicle diffusion coefficient according to the DLS equations discussed in Chapter 5. From top to bottom: 25 mM eggPC, 50 mM eggPC, 150 mM eggPC vesicles. The right plot displays the hydrodynamic diameters obtained from the vesicle diffusion coefficients using the Stokes-Einstein equation.

DLS was used to characterize the effect of the OCG detergent on the vesicle stability over the eggPC concentration range of 12 – 120 mM. Turbidity measurements are often performed to characterize the amount of OCG required to dissolve vesicles,^{14,16} however this is only useful when the absorbance of the sample is low (i.e. dilute vesicle solutions less than 10 mM in lipid concentration). For concentrated vesicle solutions (> 20 mM lipid), not enough light is transmitted through the samples for accurate measurements with our spectrophotometer, so DLS was used instead since it measures

back-scattered photons (173° scattering angle). DLS can be used to measure changes in the vesicle diffusion coefficient as detergent is added, however caution should be used in interpreting information about the hydrodynamic size from the diffusion coefficient. During vesicle titration with detergent, the vesicles change shape, often bursting and forming cylindrical micelles or planar sheets,⁸ which we observe to increase the viscosity of the sample. Therefore due to changes in the particle shape, particle concentration, and sample viscosity during detergent titration, the Stokes-Einstein equation should not be considered as an accurate way to correlate the diffusion coefficient measurements with particle size. Nonetheless, changes in the diffusion coefficient provide information on what range of OCG concentrations results in the different stages of vesicle dissolution that are outlined in Figure 7.1 – for example, when the vesicles are being broken up into mixed detergent-lipid micelles, the diffusion coefficient will increase. This is exemplified in Figure 7.4, where the diffusion coefficient for each lipid concentration decreases with OCG concentration until the [OCG]:[lipid] ratio reaches about 3.3, where most of the vesicles are expected to be ruptured and incorporated into long lipid-detergent cylindrical micelles or planar sheets that scatter more light than vesicles.^{8,14,16} As the [OCG]:[lipid] ratio increases beyond 3.3, the diffusion coefficient increases beyond the initial value, corresponding to the formation of small mixed detergent-lipid micelles. Therefore, the vesicles are considered to be completely ruptured and disassembled above [OCG]:[lipid] ratios of 3.3.

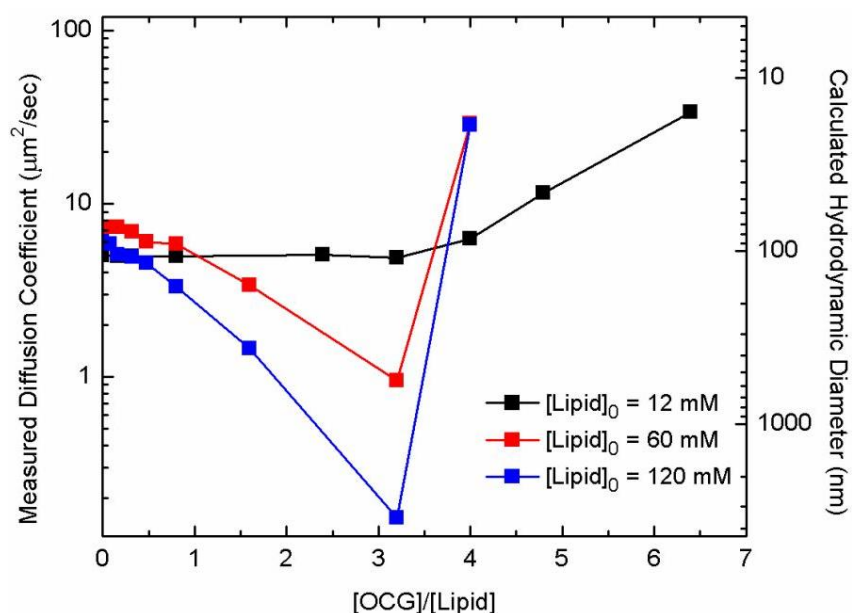


Figure 7.4. Dynamic light scattering characterization of titrating vesicles with OCG detergent. Three different initial lipid concentrations were used, 12 mM (black), 60 mM (red), and 120 mM (blue). The hydrodynamic diameter was calculated from the measured diffusion coefficient using the Stokes-Einstein equation, however the diameters should be interpreted with caution since changes in sample viscosity were not included.

7.3.2 Au-loaded Detergent Micelles

The size of pure OCG micelles was characterized by DLS. The micelle hydrodynamic diameter remains between 7 – 12 nm over the OCG concentration range of 60 – 500 mM. The OCG critical micelle concentration is about 20 mM at 25°C,¹⁶ and below 20 mM the OCG has negligible light scattering since no micelles exist in solution. The Au nanocrystals are incorporated into OCG micelles starting from a 2-phase chloroform/water emulsion followed by evaporation of the chloroform phase. The hydrodynamic diameter of the micelles is still measured to be around 12 nm for Au

nanocrystal concentrations ranging from 0.2 – 2 mg/mL. The OCG-Au micelle aqueous dispersions are stable for months at room temperature. However, aqueous OCG micelle dispersions prepared from chloroform/water emulsions will retain trace amounts of chloroform, as indicated in the ^1H NMR spectra of Figure 7.7. Even after maintaining an OCG dispersion under vacuum for 30 minutes, the dispersion retains about 3 mmol chloroform per mol of OCG. Trace amounts of chloroform will likely enhance incorporation of Au nanocrystals into vesicles as shown in Chapter 5, however the residual chloroform will present toxicity issues for biological applications.

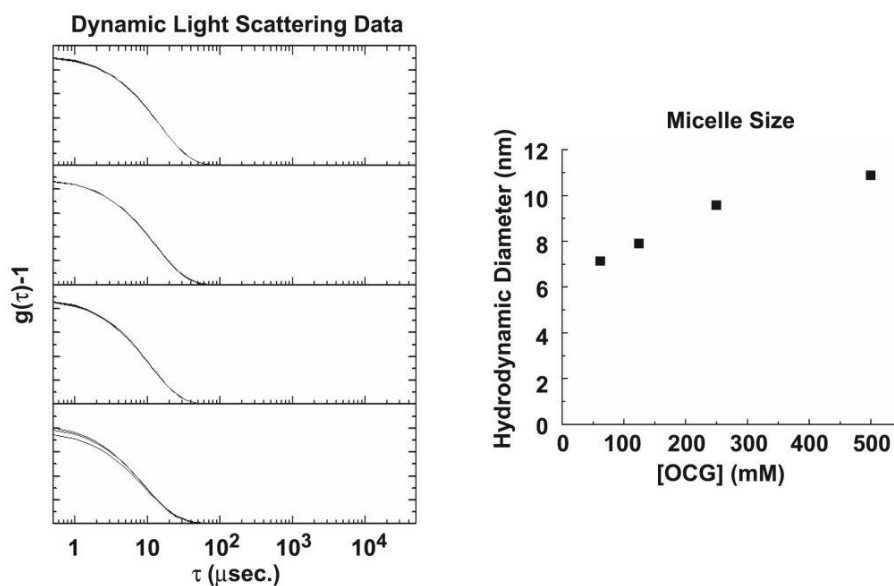


Figure 7.5. Dynamic light scattering of pure OCG micelles (no Au nanocrystals). The left series of stacked plots is the scattering intensity correlation coefficient plotted versus correlation time for different OCG concentrations, from top to bottom: 60 mM OCG, 125 mM OCG, 250 mM OCG, 500 mM OCG. Diffusion coefficients for each OCG concentration were obtained by fitting the DLS equations listed in Chapter 5 to the DLS data plotted in the left graph. The hydrodynamic diameters versus OCG concentration were obtained from the diffusion coefficients using the Stokes-Einstein equation.

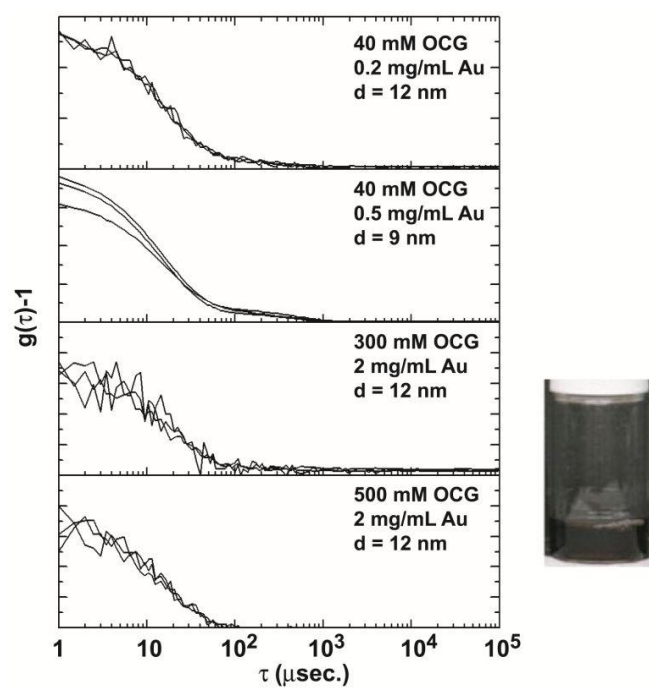


Figure 7.6. Dynamic light scattering characterization of OCG-Au nanocrystal micelles prepared at different concentrations. The hydrodynamic size does not vary much from 12 nm. The vial shows a typical dispersion of 40 mM OCG with 0.5 mg/mL Au nanocrystals.

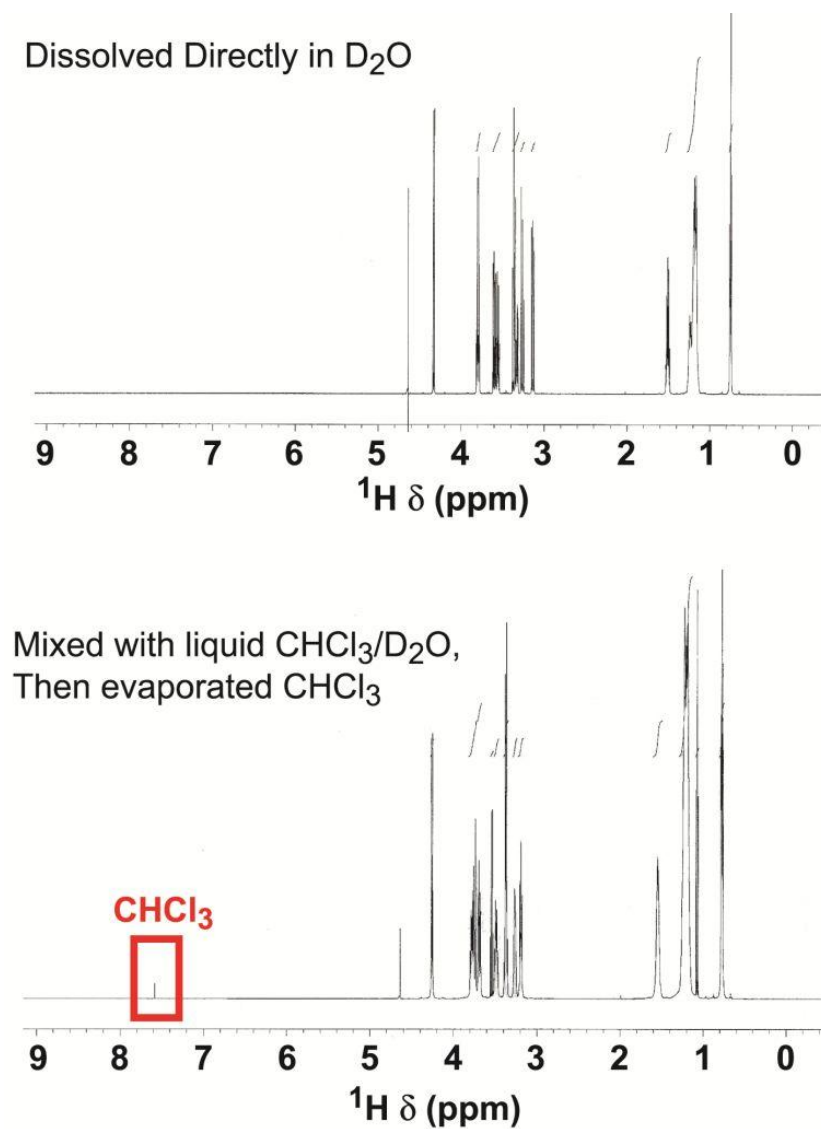


Figure 7.7. ^1H NMR characterization of OCG detergent (300 mM in D₂O). In the top spectrum, solid OCG was dissolved in D₂O with no exposure to chloroform. In the bottom spectrum, solid OCG was dissolved in chloroform, mixed with D₂O to form an emulsion, the chloroform was removed on a rotary evaporator at 50°C, and then the sample was maintained at 25°C and 50 mbar pressure for 30 minutes.

7.3.3 Au Nanocrystal Incorporation into Vesicles at 8.5 mM EggPC Concentration (2100 lipid molecules per nanocrystal)

The OCG-Au micelles were mixed with eggPC vesicles and dialyzed to remove the OCG detergent. Samples for dialysis were loaded into regenerated cellulose tubing and sealed, as shown in Figure 7.8. Since the eggPC critical micelle concentration is on the order of nanomolar,²¹ the eggPC lipids remain in lipid aggregates inside the dialysis tubing while OCG monomers readily diffuse out of the tubing during dialysis. Similarly, the dodecanethiol-coated Au nanocrystals are too large to diffuse through the dialysis tubing. In the absence of eggPC lipids, dialysis of OCG causes aggregation of hydrophobic Au nanocrystals in the dialysis tubing as shown in Figure 7.8 B1-B3. When eggPC is included in the OCG-Au micelle dispersion, the Au nanocrystals remain dispersed during dialysis, suggesting that the Au nanocrystals associate with the lipid aggregates during detergent removal.

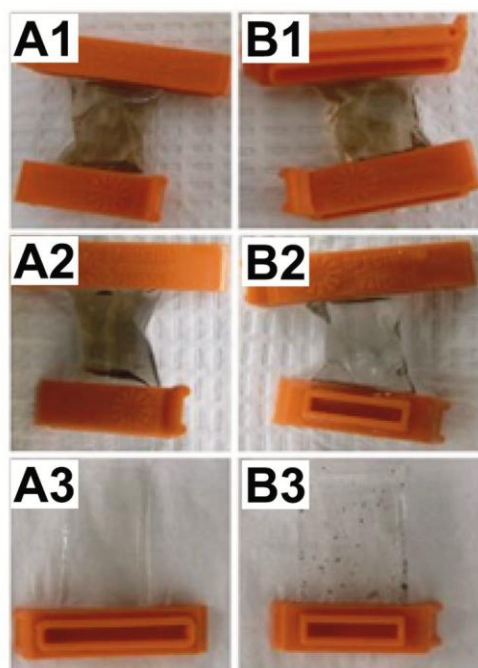


Figure 7.8. Photographs of dialysis tubings loaded with OCG-stabilized Au nanocrystals. (A1-A3) and (B1-B3) show samples obtained after dialyzing OCG-Au micelles with and without eggPC vesicles, respectively: (A1, B1) are the OCG-Au solutions in dialysis tubing before dialysis, (A2, B2) are the solutions at the end of dialysis, and (A3, B3) show the dialysis tubing after removing the solutions in (A2, B2). In B3, the precipitated Au nanocrystals can be seen on the walls of the dialysis tubing.

CryoTEM imaging shows that the Au nanocrystals load the bilayers of the eggPC lipids during OCG dialysis. The OCG and eggPC concentrations were 20 mM and 8.5 mM (2.3:1 mole ratio), respectively, at the start of dialysis. This detergent: lipid ratio was too low to result in complete break up and solubilization of the lipid vesicles by detergent (Figure 7.4),^{9,14,16} thus the vesicles simply swell with detergent molecules. Removal of the detergent forces the hydrophobic nanocrystals to associate with the vesicles to remain dispersed in water. Interestingly, the cryoTEM results in Figures 7.9

and 7.10 show that the Au nanocrystals cluster together in the lipid bilayers of the vesicles. In many cases, the lipid bilayers are half full of nanocrystals, while the other half of the vesicle's lipid bilayer can be clearly imaged and is devoid of nanocrystals. Many eggPC vesicles are completely empty as well, containing no Au nanocrystals in the lipid bilayer. The cryoTEM results also support that the vesicles remain intact during detergent addition and removal – the vesicle diameter remains around 50-70 nm, while eggPC completely solubilized in OCG micelles forms vesicles around 200 nm diameter during OCG dialysis.

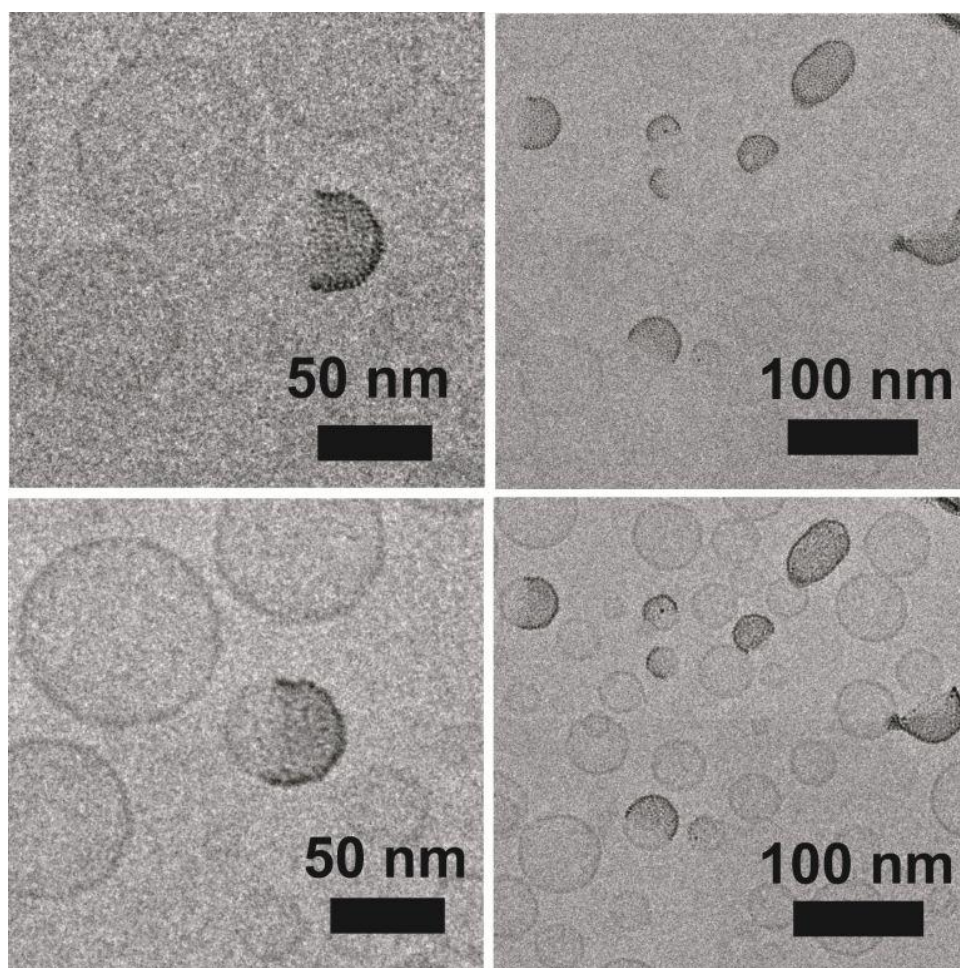


Figure 7.9. CryoTEM images of eggPC vesicles after dialysis with OCG-Au micelles. The eggPC concentration was 8.5 mM and the initial OCG concentration was 20 mM. The top row of images shows the nanocrystals in focus. The bottom row of images is the same as the top row, but with the nanocrystals out of focus, which provides better contrast to the lipid bilayers. Imaging performed with Dr. Jordi Arbiol.

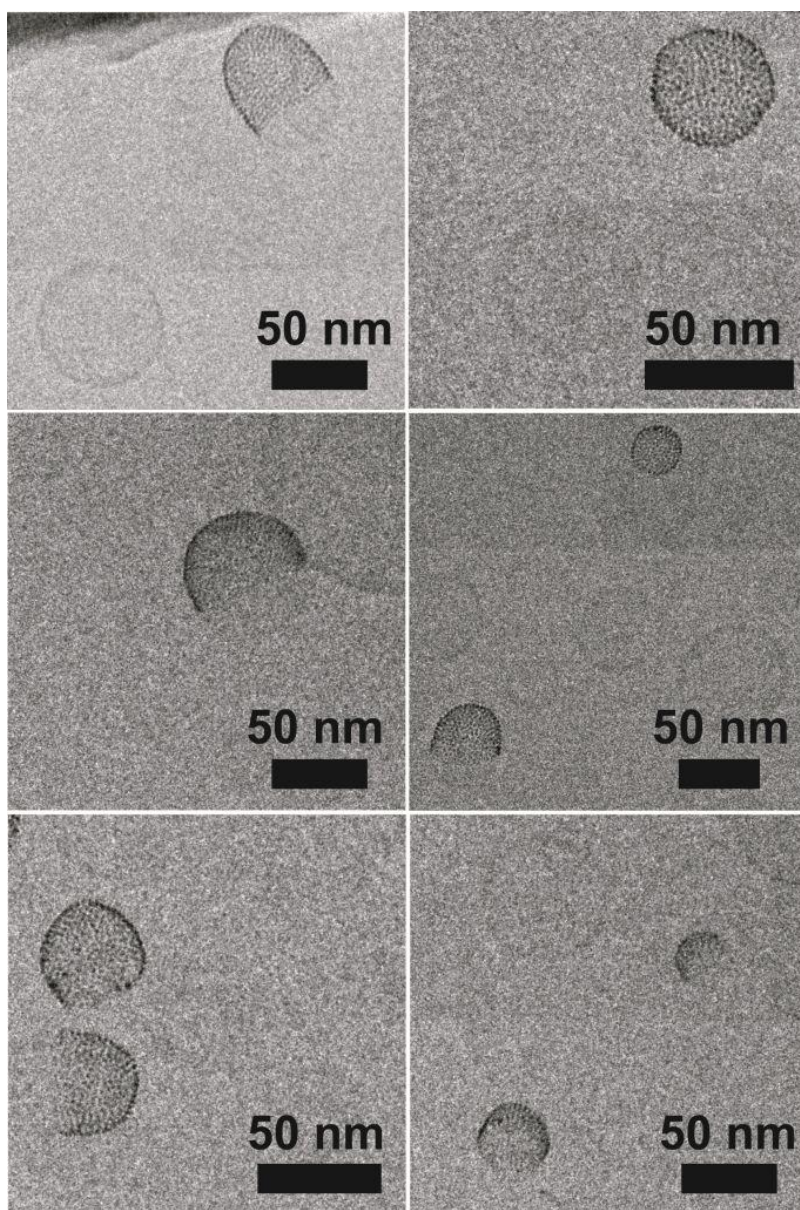


Figure 7.10. More cryoTEM images of eggPC vesicles after dialysis with OCG-Au micelles. The eggPC concentration is 8.5 mM and the initial OCG concentration was 20 mM. Imaging performed with Dr. Jordi Arbiol.

7.3.4 Au Nanocrystal Incorporation into Vesicles at 25-75 mM EggPC

Concentration (1250-3250 lipid molecules per nanocrystal).

Increasing the concentrations of vesicles and OCG-Au micelles was considered as a means to incorporate more Au nanocrystals into a greater percentage of vesicles during the dialysis process. The collision rate of two colloid particles is proportional to the product of the particle concentrations,¹⁸ therefore increasing both the vesicle and OCG-Au micelle concentrations should increase the frequency of vesicle and OCG-Au micelle collisions. Figure 7.11 shows the cryoTEM results from dialyzing a mixture of 25 mM eggPC and 150 mM OCG containing 2 mg/mL Au nanocrystals. The lipid:nanocrystal mole ratio is about 1250, which is lower than the ratio used in Chapter 7.3.3. The detergent to lipid ratio is 6, which means that the eggPC vesicles rupture when mixed with the OCG-Au micelles, and the vesicles will re-form when the detergent is removed by dialysis. The cryoTEM images in Figure 7.11 indicate that the vesicle diameter is around 200 nm, which is the result of breaking up the vesicles into mixed lipid-OCG micelles, which tend to form 200 nm diameter vesicles by detergent dialysis as described in other reports.¹² In addition to forming many vesicles that are halfway or completely loaded with Au nanocrystals, there are also many 200 nm vesicles that contain only a small cluster of Au nanocrystals in the entire lipid bilayer, indicated by the red arrows in Figure 7.11. It is not possible to tell whether the nanocrystal clusters are associated with the lipid bilayer or are OCG-Au micelles trapped inside the eggPC vesicles, since the TEM images are 2-dimensional projections of the 3-dimensional structure.

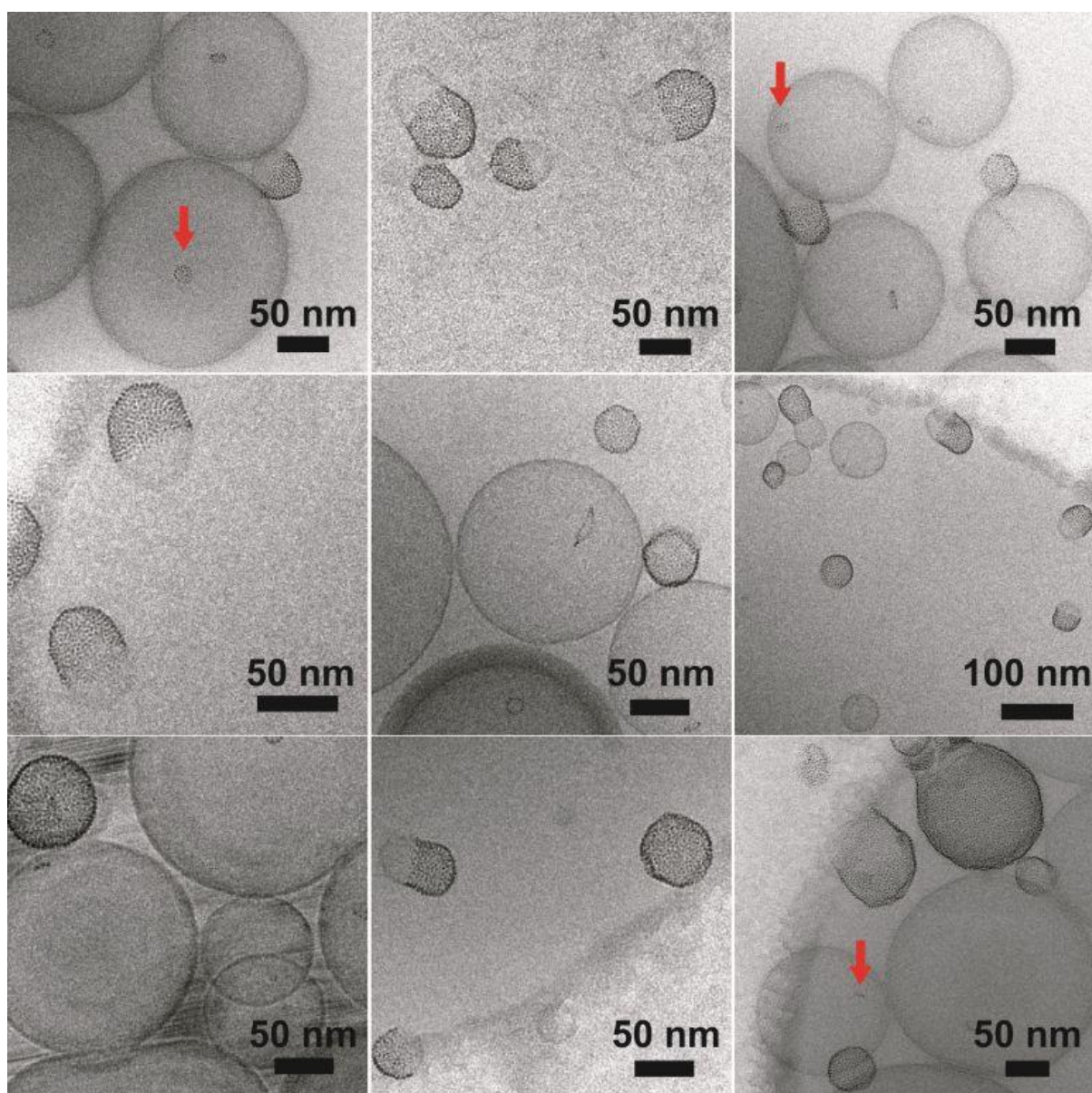


Figure 7.11. CryoTEM images of eggPC vesicles after dialysis with OCG-Au micelles. The eggPC concentration was 25 mM, the Au nanocrystal concentration was 20 μ M, and the initial OCG concentration was 150 mM. The red arrows point to small clusters of nanocrystals associating with each lipid membrane.

Increasing the OCG concentration from 150 mM to 250 mM at the start of dialysis, while keeping the eggPC and nanocrystal concentrations fixed at 25 mM and 20 μ M respectively, resulted in fewer vesicles that have high loading of Au nanocrystals in the bilayer. The cryoTEM imaging results are shown in Figure 7.12. The detergent to lipid ratio in this case is 10, so the eggPC lipids are completely solubilized by OCG micelles at the start of dialysis. Many 200 nm diameter vesicles form as expected, and all of these vesicles are associated with a cluster of Au nanocrystals. The nanocrystal cluster appears to be a short chain of Au nanocrystals that forms a closed, flexible loop. In some cases the OCG detergent was reported to form cylindrical, thread-like micelles with eggPC lipids at Stage II in Figure 7.1 of vesicle solubilization,^{14,16,22} which is because the average molecular packing factor in the OCG-eggPC cylindrical micelles is between 0.3 – 0.5. It is possible that the OCG-Au micelles assemble into chains as the detergent is removed, and that these chain micelles simultaneously become encapsulated within the 200 nm diameter vesicles that form by aggregation of OCG-eggPC micelles. Once encapsulated in vesicles, the vesicle membrane may provide a barrier to complete detergent removal from the OCG-Au micelles, and a detergent concentration gradient may persist across the vesicle bilayer. Retention of detergent monomers inside vesicles has been noted elsewhere as a barrier to complete detergent removal even for forming pure lipid vesicles,⁸ and it depends on the rate at which the encapsulated detergent can partition into the inner bilayer leaflet, flip-flop across the bilayer to the outer leaflet, and then diffuse away from the vesicle.⁸ Normally OCG has a fast rate of bilayer flip-flop,^{23,24} compared to ionic detergents like sodium cholate,²⁵ however if the OCG

detergent adsorbs to co-encapsulated hydrophobic nanocrystals then this may slow down the rate of OCG diffusion out of the vesicles.

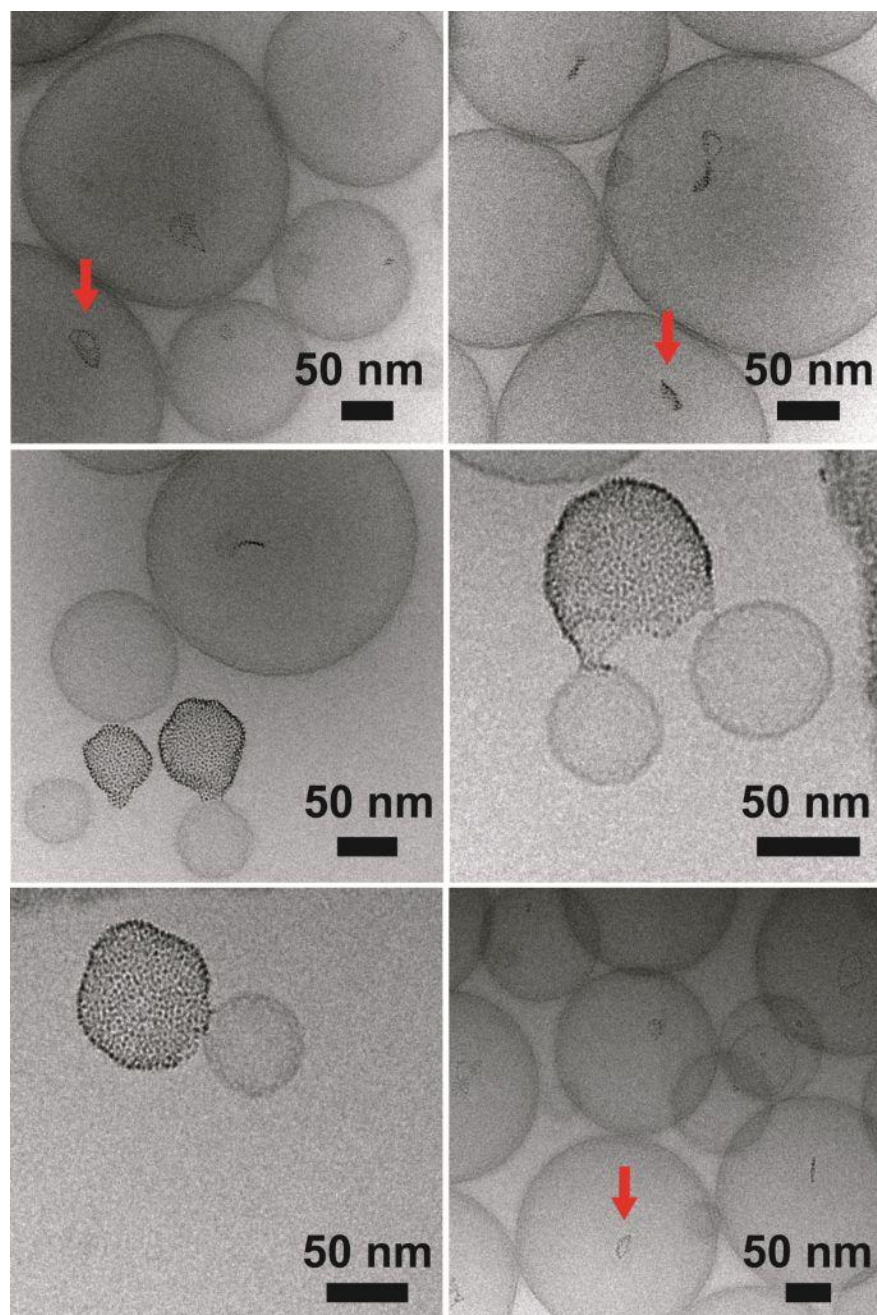


Figure 7.12. CryoTEM images of eggPC vesicles after dialysis with OCG-Au micelles. The eggPC concentration was 25 mM, the Au nanocrystal concentration was 20 μM , and the initial OCG concentration was 250 mM. The red arrows point to small clusters of nanocrystals associating with each lipid membrane.

Next, the eggPC concentration was increased to 75 mM in the dialysis dispersion. The results of dialyzing 75 mM eggPC with 150 mM OCG are shown in Figure 7.13. The detergent to lipid ratio is 2, therefore the vesicles should not break up after being mixed with the detergent. The vesicle size in most cases is around 50-100 nm, which is comparable to the initial size of the vesicles before OCG addition. This sample contains the highest concentrations of eggPC and Au nanocrystals (20 μ M), and therefore we expect that it has the highest collision rate of vesicles and nanocrystals during the dialysis process, compared to the other samples discussed previously. Every vesicle in the sample is loaded with a small cluster of about 5-10 Au nanocrystals. No vesicles were found that had a high loading of Au nanocrystals in the bilayer, as shown in Figures 7.9 – 7.12, and no empty vesicles were observed. Long chains of Au nanocrystals were not observed inside in the vesicles, and we consider that there was no nanocrystal encapsulation inside vesicles since the vesicles were not ruptured during detergent addition.

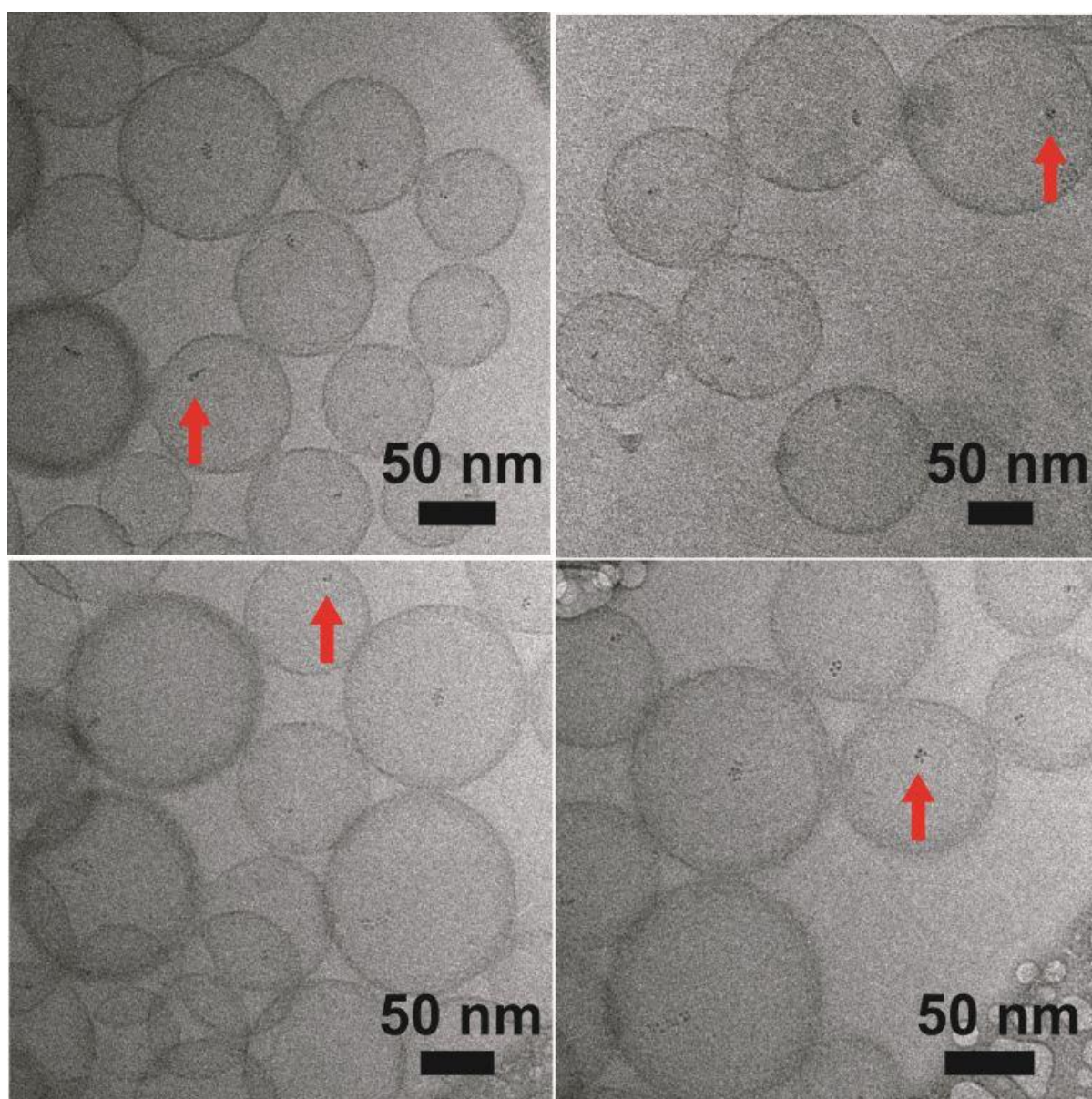


Figure 7.13. CryoTEM images of eggPC vesicles after dialysis with OCG-Au micelles. The eggPC concentration was 75 mM, the Au nanocrystal concentration was 20 μ M, and the initial OCG concentration was 150 mM. The red arrows point to small clusters of nanocrystals associating with each lipid membrane. Nearly every vesicle has a small cluster of 4-6 Au nanocrystals.

Mixing the vesicles and nanocrystals at concentrations of 75 mM eggPC, 20 μ M Au nanocrystals, and 250 mM OCG resulted in encapsulation of very long nanocrystal chains inside the vesicles. In this sample the detergent to lipid ratio is 3.3, which is at the point where the vesicles are saturated with enough detergent to begin to rupture and open. The vesicle size after dialysis is over 200 nm according to cryoTEM, consistent with the original 50 nm diameter vesicles opening, combining with other lipid bilayers stabilized by octylglucoside detergent, and then refolding of the larger vesicle bilayers during detergent removal. Figure 7.14 displays cryoTEM images, showing that numerous vesicles contain long chains of Au nanocrystals, and as mentioned previously, the chains probably contain OCG detergent. This is further supported by Figure 7.15, showing that a few freely-dispersed chains of Au nanocrystals, which were not encapsulated in vesicles, were observed in this sample. Since detergent can partition into the lipid bilayers and adsorb to the Au nanocrystals, and since this sample had the highest concentration of lipid as well as detergent, it is likely that detergent removal from this sample is slower than expected. Figure 7.16 diagrams a possible mechanism showing how OCG-Au nanocrystal micelles may incorporate into vesicles – the vesicles are initially ruptured into lipid bilayer fragments, and as detergent is removed, the bilayer fragments aggregate and enclose the OCG-Au micelle.

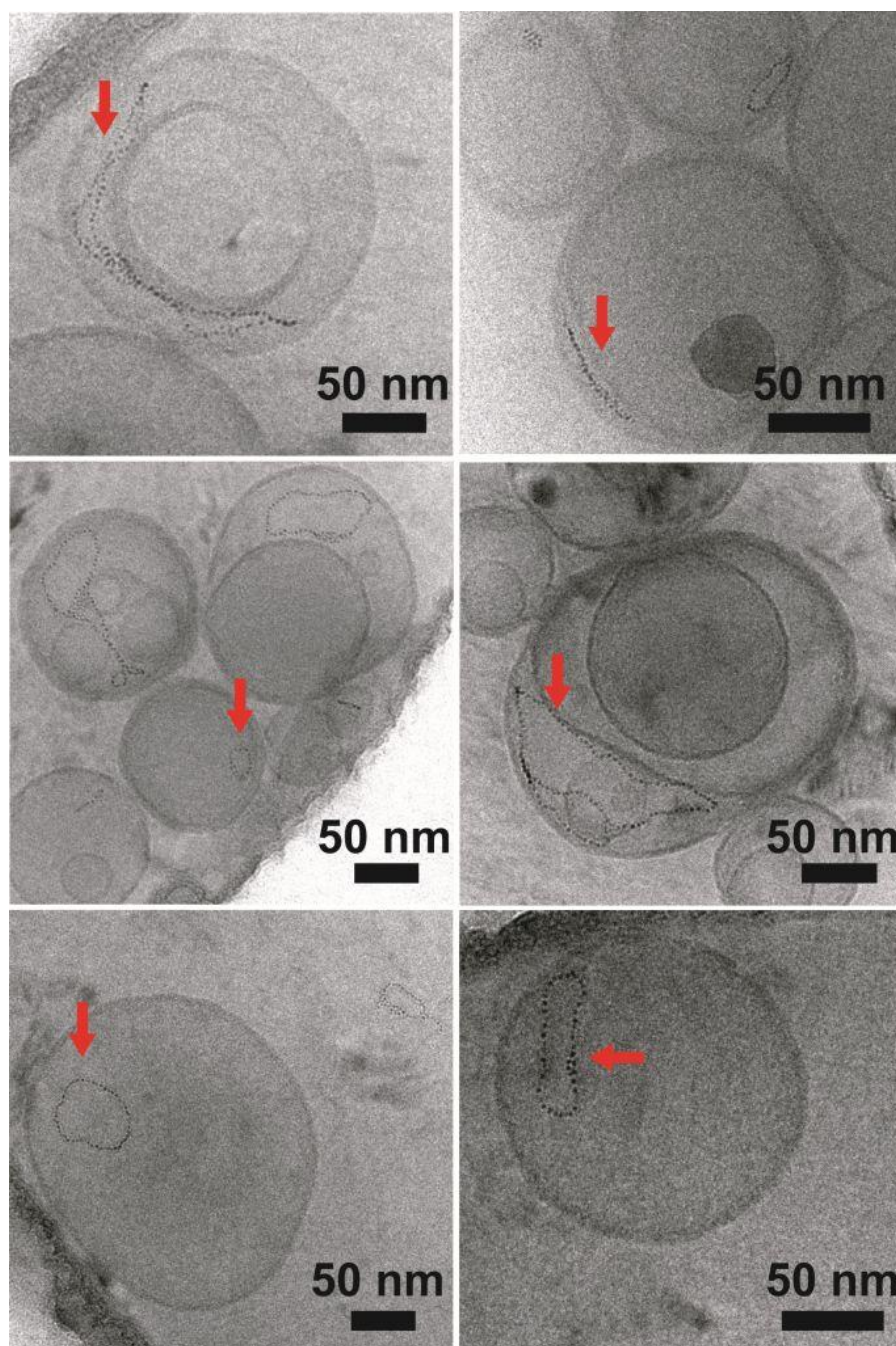


Figure 7.14. CryoTEM images of eggPC vesicles after dialysis with OCG-Au micelles. The eggPC concentration was 75 mM, the Au nanocrystal concentration was 20 μM , and the initial OCG concentration was 250 mM. The red arrows point to chains of Au nanocrystals that seem to be encapsulated within the vesicles.

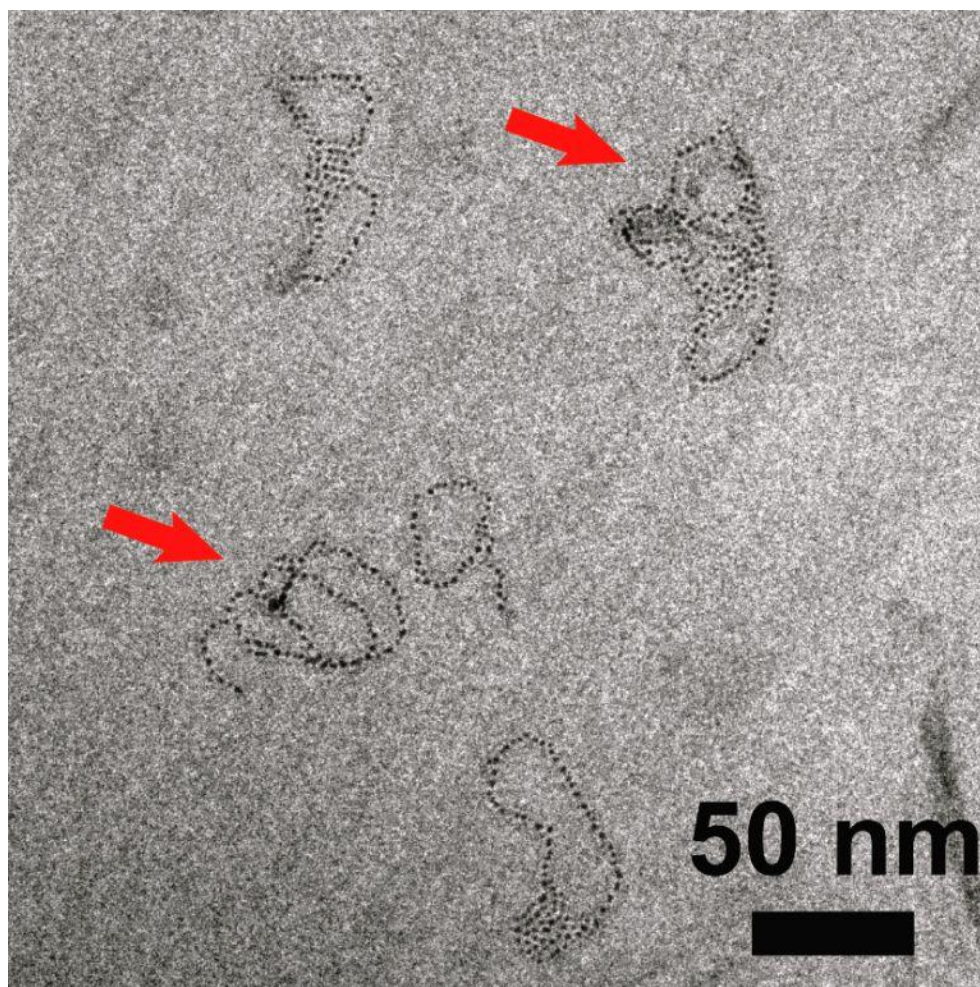


Figure 7.15. CryoTEM of Au nanocrystal chains found outside of vesicles after dialysis of 75 mM eggPC vesicles and OCG-Au micelles (250 mM OCG). The red arrows point to chains of Au nanocrystals. The chains must be coated with either OCG or and OCG-eggPC mixture.

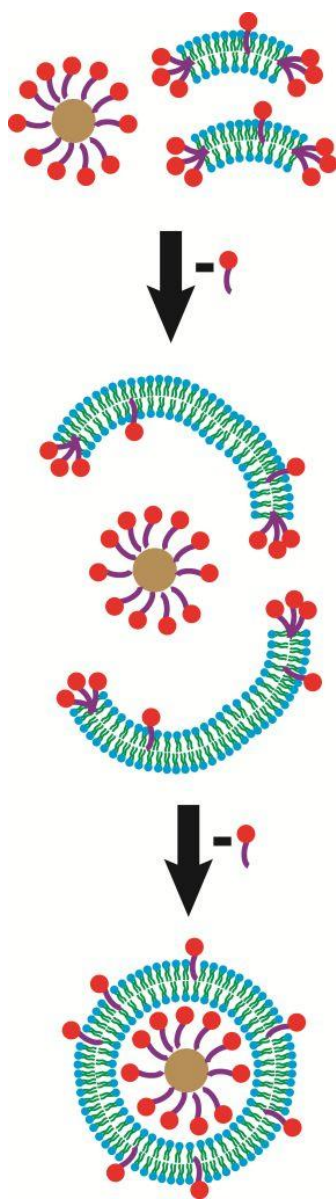


Figure 7.16. Schematic illustration of the encapsulation of OCG-Au nanocrystal micelles inside eggPC vesicles formed during detergent depletion, which begins with ruptured vesicles. In the vesicle drawn at the bottom, removing the detergent molecules adsorbed to the nanocrystal will require that they de-sorb from the nanocrystal, incorporate into the vesicle membrane, flip-flop across the membrane, and then de-sorb from the vesicle.

7.3.5 Nanocrystal Clustering Mechanism in Lipid Bilayers (Raft Formation)

The observation of vesicles loaded with rafts of hydrophobic nanocrystals is unprecedented, as far as we know. Since the Au nanocrystals are hydrophobic, there is indeed a strong thermodynamic driving force for nanocrystal insertion into the bilayer, but this also creates a mechanical deformation in the bilayer. The free energy change ΔG_{solv} , to place the hydrophobic sphere into the hydrophobic membrane from pure water is $\pi D^2 \gamma$, where γ is the liquid-vapor surface tension of water (72.0 mN/m)⁸³ and D is the nanocrystal diameter including the hydrophobic ligands.⁸⁴ Fully extended dodecanethiol ligands should add about 1.8 nm to the particle radius. Therefore, with $D=5.5$ nm diameter, $\Delta G_{\text{solv}} = 1650kT$, where k is Boltzmann's constant. Wi et al. has calculated the energy penalty to deform a dioleoylphosphatidylcholine lipid bilayer ΔG_{def} , when a hydrophobic sphere that is 5.5 nm in diameter is situated in the center of the bilayer: $\Delta G_{\text{def}} = 240kT$.⁵⁶ ΔG_{solv} is nearly an order of magnitude greater than ΔG_{def} . However, the membrane must 'un-zip' when the spherical nanocrystal is located at the center of the bilayer, as illustrated in Figure 7.17C. This un-zipping creates void space around the nanocrystal within the bilayer (red circles, Figure 7.17C) that draws other nanocrystals together in the membrane. Clustering of the nanocrystals in the lipid bilayer reduces the total void space around the nanocrystals. The minimization of ΔG_{def} may explain the formation of the Janus-type nanocrystal-vesicle hybrids, as opposed to vesicles with uniformly dispersed nanocrystals in the membrane.⁸⁵

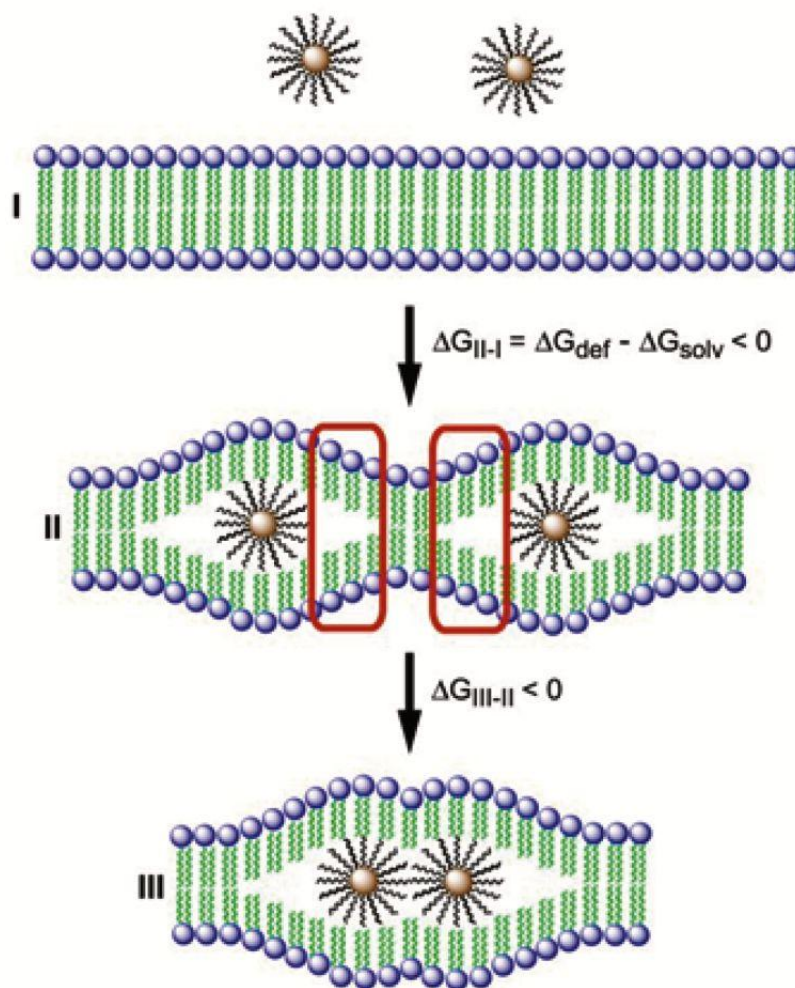


Figure 7.17. Schematic illustration considering three hypothetical states in which hydrophobic Au nanocrystals could exist, without considering the presence of detergent. In state I, the hydrophobic Au nanocrystals are placed in water outside of a lipid bilayer. In states II and III, the nanocrystals are placed inside the lipid bilayer. The insertion of a hydrophobic nanocrystal into the lipid bilayer leads to a membrane deformation and an “unzipping” of the bilayer. In the situation where two nanocrystals are present in the bilayer, as in stage II, the nanocrystals total membrane curvature is reduced by lateral aggregation of the nanocrystals, as shown in stage III. The strained regions of the lipid bilayer are circled in red in stage II.

7.4 Conclusions

The incorporation of hydrophobic Au nanocrystals into vesicles by the detergent dialysis procedure is sensitive to both the detergent:lipid ratio and the total surfactant concentration. When the detergent:lipid ratio is below the amount needed to rupture the vesicles, the vesicle size does not increase much during dialysis, and the incorporation of Au nanocrystals is affected by the total concentration (vesicles *and* nanocrystals) – at low total concentration the nanocrystals form tightly-packed rafts (containing hundreds of nanocrystals) in some vesicles while other vesicles are completely devoid of nanocrystals; at high total concentration nearly every vesicle has a small cluster of about 5-10 Au nanocrystals. Increasing the total concentration should increase the collision rate of vesicles and nanocrystals, which may be responsible for a greater proportion of vesicles colliding with nanocrystal micelles during dialysis when the concentration is higher. When the total concentration is low, the nanocrystal assembly may be more dominated by hydrophobic forces, which are long range,²⁶ causing the nanocrystals to assemble into much larger agglomerates at the relatively few sites where vesicle-nanocrystal collision results in nanocrystal incorporation into the vesicle bilayer and disrupts the lipid packing (Figure 7.17). A problem with this argument, however, is that increasing the total concentration also increases the viscosity of the dispersion, which reduces collision frequency of the dispersed particles,¹⁸ and a more detailed understanding of the relationship between vesicle-nanocrystal concentration, viscosity, and collision frequency is needed as it relates to the formation of the different Au-loaded vesicle structures demonstrated in this chapter.

Once the vesicles are allowed to rupture by using a high enough ratio of detergent to lipid molecules, then the cryoTEM imaging strongly suggests that Au nanocrystal chains are encapsulated within the vesicles. The fact that a few Au nanocrystal chains are observed outside of vesicles supports that the OCG-Au micelles likely assembly into chains during detergent dialysis. The fragmented vesicles gradually re-assemble into large vesicles over 200 nm in diameter during detergent dialysis, and the nanocrystal chains become trapped inside these vesicles. The chains likely still contain OCG detergent after dialysis, since detergents are known to be retained inside vesicles during dialysis due to slow exchange of vesicle contents with the surrounding medium.⁸

The cryoTEM images of the nanocrystal-vesicle hybrids prepared here provide new insight into how hydrophobic nanocrystals with size similar to the lipid bilayer thickness interact with vesicles. The observation of dense monolayers of tightly packed nanocrystals in the lipid bilayers of vesicles is unprecedented, however, it makes sense when one considers the significant energy penalty that occurs when nanocrystals insert into the bilayer and deform the lipid membrane.^{56,86} The clustering of the nanocrystals, as in the rather extreme case of the Janus-like nanocrystal-vesicle hybrids, contrasts previous observations of CdSe and Fe₂O₃ nanocrystal-loaded vesicles,^{3,39,47} in which the nanocrystals were apparently uniformly dispersed in the bilayer. Importantly, the results of this chapter show that it is possible to control whether vesicles contain few or many nanocrystals per bilayer by controlling the assembly parameters. It would be useful to conduct further studies that include detergent-adsorbing beads (e.g. BioBeads)^{27,28} to try and remove trace amounts of residual detergent from the vesicle dispersions, in order to

ensure that the vesicle-nanocrystal structures reach equilibrium rather than a metastable state. The possible role of trace amounts of chloroform, which was detected by NMR in the OCG-Au micelles (Figure 7.7), must be investigated as well.

7.5 References

- (1) Kudlicki, W.; Katzen, F.; Peterson, T. C. *Trends in Biotechnology* **2009**, 27, 455-460.
- (2) Seddon, A. M.; Curnow, P.; Booth, P. J. *Biochimica Et Biophysica Acta* **2004**, 1666, 105-117.
- (3) Paternostre, M. T.; Roux, M.; Rigaud, J. L. *Biochemistry* **1988**, 27, 2668-2677.
- (4) Rigaud, J. L.; Paternostre, M. T.; Bluzat, A. *Biochemistry* **1988**, 27, 2677-2688.
- (5) Saxena, K.; Shipley, G. G. *Biochemistry* **1997**, 36, 15940-15948.
- (6) Mimms, L. T.; Zampighi, G.; Nozaki, Y.; Tanford, C.; Reynolds, J. A. *Biochemistry* **1981**, 20, 833-840.
- (7) Israelachvili, J. N. *Intermolecular and Surface Forces*; 2nd ed.; Academic press Inc.: San Diego, 1992.
- (8) Ollivon, M.; Lesieur, S.; Grabielle-Madelmont, C.; Paternostre, M. *Biochimica Et Biophysica Acta* **2000**, 1508, 34-50.
- (9) Jackson, M. L.; Schmidt, C. F.; Lichtenberg, D.; Litman, B. J.; Albert, A. D. *Biochemistry* **1982**, 21, 4576-4582.
- (10) Korgel, B. A.; Monbouquette, H. G. *Journal of Physical Chemistry* **1996**, 100, 346-351.
- (11) Korgel, B. A.; van Zanten, J. H.; Monbouquette, H. G. *Biophys J* **1998**, 74, 3264-3272.
- (12) Schwendener, R. A.; Asanger, M.; Weder, H. G. *Biochem Biophys Res Commun.* **1981**, 100, 1055-1062.
- (13) Zumbuehl, O.; Weder, H. G. *Biochimica Et Biophysica Acta* **1981**, 640, 252-262.
- (14) Vinson, P. K.; Talmon, Y.; Walter, A. *Biophysical Journal* **1989**, 56, 669-681.
- (15) Leng, J.; Egelhaaf, S. U.; Cates, M. E. *Biophysical Journal* **2003**, 85, 1624-1646.
- (16) Ollivon, M.; Eidelman, O.; Blumenthal, R.; Walter, A. *Biochemistry* **1988**, 27, 1695-1703.
- (17) Kucerka, N.; Nieh, M.-P.; Katsaras, J. *Biochimica Et Biophysica Acta* **2011**, 1808, 2761-2771.

- (18) Valioulis, I. A.; List, E. J. *Advances in Colloid and Interface Science* **1984**, *20*, 1-20.
- (19) Van Zanten, J. H.; Monbouquette, H. G. *Journal of Colloid and Interface Science* **1994**, *165*, 512-518.
- (20) Pons, T.; Uyeda, H. T.; Medintz, I. L.; Mattoussi, H. *Journal of Physical Chemistry B* **2006**, *110*, 20308-20316.
- (21) Marsh, D. *CRC Handbook of Lipid Bilayers*; CRC Press, Inc.: Boca Raton, FL, 1990.
- (22) Johnsson, M.; Edwards, K. *Langmuir* **2000**, *16*, 8632-8642.
- (23) Ueno, M.; Tanford, C.; Reynolds, J. A. *Biochemistry* **1984**, *23*, 3070-3076.
- (24) Heerklotz, H.; Seelig, J. *Biophysical Journal* **2000**, *78*, 2435-2440.
- (25) El-Sayed, M. A.; Cevc, G. *Biochimica Et Biophysica Acta* **2011**, *1808*, 140-153.
- (26) Chandler, D. *Nature* **2005**, *437*, 640-647.
- (27) Sechoy, O.; Philippot, J. R.; Bienvenue, A. *Biochimica Et Biophysica Acta-Biomembranes* **1986**, *857*, 1-12.
- (28) Philippot, J. R.; Mutaftschiev, S.; Liautard, J. P. *Biochimica Et Biophysica Acta-Biomembranes* **1983**, *734*, 137-143.

Chapter 8: Assembling Fluorescent Semiconductor Nanocrystals with Phosphatidylcholine and Squalene Droplets for Cell Labeling[§]

8.1 Introduction

There have been many recent studies demonstrating that fluorescent semiconductor nanocrystals (quantum dots) may incorporate into lipid micelles¹⁻³ and vesicles.⁴ Several types of quantum dots are synthesized with a hydrophobic surface,⁵⁻⁷ and incorporating them into amphiphile aggregates renders them hydrophilic and dispersible in water,^{3,5,8} which is necessary for labeling cells and macromolecules located in aqueous biological media.^{6,9-11} While lipid micelles are adequate for dispersing hydrophobic quantum dots in aqueous media, combining the fluorescence of the quantum dots with the drug carrying capability of lipid vesicles may create particles capable of dual fluorescence imaging and therapy.¹²⁻¹⁵

Recently lipid vesicles loaded with hydrophobic CdSe quantum dots were used to label mammalian cells.^{12,14} The quantum dots were dispersed in water by lipids having a cationic headgroup, which caused the lipid-nanocrystal aggregates to bind to the cells by electrostatic adsorption.¹² Binding of cationic liposomes to cells is possible because cell membranes (excluding nerve cells) typically have a negative zeta potential.^{16,17} Dispersions of cationic lipids often are used to transfer anionic polynucleic acids into cells for non-viral gene delivery,¹⁸⁻²¹ and the same transfection protocols using cationic liposomes were adopted to load fluorescent CdSe nanocrystals in cells as well.^{22,23}

Several concerns remain however. First, there has been limited characterization of how

[§] Portions of this chapter will appear in an upcoming ACS Journal publication; draft in progress.

CdSe nanocrystals assemble with lipid vesicles; it is not clear whether the nanocrystals fully load vesicle membranes, or if they form lipid-coated agglomerates as shown with Au nanocrystals in Chapter 6. Second, cadmium-containing compounds are known to be cytotoxic,²⁴ and the safety of CdSe nanocrystals has not been fully characterized.^{25,26} To create vesicles loaded with fluorescent nanocrystals having less toxic elements, Si-loaded vesicles were prepared,²⁷ however the structure of these lipid-Si assemblies was not carefully characterized by cryoTEM. It has not been clear whether Si nanocrystals actually load lipid bilayers or simply form lipid-coated agglomerates, comparable to the Si-loaded lipid micelles used by Prasad and coworkers for fluorescent cell and tissue labeling.³

This chapter extends the vesicle preparation methods developed in Chapters 5-6 to the preparation of phosphatidylcholine lipid dispersions containing hydrophobic CdSe, Si, and CIS nanocrystals. Squalene emulsions are also prepared with the lipids and nanocrystals. CryoTEM is used to elucidate the structure of the lipid-nanocrystal aggregates. The cationic lipid dioleoyltrimethylammonium-propane (DOTAP) is included in Si-lipid dispersions and mixed with HL-60 cells to investigate whether the nanocrystals can bind to the cells. In addition, the hydrophobic fluorescent dye Nile Red was synthesized, incorporated into lipid particles, and mixed with HL-60 cells for comparison to Si-loaded lipid particles. HL-60 is a continuous human leukemia cell line that grows in suspension,²⁸⁻³⁰ and it was chosen for this work because it is simple to maintain,³¹ it has a relatively fast doubling time (24-36 hours),^{31,32} its cell membrane has a negative zeta potential for adsorption of cationic particles,¹⁶ and the binding of dye-

loaded cationic liposomes has been demonstrated.¹⁶ However, when cationic vesicles were used for transfecting actively-dividing HL-60 cells, gene transfer efficiency is reportedly low because the cells are reluctant to perform endocytosis.³³ Therefore, the fluorescent Si nanocrystals and dye molecules are expected to bind to and remain at the cell membrane by electrostatic and hydrophobic forces, rather than being transported inside the cell.

8.2 Experimental Details

8.2.1 Chemicals

Nanocrystal and Dye Synthesis. Selenium powder (99.99%), cadmium oxide (99%), trioctylphosphine (TOP, 90%), trioctylphosphine oxide (TOPO, 99%), Nile Blue chloride (99%), Trypan Blue (99%), 4-(2-hydroxyethyl)-1-piperazineethanesulfonic acid (HEPES, 99%), and squalene (99%) were from Sigma Aldrich. Tetradecylphosphonic acid (TDPA, 98%) was from Strem Chemical. Dioleoyltrimethylammonium-propane (DOTAP, 99%), dilauroylphosphatidylcholine (DLPC, 99%), dimyristoylphosphatidylcholine (DMPC, 99%), dipalmitoylphosphatidylcholine (DPPC, 99%), dipalmitoylphosphatidylglycerol (DPPG, 99%), dimyristoyl-glycero-ethylphosphocholine (eDMPC, 99%), and PEG₂₀₀₀-dipalmitoylphosphatidylethanolamine (PEG-DPPE, 99%) were from Avanti Polar Lipids. Sulfuric acid (98%), cyclohexane (98%), xylenes (98%), toluene (99%), chloroform (99%), and ethanol (99%) were from Fisher Scientific. All chemicals were used as received. Deionized water was at 17 M Ω resistance and filtered through 0.2 μ m pores.

Cell Culture. The HL60 cell line was obtained from the American Type Tissue Culture Collection (ATCC). Fetal bovine serum (FBS), Iscove's Modified Dulbecco's Medium (IMDM), Hank's Balanced Salt Solution without Phenol Red (HBSS), and dimethylsulfoxide were from ATCC. Trypan Blue powder was from Sigma Aldrich.

8.2.2 Nanocrystal Synthesis

Trioctylphosphine-coated CdSe Nanocrystals. The nanocrystal synthesis is adopted from a recent procedure.³⁴ First the precursor solutions are prepared. In a 100 mL 3-neck round bottom flask, 51.4 mg cadmium oxide, 223 mg TDPA, and 3.7768 g of TOPO are combined. A glass stir bar is added, and the flask is fitted with a glass condenser-stopcock assembly and rubber septa. A thermocouple is inserted into the flask through one of the septa. The flask is connected to a Schlenk line, placed under vacuum, heated to 100°C, and held at a pressure less than 500 mbar for 3 hours. Meanwhile, in a 25 mL 3-neck round bottom flask, 41.1 mg Se and a Teflon stir bar are added, the flask is assembled with a glass stopcock and 2 rubber septa, a thermocouple is inserted through one septum, the flask is transferred to a nitrogen-filled glovebox and loaded with 2.5 mL TOP, and then the flask is transferred to the Schlenk line while sealed under nitrogen.

Next the reaction is performed. The 100 mL flask is heated to 350°C under low N₂ (g) pressure and stirred until it turns colorless. The 25 mL flask is heated to 120°C low N₂ (g) pressure as well to dissolve the selenium. The 100 mL flask is cooled to 250°C, at which point the TOP-Se solution is drawn up into a syringe and injected into the 100 mL flask. The nanocrystals are rapidly nucleate and grow over time. Green-

emitting CdSe nanocrystals are typically formed by 3-5 minutes, while orange-emitting CdSe nanocrystals require about 45 minutes. When the reaction is complete, the 100 mL flask is cooled to room temperature in air.

The nanocrystals are purified by mixing the crude reaction solution with about 2 mL of toluene. The dispersion is transferred to glass centrifuge tubes, followed by addition of 20 mL methanol. The samples are centrifuged at 8000 rpm for 5 minutes to precipitate the nanocrystals. The precipitate is dispersed in about 1 mL of toluene. Then 10 mL of methanol is added and the dispersion is centrifuged a second time. The precipitate is dispersed in 1 mL of toluene and centrifuged at 8000 rpm for 3 minutes. The supernatant of well-dispersed nanocrystals is transferred to a clean glass vial for storage until use.

Dodecanethiol-coated CuInSeS (CIS) Nanocrystals. CIS nanocrystals were synthesized by Matthew Panthani using the methods described in Chapter 4. Steps corresponding to growth of the zinc sulfide shell were omitted, resulting in a quantum yield of 10%.

Dodecane-coated Si Nanocrystals. Si nanocrystals were synthesized by Yixuan Yu using the methods described in Chapter 4. Different ligands were used during hydrosilylation as described in the text.

8.2.3 Nile Red Synthesis

The Nile Red fluorescent dye was synthesized according to a literature protocol,³⁵ as diagrammed in Figure 8.1. First, 0.46 grams of Nile Blue chloride was dissolved in 250 mL of 0.5% v/v H₂SO₄ (aq). The solution was boiled for 2 hours at ambient

pressure, forming a mixture of Nile Blue and Nile Red. The Nile Red was separated by extracting it using three sequential 250 mL volumes of xylenes. Next, the xylene phase was mixed three 250 mL volumes of DI water to collect any remaining Nile Blue in the aqueous phase. Extraction of the xylene phase with DI water was repeated until no blue material was collected in the aqueous phase, indicating that all of the Nile Blue was removed from the xylene phase. The xylene phase was placed in a round bottom flask on a rotary evaporator, and the xylene was evaporated at 80°C and reduced pressure. The dye was dissolved in chloroform, transferred to a glass vial and stored until use.

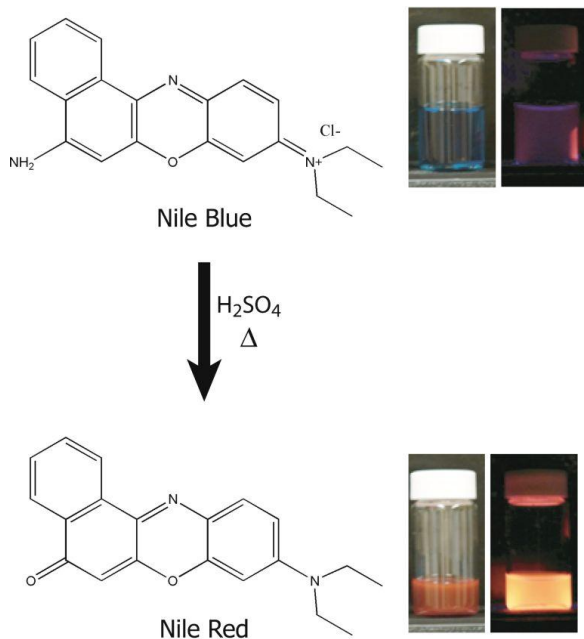


Figure 8.1. Schematic illustration of the synthesis of Nile Red dye by heating Nile Blue dye in sulfuric acid. Photographs of the vials correspond to chloroform solutions of Nile Blue (top row) and Nile Red (bottom row). The vials show each solution under room light (left vial) and a handheld ultraviolet lamp at 350 nm wavelength (right vial).

8.2.4 Formation of Lipid Dispersions and Squalene Emulsions

The dispersions of lipid vesicles and squalene emulsions were prepared as described in Chapters 5.2 and 6.2, using 4 mg of Si, 4 mg of CIS, and 3 mg of CdSe nanocrystals. For cryoTEM imaging, the lipid-nanocrystal dispersions were prepared in an aqueous pH 7.4 buffer solution of 10 mM HEPES and 10 mM NaCl. For cell culture, the dispersions were prepared in Hank's Balanced salt solution without phenol red indicator (150 mM ionic strength, pH 7.4).

With the Nile Red dye, the dye was mixed with lipids in chloroform, and then dried to a film before dispersing in water. The concentration of dye in the aqueous vesicle dispersions and emulsions was 50 $\mu\text{g/mL}$. The lipids were 30 mM DLPC and 7.5 mM DOTAP. In the aqueous Nile Red dye emulsions, the concentration of squalene was 5% by volume. The dispersions were prepared in Hank's Balanced salt solution for mixing with cells.

8.2.5 Material Characterization

Characterization of the nanocrystals by TEM, SAXS, and TGA was performed as described in chapter 4.2. CryoTEM imaging of aqueous dispersions was performed as described in Chapter 5.2. FTIR of the Nile Red dye was performed as described in Chapter 4.2. Quantum yield was calculated as described in Chapter 4.2. Dynamic light scattering was performed as described in Chapter 5, the data were fitted to the equations in Chapter 5 using non-linear least squares regression to minimize χ^2 (sum of the squared residual errors between the model and the data), and the Rayleigh approximation was

applied, which is valid for lipid particles up to about 200 nm diameter.³⁶ Using this approximation, the relative number of particles of sizes 1 and 2 (N_1 , N_2) is related to the particle diameters (d_1 , d_2) and the amplitude of scattering intensities (A_1 , A_2) by equation 8.1. Therefore if $d_1 < d_2$ and $A_1 \approx A_2$, the particles of size d_1 are much more numerous in the dispersion than the larger particles.

$$\frac{N_1}{N_2} = \frac{A_1}{A_2} \cdot \left(\frac{d_2}{d_1} \right)^6 \quad (8.1)$$

8.2.6 HL60 Cell Culture

HL60 cells were handled using standard aseptic techniques.³⁷ The cells were cultured in 20 mL of 20% v/v FBS in IMDM at 37°C, 5% CO₂, and 90% relative humidity using 75 mL vented-cap tissue culture flasks. Cultures were maintained at a cell density between 10⁵ and 2 x 10⁶ cells/mL and passaged when the measured cell concentration exceeded 1 x 10⁶ cells/mL. Cell concentration was determined by counting cells on a hemacytometer, and cell viability was checked weekly by staining cells with 0.2% w/w Trypan blue for 1 minute prior to counting.³⁷

8.2.7 Cell Labeling and Imaging

HL60 cells were cultured to a density of 10⁶ cells per mL. 5 mL of the cell suspension was placed in a sterile 15 mL centrifuge tube and centrifuged at 150g for 6 minutes. The supernatant was discarded and the cell pellet was dispersed in 5 mL of HBSS. The cells were maintained at 37°C and 5% CO₂ atmosphere for a few minutes before imaging. Prior to imaging, 50 µL of the cell suspension was added to a 2 mL

plastic centrifuge tube. Subsequently, 50 μL of the stain solution (lipid/nanocrystals, lipid/dye, or HBSS as a control) was injected into the cell suspension, the tube was then closed and gently shaken by hand to mix the contents. After about 2 minutes, the 100 μL suspension was pipetted into the 100 μL well of a Coverwell perfusion chamber (Sigma Aldrich) assembled on cover glass (number 1 thickness, autoclaved). After 1 minute, the cells were immediately imaged by placing the imaging chamber on the stage of a Leica SP2 AOBS Confocal Laser Scanning Microscope. The excitation and emission filters and detector voltages were adjusted depending on the sample.

8.3 Results and Discussion

8.3.1 Nile Red Dye Synthesis

The synthesis of the Nile Red dye is straightforward. Once the Nile Red was extracted into organic solvent, the dye exhibited orange fluorescence. The optical spectra of the dye are displayed in Figure 8.2. The photoluminescence quantum yield of the Nile Red dye was measured to be about 70% at an excitation wavelength of 500 nm, using Rhodamine 101 dye as a reference. The FTIR analysis of Nile Red, shown in Figure 8.3, confirms the formation of the carbonyl group based on the absorbance peak at 1770 cm^{-1} . Nile red is very soluble in low polarity solvents like chloroform, and it is insoluble in water.

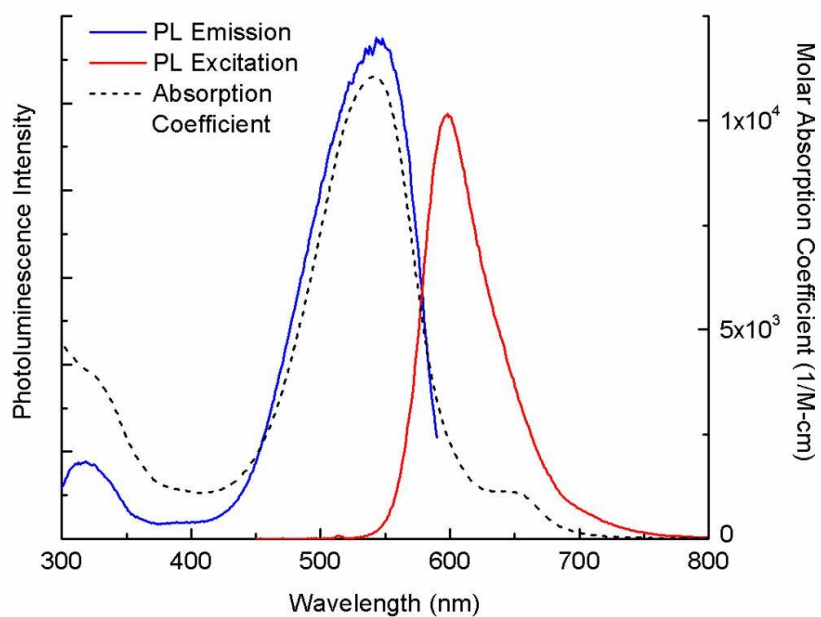


Figure 8.2. Photoluminescence (PL) spectra and molar absorption coefficient of the Nile Red dye dissolved in chloroform. The PL emission with 500 nm excitation wavelength is the red curve, the PL excitation with 620 nm emission is the blue curve, and the black dashed curve is the molar absorption coefficient determined using the Beer Lambert law and successive dilutions of the dye (Chapter 3).

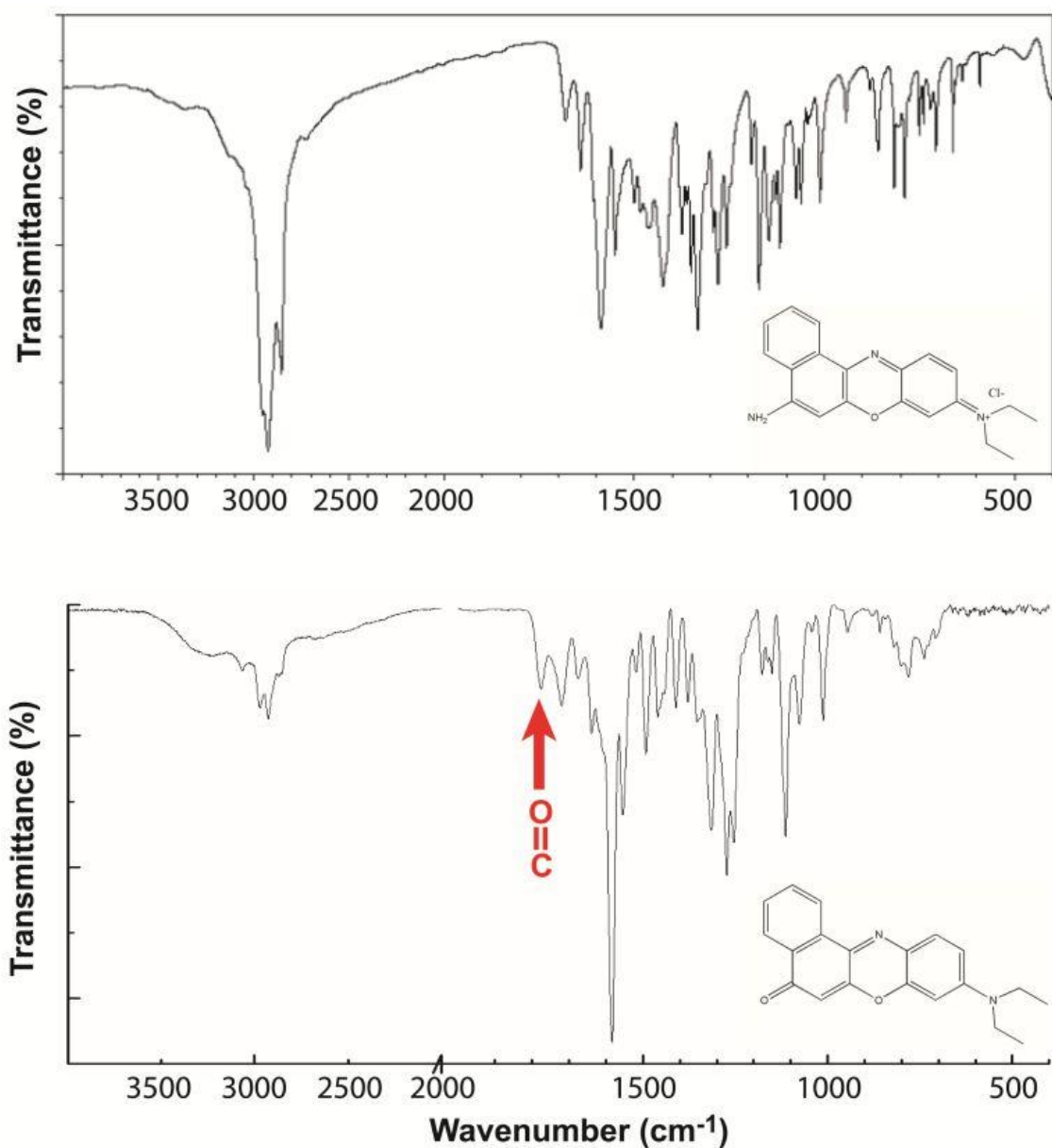


Figure 8.3. FTIR spectra of Nile Red and Nile Blue dyes. The Nile Blue spectrum (top) is from the SDBS of organic compounds.³⁸ The Nile red spectrum (bottom) was measured by ATR-FTIR. The carbonyl group of Nile Red is detected by an absorbance maximum at 1770 cm⁻¹, while Nile Blue does not have an absorbance peak between 1700 – 1800 cm⁻¹ indicating the absence of a carbonyl group in this molecule.³⁹

8.3.2 CdSe Nanocrystal Synthesis

The CdSe nanocrystals were grown for 5 minutes to yield nanocrystals that emit green light when excited at blue to UV wavelengths (Figure 8.4). The nanocrystals are coated with TOPO and TDPA ligands and are therefore hydrophobic. The stability of the nanocrystals is highly dependent on the solvent used to disperse them – toluene keeps the nanocrystals stable over many months, while the nanocrystals typically aggregate when dispersed in chloroform for a few hours, because chloroform is a better solvent than toluene for the ligands and results in rapid ligand de-sorption from the CdSe surface. The optical spectra of the CdSe nanocrystals are displayed in Figure 8.4. The nanocrystal photoluminescence quantum yield is 14%, relative to the Rhodamine 101 dye as a reference. From TEM characterization in Figure 8.5, the CdSe diameter is 4.3 ± 0.5 nm.

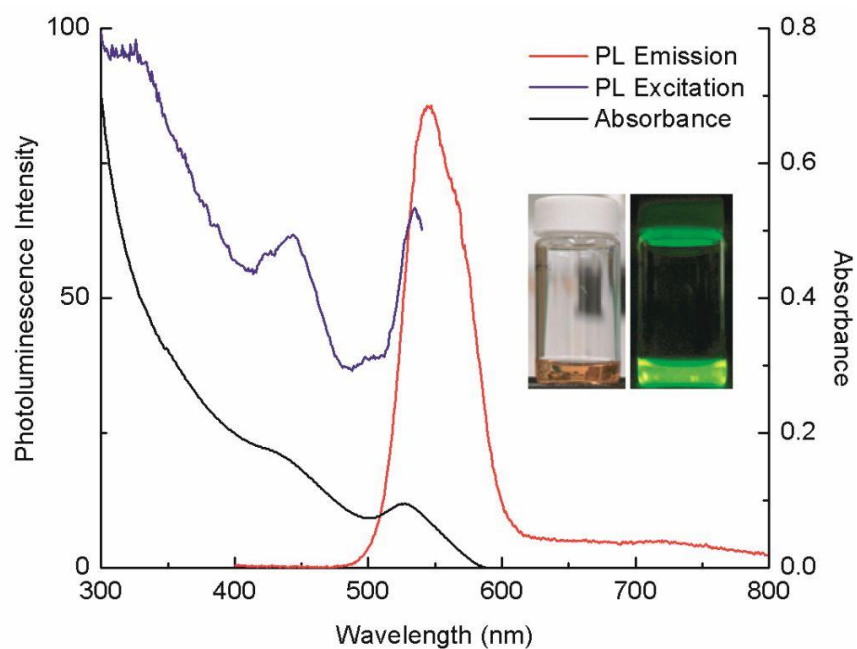


Figure 8.4. Photoluminescence (PL) and absorbance spectra of CdSe nanocrystals (5 $\mu\text{g/mL}$ concentration). The insets show vials of the nanocrystals dispersed in toluene under room light (left vial) and ultraviolet light (right vial, 350 nm excitation).

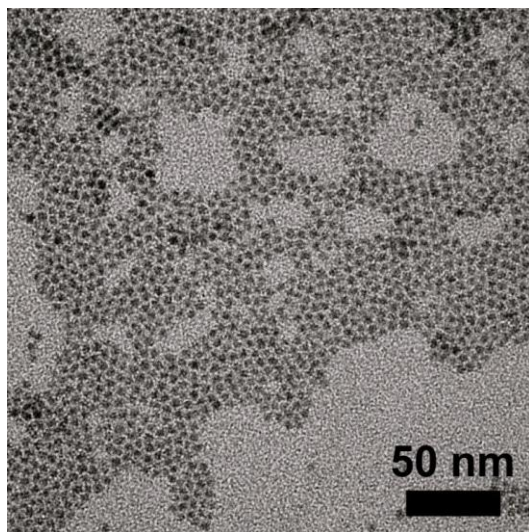


Figure 8.5. TEM image of CdSe nanocrystals coated with TOPO and TDPA ligands. The average CdSe diameter is 4.3 ± 0.5 nm.

8.3.3 Vesicles and Emulsion Particles Loaded with Nile Red Dye

Dry films of lipid and Nile Red dye readily dispersed in the aqueous buffer solution to form vesicles. Without squalene, the hydrodynamic diameter of the dispersed lipid-squalene particles was 32 nm from dynamic light scattering ($\chi^2 = 0.0008$ from fitting). The Nile Red dye emits orange-red fluorescence when dispersed in the aqueous vesicles as shown in Figure 8.6, whereas Nile Red cannot disperse in water on its own (without lipid) to make a fluorescent aqueous dispersion. The zeta potential of the samples is +20 mV. A fluorescent aqueous dispersion was also obtained when squalene was included to form an emulsion with the lipid and Nile Red dye, and the zeta potential was also +20 mV, however the particle size was 80 nm according to DLS.

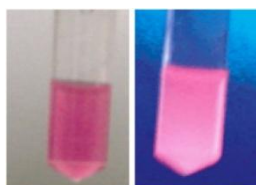


Figure 8.6. Photographs of a dispersion of vesicles loaded with Nile Red dye in Hank's Balanced salt solution without phenol red indicator. Left tube: dispersion under room light. Right tube: dispersion under UV light (350 nm excitation), showing the orange emission characteristic of Nile Red.

8.3.4 Vesicles and Emulsion Particles Loaded with CdSe

The green-fluorescent CdSe nanocrystals were dispersed in aqueous HEPES/NaCl buffer solution at pH 7.4 using DMPC, DPPC, DPPC plus squalene, and DOPC. The DOPC sample was annealed with chloroform prior to dispersing in water, since the

results of Chapter 5 indicate that this annealing improves the dispersibility of nanocrystals with the DOPC lipid. The CdSe nanocrystals dispersed in aqueous lipid particles (DMPC, DPPC, DOPC) were not fluorescent, as shown in Figure 8.7. The fluorescence of the DPPC-SQE emulsion was practically negligible. The loss of fluorescence suggests that the CdSe nanocrystal surface probably is oxidizing when transferred from organic solvent to water, in spite of the lipid coating. CdSe nanocrystals are known to oxidize in the presence of water and oxygen,⁴⁰ resulting in a loss of fluorescence. Since the CdSe-lipid dispersions are not fluorescent, they are not suitable to label cells for fluorescent imaging.

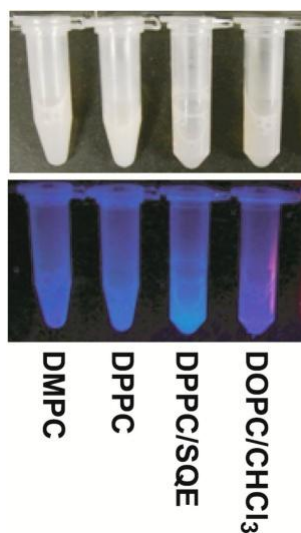


Figure 8.7. CdSe nanocrystals dispersed at 3 mg/mL concentration in aqueous vesicles and emulsion particles. Top row: aqueous dispersions under room light. Bottom row: the aqueous dispersions excited with a 350 nm ultraviolet lamp. The vesicle dispersions with DMPC, DPPC, and DOPC lipid are not fluorescent. The emulsion of DPPC lipid and squalene (SQE) has a very faint green fluorescence, and the squalene concentration is 5% by volume.

CryoTEM images of the CdSe nanocrystals dispersed in the lipid particles are displayed in Figures 8.8 – 8.11. The DMPC-CdSe dispersion, Figure 8.8, had the nanocrystals dispersed as small clusters adhering to the vesicle bilayers. No flat nanocrystal sheets of CdSe are observed as seen with the 1.8 nm Au nanocrystals in Chapter 6. Since the nanocrystals adhere to the lipid bilayer, they must remain somewhat hydrophobic even if they have oxidized a little based on the loss of fluorescence. The same results are observed with both DPPC and DOPC lipids. The CdSe nanocrystals form small clusters adhering to the faceted DPPC vesicles, shown in Figure 8.9. With DOPC, the CdSe forms clusters adhering to the vesicles as well, in spite of annealing with chloroform. The DOPC results with CdSe are comparable to results of dispersing hexadecanethiol-coated 1.8 nm Au and dodecanethiol-coated 4.1 nm Au nanocrystals with DOPC after chloroform annealing – the nanocrystals do not completely load the bilayers of the vesicles. Figure 8.11 shows the results with using DPPC and squalene to form an emulsion. The CdSe nanocrystals incorporate into the squalene droplets, and some of the nanocrystals are found to extend beyond the edge of the squalene droplet (bottom row, Figure 8.11), suggesting that the CdSe nanocrystals are somewhat hydrophilic, which may be the result of nanocrystal surface oxidation to form selenium oxides.⁴⁰

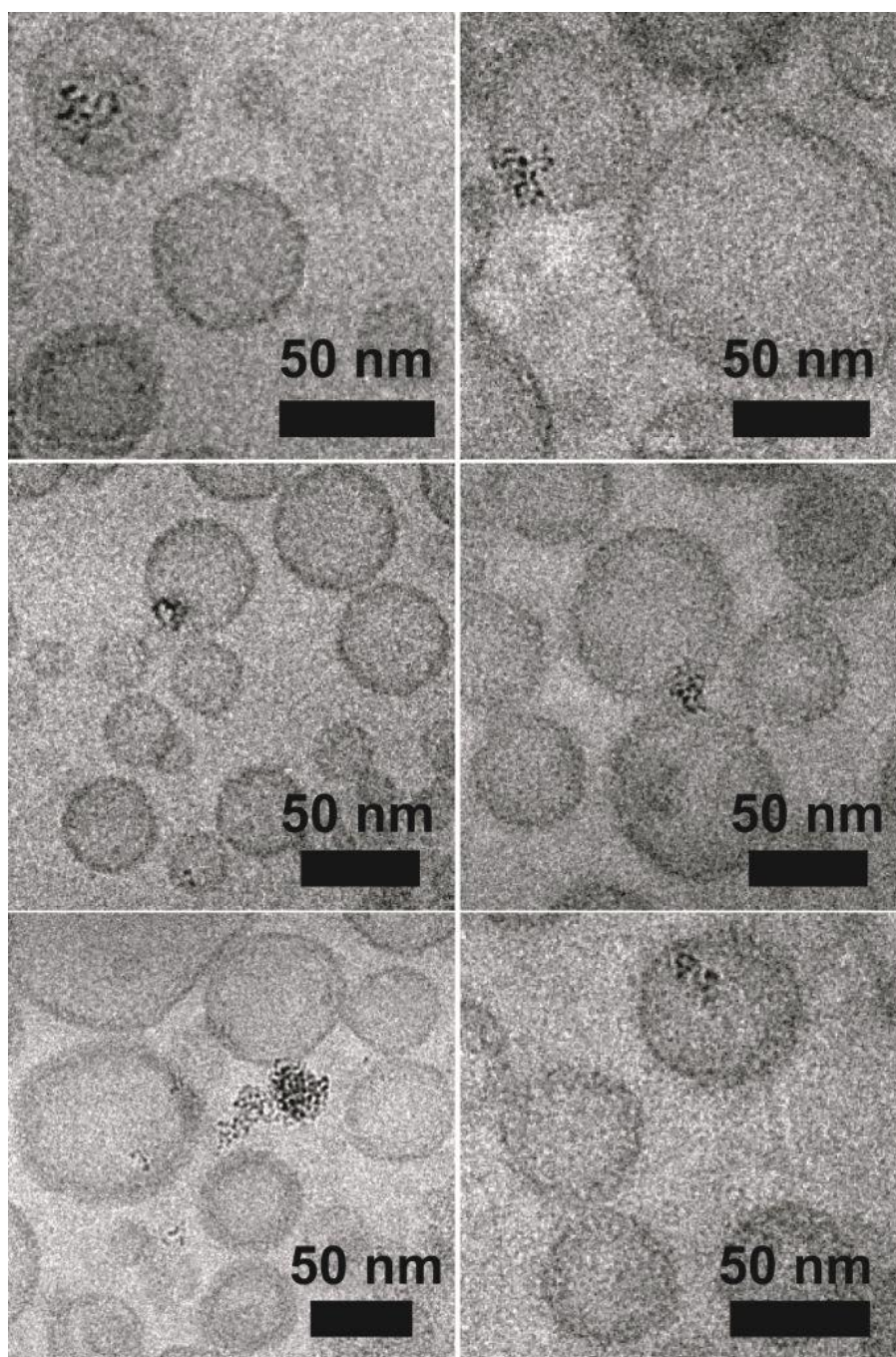


Figure 8.8. CryoTEM images of CdSe nanocrystals dispersed with DMPC lipid in water. The nanocrystals form small agglomerates adhering to the lipid bilayers.

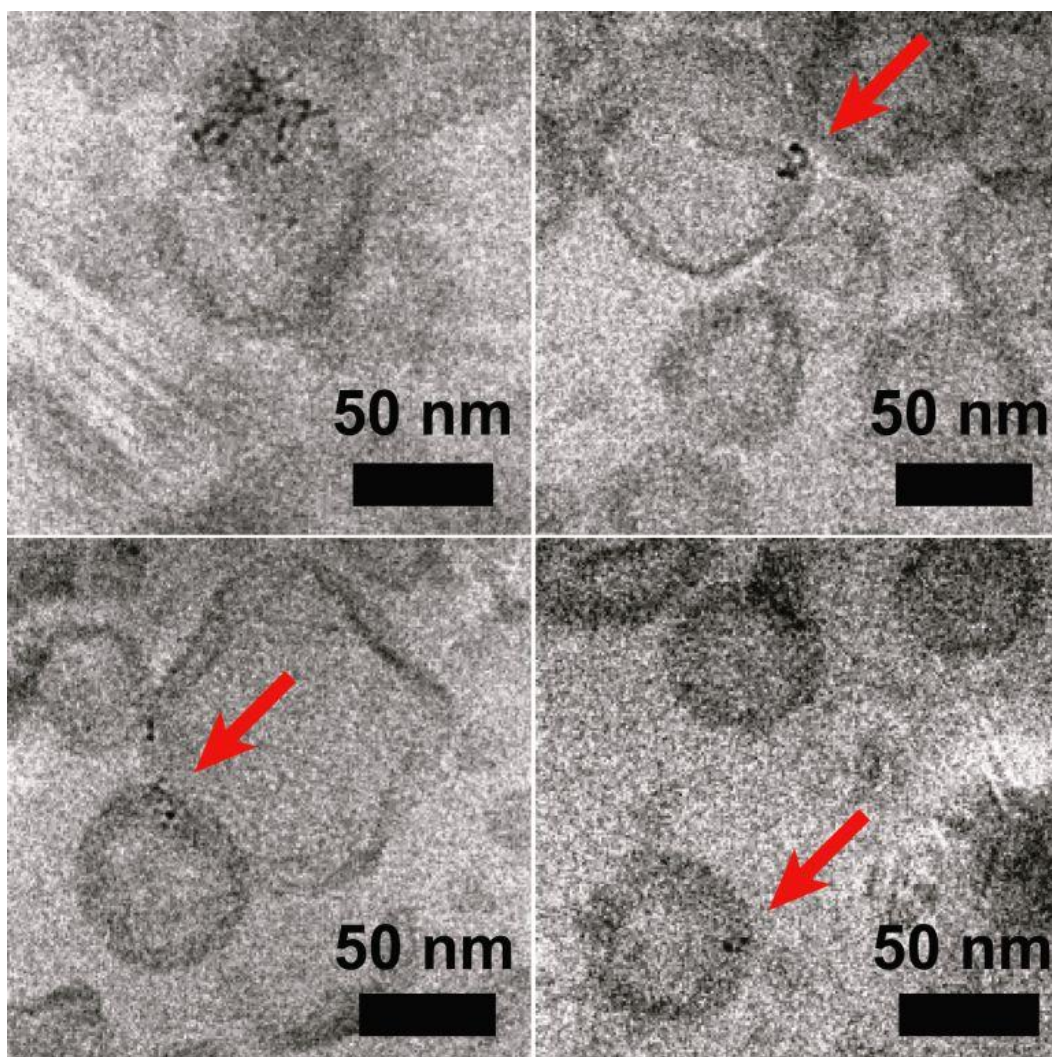


Figure 8.9. CryoTEM of CdSe nanocrystals dispersed with DPPC lipid in water. The red arrows point to CdSe nanocrystals. The sample was vitrified at 25°C, and the lipid melting temperature is 41°C.⁴¹

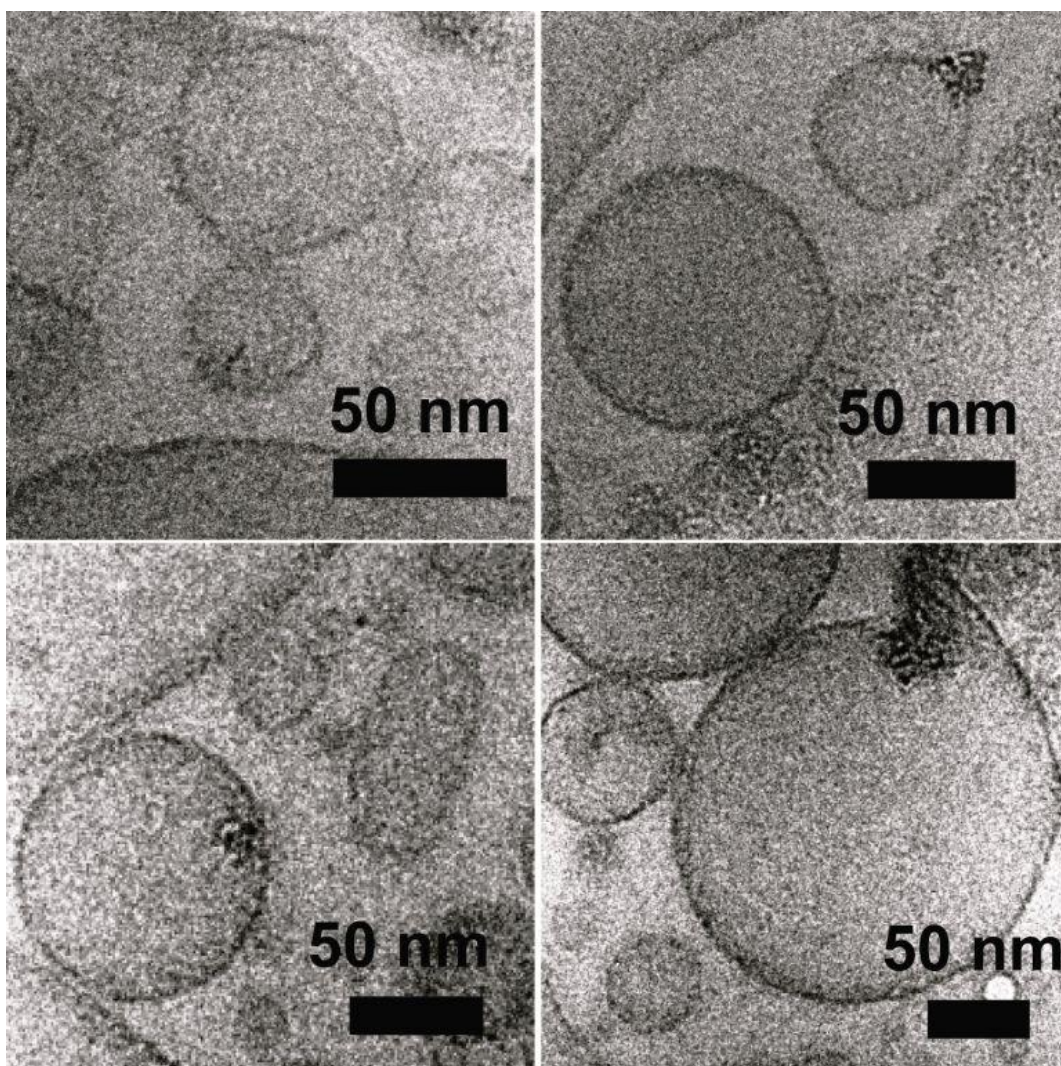


Figure 8.10. CryoTEM images of CdSe nanocrystals dispersed in water with DOPC lipid after annealing with chloroform vapor.

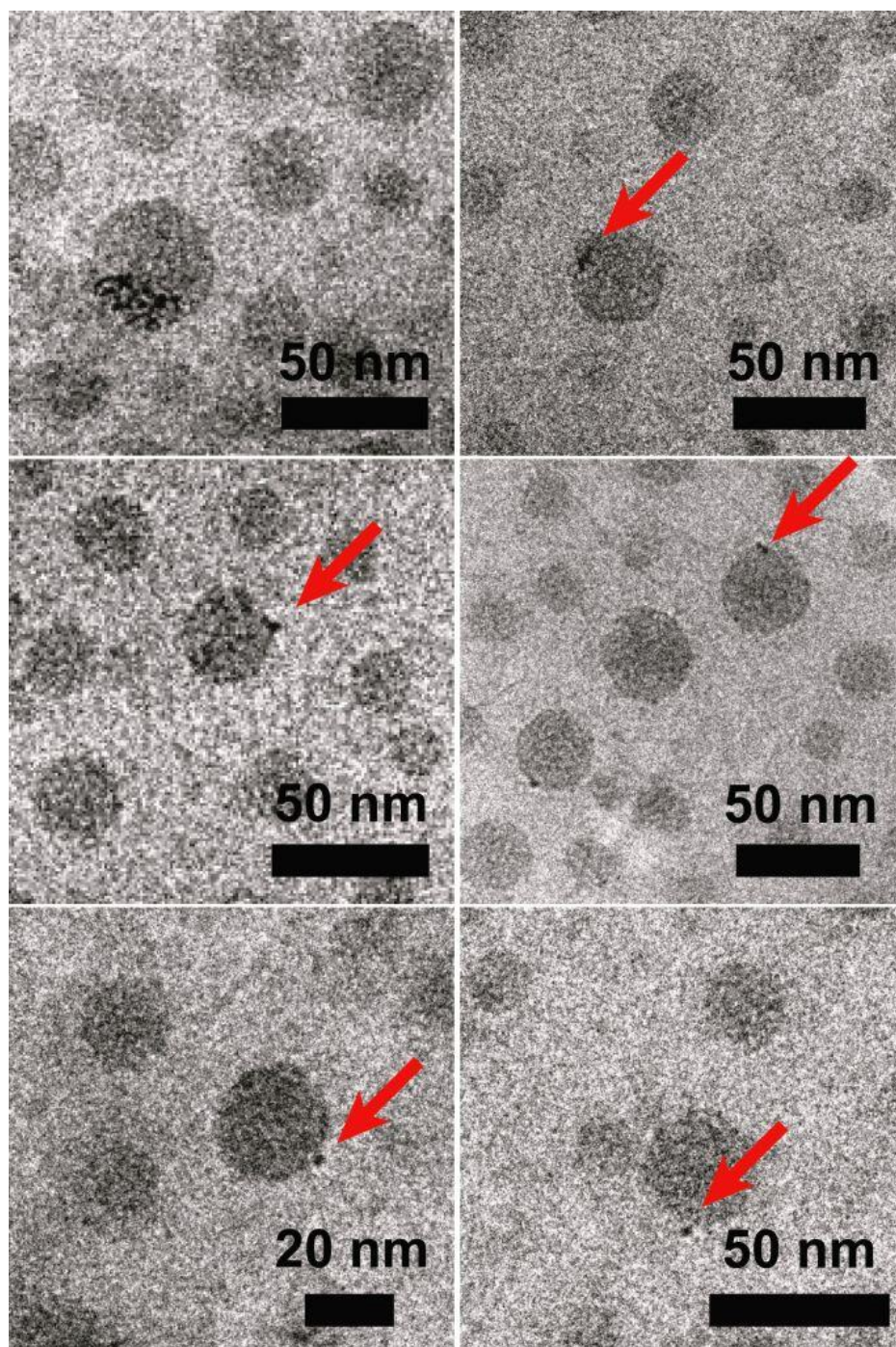


Figure 8.11. CryoTEM images of CdSe nanocrystals incorporated into squalene emulsion droplets, stabilized by DPPC lipid. The red arrows point at single CdSe nanocrystals. The squalene concentration is 5% by volume in water.

8.3.5 Vesicles and Emulsion Particles Loaded with CIS Nanocrystals

The CIS nanocrystals maintained their red luminescence when dispersed in water by lipids and squalene, as shown in Figure 8.12. CryoTEM images of the dispersions are shown in Figures 8.13 – 8.17. With DLPC lipid and 1% v/v squalene concentration, the CIS nanocrystals load the squalene droplets, but there is no obvious localization of nanocrystals at the squalene-water interface as observed with the 1.8 nm Au nanocrystals in Chapter 6. This result is surprising, given that the CIS is about the same size as the 1.8 nm Au nanocrystals and has the same capping ligand (dodecanethiol). The results with DMPC lipid and 1% v/v squalene compare more favorably to 1.8 nm Au, since some 50 nm diameter squalene droplets are fully-loaded with CIS nanocrystals and the nanocrystals are concentrated into a shell around the droplet surface (Figure 8.14). Numerous 10-20 nm diameter squalene droplets are also found in cryoTEM to contain a few CIS nanocrystals, and empty DMPC vesicles are also found. Using DSPC lipid, the shape of the CIS-lipid agglomerates is temperature-sensitive. Figure 8.15 shows the DSPC lipids vitrified at 25°C contain the CIS nanocrystals in faceted structures that adhere to the faceted lipid vesicles. At 58°C (Figure 8.16), the vesicles and CIS structures are spherical since the lipid is now in the liquid crystal phase, but the nanocrystals do not appear to be concentrated at the water interface of squalene droplets. Finally, Figure 8.17 shows the CIS nanocrystals dispersed with DOPC lipid after chloroform annealing. Surprisingly, the CIS nanocrystals only form aggregates adhering to a few lipid bilayers, and the CIS nanocrystals do not completely load the vesicle bilayers as observed with the 1.8 nm dodecanethiol-coated Au nanocrystals in Chapter 5.

Many of the CIS nanocrystals are located in complex lipid particles containing many internal, inter-lamellar attachments, suggesting that the CIS nanocrystals may de-stabilize the DOPC vesicles as observed with the hexadecanethiol-coated 1.8 nm Au and dodecanethiol-coated 4.1 nm Au nanocrystals.

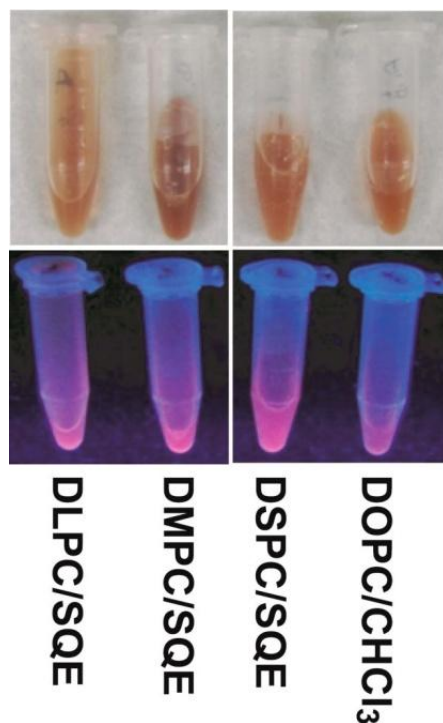


Figure 8.12. Photograph of dodecanethiol-coated CIS nanocrystals dispersed in aqueous vesicles and squalene emulsions at 4 mg/mL concentration. The squalene concentration in each of the emulsions is 1% by volume. The DOPC sample was annealed with chloroform vapor prior to dispersing in water. The solvent is deionized water. The top row shows the samples under room light, the bottom row shows the samples under an ultraviolet lamp (350 nm excitation).

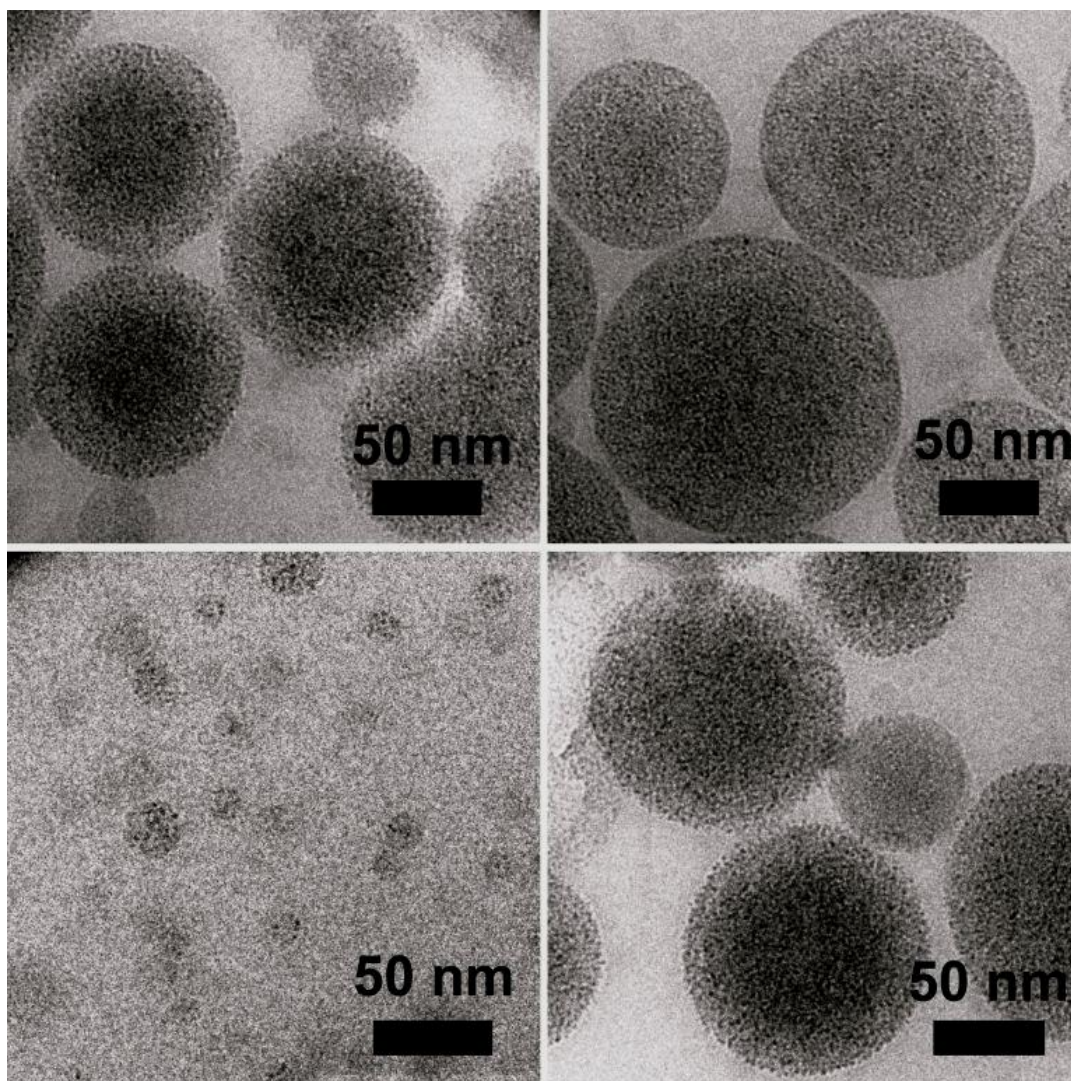


Figure 8.13. CryoTEM images of CIS nanocrystals loaded in squalene droplets, stabilized by DLPC lipid.

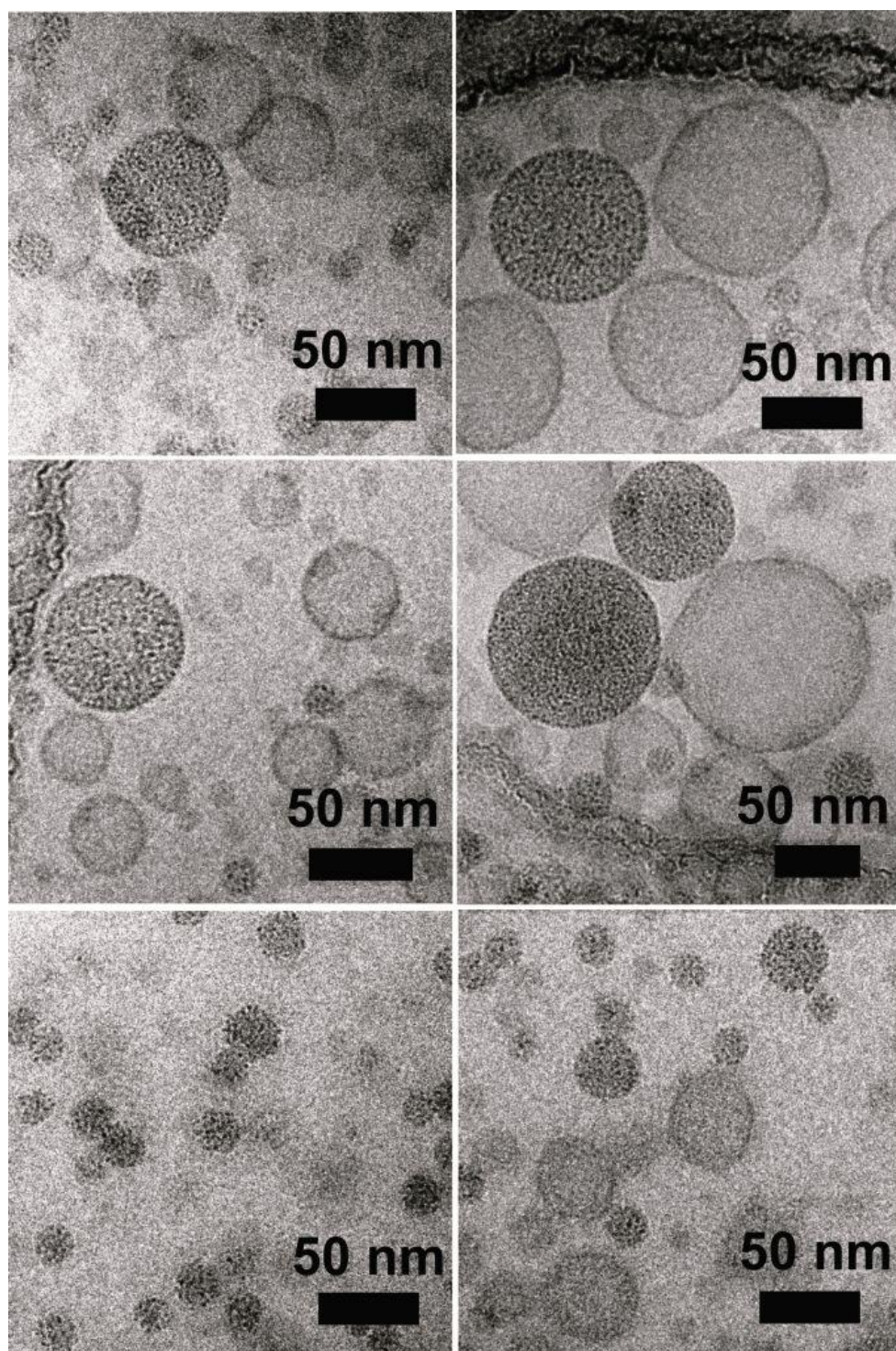


Figure 8.14. CryoTEM images of CIS nanocrystals loaded in squalene droplets, stabilized by DMPC lipid.

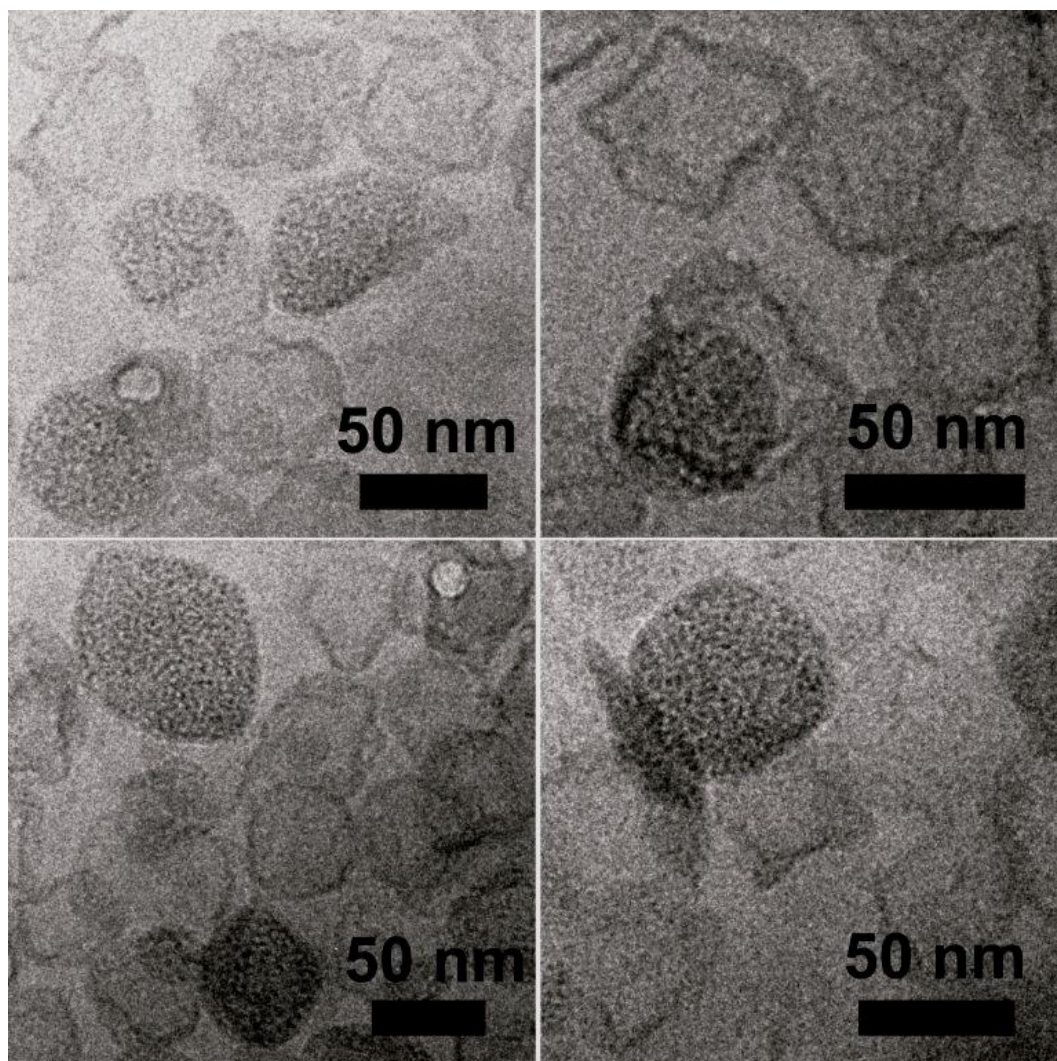


Figure 8.15. CryoTEM images of CIS nanocrystals dispersed with squalene and DSPC lipid. The sample was vitrified at 25°C. DSPC vesicles are faceted because the lipid's gel to liquid crystal phase transition temperature is 55°C.⁴¹

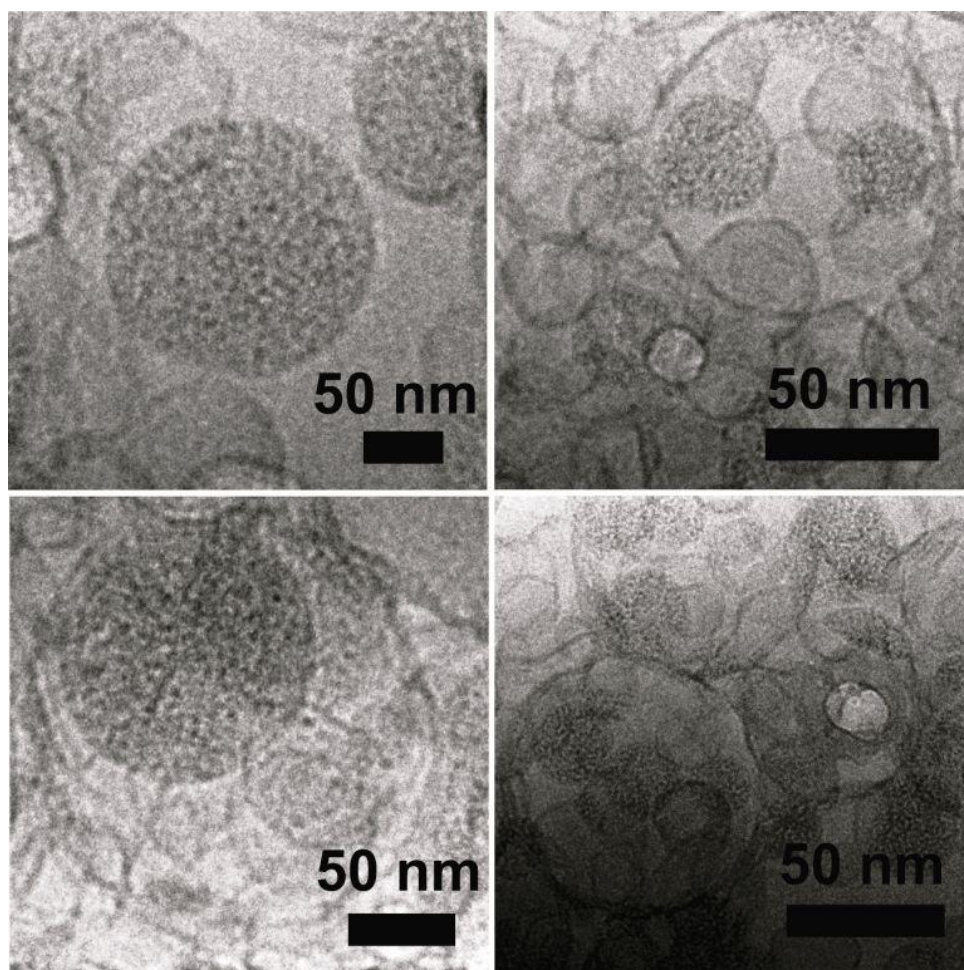


Figure 8.16. CryoTEM images of CIS nanocrystals dispersed with squalene and DSPC lipid. The sample was vitrified at 58°C, above the phase transition temperature of DSPC (55°C)⁴¹, causing the vesicles to be rounded rather than faceted.

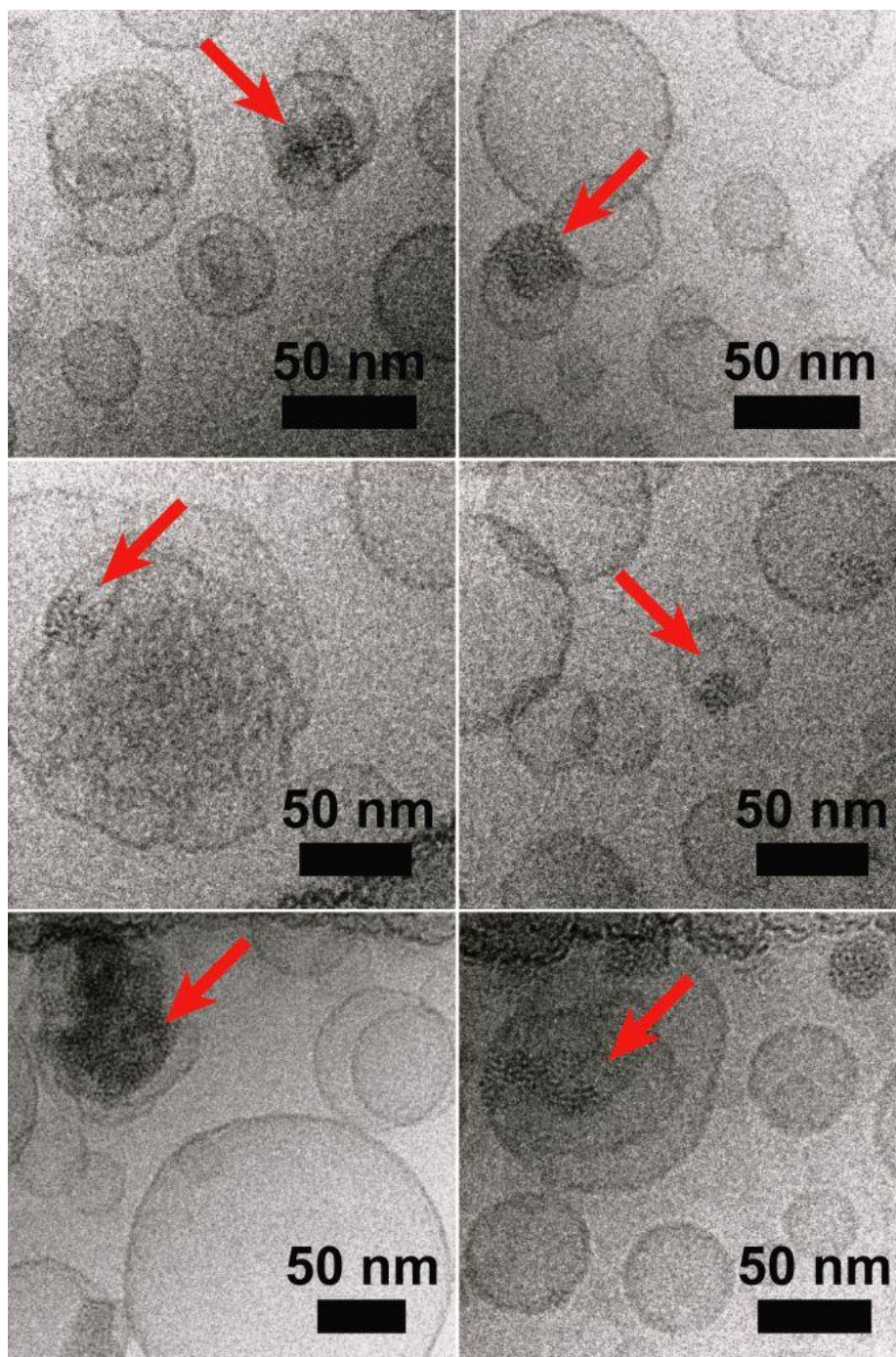


Figure 8.17. CryoTEM images of CIS nanocrystals dispersed with DOPC lipids after annealing a dry CIS/DOPC film with chloroform vapor. The arrows point to clusters of CIS nanocrystals.

8.3.6 Vesicles and Emulsion Particles Loaded with Si

The Si nanocrystals dispersed well in water with the lipids, and subsequently the nanocrystals maintained their orange fluorescence as shown in Figure 8.18. CryoTEM images of the different Si-lipid dispersions are shown in Figures 8.19 – 8.27. Figure 8.19 shows the Si nanocrystals dispersed in water with DOPC after chloroform annealing. The results are the same as with dodecanethiol-coated CIS, hexadecanethiol-coated 1.8 nm Au, and dodecanethiol-coated 4.1 nm Au nanocrystals. The Si nanocrystals form clusters adhering to multiple lipid bilayers and can be found within the complex lipid particles having multiple internal inter-lamellar attachments. The hydrodynamic diameter obtained from DLS is 85 nm ($\chi^2 = 0.0005$).

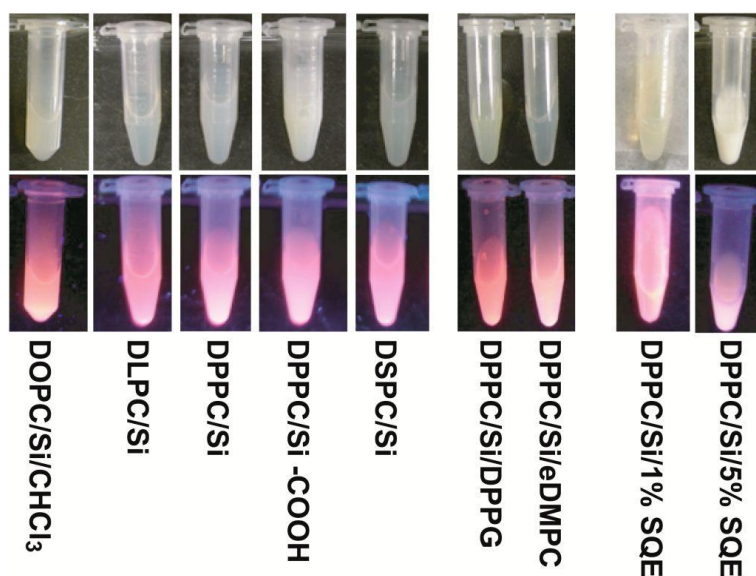


Figure 8.18. Photograph of aqueous dispersions of dodecane-coated Si nanocrystals (4 mg/mL) and different lipids. The solvent is 10 mM HEPES, 10 mM NaCl in water at pH 7.4. The DOPC sample was annealed with chloroform prior to dispersing in water. The DPPC/Si-COOH sample contains silicon nanocrystals passivated with a 100:1 mixture of dodecane and undecanoic acid.

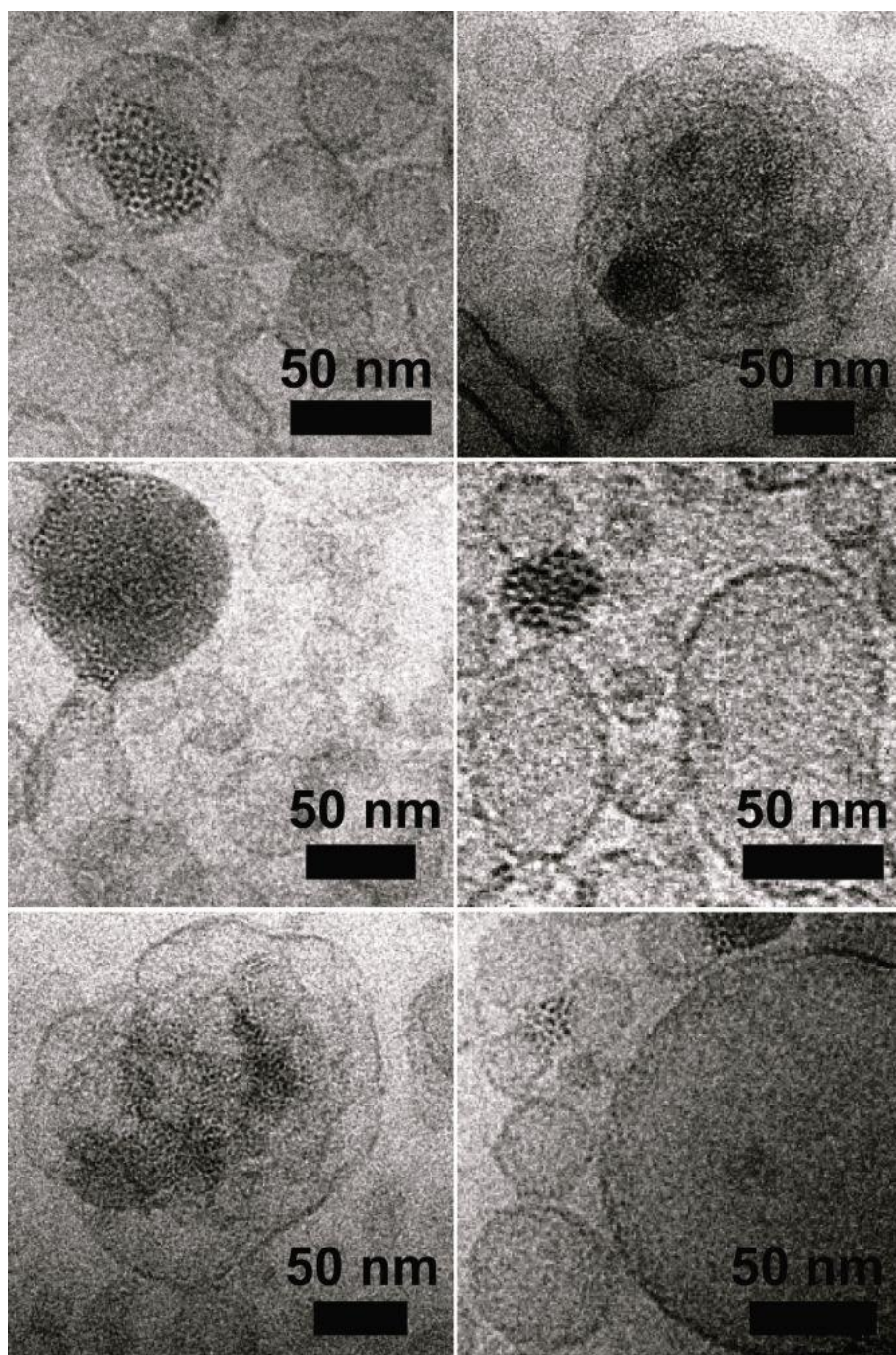


Figure 8.19. CryoTEM images of dodecane-coated Si nanocrystals dispersed in water with DOPC lipid after chloroform annealing.

The cryoTEM images of Si nanocrystals dispersed in water with different saturated lipids show that the nanocrystals form lipid-coated clusters just like the dodecanethiol-coated Au nanocrystals. In Figure 8.20, the Si nanocrystals are coated by DLPC, and no long nanocrystal chains are observed as with the 1.8 nm diameter dodecanethiol-coated Au nanocrystals. The hydrodynamic diameter in the DLPC-Si dispersion is 63 nm from DLS ($\chi^2 = 0.005$). Unlike the DLPC, many Si nanocrystal clusters associate with DPPC vesicles, as shown in Figure 8.21, and the hydrodynamic radius is 74 nm. Adhesion of the hydrophobic Si nanocrystals does not appear to affect the size or shape of the DPPC vesicles, compared to the empty vesicles having no nanocrystals observed in Figure 8.21. Imaging of the DSPC-Si dispersions also revealed that some lipid-coated Si clusters adhere to vesicles (Figure 8.22). The hydrodynamic diameter of the DSPC dispersion is 103 nm, which is larger than the DLPC and DPPC samples.

Next, we considered whether introducing a hydrophilic carboxylic acid onto the surface of the Si nanocrystals would encourage the nanocrystals to distribute throughout the vesicle bilayer to favor hydrogen bonding between the nanocrystal carboxylic acid and the ester and phosphate groups of the lipids. The ratio of 100:1 dodecane to undecanoic acid in this sample is based on the mole ratio of dodecene to undecanoic acid used during the hydrosilylation reaction used to attach the ligands to the Si nanocrystals (see Chapter 4), and it was chosen because it should allow most of the Si nanocrystal surface to be hydrophobic for insertion into the lipid bilayer. The results of the incorporating the mixed ligand Si into DPPC vesicles is shown in Figure 8.23, and the

results essentially look the same as Si nanocrystals coated with just dodecane. Also, the hydrodynamic diameter measured by DLS was 74 nm, which is the same as the sample prepared from Si having 100% dodecane on the surface. Therefore the small amount of carboxylic acid on the silicon surface does not improve nanocrystal incorporation into the lipid bilayers.

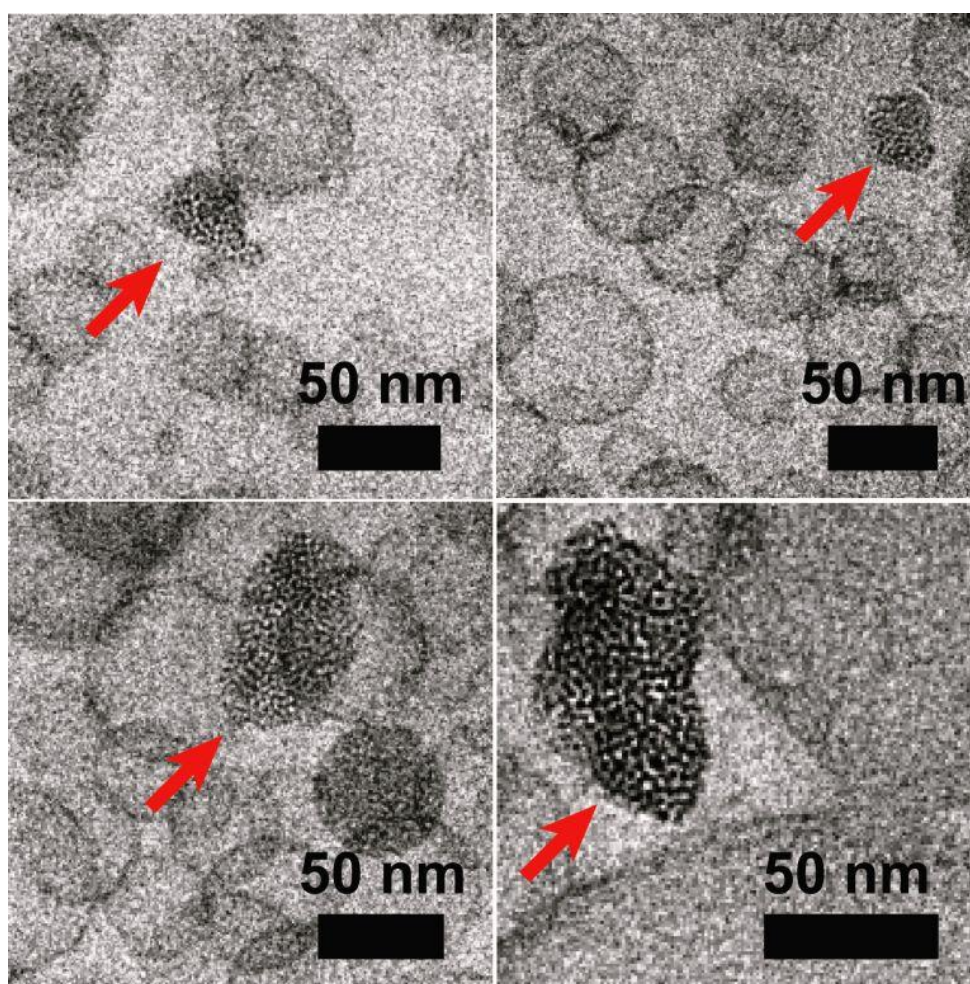


Figure 8.20. CryoTEM images of dodecane-coated Si nanocrystals dispersed in water with DLPC lipid. The red arrows point to the lipid-coated nanocrystal agglomerates.

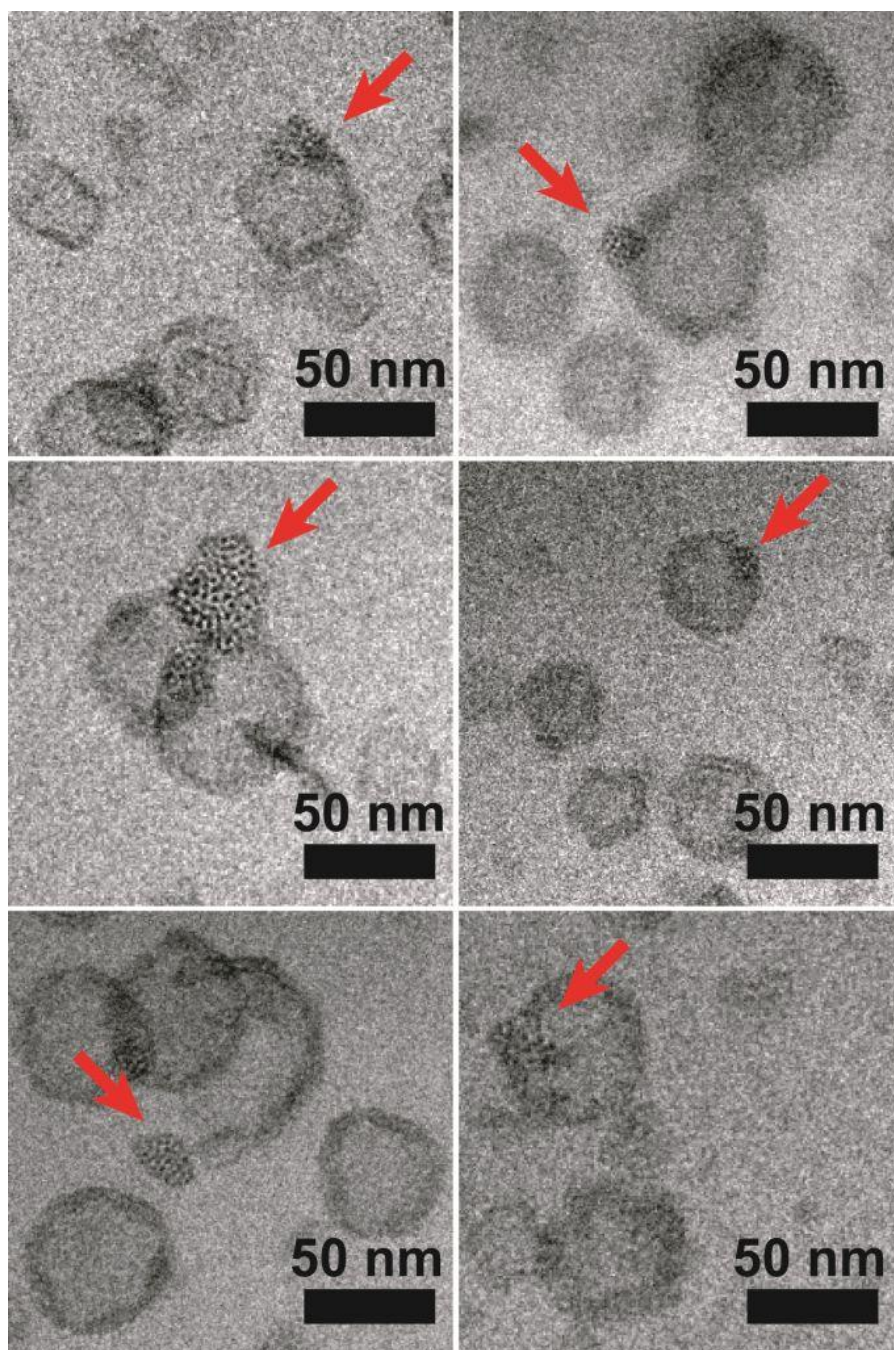


Figure 8.21. CryoTEM images of dodecane-coated Si nanocrystals dispersed in DPPC vesicles in water. The red arrows point to clusters of Si nanocrystals adhering to the vesicle bilayer. The sample was vitrified at 25°C, and the lipid melting temperature is 41°C.⁴¹

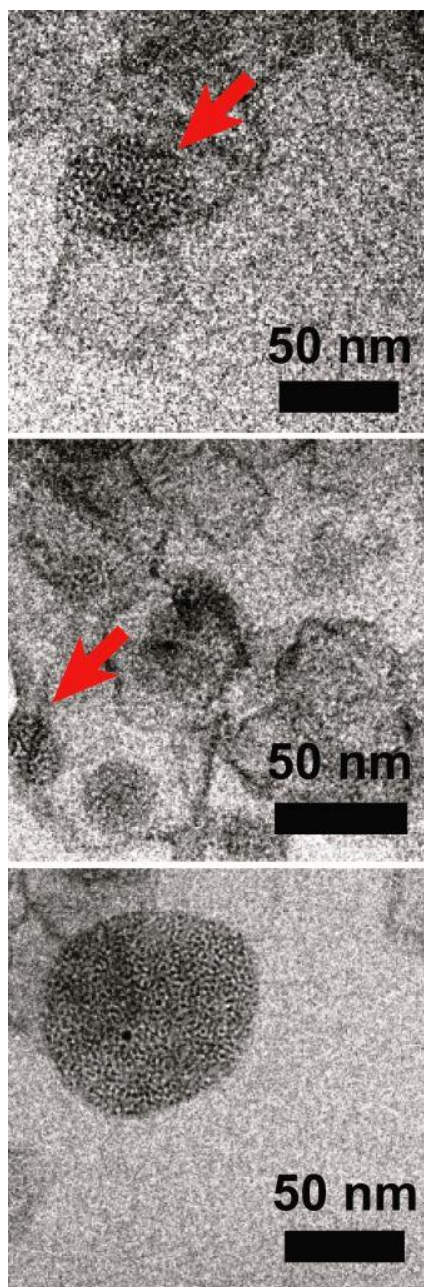


Figure 8.22. Dodecane-coated Si nanocrystals dispersed in water with DSPC lipid. The sample is vitrified at 25°C, and the lipid melting temperature is 55°C.⁴¹ The red arrows point to small clusters of Si nanocrystals that seem to stick to a vesicle bilayer.

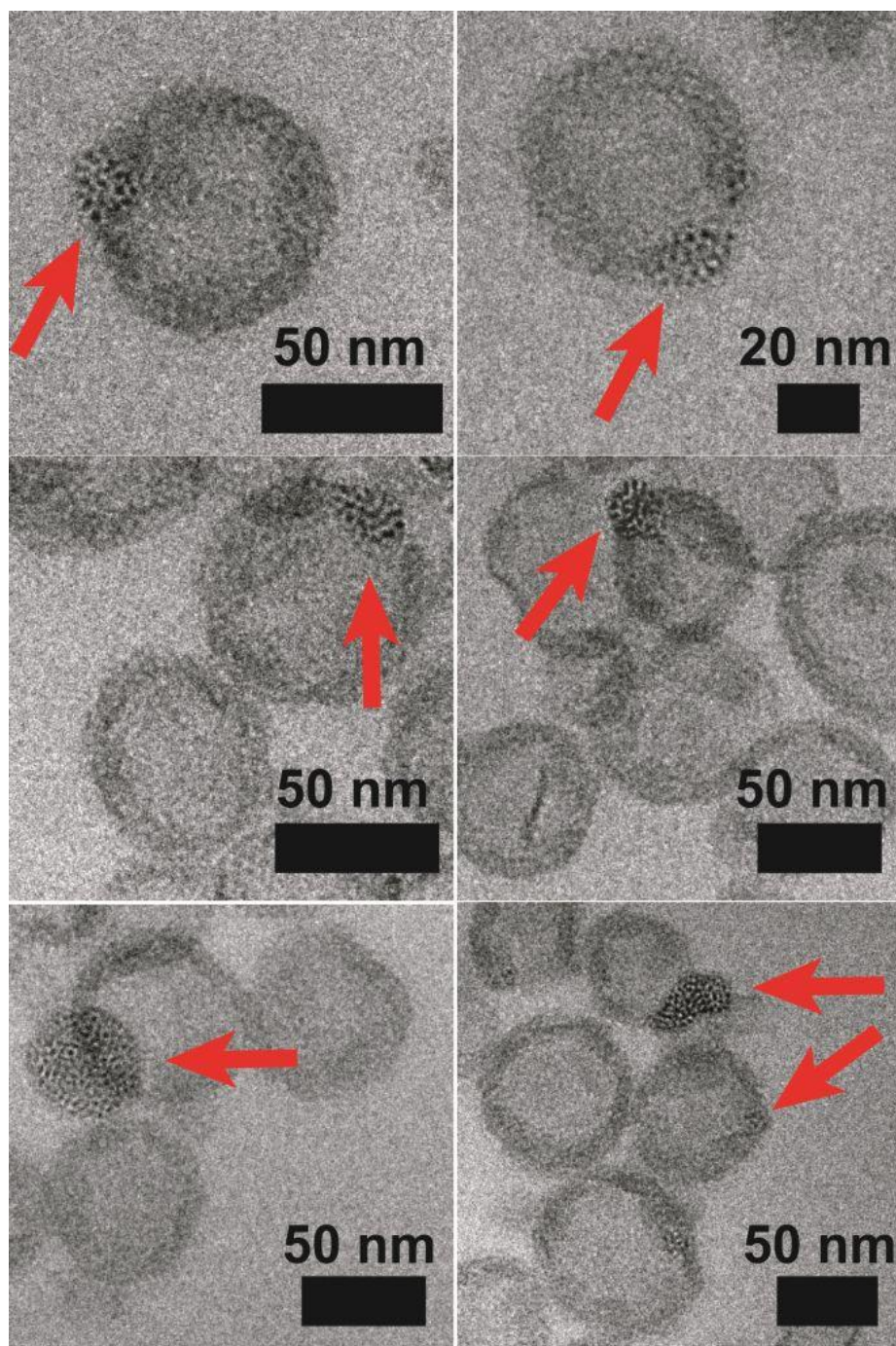


Figure 8.23. Si nanocrystals coated with a 100:1 mixture of dodecane and undecanoic acid and dispersed in DPPC vesicles. The red arrows point to Si nanocrystal clusters. The sample was vitrified at 25°C, and the lipid melting temperature is 41°C.⁴¹

Next, the dodecane-coated Si nanocrystals were dispersed in water using a mixture of DPPC and either DPPG (anionic lipid) or eDMPC (cationic lipid). Practically all of the Si nanocrystals are dispersed as nanocrystal clusters coated by lipid, but the clusters do not associate with the vesicles. The cryoTEM imaging results are shown in Figures 8.24 – 8.25. The lipid-coated Si clusters have irregular shapes. The hydrodynamic diameters of the samples were 55 nm for DPPG/DPPC and 42 nm for eDMPC/DPPC, which agrees well with the cryoTEM imaging results.

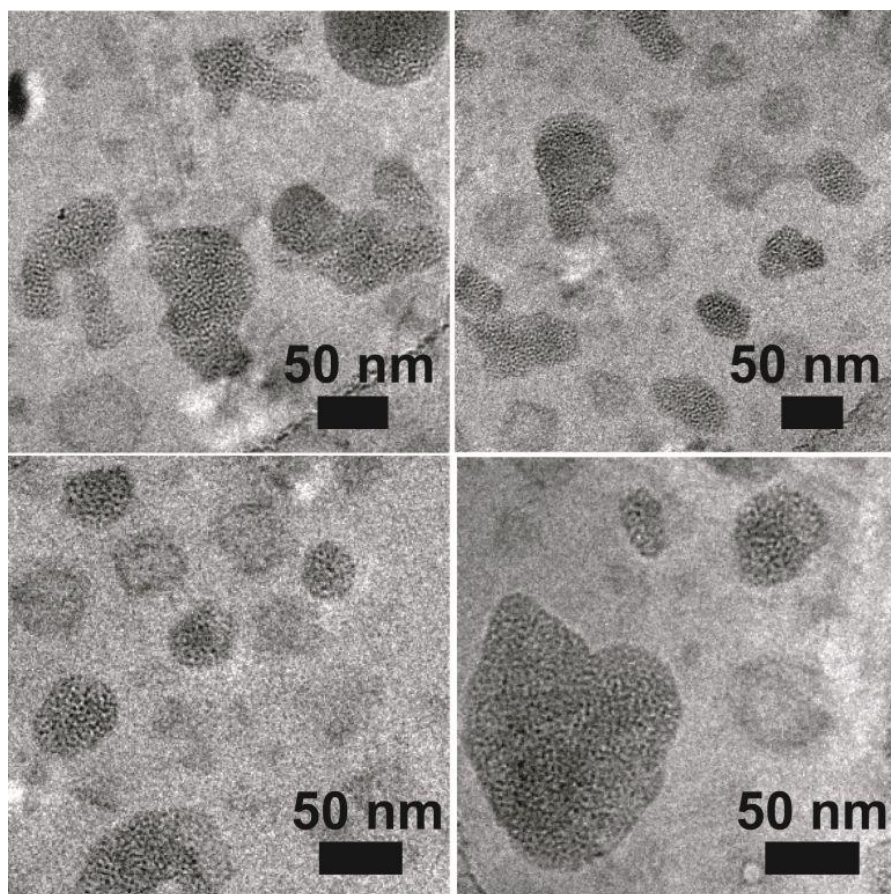


Figure 8.24. Dodecane-coated Si nanocrystals dispersed in water with a 4:1 mixture of DPPC and DPPG lipids.

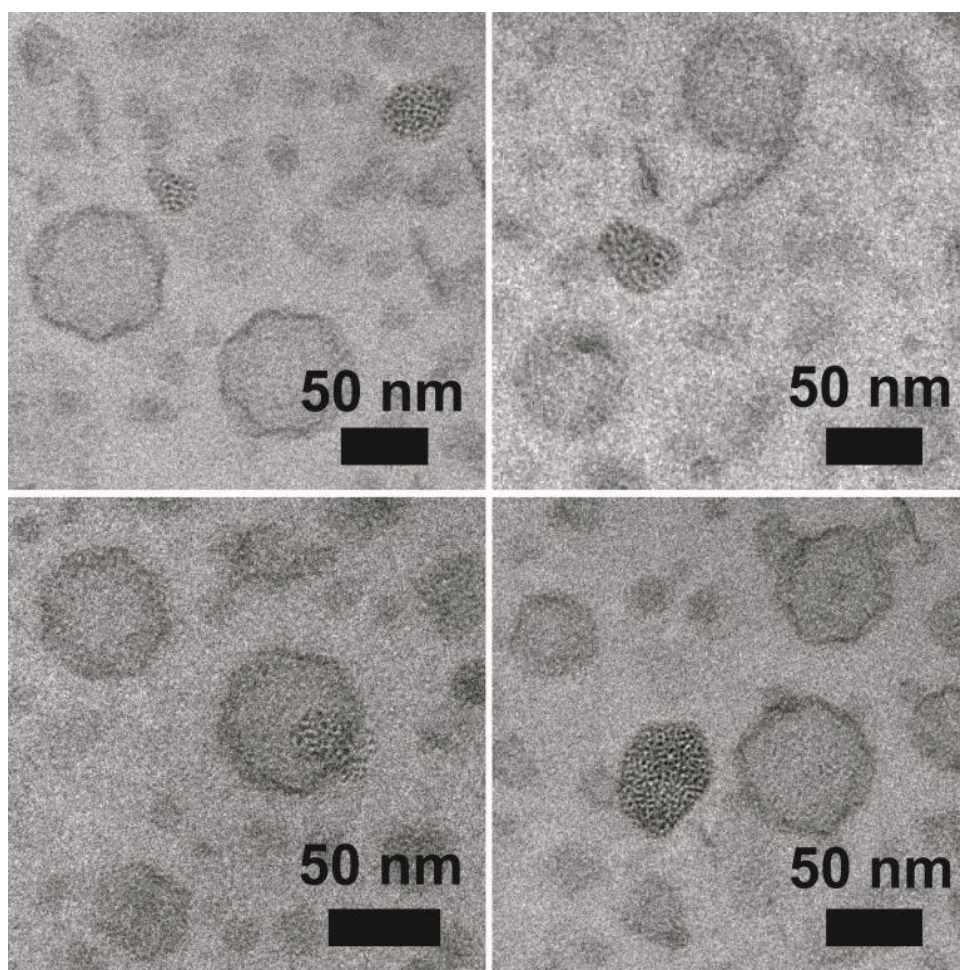


Figure 8.25. Dodecane-coated Si nanocrystals dispersed in water with a 4:1 mixture of DPPC and eDMPC lipids.

The Si nanocrystals were also incorporated into squalene emulsion droplets coated by DMPC and DPPC lipids, and the nanocrystals do not localize at the squalene-water interface. In Figure 8.26, the red arrows indicate one place in the cryoTEM imaging where the edge of the squalene droplet can be seen, showing that the Si nanocrystals are not located there. The Si-squalene emulsion particles, as well as the empty vesicles, are between 25-100 nm diameter, indicating that many small (25 nm)

diameter squalene droplets form during the processing. Figure 8.27 shows Si-lipid particles prepared with 5% squalene by volume, and the squalene droplets are still loaded with nanocrystals though the droplets do not appear to be as densely loaded with Si as in Figure 8.26 (1% squalene). The hydrodynamic diameter measured for the 5% squalene sample was 97 nm, which is a bit larger than the droplet sizes observed in cryoTEM. The smaller droplets will scatter less light than larger particles, so the scattering signal from the smaller droplets may be overwhelmed by the scattering from particles around 100 nm diameter.

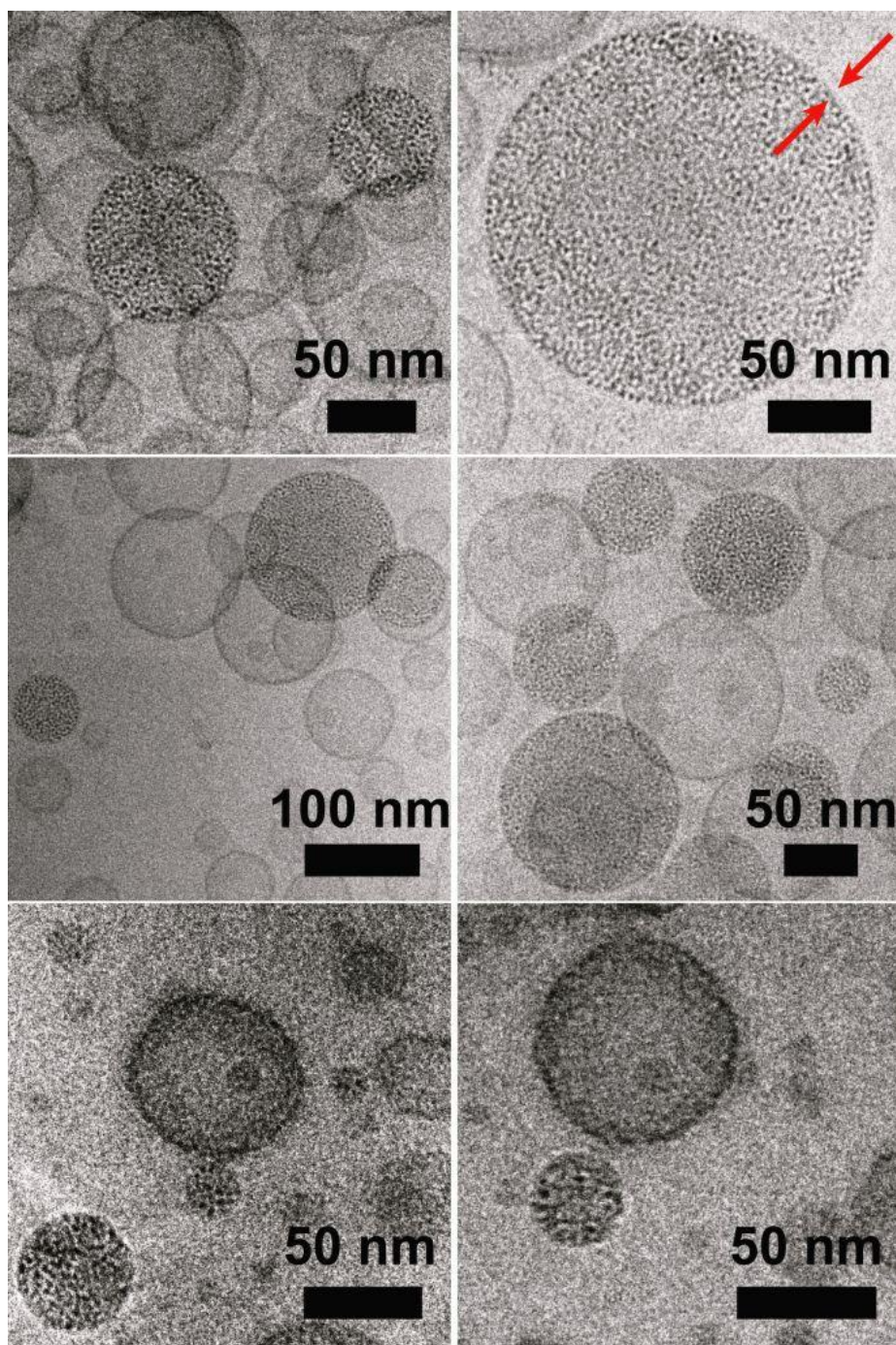


Figure 8.26. Dodecane-coated Si nanocrystals dispersed in water with DMPC lipid and 1% squalene by volume. The red arrows point to the edge of the squalene droplet, which does not seem to be occupied by nanocrystals.

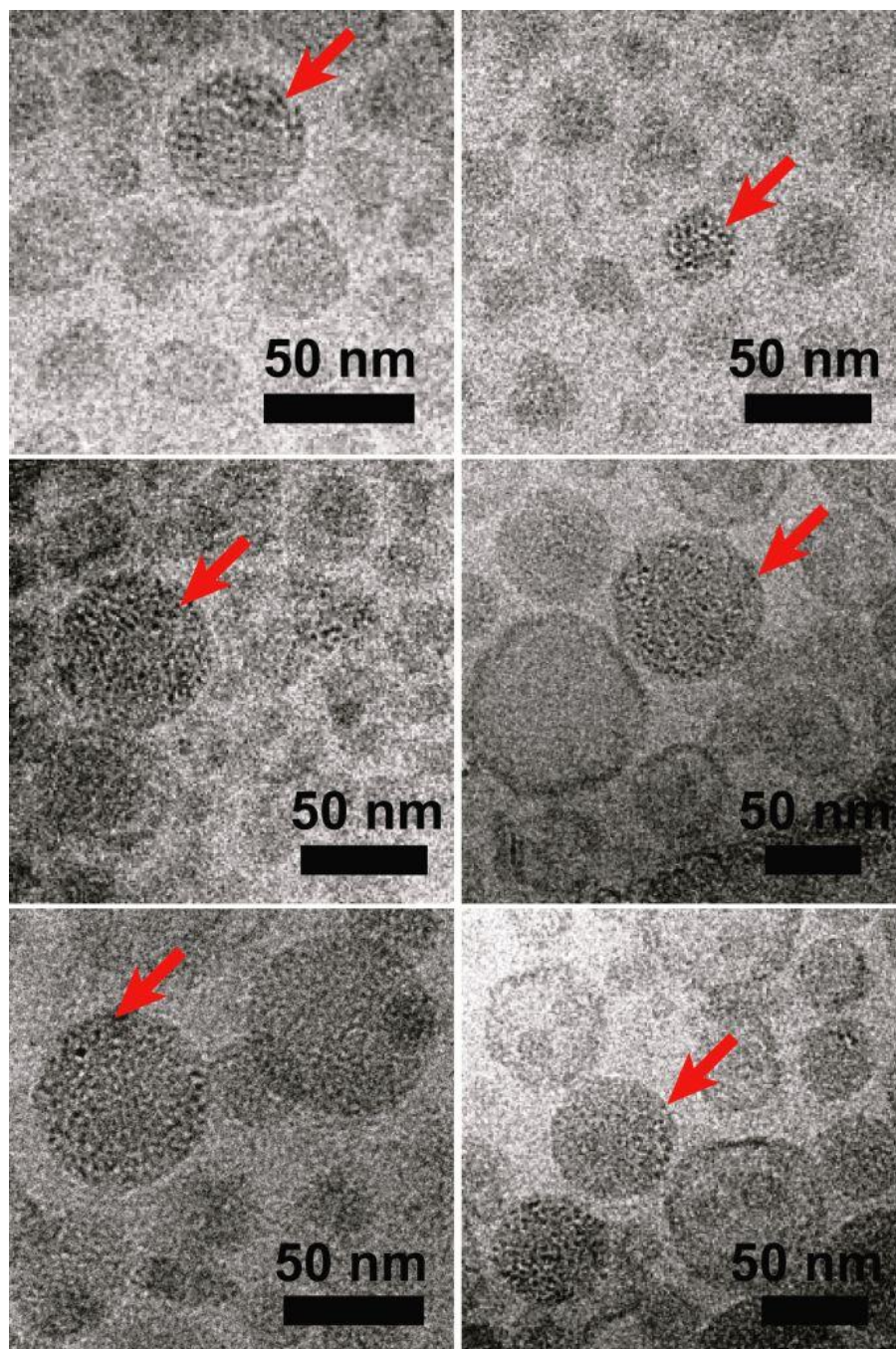


Figure 8.27. Dodecane-coated Si nanocrystals dispersed in water with DPPC lipid and 5% squalene by volume. Red arrows point to squalene droplets loaded with silicon nanocrystals.

8.3.7 HL60 Cell Labeling with Fluorescent Lipid Aggregates and Emulsion Particles

The HL-60 cells were imaged live by suspending them in a chamber sealed between two glass cover slides and a rubber gasket. The cells were exposed to a 514 nm laser, and both transmitted white light as well as the fluorescent orange light (600 – 700 nm) were detected. As the first step in imaging, the normal HL-60 cells were viewed under the microscope without mixing with any of the lipid particles (Figure 8.28). Varying the detector voltage revealed the voltage (about 700 nm) at which the detection of cell autofluorescence becomes significant in the orange detector, indicating that the detector is too sensitive at this voltage for distinguishing the probe fluorescence from autofluorescence. Cell autofluorescence at 600 – 700 nm is largely due to flavin molecules naturally found in HL-60 cells.⁴²⁻⁴⁵ At a detector voltage less than 600 V, no autofluorescence is detected by the orange detector.

The HL-60 cells mixed with the lipid particles containing Nile Red dye were imaged by confocal microscopy, and the results are shown in Figure 8.29. The lipid particles were made of squalene (5% by volume), DLPC lipid, DOTAP, and Nile Red dye. The voltage of the orange detector is 430 V, which is well below the threshold for detecting cell autofluorescence. The cell membrane has bright orange contrast relative to the surrounding medium and the inside of the cell, suggesting that Nile Red dye accumulates in the cell membrane. This suggests that the lipid particles may fuse with the cell membrane, or they may simply bind to the membrane surface and allow the Nile Red dye to escape and enter the cell membrane. No fluorescence accumulates inside the cells, which indicates that endocytosis of the lipid particles and dye does not take place.

Previous reports found that the HL-60 cells are reluctant to endocytose cationic lipid particles as well.³³ Figure 8.30 shows confocal imaging taken of a dispersion of only the cationic lipid particles containing Nile Red, without including the cells. No fluorescent structures were observed that resembled the cells in Figure 8.29.

Confocal Imaging of Cells Only (No dye or Nanocrystals)

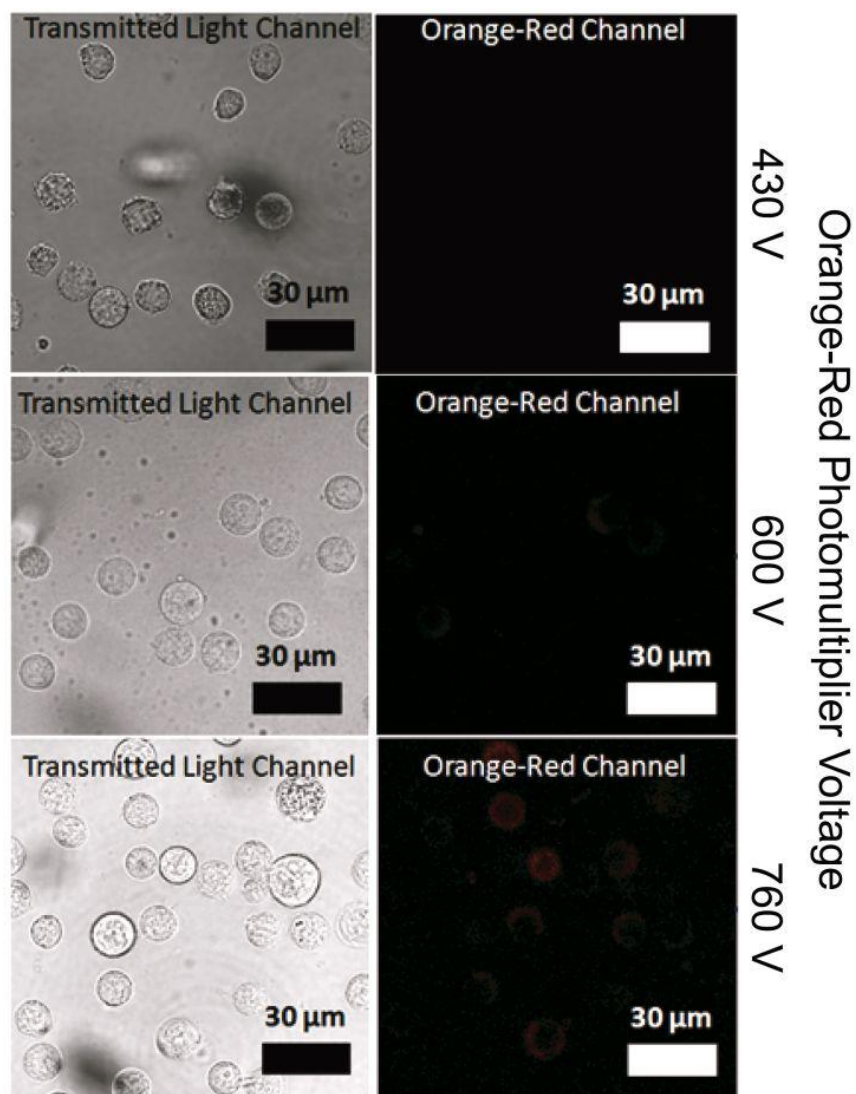


Figure 8.28. Live HL-60 cells imaged with confocal fluorescence microscopy. The photomultiplier voltage of the Orange-Red detector was varied. The left column shows transmitted light images, while the right column shows images of light detected at wavelengths between 600 – 700 nm. The excitation laser had a 514 nm wavelength and was set to 55% power. The cells were dispersed in HBSS without phenol red indicator.

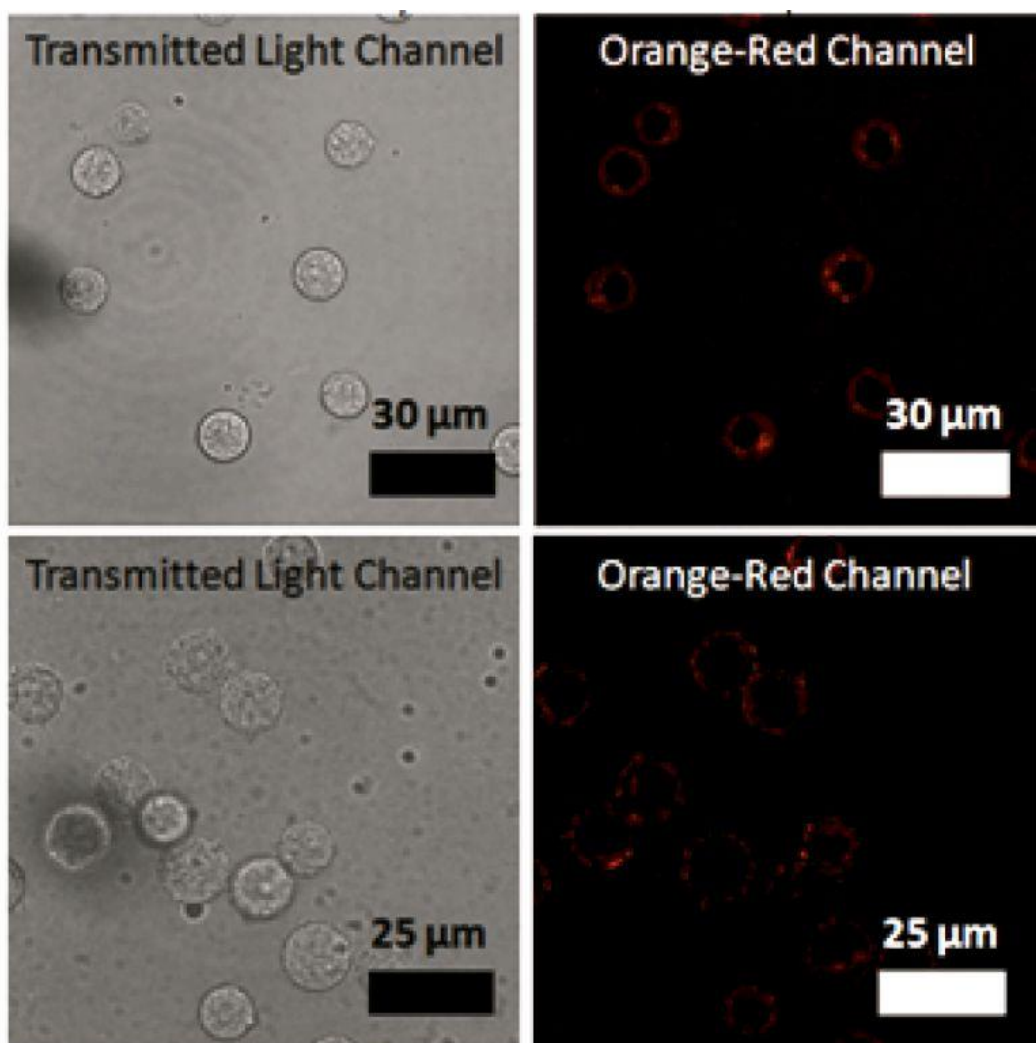


Figure 8.29. Confocal fluorescence microscopy images of live HL-60 cells mixed with Nile Red-loaded squalene droplets coated by a mixture of cationic and zwitterionic lipids. The left column shows transmitted light images, while the right column shows images of light detected at wavelengths between 600 – 700 nm. The cells were dispersed in HBSS without phenol red indicator. The excitation laser had a 514 nm wavelength and was set to 55% power. The orange-red detector's photomultiplier voltage was set to 430V, which is below the detection limit for autofluorescence observed in Figure 8.28.

No Cells

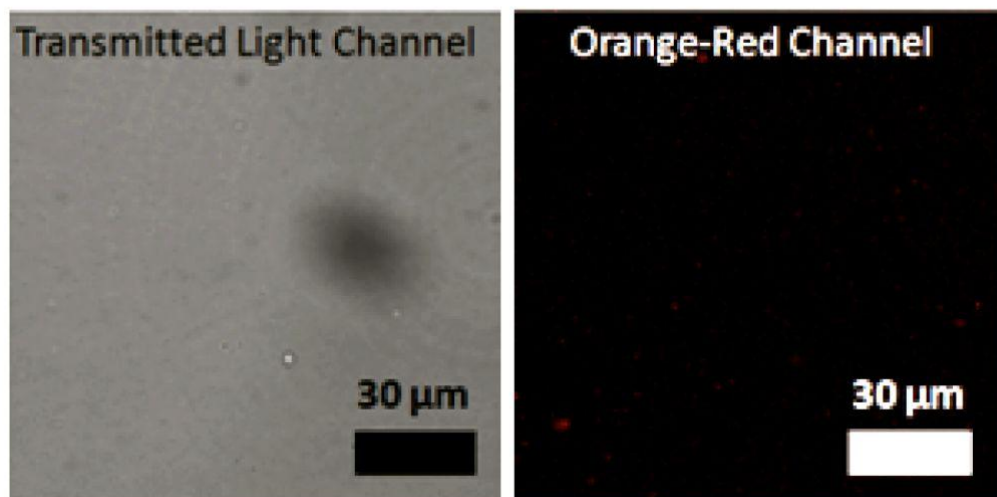


Figure 8.30. Confocal fluorescence microscopy of Nile Red-loaded squalene emulsion droplets coated by a mixture of cationic and zwitterionic lipids. The left column shows transmitted light images, while the right column shows images of light detected at wavelengths between 600 – 700 nm. The particles were dispersed in HBSS without phenol red indicator. The excitation laser had a 514 nm wavelength and was set to 55% power. The orange-red detector's photomultiplier voltage was set to 430V, which is below the detection limit for autofluorescence observed in Figure 8.28.

The Si-loaded cationic lipid particles did not give the cells enhanced fluorescence, as shown in Figure 8.31. The cationic lipid particles were prepared with dodecane-coated Si nanocrystals, DLPC, DOTAP, and 5% squalene by volume. After mixing with the Si-lipid particles, the cells are not fluorescent even up to a photomultiplier voltage of 600 V for the orange-red channel. At 760 V, the cells are autofluorescent just as observed for the cells imaged without Si (Figure 8.28). A complication that could be preventing successful cell labeling is that the cryoTEM imaging for all the Si-lipid samples showed

that the samples contain many empty lipid particles (no Si), and these empty particles could saturate the surface of the cell membranes resulting in very few Si actually sticking to the cells.

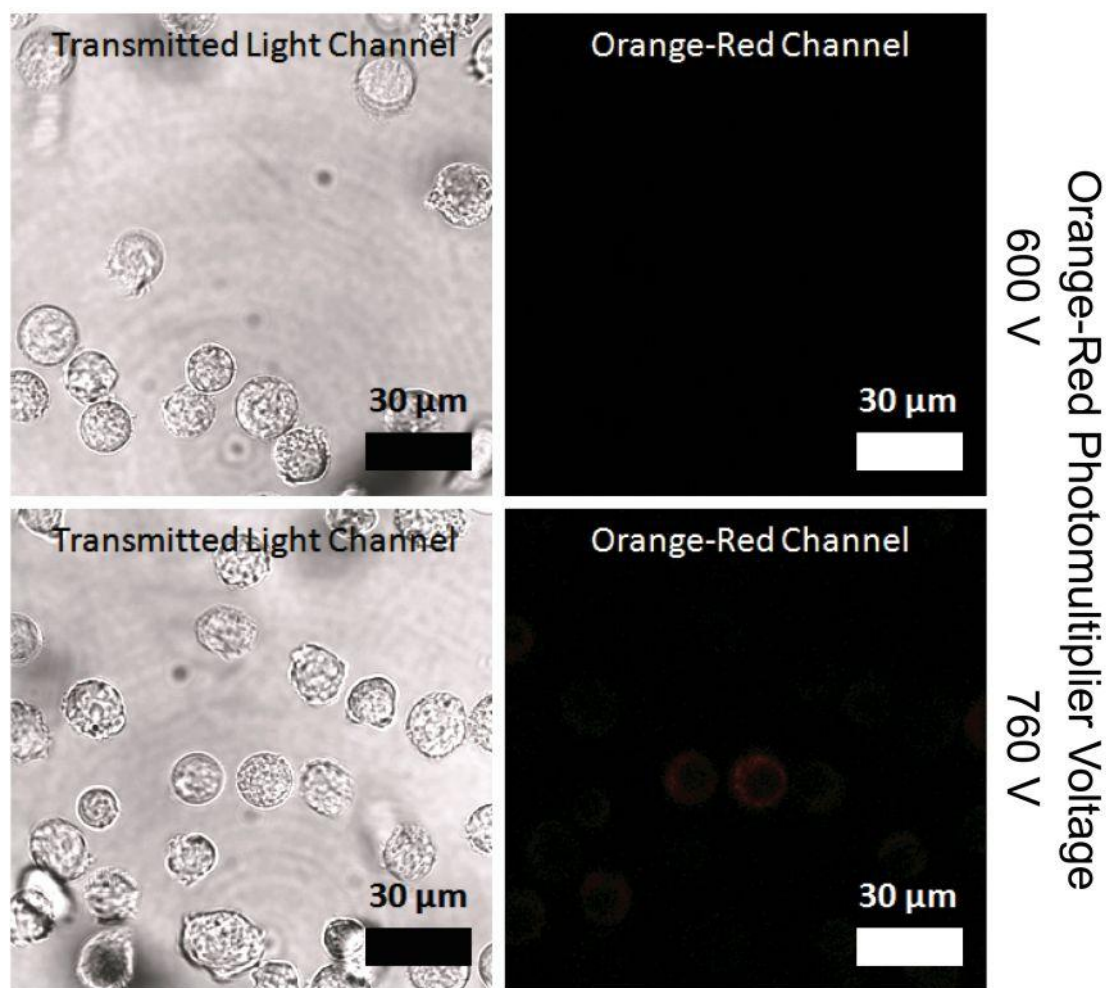


Figure 8.31. Confocal fluorescence microscopy images of live HL-60 cells mixed with squalene droplets loaded with Si nanocrystals and coated by a mixture of cationic and zwitterionic lipids. The left column shows transmitted light images, while the right column shows images of light detected at wavelengths between 600 – 700 nm. The excitation laser had a 405 nm wavelength and was set to 55% power. The orange-red detector’s photomultiplier voltage was varied.

8.4 Conclusions

The hydrophobic semiconductor nanocrystals investigated in this chapter, CdSe, CIS, and Si, did not incorporate into DOPC vesicles very well, unlike the 1.8 nm diameter dodecanethiol-coated Au nanocrystals studied in Chapter 5. With the 1.8 nm Au, the chloroform annealing method using DOPC produced vesicles having lipid bilayers fully-loaded with Au nanocrystals, while the semiconductor nanocrystals did not form any fully loaded vesicles by the same procedure. The CIS nanocrystals have about the same size (1-2 nm diameter) and the same ligand coating (dodecanethiol) as the 1.8 nm Au, yet the CIS nanocrystals do not load DOPC bilayers following chloroform annealing. Besides just the nanocrystal size and lipid composition, the nanocrystal composition also seems to be important for incorporating the nanocrystals into vesicles. Changing the nanocrystal composition from Au to another material alters the van der Waals attractive potential between particles,⁴⁶ and it may also affect the density and stability of ligands packed on the nanocrystal surface. The density of the ligands will affect the steric repulsive force between nanocrystals,⁴⁶ and if ligands easily de-sorb then the ligand density will decrease and the nanocrystals will aggregate.

The hydrophobic CdSe and Si nanocrystals formed lipid-coated agglomerates when dispersed in water with saturated lipids. In this case, the results were similar to the 1.8 nm Au nanocrystals – some of the CdSe and Si nanocrystals were in lipid-coated agglomerates adsorbed to vesicles, and some of the nanocrystal agglomerates were not adsorbed to vesicles. For the agglomerates adsorbed to vesicles, the nanocrystals did not

diffuse throughout the cell membrane, instead the semiconductor nanocrystals remained segregated into an agglomerate. Importantly, the CdSe nanocrystals lost their fluorescence when transferred to water by the lipid, which is a sign of oxidation.⁴⁰ In contrast the Si nanocrystals remained totally luminescent when dispersed in the aqueous lipid structures. The Si and CdSe incorporate into lipid-coated squalene droplets. The CdSe nanocrystals can extend beyond the edge of the liquid squalene into the water phase, suggesting that the CdSe is somewhat hydrophilic. The Si nanocrystals actually seem to pull away from the squalene water interface (Figure 8.26), suggesting that these nanocrystals may be more hydrophobic than CdSe. Nanocrystal hydrophobicity will affect how much of the nanocrystal is in contact with an oil-water interface, based on the oil-water contact angle, unfortunately the contact angle is difficult to determine for the nanocrystals since this type of measurement is done on a macroscopic planar surface (i.e. a contact angle goniometer).

The Si-lipid particles did not work well as a fluorescent label for the HL-60 cells. The cationic lipid-coated squalene droplets loaded with Si nanocrystals was shown in this chapter, and the imaging results with cationic lipid-Si agglomerates (DOTAP and phosphatidylcholine, like Figures 8.20 – 8.25) were the same. The Si did not provide any enhanced fluorescent contrast to the cells relative to background autofluorescence. The Nile Red dye did label cells, and it was delivered to the cells using the same cationic lipid formulations as used to disperse the Si. The Si-lipid dispersions contain a lot of empty lipid particles that may compete with Si-loaded lipid particles for available space on the cell surface (Figures 8.20 – 8.25), which may result in few Si nanocrystals being

adsorbed to the cell membrane at a given time. There are several improvements that can be made on this work. A different cell line that more readily performs endocytosis may be able to internalize the fluorescent nanocrystals,³³ which may result in accumulation of Si inside the cells.^{9,11,47} Synthesis of nanocrystals that have a higher quantum yield (> 10%) will provide brighter nanocrystals that can be detected at a lower photomultiplier voltage, allowing the autofluorescence signal to be filtered out. Different cationic lipids should be tested as well – the lipid Lipofectamine is used very often for binding to cells for transfection,^{20,33} although lipofectamine is only sold commercially as an aqueous formation so it would have to be freeze-dried prior to mixing with hydrophobic nanocrystals in chloroform. Ultimately active targeting of the lipid-Si agglomerates to cells is desired, in order to achieve specific labeling, which may be accomplished by attaching cell-targeting antibodies or nucleic acid aptamers to the agglomerates. HL-60 cells express insulin and transferrin receptors on their outer membrane,³² therefore attaching anti-insulin receptor or anti-transferrin receptor antibodies to the Si-lipid agglomerates is one possible approach to actively targeting the HL-60 cells in the future.

8.5 References

- (1) Carion, O.; Mahler, B.; Pons, T.; Dubertret, B. *Nature Protocols* **2007**, *2*, 2383-2390.
- (2) Erogbogbo, F.; Yong, K. T.; Roy, I.; Xu, G. X.; Prasad, P. N.; Swihart, M. T. *Acs Nano* **2008**, *2*, 873-878.
- (3) Erogbogbo, F.; Ken-Tye, Y.; Hu, R.; Law, W.; Ding, H.; Chang, C.; Prasad, P. N.; Swihart, M. T. *ACS Nano* **2010**, *4*, 5131-5138.
- (4) Al-Jamal, W. T.; Kostarelos, K. *Nanomedicine* **2007**, *2*, 85-98.
- (5) Hessel, C. M.; Rasch, M. R.; Hueso, J. L.; Goodfellow, B. W.; Akhavan, V.; Puvanakrishnan, P.; Tunnell, J. W.; Korgel, B. A. *Small* **2010**, *6*, 2026-2034.
- (6) Medintz, I. L.; Uyeda, H. T.; Goldman, E. R.; Mattoussi, H. *Nature Materials* **2005**, *4*, 435-446.
- (7) Lucey, D. W.; MacRae, D. J.; Furis, M.; Sahoo, Y.; Cartwright, A. N.; Prasad, P. N. *Chemistry of Materials* **2005**, *17*, 3754-3762.
- (8) Dubertret, B.; Skourides, P.; Norris, D. J.; Noireaux, V.; Brivanlou, A. H.; Libchaber, A. *Science* **2002**, *298*, 1759-1762.
- (9) Delehanty, J. B.; Mattoussi, H.; Medintz, I. L. *Analytical and Bioanalytical Chemistry* **2009**, *393*, 1091-1105.
- (10) Wu, X. Y.; Liu, H. J.; Liu, J. Q.; Haley, K. N.; Treadway, J. A.; Larson, J. P.; Ge, N. F.; Peale, F.; Bruchez, M. P. *Nature Biotechnology* **2003**, *21*, 452-452.
- (11) Smith, A. M.; Duan, H. W.; Mohs, A. M.; Nie, S. M. *Advanced Drug Delivery Reviews* **2008**, *60*, 1226-1240.
- (12) Gopalakrishnan, G.; Danelon, C.; Izewska, P.; Prummer, M.; Bolinger, P. Y.; Geissbuhler, I.; Demurtas, D.; Dubochet, J.; Vogel, H. *Angewandte Chemie-International Edition* **2006**, *45*, 5478-5483.
- (13) Bothun, G. D.; Rabideau, A. E.; Stoner, M. A. *Journal of Physical Chemistry B* **2009**, *113*, 7725-7728.
- (14) Al-Jamal, W. T.; Al-Jamal, K. T.; Tian, B.; Lacerda, L.; Bomans, P. H.; Frederik, P. M.; Kostarelos, K. *ACS Nano* **2008**, *2*, 408-418.
- (15) Binder, W. H.; Sachsenhofer, R.; Farnik, D.; Blaas, D. *Physical Chemistry Chemical Physics* **2007**, *9*, 6435-6441.
- (16) Alpar, H. O.; Bason, A. M.; Hickman, J. A.; Richards, F. M.; Field, W. N. *International Journal of Pharmaceutics* **1990**, *62*, 133-141.
- (17) Fontes, A.; Fernandes, H. P.; Barjas-Castro, M. L.; de Thomaz, A. A.; de Ysasa Pozzo, L.; Barbosa, L. C.; Cesar, C. L. *Proceedings of SPIE* **2006**, *6088*, 608811.
- (18) Crook, K.; Stevenson, B. J.; Dubouchet, M.; Porteous, D. J. *Gene Therapy* **1998**, *5*, 137-143.
- (19) Templeton, N. S. *Bioscience Reports* **2002**, *22*, 283-295.
- (20) Shou, Y.; Baron, S.; Poncz, M. *Journal of Biological Chemistry* **1998**, *273*, 5716-5726.
- (21) Nchinda, G.; Uberla, K.; Zschornig, O. *Bmc Biotechnology* **2002**, *2*.

- (22) Chen, A. A.; Derfus, A. M.; Khetani, S. R.; Bhatia, S. N. *Nucleic Acids Research* **2005**, *33*, e190.
- (23) Yukawa, H.; Mizufune, S.; Mamori, C.; Kagami, Y.; Oishi, K.; Kaji, N.; Okamoto, Y.; Takeshi, M.; Noguchi, H.; Baba, Y.; Hamaguchi, M.; Hamajima, N.; Hayashi, S. *Cell Transplant* **2009**, *18*, 591-599.
- (24) Satarug, S.; Baker, J. R.; Urbenjapol, S.; Haswell-Elkins, M.; Reilly, P. E. B.; Williams, D. J.; Moore, M. R. *Toxicology Letters* **2003**, *137*, 65-83.
- (25) Frasco, M. F.; Chaniotakis, N. *Analytical and Bioanalytical Chemistry* **2010**, *396*, 229-240.
- (26) Medintz, I. L.; Mattoussi, H.; Clapp, A. R. *International Journal of Nanomedicine* **2008**, *3*, 151-167.
- (27) Jang, H.; Pell, L. E.; Korgel, B. A.; English, D. S. *Journal of Photochemistry and Photobiology a-Chemistry* **2003**, *158*, 111-117.
- (28) Dalton, W. T. J.; Ahearn, M. J.; McCredie, K. B.; Fleireich, E. J.; Stass, S. A.; Trujillo, J. M. *Blood* **1988**, *71*, 242-247.
- (29) Gallagher, R.; Collins, S.; Trujillo, J.; McCredie, K.; Ahearn, M.; Tsai, S.; Metzgar, R.; Aulakh, G.; Ting, R.; Ruscetti, F.; Gallo, R. *Blood* **1979**, *54*, 713-733.
- (30) Collins, S. J. *Blood* **1987**, *70*, 1233-1244.
- (31) Fleck, R. A.; Romero-Steiner, S.; Nahm, M. H. *Clinical and Diagnostic Laboratory Immunology* **2005**, *12*, 19-27.
- (32) Birnie, G. D. *British Journal of Cancer* **1988**, *58*, 41-45.
- (33) Esendagli, G.; Canpinar, H.; Dogan, A. L.; Akkaya, M.; Kansu, E.; Guc, D. *Cytotechnology* **2009**, *61*, 45-53.
- (34) Chu, T. C.; Shieh, F.; Lavery, L. A.; Levy, M.; Richards-Kortum, R.; Korgel, B. A.; Ellington, A. D. *Biosensors & Bioelectronics* **2006**, *21*, 1859-1866.
- (35) Greenspan, P.; Fowler, S. D. *Journal of Lipid Research* **1985**, *26*, 781-789.
- (36) Van Zanten, J. H.; Monbouquette, H. G. *Journal of Colloid and Interface Science* **1994**, *165*, 512-518.
- (37) Fereshney, R. I. *Culture of Animal Cells: A Manual of Basic Technique and Specialized Applications*; 6th ed.; John Wiley & Sons, Inc.: Hoboken, 2010.
- (38) SDBSWeb : <http://riodb01.ibase.aist.go.jp/sdbs/> (National Institute of Advanced Industrial Science and Technology, July 2012)
- (39) Coates, J. In *Encyclopedia of Analytical Chemistry*; Meyers, R. A., Ed.; John Wiley & Sons Ltd: Chichester, 2000, p 10815-10837.
- (40) Pechstedt, K.; Whittle, T.; Baumberg, J.; Melvin, T. *Journal of Physical Chemistry C* **2010**, *114*, 12069-12077.
- (41) Marsh, D. *CRC Handbook of Lipid Bilayers*; CRC Press, Inc.: Boca Raton, FL, 1990.
- (42) Monici, M.; Pratesi, R.; Bernabei, P. A.; Caporale, R.; Ferrini, P. R.; Croce, A. C.; Balzarini, P.; Bottiroli, G. *Journal of Photochemistry and Photobiology B: Biology* **1995**, *30*, 29-37.
- (43) Aubin, J. E. *Journal of Histochemistry and Cytochemistry* **1979**, *27*, 36.

- (44) Xiao, L.; Liao, X.; Lin, L.; Huang, H.; Chen, Y.; Li, B. *Proceedings of SPIE* **2010**, 7845, 78452G.
- (45) Rhee, H.-W.; Choi, H.-Y.; Han, K.; Hong, J.-I. *Journal of the American Chemical Society* **2007**, 129, 4525-4525.
- (46) Israelachvili, J. N. *Intermolecular and Surface Forces*; 2nd ed.; Academic press Inc.: San Diego, 1992.
- (47) Delehanty, J. B.; Bradburne, C. E.; Medintz, I. L.; Farrell, D.; Pons, T.; Brunel, F. M.; Dawson, P. E.; Mattoussi, H. *Colloidal Quantum Dots for Biomedical Applications Iii* **2008**, 6866, K8660.

Chapter 9: Conclusions and Outlook

9.1 Conclusions

9.1.1 Amphiphilic Polymer Coating

Chapters 3 and 4 demonstrate the synthesis of an amphiphilic polymer that can coat hydrophobic semiconductor nanocrystals, enabling the nanocrystals to disperse in water. The polymer coating is a simple and robust method to transfer the hydrophobic nanocrystals into water, since it works for nanocrystals having various inorganic cores, sizes, and ligand compositions.¹⁻³ Importantly, the polymer coating preserves the optical properties of the nanocrystals when they are transferred into water, which was important for testing them in biological media. The polymer coating keeps the hydrodynamic diameter of the nanocrystals in water between 20-50 nm, which is desired to encourage the nanocrystals to be retained in tissue long enough to perform measurements or therapy. The polymer coating contains numerous carboxylate groups, which should offer sites for cross-linking to biological targeting molecules (e.g. antibodies or aptamers); however, these carboxylate groups also control the ionic strength- and pH-dependent stability of the polymer coated nanocrystals in water. If the carboxylate groups on the polymer are protonated at low pH (< 7), or if the electric double layer they help establish around the polymer is screened by increasing the ionic strength (> 2 M), then the polymer-coated nanocrystals flocculate. Preliminary tests with adsorbing albumin protein to the polymer-coated nanocrystals suggest that protein adsorption creates a barrier to particle flocculate at low pH.

9.1.2 Au Nanoshells, Au Nanorods, and Cu_{2-x}Se Nanocrystals for Photothermal Therapy

Chapters 2 and 3 demonstrate the synthesis of Au nanoshells, Au nanorods, and Cu_{2-x}Se nanocrystals and compare their photothermal transduction efficiencies when excited with a near infrared laser. The key results were that the photothermal transduction efficiency of the Cu_{2-x}Se nanocrystals was comparable with that of the Au nanorods and Au nanoshells, the Cu_{2-x}Se nanocrystals do not appear to cause any acute toxicity to cells, and the Cu_{2-x}Se nanocrystals enhanced cell death under laser irradiation. The photothermal transduction efficiency of the Au nanoshells was noticeably lower than the Cu_{2-x}Se nanocrystals and Au nanorods, and this is attributed to the nanoshells scattering much more light than the other nanoparticles,³ since the nanoshells have a much larger diameter (and therefore a larger scattering cross section). The nanoshell diameter was 140 nm, while the effective diameter of the Au nanorods and the Cu_{2-x}Se nanocrystals was around 16 nm.

In Chapter 2, the synthesis of smaller (< 100 nm) diameter Au nanoshells was investigated, and it was found to be very challenging compared to making nanoshells larger than 100 nm diameter. Growing Au nanoshells on silica core particles between 20 – 40 nm is complicated by the tendency of the core particles to stick together, which results in the formation of a network of Au-silica aggregates during Au shell deposition. The absorbance maximum of the Au nanoshells grown on 20 – 40 nm could not be tuned past 650 nm, and this is undesirable for photothermal therapy since near infrared excitation is needed to minimize the absorption of the excitation light by tissue.⁴ The

nanoshell absorbance maximum (i.e. the plasmon resonance frequency) is determined by the nanoshell geometry – the thickness of the Au shell divided by the radius of the silica core – and reducing the shell/core size ratio shifts the absorbance maximum from visible to near infrared wavelengths.⁵ The nanoshells are grown from 2-3 nm diameter Au seed particles deposited on the silica core, and decreasing the silica core size increases the minimum shell/core ratio that can possibly be attained with this chemistry. Therefore the minimum Au nanoshell size that can be produced with this chemistry, yielding nanoshells with significant absorbance in the near infrared, is around 140 nm. Producing smaller diameter nanoshells with stronger near infrared absorbance will require the development of new chemistry.

9.1.3 Loading Hydrophobic Au Nanocrystals into Phospholipid Vesicles

Vesicles are being widely investigated for transporting both hydrophilic and hydrophobic drugs,^{6,7} and incorporating nanocrystals into vesicles may create a hybrid nanomaterial capable of simultaneous drug delivery, biomedical imaging, and therapy.⁸⁻¹⁰ Dodecanethiol-coated Au nanocrystals were used to investigate the incorporation of hydrophobic nanocrystals into vesicle bilayers. The Au nanocrystals were of interest because they can be easily synthesized, and the nanocrystal diameter is tunable by controlling the synthesis conditions.^{11,12} Chapters 5-7 show different ways in which the hydrophobic Au nanocrystals were incorporated into lipid vesicles, and the results were found to depend on the nanocrystal size, the molecular structure of the lipids, and the use of additives during the vesicle formation process.

In Chapter 5, it is shown that the incorporation of dodecanethiol-coated 1.8 nm diameter Au nanocrystals into vesicles made of unsaturated phosphatidylcholine lipids was greatly enhanced by including residual chloroform solvent in the vesicles. Without chloroform, the 1.8 nm diameter Au nanocrystals agglomerate when dispersed in water with the unsaturated lipids and do not load the vesicle bilayers. When the lipids absorb a small amount of chloroform, the 1.8 nm diameter Au nanocrystals incorporate into the unsaturated lipid bilayers, forming a tightly-packed monolayer shell of nanocrystals inside the lipid bilayer. The incorporation of Au nanocrystals into the lipid bilayers was also dependent on nanocrystal size – even with chloroform present, dodecanethiol-coated 4.1 nm Au and hexadecanethiol-coated 1.8 nm Au nanocrystals did not completely load the unsaturated lipid bilayers, and instead the larger nanocrystals seemed to cause the fusion of lipid bilayers and the collapse of vesicles into complex lipid particles having many internal, crisscrossing lamellae. Chloroform is known to alter the properties of lipid bilayers, such as decreasing the viscosity,^{13,14} altering the lateral pressure distribution,^{13,15-17} and increasing the bilayer thickness.¹³ It is expected that some combination of these changes are responsible for the greatly enhanced incorporation of Au nanocrystals into the lipid bilayer, however the bilayer viscosity and lateral pressure distribution are difficult to measure reliably at this point.¹⁷ Accurately probing the lipid bilayer thickness requires synchrotron x-ray scattering or neutron scattering measurements,¹⁸ which require specialized facilities.

In Chapter 6, the 1.8 nm and 4.1 nm diameter dodecanethiol-coated Au nanocrystals were shown to disperse in water with saturated phosphatidylcholine lipids

having different fatty acid chain lengths, but cryoTEM imaging revealed that the nanocrystals merely form lipid-coated agglomerates. The agglomerates adhere to pure lipid vesicles or float freely in the dispersion. Interestingly, with the 1.8 nm Au, the shape of the lipid-nanocrystals agglomerates varied with the fatty acid chain length of the lipids, going from linear nanocrystal chains to flat nanocrystal sheets and finally 3-dimensional agglomerates as the fatty acid length was increased from 12 to 18 carbons. Chloroform annealing was tested with dilauroylphosphatidylcholine (DLPC), which has the shortest saturated fatty acid chains (12 C) and exists in the liquid crystal lamellar phase at room temperature,^{19,20} but chloroform provided limited improvement for incorporation of nanocrystals into the lipid bilayer of vesicles (Appendix A.2).²¹ Instead, squalene was introduced into the lipid-nanocrystal dispersions to try altering the properties of the dispersed phase, but the squalene formed lipid-coated oil droplets instead of incorporating into the vesicle bilayers.²² The Au nanocrystals loaded the squalene droplets, and the number of Au nanocrystals per droplet was controlled by changing the ratio of squalene to nanocrystals. Importantly, cryoTEM imaging revealed that the Au nanocrystals are located at the squalene-lipid-water interface.

9.1.4 Loading Hydrophobic Semiconductor Nanocrystals into Phospholipid Vesicles

In Chapter 8, the methods developed for preparing vesicles and squalene emulsion droplets loaded with Au nanocrystals were extended to hydrophobic semiconductor nanocrystals (CdSe, Si, CIS), and the results had limited success. None of the hydrophobic semiconductor nanocrystals were able to completely load unsaturated lipid bilayers when chloroform was included. With CdSe and Si, the nanocrystal diameter

ranged from 2-4 nm, so these particles may be too large to fully load the lipid bilayers, as found for the 4.1 nm diameter Au nanocrystals in Chapter 5. However, the dodecanethiol-coated CIS nanocrystals were 1.8 nm diameter, and they did not fully-load lipid bilayers, which suggests that the nanocrystal composition rather than its size alone may be another important factor for lipid bilayer incorporation. The CdSe, CIS, and Si nanocrystals formed agglomerates that adhered to the unsaturated DOPC lipid bilayers. The CIS and Si nanocrystals remained luminescent, however the CdSe nanocrystal fluorescence disappeared when dispersed in water with DOPC, which strongly suggests that the CdSe nanocrystals may have oxidized.²³

Dispersing hydrophobic CdSe and Si nanocrystals in water with saturated phosphatidylcholines, the nanocrystals formed lipid-coated aggregates adhering to vesicles, similar to observation with the 1.8 nm Au nanocrystals. No nanocrystal chains formed when using the DLPC lipid. The CdSe nanocrystals were not luminescent in the dispersions, while the Si nanocrystals maintained their luminescence when dispersed with lipids in water. Saturated lipids having cationic and anionic head groups were combined with the lipid-Si nanocrystal dispersions, but it was found that the Si agglomerates no longer adhered to the vesicle membranes and were freely floating in the dispersion.

The hydrophobic CIS, CdSe, and Si nanocrystals were dispersed in squalene emulsion droplets stabilized by saturated phosphatidylcholines. Like the Au nanocrystals, the semiconductor nanocrystals seem to incorporate into the squalene droplets. Based on cryoTEM imaging, many of the CdSe nanocrystals located at the squalene-water interface seem to be more on the water side of the interface than any of

the other nanocrystals being characterized, suggesting that these nanocrystals are probably the most hydrophilic (lowest oil-water contact angle). If the CdSe nanocrystal surfaces partially oxidize to form selenium oxide,²³ which is polar and water soluble,²⁴ then this could make the nanocrystals partially hydrophilic. The CIS nanocrystals often had no preferential location in the squalene droplets, though a few examples were found where the CIS nanocrystals appeared to be located at the squalene-lipid-water interface as found with the Au nanocrystals. The Si nanocrystals had no preferential location in the squalene droplets, and even appeared to pull away from the squalene-water interface in some droplets, which may suggest that the Si nanocrystals are the most hydrophobic (largest oil-water contact angle) of the nanocrystals studied. The CIS and Si nanocrystals remained luminescent in the dispersed squalene droplets, while the luminescence of CdSe was negligible.

Since the Si nanocrystals remained luminescent in aqueous dispersions of cationic lipids and squalene, the nanocrystal dispersions were mixed with live leukemia cells to see whether the nanocrystals would bind to the cell surface as a fluorescent label. The cell membrane has a negative zeta potential,²⁵ so cationic particles should bind to the cell surface by electrostatic adsorption.²⁵⁻²⁸ Unfortunately the Si nanocrystals did not provide enhanced fluorescence contrast to the cells, indicating that a negligible amount of nanocrystals adsorb to the cell surface. This result contrasts the use of cationic lipid particles and squalene emulsions loaded with the hydrophobic dye Nile Red, since the dye is able to clearly label the membrane of the cells. The Si nanocrystals may not work because, as shown in cryoTEM, numerous empty lipid particles exist alongside those

loaded with Si nanocrystals, so it is possible that the empty lipid particles adsorb to the cells and lower the amount of cell surface area available for Si-lipid particles to adsorb.

Finally, the detergent-mediated loading of nanocrystals into vesicles seems promising. By controlling the total concentration of vesicles and nanocrystal-detergent micelles, vesicle bilayers were loaded with either small clusters of 5-10 nanocrystals or nanocrystal rafts containing hundreds of nanocrystals. This procedure so far has only worked well for the dodecanethiol-coated 1.8 nm Au nanocrystals. Attempts to disperse Si nanocrystals in OCG micelles led to significant nanocrystal aggregation.

9.2 Future Work

9.2.1 Polymer coated Nanocrystals and Photothermal Therapy

Much more work is needed on developing the polymer-coated nanocrystals for biomedical applications. First, more work should be done to try and separate polymer-coated nanocrystals from empty polymer micelles, and this might be accomplished by gel permeation chromatography or gel electrophoresis if the nanocrystals have a different mobility in these matrices than the empty polymer micelles.² The cytotoxicity of the amphiphilic polymer should be carefully characterized. Preliminary tests using an MTT assay to measure cell metabolism found that the amphiphilic polymer (without nanocrystals) does not affect the metabolism of HL-60 cells over the concentration range of (1 mg/mL – 1000 mg/mL) when exposed to the cells for 3 hours. Additional tests such as lactate dehydrogenase (LDH) and caspase activity assays should provide more indications about whether the polymer is toxic to the cells. Cytotoxicity tests performed in the presence of nanocrystals are complicated by the strong absorbance or fluorescence

of the nanocrystals, since most assays rely on the change in optical properties of a chromophore in order to quantify cytotoxicity, and more careful consideration is needed when using nanocrystals. The *in vivo* distribution of the polymer should also be characterized, to determine whether the polymer accumulates in living organisms. The bio-distribution could be characterized by conjugating a radioisotope-labeled amine molecule to the amphiphilic polymer and measuring the isotope's radioactivity over time in different tissues. This approach would be amenable to the use of nanocrystals, which should not alter the radioactive decay of the isotope.

The polymer-coated Cu_{2-x}Se nanocrystals are a promising alternative to Au nanoshells for photothermal therapy. The Cu_{2-x}Se nanocrystals perform just as well as Au nanorods, while the Cu_{2-x}Se does not contain cytotoxic CTAB molecules.³ The Cu_{2-x}Se nanocrystals were not acutely toxic to cells, but more tests are needed to characterize their long-term cytotoxicity, their distribution in organs, and their photothermal heating performance in tissue specimens (rather than just a cell monolayer). With the nanocrystal synthesis, further experiments should be done to try incorporating different vacancies (such as phosphorous)²⁹ within the Cu_{2-x}Se nanocrystals to see how this impacts the plasmon resonance frequency,³⁰ and whether this frequency can be carefully tuned by controlling the dopant concentration.

9.2.2 Nanocrystal-loaded Vesicles

More work is needed to probe the structure of lipid bilayers fully loaded with Au nanocrystals using chloroform. Preliminary small angle x-ray scattering results

performed with synchrotron radiation (at Cornell) on a concentrated dispersion of DOPC vesicles fully loaded with Au nanocrystals indicate that the lipid bilayer thickness is about 9 nm, which was larger than the 4 nm thickness of DOPC bilayers containing chloroform but no Au nanocrystals. Using a combination of synchrotron x-ray scattering and neutron scattering should reveal a more complete picture of how the nanocrystals are situated in the lipid bilayer relative to the different functional groups of the lipids.¹⁸ It would be interesting to test other non-polar anesthetic liquids (e.g. isoflurane) or even gaseous xenon for improving nanocrystal loading in lipid bilayers, since chloroform is quite toxic.^{31,32} Regarding the use of other nanocrystals, different ligand chemistries should be explored, such as hydrocarbons of different lengths, which will affect the overall nanocrystal size and the inter-particle forces.³³

The work focused on detergent-mediated loading of nanocrystals into vesicles would benefit from more thorough attempts to remove trace amounts of detergent from the vesicles. A few nanocrystal chains were observed outside of vesicles by cryoTEM, which suggests that some detergent may be retained in the sample to keep the nanocrystals dispersed outside of vesicles. The hydrophobic nanocrystals probably slow down the rate of detergent removal, since the detergent is bound to the nanocrystal surface by hydrophobic forces. Gel permeation beads or detergent-adsorbing resins may help approach 100% detergent removal from the samples. More work is also needed to try dispersing Si nanocrystals in the OCG-micelles for application to this method, and it will probably be useful to test different Si nanocrystals with different lengths of surface ligands.

The squalene emulsion droplets loaded with nanocrystals could be useful for the delivery of hydrophobic drugs. The Au nanocrystals are located at the squalene-water interface, which might act as a physical barrier to the diffusion of hydrophobic drugs out of the squalene droplet, so controlled release studies should be performed with this material. In addition, the nanocrystals may act as a weighting agent to improve the stability of the droplets. The nanocrystal-loaded squalene droplets should be purified from empty squalene droplets by ultracentrifugal filtration, and a series of tests should be done to optimize the separation of nanocrystal-loaded droplets, pure squalene droplets, and pure lipid vesicles. This purification should improve the efficiency of delivering the nanocrystals to cells by removing droplets that do not contain nanocrystals.

The cell labeling experiments would benefit from several improvements. First, a different cell line might be considered that more readily performs endocytosis, since this should encourage accumulation of nanocrystals in cells.³⁴ Different cationic lipids should be tested, especially lipofectamine which is commonly used to bind to cell membranes.³⁵ Making brighter nanocrystals, with quantum yield >10% and approaching that of the Nile Red dye (70%), will enhance the signal of nanocrystals relative to cell autofluorescence.^{34,36} Testing longer nanocrystal incubation times might also promote accumulation of nanocrystals on the surface of cells. Finally, attaching antibodies (e.g. anti-insulin receptor)³⁷ to the nanocrystal-loaded lipid particles promote binding to the HL-60 cells.

9.3 References

- (1) Hessel, C. M.; Rasch, M. R.; Hueso, J. L.; Goodfellow, B. W.; Akhavan, V.; Puvanakrishnan, P.; Tunnell, J. W.; Korgel, B. A. *Small* 2010, 6, 2026-2034.
- (2) Lin, C. A. J.; Sperling, R. A.; Li, J. K.; Yang, T. Y.; Li, P. Y.; Zanella, M.; Chang, W. H.; Parak, W. G. J. *Small* 2008, 4, 334-341.
- (3) Hessel, C. M.; Pattani, V. P.; Rasch, M. R.; Panthani, M. G.; Koo, B.; Tunnell, J. W.; Korgel, B. A. *Nano Letters* 2011, 11, 2560-2566.
- (4) Weissleder, R. *Nature Biotechnology* 2001, 19, 316-317.
- (5) Oldenburg, S. J.; Averitt, R. D.; Westcott, S. L.; Halas, N. J. *Chemical Physics Letters* 1998, 288, 243-247.
- (6) Torchilin, V. P.; Sawant, R. R. *Soft Matter* 2010, 6, 4026-4044.
- (7) Torchilin, V. P. *Nature Reviews Drug Discovery* 2005, 4, 145-160.
- (8) Al-Jamal, W. T.; Kostarelos, K. *Nanomedicine* 2007, 2, 85-98.
- (9) Chen, Y.; Bose, A.; Bothun, G. D. *ACS Nano* 2010, 4, 3215-3221.
- (10) Amstad, E.; Kohlbrecher, J.; Muller, E.; Schweizer, T.; Textor, M.; Reimhult, E. *Nano Letters* 2011, 11, 1664-1670.
- (11) Brust, M.; Walker, M.; Bethell, D.; Schiffrin, D. J.; Whyman, R. *Journal of the Chemical Society, Chemical Communications* 1994, 801-802.
- (12) Sigman, M. B.; Saunders, A. E.; Korgel, B. A. *Langmuir* 2004, 20, 978-983.
- (13) Reigada, R. *Journal of Physical Chemistry B* 2011, 115, 2527-2535.
- (14) Regen, S. L.; Turkyilmaz, S.; Chen, W. H.; Mitomo, H. *Journal of the American Chemical Society* 2009, 131, 5068-+.
- (15) Phonphok, N.; Chidichimo, G.; Westerman, P. W. *Chemistry and Physics of Lipids* 1996, 83, 25-37.
- (16) Cantor, R. S. *Biochemistry* 1997, 36, 2339-2344.
- (17) Alakoskela, J. M.; Vitovic, P.; Kinnunen, P. K. J. *Chemmedchem* 2009, 4, 1224-1251.
- (18) Kucerka, N.; Nieh, M.-P.; Katsaras, J. *Biochimica Et Biophysica Acta* 2011, 1808, 2761-2771.
- (19) The unsaturated lipids studied in Chapter 5 are also in the liquid crystal lamellar phase at room temperature.
- (20) Marsh, D. *CRC Handbook of Lipid Bilayers*; CRC Press, Inc.: Boca Raton, FL, 1990.
- (21) The lipids with longer fatty acid chains have a gel to liquid crystal phase transition above room temperature. Dispersing these lipid in water at elevated temperature will require annealing the lipid films with chloroform at high temperature as well. This will increase the vapor pressure of chloroform, approaching its boiling point around 60C. This was considered to be dangerous, and therefore was not performed.

- (22) Simon, S. A.; Lis, L. J.; MacDonald, R. C.; Kauffman, J. W. *Biophysical Journal* 1977, *19*, 83-90.
- (23) Pechstedt, K.; Whittle, T.; Baumberg, J.; Melvin, T. *Journal of Physical Chemistry C* 2010, *114*, 12069-12077.
- (24) Holleman, A. F.; Wiberg, E. *Inorganic Chemistry*; Academic Press: San Diego, 2001.
- (25) Alpar, H. O.; Bason, A. M.; Hickman, J. A.; Richards, F. M.; Field, W. N. *International Journal of Pharmaceutics* 1990, *62*, 133-141.
- (26) Goldman, E. R.; Mattoussi, H.; Anderson, G. P.; Medintz, I. L.; Mauro, J. M. In *NanoBiotechnology Protocols*; Rosenthal, S. J., Wright, D. W., Eds.; Humana Press: Totowa, 2005, p 19.
- (27) Haugen, A.; May, S. *Journal of Chemical Physics* 2007, *127*, -.
- (28) Sens, P.; Joanny, J.-F. *Physical Review Letters* 2000, *84*, 4862-4865.
- (29) Stegner, A. R.; Pereira, R. N.; Klein, K.; Lechner, R.; Dietmueller, R.; Brandt, M. S.; Stutzmann, M. *Physical Review Letters* 2008, *100*, 026803.
- (30) Kriegel, I.; Jiang, C.; Rodriguez-Fernandez, J.; Schaller, R. D.; Talapin, D. V.; da Como, E.; Feldmann, J. *Journal of the American Chemical Society* 2012, *134*, 1583-1590.
- (31) Abbassi, R.; Chamkhia, N.; Sakly, M. *Toxicology and Industrial Health* 2010, *26*, 487-496.
- (32) Brennan, R. J.; Schiestl, R. H. *Mutation Research* 1998, *397*, 271-278.
- (33) Israelachvili, J. N. *Intermolecular and Surface Forces*; 2nd ed.; Academic press Inc.: San Diego, 1992.
- (34) Delehanty, J. B.; Mattoussi, H.; Medintz, I. L. *Analytical and Bioanalytical Chemistry* 2009, *393*, 1091-1105.
- (35) Esendagli, G.; Canpinar, H.; Dogan, A. L.; Akkaya, M.; Kansu, E.; Guc, D. *Cytotechnology* 2009, *61*, 45-53.
- (36) Smith, A. M.; Duan, H. W.; Mohs, A. M.; Nie, S. M. *Advanced Drug Delivery Reviews* 2008, *60*, 1226-1240.
- (37) Birnie, G. D. *British Journal of Cancer* 1988, *58*, 41-45.

Appendix

A.1. DLS Data for Chapter 5

For each annealing condition in Figure 5.17, DLS was performed at each of the three stages of vesicle formation – immediately after dispersing the films in DI water by sonication, after centrifuging the sonicated dispersions to remove agglomerates, and after extruding the dispersions through 100 nm pores. A Zetasizer Nano ZS instrument (Malvern) was used for collecting the DLS data. The wavelength of the Zetasizer laser (λ) was 630 nm and the scattering angle of the detector (θ) was 173°. The instrument measured the correlation in light scattering intensity over time and reported the data as the intensity autocorrelation function given by equation A1. For each dispersion, $g_2(t)$ was measured in triplicate.

$$g_2(t) = \frac{\langle I(t)I(0) \rangle}{\langle I(0) \rangle^2} \quad (\text{A1})$$

The intensity autocorrelation function (g_2) is related to the electric field autocorrelation function (g_1) by the well known Siegert relationship, equation A2. In A2, the β term is a constant.

$$g_2(t) = 1 + \beta \cdot |g_1(t)|^2 \quad (\text{A2})$$

Each scattering particle contributes a single exponential decay to the correlation in light scattering intensity, thus the general form of g_1 is the following:

$$g_1(t) = \sum_{i=1}^m A_i e^{-\Gamma_i t} \quad (\text{A3})$$

In equation A3, each particle size (i) has a constant pre-exponential term A_i and a scattering intensity decay rate Γ_i . Equation A4 shows how the decay rate is related to the scattering vector q and the particle diffusion coefficient D_i . Also, equation A4 employs the Stokes-Einstein relationship to relate the decay rate directly to the particle hydrodynamic diameter d_i . The constant n is the refractive index of water (1.333), η is the water dynamic viscosity at 25°C (0.89 cP), k is the Boltzmann constant ($1.38 \cdot 10^{-23}$ J/K), and T equals 298 K.

$$\Gamma_i = q^2 \cdot D_i = \left(\frac{4n}{\lambda} \sin\left(\frac{\theta}{2}\right) \right)^2 \cdot \left(\frac{kT}{3\eta \cdot d_i} \right) \quad (\text{A4})$$

Thus, obtaining particle sizes requires fitting equations A2-A4 to the experimental data $g_2(t)$ given by equation A1. Unfortunately this problem has many solutions when m in equation A3 is greater than 3, or if the particles are considered to have a multimodal, polydisperse size distribution. In this experiment though, we actually found that the DLS data were very well represented by simply assuming that there are only two particle sizes, so that $m = 2$ in equation A3. In this case, the two pre-exponentials represent the relative amplitude of scattering from each particle size, so $A_I + A_{II} = 1$.^{1,2}

For each dispersion, equations A2-A4 were fit to the three replicate measurements of $g_2(t)$ using non-linear least squares regression, assuming only non-negative solutions were valid. The regression minimized χ^2 in equation A5, the sum of the squared differences between the experimental correlation function $g_2(t)|_{\text{exp}}$ (equation A1) and the correlation function calculated by the model $g_2(t)|_{\text{model}}$ (equation A3).

$$\chi^2 = \sum \left(g_2(t)|_{\text{exp}} - g_2(t)|_{\text{model}} \right)^2 \quad (\text{A5})$$

Table A1 lists the numerical results of the fitting, and Supporting Figure A.1 shows the fitted correlation functions overlaid with the experimentally measured correlation functions. The fitted correlation functions are plotted in Figure 5.17. Table A2 lists the numerical results for fitting only a single exponential ($A_{II} = 0$) to $g_2(t)$, assuming only a single particle size exists in the dispersions. Table A2 also shows the correspondence between the sample numbers used in Tables A1 and A2 and the sample preparation conditions. Supporting Figure A.2 plots χ^2 versus sample number for the fit results in Tables A1 and A2, showing that the double exponential form of equation A3 is a better representation of the light scattering than a single exponential.

Table A1. Fit Parameters to DLS Data, Obtained by Assuming Two Particle Size Populations

Gold Core Size (nm)	Annealing Condition	d_I (nm)	d_{II} (nm)	A_I	A_{II}	β	Γ_I (ms ⁻¹)	Γ_{II} (ms ⁻¹)	χ^2
1.8	No Anneal	748	10088	0.213	0.787	0.474	0.458	0.034	0.023
1.8	No Anneal	89	357	0.499	0.501	0.851	3.856	0.960	0.011
1.8	No Anneal	32	102	0.082	0.918	0.887	8.540	2.709	0.001
1.8	Anneal, then vacuum	210	5231	0.262	0.738	0.578	1.630	0.065	0.060
1.8	Anneal, then vacuum	49	172	0.172	0.828	0.899	6.947	1.990	0.002
1.8	Anneal, then vacuum	34	105	0.116	0.884	0.907	9.994	3.263	0.001
1.8	Vacuum, then anneal	108	527	0.315	0.685	0.785	3.175	0.650	0.006
1.8	Vacuum, then anneal	65	234	0.217	0.783	0.815	5.290	1.465	0.002
1.8	Vacuum, then anneal	43	145	0.132	0.868	0.896	8.020	2.368	0.004
4.1	No Anneal	304	4767	0.357	0.643	0.481	1.128	0.072	0.025
4.1	No Anneal	50	164	0.170	0.830	0.918	6.813	2.090	0.003
4.1	No Anneal	59	155	0.352	0.648	0.889	5.801	2.206	0.002
4.1	Anneal, then vacuum	451	5102	0.272	0.728	0.517	0.759	0.067	0.097
4.1	Anneal, then vacuum	50	155	0.169	0.831	0.931	6.790	2.208	0.002
4.1	Anneal, then vacuum	53	133	0.242	0.758	0.937	6.416	2.574	0.001
4.1	Vacuum, then anneal	144	610	0.344	0.656	0.512	2.384	0.561	0.001
4.1	Vacuum, then anneal	90	308	0.331	0.669	0.680	3.821	1.111	0.002
4.1	Vacuum, then anneal	43	151	0.064	0.936	0.704	7.891	2.268	0.001

*Amplitude weighted diameter = $A_I d_I + A_{II} d_{II}$

Table A2. Fit Parameters to DLS Data, Obtained by Assuming One Particle Size Population

Gold Core Size (nm)	Annealing Condition	Step of Dispersing	d (nm)	β	Γ (ms ⁻¹)	χ^2
1.8	No Anneal	Sonicated	5151	0.461	0.066	0.1591
1.8	No Anneal	Centrifuged	162	0.841	2.108	0.0461
1.8	No Anneal	Extruded	92	0.883	3.006	0.0044
1.8	Anneal, then vacuum	Sonicated	1918	0.546	0.179	0.5665
1.8	Anneal, then vacuum	Centrifuged	135	0.890	2.533	0.0166
1.8	Anneal, then vacuum	Extruded	91	0.901	3.766	0.0064
1.8	Vacuum, then anneal	Sonicated	293	0.773	1.168	0.0665
1.8	Vacuum, then anneal	Centrifuged	170	0.806	2.011	0.0211
1.8	Vacuum, then anneal	Extruded	121	0.888	2.833	0.0131
4.1	No Anneal	Sonicated	1354	0.464	0.253	0.2466
4.1	No Anneal	Centrifuged	131	0.910	2.620	0.0150
4.1	No Anneal	Extruded	107	0.882	3.214	0.0118
4.1	Anneal, then vacuum	Sonicated	2257	0.503	0.152	0.2429
4.1	Anneal, then vacuum	Centrifuged	125	0.924	2.730	0.0121
4.1	Anneal, then vacuum	Extruded	104	0.931	3.287	0.0075
4.1	Vacuum, then anneal	Sonicated	341	0.506	1.003	0.0197
4.1	Vacuum, then anneal	Centrifuged	193	0.673	1.771	0.0183
4.1	Vacuum, then anneal	Extruded	138	0.701	2.477	0.0029

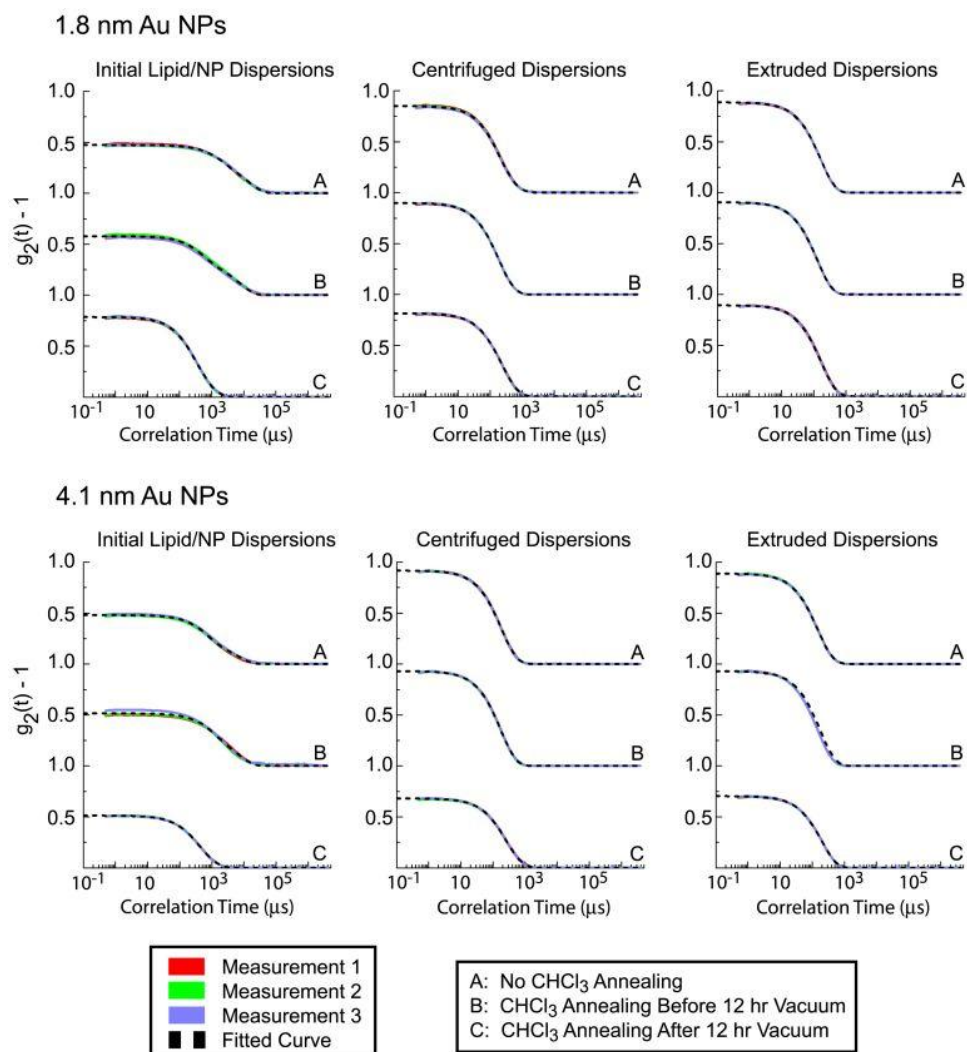


Figure A.1. Experimental DLS data plotted for each dispersion, along with the fitted light scattering model overlaid on the measured data. The gold nanoparticles are coated with dodecanethiol in this case. The fitted curves are plotted in the main text.

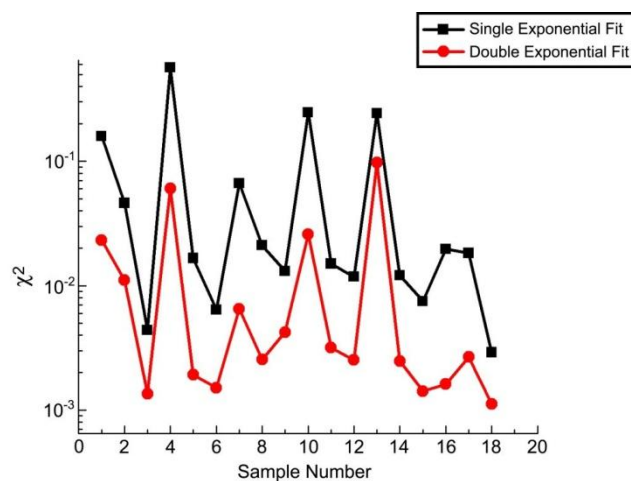


Figure A.2. Comparison of the least squares fit parameters (χ^2) of two different DLS models – a single exponential (one particle size) and a double exponential (two particle sizes) – fit to the experimental DLS data shown in Figure A.1. The lowest fit parameter is always achieved using the double exponential model. The sample numbers refer to the entries in column 1 of Table A2.

DLS Sizing – Hexadecanethiol-coated Au Nanocrystals. Figure A.3 shows DLS data of the dispersions prepared from DOPC and hexadecanethiol-coated 1.8 nm gold nanoparticles with chloroform vapor absorbed in the initial film. The DLS results for the DOPC and hexadecanethiol-gold nanoparticle dispersions are very similar to the dodecanethiol-coated 1.8 nm gold nanoparticles.

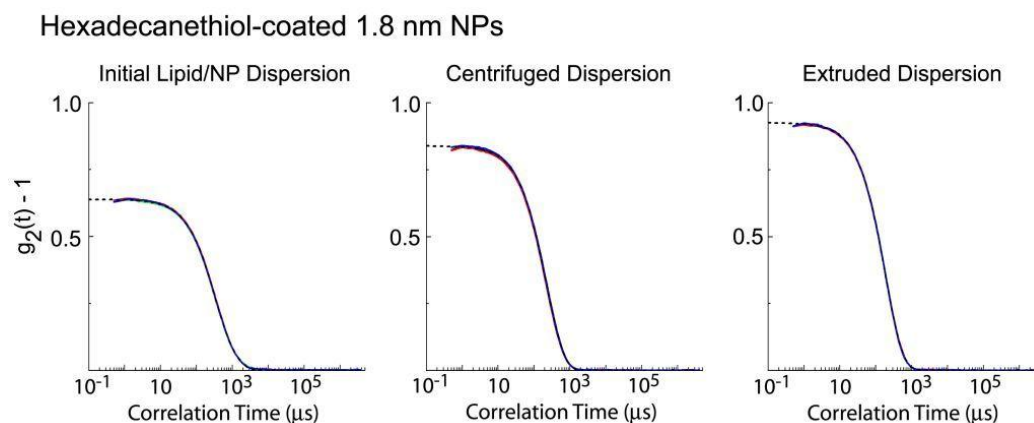


Figure A.3. DLS data of DOPC and hexadecanethiol-coated 1.8 nm NPs dispersed in water immediately after chloroform annealing. The green, red, and blue solid lines are the experimentally measured data, while the black dashed line is the DLS model fit to the experimental data.

DLS Sizing for NMR Experiments. The hydrodynamic diameters of the DOPC and DOPC-Au nanocrystal dispersions prepared for NMR are listed below in Table A3, while the DLS data is shown in Figure A.4. The DLS data show that the pure DOPC vesicles, without chloroform, are larger in size than the DOPC vesicles made with chloroform annealing. The pure DOPC vesicles are also larger than the Au-loaded DOPC sample after chloroform annealing and extrusion.

Table A3. Fit Parameters to DLS Data of Samples Prepared for NMR Experiments, Obtained by Assuming Two Particle Size Populations

Sample	d_I (nm)	d_{II} (nm)	A_I	A_{II}	β	χ^2
DOPC, No Chloroform, No Au	187	7133	0.32	0.68	0.62	0.067
DOPC, With Chloroform, No Au	47	229	0.27	0.73	0.90	0.0055
DOPC, With Chloroform, Au NCs	84	356	0.22	0.78	0.78	0.0013
DOPC, With Chloroform, Au NCs, Extruded	51	186	0.12	0.88	0.78	0.026

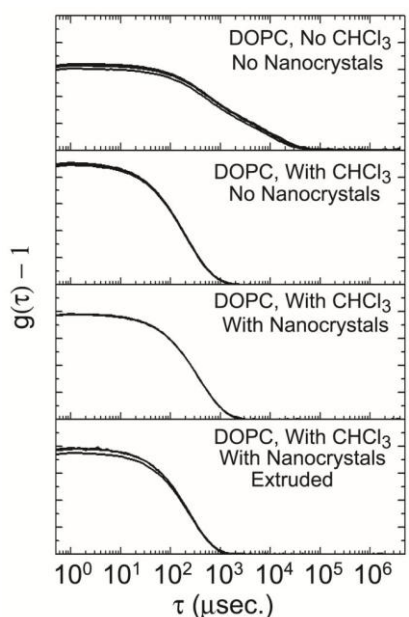


Figure A.4. DLS data of the DOPC and DOPC-Au nanocrystal samples prepared for NMR characterization.

A.2. Chloroform Annealing with Dilauroylphosphatidylcholine and 1.8 nm Au Nanocrystals

The chloroform annealing and vesicle formation procedure described in Chapter 5 with DOPC lipid was extended to the saturated lipid dilauroylphosphatidylcholine (DLPC). DLPC has a gel to liquid crystal phase transition temperature of -1°C , so the vesicle formation was carried out at the same temperature as with DOPC. A film of 30 μmol DLPC and 3 mg Au nanocrystals was annealed for 60 minutes with chloroform vapor at 25°C , dispersed in 1.0 mL of deionized water by sonication, centrifuged at 1000g for 5 minutes to remove poorly-dispersed material, and then extruded through 100 nm pores. The cryoTEM imaging of the sample is shown in Figure A5. The Au

nanocrystals are still primarily found in long chains extending several hundred nanometers in length and often terminating in DLPC vesicle bilayers. However, a few vesicles appeared to be fully-loaded with Au nanocrystals, shown in the bottom row of Figure A5. These loaded vesicles were quite rare, but it suggests that it should be possible to form the loaded vesicles with other lipids besides just DOPC or eggPC. Chloroform annealing with saturated lipids having fatty acids longer than 12 carbons was not investigated for safety reasons – the annealing and vesicle formation would have to be done at elevated temperature to ensure that the lipids are in the liquid crystal phase, and chloroform's vapor pressure increases with temperature, so the experimenter would be exposed to high levels of chloroform vapor during the process.

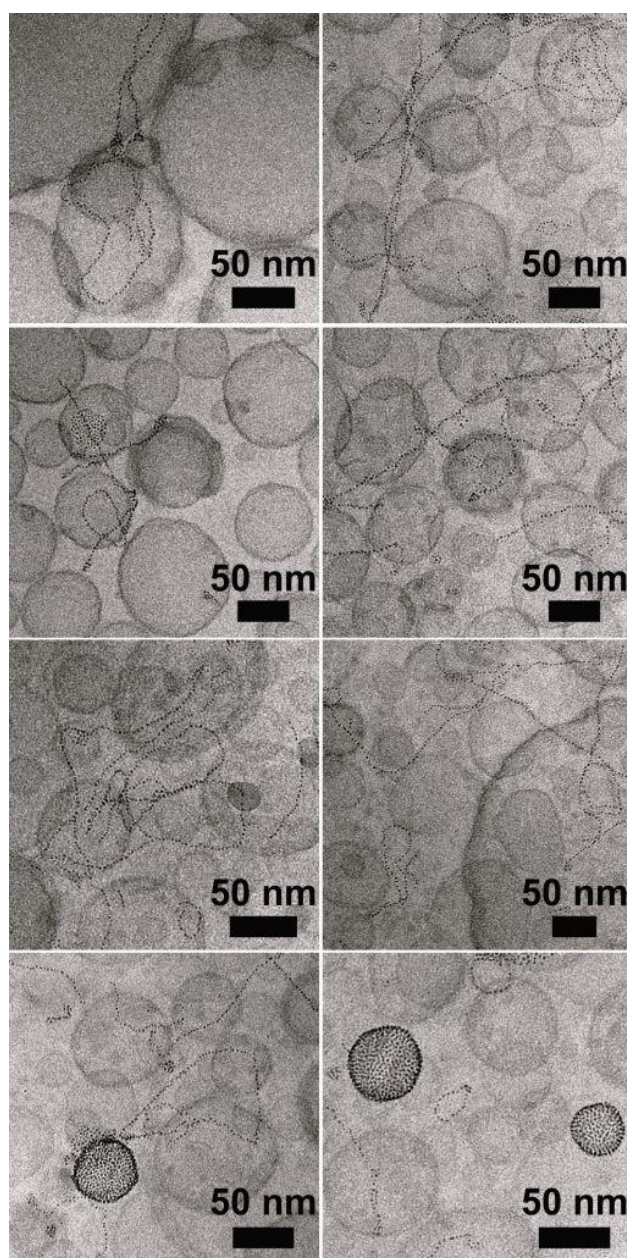


Figure A5. CryoTEM images of DLPC vesicles prepared with 1.8 nm Au nanocrystals and chloroform vapor annealing. The nanocrystals are primarily observed in lipid-coated chains, just as in the absence of chloroform annealing. However, a few Au-loaded vesicles were found in the sample as well (bottom row).

References

- (1) Yan, Y. D.; Clarke, J. H. R. *Journal of Chemical Physics* **1990**, 93, 4501-4509.
- (2) Zulauf, M.; Eicke, H. F. *Journal of Physical Chemistry* **1979**, 83, 480-486.

Bibliography

- Aagaard, T. H.; Kristensen, M. N.; Westh, P. "Packing properties of 1-alkanols and alkanes in a phospholipid membrane", *Biophysical Chemistry* **2006**, *119*(1): 61-68.
- Abbassi, R.; Chamkhia, N.; Sakly, M. "Chloroform-induced oxidative stress in rat liver: Implication of metallothionein", *Toxicology and Industrial Health* **2010**, *26*(8): 487-496.
- Abdulreda, M. H.; Moy, V. T. "Atomic force microscope studies of the fusion of floating lipid bilayer", *Biophysical Journal* **2007**, *92*(12): 4369-4378.
- Aggazzotti, G.; Fantuzzi, G.; Tartoni, L.; Predieri, G. "Plasma chloroform concentrations in swimmers using indoor pools", *Archives of Environmental Health: An International Journal* **1990**, *45*(3): 175-179.
- Alakoskela, J. M.; Vitovic, P.; Kinnunen, P. K. J. "Screening for the Drug-Phospholipid Interaction: Correlation to Phospholipidosis", *Chemmedchem* **2009**, *4*(8): 1224-1251.
- Alexeev, A.; Uspal, W. E.; Balazs, A. C. "Harnessing Janus nanoparticles to create controllable pores in membranes", *ACS Nano* **2008**, *2*(6): 1117-1122.
- Alivisatos, A. P. "Semiconductor clusters, nanocrystals, and quantum dots", *Science* **1996**, *271*: 933-937.
- Al-Jamal, W. T.; Al-Jamal, K. T.; Bomans, P. H.; Frederik, P. M.; Kostarelos, K. "Functionalized-quantum-dot-liposome hybrids as multimodal nanoparticles for cancer", *Small* **2008**, *4*(9): 1406-1415.
- Al-Jamal, W. T.; Al-Jamal, K. T.; Tian, B.; Lacerda, L.; Bomans, P. H.; Frederik, P. M.; Kostarelos, K. "Lipid-quantum dot bilayer vesicles enhance tumor cell uptake and retention in vitro and in vivo", *ACS Nano* **2008**, *2*(3): 408-418.
- Al-Jamal, W. T.; Kostarelos, K. "Liposome-nanoparticle hybrids for multimodal diagnostic and therapeutic applications", *Nanomedicine* **2007**, *2*(1): 85-98.
- Alkilany, A. M.; Nagaria, P. K.; Hexel, C. R.; Shaw, T. J.; Murphy, C. J.; Wyatt, M. D. "Cellular uptake and cytotoxicity of gold nanorods: molecular origin of cytotoxicity and surface effects ", *Small* **2009**, *5*(6): 701-708.
- Almgren, M.; Edwards, K.; Karlsson, G. "Cryo transmission electron microscopy of liposomes and related structures", *Colloids and Surfaces a-Physicochemical and Engineering Aspects* **2000**, *174*: 3-21.

Alpar, H. O.; Bason, A. M.; Hickman, J. A.; Richards, F. M.; Field, W. N. "Estimation by FACS of the delivery of liposome encapsulated macromolecules into myeloid cells", *International Journal of Pharmaceutics* **1990**, 62(2-3): 133-141.

Alper, J.; Hamad-Schifferli, K. "Effect of ligands on thermal dissipation from gold nanorods", *Langmuir* **2010**, 26(6): 3786-3789.

Amstad, E.; Kohlbrecher, J.; Muller, E.; Schweizer, T.; Textor, M.; Reimhult, E. "Triggered Release from Liposomes through Magnetic Actuation of Iron Oxide Nanoparticle Containing Membranes", *Nano Letters* **2011**, 11(4): 1664-1670.

Anglin, E. J.; Cheng, L. Y.; Freeman, W. R.; Sailor, M. J. "Porous silicon in drug delivery devices and materials", *Advanced Drug Delivery Reviews* **2008**, 60(11): 1266-1277.

Appell, J.; Porte, G.; Buhler, E. "Self-diffusion and collective diffusion of charged colloids studied by dynamic light scattering", *Journal of Physical Chemistry B* **2005**, 109(27): 13186-13194.

Arriagada, F. J.; Osseo-Asare, K. "Synthesis of Nanosize Silica in a Nonionic Water-in-Oil Microemulsion: Effects of the Water/Surfactant Molar Ratio and Ammonia Concentration ", *Journal of Colloid and Interface Science* **1999**, 211(2): 210-220.

Arruebo, M.; Fernandes-Pacheko, R.; Ibarra, M. R.; Santamaria, J. "Magnetic nanoparticles for drug delivery", *Nano Today* **2007**, 2(3): 22-32.

Aubin, J. E. "Autofluorescence of viable cultured mammalian cells", *Journal of Histochemistry and Cytochemistry* **1979**, 27: 36.

Balogh, L.; Nigavekar, S. S.; Nair, B. M.; Lesniak, W.; Zhang, C.; Sung, L. Y.; Kariapper, M. S. T.; El-Jawahri, A.; Llanes, M.; Bolton, B.; Mamou, F.; Tan, W.; Huston, A.; Minc, L.; Khan, M. K. "Significant effect of size on the in vivo biodistribution of gold composite nanodevices in mouse tumor models ", *Nanomedicine* **2007**, 3(4): 281-296.

Banerjee, R. "Nanocarriers for overcoming multidrug resistance in cancers ", *Nanomedicine* **2006**, 1(4): 481-485.

Beaune, G.; Menager, C.; Cabuil, V. "Location of magnetic and fluorescent nanoparticles encapsulated inside giant liposomes", *Journal of Physical Chemistry B* **2008**, 112(25): 7424-7429.

Beddowes, E. J.; Faux, S. P.; Chipman, J. K. "Chloroform, carbon tetrachloride and glutathione depletion induce secondary genotoxicity in liver cells via oxidative stress", *Toxicology* **2003**, 2003(2-3): 101-115.

Bernstorff, S.; Dubček, P.; Kovačević, I.; Radić, N.; Pivac, B. "Si nanocrystals in SiO₂ films analyzed by small angle X-ray scattering ", *Thin Solid Films* **2007**, 515(14): 5637-5640.

Bianco, I. D.; Fidelio, G. D.; Yu, R. K.; Maggio, B. "Degradation of Dilauroylphosphatidylcholine by Phospholipase A₂ in Monolayers

Containing Glycosphingolipids", *Biochemistry* **1991**, 30(6): 1709-1714.

Biggs, S.; Mulvaney, P. "Measurement of the forces between gold surfaces in water by atomic force microscopy ", *Journal of Chemical Physics* **1994**, 100(11): 8501-8505.

Binder, W. H.; Sachsenhofer, R.; Farnik, D.; Blaas, D. "Guiding the location of nanoparticles into vesicular structures: a morphological study", *Physical Chemistry Chemical Physics* **2007**, 9(48): 6435-6441.

Binks, B. P. "Particles as surfactants similarities and differences", *Current Opinion In Colloid & Interface Science* **2002**, 7: 21-41.

Birnie, G. D. "The HL60 cell line: A model system for studying human myeloid cell differentiation", *British Journal of Cancer* **1988**, 58(Suppl. IX): 41-45.

Blaurock, A. E.; Gamble, R. C. "Small phosphatidylcholine vesicles appear to be faceted below the thermal phase transition", *Journal of Membrane Biology* **1979**, 50: 187-204.

Bohren, C. F.; Huffman, D. R., *Absorption and Scattering of Light by Small Particles*. John Wiley: New York, 1983.

Bonnemain, B. "Superparamagnetic Agents in Magnetic Resonance Imaging: Physicochemical Characteristics and Clinical Applications A Review", *Journal of Drug Targeting* **1998**, 6(3): 167-174.

Bota, A.; Varga, Z.; Goerigk, G. "Vesicles as reactors of nanoparticles: an anomalous small-angle X-ray scattering study of the domains rich in copper ions", *Journal of Applied Crystallography* **2007**, 40: S259-S263.

Bothun, G. D. "Hydrophobic silver nanoparticles trapped in lipid bilayers: Size distribution, bilayer phase behavior, and optical properties", *Journal of Nanobiotechnology* **2008**, 6(13).

Bothun, G. D.; Rabideau, A. E.; Stoner, M. A. "Hepatoma Cell Uptake of Cationic Multifluorescent Quantum Dot Liposomes", *Journal of Physical Chemistry B* **2009**, *113*(22): 7725-7728.

Brennan, R. J.; Schiestl, R. H. "Chloroform and carbon tetrachloride induce intrachromosomal recombination and oxidative free radicals in *Saccharomyces cerevisiae*", *Mutation Research* **1998**, *397*(2): 271-278.

Brewer, S. H.; Glomm, W. R.; Johnson, M. C.; Knag, M. K.; Franzen, S. "Probing BSA binding to citrate-coated gold nanoparticles and surfaces", *Langmuir* **2005**, *21*(20): 9303-9307.

Brinker, C. J.; Dunphy, D. R.; Alam, T. M.; Tate, M. P.; Hillhouse, H. W.; Smarsly, B.; Collord, A. D.; Carnes, E.; Baca, H. K.; Kohn, R.; Sprung, M.; Wang, J. "Characterization of Lipid-Templated Silica and Hybrid Thin Film Mesophases by Grazing Incidence Small-Angle X-ray Scattering", *Langmuir* **2009**, *25*(16): 9500-9509.

Brinker, C. J.; Dunphy, D. R.; Garcia, F. L.; Jiang, Z.; Strzalka, J.; Wang, J. "X-Ray characterization of self-assembled long-chain phosphatidylcholine/bile salt/silica mesostructured films with nanoscale homogeneity", *Chemical Communications* **2011**, *47*(6): 1806-1808.

Brinson, B. E.; Lassiter, J. B.; Levin, C. S.; Bardhan, R.; Mirin, N.; Halas, N. J. "Nanoshells Made Easy: Improving Au Layer Growth on Nanoparticle Surfaces", *Langmuir* **2008**, *24*(24): 14166-14171.

Brown, W.; Mortensen, K., *Scattering in Polymeric and Colloidal Systems*. Gordon and Breach: Singapore, 2000.

Brust, M.; Walker, M.; Bethell, D.; Schiffrin, D. J.; Whyman, R. "Synthesis of Thiol-derivatised Gold Nanoparticles in a Two-phase Liquid-Liquid System", *Journal of the Chemical Society, Chemical Communications* **1994**, (7): 801-802.

Burda, C.; Chen, X.; Narayanan, R.; El-Sayed, M. A. "Chemistry and Properties of Nanocrystals of Different Shapes", *Chemical Reviews* **2005**, *105*(4): 1025-1102.

Burnell, E. E.; Cullis, P. R.; Kruijff, B. D. "Effects of tumbling and lateral diffusion on phosphatidylcholine model membrane ³¹P-NMR lineshapes", *Biochim Biophys Acta* **1980**, *603*: 63-69.

Buzea, C.; Pacheco, I. I.; Robbie, K. "Nanomaterials and nanoparticles: Sources and toxicity", *Biointerphases* **2007**, *2*(4): Mr17-Mr71.

- Cantor, R. S. "The lateral pressure profile in membranes: A physical mechanism of general anesthesia", *Biochemistry* **1997**, 36(9): 2339-2344.
- Carion, O.; Mahler, B.; Pons, T.; Dubertret, B. "Synthesis, encapsulation, purification and coupling of single quantum dots in phospholipid micelles for their use in cellular and in vivo imaging", *Nature Protocols* **2007**, 2(10): 2383-2390.
- Cassette, E.; Pons, T.; Bouet, C.; Helle, M.; Bezdetnaya, L.; Marchal, F.; Dubertret, B. "Sol-gel emulsion synthesis of biphotonic core-shell nanoparticles based on lanthanide doped organic-inorganic hybrid materials ", *Chemistry of Materials* **2010**, 22(13): 6117-6124.
- Chamberland, D. L.; Agarwal, A.; Kotov, N.; Fowlkes, J. B.; Carson, P. L.; Wang, X. "Photoacoustic tomography of joints aided by an Etanercept-conjugated gold nanoparticle contrast agent - an ex vivo preliminary rat study", *Nanotechnology* **2008**, 19(9): 095101.
- Chan, V. S. W. "Nanomedicine: An unresolved regulatory issue", *Regulatory Toxicology and Pharmacology* **2006**, 46(3): 218-224.
- Chandler, D. "Interfaces and the driving force of hydrophobic assembly", *Nature* **2005**, 437(7059): 640-647.
- Chang, A. C.; Pfeiffer, W. F.; Guillaume, B.; Baral, S.; Fendler, J. H. "Preparation and Characterization of Selenide Semiconductor Particles in Surfactant Vesicles", *Journal of Physical Chemistry* **1990**, 94(10): 4284-4289.
- Charamisinau, I.; Happawana, G.; Evans, G.; Rosen, A.; Hsi, R. A.; Bour, D. "Semiconductor laser insert with uniform illumination for use in photodynamic therapy ", *Applied Optics* **2005**, 44(24): 5055-5068.
- Chattopadhyay, P. K.; Price, D. A.; Harper, T. F.; Betts, M. R.; Yu, J.; Gostick, E.; Perfetto, S. P.; Goepfert, P.; Koup, R. A.; De Rosa, S. C.; Bruchez, M. P.; Roederer, M. "Quantum dot semiconductor nanocrystals for immunophenotyping by polychromatic flow cytometry", *Nature Medicine* **2006**, 12(8): 972-977.
- Chaudhuri, R. G.; Paria, S. "Core/Shell Nanoparticles: Classes, Properties, Synthesis Mechanisms, Characterization, and Applications", *Chemical Reviews* **2012**, 112: 2373-2433.
- Chen, A. A.; Derfus, A. M.; Khetani, S. R.; Bhatia, S. N. "Quantum dots to monitor RNAi delivery and improve gene silencing", *Nucleic Acids Research* **2005**, 33(22): e190.

Chen, J. Y.; Glaus, C.; Laforest, R.; Zhang, Q.; Yang, M. X.; Gidding, M.; Welch, M. J.; Xia, Y. N. "Gold Nanocages as Photothermal Transducers for Cancer Treatment ", *Small* **2010**, 6(7): 811-817.

Chen, J. Y.; Wang, D. L.; Xi, J. F.; Au, L.; Siekkinen, A.; Warsen, A.; Li, Z. Y.; Zhang, H.; Xia, Y. N.; Li, X. D. "Immuno Gold Nanocages with Tailored Optical Properties for Targeted Photothermal Destruction of Cancer Cells ", *Nano Letters* **2007**, 7(5): 1318-1322.

Chen, Y.; Bose, A.; Bothun, G. D. "Controlled Release from Bilayer-Decorated Magnetoliposomes via Electromagnetic Heating", *ACS Nano* **2010**, 4(6): 3215-3221.

Cheon, J.; Lee, J.-H. "Synergistically Integrated Nanoparticles as Multimodal Probes for Nanobiotechnology", *Accounts of Chemical Research* **2008**, 41(12): 1630-1640.

Choi, H. S.; Liu, W.; Misra, P.; Tanaka, E.; Zimmer, J. P.; Ipe, B. I.; Bawendi, M. G.; Frangioni, J. V. "Renal clearance of quantum dots", *Nature Biotechnology* **2007**, 25(10): 1165-1170.

Christina, V.; Green, C. S. "Colloidal gold solution. The preparation of gold solutions and their titration with permanent hydrogen-ion concentration standards ", *Journal of Laboratory and Clinical Medicine* **1928**, 13: 678.

Chu, T. C.; Shieh, F.; Lavery, L. A.; Levy, M.; Richards-Kortum, R.; Korgel, B. A.; Ellington, A. D. "Labeling tumor cells with fluorescent nanocrystal-aptamer bioconjugates", *Biosensors & Bioelectronics* **2006**, 21(10): 1859-1866.

Coates, J., Interpretation of Infrared Spectra, A Practical Approach. In *Encyclopedia of Analytical Chemistry*, Meyers, R. A., Ed. John Wiley & Sons Ltd: Chichester, 2000; pp 10815-10837.

Cole, J. R.; Mirin, N. A.; Knight, M. W.; Goodrich, G. P.; Halas, N. J. "Photothermal Efficiencies of Nanoshells and Nanorods for Clinical Therapeutic Applications ", *Journal of Physical Chemistry C* **2009**, 113(28): 12090-12094.

Cole, L. K.; Vance, J. E.; Vance, D. E. "Phosphatidylcholine biosynthesis and lipoprotein metabolism", *Biochim Biophys Acta* **2012**, 1821(5): 754-761.

Collins, S. J. "The HL-60 promyelocytic leukemia cell line: proliferation, differentiation, and cellular oncogene expression", *Blood* **1987**, 70: 1233-1244.

Crook, K.; Stevenson, B. J.; Dubouchet, M.; Porteous, D. J. "Inclusion of cholesterol in DOTAP transfection complexes increases the delivery of DNA to cells in vitro in the presence of serum", *Gene Therapy* **1998**, 5: 137-143.

Cubeddu, R.; Pifferi, A.; Taroni, P.; Torricelli, A.; Valentini, G. "Noninvasive absorption and scattering spectroscopy of bulk diffusive media: An application to the optical characterization of human breast ", *Applied Physics Letters* **1999**, 74(6): 874-876.

Dalton, W. T. J.; Ahearn, M. J.; McCredie, K. B.; Fleireich, E. J.; Stass, S. A.; Trujillo, J. M. "HL-60 cell line was derived from a patient with FAB-M2 and not FAB-M3", *Blood* **1988**, 71: 242-247.

Daniel, M.; Astruc, D. "Gold Nanoparticles: Assembly, Supramolecular Chemistry, Quantum-Size-Related Properties, and Applications toward Biology, Catalysis, and Nanotechnology", *Chemical Reviews* **2004**, 104(1): 293-346.

Dashiti, M.; Kulik, W.; Hoek, F.; Veerman, E. C.; Peppelenbosch, M. P.; Rezaee, F. "A Phospholipidomic Analysis of All

Defined Human Plasma Lipoproteins", *Scientific Reports* **2011**, 1(139): 1-11.

De Jong, W. H.; Hagens, W. I.; Krystek, P.; Burger, M. C.; Sips, A.; Geertsma, R. E. "Particle size-dependent organ distribution of gold nanoparticles after intravenous administration ", *Biomaterials* **2008**, 29(12): 1912-1919.

De Luca, G.; Pisula, W.; Credgington, D.; Treossi, E.; Fenwick, O.; Lazzerini, G. M.; Dabirian, R.; Orgiu, E.; Liscio, A.; Palermo, V.; Mullen, K.; Cacialli, F.; Samori, P. "Non-conventional Processing and Post-processing Methods for the Nanostructuring of Conjugated Materials for Organic Electronics", *Advanced Functional Materials* **2011**, 21(7): 1279-1295.

Deen, W. M., *Analysis of Transport Phenomena*. Oxford University Press Inc.: New York, 1998.

Deka, S.; Genovese, A.; Zhang, Y.; Miszt, K.; Bertoni, G.; Krahne, R.; Giannini, C.; Manna, L. "Phosphine-Free Synthesis of p-Type Copper(I) Selenide Nanocrystals in Hot Coordinating Solvents ", *Journal of the American Chemical Society* **2010**, 132(26): 8912-8914.

Delehanty, J. B.; Bradburne, C. E.; Medintz, I. L.; Farrell, D.; Pons, T.; Brunel, F. M.; Dawson, P. E.; Mattoussi, H. "Specific cellular delivery and intracellular fate of quantum dot-peptide and quantum dot-polymer nanoassemblies", *Colloidal Quantum Dots for Biomedical Applications Iii* **2008**, 6866: K8660-K8660.

Delehanty, J. B.; Mattoussi, H.; Medintz, I. L. "Delivering quantum dots into cells: strategies, progress and remaining issues", *Analytical and Bioanalytical Chemistry* **2009**, 393(4): 1091-1105.

Derfus, A. M.; Chan, W. C. W.; Bhatia, S. N. "Probing the Cytotoxicity of Semiconductor Quantum Dots", *Nano Letters* **2004**, 4(1): 11-18.

Deserno, M.; Gelbart, W. M. "Adhesion and wrapping in colloid-vesicle complexes", *Journal of Physical Chemistry B* **2002**, 106(21): 5543-5552.

Dickinson, E.; McClements, D. J., *Advances in Food Colloids*. Blackie Academic & Professional: Glasgow, 1996.

Dietrich, C.; Angelova, M.; Pouligny, B. "Adhesion of latex spheres to giant phospholipid vesicles: Statics and dynamics", *Journal De Physique II* **1997**, 7(11): 1651-1682.

Donega, C. D.; Bode, M.; Meijerink, A. "Size- and temperature-dependence of exciton lifetimes in CdSe quantum dots", *Physical Review B* **2006**, 74: 085320.

Dubertret, B.; Skourides, P.; Norris, D. J.; Noireaux, V.; Brivanlou, A. H.; Libchaber, A. "In vivo imaging of quantum dots encapsulated in phospholipid micelles", *Science* **2002**, 298(5599): 1759-1762.

Dubois, M.; Deme, B.; Gulik-Krzywicid, T.; Dedieu, J.-C.; Vautrin, C.; Desert, S.; Perez, E.; Zemb, T. "Self-assembly of regular hollow icosahedra in salt-free catanionic solutions", *Nature* **2001**, 411: 672-675.

Duff, D. G.; Baiker, A.; Edwards, P. P. "A New Hydrosol of Gold Clusters .1. Formation and Particle-Size Variation", *Langmuir* **1993**, 9(9): 2301-2309.

Duguet, E.; Vasseur, S.; Mornet, S.; Devoisselle, J. "Magnetic nanoparticles and their applications in medicine", *Nanomedicine* **2006**, 1(2): 157-168.

Edgar, R.; McKinstry, M.; Hwang, J.; Oppenheim, A. B.; Fekete, R. A.; Giulian, G.; Merrill, C.; Nagashima, K.; Adhya, S. "High-sensitivity bacterial detection using biotin-tagged phage and quantum-dot nanocomplexes", *Proceedings of the National Academy of Sciences of the United States of America* **2006**, 103(13): 4841-4845.

Efrat, R.; Kesselman, E.; Aserin, A.; Garti, N.; Danino, D. "Solubilization of Hydrophobic Guest Molecules in the Monoolein Discontinuous Q(L) Cubic Mesophase and Its Soft Nanoparticles", *Langmuir* **2009**, 25(3): 1316-1326.

El-Sayed, I. H.; Huang, X. H.; El-Sayed, M. A. "Selective laser photo-thermal therapy of epithelial carcinoma using anti-EGFR antibody conjugated gold nanoparticles", *Cancer Letters* **2006**, 239: 129-135.

El-Sayed, M. A.; Cevc, G. "The vesicle-to-micelle transformation of phospholipid–cholate mixed aggregates: A state of the art analysis including membrane curvature effects", *Biochimica Et Biophysica Acta* **2011**, 1808: 140-153.

Erathodiyil, N.; Ying, J. Y. "Functionalization of Inorganic Nanoparticles for Bioimaging Applications", *Accounts of Chemical Research* **2011**, 44(10): 925-935.

Erogbogbo, F.; Ken-Tye, Y.; Hu, R.; Law, W.; Ding, H.; Chang, C.; Prasad, P. N.; Swihart, M. T. "Biocompatible Magnetofluorescent Probes: Luminescent Silicon Quantum Dots Coupled with Superparamagnetic Iron(III) Oxide ", *ACS Nano* **2010**, 4(9): 5131-5138.

Erogbogbo, F.; Yong, K. T.; Roy, I.; Xu, G. X.; Prasad, P. N.; Swihart, M. T. "Biocompatible luminescent silicon quantum dots for imaging of cancer cells", *ACS Nano* **2008**, 2(5): 873-878.

Esendagli, G.; Canpinar, H.; Dogan, A. L.; Akkaya, M.; Kansu, E.; Guc, D. "Transfection of myeloid leukaemia cell lines is distinctively regulated by fibronectin substratum", *Cytotechnology* **2009**, 61: 45-53.

Evans, E.; Heinrich, V.; Ludwig, F.; Rawicz, W. "Dynamic tension spectroscopy and strength of biomembranes", *Biophysical Journal* **2003**, 85(4): 2342-2350.

Feng, L. Y.; Kong, X. G.; Chao, K. F.; Sun, Y. J.; Zeng, Q. H.; Zhang, Y. L. "Efficient phase transfer of hydrophobic CdSe quantum dots: From nonpolar organic solvent to biocompatible water buffer", *Materials Chemistry and Physics* **2005**, 93(2-3): 310-313.

Fereshney, R. I., *Culture of Animal Cells: A Manual of Basic Technique and Specialized Applications*. 6th ed.; John Wiley & Sons, Inc.: Hoboken, 2010.

Fleck, R. A.; Romero-Steiner, S.; Nahm, M. H. "Use of HL-60 Cell Line To Measure Opsonic Capacity of Pneumococcal Antibodies", *Clinical and Diagnostic Laboratory Immunology* **2005**, 12(1): 19-27.

Fontes, A.; Fernandes, H. P.; Barjas-Castro, M. L.; de Thomaz, A. A.; de Ysasa Pozzo, L.; Barbosa, L. C.; Cesar, C. L. "Red blood cell membrane viscoelasticity, agglutination, and zeta potential measurements with double optical tweezers", *Proceedings of SPIE* **2006**, 6088: 608811.

Fortina, P.; Kricka, L. J.; Graves, D. J.; Park, J.; Hyslop, T.; Tam, F.; Halas, N. J.; Surrey, S.; Waldman, S. A. "Applications of nanoparticles to diagnostics and therapeutics in colorectal cancer", *Trends in Biotechnology* **2007**, 25(4): 145-152.

Fox, C. B. "Squalene Emulsion for Parenteral Vaccine and Drug Delivery", *Molecules* **2009**, 14: 3286-3312.

Frasco, M. F.; Chaniotakis, N. "Bioconjugated quantum dots as fluorescent probes for bioanalytical applications", *Analytical and Bioanalytical Chemistry* **2010**, 396(1): 229-240.

Freeman, C.; Halperin, E. C.; Brady, L. W.; Wazer, D. E., *Perez and Brady's Principles and Practice of Radiation Oncology*. Wolters Kluwer Health/Lippincott Williams & Wilkins: Philadelphia, 2008.

Friskén, B. J. "Revisiting the method of cumulants for the analysis of dynamic light-scattering data", *Applied Optics* **2001**, 40(24): 4087-4091.

Gallagher, R.; Collins, S.; Trujillo, J.; McCredie, K.; Ahearn, M.; Tsai, S.; Metzgar, R.; Aulakh, G.; Ting, R.; Ruscetti, F.; Gallo, R. "Characterization of the continuous, differentiating myeloid cell line (HL-60) from a patient with acute promyelocytic leukemia", *Blood* **1979**, 54: 713-733.

Gao, H. J.; Shi, W. D.; Freund, L. B. "Mechanics of receptor-mediated endocytosis", *Proceedings of the National Academy of Sciences of the United States of America* **2005**, 102(27): 9469-9474.

Gao, J.; Gu, H.; Xu, B. "Multifunctional Magnetic Nanoparticles: Design, Synthesis, and Biomedical Applications", *Accounts of Chemical Research* **2009**, 42(8): 1097-1107.

Gao, X.; Cui, Y.; Levenson, R. M.; Chung, L. W. K.; Nie, S. "In vivo cancer targeting and imaging with semiconductor quantum dot", *Nature Biotechnology* **2004**, 22: 969-976.

Garcia, M. A. "Surface plasmons in metallic nanoparticles: fundamentals and applications", *Journal of Physics D-Applied Physics* **2011**, 44: 283001.

Gianella, A.; Jarzyna, P. A.; Mani, V.; Ramachandran, S.; Calcagno, C.; Tang, J.; Kann, B.; Dijk, W. J. R.; Thijssen, V. L.; Griffioen, A. W.; Storm, G.; Fayad, Z. A.; Mulder, W. J. M. "Multifunctional Nanoemulsion Platform for Imaging Guided Therapy Evaluated in Experimental Cancer", *ACS Nano* **2011**, 5(6): 4422-4433.

Gill, R.; Zayats, M.; Willner, I. "Semiconductor quantum dots for bioanalysis", *Angewandte Chemie-International Edition* **2008**, 47(40): 7602-7625.

Ginzburg, V. V.; Balijepailli, S. "Modeling the thermodynamics of the interaction of nanoparticles with cell membranes", *Nano Letters* **2007**, 7(12): 3716-3722.

Glatter, O.; Kratky, O.; Eds., *Small-Angle X-Ray Scattering*. Academic Press: New York, 1982.

Glogowski, E.; He, J.; Russell, T. P.; Emrick, T. "Mixed monolayer coverage on gold nanoparticles for interfacial stabilization of immiscible fluids", *Chemical Communications* **2005**: 4050-4052.

Gobin, A. M.; Lee, M. H.; Halas, N. J.; James, W. D.; Drezek, R. A.; West, J. L. "Near-Infrared Resonant Nanoshells for Combined Optical Imaging and Photothermal Cancer Therapy ", *Nano Letters* **2007**, 7: 1929-1934.

Goldman, E. R.; Mattoussi, H.; Anderson, G. P.; Medintz, I. L.; Mauro, J. M., Fluoroimmunoassays Using Antibody-Conjugated Quantum Dots. In *NanoBiotechnology Protocols*, Rosenthal, S. J.; Wright, D. W., Eds. Humana Press: Totowa, 2005; p 19.

Gopalakrishnan, G.; Danelon, C.; Izewska, P.; Prummer, M.; Bolinger, P. Y.; Geissbuhler, I.; Demurtas, D.; Dubochet, J.; Vogel, H. "Multifunctional lipid/quantum dot hybrid nanocontainers for controlled targeting of live cells", *Angewandte Chemie-International Edition* **2006**, 45(33): 5478-5483.

Grabar, K. C.; Smith, P. C.; Musick, M. D.; Davis, J. A.; Walter, D. G.; Jackson, M. A.; Guthrie, A. P.; Natan, M. J. "Kinetic Control of Interparticle Spacing in Au Colloid-Based Surfaces: Rational Nanometer-Scale Architecture ", *Journal of the American Chemical Society* **1996**, 118(5): 1148-1153.

Gracin, D.; Bernstorff, S.; Dubcek, P.; Gajovic, A.; Juraic, K. " Study of amorphous nanocrystalline thin silicon films by grazing-incidence small-angle X-ray scattering ", *Journal of Applied Crystallography* **2007**, 40(S1): s373-s376.

Greenspan, P.; Fowler, S. D. "Spectrofluorometric studies of the lipid probe, Nile red", *Journal of Lipid Research* **1985**, 26(7): 781-789.

Greenwood, A. I.; Tristram-Nagle, S.; Nagle, J. F. "Partial molecular volumes of lipids and cholesterol", *Chemistry and Physics of Lipids* **2006**, 143(1-2): 1-10.

Guinier, A.; Fournet, G., *Small-Angle Scattering of X-Rays*. Wiley: New York, 1955.

Gustafsson, J.; Ljusberg-Wahren, H.; Almgren, M.; Larsson, K. "Submicron Particles of reversed lipid phases in water stabilized by a nonionic amphiphilic polymer", *Langmuir* **1997**, 13(26): 6964-6971.

Halas, N. J. "Playing with plasmons: tuning the optical resonant properties of metallic nanoshells ", *Mrs Bulletin* **2005**, 30(5): 362-367.

Hall, R. A.; Thistlethwaite, P. J.; Grieser, F. "An Investigation of Miscibility in Guest-Host Monolayers by Surface Pressure and Fluorescence Methods", *Langmuir* **1993**, 9(8): 2128-2132.

Hantash, B. M.; Mahmood, M. B. "Fractional Photothermolysis: A Novel Aesthetic Laser Surgery Modality", *Dermatologic Surgery* **2007**, 33: 525-534.

Hardman, R. "A Toxicologic Review of Quantum Dots: Toxicity Depends on Physicochemical and Environmental Factors", *Environmental Health Perspectives* **2006**, 114(2): 165-172.

Harris, D. C., *Quantitative Chemical Analysis*. W. H. Freeman: New York, 2003.

Haugen, A.; May, S. "The influence of zwitterionic lipids on the electrostatic adsorption of macroions onto mixed lipid membranes", *Journal of Chemical Physics* **2007**, 127(21): -.

Hauss, T.; Dante, S.; Dencher, N. A.; Haines, T. H. "Squalane is in the midplane of the lipid bilayer: implications for its function as a proton permeability barrier", *Biochimica Et Biophysica Acta* **2002**, 1556: 149-154.

Haynes, W. M.; Lide, D. R., *CRC Handbook of Chemistry and Physics*. 91st ed.; CRC Press: Boca Raton, FL, 2011.

Heerklotz, H.; Seelig, J. "Correlation of Membrane/Water Partition Coefficients of Detergents with the Critical Micelle Concentration", *Biophysical Journal* **2000**, 78: 2435-2440.

Heitsch, A. T.; Smith, D. K.; Patel, R. N.; Ress, D.; Korgel, B. A. "Multifunctional particles: Magnetic nanocrystals and gold nanorods coated with fluorescent dye-doped silica shells", *Journal of Solid State Chemistry* **2008**, 181(7): 1590-1599.

Hermanson, G. T., *Bioconjugate Techniques*. Second ed.; Academic Press, Inc.: San Diego, 2008.

Hermansson, M.; Hokynar, K.; Somerharju, P. "Mechanisms of glycerophospholipid homeostasis in mammalian cells", *Progress in Lipid Research* **2011**, 50: 240-257.

Hessel, C. M.; Henderson, E. J.; Veinot, J. G. C. "Hydrogen Silsesquioxane: A Molecular Precursor for Nanocrystalline Si-SiO₂ Composites and Freestanding Hydride-Surface-Terminated Silicon Nanoparticles ", *Chemistry of Materials* **2006**, *18*(26): 6139-6146.

Hessel, C. M.; Henderson, E. J.; Veinot, J. G. C. "An Investigation of the Formation and Growth of Oxide-Embedded Silicon Nanocrystals in Hydrogen Silsesquioxane-Derived Nanocomposites ", *Journal of Physical Chemistry C* **2007**, *111*(9): 6956-6961.

Hessel, C. M.; Pattani, V. P.; Rasch, M. R.; Panthani, M. G.; Koo, B.; Tunnell, J. W.; Korgel, B. A. "Copper selenide nanocrystals for photothermal therapy", *Nano Letters* **2011**, *11*(6): 2560-2566.

Hessel, C. M.; Rasch, M. R.; Hueso, J. L.; Goodfellow, B. W.; Akhavan, V.; Puvanakrishnan, P.; Tunnell, J. W.; Korgel, B. A. "Alkyl Passivation and Amphiphilic Polymer Coating of Silicon Nanocrystals for Diagnostic Imaging", *Small* **2010**, *6*(18): 2026-2034.

Heywood, B. R.; Fendler, J. H.; Mann, S. "Insitu Imaging of Cds and Zns Semiconductor Particles in Surfactant Vesicles", *Journal of Colloid and Interface Science* **1990**, *138*(1): 295-298.

Hirsch, L. R.; Stafford, R. J.; Bankson, J. A.; Sershen, S. R.; Rivera, B.; Price, R. E.; Hazle, J. D.; Halas, N. J.; West, J. L. "Nanoshell-mediated near-infrared thermal therapy of tumors under magnetic resonance guidance", *Proceedings of the National Academy of Sciences of the United States of America* **2003**, *100*(23): 13549-13554.

Ho, Y. P.; Leong, K. W. "Quantum dot-based theranostics", *Nanoscale* **2010**, *2*(1): 60-68.

Holleman, A. F.; Wiberg, E., *Inorganic Chemistry*. Academic Press: San Diego, 2001.

Huang, X.; El-Sayed, I. H.; Qian, W.; El-Sayed, M. A. "Cancer Cell Imaging and Photothermal Therapy in the Near-Infrared Region by Using Gold Nanorods", *Journal of the American Chemical Society* **2006**, *128*: 2115-2120.

Huang, X. H.; Jain, P. K.; El-Sayed, I. H.; El-Sayed, M. A. "Plasmonic photothermal therapy (PPTT) using gold nanoparticles", *Lasers in Medical Science* **2008**, *23*(3): 217-228.

Huang, X. H.; Neretina, S.; El-Sayed, M. A. "Gold Nanorods: From Synthesis and Properties to Biological and Biomedical Applications", *Advanced Materials* **2009**, *21*(48): 4880-4910.

Hurst, S. J., *Biomedical Nanotechnology Methods and Protocols*. Human Press: New York, 2011.

Hutchinson, J. L.; Mann, S.; Skarnulis, A. J.; Williams, R. J. P. "Preparation of silver oxide crystallites within phospholipid vesicles and their use in nucleation studies ", *Journal of the Chemical Society, Chemical Communications* **1980**, (13): 634-635.

Hyeon, T.; Lee, S. S.; Park, J.; Chung, Y.; Bin Na, H. "Synthesis of highly crystalline and monodisperse maghemite nanocrystallites without a size-selection process", *Journal of the American Chemical Society* **2001**, 123(51): 12798-12801.

Islam, T.; Josephson, L. "Current state and future applications of active targeting in malignancies using superparamagnetic iron oxide nanoparticles", *Cancer Biomarkers* **2009**, 5(2): 99-107.

Israelachvili, J. N., *Intermolecular and Surface Forces*. 2nd ed.; Academic press Inc.: San Diego, 1992.

Jackson, M. L.; Schmidt, C. F.; Lichtenberg, D.; Litman, B. J.; Albert, A. D. "Solubilization of Phosphatidylcholine Bilayers by Octyl Glucoside", *Biochemistry* **1982**, 21(19): 4576-4582.

Jagminas, A.; Juskenas, R.; Gailiute, I.; Statkute, G.; Tomasiunas, R. "Electrochemical synthesis and optical characterization of copper selenide nanowire arrays within the alumina pores ", *Journal of Crystal Growth* **2006**, 294(2): 343-348.

Jain, P. K.; El-Sayed, I. H.; El-Sayed, M. A. "Au nanoparticles target cancer", *Nano Today* **2007**, 2(1): 18-29.

Jain, P. K.; Huang, X. H.; El-Sayed, I. H.; El-Sayed, M. A. "Noble Metals on the Nanoscale: Optical and Photothermal Properties and Some Applications in Imaging, Sensing, Biology, and Medicine", *Accounts of Chemical Research* **2008**, 41(12): 1578-1586.

Jain, P. K.; Lee, K. S.; El-Sayed, I. H.; El-Sayed, M. A. "Calculated Absorption and Scattering Properties of Gold Nanoparticles of Different Size, Shape, and Composition: Applications in Biological Imaging and Biomedicine ", *Journal of Physical Chemistry B* **2006**, 110(14): 7238-7248.

Jana, N. R.; Gearheart, L.; Murphy, C. J. "Wet chemical synthesis of high aspect ratio cylindrical gold nanorods ", *Journal of Physical Chemistry B* **2001**, 105(19): 4065-4067.

Jang, H.; Pell, L. E.; Korgel, B. A.; English, D. S. "Photoluminescence quenching of silicon nanoparticles in phospholipid vesicle bilayers", *Journal of Photochemistry and Photobiology a-Chemistry* **2003**, *158*(2-3): 111-117.

Jarzyna, P. A.; Skajaa, T.; Gianella, A.; Cormode, D. P.; Samber, D. D.; Dickson, S. D.; Chen, W.; Griffioen, A. W.; Fayad, Z. A.; Mulder, W. J. M. "Iron oxide core oil-in-water emulsions as a multifunctional nanoparticle

platform for tumor targeting and imaging", *Biomaterials* **2009**, *30*: 6947-6954.

Jelinek, R.; Mogilevsky, A.; Volinsky, R.; Dayagi, Y.; Markovich, N. "Gold Nanoparticle Self-Assembly in Saturated Phospholipid Monolayers", *Langmuir* **2010**, *26*(11): 7893-7898.

Jesorka, A.; Orwar, O. "Liposomes: Technologies and Analytical Applications", *Annual Review of Analytical Chemistry* **2008**, *1*: 801-832.

Ji, X. J.; Shao, R. P.; Elliott, A. M.; Stafford, R. J.; Esparza-Coss, E.; Bankson, J. A.; Liang, G.; Luo, Z. P.; Park, K.; Markert, J. T.; Li, C. "Bifunctional gold nanoshells with a superparamagnetic iron oxide-silica core suitable for both MR imaging and photothermal therapy", *Journal of Physical Chemistry C* **2007**, *111*(17): 6245-6251.

Jiang, M.; Liu, Z. "Reversible aggregation of gold nanoparticles driven by inclusion complexation", *Journal of Materials Chemistry* **2007**, *17*(40): 4249-4254.

Jiang, W.; Kim, B. Y. S.; Rutka, J. T.; Chan, W. C. W. "Nanoparticle-mediated cellular response is size-dependent", *Nature Nanotechnology* **2008**, *3*(3): 145-150.

Johnsson, M.; Edwards, K. "Interactions between Nonionic Surfactants and Sterically Stabilized Phosphatidyl Choline Liposomes", *Langmuir* **2000**, *16*(23): 8632-8642.

Johnsson, M.; Edwards, K. "Liposomes, disks, and spherical micelles: Aggregate structure in mixtures of gel phase phosphatidylcholines and poly(ethylene glycol)-phospholipids", *Biophysical Journal* **2003**, *85*(6): 3839-3847.

Jori, G.; Spikes, J. D. "Photothermal Sensitizers: Possible Use in Tumor Therapy", *Journal of Photochemistry and Photobiology B: Biology* **1990**, *6*: 93-101.

Jung, H. T.; Coldren, B.; Zasadzinski, J. A.; Iampietro, D. J.; Kaler, E. W. "The origins of stability of spontaneous vesicles", *Proceedings of the National Academy of Sciences of the United States of America* **2001**, *98*(4): 1353-1357.

- Kairdolf, B. A.; Smith, A. M.; Nie, S. "One-pot synthesis, encapsulation, and solubilization of size-tuned quantum dots with amphiphilic multidentate ligands", *Journal of the American Chemical Society* **2008**, *130*(39): 12866-+.
- Kam, N. W. S.; O'Connell, M.; Wisdom, J. A.; Dai, H. J. "Carbon nanotubes as multifunctional biological transporters and near-infrared agents for selective cancer cell destruction ", *Proceedings of the National Academy of Sciences of the United States of America* **2005**, *102*(33): 11600-11605.
- Katz, E.; Willner, I. "Integrated nanoparticle-biomolecule hybrid systems: Synthesis, properties, and applications", *Angewandte Chemie-International Edition* **2004**, *43*(45): 6042-6108.
- Kelly, K. L.; Coronado, E.; Zhao, L. L.; Schatz, G. C. "The Optical Properties of Metal Nanoparticles: The Influence of Size, Shape, and Dielectric Environment", *Journal of Physical Chemistry B* **2003**, *107*(3): 668-677.
- Kennedy, M. T.; Korgel, B. A.; Monbouquette, H. G.; Zasadzinski, J. A. "Cryo-transmission electron microscopy confirms controlled synthesis of cadmium sulfide nanocrystals within lecithin vesicles", *Chemistry of Materials* **1998**, *10*(8): 2116-2119.
- Kim, T.; Lee, K.; Gong, M.; Joo, S. "Control of Gold Nanoparticle Aggregates by Manipulation of Interparticle Interaction", *Langmuir* **2005**, *21*(21): 9524-9528.
- Kitano, T.; Kataoka, T.; Shirota, T. "An empirical equation of the relative viscosity of polymer melts filled with various inorganic fillers", *Rheologica Acta* **1981**, *20*(2): 207.
- Klimov, V.; Bolivar, P. H.; Kurz, H.; Karavanskii, V.; Krasovskii, V.; Korkishko, Y. "Linear and nonlinear transmission of CuxS quantum dots ", *Applied Physics Letters* **1995**, *67*(5): 653-655.
- Koo, B.; Patel, R. N.; Korgel, B. A. "Synthesis of CuInSe₂ Nanocrystals with Trigonal Pyramidal Shape ", *Journal of the American Chemical Society* **2009**, *131*(9): 3134-3135.
- Korgel, B. A.; Fitzmaurice, D. "Small-angle x-ray-scattering study of silver-nanocrystal disorder-order phase transitions", *Physical Review B* **1999**, *59*(22): 14191-14201.
- Korgel, B. A.; Fullam, S.; Connolly, S.; Fitzmaurice, D. "Assembly and self-organization of silver nanocrystal superlattices: Ordered "soft spheres"", *Journal of Physical Chemistry B* **1998**, *102*(43): 8379-8388.

Korgel, B. A.; Monbouquette, H. G. "Synthesis of size-monodisperse CdS nanocrystals using phosphatidylcholine vesicles as true reaction compartments", *Journal of Physical Chemistry* **1996**, *100*(1): 346-351.

Korgel, B. A.; Monbouquette, H. G. "Controlled synthesis of mixed core and layered (Zn,Cd)S and (Hg,Cd)S nanocrystals within phosphatidylcholine vesicles", *Langmuir* **2000**, *16*(8): 3588-3594.

Korgel, B. A.; van Zanten, J. H.; Monbouquette, H. G. "Vesicle size distributions measured by flow field-flow fractionation coupled with multiangle light scattering", *Biophys J* **1998**, *74*(6): 3264-3272.

Krack, M.; Hohenberg, H.; Kornowski, A.; Lindner, P.; Weller, H.; Forster, S. "Nanoparticle-loaded magnetophoretic vesicles", *Journal of the American Chemical Society* **2008**, *130*(23): 7315-7320.

Kriegel, I.; Jiang, C.; Rodriguez-Fernandez, J.; Schaller, R. D.; Talapin, D. V.; da Como, E.; Feldmann, J. "Tuning the Excitonic and Plasmonic Properties of Copper Chalcogenide Nanocrystals", *Journal of the American Chemical Society* **2012**, *134*: 1583-1590.

Kucerka, N.; Nieh, M.-P.; Katsaras, J. "Fluid phase lipid areas and bilayer thicknesses of commonly used phosphatidylcholines as a function of temperature", *Biochimica Et Biophysica Acta* **2011**, *1808*: 2761-2771.

Kudlicki, W.; Katzen, F.; Peterson, T. C. "Membrane protein expression: no cells required", *Trends in Biotechnology* **2009**, *27*(8): 455-460.

Kumar, P. S.; Pastoriza-Santos, I.; Rodriguez-Gonzalez, B.; Garcia de Abajo, F. J.; Liz-Marzan, L. M. "High-yield synthesis and optical response of gold nanostars ", *Nanotechnology* **2008**, *19*(1): 015606.

Kundu, S. K., S. "Layer-by-Layer Assembly of Thiol-Capped Au Nanoparticles on a Water Surface and Their Deposition on H-Terminated Si(001) by the Langmuir-Blodgett Method", *Langmuir* **2011**, *27*(7): 3930-3936.

Kuzuya, T.; Itoh, K.; Sumiyama, K. "Low polydispersed copper-sulfide nanocrystals derived from various Cu-alkyl amine complexes ", *Journal of Colloid and Interface Science* **2008**, *319*(2): 565-571.

Lal, S.; Clare, S. E.; Halas, N. J. "Nanoshell-Enabled Photothermal Cancer Therapy: Impending Clinical Impact", *Accounts of Chemical Research* **2008**, *41*(12): 1842-1851.

Lambert, T. N.; Andrews, N. L.; Gerung, H.; Boyle, T. J.; Oliver, J. M.; Wilson, B. S.; Han, S. M. "Water-soluble germanium(0) nanocrystals: cell recognition and near-infrared photothermal conversion properties ", *Small* **2007**, 3(4): 691-699.

Landry, J.; Samson, S.; Chretien, P. "Hyperthermia-induced Cell Death, Thermotolerance, and Heat Shock Proteins in Normal, Respiration-deficient, and Glycolysis-deficient Chinese Hamster Cells", *Cancer Research* **1990**, 46: 324-327.

Larson, T. A.; Bankson, J. A.; Aaron, J.; Sokolov, K. "Hybrid plasmonic magnetic nanoparticles as molecular specific agents for MRI/optical imaging and photothermal therapy of cancer cells ", *Nanotechnology* **2007**, 18(32): 325101.

Lasic, D. D. "The mechanism of vesicle formation", *Biochemical Journal* **1988**, 256(1): 1-11.

Lassiter, J. B.; Aizpurua, J.; Hernandez, L. I.; Brandl, D. W.; Romero, I.; Lal, S.; Hafner, J. H.; Nordlander, P.; Halas, N. J. "Close Encounters between Two Nanoshells ", *Nano Letters* **2008**, 8(4): 1212-1218.

Laurent, S.; Boutry, S.; Mahieu, I.; Vander Elst, L.; Muller, R. N. "Iron Oxide Based MR Contrast Agents: from Chemistry to Cell Labeling", *Current Medicinal Chemistry* **2009**, 16(35): 4712-4727.

Lee, C.; Kim, H.; Hong, C.; Kim, M.; Hong, S.; Lee, D. H.; Lee, W. I. "Porous silicon as an agent for cancer thermotherapy based on near-infrared light irradiation ", *Journal of Materials Chemistry* **2008**, 18(40): 4790-4795.

Lee, D. C.; Mikulec, F. V.; Pelaez, J. M.; Koo, B.; Korgel, B. A. "Synthesis and magnetic properties of silica-coated FePt nanocrystals", *Journal of Physical Chemistry B* **2006**, 110(23): 11160-11166.

Lee, J. E.; Lee, N.; Kim, T.; Kim, J.; Hyeon, T. "Multifunctional Mesoporous Silica Nanocomposite Nanoparticles for Theranostic Applications", *Accounts of Chemical Research* **2011**, 44(10): 893-902.

Lee, K.; Sathyagal, A. N.; McCormick, A. V. "A closer look at an aggregation model of the Stober process ", *Colloids and Surfaces a-Physicochemical and Engineering Aspects* **1998**, 144(1-3): 115-125.

Leng, J.; Egelhaaf, S. U.; Cates, M. E. "Kinetics of the micelle-to-vesicle transition: Aqueous lecithin-bile salt mixtures", *Biophysical Journal* **2003**, 85(3): 1624-1646.

Levin, C. S.; Bishnoi, S. W.; Grady, N. K.; Halas, N. J. "Determining the Conformation of Thiolated Poly(ethylene glycol) on Au Nanoshells by Surface-Enhanced Raman Scattering Spectroscopic Assay ", *Analytical Chemistry* **2006**, *78*(10): 3277-3281.

Levin, C. S.; Kundu, J.; Janesko, B. G.; Scuseria, G. E.; Raphael, R. M.; Halas, N. J. "Interactions of Ibuprofen with Hybrid Lipid Bilayers Probed by Complementary Surface-Enhanced Vibrational Spectroscopies", *Journal of Physical Chemistry B* **2008**, *112*(45): 14168-14175.

Li, L.; Daou, T. J.; Texier, I.; Tran, T. K. C.; Nguyen, Q. L.; Reiss, P. "Highly Luminescent CuInS₂/ZnS Core/Shell Nanocrystals: Cadmium-Free Quantum Dots for In Vivo Imaging", *Chemistry of Materials* **2009**, *21*(12): 2422-2429.

Li, Y. B.; Lu, W.; Huang, Q. A.; Huang, M. A.; Li, C.; Chen, W. "Copper sulfide nanoparticles for photothermal ablation of tumor cells ", *Nanomedicine* **2010**, *5*(8): 1161-1171.

Li, Z. F.; Ruckenstein, E. "Water-soluble poly(acrylic acid) grafted luminescent silicon nanoparticles and their use as fluorescent biological staining labels", *Nano Letters* **2004**, *4*(8): 1463-1467.

Lian, W.; Litherland, S. A.; Badrane, H.; Tan, W.; Wu, D.; Baker, H. V.; Gulig, P. A.; Lim, D. V.; Jin, S. "Ultrasensitive detection of biomolecules with fluorescent dye-doped nanoparticles ", *Analytical Biochemistry* **2004**, *334*(1): 135-144.

Liang, H.; Wan, L.; Bai, C.; Jiang, L. "Gold Hollow Nanospheres: Tunable Surface Plasmon Resonance Controlled by Interior-Cavity Sizes ", *Journal of Physical Chemistry B* **2005**, *109*(16): 7795-7800.

Liao, H.; Nehl, C. L.; Hafner, J. H. "Biomedical applications of plasmon resonant metal nanoparticles ", *Nanomedicine* **2006**, *1*(2): 201-208.

Lin, C. A. J.; Sperling, R. A.; Li, J. K.; Yang, T. Y.; Li, P. Y.; Zanella, M.; Chang, W. H.; Parak, W. G. J. "Design of an amphiphilic polymer for nanoparticle coating and functionalization", *Small* **2008**, *4*(3): 334-341.

Lin, W. B.; Hyeon, T.; Lanza, G. M.; Zhang, M. Q.; Meade, T. J. "Magnetic Nanoparticles for Early Detection of Cancer by Magnetic Resonance Imaging", *Mrs Bulletin* **2009**, *34*(6): 441-448.

Link, S.; El-Sayed, M. A. "Spectral Properties and Relaxation Dynamics of Surface Plasmon Electronic Oscillations in Gold and Silver Nano-dots and Nano-rods", *Journal of Physical Chemistry B* **1999**, *103*(40): 8410-8426.

Link, S.; El-Sayed, M. A. "Shape and size dependence of radiative, non-radiative and photothermal properties of gold nanocrystals", *International Reviews in Physical Chemistry* **2000**, *19*(3): 409-453.

Liu, H.; Graff, G. L.; Hyde, M.; Sarikaya, M.; Aksay, I. A. "Synthesis of Ultrafine, Multicomponent Particles Using Phospholipid-Vesicles", *Materials Synthesis Based on Biological Processes* **1991**, *218*: 115-121.

Liu, R. H.; Kay, B. K.; Jiang, S. Y.; Chen, S. F. "Nanoparticle Delivery: Targeting and Nonspecific Binding", *Mrs Bulletin* **2009**, *34*(6): 432-440.

Liu, Z.; Song, H.; Yu, L.; Yang, L. "Fabrication and near-infrared photothermal conversion characteristics of Au nanoshells ", *Applied Physics Letters* **2005**, *86*(11): 113109.

Lohner, K. "Effects of Small Organic-Molecules on Phospholipid Phase-Transitions", *Chemistry and Physics of Lipids* **1991**, *57*(2-3): 341-362.

Loo, C.; Lin, A.; Hirsch, L. R.; Lee, M.; Barton, J. K.; Halas, N. J.; West, J. L.; Drezek, R. A. "Nanoshell-enabled photonics-based imaging and therapy of cancer ", *Cancer Research and Treatment* **2004**, *3*(1): 33-40.

Loo, C.; Lowery, A.; Halas, N. J.; West, J. L.; Drezek, R. A. "Immunotargeted Nanoshells for Integrated Cancer Imaging and Therapy ", *Nano Letters* **2005**, *5*(4): 709-711.

Lucey, D. W.; MacRae, D. J.; Furis, M.; Sahoo, Y.; Cartwright, A. N.; Prasad, P. N. "Monodispersed InP quantum dots prepared by colloidal chemistry in a noncoordinating solvent", *Chemistry of Materials* **2005**, *17*(14): 3754-3762.

Luther, J. M.; Jain, P. K.; Ewers, T.; Alivisatos, A. P. "Localized surface plasmon resonances arising from free carriers in doped quantum dots ", *Nature Materials* **2011**, *10*(5): 361-366.

Luzzati, V.; Tardieu, A. "Lipid Phases - Structure and Structural Transitions", *Annual Review of Physical Chemistry* **1974**, *25*: 79-94.

Lyon, J. L.; Fleming, D. A.; Stone, M. B.; Sciffer, P.; Williams, M. E. "Synthesis of Fe Oxide Core/Au Shell Nanoparticles by Iterative Hydroxylamine Seeding", *Nano Letters* **2004**, *4*(4): 719-723.

Mandal, T. K.; Si, S. "pH-controlled reversible assembly of peptide-functionalized gold nanoparticles", *Langmuir* **2007**, *23*(1): 190-195.

- Mann, S. "Molecular Tectonics in Biomineralization and Biomimetic Materials Chemistry", *Nature* **1993**, 365(6446): 499-505.
- Mann, S.; Hannington, J. P. "Formation of Iron-Oxides in Unilamellar Vesicles", *Journal of Colloid and Interface Science* **1988**, 122(2): 326-335.
- Mann, S.; Hannington, J. P.; Williams, R. J. P. "Phospholipid-Vesicles as a Model System for Biomineralization", *Nature* **1986**, 324(6097): 565-567.
- Marangoni, A. G.; Narine, S. S., Elasticity of Fractal Aggregate Networks: Mechanical Arguments. In *Crystallization and Solidification Properties of Lipids*, Widlak, N.; Hartel, R.; Narine, S., Eds. AOCS Press: Champaign, 2001; pp 153-159.
- Marsh, D., *CRC Handbook of Lipid Bilayers*. CRC Press, Inc.: Boca Raton, FL, 1990.
- Marsh, D. "General Features of Phospholipid Phase-Transitions", *Chemistry and Physics of Lipids* **1991**, 57(2-3): 109-120.
- Marsh, D. "Lateral Pressure Profile, Spontaneous Curvature Frustration, and the Incorporation and Conformation of Proteins in Membranes", *Biophysical Journal* **2007**, 93(11): 3884-3899.
- Mason, T. G.; Wilking, J. N.; Meleson, K.; Chang, C. B.; Graves, S. M. "Nanoemulsions: formation, structure, and physical properties", *Journal of Physics: Condensed Matter* **2006**, 18: R635-R666.
- Matsumoto, T.; Suzuki, J. I.; Ohnuma, M.; Kanemitsu, Y.; Masumoto, Y. *Physical Review B* **2001**, 63: 1953221-1953225.
- McCarthy, J. R.; Kelly, K. A.; Sun, E. Y.; Weissleder, R. "Targeted delivery of multifunctional magnetic nanoparticles", *Nanomedicine* **2007**, 2(2): 153-167.
- McClements, D. J., *Food Emulsions: Principles, Practice, and Techniques*. CRC Press LLC: Boca Raton, 1999.
- McIntosh, T. J.; Simon, S. A.; MacDonald, R. C. "The organization of n-alkanes in lipid bilayers", *Biochim Biophys Acta* **1980**, 597(3): 445-463.
- McNeil, S. E., *Characterization of Nanoparticles Intended for Drug Delivery*. Humana Press: Totawa, N.J., 2011.
- Medintz, I. L.; Mattoussi, H.; Clapp, A. R. "Potential clinical applications of quantum dots", *International Journal of Nanomedicine* **2008**, 3(2): 151-167.

Medintz, I. L.; Uyeda, H. T.; Goldman, E. R.; Mattoussi, H. "Quantum dot bioconjugates for imaging, labelling and sensing", *Nature Materials* **2005**, 4(6): 435-446.

Melancon, M. P.; Lu, W.; Yang, Z.; Zhang, R.; Cheng, Z.; Elliot, A. M.; Stafford, J.; Olson, T.; Zhang, J. Z.; Li, C. "In vitro and in vivo targeting of hollow gold nanoshells directed at epidermal growth factor receptor for photothermal ablation therapy ", *Molecular Cancer Therapeutics* **2008**, 7(6): 1730-1739.

Michalet, X.; Pinaud, F. F.; Bentolila, L. A.; Tsay, J. M.; Doose, S.; Li, J. J.; Sundaresan, G.; Wu, A. M.; Gambhir, S. S.; Weiss, S. "Quantum dots for live cells, in vivo imaging, and diagnostics", *Science* **2005**, 307(5709): 538-544.

Migo, V. P.; Del Rosario, E. J.; Matsumura, M. "Flocculation of Melanoidins Induced by Inorganic Ions", *Journal of Fermentation and Bioengineering* **1997**, 83(3): 287-291.

Mimms, L. T.; Zampighi, G.; Nozaki, Y.; Tanford, C.; Reynolds, J. A. "Phospholipid Vesicle Formation and Transmembrane Protein Incorporation Using Octyl Glucoside", *Biochemistry* **1981**, 20(4): 833-840.

Mirkin, C. A.; Hurst, S. J.; Hill, H. D.; Macfarlane, R. J.; Wu, J. S.; Dravid, V. P. "Synthetically Programmable DNA Binding Domains in Aggregates of DNA-Functionalized Gold Nanoparticles", *Small* **2009**, 5(19): 2156-2161.

Monici, M.; Pratesi, R.; Bernabei, P. A.; Caporale, R.; Ferrini, P. R.; Croce, A. C.; Balzarini, P.; Bottiroli, G. "Natural fluorescence of white blood cells", *Journal of Photochemistry and Photobiology B: Biology* **1995**, 30: 29-37.

Moon, H. K.; Lee, S. H.; Choi, H. C. "In Vivo Near-Infrared Mediated Tumor Destruction by Photothermal Effect of Carbon Nanotubes ", *ACS Nano* **2009**, 3(11): 3707-3713.

Mornet, S.; Lambert, O.; Duguet, E.; Brisson, A. "The formation of supported lipid bilayers on silica nanoparticles revealed by cryoelectron microscopy", *Nano Letters* **2005**, 5(2): 281-285.

Mueller, W.; Koynov, K.; Fischer, K.; Hartmann, S.; Pierrat, S.; Basche, T.; Maskos, M. "Hydrophobic Shell Loading of PB-b-PEO Vesicles", *Macromolecules* **2009**, 42(1): 357-361.

Muir, B. W.; Moffat, B. A.; Harbour, P.; Coia, G.; Zhen, G. L.; Waddington, L.; Scoble, J.; Krah, D.; Thang, S. H.; Chong, Y. K.; Mulvaney, P.; Hartley, P. "Combinatorial Discovery of Novel Amphiphilic Polymers for the Phase Transfer of Magnetic Nanoparticles", *Journal of Physical Chemistry C* **2009**, 113(38): 16615-16624.

Murray, C. B.; Kagan, C. R.; Bawendi, M. G. "Synthesis and characterization of monodisperse nanocrystals and close-packed nanocrystal assemblies", *Annual Review of Materials Science* **2000**, *30*: 545-610.

Nadejda, R.; JinZhong, Z. "Photothermal ablation therapy for cancer based on metal nanostructures", *Science in China Series B-Chemistry* **2009**, *52(10)*: 1559-1575.

Nagle, J. F.; Pan, J.; Tristram-Nagle, S.; Kucerka, N. "Temperature dependence of structure, bending rigidity, and bilayer interactions of dioleoylphosphatidylcholine bilayers", *Biophysical Journal* **2008**, *94(1)*: 117-124.

Nchinda, G.; Uberla, K.; Zschornig, O. "Characterization of cationic lipid DNA transfection complexes differing in susceptibility to serum inhibition", *Bmc Biotechnology* **2002**, *2(12)*.

Nehl, C. L.; Grady, N. K.; Goodrich, G. P.; Tam, F.; Halas, N. J.; Hafner, J. H. "Scattering Spectra of Single Gold Nanoshells ", *Nano Letters* **2004**, *4(12)*: 2355-2359.

Nelson, P., *Biological Physics: Energy, Information, Life*. W. H. Freeman and Company: New York, 2004.

Nikoobakht, B.; El-Sayed, M. A. "Preparation and growth mechanism of gold nanorods (NRs) using seed-mediated growth method ", *Chemistry of Materials* **2003**, *15(10)*: 1957-1962.

O'Farrell, N.; Houlton, A.; Horrocks, B. R. "Silicon nanoparticles: applications in cell biology and medicine", *International Journal of Nanomedicine* **2006**, *1(4)*: 451-472.

Olbrich, K.; Rawicz, W.; Needham, D.; Evans, E. "Water permeability and mechanical strength of polyunsaturated lipid bilayers", *Biophysical Journal* **2000**, *79(1)*: 321-327.

Oldenburg, S. J.; Averitt, R. D.; Westcott, S. L.; Halas, N. J. "Nanoengineering of optical resonances ", *Chemical Physics Letters* **1998**, *288(2, 3, 4)*: 243-247.

Oldenburg, S. J.; Jackson, J. B.; Westcott, S. L.; Halas, N. J. "Infrared extinction properties of gold nanoshells ", *Applied Physics Letters* **1999**, *75(19)*: 2897-2899.

Ollivon, M.; Eidelman, O.; Blumenthal, R.; Walter, A. "Micelle Vesicle Transition of Egg Phosphatidylcholine and Octyl Glucoside", *Biochemistry* **1988**, *27(5)*: 1695-1703.

Ollivon, M.; Lesieur, S.; Grabielle-Madelmont, C.; Paternostre, M. "Vesicle Reconstitution from lipid-detergent mixed micelles", *Biochimica Et Biophysica Acta* **2000**, *1508*: 34-50.

O'Neal, D. P.; Hirsch, L. R.; Halas, N. J.; Payne, J. D.; West, J. L. "Photo-thermal tumor ablation in mice using near infrared-absorbing nanoparticles ", *Cancer Letters* **2004**, *209*(2): 171-176.

Osaki, F.; Kanamori, T.; Sando, S.; Sera, T.; Aoyama, Y. " A Quantum Dot Conjugated Sugar Ball and Its Cellular Uptake. On the Size Effects of Endocytosis in the Subviral Region ", *Journal of the American Chemical Society* **2004**, *126*(21): 6520-6521.

Paasonen, L.; Laaksonen, T.; Johans, C.; Yliperttula, M.; Kontturi, K.; Urth, A. "Gold nanoparticles enable selective light-induced contents release from liposomes", *Journal of Controlled Release* **2007**, *122*(1): 86-93.

Pankhurst, Q. A.; Thanh, N. K. T.; Jones, S. K.; Dobson, J. "Progress in applications of magnetic nanoparticles in biomedicine", *Journal of Physics D-Applied Physics* **2009**, *42*(22): 220301.

Pansu, B.; Lecchi, A.; Constantin, D.; Clerc-Imperator, M.; Veber, M.; Dozov, I. "Insertion of Gold Nanoparticles in Fluid Mesophases: Size Filtering and Control of Interactions", *Journal of Physical Chemistry C* **2011**, ASAP: DOI: 10.1021/jp2046189.

Panthani, M. G.; Akhavan, V.; Goodfellow, B. W.; Schmidtke, J. P.; Dunn, L.; Dodabalapur, A.; Barbara, P. F.; Korgel, B. A. "Synthesis of CuInS₂, CuInSe₂, and Cu(In_xGa_{1-x})Se₂ (CIGS) Nanocrystal "Inks" for Printable Photovoltaics ", *Journal of the American Chemical Society* **2008**, *130*(49): 16770-16777.

Park, J.; Estrada, A.; Sharp, K.; Sang, K.; Schwartz, J. A.; Smith, D. K.; Coleman, C.; Payne, J. D.; Korgel, B. A.; Dunn, A. K.; Tunnell, J. W. "Two-photon-induced photoluminescence imaging of tumors using near-infrared excited gold nanoshells", *Optics Express* **2008**, *16*(3): 1590-1599.

Park, J. H.; Gu, L.; von Maltzahn, G.; Ruoslahti, E.; Bhatia, S. N.; Sailor, M. J. "Biodegradable luminescent porous silicon nanoparticles for in vivo applications", *Nature Materials* **2009**, *8*(4): 331-336.

Park, J. H.; von Maltzahn, G.; Ruoslahti, E.; Bhatia, S. N.; Sailor, M. J. "Micellar hybrid nanoparticles for simultaneous magnetofluorescent imaging and drug delivery", *Angewandte Chemie-International Edition* **2008**, *47*(38): 7284-7288.

Park, J.-H.; von Maltzahn, G.; Ong, L. L.; Centrone, A.; Hatton, T. A.; Ruoslahti, E.; Bhatia, S. N.; Sailor, M. J. "Cooperative Nanoparticles for Tumor Detection and Photothermally Triggered Drug Delivery", *Advanced Materials* **2010**, *22*: 880-885.

Park, S.; Park, M.; Han, P.; Lee, S. "The effect of pH-adjusted gold colloids on the formation of gold clusters over APTMS-coated silica cores ", *Bulletin of the Korean Chemical Society* **2006**, 27(9): 1341-1345.

Park, S. H.; Oh, S. G.; Mun, J. Y.; Han, S. S. "Loading of gold nanoparticles inside the DPPC bilayers of liposome and their effects on membrane fluidities", *Colloids and Surfaces B-Biointerfaces* **2006**, 48(2): 112-118.

Park, S. H.; Oh, S. G.; Suh, K. D.; Han, S. H.; Chung, D. J.; Mun, J. Y.; Han, S. S.; Kim, J. W. "Control over micro-fluidity of liposomal membranes by hybridizing metal nanoparticles", *Colloids and Surfaces B-Biointerfaces* **2009**, 70(1): 108-113.

Paternostre, M. T.; Roux, M.; Rigaud, J. L. "Mechanisms of Membrane-Protein Insertion into Liposomes during Reconstitution Procedures Involving the Use of Detergents .1. Solubilization of Large Unilamellar Liposomes (Prepared by Reverse-Phase Evaporation) by Triton X-100, Octyl Glucoside, and Sodium Cholate", *Biochemistry* **1988**, 27(8): 2668-2677.

Patri, A. K.; Kulowska-Latallo, J. F.; Baker, J. R. J. "Targeted drug delivery with dendrimers: comparison of the release kinetics of covalently conjugated drug and non-covalent drug inclusion complex", *Advanced Drug Delivery Reviews* **2005**, 57(15): 2203-2214.

Pechstedt, K.; Whittle, T.; Baumberg, J.; Melvin, T. "Photoluminescence of Colloidal CdSe/ZnS Quantum Dots: The Critical Effect of Water Molecules", *Journal of Physical Chemistry C* **2010**, 114: 12069-12077.

Petros, R. A.; DeSimone, J. M. "Strategies in the design of nanoparticles for therapeutic applications", *Nature Reviews Drug Discovery* **2010**, 9(8): 615-627.

Philippot, J. R.; Mutaftschiev, S.; Liautard, J. P. "A very mild method allowing the encapsulation of very high amounts of macromolecules into very large (1000 nm) unilamellar liposomes", *Biochimica Et Biophysica Acta-Biomembranes* **1983**, 734(2): 137-143.

Phonphok, N.; Chidichimo, G.; Westerman, P. W. "Disposition of chloroform in phosphatidylcholine membranes: A H-2- and P-31-NMR study", *Chemistry and Physics of Lipids* **1996**, 83(1): 25-37.

Pichot, R.; Spyropoulos, F.; Norton, I. T. "O/W emulsions stabilised by both low molecular weight surfactants and colloidal particles: The effect of surfactant type and concentration", *Journal of Colloid and Interface Science* **2010**, 352(1): 128-135.

Pierret, R. F., *Semiconductor Fundamentals*. Addison-Wesley Publishing Co.: New York, 1988; Vol. 1.

Pochan, D. J.; Cui, H.; Hodgdon, T. K.; Kaler, E. W.; Abezgauz, L.; Danino, D.; Lubovsky, M.; Talmon, Y. "Elucidating the assembled structure of amphiphiles in solution via cryogenic transmission electron microscopy", *Soft Matter* **2007**, 3(8): 945-955.

Pochan, D. J.; Zhong, S. "Cryogenic Transmission Electron Microscopy for Direct Observation of Polymer and Small-Molecule Materials and Structures in Solution", *Polymer Reviews* **2010**, 50(3): 287-320.

Pons, T.; Pic, E.; Lequex, N.; Cassette, E.; Bezdetnaya, L.; Guillemin, G.; Marchal, F.; Dubertret, B. "Cadmium-Free CuInS₂/ZnS Quantum Dots for Sentinel Lymph Node Imaging with Reduced Toxicity ", *ACS Nano* **2010**, 4(5): 2531-2538.

Pons, T.; Uyeda, H. T.; Medintz, I. L.; Mattoussi, H. "Hydrodynamic dimensions, electrophoretic mobility, and stability of hydrophilic quantum dots", *Journal of Physical Chemistry B* **2006**, 110(41): 20308-20316.

Pornpattananangkul, D.; Olson, S.; Aryal, S.; Sartor, M.; Huang, C. M.; Vecchio, K.; Zhang, L. "Stimuli-Responsive Liposome Fusion Mediated by Gold Nanoparticles", *ACS Nano* **2010**, 4(4): 1935-1942.

Prodan, E.; Radloff, C.; Halas, N. J.; Nordlander, P. "A hybridization model for the plasmon response of complex nanostructures ", *Science* **2003**, 302(5644): 419-422.

Puvanakrishnan, P.; Park, J.; Diagaradjane, P.; Schwartz, J. A.; Coleman, C. L.; Gill-Sharp, K. L.; Sang, K. L.; Payne, J. D.; Krishnan, S.; Tunnell, J. W. " Near-infrared narrow-band imaging of gold/silica nanoshells in tumors ", *Journal of Biomedical Optics* **2009**, 14(2): 024044.

Quemeneur, F.; Quilliet, C.; Faivre, M.; Viallat, A.; Pepin-Donat, B. "Gel Phase Vesicles Buckle into Specific Shapes", *Physical Review Letters* **2012**, 108: 108303.

Rangel-Yagui, C. O.; Pessoa, A. J.; Tavares, L. C. "Micellar solubilization of drugs", *Journal of Pharmacy and Pharmaceutical Sciences* **2005**, 8(2): 147-163.

Rasch, M. R.; Rossinyol, E.; Hueso, J. L.; Goodfellow, B. W.; Arbiol, J.; Korgel, B. A. "Hydrophobic Gold Nanoparticle Self-Assembly with Phosphatidylcholine Lipid: Membrane-Loaded and Janus Vesicles", *Nano Letters* **2010**, 10(9): 3733-3739.

Rasch, M. R.; Sokolov, K. V.; Korgel, B. A. "Limitations on the Optical Tunability of Small Diameter Gold Nanoshells", *Langmuir* **2009**, *25*(19): 11777-11785.

Rauf, S.; Glidle, A.; Cooper, J. M. "Production of Quantum Dot Barcodes Using Biological Self-Assembly", *Advanced Materials* **2009**, *21*(40): 4020-+.

Regen, S. L.; Turkyilmaz, S.; Chen, W. H.; Mitomo, H. "Loosening and Reorganization of Fluid Phospholipid Bilayers by Chloroform", *Journal of the American Chemical Society* **2009**, *131*(14): 5068-+.

Reigada, R. "Influence of Chloroform in Liquid-Ordered and Liquid-Disordered Phases in Lipid Membranes", *Journal of Physical Chemistry B* **2011**, *115*(11): 2527-2535.

Reiss, P.; Protiere, M.; Li, L. "Core/Shell Semiconductor Nanocrystals", *Small* **2009**, *5*(2): 154-168.

Resch-Genger, U.; Grabolle, M.; Cavaliere-Jaricot, S.; Nitschke, R.; Nann, T. "Quantum dots versus organic dyes as fluorescent labels", *Nature Methods* **2008**, *5*(9): 763-775.

Rhee, H.-W.; Choi, H.-Y.; Han, K.; Hong, J.-I. "Selective Fluorescent Detection of Flavin Adenine Dinucleotide in Human Eosinophils by Using Bis(Zn²⁺-Dipicolylamine) Complex", *Journal of the American Chemical Society* **2007**, *129*: 4525-4525.

Rigaud, J. L.; Paternostre, M. T.; Bluzat, A. "Mechanisms of Membrane-Protein Insertion into Liposomes during Reconstitution Procedures Involving the Use of Detergents .2. Incorporation of the Light-Driven Proton Pump Bacteriorhodopsin", *Biochemistry* **1988**, *27*(8): 2677-2688.

Roiter, Y.; Ornatska, M.; Rammohan, A. R.; Balakrishnan, J.; Heine, D. R.; Minko, S. "Interaction of nanoparticles with lipid membrane", *Nano Letters* **2008**, *8*(3): 941-944.

Roiter, Y.; Ornatska, M.; Rammohan, A. R.; Balakrishnan, J.; Heine, D. R.; Minko, S. "Interaction of Lipid Membrane with Nanostructured Surfaces", *Langmuir* **2009**, *25*(11): 6287-6299.

Roper, D. K.; Ahn, W.; Hoepfner, M. J. "Microscale Heat Transfer Transduced by Surface Plasmon Resonant Gold Nanoparticles ", *Journal of Physical Chemistry C* **2007**, *111*(9): 3636-3641.

Sadauskas, E.; Wallin, H.; Stoltenberg, M.; Vogel, U.; Doering, P.; Larsen, A.; Danscher, G. "Kupffer cells are central in the removal of nanoparticles from the organism", *Particle and Fiber Toxicology* **2007**, *4*: 10.

Santos, H. M.; Lodeiro, C.; Capelo-Martinez, J.-L., *Ultrasound in Chemistry: Analytical Applications*. In Capelo-Martinez, J.-L., Ed. Wiley-VCH Verlag GmbH & Co.: Weinheim, 2009.

Sapsford, K. E.; Spindel, S.; Jennings, T.; Tao, G.; Triulzi, R. C.; Algar, W. R.; Medintz, I. L. "Optimizing Two-Color Semiconductor Nanocrystal Immunoassays in Single Well Microtiter Plate Formats", *Sensors* **2011**, *11*: 7879-7891.

Satarug, S.; Baker, J. R.; Urbenjapol, S.; Haswell-Elkins, M.; Reilly, P. E. B.; Williams, D. J.; Moore, M. R. "A global perspective on cadmium pollution and toxicity in non-occupationally exposed population", *Toxicology Letters* **2003**, *137*: 65-83.

Saunders, A. E.; Korgel, B. A. "Second Virial Coefficient Measurements of Dilute Gold Nanocrystal Dispersions Using Small-Angle X-ray Scattering", *Journal of Physical Chemistry B* **2004**, *108*(43): 16732-16738.

Saxena, K.; Shipley, G. G. "Structural studies of detergent-solubilized and vesicle-reconstituted low-density lipoprotein (LDL) receptor", *Biochemistry* **1997**, *36*(50): 15940-15948.

Schipper, M. L.; Iyer, G.; Koh, A. L.; Cheng, Z.; Ebenstein, Y.; Aharoni, A.; Keren, S.; Bentolila, L. A.; Li, J. Q.; Rao, J. H.; Chen, X. Y.; Banin, U.; Wu, A. M.; Sinclair, R.; Weiss, S.; Gambhir, S. S. "Particle Size, Surface Coating, and PEGylation Influence the Biodistribution of Quantum Dots in Living Mice", *Small* **2009**, *5*(1): 126-134.

Schwendener, R. A.; Asanger, M.; Weder, H. G. "n-Alkyl-glucosides as detergents for the preparation of highly homogeneous bilayer liposomes of variable sizes (60-240 nm phi) applying defined rates of detergent removal by dialysis.", *Biochem Biophys Res Commun.* **1981**, *100*(3): 1055-1062.

Sechoy, O.; Philippot, J. R.; Bienvenue, A. "Preparation and characterization of F-protein vesicles isolated from Sendai virus by means of octyl glucoside", *Biochimica Et Biophysica Acta-Biomembranes* **1986**, *857*(1): 1-12.

Seddon, A. M.; Curnow, P.; Booth, P. J. "Membrane proteins, lipids and detergents: not just a soap opera", *Biochimica Et Biophysica Acta* **2004**, *1666*: 105-117.

Seddon, J. M. "Structure of the Inverted Hexagonal (Hii) Phase, and Non-Lamellar Phase-Transitions of Lipids", *Biochimica Et Biophysica Acta* **1990**, *1031*(1): 1-69.

Selvan, S. T.; Tan, T. T. Y.; Yi, D. K.; Jana, N. R. "Functional and Multifunctional Nanoparticles for Bioimaging and Biosensing", *Langmuir* **2010**, *26*(14): 11631-11641.

Sens, P.; Joanny, J.-F. "Counterion Release and Electrostatic Adsorption", *Physical Review Letters* **2000**, *84*(21): 4862-4865.

Shah, J.; Park, S.; Aglyamov, S.; Larson, T.; Ma, L.; Sokolov, K.; Johnston, K.; Milner, T.; Emelianov, S. Y. "Photoacoustic imaging and temperature measurement for photothermal cancer therapy", *Journal of Biomedical Optics* **2008**, *13*(3): 034024.

Sherlock, S. P.; Tabakman, S. M.; Xie, L.; Dai, H. "Photothermally Enhanced Drug Delivery by Ultrasmall Multifunctional FeCo/Graphitic Shell Nanocrystals ", *ACS Nano* **2011**, *5*(2): 1505-1512.

Shou, Y.; Baron, S.; Poncz, M. "An Sp1-binding Silencer Element Is a Critical Negative Regulator of the Megakaryocyte-specific α IIb Gene", *Journal of Biological Chemistry* **1998**, *273*(10): 5716-5726.

Shukla, A.; Neubert, R. H. H. "Diffusion behavior of pharmaceutical O/W microemulsions studied by dynamic light scattering", *Colloid and Polymer Science* **2006**, *284*(5): 568-573.

Sigman, M. B.; Saunders, A. E.; Korgel, B. A. "Metal nanocrystal superlattice nucleation and growth", *Langmuir* **2004**, *20*(3): 978-983.

Silbert, L. E. "Jamming of frictional spheres and random loose packing", *Soft Matter* **2010**, *6*: 2918-2924.

Simon, S. A.; Lis, L. J.; MacDonald, R. C.; Kauffman, J. W. "The Noneffect of a Large Linear Hydrocarbon, Squalene, on the Phosphatidylcholine Packing Structure", *Biophysical Journal* **1977**, *19*: 83-90.

Sjolund, M.; Lindblom, G.; Rilfors, L.; Arvidson, G. "Hydrophobic Molecules in Lecithin Water-Systems .1. Formation of Reversed Hexagonal Phases at High and Low Water Contents", *Biophysical Journal* **1987**, *52*(2): 145-153.

Slocik, J. M.; Tam, F.; Halas, N. J.; Naik, R. R. "Peptide-Assembled Optically Responsive Nanoparticle Complexes ", *Nano Letters* **2007**, *7*(4): 1054-1058.

Smith, A. M.; Duan, H. W.; Mohs, A. M.; Nie, S. M. "Bioconjugated quantum dots for in vivo molecular and cellular imaging", *Advanced Drug Delivery Reviews* **2008**, *60*(11): 1226-1240.

Smith, A. M.; Nie, S. "Semiconductor Nanocrystals: Structure, Properties, and Band Gap Engineering", *Accounts of Chemical Research* **2010**, *43*(2): 190-200.

Smith, D. K.; Goodfellow, B. W.; Smilgies, D. M.; Korgel, B. A. "Self-assembled simple hexagonal ab2 binary nanocrystal superlattices: SEM, GISAXS and Defects", *Journal of the American Chemical Society* **2009**, *131*(9): 3281-3290.

Smith, D. K.; Miller, N. R.; Korgel, B. A. "Iodide in CTAB Prevents Gold Nanorod Formation", *Langmuir* **2009**, *25*(16): 9518-9524.

Smoluchowski, M. V. *Bulletin International de l'Academie des sciences de Cracovie* **1903**: 184.

Song, C.; Wang, P.; Makse, H. A. "A phase diagram for jammed matter", *Nature* **2008**, *453*: 629-632.

Song, Y. J.; Garcia, R. M.; Dorin, R. M.; Wang, H. R.; Qiu, Y.; Shelnutt, J. A. "Synthesis of platinum nanocages by using liposomes containing photocatalyst molecules", *Angewandte Chemie-International Edition* **2006**, *45*(48): 8126-8130.

Soo Choi, H.; Liu, W.; Mista, P.; Tanaka, E.; Zimmer, J. P.; Itty, I. B.; Bawendi, M. G.; Frangioni, J. V. "Renal clearance of quantum dots ", *Nature Biotechnology* **2007**, *25*(10): 1165-1170.

Spanova, M.; Daum, G. "Squalene - biochemistry, molecular biology, process biotechnology, and applications", *European Journal of Lipid Science and Technology* **2011**, *113*: 1299-1320.

Sperling, R. A.; Pellegrino, T.; Li, J. K.; Chang, W. H.; Parak, W. J. "Electrophoretic separation of nanoparticles with a discrete number of functional groups ", *Advanced Functional Materials* **2006**, *16*(7): 943-948.

Stegner, A. R.; Pereira, R. N.; Klein, K.; Lechner, R.; Dietmueller, R.; Brandt, M. S.; Stutzmann, M. "Electronic Transport in Phosphorus-Doped Silicon Nanocrystal Networks", *Physical Review Letters* **2008**, *100*: 026803.

Stillwell, W.; Shaikh, S. R.; Dumauval, A. C.; Jenski, L. J. "Lipid phase separation in phospholipid bilayers and monolayers modeling the plasma membrane", *Biochimica Et Biophysica Acta-Biomembranes* **2001**, *1512*(2): 317-328.

Sudhir, B.; Kumar, S. "Existence of a new force in colloidal systems - hydrophobic attraction between macroscopic surfaces ", *Resonance* **2002**, *7*(4): 67-81.

Suhara, T.; Shimano, F.; Sato, Y.; Fukui, H.; Yamaguchi, M. "Fine silica powder modified with quaternary ammonium group. 4. Bactericidal activity ", *Colloids and Surfaces a-Physicochemical and Engineering Aspects* **1996**, *119*(2/3): 105-114.

Tam, J. M.; Tam, J. O.; Murthy, A.; Ingram, D. R.; Ma, L. L.; Travis, K.; Johnston, K. P.; Sokolov, K. V. "Controlled Assembly of Biodegradable Plasmonic Nanoclusters for Near-Infrared Imaging and Therapeutic Applications", *ACS Nano* **2010**, 4(4): 2178-2184.

Tambe, D. E.; Sharma, M. M. "Factors Controlling the Stability of Colloid-stabilized Emulsions", *Journal of Colloid and Interface Science* **1993**, 157: 244-253.

Taurozzi, J. S.; Hackley, V. A.; Wiesner, M. R. "Ultrasonic dispersion of nanoparticles for environmental, health and safety assessment – issues and recommendations", *Nanotoxicology* **2011**, 5(4): 711-729.

Templeton, N. S. "Cationic Liposome-mediated Gene Delivery In vivo", *Bioscience Reports* **2002**, 22(2): 283-295.

Thomas, D. G. "Transport characteristics of suspension: VIII. A note on the viscosity of Newtonian suspensions of uniform spherical particles", *Journal of Colloid and Interface Science* **1965**, 20(3): 267.

Tilborg, G. A. F.; Cormode, D. P.; Jarzyna, P. A.; van der Toorn, A.; van der Pol, S. M. A.; van Bloois, L.; Fayad, Z. A.; Storm, G.; Mulder, W. J. M.; de Vries, H. E.; Dijkhuizen, R. M. "Nanoclusters of Iron Oxide: Effect of Core Composition on Structure,

Biocompatibility, and Cell Labeling Efficacy", *Bioconjugate Chemistry* **2012**, 23: 941-950.

Tilcock, C. P. S.; Cullis, P. R.; Gruner, S. M. "On the validity of ³¹P-NMR determinations of phospholipid polymorphic phase behavior", *Chemistry and Physics of Lipids* **1986**, 40: 47-56.

Torchilin, V. P. "Recent advances with liposomes as pharmaceutical carriers", *Nature Reviews Drug Discovery* **2005**, 4(2): 145-160.

Torchilin, V. P.; Sawant, R. R. "Liposomes as 'smart' pharmaceutical nanocarriers", *Soft Matter* **2010**, 6(17): 4026-4044.

Torchilin, V. P.; Weissig, V., *Liposomes: A Practical Approach*. 2nd ed.; Oxford: New York, 2003.

Tricot, Y. M.; Fendler, J. H. "Insitu Generated Colloidal Semiconductor Cds Particles in Dihexadecyl Phosphate Vesicles - Quantum Size and Asymmetry Effects", *Journal of Physical Chemistry* **1986**, 90(15): 3369-3374.

Tsuchida, E.; Sou, K.; Nakagawa, A.; Sakai, H.; Komatsu, T.; Kobayashi, K. "Artificial Oxygen Carriers, Hemoglobin Vesicles and Albumin-Hemes, Based on Bioconjugate Chemistry", *Bioconjugate Chemistry* **2009**, 20(8): 1419-1440.

Ueno, M.; Tanford, C.; Reynolds, J. A. "Phospholipid Vesicle Formation Using Nonionic Detergents with Low Monomer Solubility. Kinetic Factors Determine Vesicle Size and Permeability", *Biochemistry* **1984**, 23: 3070-3076.

Valioulis, I. A.; List, E. J. "Collision Efficiencies of Diffusing Spherical Particles: Hydrodynamic, Van der Waals and Electrostatic Forces", *Advances in Colloid and Interface Science* **1984**, 20(1): 1-20.

Van Zanten, J. H.; Monbouquette, H. G. "Phosphatidylcholine Vesicle Diameter, Molecular-Weight and Wall Thickness Determined by Static Light-Scattering", *Journal of Colloid and Interface Science* **1994**, 165(2): 512-518.

Vincent, B. "The van der Waals attraction between colloid particles having adsorbed layers. II. Calculation of interaction curves ", *Journal of Colloid and Interface Science* **1973**, 42(2): 270-285.

Vinson, P. K.; Talmon, Y.; Walter, A. "Vesicle-Micelle Transition of Phosphatidylcholine and Octyl Glucoside Elucidated by Cryo-Transmission Electron-Microscopy", *Biophysical Journal* **1989**, 56(4): 669-681.

Volodkin, D. V.; Skirtach, A. G.; Mohwald, H. "Near-IR Remote Release from Assemblies of Liposomes and Nanoparticles", *Angewandte Chemie-International Edition* **2009**, 48(10): 1807-1809.

Von White, I. G.; Chen, Y.; Roder-Hanna, J.; Bothun, G. D.; Kitchens, C. L. "Structural and Thermal Analysis of Lipid Vesicles Encapsulating Hydrophobic Gold Nanoparticles", *ACS Nano* **2012**, ASAP online.

Wall, J. F.; Grieser, F.; Zukoski, C. F. "Monitoring chemical reactions at the gold/solution interface using atomic force microscopy", *Journal of the Chemical Society-Faraday Transactions* **1997**, 93(22): 4017-4020.

Wang, C.; Gao, X.; Su, X. G. "In vitro and in vivo imaging with quantum dots", *Analytical and Bioanalytical Chemistry* **2010**, 397(4): 1397-1415.

Wang, J.; Yang, F.; Tan, J.; Liu, G.; Xu, J.; Sun, D. "Pickering Emulsions Stabilized by a Lipophilic Surfactant and Hydrophilic Platelike Particles", *Langmuir* **2010**, 26(8): 5397-5404.

Wang, M. F.; Zhang, M.; Siegers, C.; Scholes, G. D.; Winnik, M. A. "Polymer Vesicles as Robust Scaffolds for the Directed Assembly of Highly Crystalline Nanocrystals", *Langmuir* **2009**, 25(24): 13703-13711.

Wang, Y.; Qian, W.; Tan, Y.; Ding, S. "A label-free biosensor based on gold nanoshell monolayers for monitoring biomolecular interactions in diluted whole blood ", *Biosensors & Bioelectronics* **2008**, 23(7): 1166-1170.

Wang, Y.; Qian, W.; Tan, Y.; Ding, S.; Zhang, H. "Direct electrochemistry and electroanalysis of hemoglobin adsorbed in self-assembled films of gold nanoshells ", *Talanta* **2007**, 72(3): 1134-1140.

Watzke, H.; Fendler, J. H. "Quantum size effects of in situ generated colloidal cadmium sulfide particles in dioctadecyldimethylammonium chloride surfactant vesicles", *Journal of Physical Chemistry* **1987**, 91(4): 854-861.

Weissleder, R. "A clearer vision for in vivo imaging ", *Nature Biotechnology* **2001**, 19(4): 316-317.

Westcott, S. L.; Oldenburg, S. J.; Lee, T. R.; Halas, N. J. "Formation and adsorption of clusters of gold nanoparticles onto functionalized silica nanoparticle surfaces", *Langmuir* **1998**, 14(19): 5396-5401.

Wi, H. S.; Lee, K.; Pak, H. K. "Interfacial energy consideration in the organization of a quantum dot-lipid mixed system", *Journal of Physics-Condensed Matter* **2008**, 20(49): 494211.

Williams, K. R.; Gupta, K.; Wasilik, M. J. *Journal of Micromechanical Systems* **2003**, 12: 761-778.

Winter, J.; Schmidt, C.; Korgel, B. "Optimization of quantum dot - Nerve cell interfaces", *Quantum Dots, Nanoparticles and Nanowires* **2004**, 789: 119-122

429.

Winter, J. O.; Liu, T. Y.; Korgel, B. A.; Schmidt, C. E. "Recognition molecule directed interfacing between semiconductor quantum dots and nerve cells", *Advanced Materials* **2001**, 13(22): 1673-1677.

Woodward, R. T.; Olariu, C. I.; Hasan, E. A.; Yiu, H. H. P.; Rosseinsky, M. J.; Weaver, J. V. M. "Multi-responsive polymer-stabilized magnetic engineered emulsions as

liquid-based switchable magneto-responsive actuators", *Soft Matter* **2011**, 7: 4335.

Wu, X. Y.; Liu, H. J.; Liu, J. Q.; Haley, K. N.; Treadway, J. A.; Larson, J. P.; Ge, N. F.; Peale, F.; Bruchez, M. P. "Immunofluorescent labeling of cancer marker Her2 and other cellular targets with semiconductor quantum dots", *Nature Biotechnology* **2003**, *21*(4): 452-452.

Wu, Z.; Xiang, H.; Kim, T.; Chun, M.; Lee, K. "Surface properties of submicrometer silica spheres modified with aminopropyltriethoxysilane and phenyltriethoxysilane ", *Journal of Colloid and Interface Science* **2006**, *304*(1): 119-124.

Xia, X.; Liu, Y.; Backman, V.; Ameer, G. A. "Engineering sub-100 nm multi-layer nanoshells ", *Nanotechnology* **2006**, *17*(21): 5435-5440.

Xia, Y.; Xiong, Y.; Lim, B.; Skrabalak, S. E. "Shape-controlled synthesis of metal nanocrystals: simple chemistry meets complex physics?", *Angewandte Chemie-International Edition* **2009**, *48*(1): 60-103.

Xiao, L.; Liao, X.; Lin, L.; Huang, H.; Chen, Y.; Li, B. "Autofluorescence characteristics of human leukemia cells and mononuclear cells", *Proceedings of SPIE* **2010**, *7845*: 78452G.

Yaacob, I. I.; Bhandarkar, S.; Bose, A. "Synthesis of Aluminum Hydroxide Nanoparticles in Spontaneously Generated Vesicles", *Journal of Materials Research* **1993**, *8*(3): 573-577.

Yan, Y. D.; Clarke, J. H. R. "Dynamic Light-Scattering from Concentrated Water-in-Oil Microemulsions the Coupling of Optical and Size Polydispersity", *Journal of Chemical Physics* **1990**, *93*(7): 4501-4509.

Yang, K.; Zhang, S. A.; Zhang, G. X.; Sun, X. M.; Lee, S. T.; Liu, Z. A. "Graphene in Mice: Ultrahigh In Vivo Tumor Uptake and Efficient Photothermal Therapy ", *Nano Letters* **2010**, *10*(9): 3318-3323.

Yang, P.; Lipowsky, R.; Dimova, R. "Nanoparticle formation in giant vesicles: synthesis in biomimetic compartments", *Small* **2009**, *5*(18): 2033-2037.

Yin, Y.; Alivisatos, A. P. "Colloidal nanocrystal synthesis and the organic–inorganic interface", *Nature* **2005**, *437*: 664-670.

Yokoyama, M. "Polymeric micelles as a new drug carrier system and their required considerations for clinical trials", *Expert Opinion in Drug Delivery* **2010**, *7*(2): 145-158.

Yong, K. T.; Roy, I.; Swihart, M. T.; Prasad, P. N. "Multifunctional nanoparticles as biocompatible targeted probes for human cancer diagnosis and therapy", *Journal of Materials Chemistry* **2009**, *19*(27): 4655-4672.

Yong, K. T.; Sahoo, S. K.; Swihart, M. T.; Prasad, P. N. "Synthesis and plasmonic properties of silver and gold nanoshells on polystyrene cores of different size and of gold-silver core-shell nanostructures ", *Colloids and Surfaces a-Physicochemical and Engineering Aspects* **2006**, *290*(1-3): 89-105.

Yu, M. K.; Park, J.; Jon, S. "Targeting Strategies for Multifunctional Nanoparticles in Cancer Imaging and Therapy", *Theranostics* **2012**, *2*(1): 3-44.

Yukawa, H.; Mizufune, S.; Mamori, C.; Kagami, Y.; Oishi, K.; Kaji, N.; Okamoto, Y.; Takeshi, M.; Noguchi, H.; Baba, Y.; Hamaguchi, M.; Hamajima, N.; Hayashi, S. "Quantum dots for labeling adipose tissue-derived stem cells", *Cell Transplant* **2009**, *18*(5): 591-599.

Zhang, L. F.; Granick, S. "How to stabilize phospholipid liposomes (using nanoparticles)", *Nano Letters* **2006**, *6*(4): 694-698.

Zhang, X.; Neiner, D.; Wang, S.; Louie, A. Y.; Kauzlarich, S. M. "A new solution route to hydrogen-terminated silicon nanoparticles: synthesis, functionalization and water stability", *Nanotechnology* **2007**, *18*(9): 095601.

Zhang, X. W.; Yang, Y. F.; Tian, J.; Zhao, H. Y. "Vesicles fabricated by hybrid nanoparticles", *Chemical Communications* **2009**, (25): 3807-3809.

Zhao, Y.; Pan, H.; Lou, Y.; Qiu, X.; Zhu, J.; Burda, C. J. "Plasmonic Cu_{2-x}S Nanocrystals: Optical and Structural Properties of Copper-Deficient Copper(I) Sulfides ", *Journal of the American Chemical Society* **2009**, *131*(12): 4253-4261.

Zhao, Y.; Trewyn, B. G.; Slowing, I. I.; Lin, V. S. Y. "Mesoporous Silica Nanoparticle-Based Double Drug Delivery System for Glucose-Responsive Controlled Release of Insulin and Cyclic AMP", *Journal of the American Chemical Society* **2009**, *131*(24): 8398-8400.

Zharov, V. P.; Galanzha, E. I.; Shashkov, E. V.; Kim, J. W.; Khlebtsov, N. G.; Tuchin, V. V. "Photoacoustic flow cytometry: principle and application for real-time detection of circulating single nanoparticles, pathogens, and contrast dyes in vivo", *Journal of Biomedical Optics* **2007**, *12*(5): 051503.

Zulauf, M.; Eicke, H. F. "Inverted Micelles and Microemulsions in the Ternary-System H₂O-Aerosol-Ot-Isooctane as Studied by Photon Correlation Spectroscopy", *Journal of Physical Chemistry* **1979**, 83(4): 480-486.

Zumbuehl, O.; Weder, H. G. "Liposomes of Controllable Size in the Range of 40 to 180 Nm by Defined Dialysis of Lipid-Detergent Mixed Micelles", *Biochimica Et Biophysica Acta* **1981**, 640(1): 252-262.

Vita

Michael Rasch is from Allentown, PA, and graduated from Emmaus High School in 2002. He attended the University of Delaware from 2002 – 2006, graduating *cum laude* with a Bachelor's degree in Chemical Engineering and minors in Chemistry, Economics, and Biochemical Engineering. In August of 2006, he entered graduate school at the University of Texas at Austin in the Department of Chemical Engineering. He joined Dr. Brian Korgel's research group, investigating nanomaterials chemistry and lipid particles.

Permanent address: 3870 Pleasant Avenue, Allentown, PA 18103

This dissertation was typed by the author.